

Field Cycling NMR Studies of Molecular Dynamics in Liquid Crystals

**A thesis submitted for the award of the Degree of
Doctor of Philosophy**

**by
D. Loganathan**



**School of Physics
University of Hyderabad
Hyderabad - 500 046
INDIA**

August 2000

Dedicated to my loving

Parents

Brothers

And

Mama

DECLARATION

I hereby declare that the matter embodied in this thesis entitled. **"Field Cycling NMR studies of Molecular Dynamics in Liquid Crystals"**, is the result of investigations carried out by me in the School of Physics. University of Hyderabad, Hyderabad. India, under the supervision of Dr K Venu.

Place **Hyderabad**

Date : **30.08.2000.**



(I). Loganathan)

CERTIFICATE

This is to certify that the work described in this dissertation entitled, "**Field Cycling NMR studies of Molecular Dynamics in Liquid Crystals**", has been carried out by Mr. D. **Loganathan** under my supervision for the full period prescribed under Ph. D ordinances of the University and the same has not been submitted for any other degree or diploma at this or any other University.

Place : Hyderabad

Date :

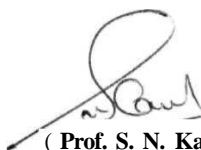


(**Dr. K. Venu**)

School of Physics

University of Hyderabad

Hyderabad - 500 046. INDIA



(**Prof. S. N. Kaul**)

Dean

School of Physics

University of Hyderabad

Hyderabad - 500 046, INDIA.

Acknowledgements

I wish to express my thanks to Dr. K. Venu, my thesis **supervisor**, for his great support and guidance during every crucial phase of the **FCNMR** instrumentation work. I also thank him for the useful discussions **during** my thesis work.

My sincere thanks to **Prof. V. S. S. Sastry** for his involvement and continuous encouragement throughout this **work**. I wish to express my thanks to him for spending his valuable time in reading my thesis and making valuable suggestions.

I thank Prof. S. N. **Kaul**, Dean, School of Physics for providing me the necessary facilities to carry out this work. I also thank all the erstwhile Dean's, Prof. A. P. Pathak, Prof. K. N. Shrivatsava, and Prof. A. K. Bhatnagar for the same. My sincere thanks to **Prof. V. Srinivasan** for his help and encouragement. I wish to express my heartfelt thanks to all the faculty members of the School of Physics, for their support and **encouragement**.

I thank all the staff members of the School of Physics especially to Mr. **Abragam**, Mr. Pentaiah, Mr. Veerraju, Mr. Sureshababu, Mr. Anand, Mr. Chandrapal, Mr. Mukunda reddy, Mr. Bansilal, Mr. Satyanand and Mr. Narsinga Rao. I thank all the staff of the **CIL**, glass blowing section, NRS Hostel, Health center, Library, Administration and Central workshop for their help and affection.

I thank my colleagues Dr. G. Ravindranath, Dr. B. Jagadeesh, Dr. P. K. Rajan, Dr. A. S. Sailaja, Dr. R. K. **Subramanian**, Ms. Kavita, Dr. Uma, Mr. V. Satheesh and Mr. Bharadwaj for their support. My special thanks to Rajan and Jagadeesh and their families for their love and affection.

I thank Phani **kumar** for his timely help and support. A special word of thanks is in order to my dear friend Venkat Reddy for his help in preparing this thesis. I thank all my friends and colleagues in the school of physics, especially GV Rao, Murali, Shiva, Haribabu, Venu, Prasanna, P. D. Babu, Harish, **Issac**, Suresh, **Nirmal**,

Balakrishnan, Ravikanth, **Ramkumar**, Murali, Srinath, **Sudhakar**, Azhar, Prakash, Phani Murali, Hari, Sarkar, Anita, **Senthil**, Dr. Hari, Dr. Nagaraj Kumar, Gurappa, **Sunil**, **Srinivas** Reddy and others.

My thanks to my dear friends in the university, Ramanathan, Sahoo, Bakthadoss, Muthaiah, Appaji, Gurubaran, Ravichandran, Pandiaraja, **Nachimuthu**, Narkunan, **Rambo**, Mustafa, **Davuluri**, Nagarjuna and all the other **friends**.

I thank **Prof.** Ramanan and **family**, **Prof.** M. Periasamy, **Prof.** R.Jagannathan and family, Dr. **Sivakumar** and Ms. Chandra, Dr. C. S Sunandana and family for their affection.

My special thanks to my friend Ms. Vaishnavi for her help and support. My thanks to Mr. Sajjan for his help. I thank my friends Guravaiah and Rajasekhar for their support.

My thanks to all my family members and relatives for their love and affection.

I thank the Department of Atomic Energy, India for funding the FCNMR Instrumentation project and also for providing me Junior Research Fellowship. I would like to thank **CSIR**, India for providing me Senior Research Fellowship.

Preface

This Ph. D thesis is separated in to two units.

- > Unit I - presents the fabrication details of the Field Cycling **NMR** Spectrometer.
- > Unit **II** - presents NMRD studies of Molecular Dynamics in Liquid Crystals.

Unit – I

Study of molecular dynamics in complex fluids such as liquid crystals poses both experimental and theoretical challenges, due to the complexity of the molecules and the presence of a wide variety of dynamic processes (with possible couplings between them). The Field Cycling NMR technique in this connection offers a very distinct advantage due to its sensitivity to probe microscopic details and capability to access, and map out, a wide frequency window (particularly in the low frequency region) selectively - thanks to the resonance nature of its relaxation process.

In contrast to the conventional NMR technique (constant **Zeeman** magnetic field is applied during Preparation, Evolution and Detection periods of the NMR experiment) FCNMR technique cycles the Zeeman field to different levels in different periods of the experiment. Evolution of the spin system takes place at a lower magnetic field, and thereby facilitating measurements at very low **Larmor** frequencies, which are not accessible to the conventional NMR **methodology**

Field Cycling NMR spectrometer operating at 3 MHz was fabricated and standardized, as a part of this **thesis**, which mainly consists of a pulsed *rf* spectrometer and a Field Cycling Network which enables fast switching of the Zeeman fields in times very short compared to the NMR relaxation times of the systems under study.

The crucial part in the fabrication of FCNMR spectrometer is the construction of the field cycling network, which permits fast switching of the currents in the induction coil. The Field Cycling Network consists of, a controller, current driver

circuit consisting of 20 MOSFETs with independent gate drivers, a MOSFET switch with an optically coupled gate driver circuit and a energy storage capacitor **network** necessary to employ the well known 'energy storage principle', was built for this FCNMR spectrometer.

The fabrication details and operational procedures are presented in the chapter 2 of unit I. Chapter 3 presents the fabrication details the complete FCNMR spectrometer capable of providing **NMRD** data ranging from 20 kHz to 4 MHz. The fabrication details of the other parts of a *rf* spectrometer namely transmitter, probe, receiver and a temperature control assembly are also presented in the chapter -3.

Unit II

*Structure-dynamics relationship in **Butyloxybenzylidene Alkylanilines (4O.m)**:*

Liquid crystals are formed by molecules with highly anisotropic shapes. From the basic viewpoint, the study of the partial orientational and positional ordering of such changing, highly anisotropic shapes in condensed phases is one of the most challenging problems in the statistical physics of many bodies. The ever-increasing range of technological applications of liquid crystals in recent years resulted in an increasing interest in these systems. The choice of the system for a given application is critically dependent on its physical properties such as **visco-elastic** coefficients, density, refractive index, phase stability and **etc.**, Typical mesogenic molecules are made up of rigid or semi rigid parts such as aromatic groups, and flexible end chains, both contribute in determining the properties of the mesophase. From studies of homologous series of molecules it is generally observed that the nematic-isotropic phase transition temperatures and the transitional properties depend on the length of the flexible end chain, showing the characteristic odd-even alteration. An appreciation of the dependence of the physical properties of liquid **crystals**, on the dynamic environment of the constituent molecules is essential for liquid crystal engineering, and is still not available.

The effect of end chain structure on the molecular dynamics using the **FCNMR** technique, in the homologous **series** of butyloxybenzylidene alkylanilines (**40.m**: **m** = 2, 3, 4, 5, 7, 8 and 9) was carried out as a part of this thesis. In particular the molecular level understanding of the well-known 'odd-even effects', chain length effects and the effect of '**symmetric** end chains' is the aim of this experimental work. Present systems provide an opportunity to probe all these properties. Experiments were carried out to collect proton NMRD (Nuclear Magnetic Relaxation **Dispersion- T_1** as a function of Larmor frequency) profiles over a wide range of frequencies on the homologous series, which were studied earlier using conventional NMR spectrometer in this laboratory.

The application of existing theoretical formalism to extract useful information from the NMRD profiles, on visco-elastic properties of the medium, however requires certain improvements. Moreover, the situation is more complex in **nematics** with underlying **smectic A_d** phases: The presence of molecular associations (**dimers** and clusters) may lead to additional contribution to relaxation and restrictions on the DF modes leading to the upper and lower cut-off frequencies. Analysis of the data was done based on a composite model incorporating the three relevant molecular mechanisms [director fluctuations (**DF**), molecular self-diffusion (**SD**) and individual reorientations (**R**)], reflecting the differing influences of the microscopic dynamics on the magnetic dipolar interactions among the spins. The observed spin-lattice relaxation rate ($R_1 \sim T_1^{-1}$) is a sum of the contributions from these mechanisms. The mechanisms mediating spin-lattice relaxation in different **mesophases** are listed below.

- R_{DF}, R_{SD}, R_m in the case of nematics without underlying smectic **A_d** phase,
- R_{IL}, R_{ISD}, R_m in the case of smectic A phase,
- $R_{DF}, R_{ISD}, R_{IR}, R_{IF}$ in the case of frustrated nematics
- R_{DF}, R_{ISD}, R_{IR} and R_{IF} in the case of smectic **A_d** phase.

Separating out the various molecular motions mediating spin lattice relaxation in liquid crystals is major experimental challenge and it is very difficult to get information about all the important molecular motions using conventional NMR methodology **alone**. The Field Cycling NMR data along with the earlier conventional

NMR data on these systems made this task possible. The relative contributions of these three dynamical parameters and the dynamic parameters associated with them at different mesophases (nematic, smectic A, **smectic A_d** and **smectic B** phases are studied and presented in this thesis). The effect of the formation of the various degrees of orientational and positional orders on the molecular dynamics in liquid crystals is also addressed in this study to some extent. The observed end chain structure-molecular dynamics relationships are presented in the thesis. Analysis done using isotropic and anisotropic elastic constants are also compared.

Molecular dynamics of binary mixtures exhibiting Induced Smectic Phases:

It is known that liquid crystals consisting of molecules with a strongly polar end group (usually -CN) differ in many aspects from the more classical liquid crystals like the homologous series (nO.m). The most spectacular effects are reentrant nematic phases and induced smectic phase (ISP). The delicate balance between attractive forces and packing effects that determine the stability of the smectic phases have been studied using various techniques by various researchers. The ability of the polar molecules to establish different liquid crystal phases depends on the following factors:

- The length of the terminal chain,
- > Odd-even effects,
- The length of the rigid core and
- The polarity of the terminal group.

It is not possible to vary nematic and smectic temperature ranges by changing the **alkyl** chain length. Another way of changing the mesophase range can be done by mixing two different liquid crystals. By doing **so**, it is possible to alter the interactions aiding and opposing layer formation. Mixing two molecules of different polarities and end chain properties leads to a very complex phase such as **Induced** Smectic Phases (ISP).

Finding out a connection between the individual molecular properties and **the** alteration of various forces aiding and opposing the liquid crystalline formation **due** to mixing two different molecules is the aim of this work on binary liquid crystal **mixture**

of 8CN and 7BCB. In this mixture of the compounds at a particular range of compositions the induced smectic phase (ISP) appears, whereas the pure compounds does not show any smectic phase. A recent theoretical model developed by (Kyū et al.,) explaining the formation of the ISP, highlights the factors responsible for this interesting phase diagram.

The pure system 7BCB has a smectic forming tendency and it is frustrated phase. The next one in the same series (8BCB) has a stable smectic A phase. The nematic stability can be altered by either increasing the end chain length or by mixing a strongly polar compound (8CN). Formation of dimers and the frustration phenomenon in the polar liquid crystals are very important in the formation of the induced smectic phases. Effects of chain length as well as dimer formation plays pivotal role in deciding the phase diagrams in these mixtures.

Dimerization and frustration lead to an additional dynamic mechanism, namely the 'creation and segregation of the molecular associations'. This special mechanism is considered by many researchers in the analysis of NMRD data. A contribution with a correlation time associated with the creation and segregation of molecules has to be incorporated along with the usual dynamic mechanisms mentioned above.

The dynamic behavior connected with the formation of ISP is discussed in this thesis along with the separation of different dynamic mechanisms responsible for spin relaxation in nematic and smectic A_d phases. According to the theoretical model the ISP is formed as a consequence of the reduction of the nematic free energy at specific compositions of the two constituents forming binary mixture. The dynamic parameters in the pure nematic phases and the nematic phases with underlying smectic A_d phases are found to be very different. The role of DF mechanism on the stability of the nematic phase is also discussed. Thus a logical connection is established among the end chain length, odd-even effects, end chain symmetry, dimer formation and frustration in order to explain phase stability in terms microscopic dynamic behavior in the binary mixtures exhibiting ISP.

Organization of the Thesis:

Unit I consists three chapters Experimental challenges and the theoretical details connected with the implementation of the FCNMR technique are presented in the **chapter-1**. **Chapter 2** presents the details of the fabrication of the Field Cycling Network **Chapter 3** presents the details of the complete FCNMR spectrometer. References and conclusions for this unit are given at the end

Unit II consists of four chapters **Chapter 4** describes a review of chemical structure-physical properties with a special reference to the end chain properties like, odd-even effects, chain length and symmetry effects based on various experimental and theoretical studies on liquid crystals. Various ways of forming different phase diagrams and the underlying physics of the phase transitions are also discussed. References are given at the end. **Chapter 5** deals with the theory of NMR relaxation in liquid crystals and the models used in the NMRD data analysis References are given at the end of the chapter

Chapter 6 deals with experimental work carried out on the homologous series (4O.m) of liquid crystals Data analysis and results obtained on the liquid crystalline systems 4O.2, 4O.3, 4O.4, 4O.5, 4O.7, 4O.8 and 4O.9 are presented in separate sections (section 2 to section 8). A comparative study of dynamic parameters obtained on different systems is presented in the concluding section (section 9). References for this chapter are given separately.

Chapter 7 presents the NMRD study of nematics and smectic A_d phases of systems 8CN and 7BCB and their mixtures. The details of the experimental work and the analysis of the NMRD profiles are discussed separately in different sections. **The** composition dependent dynamic parameters are discussed in the concluding section of this chapter.

Abbreviations

<i>Notation</i>	<i>Description</i>
NMRD	Nuclear magnetic relaxation dispersion
FCNMR	Field Cycling NMR
T_1	Spin-Lattice relaxation time
R_{1DF}	Relaxation rate
R_{1SD}	Relaxation rate
R_{1R}	Relaxation rate
R_{1LU}	Relaxation rate
R_{1F}	Relaxation rate
DF	Director Fluctuations
OF	Order Fluctuations
LU	Layer Undulations
SD	Self-Diffusion
R	Rotations
F	Frustration
T_1	Spin-Lattice relaxation time
T_{11}	Dipolar relaxation time
T_{1F}	Relaxation time in the rotating frame
R_{1DF}	Relaxation rate due to DF mechanism
R_{1SD}	Relaxation rate due to SD mechanism
R_{1R}	Relaxation rate due to R mechanism
R_{1LU}	Relaxation rate due to LU mechanism
R_{1F}	Relaxation rate due to F mechanism
B	Constant quantifying the SD contribution
C	Constant quantifying the R contribution or Capacitance
F	Constant quantifying the F contribution
I)	Self-Diffusion constant
τ_R	Correlation time for rotations
τ_{ca}	Correlation time for creasion and segregation of molecular associations
τ_d	Correlation time for diffusion
K_{11}	Splay elastic constant
K_{22}	Twist elastic constant
K_{33}	Bend elastic constant
η_i	viscosities
γ	gyromagnetic ratio or rotational viscosity
γ	a constant quantifying DF contribution
$f_{\omega cl}$	lower cut-off frequency of DF modes in the direction parallel to nematic director n .
$f_{\omega ch}$	upper cut-off frequency of DF modes in the direction parallel to nematic director n .
$f_{\omega cl}$	lower cut-off frequency of DF modes in the direction perpendicular to nematic director n .

λ_{zcl}		lower cut-off wavelength of DF modes in the direction parallel to nematic director <i>n</i> .
λ_{zch}		upper cut-off wavelength of DF modes in the direction parallel to nematic director <i>n</i> .
λ_{icl}	lower cut-off	wavelength of OF modes in the direction perpendicular to nematic director <i>n</i> .
q		wave vector
LC		Liquid Crystal
S		Nematic order parameter
N		Nematic director
I-N		Isotropic-Nematic
N-S_A		Nematic-Smectic A
X	Crystal	phase
S_G		Smectic G phase
S_C		Smectic C phase
S_B		Smectic B
B		Magnetic field
B_p	Polarization	field
B_D	Detection	field
B_E	Evolution	field
M		Nuclear Magnetization
M_p		Magnetization in the polarization period
M_D		Magnetization in the Detection period
M_E		Magnetization in the Evolution period
PID		Proportional Integrator and Differentiator
FID		Free Induction Decay
L		Inductance
I		Current
S/N		Signal to Noise ratio
O	Quality	factor
nO.m		Alkyloxybenzylidenealkylanilines
40.2		Butyloxybenzylideneethyl aniline
40.3		Butyloxybenzylidene propylaniline
40.4		Butyloxybenzylidene butylaniline
40.5		Butyloxybenzylidene pentyl aniline
40.7		Butyloxybenzylidene heptylaniline
40.8		Butyloxybenzylidene octylaniline
40.9		Butyloxybenzylidene nonyl aniline
8CN		4-cyanophenyl 4-octylbenzoate
7BCB		4-cyanobiphenyl 4-heptylbenzoate
PAA		p-azoxyanisole
MBBA		Methyloxybenzylidene butylanilene

CONTENTS

Unit I

Fabrication details of the Field Cycling NMR Spectrometer

Chapter 1

Field Cycling NMR technique

1.1 Slow dynamics in complex systems	3
1.2. Field cycling Principle	5
1.3. Mechanical and Electronic methods	6
1.4. Magnetization during the transits	7
1.4.1. Ideal Field cycling	7
1.4.2. Experimental situation	10
1.5. Modern Field Cycling NMR Relaxometry	14
1.5.1. NMRD studies using FCNMR technique	14
1.5.1.1. Measurement of Spin-Lattice relaxation time (T_1)	18
1.5.1.1.1. Saturation Recovery Sequence	18
1.5.1.1.2. Inversion Recovery Sequence	23
1.5.1.1.3. Saturation Burst Sequence	27
1.5.2. Spin-Spin Relaxation time (T_2)	29
1.5.3. Adiabatic Demagnetization in the Laboratory Frame (ADLF)	30
1.5.4. Jeener-Brockaert pulse sequence $[(\pi/2)_Y - t - (\pi/4)_X - \tau - (\pi/4)_X \text{ or } Y]$	31
1.5.5. Spin-Lock Adiabatic Field cycling Imaging Relaxometry (SLOAFI)	34
1.6. The requirements and demands for the FCNMR Spectrometer	39

Chapter 2

Fabrication details of the Field Cycling Network

2.1. Introduction	41
2.2. Induction coil	43
2.2.1. Homogeneity with outer notches	46
2.3. Switchable magnetic field	49
2.3.1. Without the energy storage principle	49
2.3.2. With the energy storage principle	53
2.4. Current switching and control devices	58
2.4.1. Controller circuit	59
2.4.1.1. The reference	60
2.4.1.2. Feedback	60
2.4.1.3. Polc Zero pair amplifier	64
2.4.1.4. Compensation	65
2.4.1.5. Evolution field control	69

2.4.2. Working of the controller	70
2.4.2.1. Polarization and Detection fields	70
2.4.2.2. Evolution Period operation	70
2.4.2.3. ON/OFF periods and compensation	71
2.5. MOSFET current driver circuits	72
2.6. MOSFET switch	74
2.7. MOSFET switch driver circuit	74
2.8. Working of the Field Cycling Network	77
2.8.1. Polarization and Detection Periods	77
2.8.2. Switch OFF operation	78
2.8.3. Evolution Period	80
2.8.4. Switch ON operation	80
2.8.5. Detection Period	82
2.9. Standardization and Calibration	83

Chapter 3

Field Cycling NMR Spectrometer

3.1. Transmitter	87
3.1.1. rf generator	87
3.1.2. Pulse and delay generators	88
3.1.3. Double Balanced Mixer	91
3.1.4. Medium power amplifier	94
3.1.5. High power amplifier	94
3.2. Matching network	97
3.2.1. Series resonant circuit	98
3.2.2. Parallel resonant circuit	99
3.3. Receiver	101
3.3.1. Fast recovery preamplifier	102
3.3.2. Timed Amplifiers	103
3.3.3. PSD and phase shifter	103
3 3.4. Filter and signal averager	104
3.4. Temperature Controller	105
3.5. Automation	107
conclusions	108
References	

Unit II

Molecular Dynamics of Liquid Crystals Studied by FCNMR Technique

Chapter 4

Structure-Property Relationships in Liquid Crystals

Section A

Chemical structure and Thermal stability in Liquid Crystals

4.1 Introduction	117
4.2. Types of Liquid Crystals	119
4.2.1. Nematic and Smectic Phases	119
4.3. Chemical Structure and thermal stability	122
4.3.1. Physical properties and substituents	123
4.3.1.1. Role of the core	123
4.3.1.2. Role of linking groups	123
4.3.1.3. Role of the lateral substituents	124
4.3.1.4. Role of the terminal substituents	124
4.3.2. Nematic phase stability and terminal chains	125
4.3.2.1. Odd-Even effects	125
4.3.2.2. Alkyl chain length	125
4.3.2.3. Symmetric end chains	127
4.4. References	

Section B

Theories and experiments on Phase Transitions, Physical properties and Molecular Dynamics in Liquid Crystals

4.5 Introduction	131
4.6. Order parameter	132
4.7. Onsagar approach (repulsive forces)	133
4.7.1. Isotropic-Nematic transition	133
4.8. Mean field approach (attractive potentials)	136
4.8.1 Nematic-Smectic A phase transition	137
4.9. Generalized models	142
4.9.1. Formation of the mesophases	143
4.9.2. Role of dipolar forces	144
4.10. Theoretical explanation for odd-even effects	144

4.10.1 Intrachain constraints and rotational dynamics	146
4.10.2. Intrachain constraints and physical properties	147
4.10.3. Other models and computer simulations	148
4.11. Theorics and experiments on clastic constants	148
4.11.1. Molecular length and elastic constants	149
4.11.2. Order parameters and clastic constants	150
4.11.3. Cybotactic clusters and elastic constants	153
4.12. Anisotropic physical properties and molecular dynamics	153
4.12.1. Optical anisotropy	153
4.12.2. Anisotropic viscosity coefficients	154
4.12.3. Anisotropic rotational motions	154
4.12.4. Anisotropy in Self-Diffusion	156
4.1.3. <i>references</i>	

Chapter 5

Nuclear Magnetic Relaxation Dispersion (NMRD) Theory of Liquid Crystals

5.1. Nuclear Magnetic Relaxation Dispersion (NMRD)	162
5.1.1 Laboratory-Frame Spin-Lattice Relaxation	168
5.1.1.1. Dipolar Interaction	168
5.1.1.2. Scalar Coupling	171
5.1.1.3. Quadrupolar coupling	171
5.1.1.4. Chemical-Shift Anisotropy	172
5.1.2. Rotating-Frame Spin-Lattice Relaxation by Dipolar Coupling	172
5.2. Director Fluctuations and Spin Relaxation	173
5.2.1. Curvature elastic constants	173
5.2.2 The one constant expansion for $J_1(\omega_0)$	179
5.2.3. Anisotropic elastic Constants	180
5.2.4. Generalized Model (Upper and Lower cut-off frequencies)	184
5.2.5. Smectic Phases	186
5.3. Self Diffusion	191
5.3.1. Isotropic Phase	191
5 3.2. Nematic phase	197
5.3.3. Smectic A Phase	201
5.3.4. Smectic B and ordered Smectics	202
5.4. Reorientations	203
5.4.1. Nematic Phase	206
5.4.2. Smectic Phases	207
5.5. <i>References</i>	

Chapter 6

Field Cycling NMR Studies of Molecular Dynamics in Butyloxy Benzylidene Alkylanilines (40.m)

6.1	Earlier studies and present objectives of molecular dynamics in Liquid Crystals	214
6.1.1.	Introduction	214
6.1.2.	Motivation and objectives	214
6.1.3	Review of earlier studies on nO.m compounds	220
6.1.4.	Earlier NMR relaxation measurements in Homologous series	221
6.1.4.1	Earlier observations on Order and Director Fluctuations (OF and DF)	223
6.1.5.	Experimental Details	225
6.1.6.	Data analysis	226
6.1.6.1.	Nematic Director fluctuations (DF)	226
6.1.6.1.1.	Isotropic elastic constants model	227
6.1.6.1.2.	Anisotropic elastic constants model	227
6.1.6.2.	Smectic layer undulation modes (LU)	230
6.1.6.3.	Rotations about the short axis (R)	232
6.1.6.4.	Self-Diffusion (SD)	233
6.1.7.	Ordered smectic Phases	234
6.2.	NMRD study of Butyloxybenzylidene ethylaniline (40.2)	239
6.2.1.	Experimental Details	239
6.2.2.	Data analysis	242
6.2.2.1.	Nematic Phase	242
6.2.2.1.1.	Isotropic elastic constants model	242
6.2.2.1.1.	Anisotropic elastic constants model	244
6.2.2.2.	Ordered smectic phase (S_C)	247
6.3.	NMRD study of Butyloxybenzylidene propylaniline (40.3)	248
6.3.1.	Experimental Details	248
6.3.2.	Data analysis	250
6.3.2.1.	Nematic Phase	250
6.3.2.1.1.	Isotropic elastic constants model	250
6.3.2.1.2.	Anisotropic elastic constants	254
6.3.2.2.	Solid phase	256
6.4.	NMRD study of Butyloxybenzylidene Butylaniline (40.4)	257
6.4.1.	Experimental Details	257
6.4.2.	Data analysis	260
6.4.2.1.	Nematic Phase	260
6.4.2.1.1.	Isotropic elastic constants model	260
6.4.2.1.2.	Anisotropic elastic constants model	264
6.4.2.2.	Comparison with the ordered smectic phases	265

6.5. NMRD study of Butyloxybenzylidene Pentyaniline (40.5)	267
6.5.1. Experimental Details	267
6.5.2. Data analysis	270
6.5.2.1. Nematic Phase	270
6.5.2.1.1. Isotropic clastic constants model	270
6.5.2.1.2. Anisotropic clastic constants model	273
6.5.2.2 Smectic A phase	275
6.5.2.3. Ordered smectic Phases	277
6.6. NMRD study of Butyloxybenzylidene Heptyaniline (40.7)	280
6.6.1. Experimental Details	280
6.6.2.Data analysis	283
6.6.2.1. Nematic Phase	283
6.6.2.1.1. Isotropic clastic constants model	283
6.6.2.1.2. Anisotropic elastic constants	286
6.6.2.2. Smectic A phase	288
6.6.2.3. Comparison with the ordered smectic phase	290
6.7. NMRD study of Butyloxybcnzylidenc Octylaniline (40.8)	291
6.7.1. Experimental Details	291
6.7.2. Data analysis	292
6.7.2.1. Nematic Phase	292
6.7.2.1.1. Isotropic elastic constants model	292
6.7.2.1.2. Anisotropic elastic constants	295
6.8. NMRD study of Butyloxybenzylidene Nonylanilinc (40.9)	298
6.8.1. Experimental Details	298
6.8.2. Data analysis	302
6.8.2.1. Nematic Phase	302
6.8.2.1.1. Isotropic clastic constants model	302
6.8.2.1.2. Anisotropic clastic constants	305
6.8.2.1.3. Comparison with high frequency study	307
6.8.2.2. Smectic A phase	308
6.8.2.3. Ordered Smectic phase (S_R)	311
6.9. Conclusions	315
6.9.1. Effect of end chain length on T,	315
6.9.2. Director fluctuations and end chains	317
6.9.3. Self Diffusion and end chain length	320
6.9.4. Rotations about the short axis	320
6.9.5 Relative percentage contributions	326
6.10. References	

Chapter 7

NMRD Studies of Binary Liquid Crystal Mixtures exhibiting Induced Smectic A₁ Phases

7.1. Liquid crystal mixtures	339
7.1.1. Introduction	339
7.1.2. Theoretical review of binary liquid crystal mixtures	340
7.1.2.1. Linear and non-linear behaviors of phase diagram	340
7.1.2.2. Molecular flexibility	341
7.1.3. Theoretical models for the Induced Smectic Phases (ISP)	341
7.1.4. Experimental observations of Induced Smectic Phases	346
7.1.5. Nematic gap	347
7.2. Frustration. Dimerization and Molecular Dynamics in Induced Smectic Phases	348
7.2.1. Introduction	348
7.2.2. Frustration	348
7.2.3. Frustration in Liquid crystals	348
7.2.4. Mean field and Frustration strategies	349
7.2.5. Dimerization and the formation of the ISP	350
7.2.6. Role of the alkyl chains on the stability of the frustrated phases	351
7.2.7. Factors responsible for the ISP in the mixture of 8CN+7BCB	353
7.2.8 Molecular dynamics in frustrated phases	359
7.3. NMRD study of the polar liquid crystal 8CN	360
7.3.1. Experimental Details	360
7.3.2. Data analysis	363
7.3.2.1. Nematic Director fluctuations (DF)	363
7.3.2.2. Rotations about the short molecular axis and Self-diffusion	365
7.3.3. Results and Discussion	365
7.4. NMRD study of frustrated nematic liquid crystal 7BCB	371
7.4.1. Experimental Details	371
7.4.2. Data analysis	373
7.4.2.1. NMRD model for frustration and other dynamics	373
7.4.3. Results and Discussion	375
7.5. NMRD studies of the binary mixture of 70% 8CN + 30% 7BCB	379
7.5.1. Experimental Details	379
7.5.2. Nematic Phase	381
7.5.2.1. Results and Discussion	383
7.5.2.2. Dynamic parameters for DF modes	383
7.5.2.3. Dynamic parameters for SD. R and F	385
7.5.2.4. Percentage contributions	386
7.5.3. Smectic A₁ phase	387
7. 6. NMRD studies of the binary mixture of 40% 8CN + 60% 7BCB	392

7.6.1. Experimental Details	392
7.6.2. Data analysis	394
7.6.2.1. Nematic Phase	394
7.6.2.1.1. Dynamic parameters for DF modes	394
7.6.2.1.2. Dynamic parameters for SD, R and F	396
7.6.2.1.3. Percentage contributions	398
7.6.2.2. Smectic A _l phase	399
7.7. Conclusions	403
<i>Molecular Dynamics as a function of Composition in the Binary Mixtures of Polar Liquid Crystals</i>	
7.7.1. Relaxation times and composition	403
7.7.2. Director fluctuations	405
7.7.3. Self-Diffusion	407
7.7.4. Rotations	408
7.7.5. Frustration	410
7.7.6. Percentage contributions	411
7.8. References	

Unit I

Fabrication details of the Field Cycling NMR Spectrometer

This unit presents fabrication details of the Field Cycling NMR spectrometer, built as a part of this Ph.D. thesis. The unit consists of three chapters.

The first chapter, "Field Cycling NMR technique", presents the field cycling principle, the differences between ideal field cycling and practically feasible field cycling, various possible experiments using the FCNMR technique and their conventional NMR counterparts, discussed in detail. Finally, the experimental challenges involved in building the FCNMR spectrometer are presented at the end of the first chapter.

The second chapter, "Fabrication details of the Field Cycling Network", presents the most crucial part of the field cycling NMR spectrometer. Following the ideas presented in the pioneering work done by Noack and co-workers, a very simple FCNMR Spectrometer has been fabricated. A novel, problem-free switching circuit was built, using a simple power MOSFET and an optical coupler. This switching circuit is not only economical, but also convenient since, the possibility of a damage is negligible, when compared to the usually used GTO based switches.

Another, very important circuit called "*the controller*" has been built, with a special component called the "compensating amplifier", which takes care of the overmodulation of the current while switching from the evolution field to detection field. The implementation of the compensation is done in a special manner, such that the circuit automatically takes care of the overmodulation and this arrangement leads

to an almost ideal field cycling. The timing diagram and the pulse programming procedure designed for this spectrometer provides a free access to the operator and acts as an interface, in order to adjust the settings such that one can obtain the required field cycle. MOSFET current driver circuits (20 units connected parallelly) had also been built and optimized for the best performance. Among the other components of the field cycling network, such as various power supplies for the control and switching circuits, energy storage capacitor network, different decoupling diodes, **etc.**, the author has used commercially available components and units, but smaller power supplies and circuits were built for specific **applications**. A cylindrical coil already available in this laboratory was used in this **instrumentation**.

Chapter three, "Field Cycling NMR Spectrometer", presents the complete picture of the FCNMR spectrometer, the combination of the field cycling network and the conventional low field (operating at 3 to 4 MHz) NMR spectrometer. The author has built some of the crucial units like, the probe, a novel temperature control assembly, pre-amplifier, high power amplifier and a filter, which are interfaced with the field cycling network, used for NMRD measurements on liquid crystals.

After the completion of this work, the author could calibrate and standardize the spectrometer, and could collect proton ¹H data for the first time in this laboratory. Further improvements were made throughout the period of this work. The data obtained using this spectrometer on the standard samples, proved that the results were reliable and repeatable, within the error limits given in this **thesis**. The present FCNMR spectrometer is capable of providing proton NMRD data, from about 20 kHz, to about 3 MHz. Experiments were performed on **nematic** and **smectic** liquid crystals, and certain liquids. The spectrometer is used routinely for temperature and frequency dependent relaxation studies.

./ Slow dynamics in complex systems

The power of NMR relaxation spectroscopy to probe molecular motions in a variety of systems is rather well known. Apart from being a non-invasive local probe, this technique is capable of probing relatively low frequency **region**. i.e., in radio frequency range and below. While this property facilitates the investigation of many dynamic processes, like reorientations, translational diffusion etc., there are many dynamic processes that are slower, taking place below the MHz region, like director fluctuations in **nematic** liquid crystals, tunnel rotation of symmetric molecular groups in solids, back-bone fluctuations in polymers etc., which are not accessible to conventional NMR relaxation spectroscopy [12]. This limitation is mainly due to the unacceptable signal strength and other instrumentation difficulties below few MHz, which would be explained a little later. The field cycling NMR method is a powerful approach for investigating such complex distributions of motions in various materials, which often span a broad range of time scales (10^{-2} to 10^{-12} sec).

Among the several procedures which are useful in separating the relaxation mechanisms of different spin order, such as that of the **Zeeman**, dipolar, or quadrupolar energies, fast Field cycling NMR is considered to be the most obvious and general technique due to its capacity to probe spectral densities over a wide frequency range. Comparing the characteristic Nuclear Magnetic Relaxation Dispersions (NMRD) of various substances, a better understanding could be gained, of their microscopic behaviour in relation to the observed microscopic material properties. It is also well known that broad distributions of molecular motions exist in synthetic polymers, proteins, **lipid** bilayers and liquid crystals. The high frequency individual molecular motions and conformational motions are manifest predominantly in the local dynamics whereas, low frequency motions like collective fluctuations are typically associated with rheological properties of the assembly, including the elastic, viscous, and other

characteristic macroscopic **properties** In the case of biological membranes, lipids and proteins, the T_1 behaviour may be associated with their biological activity. It is therefore, important to study various types of such motions, their corresponding rates, and the relative importance of such motions quantitatively over a broad range of frequencies as a means of achieving a comprehensive description of the dynamics of these and related materials. By systematically changing the structure of the molecule forming the material, the structure-dynamics relationship can be obtained using detailed NMRD studies

In the present chapter, the details of the field cycling NMR technique, theoretical explanation of the experimentation, differences between the ideal spectrometer and the realistic case, the methodology of various experiments possible with field cycling NMR, which has their equivalents in conventional NMR, would be discussed in detail.

A conventional NMR relaxation experiment, say a spin-lattice relaxation time (T_1) measurement as a function of the static magnetic field strength, probes the spectral densities of the fluctuations ($J_m(\omega)$) typically at the corresponding Larmor frequency (ω), which in turn are Fourier transforms of the correlation functions $G_m(\nu)$, where m is the magnetic projection index. The correlation functions describe fluctuations of the second rank molecular interactions, generated by molecular motions, which enable various relaxation processes to occur. Thus, to probe fluctuations taking place below the MHz region, the Larmor frequency should be below MHz. As the signal strength varies from ω^{-5} to ω^2 , the signal to noise ratio (S/N), in conventional NMR becomes very unfavorable below the MHz region. It is difficult to detect the proton NMR signal in magnetic fields below 0.1 Tesla (resonance frequency of about 3 MHz), due to very weak nuclear induction and the acoustical ringing induced in the NMR probe. Moreover, it is difficult to produce short, high power rf pulses at frequencies in the low MHz range to detect nuclear induction signals from solid and liquid crystal phases which have relatively short transverse relaxation times (T_2). T_2 is related to the quality factor (Q) of the NMR probe which is decreased significantly at lower frequencies.

Other instrumentation difficulties like the increased dead time of the receiver also crop up in this frequency range.

There are NMR techniques like line width, spin-lattice relaxation time in rotating frame ($T_{1\rho}$), and dipolar relaxation time (T_{1D}) measurements that probe fluctuation spectrum towards the low frequency region upto 100 kHz. Between 100 kHz and 3 MHz, a large frequency gap exists, which could not be covered by any NMR method. This leads to a major problem of mapping the frequency dispersion over the entire range, including the important region between the high and low frequencies. Field cycling NMR (FCNMR) technique, on the other hand, facilitates the measurement of NMR parameters at low frequencies, continuously, in principle, all the way to zero frequency. Further, using the FCNMR technique, any frequency dependent study between a given minimum and maximum obtainable frequencies can be easily done without having to tune the spectrometer independently at each frequency (as the frequency where the signal is detected is not altered in this technique). Using the typical field cycling procedure, one can obtain proton NMR relaxation times in the frequency range from 10^3 Hz to 10^8 Hz and for deuterons, this range is from 10^2 to 10^7 Hz by orders of magnitude.

1.2. Field cycling Principle

The basic methodology in the FCNMR technique is to use a high enough magnetic field strength at the time of polarizing the spin system (called polarization field, B_p) and at the time of sampling the remaining coherence (detection field, B_D), but switch the field to a low value at the time of the evolution of the spin system (evolution field, B_E) as shown in figure 1.1,

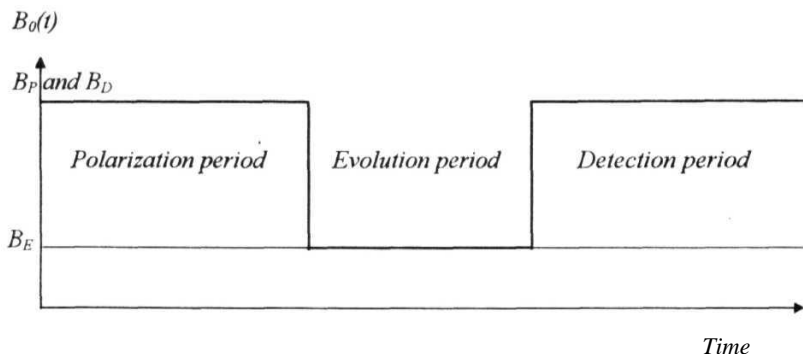


Figure 1.1. Ideal Field cycling procedure

This technique, while providing comfortable signal to noise ratio (S/N) corresponding to B_P and B_D , allows the measurement of the relaxation times corresponding to B_E , making it a useful technique for the low as well the high frequency (conventional NMR) range. This technique requires that the magnetic field be switched from B_P to B_E and back to B_D in times very short, compared to NMR relaxation times, but at the same time not too fast as to exceed the adiabatic fast passage condition or to create Fourier components of the resulting transients at ω^2 .

1.3. Mechanical and Electronic methods

The desired field cycle (figure 1.1) can be obtained by two methods. The first is by a mechanical movement of the sample between the chosen magnetic fields [1-8]. The other method involves electronic switching wherein field cycling is achieved by varying the current through an inductive load [9-10]. Mechanical cycling can be performed with a simple apparatus and moreover, there is no limit on the obtainable polarization and detection field levels. However, the mechanical approach is limited by the time it takes to physically shuttle the sample from one position to another.

A simple, mechanical field switch was first developed by Pound [1] in 1951. Electronic field cycling instruments have been developed very recently with magnet

coils using high power switching **components**. Such electronic switches offer the most advanced and versatile capabilities, and in principle, enable switching times of less than 1ms. Initial field cycling NMR spectrometers were made possible due to the pioneering work by Redfield et al., in 1968 [11], on the '**energy storage principle**' and field cycling procedure, by utilizing networks of transistor field switches and storage capacitors, to boost the voltage over the magnet coils [12]. Later, GTO thyristor switches have found use as a substitute for the transistor switch, and most recently, the utilization of MOSFETs for regulation has been proposed to **simplify** the total current control [13]. Using commercially available 'pulse width modulation switching current amplifier', having a low internal power dissipation and a fast current settling time, Job et al., [44] have developed a PC based FCNMR spectrometer very recently. They have used the 'waveform electronics control and pulse width modulation amplifiers', which are high performance current control amplifiers optimized to drive the gradient coils in MRI systems [44].

Another important development of FCNMR is the zero field or, low field NMR relaxation [14-21] where, the Zeeman energy and consequently line broadening caused by the distribution of molecular orientations due to the Zeeman field vanish, thus enhancing the spectral resolution. Apart from frequency dispersion studies over a wide frequency range, FCNMR spectrometer can be used in level crossing experiments [22-24], in detection of weak and low frequency resonance signals [25], cross relaxation spectroscopy [26-33] and in certain 2D experiments [34]. Some of the manifold applications of FCNMR were illustrated by Kimmich et al.,[35-37].

1.4. Magnetization during the transits

1.4.1. Ideal Field cycling

In the conventional NMR, macroscopic nuclear magnetization is under the influence of a constant Zeeman field i.e., Zeeman field is not changed during the polarization, evolution, and detection periods. But in the case of FCNMR, the Zeeman field is modulated during these periods, and hence the effects of this modulation on the

magnetization along with the effects due to the pulsed rf magnetic field, also is to be considered (since the behavior of spins in the evolution period necessarily depends on the behavior during the other periods of the cycle and especially during **transits**) Considering the equilibrium value of the magnetization to be M_0 and the spin-lattice relaxation time T , to be field dependent, the **Bloch** equation for the magnetization parallel to the external field, M_z can be written as

$$\frac{dM_z}{dt} = \gamma [M_z(t) \times B_0] - \frac{1}{T_{1B}} [M_z(t) - M_{zB}] \quad 1.1)$$

where T_{1B} is the field dependent spin-lattice relaxation time. Let the equilibrium values of M_z in the polarization, evolution and detection periods be M_P , M_E and M_D with corresponding spin-lattice relaxation times T_{1P} , T_{1E} and T_{1D} , respectively. The conditions mentioned earlier, on the transit times, is that the switching is fast compared to the relaxation times, and the switching should be slow enough compared to the **Larmor** frequency ω_0 , so that the magnitude and angle between $M_0(t)$ and $B_0(t)$ is preserved.

These conditions ensure that, there is no change in magnetization during the transits and hence the magnetization after the transits is constant and parallel to the applied field, just before the transits. In this ideal field cycle, magnetization during switching *down*, from polarization field (B_P) to detection field (B_E), the magnetization is constant at a value M_P . Similarly, during switching *up* from evolution field (B_E) to detection field (B_D), the magnetization should be same as the value at M_E . The development of the magnetization in the different regimes in the ideal cycle are shown in figure 1.2 and the equations describing them are also given in equations 1.2a-e.

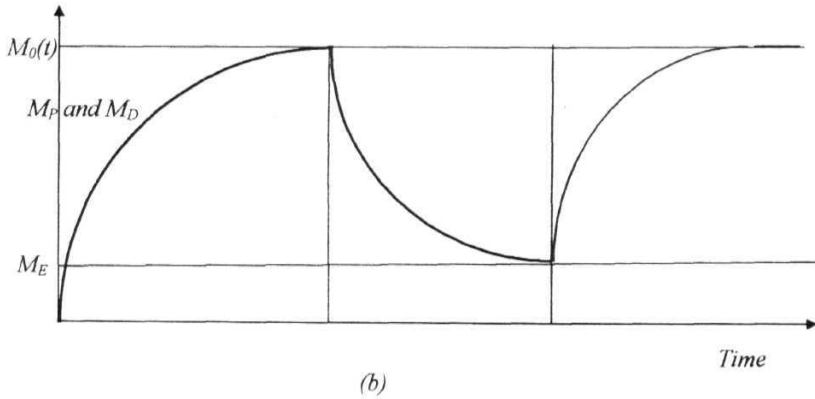
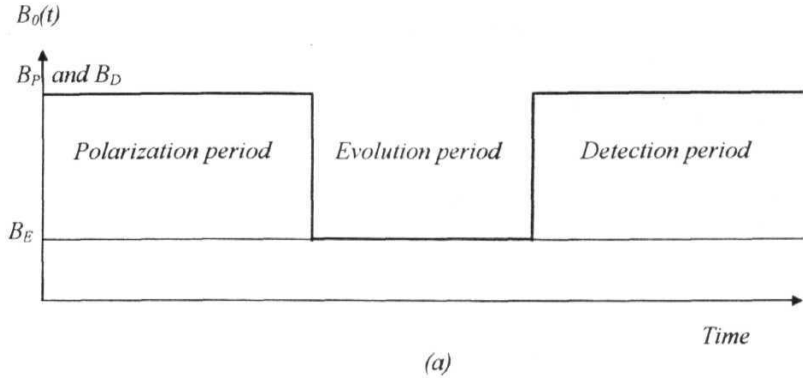


Figure 1.2.(a). Magnetic field with time during ideal field cycle.

(b). Magnetization during different periods

Polarization period:

$$M_z(t) = M_D = M_P \quad \text{during } t < t_P \quad (1.2a)$$

Switching down period:

$$M_z(t) = M_z(t_P) = M_P = \text{constant} \quad (1.2b)$$

Evolution period:

$$M_z(t) = M_P - (M_P - M_E) \left[1 - e^{-\left(\frac{t-t_P}{T_{1D}}\right)} \right] \quad \text{during } t_P < t < t_E \quad (1.2c)$$

Switching *up* period

$$M_z(t) = M_z(t_E) = \text{constant} \quad (1.2d)$$

Detection **period**:

$$M_z(t) = M_z(t_E) + \left[M_D - M_z(t_E) \right] e^{-\left[\frac{t - t_E + t_P}{T_{1D}} \right]} \quad (12e)$$

during $t_P + t_E < t < t_P + t_E + t_D$

Thus field cycling NMR measurements enable the measurement of $M_z(t)$ as a function of the magnitude of the evolution field B_E . Though most field cycling NMR experiments are concerned with longitudinal relaxation processes, any other NMR parameters which follow general Bloch type relations, such as diffusion constant, cross relaxation rate etc., are also measurable through the suitable combination of standard NMR procedures with the field cycling procedure (with suitable *Ho* cycles).

1.4.2. *Experimental situation*

In order to analyze the behaviour of spins in the evolution period (T_E) of field cycling NMR experiment, it is necessary to calculate the magnetization during transits and during the other periods. Exact variation in the magnetic field due to field cycling and its effects on the magnetization are difficult to calculate, but the experimental procedures, and data fitting methods take care of this problem. Therefore, it is important to mention the difference between an ideal field cycle and a practically feasible cycle. The correct requirement for an ideal cycle is that, with almost a zero evolution period the polarization produced should be detected without any loss. In other words, a perfect 'reversibility' of the cycle should be observed, which is possible only when the switching takes place in no time. In the case of longer switching times, comparable with the relaxation times at the evolution fields, the losses in the magnetization do not lead to any systematic experimental errors, though they affect the sensitivity of the experiment. During the switching periods, all quantities in Bloch's equation for the z-magnetization become time dependent. This is given by

$$\frac{dM_z(t)}{dt} = -\frac{M_z(t) - M_0(t)}{T_1(t)} \quad (1.3)$$

where $M_0(t)$, is the instantaneous equilibrium magnetization, and $T_1(t)$ is the instantaneous relaxation time. This can be rewritten as

$$\frac{dM_z(t)}{dt} + \left(\frac{1}{T_1(t)} \right) M_z(t) = \frac{M_0(t)}{T_1(t)} \quad (1.4)$$

By defining

$$P(t) \equiv \int_{t_0}^t \frac{1}{T_1(t')} dt' \quad (1.5)$$

in the switching interval $t_0 < t \leq t_0 + \Delta t$ the integral can be expressed [36] as,

$$M_z(t_0 + \Delta t) = e^{-P(t_0 + \Delta t)} \left[\int_0^{t_0 + \Delta t} e^{P(t'')} \frac{M_0(t'')}{T_1(t'')} dt'' + M_z(t_0) \right] \quad (1.6)$$

$$M_z(t_0 + \Delta t) = M_z(t_0) e^{-C_1} + C_2 \quad (1.8)$$

where

$$C_1 = P(t_0 + \Delta t) = \int_{t_0}^{t_0 + \Delta t} \frac{1}{T_1(t')} dt' = \text{constant} \quad (1.9)$$

$$C_2 = e^{-C_1} \int_{t_0}^{t_0 + \Delta t} e^{P(t'')} \frac{M_0(t'')}{T_1(t'')} dt'' = \text{constant} \quad (1.10)$$

are the switching constants.

When the magnetic field is switched *down* from polarization field (B_P) to evolution field (B_E), in the interval $(\Delta t)_d$ beginning at $t_0=0$, magnetization reduces from $M_z(0)=M_P$ to M_z [(Aid)] where M_P is the equilibrium magnetization in the polarization field. Designing switching constants (c_1^d and c_2^d) for this period, using the above equations 1.9 and 1.10, one can get the magnetization at the beginning of the relaxation interval as

$$M_z[(\Delta t)_d] = M_P e^{-c_1^d} + c_2^d \quad (1.11)$$

and the condition,

$$M_z[(\Delta t)_d] \gg M_E \quad (1.12)$$

is very important for field cycling experiment

During the evolution period (7.) the magnetization relaxes with time T_{1E} obeying the equation given by

$$M_z[T_E + (\Delta t)_d] = (M_z[(\Delta t)_d] - M_E) e^{-\frac{T_E}{T_{1E}}} + M_E \quad (1.13)$$

where T_{1E} is the spin-lattice relaxation time in the evolution field.

The switching constants for switching *up* period (the switching *up* period $(\Delta t)_u$, starts at the end of the evolution, i.e., at $t_0=T_E+(\Delta t)_d$), can be denoted as c_1^u and c_2^u and the magnetization at the beginning of the detection interval is represented by

$$M_z[T_E + (\Delta t)_d + (\Delta t)_u] = M_z[T_E + (\Delta t)_d] e^{-c_1^u} + c_2^u \quad (1.14)$$

The magnetization, during the detection period can be written [36] as

$$M_z[T_E + (\Delta t)_d + (\Delta t)_u] = \left[M_z[T_E + (\Delta t)_d + (\Delta t)_u] e^{-\frac{T_E}{T_{1E}}} + M_E \right] e^{-c_1^u} + c_2^u \quad (1.15)$$

and the relaxation behaviour to be evaluated is of the form

$$M_Z \left[T_E + (\Delta t)_d + (\Delta t)_u \right] - M_Z(\infty) = \left(M_Z \left[(\Delta t)_d \right] - M_E \right) e^{-c_1 u} e^{-\frac{T_E}{T_{1E}}} \quad (1.16)$$

$$= \Delta M_Z^{eff} e^{-\frac{T_E}{T_{1E}}} \quad (1.17)$$

This relation shows that the relaxation is a function of T_{1E} , and the switching intervals do not cause any systematic error in the experiment. The effective range of variation of the magnetization decides the accuracy of the experiment

$$(1.18)$$

If the range of variation is more, the experimental error would be less.

7.5. Modern Field Cycling NMR Relaxometry

Though the main object of field cycling NMR experiments is to obtain information on the spectral densities of the fluctuating spin interactions in a frequency range as wide as possible, with the basic interest of understanding and **characterizing** the molecular dynamical processes in a direct and quantitative way, there are several new experimental methods which made field cycling NMR relaxometry, the most exciting technique [12,36]. Apart from just lowering the intensity of the fields (and hence induction B_0), field cycling may, as well include evolution periods with higher field intensity than the detection field, or even changing the **direction** of the field, and hence this technique offers capabilities which go far beyond the original intentions. Cycling of the orientation at high speed facilitates the angular dependent relaxation and diffusion measurements [12] in liquid crystals with relative ease, compared to other cumbersome methods of field rotation. It is well known, that the accuracy of relaxation time measurements depends on how well defined and homogeneously, the initial non-equilibrium state is produced in a sample. In contrast to the conventional NMR method, the non-equilibrium state is reached by switching the main magnetic flux to the new level, in the field cycling NMR method. This new low evolution field has a very good homogeneity than that of the rf pulse homogeneity, which is used in the conventional method to arrive at a new non-equilibrium. Field cycling NMR relaxometry is therefore, a rather reliable technique in this respect [36].

7.5. /. NMRD studies using FCNMR technique

Conventionally, NMR experiments can be performed either in a frequency domain or in a time domain. In the frequency domain experiments, a low power rf radiation is applied to the sample, which is kept in a high Zeeman magnetic field. Either the frequency of rf or, the strength of the Zeeman magnetic field is slowly swept through resonance. On the other hand, in a time domain experiment, the response of the spin system, excited by an intense burst of high power resonant rf magnetic field applied for a short duration, is

monitored. The results obtained from these two methods are related by Fourier transformations, and hence, the same spectral information can be obtained from both these methods. The time domain method is found to be more efficient, due to its economy in time and better sensitivity.

The general experimental methods followed in measuring the spin-lattice relaxation time (T_1) would be discussed here. Conventional NMR procedures are adopted (modified in some cases, keeping the switchable nature of the **Zeeman** magnetic field in mind) in case of the FCNMR technique, too. Incorporation of conventional pulse sequences with the field cycling procedure would also be discussed here. The Zeeman interaction of a spin kept in a static magnetic field \mathbf{H}_o , which is applied along the z-axis, can be written as

$$\mathcal{H} = -\gamma\hbar H_o I_z \quad (1.19)$$

the eigen values of a state $|l, m\rangle$ are then given by

$$E_m = -\gamma\hbar H_o m \quad (1.20)$$

therefore, E_m can have $2l+1$ values, giving rise to $2l+1$ equally spaced energy levels with a separation of $\gamma\hbar H_o$. Transitions among these states can be induced by applying electromagnetic radiation with a frequency $\omega_o = \gamma H_o$ (Larmor frequency). To induce transitions, the radiation field should be applied in a direction perpendicular to the static field \mathbf{H}_o , i.e., in the x-y plane.

A nuclear magnetic moment $\boldsymbol{\mu}$ ($=\gamma\mathbf{I}$), under the influence of an external magnetic field \mathbf{H} experiences a torque $\boldsymbol{\mu} \times \mathbf{H}$, which is equal to the rate of change of angular momentum. The resultant equation of motion of the magnetic moment in a laboratory frame is given by

$$\frac{d\boldsymbol{\mu}}{dt} = \gamma(\boldsymbol{\mu} \times \mathbf{H}) \quad (1.21)$$

since $\sum \boldsymbol{\mu}_i = \mathbf{M}$, the total magnetization of the system, the equation of motion can be written as

$$\frac{d\mathbf{M}}{dt} = \gamma(\mathbf{M} \times \mathbf{H}) \quad (1.22)$$

The application of a perturbing *rf* field, $\mathbf{H}_1(t)$ (with a frequency ω), in a plane perpendicular to H (in x-y plane) modifies the above equation (1.22) as,

$$\frac{d\mathbf{M}}{dt} = \gamma \left[\mathbf{M} \times \left[H + H_1(t) \right] \right] \quad (1.23)$$

The solution of the above equation (1.23) is simplified when viewed from a different coordinate system ($x' y' z'$), which is rotating with respect to the laboratory frame (xyz), about some axis, say the z-axis, with an angular frequency same as that of *rf* field as shown in the figure 1.3. The equation of motion of the magnetization in this frame is similar to that in the laboratory frame, with the magnetic field replaced by an effective field given by,

$$H_{eff} = \left[\left(H + \frac{\omega}{\gamma} \right) + H_1(t) \right] \quad (1.24)$$

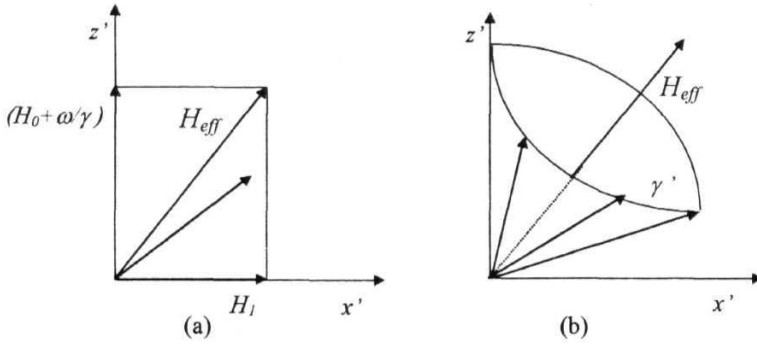


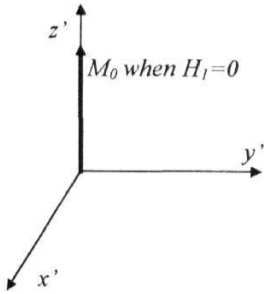
Figure. 1.3. a) Rotating frame and effective field

b) Motion of the magnetic moment around the effective field.

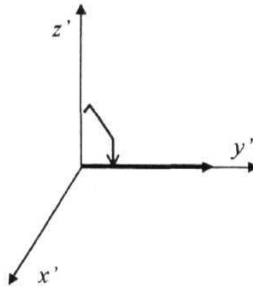
Thus, the spin precesses about the effective field in the rotating frame, with an angular frequency, $\gamma \mathbf{H}_{eff}$. Choosing H to be along the z-axis of the laboratory frame i.e., $H = H_0 \mathbf{k}$ (\mathbf{k} is a unit vector along z-axis), the effective field is modified to

$$\mathbf{H}_{eff} = \left[\left(H_0 + \frac{\omega}{\gamma} \right) \mathbf{k} + i H_1(t) \right] \quad (1.25)$$

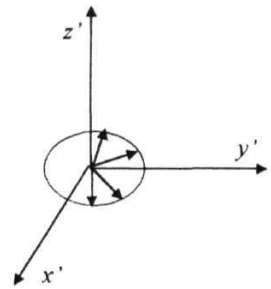
Also choosing the frequency of the rotating frame to be equal to that of the Larmor frequency i.e., $\omega = \omega_0 = -\gamma H_0$, it can be seen that the effective field in the rotating frame is $i H_1$, and hence the magnetization that was initially parallel to H_0 now precesses about H_1 in the $y'z'$ plane. If such an rf is applied for a time t_w , the angle by which the magnetization precesses is given by $\theta = \gamma H_1 t_w$.



(a) M_0 when $H_1 = 0$

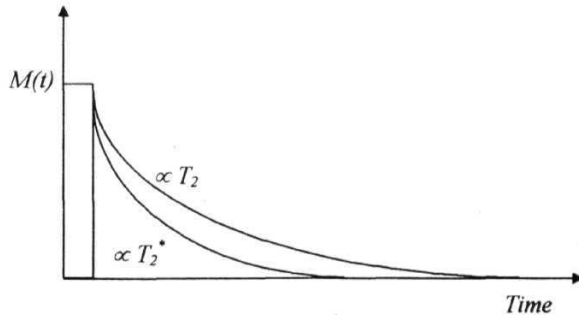


(b) magnetization after $\pi/2$ pulse

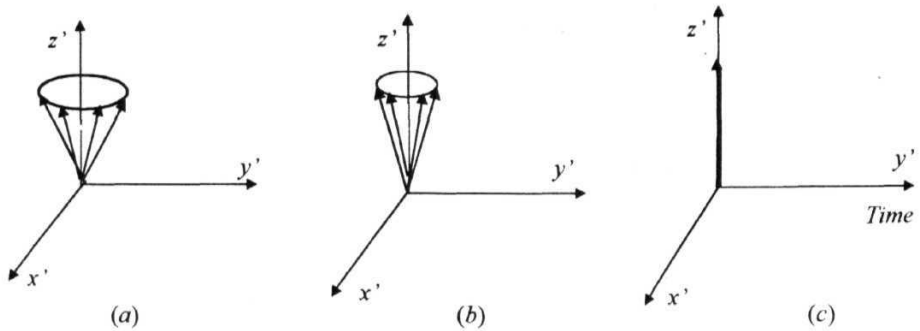


(c) spin-spin
relaxation

1.4. Effect of $\pi/2$ pulse on the equilibrium magnetization



1.5. Spin - Spin relaxation.



1.6. Spin-Lattice relaxation process.

Thus, with an appropriate combination of the intensity and the duration of the rotating magnetic field, magnetization can be flipped from the z -axis by any desired angle. For a given H_1 , a pulse applied such that the magnetization rotated by 90° is called a $\pi/2$ pulse (Figure. 1.4) and a pulse applied such that tilt angle $\theta=180^\circ$ is called a π pulse. The pick up coil is sensitive only to the component of magnetization perpendicular to the z -axis and the magnetization that is developed along z -axis due to T_1 process (Figure 1.6), is detectable only after it is rotated away from the quantization axis. The rf pulse sequences which are useful in T_1 measurements would be discussed here. The T_2 process is explained in figure 1.5.

1.5.1.1. Measurement of Spin-Lattice relaxation time (T_1)

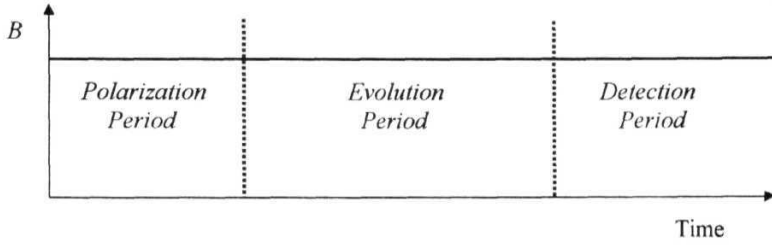
1.5.1.1.1. Saturation Recovery Sequence

For the sake of convenience, the experimental period (time) is divided into three parts as shown in figure 1.7a. In the conventional NMR relaxometry, the Zeeman field is the same throughout the period of the experiment. In the practical case, this cycle repeats again and again in order to do the averaging of the signal. Evolution period is varied to obtain the magnetization recovery profiles as a function of evolution time. The conventional *saturation recovery sequence* consists of a $\pi/2$ pulse followed by another $\pi/2$

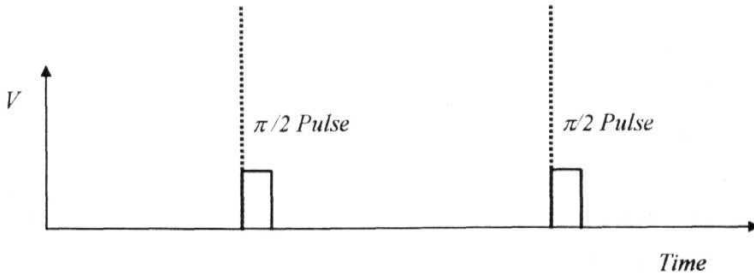
pulse which is applied after a variable evolution time τ (Figure 1.7b). The first $\pi/2$ pulse is the polarization pulse, which flips the magnetization away from the z-direction to the x-y plane. After allowing the magnetization to evolve in the z-direction for a time τ , another $\pi/2$ pulse is applied, which brings the z-magnetization, developed in the time τ [$M(\tau)$], to the x-y plane, as shown in figure 1.7c. The corresponding magnetization has an amplitude $A(\tau)$, at a fixed time from the sampling pulse, develops from zero at $\tau=0$ to A_0 at time $\tau=\infty$, which is proportional to $M(\tau)$, and varies as

$$A(\tau) = A_0 \left[1 - \exp\left(-\tau/T_1\right) \right] \quad (126)$$

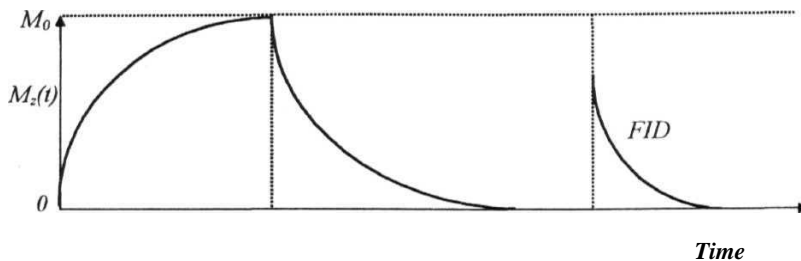
$A(x)$ is measured at a fixed point on the FID, following the sampling pulse. By repeating the measurement for different values of τ and then fitting data to the equation 1.26, T_1 is obtained.



1.7a. Zeeman magnetic field with time in a conventional T_1 measurement.



1.7b. Conventional Saturation recovery pulse sequence.

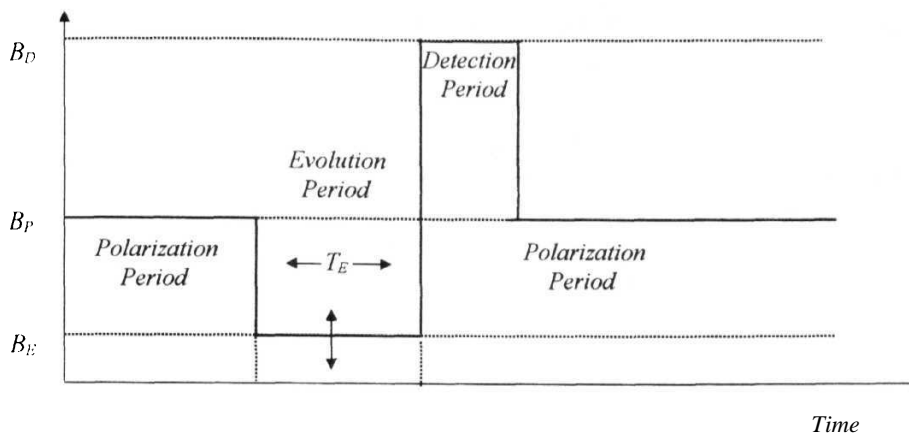


1.7c. Evolution of magnetization with time

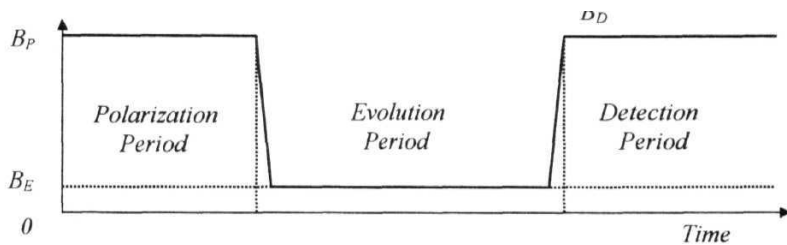
FCNMR equivalent of saturation recovery sequence

A simple, *field cycling procedure* used by the Noack's and Kimmich's groups [12,36] are shown in the figure 1.8. In this case, they have used different magnetic fields during polarization and detection periods. They have used very high magnetic fields for detection, which has enabled them to have a good signal to noise ratio. The polarization field is kept at a value where sufficient magnetization is prepared and made available for evolution. The evolution time is varied to get the magnetization recovery to the new equilibrium set by the evolution field. The relaxation takes place in this field, and the measured T_1 's are corresponding to the evolution field. The evolution field is varied, keeping other fields during the polarization and detection periods constant, in order to obtain relaxation dispersion (NMRD) over a very wide range of frequencies

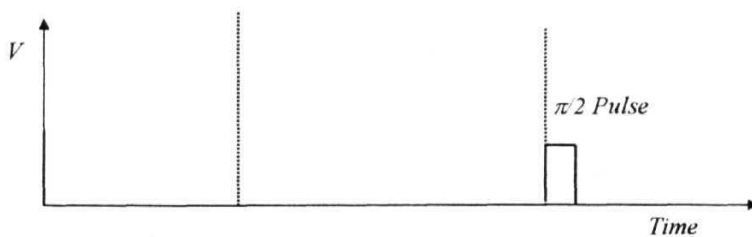
In the **present** FCNMR case, a constant field is used for polarization and detection periods, whereas the evolution field is varied from a maximum of B_p to a minimum of about a few gauss. The detection field is stable and repeatable accurately over the experimental time, which is very essential for an accurate determination of T_1 of the order of milliseconds. The simplified equation used to fit the magnetization recovery as a function of evolution period, in order to get T , is given below 1.28. The original equation and the need for the modification of that equation are discussed in the previous section



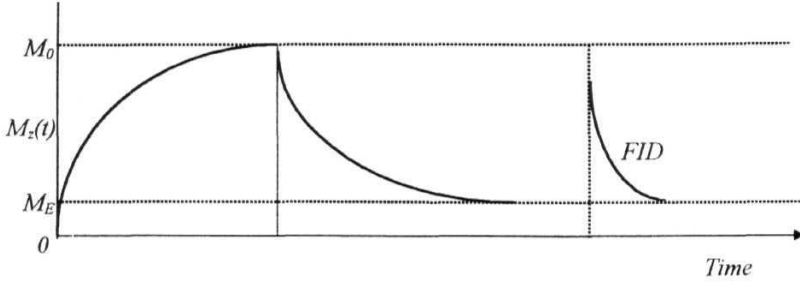
1.8. Field cycling procedure [36] with higher detection field.



1.9a. Zeeman magnetic field cycle in the present case.



1 9b Single pulse sequence (FCNMR equivalent of saturation recovery sequence).



1.9c. Evolution of magnetization.

In the field cycling NMR version of the saturation recovery sequence, the first rf pulse is not necessary, since the polarization field is suddenly removed from one value to the other (to low evolution field) and hence magnetization is forced to set to the new equilibrium value corresponding to the B_E . This switching process replaces the need for the first $\pi/2$ pulse (Figure 1.9b). The new non-equilibrium is set by B_E , and is combined with a $B_1(t)$ sequence to sample the evolving magnetization or the spin temperature belonging to the evolution period i.e.,

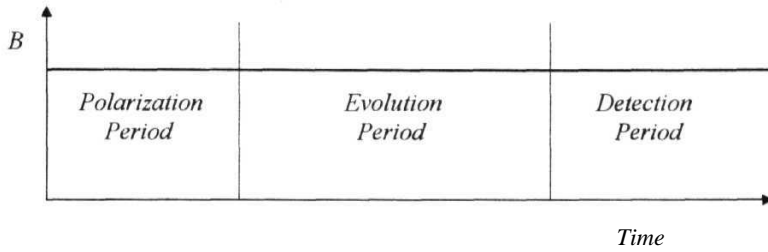
$$M_z(t_E) = M_z(t_E = 0) - (M_z(t_E = 0) - M_{0E}) \left[1 - \exp\left(-\frac{t_E}{T_{1E}}\right) \right] \quad (1.27)$$

As shown in the figure 1.9c, the magnetization, M_z increases to a high equilibrium value, M_p , at the end of the sufficiently long polarization period, t_p . When the Zeeman field is switched to a lower value (evolution field, B_E), the magnetization, $M_z(t)$ relaxes with the increase in the evolution period with a time constant T_{1E} , towards the new equilibrium value M_E . After this, the Zeeman field is brought back to the high value (detection field, $B_D=B_p$) and a sampling $\pi/2$ pulse is applied. Sampling pulse flips the magnetization into the plane perpendicular to B_p . This transverse magnetization $M_x(t_D=0)$ i.e., $M_z(t-T_E)$, now relaxes under the influence of B_p , with Larmor frequency ω_0 giving rise to FID in the sample coil. The FID height decays proportional to the magnitude of M_z at $t=T_E$, i.e., the height of the FID obtained decays exponentially with a time

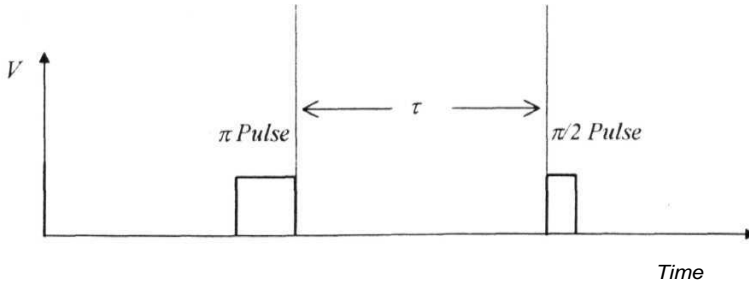
constant T_{1E} as a function of the evolution period time, T_E . Thus the relaxation time T_{1E} , at any selected evolution field is measured directly from the height of the FID by varying the evolution period T_E . The equation used to get the T_{1E} is given below (1.28). A non-linear least square fit involving three variables (A , B , and T_{1E}) with $M_Z(T_E)$ and T_E as **inputs**, is used to get the T_{1E} values.

$$M_Z(T_E) = A \exp [-T_E / T_{1E}] + B \quad (1.28)$$

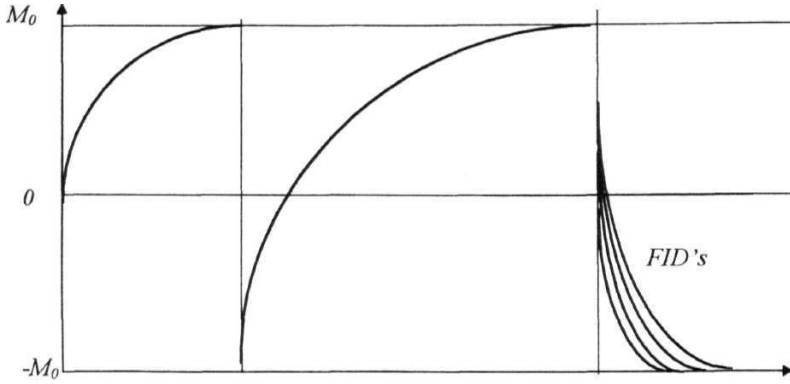
1.5.1.1.2. Inversion Recovery Sequence



1.10a. Zeeman magnetic field with time in the conventional inversion recovery sequence.



1.10b. Inversion recovery pulse sequence.



1 10c. Magnetization in the case of inversion recovery pulse sequence.

The pulse sequence here is π - τ - $\pi/2$ (Figure 1.1 Ob). The preparation pulse (π pulse) tilts the magnetization, from the +z axis to the -z axis, and then, the evolution along +z direction is monitored by another $\pi/2$ pulse after a delay τ (Figure 1.10c). As usual in the conventional NMR τ experiment the Zeeman field is constant over time (Figure 1.10a) and in the case of the FCNMR the Zeeman field changes, when this sequence is convenient (evolution field close to detection field) in measurement of τ as shown in the figure 1.11a.

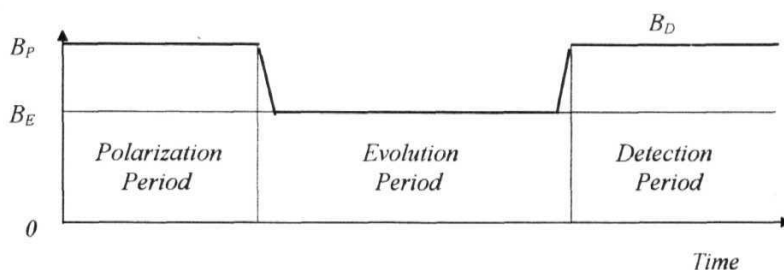
The preparation pulse (π pulse) inverts the spin population (+z-axis to -z axis) and hence the z-component of magnetization recovers from $-M_0$ to M_0 , which follows the equation

$$\int A(\tau) = A_0 \left[1 - 2 \exp\left(-\tau/T_1\right) \right] \quad (129)$$

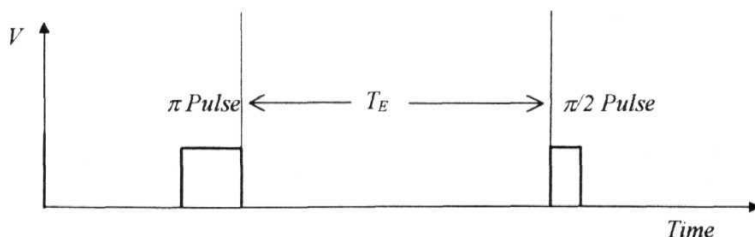
A_0 being the amplitude of the FID after a time $\tau = \infty$.

The inversion recovery sequence is very useful in FCNMR, when the evolution field is very close to the value of the preparation and detection fields. Under this situation

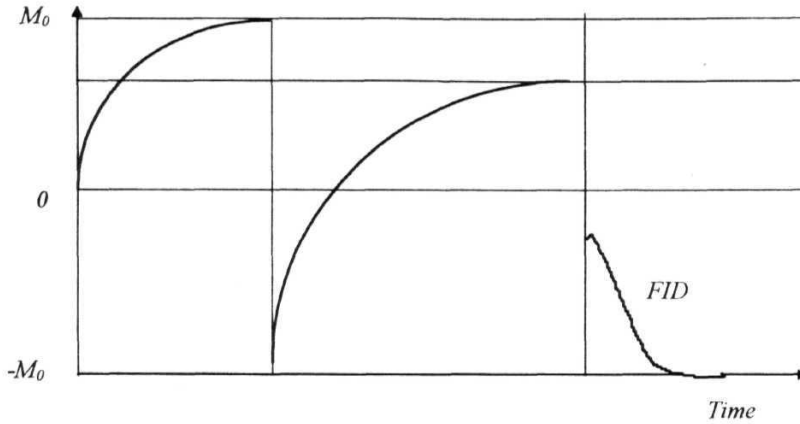
the variation of the magnetization is very less in case of the single pulse, saturation recovery sequence. To have the variation in the magnetization maximum, the first n pulse applied at the end of the polarization period, tilts the magnetization to $-\mathcal{M}_P$ and this evolves to the $+\mathcal{M}_E$ level with the evolution period. This pulse sequence is very useful when $+\mathcal{M}_E$ is close to $+\mathcal{M}_P$ and this has all the advantageous of the conventional inversion recovery sequence as long as the evolution field is not very low. This sequence is essential when the relaxation experiment is done at very low frequencies, i.e., very close to zero frequency. The experimental procedure with a typical situation where (the evolution field is close to the preparation field) this pulse sequence is very **useful**, is shown in the figure 1.11a. The same equation (1.28) is used to fit the FID amplitude with T_E , to get T_{1E} .



1.11a. Typical field cycle in the FCNMR version of inversion recovery sequence.



1.11b. Field cycling NMR version of inversion recovery pulse sequence.

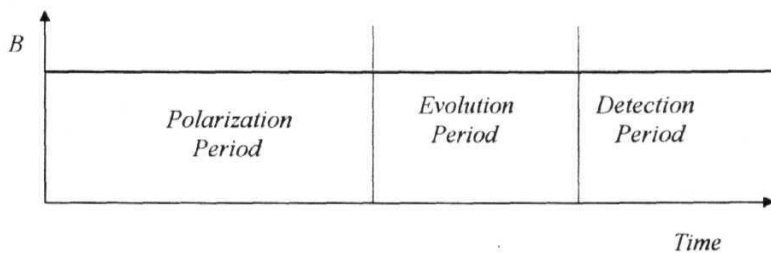


1.11c. Evolution of magnetization with time.

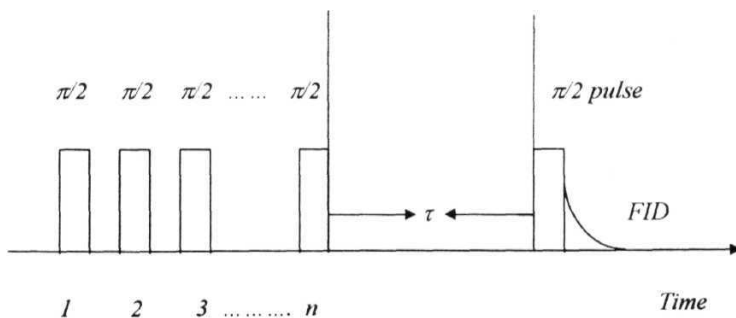
The advantages of conventional π - τ - $\pi/2$ sequence over $\pi/2$ - τ - $\pi/2$ is that the recovery has twice the dynamic range (M_o to $+M_o$) as compared to the saturation recovery sequence (0 to M_o). The demerit is that the sequence can be repeated only after a considerable time i.e., at least $5T_1$ time has to be spent in waiting for the magnetization to reach the equilibrium value M_o after the sampling $\pi/2$ pulse is applied. This is because, the next preparation pulse (π pulse) is expected to create a non-equilibrium situation which is possible only if $M_z = -M_o$. In the case of field cycling NMR version too, this waiting time is necessary. The main advantage of conventional saturation recovery sequence over the inversion recovery sequence is, for a given transmitter power, its spectral width which yields a better line shape and intensity for broad lines. The new equilibrium is decided by the evolution field in the case of FCNMR, which has an advantage in having the correct final magnetization as already mentioned, and overcoming the disadvantage of both of these conventional pulse sequences is that, of the preparation pulse width is not exactly set ($\pi/2$ or π), which is after the case, or if $H_1(t)$ is not homogeneous, the initial condition of the magnetization (0 or $-M_o$) is not met with, hence leading to reduction in the signal strength.

1.5.1.1.3. Saturation Burst Sequence

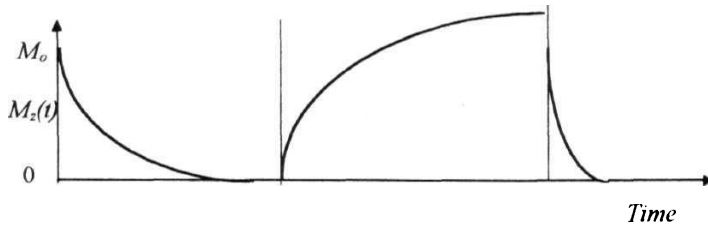
The demerits of the $\pi/2$ - τ - $\pi/2$ and π - τ - $\pi/2$ sequences can be overcome by using another pulse sequence called the *saturation burst sequence*. This is a version of saturation recovery sequence, which ensures the initial non-equilibrium condition corresponding to a situation (zeroing of the magnetization), even if the pulse width is not exactly set to $\pi/2$ or if $H_1(t)$ is slightly inhomogeneous. This sequence consists of a burst of closely spaced $\pi/2$ pulses (usually 5 to 10) for the preparation and is followed by a sampling pulse ($\pi/2$ pulse) after a variable time, τ as shown in figure 1.12.



1.12a. Zeeman field with time.



1 12b. Saturation burst A/pulse sequence.



1.12c. Evolution of Magnetization in the saturation burst sequence.

The spacing between the pulses in the burst is chosen to be greater than the spin-spin relaxation time (T_2), but much less than T_1 . The evolution of magnetization after applying the sampling pulse follows the equation

$$A(\tau) = A_o \left[1 - \exp\left(-\tau/T_1\right) \right] \quad (1.30)$$

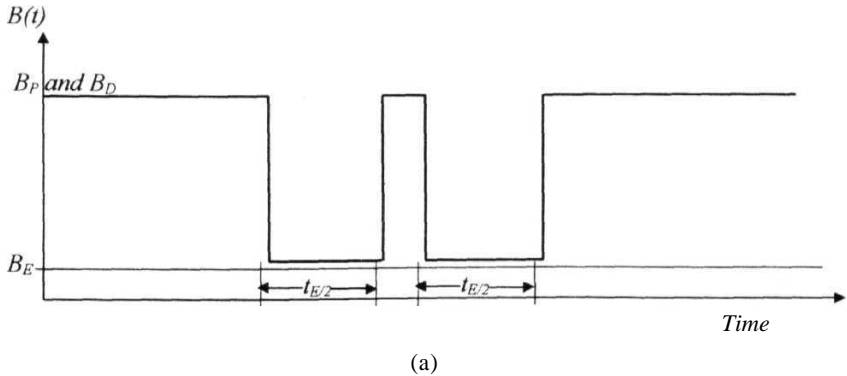
The other advantage of this sequence over the inversion recovery sequence is that the long waiting time ($>5T_1$) for long T_1 measurements is eliminated, as there is no need to allow the magnetization to recover fully before the sequence is repeated. In the actual experiments, the first pulse of the next burst can be used as the sampling pulse. This pulse sequence is used for T_1 measurements in the conventional NMR spectrometer.

1.5.2. Spin-Spin Relaxation time (T_2)

With the FCNMR technique, the transverse relaxation time, T_2 , can be measured using a similar procedure used in the conventional NMR, though this experiment can be effectively done only in systems having long T_2^* , which is possible only when $T_2 \cong T_1$. From the Bloch equation, the transverse nuclear magnetization M_{\perp} following the $\pi/2$ pulse, can be written as

$$\frac{dM_{\perp}}{dt} = \gamma [M(t) \times B_0] - \frac{M_{\perp}(t)}{T_2} \quad (1.31)$$

The relaxation time T_{2E} in the evolution period may be measured from the **FID** created by a $\pi/2$ pulse in the polarization period and sampled as a function of the time, T_E . But, a *spin echo technique* is a better option, due to the inhomogeneities in the Zeeman field. A typical *Carr-Purcell spin echo sequence* applicable with the field cycling procedure is given in figure 1.13, in which, shortly before the end of polarization period, the magnetization is flipped into the x-y plane by the $n/2$ pulse and the subsequent field switch changes the relaxation time from T_{2P} to T_{2E} . The n pulse which refocuses the dephasing spins is applied in the middle of the evolution period with a spacing $\Delta t = TE/2$.



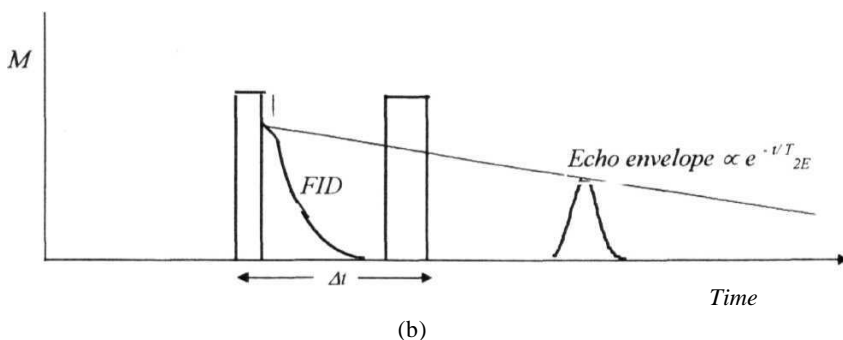


Figure. 1.13. Carr-Purcell spin echo sequence with FCNMR.

a) Zeeman field with time b). Carr-Purcell sequence and spin-echo

7.5.5. Adiabatic Demagnetization in the Laboratory Frame (ADLF)

Adiabatic demagnetization-remagnetization in rotating frame (ADRF) is one of the methods used in the conventional NMR relaxometry to study low frequency motions by measuring dipolar spin relaxation time, T_{1D} . This is done by transferring Zeeman order to the dipolar order and measuring the decay of magnetization. The pulse sequence shown in figure 1.14 is used to measure the dipolar relaxation time by demagnetization of//, following a spin locking pulse.

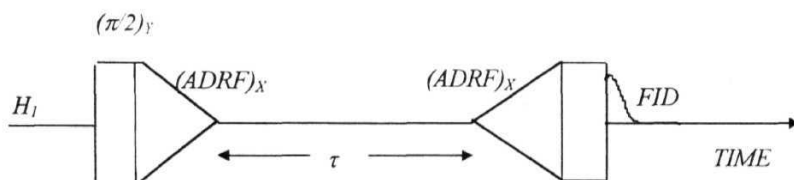


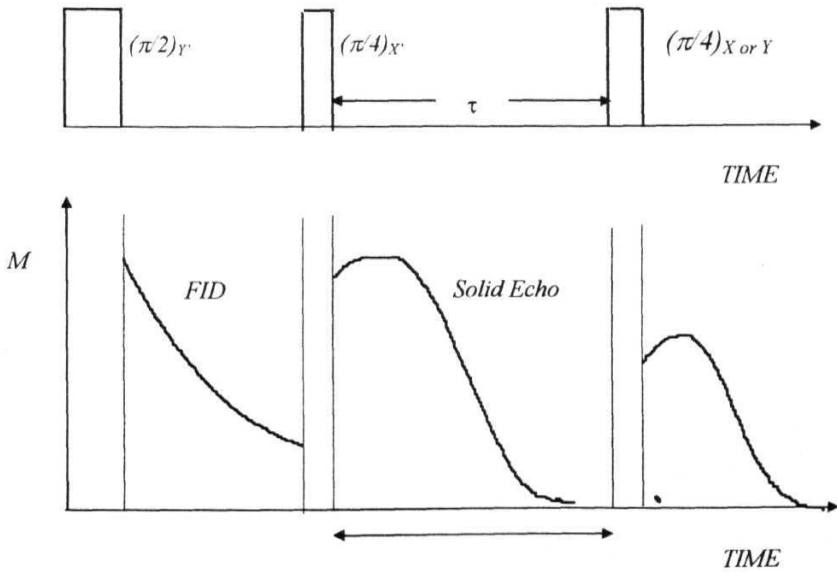
Figure. 1.14. Adiabatic demagnetization-remagnetization in the rotating frame (ADRF)

The first $\pi/2$ pulse tilts the magnetization from the z -axis to along x -axis. Immediately, a 90° phase shifted pulse corresponding to a field of H_{ap} is applied. This

field is adiabatically reduced to zero, by which the Zeeman order is transferred to a dipolar order. Then, after allowing the magnetization to decay in the dipolar fields for a time τ , the H_{app} is increased adiabatically back to the initial value. This converts the remaining dipolar order back to the Zeeman order, which is observed in the form of a FID following the turn-off of the rf pulse. This method is not useful when T_{ID} 's are less than 1 msec and hence another method proposed by Jeener-Broekaert [76] is used to measure T_{ID} .

1.5.4. Jeener-Broekaert pulse sequence $[(\pi/2)_Y - t - (\pi/4)_X - \tau - (\pi/4)_{X \text{ or } Y}]$:

In this method, two closely spaced pulses which are 90° out of phase are applied to transfer the Zeeman order to dipolar order, and the magnetization is transferred back to the Zeeman order, after evolution in the dipolar fields, using a third pulse in the x - y plane as shown in the figure 1.15.



1.15. Jeener-Broekaert pulse sequence and the magnetization [76]

By having both second and third pulses to be $\pi/4$, the maximum efficiency that can be achieved is about 56%. The phase of the third pulse can be anything because dipolar order is not aligned along any particular direction. But, to see the dipolar signal and not a FID after the third pulse, the receiver reference should be 90° out of phase with respect to the rf of the third pulse. Thus, the phase of the receiver is adjusted such that FID is maximum after the **first pulse**. Then, it is ensured that second and third pulses are 90° out of phase. An echo is observed after the third pulse, which is a measure of the remaining dipolar order. The decay of the amplitude of the dipolar echo as a **function** of the delay between the second and third pulses is given by

$$A(\tau) = A_0 \exp\left(\frac{-\tau}{T_{1D}}\right) \quad (132)$$

where τ is the variable time between the second and the third pulses. The third pulse is followed by a FID, which is 90° out of phase with the dipolar echo, while the second pulse is followed by the solid echo. Hence, for detecting the dipolar echo alone, it should be ensured that the reference signal to the phase sensitive detector is 90° out of phase with respect to the FID. In the actual experiment, phase of the reference rf given to the receiver is adjusted to maximize the FID following the first pulse and the third pulse is set to be 90° out of phase with respect to the first pulse. In addition, to maximize the echo, it is necessary to place the second pulse at the steepest part of the FID after the first pulse. The efficiency of this sequence in setting up the dipolar order is maximum when the second and the third pulses are 45° out of phase. The major disadvantage with this sequence is that its efficiency is only 56% whereas the efficiency of ADRF is 100%, but here, the pulsing technique is relatively simple.

In the field cycling procedure, there is no limit to the field variation rate with respect to the adiabatic condition as long as the field direction remains **unchanged**. However, at very low external fields the local fields caused by spin interactions begin to dominate the quantization field. The directions of these fields are randomly distributed. There are two possible choices in this situation. First, it is possible to vary the field adiabatically, so that dipolar or quadrupolar order is **produced**. This "adiabatic demagnetization in the laboratory frame (ADLF) method" is the field cycling

counterpart of the **Jeener-Broekaert** (J-B) pulse sequence and of the "adiabatic demagnetization in the rotating frame (ADRF) method". This frequency dependent study of T_{1D} on liquid crystals can be done between 10^3 to 10^7 Hz [38], with the aim of understanding collective director fluctuations (DF) through dipolar relaxation. The experimental procedure is shown in the figure 1.16.

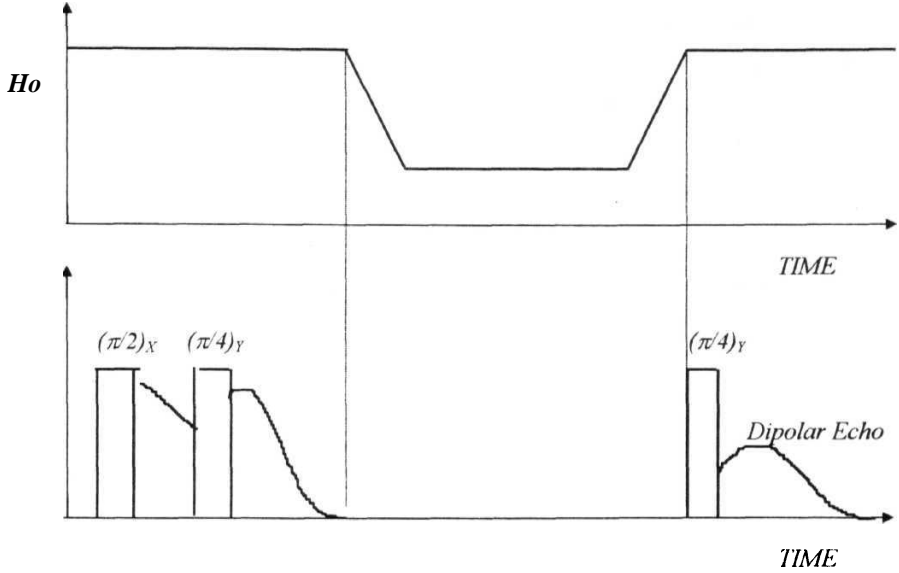


Figure. 1.16. Field cycling-adiabatic demagnetization in the laboratory frame (ADLF) Method [38].

This ADLF method is used to get frequency dependent dipolar relaxation times in liquid crystals and other complex systems at low frequencies, where dipolar energy relaxation measurements using the conventional J-B sequence becomes a difficult experiment for **Larmor** frequencies under 2 MHz. In low frequencies, the signal to noise ratio of the dipolar echo becomes smaller due to the poor spin polarization. The field cycling method becomes **useful** because, the polarization of the spin system and the **Zeeman** to dipolar order transfer is done at high magnetic fields. In this method, the polarizing magnetic field is switched *on* to acquire the dipolar echo.

7.5.5. **Spin-Lock**Adiabatic Field cycling Imaging Relaxometry (**SLOAFI**)

Field cycling NMR techniques like ADLF can also be combined with NMR imaging techniques so that the whole frequency range accessible, is probed at each transient. The imaging procedures can be of either laboratory frame (B_0 gradient) or rotating frame (B_1 gradient) variants. Using these methods, one can obtain spin-lattice relaxation times in the rotating frame under off-resonance conditions also [36]. Spin-lattice relaxation time in the rotating frame method (Figure 1.17) and its field cycling NMR counterpart will be discussed here. The relaxation process, where magnetization is allowed to evolve under the influence of the *rf* field in the rotating frame, instead of the Zeeman field, is termed as the spin-lattice relaxation in the rotating frame, with the corresponding time constant referred to as the spin-lattice relaxation time constant, $T_{1\rho}$. The methodology of such an experiment to measure $T_{1\rho}$ involves locking the spin system to a small //field, H_1 , in the rotating frame and observing the magnetization as it evolves from the initial equilibrium value corresponding to H_0 to the final equilibrium value corresponding to H_1 .

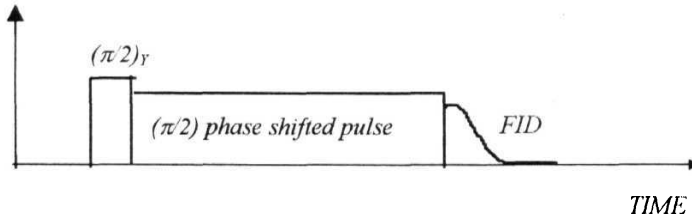
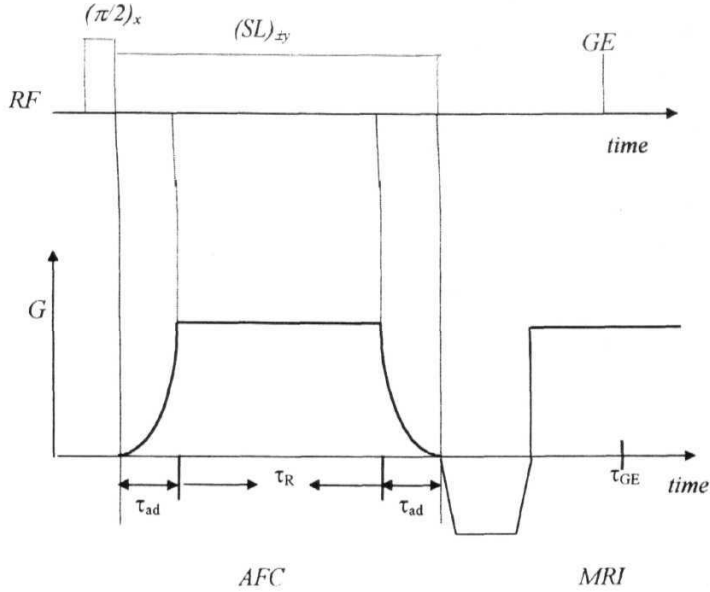


Figure. 1.17. Spin-lattice relaxation time in the rotating frame NMR method

The first $n/2$ pulse, flips the magnetization from the *z*-axis into the *x'y'* plane. The second 90° phase shifted pulse applied immediately after the first pulse of variable width, locks the spin system to H_1 since the *rf* field and the magnetization are in the same direction in the rotating frame. Now, the magnetization evolving in the presence of the rotating frame magnetic field is given by

$$A(\tau) = A_0 \exp\left(\frac{-\tau}{T_{1\rho}}\right) \quad (1.33)$$

where τ is the variable time for which the locking field is applied. Here, $A(x)$ corresponds to the amplitude of the FID after an evolution time T . By fitting the experimental data to the above equation (1.33), $T_{1\rho}$ can be calculated. The SLOAFI method [36] is useful for the study of spin-lattice relaxation in the rotating frame.



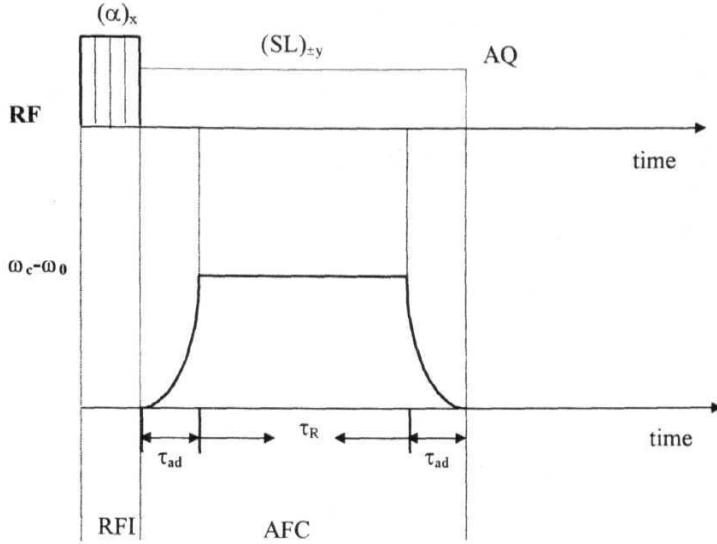
1.18. The pulse and field cycling procedure for lab-frame imaging relaxometry [36]

A 90° excitation pulse followed by a 90° phase shifted pulse is applied to make sure that the magnetization is spin-locked. At the beginning, the spin-lock pulse is resonant. The magnetic field-gradient pulse is then adiabatically switched **on**, so that the carrier frequency deviates from resonance depending on the position along the field-gradient direction. Depending on the position of the sample, the effective field is tilted towards the z -direction at angles other than 90° . The tilt angle thus becomes **a** function of the position in the sample. The adiabatic characteristic of **the** gradient pulse ensures **that the local** magnetization follows the effective field and remains spin locked at all instants. According to the applied field-gradient, the deviation from

resonance varies across the sample, i.e., in the interval τ_R , the spin-lattice relaxation is determined by the effective angular frequencies which are spatially distributed according to the field-gradient. At the end of the interval τ_R , the field-gradient is adiabatically switched **off**.

Thus, the local magnetization is brought back to resonant spin-locking at all positions within the sample. Depending on the duration of the relaxation interval TR and on the specially dependent effective angular frequency, the magnetization profile along the field-gradient can be **obtained**. To obtain an image of this partially relaxed magnetization profile, the free induction decay (FID) following the spin-lock pulse is refocussed and read in the form of a gradient echo. The one-dimensional image obtained after the Fourier transformation directly reflects the magnetization profile. These profiles for various intervals of τ_R incremented in subsequent transients permits the evaluation of the relaxation curves at different positions of the magnetization **profile**

The second method, is where the effective field is adiabatically cycled by modulating the carrier frequency of the spectrometer. Instead of a magnetic field (B_0) gradient, the amplitude of the *rf* field now is a function of the position (x coordinate of the laboratory frame, so that $B_1=B_1(x)$) for the spin-lock pulse as well as for the initial excitation pulse. Based on this B_1 gradient, the profile of the partially relaxed magnetization can be rendered as an image by combining *spin-lock field cycling* with the *rotating-frame imaging* procedure (Figure 1.19). The length or the amplitude of the initial excitation pulse is incremented in subsequent transients. The FID is then acquired as a function of the excitation pulse width and of the relaxation interval TR .



1.19. Spin-lock field cycling with rotating-frame imaging procedure (36).

The main advantage of the B_1 gradient Spin-Lock Adiabatic Field cycling Imaging Relaxometry (SLOAFI) technique is that the FIDs are recorded in the absence of field-gradients. That is, the full spectroscopic information is preserved. The rf frequency can be varied freely in a programmable way. Fringe field of a solenoid rf probe coil can be used as a source of B_1 gradients as they are used in standard NMR probes. Other probe geometries such as cavity detectors or coaxial resonators are also of interest in this context [36].

There are so many attempts to incorporate almost all NMR features into FCNMR in the recent past [37]. A doubly rotating frame field cycling method is being used by Krushelnitsky et al., [39] to study slow protein dynamics, by averaging of the local magnetic field by means of magnetization rotation under the magic angle condition and in this way much slower motions become accessible. In this method, two fields are simultaneously applied to the nuclear system, one is the standard B_1 , and the other a weak field B_2 . The latter is created by phase modulation of B_1 , and the

depth of this modulation defines the resonance frequency in the doubly rotating frame. The relaxation time measured in this way contains information on spectral densities of motion at two resonance frequencies, ω_1 and ω_2 . The latter can easily be **changed**, by varying the depth of phase modulation of the field B , field within the range 200 Hz to 10 Hz. This relaxation time is sensitive to the motion of the three nuclei with respect to each other, whereas the standard relaxation is defined, by a pair-wise nuclear interaction.

Using the fast field cycling method, Pusiol et al., [40], have studied Nuclear Quadrupole Double Resonance in liquid crystals. The experiment involves fast field cycling NMR of protons, together with the irradiation of the quadrupole ^{14}N nuclei by means of a second *rf* pulse just during the period of zero-magnetic field. As the dipolar interaction between protons and nitrogens is quenched at zero field, the spin-mixing by level crossing procedure (LCNQDOR) was used. This LCNQDOR procedure combines electronic fast field cycling and two **different** radio-frequency excitations of the sample. The experiment consists of three phases as given below [40]

- Polarization of the field with high magnetic field at lattice temperature.
- Irradiation of quadrupole transitions at zero-field, where the external field is adiabatically switched off, and an allowed ^{14}N quadrupole transition is irradiated with a pulsed *rf* with a frequency matching with quadrupolar splitting.
- Detection of the proton NMR signal, after increasing the magnetic field to the high detection field level. During raising and lowering of the external field, all ^{14}N quadrupole transitions are "level crossed" by the Zeeman splitting, and the thermal contact between the different spin systems takes place and polarization is transferred from one spin system to the other which leads to the "quadrupolar dip" in the proton NMR signal.

Struppe et al., [41] have studied deuterium nuclear quadrupole resonance dips in the proton spin relaxation dispersion of deuterated liquid crystals. Recently, there were efforts [42,43] to combine the sensitivity of X-band EPR and the resolution of zero-field EPR by field cycling spectroscopy, with excitation of transitions between

splittings in the zero field and detection in the high field. The pulsed version of this is called "pulsed field cycled ENDOR spectroscopy".

1.6. The requirements and demands for the FCNMR Spectrometer

The following requirements and demands for optimization of the switchable magnet (Field Cycling Network), which is essential for a good FCNMR spectrometer, are kept in mind while building such a facility under this Ph. D project.

1. The limit on homogeneity and transit times depends on the type of systems under investigation i.e., liquids have smaller line widths and hence require more homogenous fields. On the other hand, solids require an enhanced B_0 and dB/dt , with a moderate homogeneity since they have larger line-widths. The transit times must be shorter, compared to relaxation times but longer, compared to the Larmor frequency. The polarization field should be sufficiently high for good initial magnetization. The detection field should be sufficiently high and homogenous to ensure good S/N. The maximum induction and the rate of change of the induction must be optimized simultaneously. Keeping these factors in view, a field cycling network [74] with necessary electronic circuits to control and switch the field is designed, the details of which are given in chapter-2.

2. Various pulses required in implementing field cycling technique (during the periods of switching, evolution, compensation and detection periods) should be effectively synchronized with the pulses used in producing high power *rf* pulses, for the manipulation of the macroscopic nuclear magnetization of the spin system.

3. Efficient handling of the drift in the detection magnetic field (over the period of an experiment) by effective cooling of the magnet and the electronic circuitry.

4. Construction of a receiver, which could provide good S/N and shorter dead time at relatively low Larmor frequencies (in the present case the detection is done at 3-4 MHz). As the signal strength varies from $\omega^{1.5}$ to ω^2 , as a function of the detection field,

signal to noise ratio (S/N) becomes very unfavorable at lower frequencies. It is therefore, difficult to detect the proton NMR signal in magnetic fields below 0.1 T (resonance frequency of about 3 MHz) due to very weak nuclear induction and the acoustical ringing induced in the NMR probe at these **frequencies**. Moreover, it is difficult to produce short, high power *rf* **pulses** at frequencies in the low MHz range to detect nuclear induction signals from solid and liquid crystal phases, which have relatively short transverse relaxation times (T_2), which is related to the quality factor (Q) of the NMR probe which is decreased significantly at lower **frequencies**.

5. Temperature control facility, which could effectively work under the constraints such as small magnet bore and magnet heating (due to the magnet power dissipation). The design of a cryostat set up and temperature control circuitry, to handle this situation is very crucial.

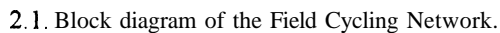
2.1. Introduction

Fabrication of a fast switchable, drift free Field Cycling Network is the crucial part of the FCNMR instrumentation. Apart from the usual specifications of a NMR magnet, such as maximum induction, homogeneity and stability etc., a field cycling NMR magnet is characterized by an additional feature i.e., the geometry of the coil, which enable fast switching. The highest obtainable field $(B_0)_{max}$ and the maximum rate of change of induction $(dB/dt)_{max}$ characterizing the induction coil are inter-dependent through the coil parameters like inductance, permeability, volume, etc. The optimization of all these parameters and the details of the fabrication of the field cycling network would be discussed in this chapter.

The most important concept used in the FCNMR instrumentation is called, "energy storage principle", first introduced by Redfield [11], which is implemented using 'energy storage capacitor network' and a 'MOSFET switch'. The important sub units used are listed below.

- An induction coil capable of fast switching.
- A power supply having variable current and voltage capabilities, to energize the magnet (N_1).
- Decoupling diodes (D 's), capable of handling high currents and voltages.
- A control circuit (*controller*) with various options.
- A current driver circuit using MOSFETs (20 MOSFETs with independent gate drivers).
- An energy storage capacitor network (C).
- A precharging power supply for energy storage capacitor network (N_2).

- The block diagram of the 'field cycling network' comprises all these units, which is used to control and switch the current through the magnet is given in figure 2.1.



42

necessary feedback to the controller. The action of the energy storage capacitor network, C (five capacitors in parallel, CSI Capacitors, 100 μ F, 2 KVDC, Part No. 2W365TN) is enhanced by precharging, with the help of an additional power supply N_2 with negligible current demand (1200V/1Amp, APLAB make, No. 7323), so as to provide extra driving power required during the transits. The charging diode D_2 allows the charging of the capacitor network C, and also decouples the coil from the source N_2 , during the transits. The free wheel diode D_3 (Nihon model No: 45MLA120), provides a path for current during the turn OFF interval, where the excess energy available across the coil is transferred to the capacitor. The diode, D_3 (45MLA120) provides a path to the current during the turn OFF interval as explained below. The MOSFET switch (1RFPG40) with an opto-coupler (TIL 113) based gate driver circuit provides the current path during the transit from low to high field.

2.2. Induction coil

Maximum Induction Vs. Fast Switching (Optimization of B_0 and dB_0/dt)

A high magnetic field requires high inductance (high coil volume) and high current density, which are also the basic constraints in achieving the faster switching times, since the switching times depend on the coil volume and it should be very small for fast switching. Small resistive, high-field magnets stipulate a good cooling efficiency. In overcoming these difficulties, various new technologies such as superconducting magnet coils [45], liquid-nitrogen cooled resistive coils are generally used. But, these cryogenic designs have their drawbacks due to the handling problems and larger consumption of coolants. Some of the latest instruments use high-pressure oil-cooled copper magnets optimized for the circulation properties of the cooling medium as well as for the spatial distribution of the current density [46-49]. So, it is important to achieve homogeneous high field for a good signal sensitivity, shorter switching times for experimental accuracy of spin-lattice and spin-spin relaxation time measurements. Of the various geometries for the design of the induction coil available in the literature [11,13,51-55], the Helmholtz ring pair and cylindrical geometries (Figure. 2.2) are rather well known. Although, the Helmholtz ring pair arrangements, has an advantage of well understood mathematics and a convenient radial access to the

center, it is limited by the marked reduction in the induction at the center of the coil compared to that near the windings. Further, good homogeneity is limited to a relatively small area around the center. In this respect, cylindrical coils are found to be superior to Helmholtz ring pairs with regard to many specifications like maximum induction, homogeneity and total field volume, since, for a given volume, cylindrical geometry provides a better B_0/I ratio. However, the inconvenience of having only axial access to the field (at the center) is a disadvantage to be accepted with the above advantages. Due to the above reasons, in the present case a cylindrical geometry [74] is chosen.

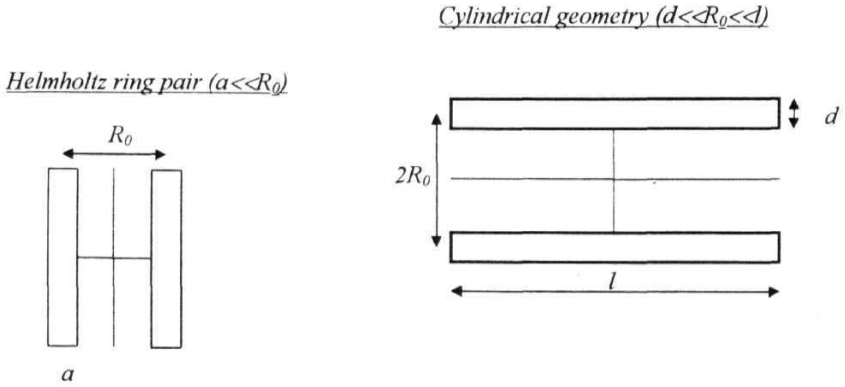


Figure. 2.2. Different geometries of the NMR magnets.

Optimization of both these parameters, B_0 and dB/dt , necessitates the critical consideration of the relationship between them. Due to the large number of parameters involved, an empirical approach (involving standard formulae on the magnetic field for different geometries) is usually adopted during the construction of an FCNMR magnet [12,25,74]. The induction along the axis of a long solenoid of length l , radius r and number of turns n in a medium of permeability μ is given by

$$B_0 = \mu H_0 = \mu \frac{n}{l} \left[1 + \left(\frac{r}{l} \right)^2 \right]^{-\frac{1}{2}} I \quad (1.34)$$

where I is the current through the coil. The rate of change of current through the coil, dI/dt , for an applied voltage ' U ' is given by the Faraday's law of induction as

$$\frac{dI}{dt} = \frac{U - I R_s}{L}$$

where R_s is the series resistance and L is the inductance of the coil, given by

$$L = \frac{\mu n^2 \pi r^2}{l} \quad (1.36)$$

The above equations 1.34 to 1.36 clearly indicate that B_0 and dB/dt cannot be optimized independently since maximization of one, changes the other. Thus, a compromise has to be laid down between them, for efficient switching. Equations 1.34 and 1.35 can be rewritten in terms of the volume V of the coil and inductance L as

$$B_0|_{\max} = \sqrt{\frac{\mu L}{V}} I \quad (1.37a)$$

$$\left. \frac{dB}{dt} \right|_{\max} = \sqrt{\frac{\mu}{VL}} U \quad (1.37b)$$

from these two equations,

$$\left(B_0 \right)_{\max} \times \left(\frac{dB}{dt} \right)_{\max} \approx \frac{\mu}{V} \quad (1.38)$$

Analysis of this equation shows that it is not possible to produce higher magnetic fields with fast switchable properties in a simple way. It also shows simultaneous maximization of B_0 and dB/dt depends on the effective volume V of the coil, and the permeability μ of the core material used, and is independent of other quantities, and hence lays restrictions on coil volume. The obvious choice thus, is to maximize both the quantities simultaneously i.e., $(B_0)_{\max} \times (dB/dt)_{\max} \sim \mu V$, where V is the **effective** volume enclosed by the coil. Thus, a good field cycling NMR coil should be very small and filled with magnetic material of large permeability (in the regions not occupied by the **sample**) However, both aspects are bound by mathematical and

technical problems, which are **complicated**. For example, the choice of the magnetic material is limited since ferromagnetic materials are completely inadequate due to poor **frequency** response and hysteresis effects, while **ferrimagnetic** materials are **not** very promising due to their **low $\mu (B_0)$** saturation [12]. Similarly, reduction of volume is limited by the technical requirements on the cooling facility and also a minimum size of the sample and cryostat required for temperature variation **measurements**.

2.2.1. Homogeneity with outer notches

Other important NMR specifications, after achieving the required fast switchable field, are homogeneity over sample and stability of the magnetic field over experiment time. After choosing the cylindrical configuration for the magnet coil, it is also important to have a sufficiently long coil for better homogeneity. It is very difficult to handle very long magnets, and hence short magnets with suitable refinements were suggested for improved field homogeneity in the literature [56-58]. Grossel et al., [47] have added 'outer notches' to the induction coil for better homogeneity at the sample coil, which has the advantage of providing accurate field values in a considerable volume around the center of the solenoid. A home-built induction coil with an efficient cooling facility [74], following the Grossel et al., method [47] is used in the fabrication of the field cycling network. The geometrical parameters of the coil optimized for good homogeneity is shown in figure 2.3a. The geometrical parameters are denoted as $\alpha = R_o/R_i$, $\beta = l/2R_i$, $\eta = l_k/l$, and

$$R = \frac{1}{2}(\alpha + 1)R_i,$$

is the mean radius and C is the layer thickness given by $(\alpha - 1)R_i$. The relative axial and radial variables are $x = l_o/l$ and $y = R_o/R_i$. This procedure consists of optimizing the quantity $B \times dB/dt$ for a given peak input power. The solutions of the elliptic integrals obtained [47] result in the switching time, being proportional to the square of the flux density

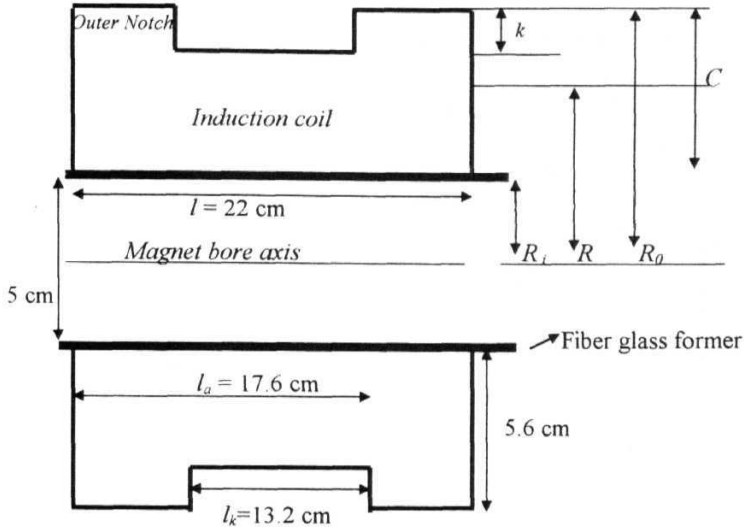


Figure. 2.3a. Geometrical parameters and dimensions of the magnet [47]

The inductance of the coil is 66 mH with a resistance of 7 ohms. Outer notches consist of 352 windings of the copper wire, which include in the total number of 2552 windings [74]. The maximum magnetic induction of 0.15 Tesla can be obtained with current about 10 A. With the above specifications an induction coil was built (by Electromagnetic Devices Private Limited, Hyderabad, India). The coil is kept in the oil bath, which is cooled by chilled water flowing through the oil bath. Copper tubes are used for circulation of water. The overall view of the magnet is shown in figure 2.3b.

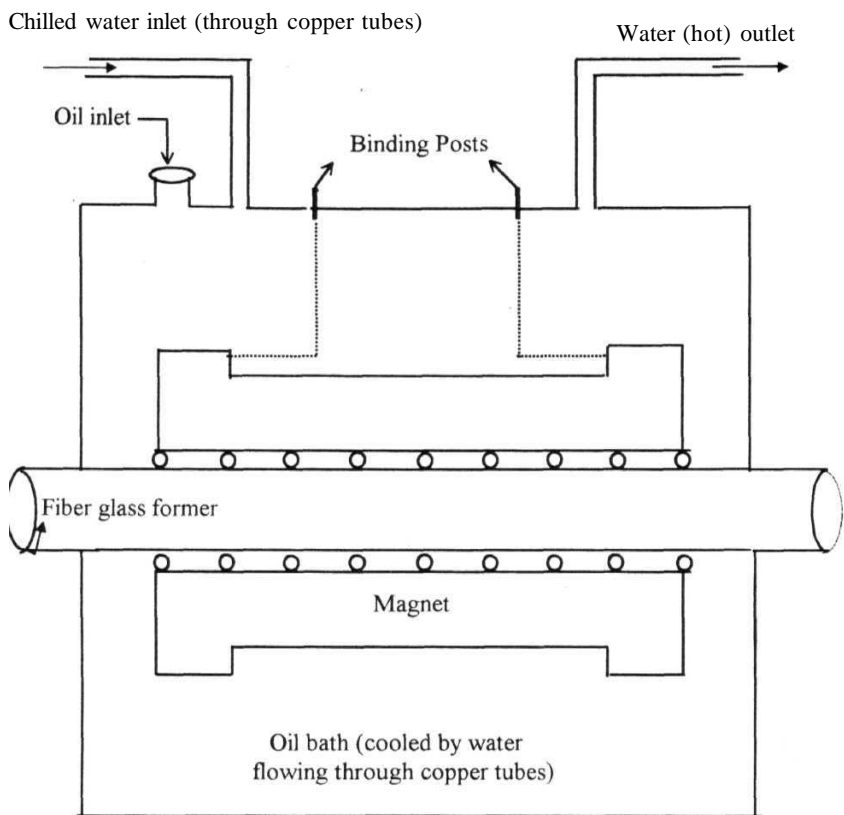


Figure. 2.3. Overall view of the magnet with cooling arrangement [74].

2.3. Switchable magnetic field

2.3.1. Without the energy storage principle

The basic switch characteristics of the fast field cycling network are determined by the efficiency of the switching and controlling circuits available. The very first attempt was made by Packard and Varian [60], and by Bloom and Mansir [60], much before the very famous contribution of Redfield et al., [11]. The basic form of the circuitry [12] is shown in figure 2.4, which facilitates the switching between two different levels, by means of some switch, that may be a relay, a thyristor or a transistor.

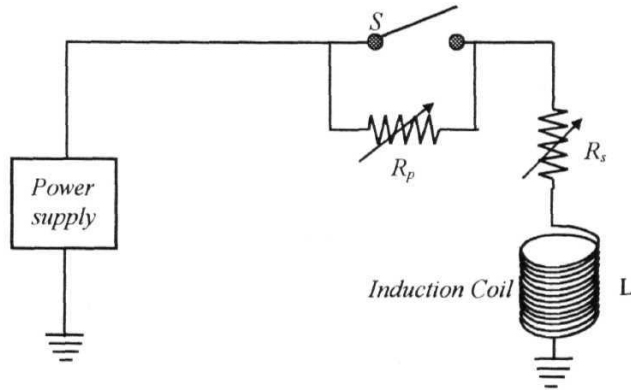


Figure. 2.4. Basic magnetic field switch.

The power supply generates two current levels in the coil of inductance L and a series resistance R_s , through a switch S and adjustable parallel resistance R_p . The sum $R_p + R_s$ determines the lower level of current, I_{min} , while R_s determines the upper level of the current, I_{max} . Initially, when the switch S is closed, the parallel resistance R_p is

short circuited by S , and therefore, the voltage “ U_0 ” applied to the coil increases the current (7) with a time constant,

$$\begin{aligned} T_{on} &= \frac{L}{R_s} \quad \text{i.e.,} \\ U_0 - L \frac{dI}{dt} &= IR_s \end{aligned} \quad (1.39)$$

By solving the equation 1.39 with the suitable initial condition [12], the following equation (1.40), is obtained for the exponentially increasing current in the coil.

$$I_{on}(t') = I_{\min} + [I_{\max} - I_{\min}] \left(1 - \exp\left(-\frac{R_s}{L} t' \right) \right) \quad (1.40)$$

where the initial condition is given by,

$$I(t' = 0) = I_{\min} = \frac{U_0}{R_s + R_p} \quad (1.41)$$

and the maximum possible current, in the absence of parallel resistance is

$$I_{\max} = \frac{U_0}{R_s} \quad (1.42)$$

Similarly, when the switch S is open, the voltage across the coil decreases with a time constant

$$T_{off} = \frac{L}{R_s + R_p} \quad \text{i.e.,} \quad U_0 - L \frac{dI}{dt} = I(R_s + R_p) \quad (1.43)$$

And by solving the equation 1.43 it is possible to obtain [12],

$$I_{off}(t'') = I_{\min} + [I_{\max} - I_{\min}] \exp\left(-\frac{R_s + R_p}{L} t'' \right) \quad (1.44)$$

with the initial condition,

$$I(t''=0) = I_{\max} = \frac{U_0}{R_s} \quad (1.45)$$

From these equations, it is clear that the transit times are shorter for larger values of R_s and R_p and smaller values of L . The increase in the values of R_s and R_p are limited by the fact that, the increase in R , beyond a point results in an enormous increase of supply voltage (for a given maximum current), and an increase in R_p fails to

suppress the excessive voltages induced due to the sudden decrease in the current during turn OFF. So, it is clear from the ON and OFF characteristics that, though the equilibrium state is reached faster for higher values of R_s and R_p , the fastest rate of increase or decrease of current are independent of R_s and R_p , since

$$\left| \frac{dI}{dt} \right|_{\max} = \left| \frac{U_0}{L} \right| \quad (1.46)$$

The ON and OFF current characteristics of the coil, for certain magnitudes of R_s and R_p are shown in the figures 2.5a and 2.5b [121].

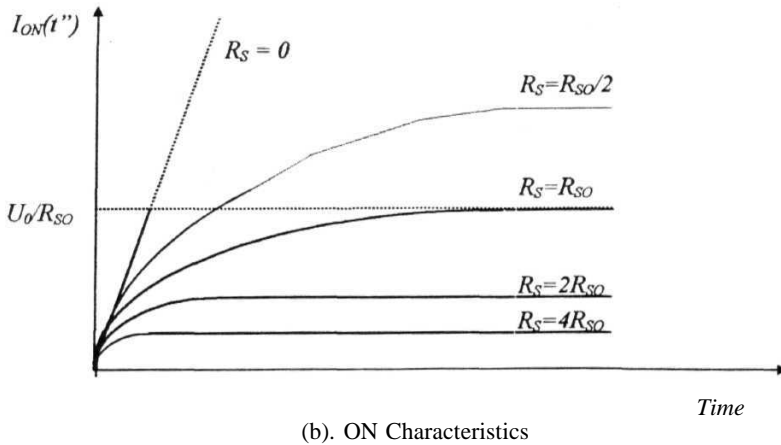
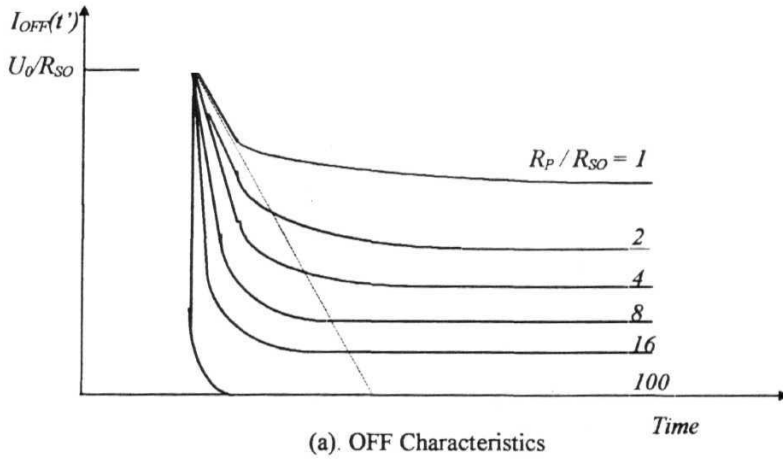


Figure. 2.5. ON/OFF current characteristics of the induction coil. R_s and R_p are measured in arbitrary units R_{so} , which is the reference.

From the equation (1.40) for I_{on} , the damping time constant (τ_{on}) for ON time can be defined as

$$\tau_{on} = \frac{L}{R_s} \quad (1.47)$$

Similarly from the equation (1.44) for I_{off} , the damping time constant (τ_{off}) for OFF period can be written as

$$\tau_{off} = \frac{L}{R_s + R_p} \quad (1.48)$$

The equation for the ratio of the transit times can be obtained from the equations 1.47 and 1.48 as

$$\frac{t_{off}}{t_{on}} = \frac{\tau_{off}}{\tau_{on}} \left[\ln \frac{1}{\varepsilon} + \ln \left(\frac{I_{max} - I_{min}}{I_{max}} \right) \right] \quad (1.49)$$

where ε is the accuracy of current with which one can attain a new state in times τ_{off} and τ_{on} given by

$$\varepsilon = \frac{|I(t) - I(\infty)|}{I_{max}} \quad (1.50)$$

The typical s value ranges from 10^{-7} to 10^{-5} and $\ln(1/\varepsilon)$ runs from 9.2 to 13.8 for the required FCNMR standards [12]. The second term in the equation 1.49 becomes zero when $I_{min}=0$. Handling the OFF switch is easier than the ON switch, because of the larger resistances involved in τ_{off} compared to τ_{on} . From the relation, $\tau_{on}=L/R_s$, for any fixed value of L , lowering the value of R_s can be regarded as the proper choice, to shorten the ON interval. It is also known that lowering the value of L is very important for any switching. So, it is important to replace iron-core magnets with air-core magnets having small L values. Hence, more sophisticated concepts than simple resistance and inductance adjustments should be taken into consideration in order to reduce the transit intervals.

2.3.2. With the energy storage principle

The total energy (ET) required for different loads of the field cycling network during the high field interval is composed of two parts, 1. The magnetic field energy (E_L) due to inductive load of the coil, and 2. The energy dissipated in the form of Joule losses in the resistor (E_R), so that

$$E_{Tot} = E_L + E_R \quad (1.51)$$

with

$$E_L = \frac{1}{2} L I_0^2 \quad (1.52)$$

and

$$E_R = \int_0^{t_{on}} R_s I^2(t) dt \quad (1.53)$$

It is very important to lower the value of E_R , to reduce the Joule heating. It is also known that [12] the energy storage principle demands $E_R < E_L$, for fast switching properties. These requirements necessitate lower ER . It is very crucial to remove the magnetic field energy from the coil during the turn OFF interval, since there is no way to transfer the energy back to the energy source. The other alternative is to dissipate it in the circuit elements. The provision of the energy storage capacitor requires transformation of such magnetic energy of the coil (E_L), into electrostatic energy (E_C). In this process voltage transients (surges) would be expected, which can damage the components of the switching circuit and the induction coil. The solution for this problem would be discussed later.

Apart from the energy storage principle, there are other methods used in implementing the switching of magnetic field to various levels, such as, the **RLC** network with an oscillatory mode, which has a similarity to the energy storage principle. The RIX makes it possible to control the changeover from one current level to another by adjusting the **capacitance**. Adding and enlarging the capacitive component shortens the transit times. The details of this are given by Noack [12]. Later, most of the experimentalists utilized this technique in building fast field cycling

NMR spectrometers. Kimmich [36] had used a cascade circuit to produce a high voltage required to switch ON the magnet. Blanz et al., [46] have used a combination of FETs and Darlington transistors, for switching. A commercial, constant voltage source is used [46], with the external MOSFET current control circuitry, which essentially is the current source. Therefore, the components should be chosen keeping these high voltage transients in mind. Free wheeling diode, Ohmic resistor, transient absorbing Zener diode and voltage dependent resistor are some of the possible solutions recommended in the literature [61-65].

Rommel et al., [13,46] had introduced a modification to store the energy released during switching also. In this case, the additional energy source, used to pre-charge the capacitor, takes care of the Ohmic losses. Rommel's [13,46] modifications using MOSFETs were successfully implemented by Schweikert [25] by parallelly connecting them with independent gate drivers. The switching times are further reduced by precharging C through a power supply P_2 . Other concepts [12] like the 'cryomagnet limit' with linear $I(t)$ characteristics and, the 'current and voltage dependent resistors', basically deal with the resistance of the induction coil, whereas "the energy storage principle", is connected with the power supply, used to energize the coil.

The energy storage principle leading to an increased slope in $I(t)$ characteristics is explained here, before describing the details of the present setup. Considering the energy transfer from the power supply to the inductive load, it is clear from the equations 1.39,1.40,1.43, and 1.44 that, the total available power is dissipated in the circuit elements only during high fields of the polarization and detection periods. During the evolution period and transits, this power is not utilized. This redundant energy which can be defined by

$$E_{red} = \int_0^T [P_0 - P(t)]dt \quad (1.54)$$

where,

$$P_0 = I_0 U_0 \quad (1.55)$$

is the total available power during high fields and

$$P(t) = I(t) U_0 \quad (156)$$

is the power dissipated during low evolution period, which can be stored using suitable storage capacitors instead of dissipating it in the circuit elements, such as damping resistors. This stored energy can be recycled to accelerate the switching speed. The voltage developed due to this redundant energy can be defined by

$$U_c = \left[\frac{2}{C} \int_0^t [P_0 - P(t)] dt \right]^{1/2} \quad (157)$$

This voltage U_c available across the capacitor, added with the supply voltage U_0 in the interval $0 < t'' \leq t_{on}$ is used to get shorter ON times, according to the equation [12]

$$I_{on}(t') = I_{min} + \left[\frac{U_0 + U_c}{R_s} - I_{min} \right] \left[1 - \exp\left(-\frac{R_s}{L} t'\right) \right] \quad (158)$$

Similarly inverting the driving voltage $U_0 + U_c$ for the period $0 \leq t' \leq t_{off}$ has similar **effect** on OFF time, which leads to the equation

$$I_{off}(t'') = I_{min} + \left[\frac{U_0 + U_c}{R_s} - I_{min} \right] \left[1 - \exp\left(-\frac{(R_s + R_p)}{L} t''\right) \right] \quad (159)$$

These effects with energy storage, and without the energy storage capacitor are shown in the figure 2.6 and 2.7.

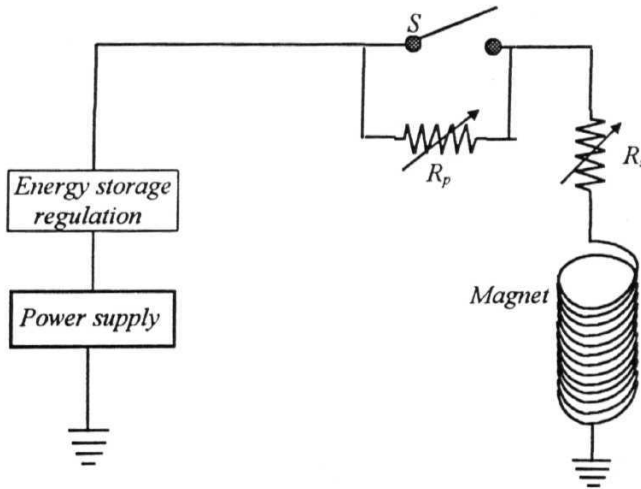


Figure. 2.6. A simple magnetic field switch with energy storage capacitor.

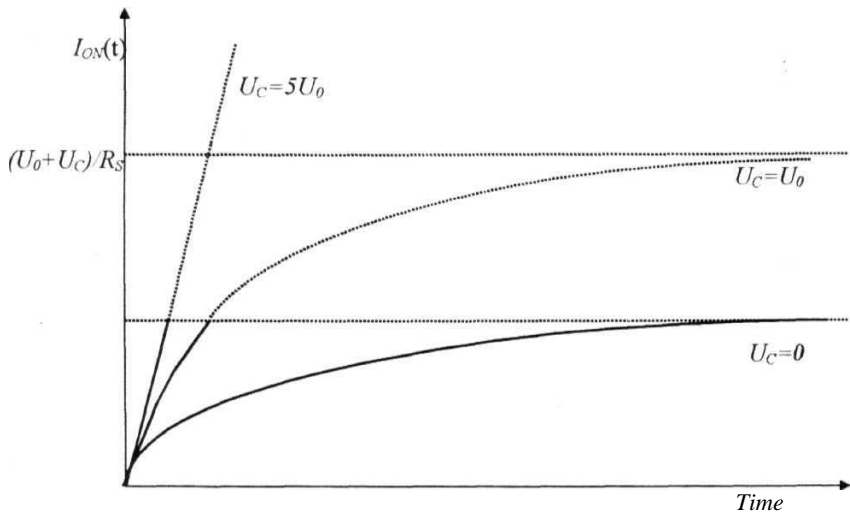


Figure. 2.7. Switch ON characteristics with Energy Storage Capacitor [12].

The new current characteristics shown in figure 2.7 are not only advantageous in reducing the ON time but also increase the maximum possible detection field. Inclusion of a pre-charging power supply improves the function of the instrument, which can be understood with a simple analysis [12,25]. It is also considered here, the case in which a precharging power supply is used to keep the energy storage capacitor voltage above some minimum value rather than zero voltage, before storage is started by diverting the excess energy available in the magnet. So, the components involved in the voltage balance equation are the inductance L of the magnet, the Ohmic resistance R of the circuit and the magnet, the storage capacitor with capacitance C , and a precharging power supply. Now, the balance equation applying Kirchhoff voltage rule is given by

$$L \frac{dI}{dt} - LI_0 + \frac{1}{C} \int_0^t I dt - U_c + RI = 0 \quad (1.60)$$

where, I_0 is the value of the initial current / and U_c is the precharged voltage over the storage capacitor. Electrical current as a function of time can be computed using the equation

$$L \frac{d^2 Q}{dt^2} + R \frac{dQ}{dt} + \frac{Q}{C} = U_C + LI_0, \quad (1.61)$$

where Q is the charge. This equation 1.61 can be solved to get the electrical current as a function time, using the Laplace transform method [44] Inserting component values as inputs and considering initial precharged voltage of the capacitor U_C , and the initial current values, it is possible to calculate electrical current as a function of the time for a low to high transit interval. Similarly, by inserting the initial values one finds the current characteristics for a high to low interval in a quantitative manner. The pre-charged value of the voltage is an important factor that controls the function of the energy storage principle in a more refined way and hence, achievement of higher currents is made possible.

Implementing the energy storage principle has technical difficulties due to the high voltages developed across the energy storage capacitor and subsequent application of such high voltages in the circuit. It is very difficult to stop the suddenly increased current at a preselected level, with a stability of NMR experimental requirements This needs a control signal with 'compensation' for overmodulation. The details of the controller and the compensation, which solve these problems, would be discussed later in the following sections.

2.4. Current switching and control devices

The crucial units made up of electronic circuits and modern semiconductor devices, used in the fabrication of the 'Field Cycling Network' are listed below and shown in the figure 2.8.

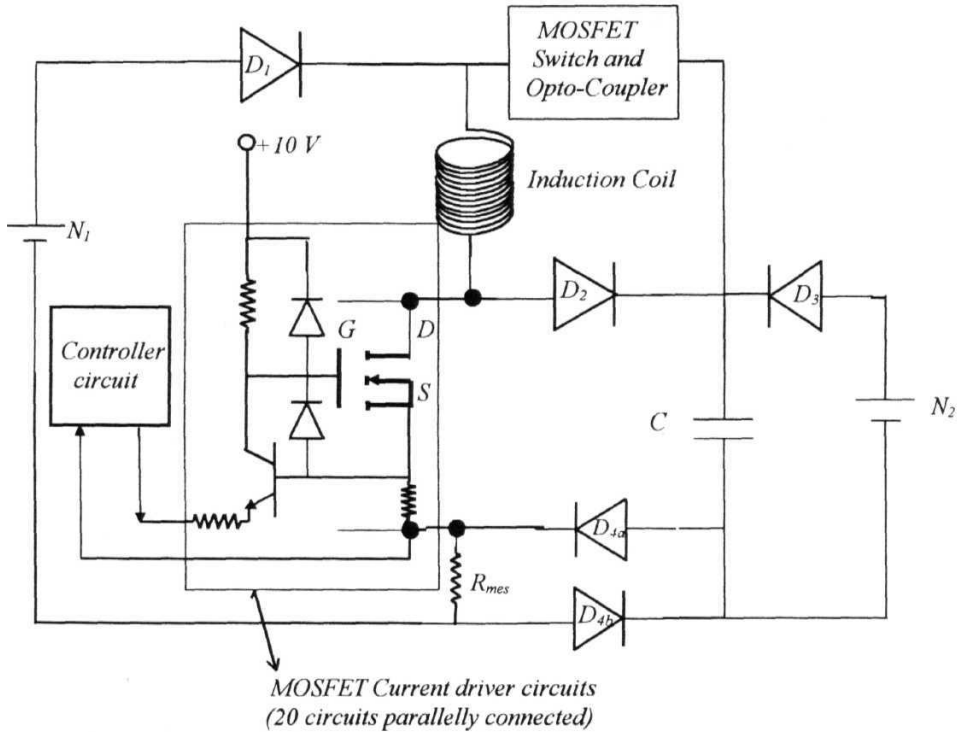


Figure 2.8. Interconnection details of the sub-units of the Field Cycling Network.

1. The *controller circuit* gives the required control signal to the gates of the MOSFETs, which are capable of controlling and switching high currents.
2. 20 independent *gate driver* circuits used to drive the gates of 20 MOSFETs, in order to avoid the oscillations due to mismatch in the behaviors of the MOSFETs.

This network of MOSFETs and their gate drivers are used to control and regulate the current through the **magnet**. It is termed as the '*current driver circuit*' in this thesis.

3. MOSFET *switch* with an *opto-coupler* based *gate driver* is used to switch the energy storage capacitor, *in* and *out* of the field cycling network, in order to facilitate the application of the energy storage principle. It is also useful in isolating the high voltage capacitor stage from the low voltage components, such as the controller and the current driver circuits.

Apart from these major units, various diodes called decoupling diodes (D_1 and D_3), free wheel diode (D_2), high voltage (2000V) high capacitance ($500\mu F$) capacitors (C), power supplies (180V, 25A, APLAB make) for energizing the magnet (N_1) and a 1200V power supply (N_2) for precharging the energy storage capacitor network, pulse amplifiers built using operational amplifiers (OP27), a MOSFET switch, home made pulse generators and commercial delay generators (EG&G make) are used in the fabrication of the field cycling network.

2.4.1. *Controller circuit*

A special power regulating system is required in order to achieve a drift-free, modulation-free control of current passing through the induction coil. Since the current regulation is done by the 'MOSFET current driver' circuits, it is very important to give a perfect gate input signal to the MOSFETs. This gate input is obtained with the help of the gate driver circuits. Depending on the Larmor frequencies of operation, a dynamic regulation of $1:10^5$ is required, i.e., in the present case the accuracy required is about a few mA when the maximum current is about 6 to 10 A. The control signal driving gates of the MOSFETs is achieved using a PID type (Proportional, Integrator, and Differentiator) controller circuit. The PID type controller used by Schweikert [25] is modified and used here to realize an overmodulation-free, drift-free current regulation. This controller circuit acts as an interface between the user and the high voltage, high current circuits of the field cycling network. The block diagram of the controller circuit is shown in figure 2.9

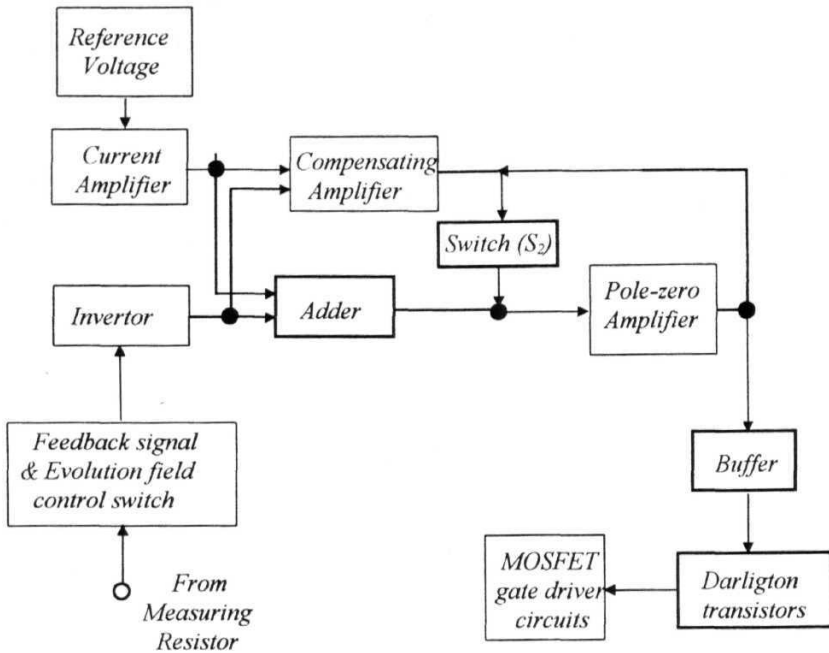


Figure 2.9. Bloch diagram of the controller

2.4.1.1. The reference

The *reference voltage* is adjustable through variable potentiometers (20K for coarse variation and 100Ω for fine variation) for coarse and fine current variations as shown in figure 2.10. A buffer (using OP27, Motorola make) gives the necessary driving capabilities to this signal.

2.4.1.2. Feedback

A *feedback input* {V_j} is taken from the measuring resistor, R_{mes} , placed in the path of the coil current. The fluctuations or variations in the coil current are fed back to the controller in such a sense, with respect to the reference, that the output of this controller responds to cancel the fluctuations in the current. Any fluctuations or

variations in the coil current are to be fed back to the controller in the right sense. For this, the current measuring resistor R_{mes} , should be capable of reading the current in the coil without error. Apart from sensing the oscillations and measuring the current passing through the magnet, the voltage across the R_{mes} is also used to vary the evolution field. This part of the circuit is shown separately in figure 2.11.

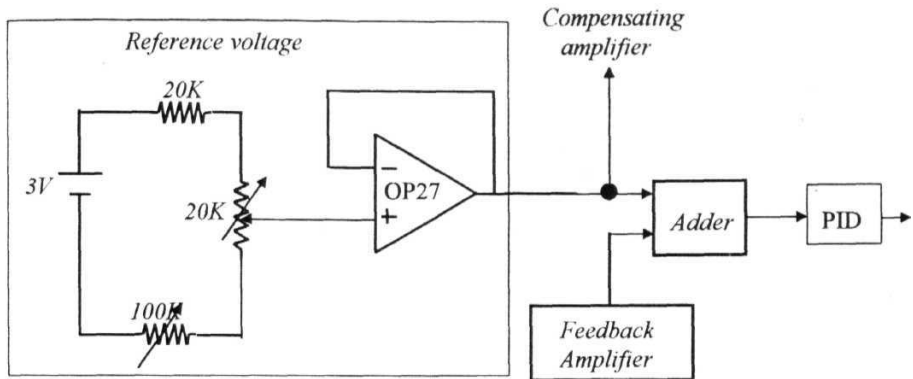


Figure 2.10. Reference amplifier (Detection field control).

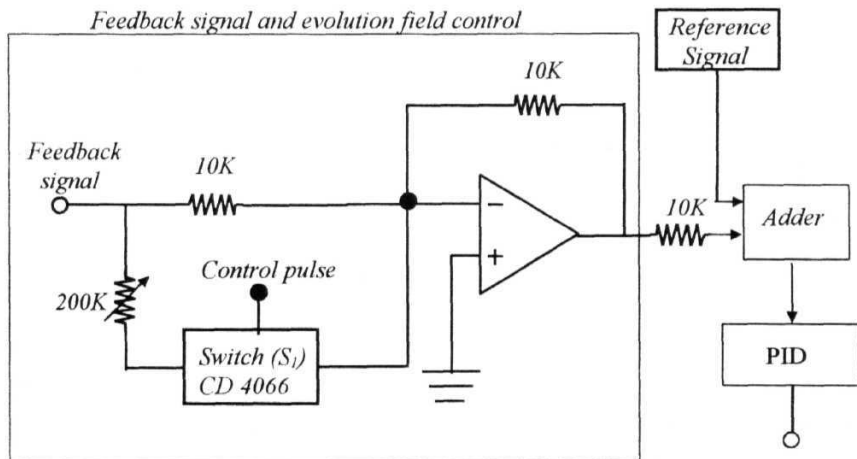


Figure 2.11. Feedback and evolution field control circuit with other units.

A solid state switch (CD 4066) is used to connect an additional resistive load in the feedback path, during the evolution period, with a variable resistor available in the feedback amplifier. The signal coming from the measuring resistor is amplified by the feedback amplifier, and the gain is adjusted to get the required control signals for different evolution fields.

The position and value of the measuring resistor R_{mes} are selected, following Schweikert suggestions [25]. The possible positions of the measuring resistor in the field cycling network are shown in the figure 2.12. The position selected is also shown with the closed box/ labeled as '*measuring resistor*'.

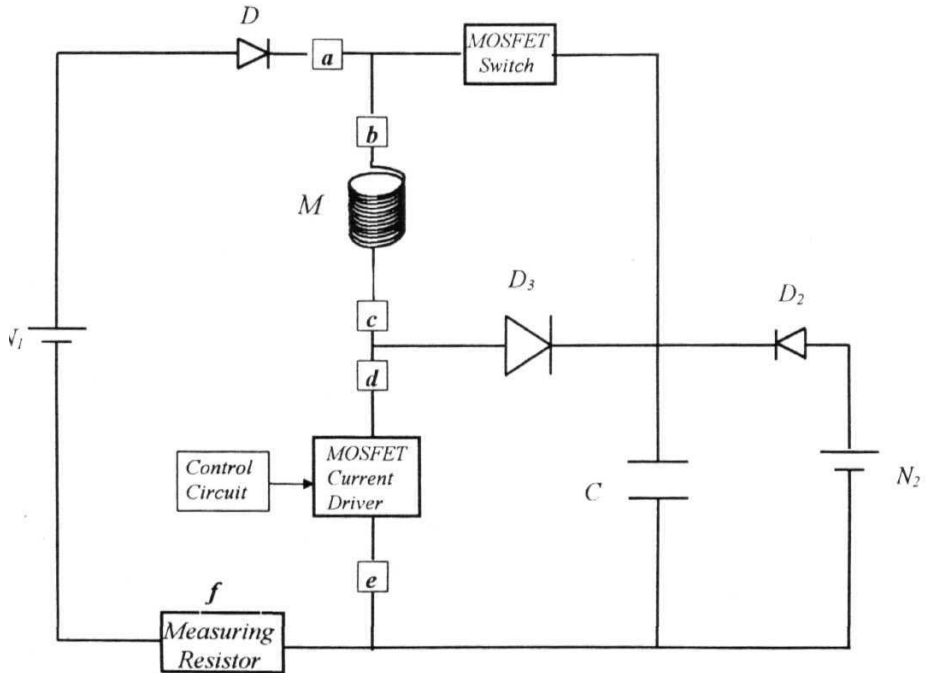


Figure 2.12. Possible positions (the boxes a , b , c , d , e and f) considered for current measuring resistor.

Positions a and b do not hold ON, OFF currents directly and are at a high variable potential with respect to the ground. Hence a direct and precise transmission

of the signal to the control circuit is not possible. Positions c and d are directly in the magnet power supply lines, and hence measurement of the current without any error is possible, but they are at a higher potential with respect to the ground. The positions e and f are at easily operating positions but at e , the driving current for the MOSFET current driver falsifies the data apart from the improper OFF current measurement. The position f has the most favorable characteristics and is chosen for positioning the measuring resistor. The circuit is modified slightly to hold the input current properly as shown in figure 2.13 with two more diodes (D_{4a} and D_{4b}).

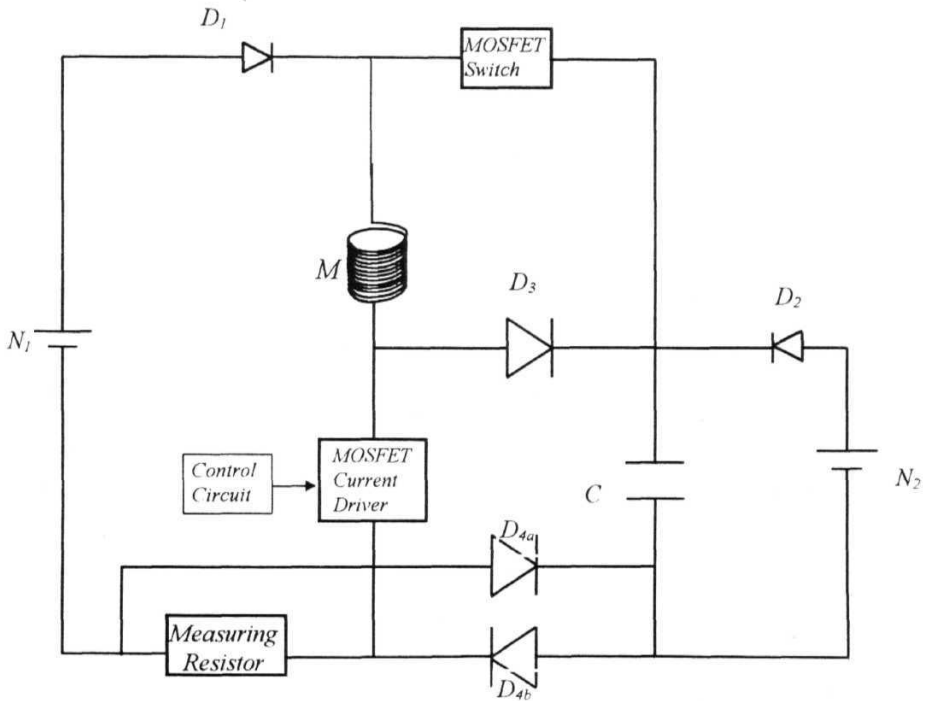


Figure 2.13. Modified (final) version of the Field Cycling Network

The choice of the value of R_{mes} is also very critical. On one hand, it must be large enough for the voltage drop to be strong enough to measure, the feedback signal

which is sensitive to the modulations in the coil current. On the other hand, it should be small so that, the heat dissipated is minimal to ensure a stable operation. In the present case, a $150\text{ m}\Omega$ resistor satisfies the requirements, since it results in a minimum voltage drop of about 1 V for a value of coil current of about 6 Amperes . The power dissipation across R_{mes} is about 7 watt .

2.4.1.3. Pole Zero pair amplifier

The gain of the *Pole Zero Pair Amplifier* (A_s), which is the most crucial part of the controller, is chosen to be high enough to obtain high stability of the current (and the field). The circuit (with the values of the resistors and capacitor chosen) is shown in figure 2.14.

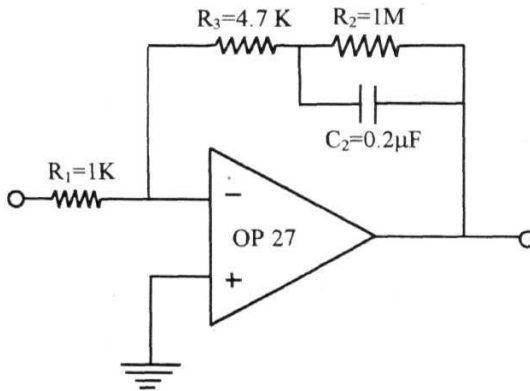


Figure 2.14. Pole Zero pair amplifier

The position of the *pole* and *zero* of the circuit are adjusted by trial and error method. The frequency response characteristics of pole zero pair amplifier chosen here are given in figure 2.15. The low frequency part // is responsible for the stability with the drift compensated input. The next region I_2 , coupled with the high frequency region adjusts the control parameter to a high frequency limit. The third part P allows

the controller to work in the regulation region (**proportional**) The *pole* and *zero* of the circuit are given by

$$f_p = -\frac{1}{R_2 C_2} \quad (1.62)$$

$$f_z = \frac{R_3 R_2 C_2}{R_3 + R_2}$$

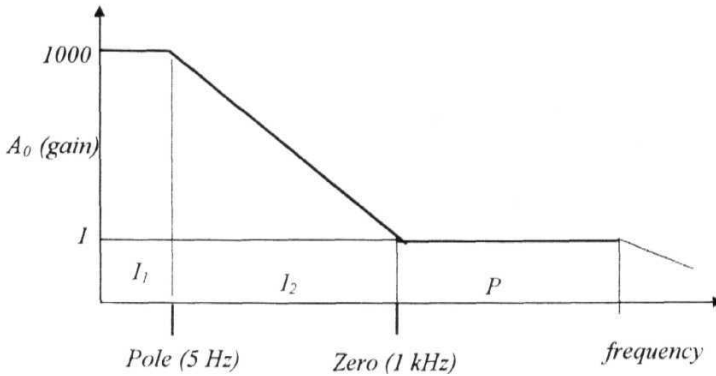


Figure 2.15. Characteristics of Pole Zero pair amplifier

and the *dc* gain of this amplifier is given by

$$A_0 = \frac{R_2 + R_3}{R_1} \quad (1.63)$$

The *dc* gain in the present case is about a 1000. The pole and zero are adjusted for good performance and the values of the resistors and capacitor are set such that Pole is at $(f_p) = 5$ Hz and Zero at $(f_z) = 1$ kHz.

2.4.1.4. Compensation

Switching of the current from one value to the other results in the **overmodulation** of the current from the required level, due to the finite time constant of the pole-zero circuit. The MOSFETs, which control the current, respond to this unwanted signal and lead to sudden increase in the current through the coil as shown in

figure 2.16. It takes a while to settle at the required level of current chosen, for polarization or detection.

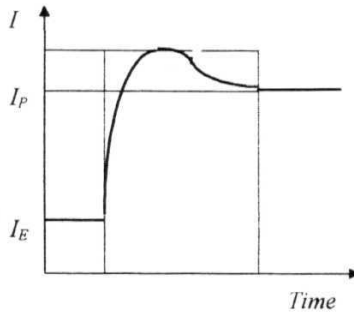


Figure 2.16. Over modulation (without compensation).

This unwanted **overmodulation** is a very serious problem in achieving the ideal switching properties expected for NMR field cycling experiments. In order to obtain **effective** and reliable field cycling performance, overmodulations should be corrected. Lesser the time it takes to settle, better the sensitivity of the NMR **experiment**. Getting a flat, predetermined response of the new level (figure 2.17) can be achieved by adding “a compensating amplifier” in the controller as shown in figure 2.18.

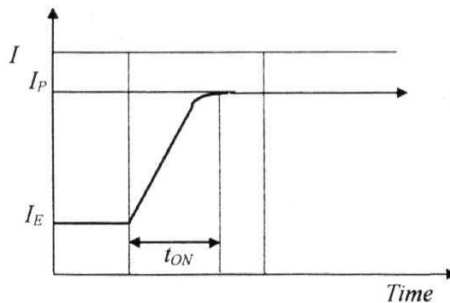


Figure 2.17. Magnetic field after compensation

A simple procedure (Figure 2.18) to be followed to overcome the over modulation is to disable the high gain pole zero amplifier during transits, and during

the period of **overmodulation**. By adding another feedback path through a resistor of **1K Ohms**, by closing a solid state switch (CD 4066), it is possible to drastically reduce the gain of the pole zero pair **amplifier**. This feedback amplifier converts the high gain pole zero amplifier into a unit gain inverting amplifier. The sudden reduction of the gain leads to a change in the input signal to the gates of the current control **MOSFETs**. It is important to compensate the controller output signal, by adding a compensating amplifier, which is made to provide the required control signal with the help of a potentiometer and a switch S, (CD 4066) The compensating signal is taken from both the measuring resistor and the reference amplifier added together before giving this to the compensating **amplifier**. Different pulses are used for switching the field and for including the compensating arm in to the field cycling network. These pulses would be described later with a timing diagram later.

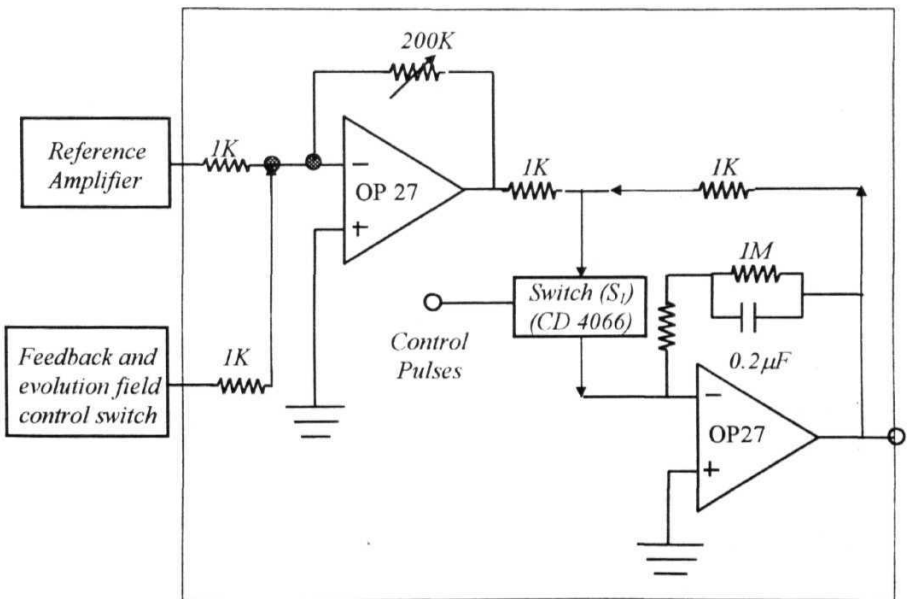


Figure 2.18. Compensating amplifier

The current control during the compensation period is not as good as the PID controlled current, but it helps the field cycle to behave as expected (without **overmodulation**). This can be seen visually with the help of a digital storage oscilloscope, by monitoring the voltage across the measuring resistor,

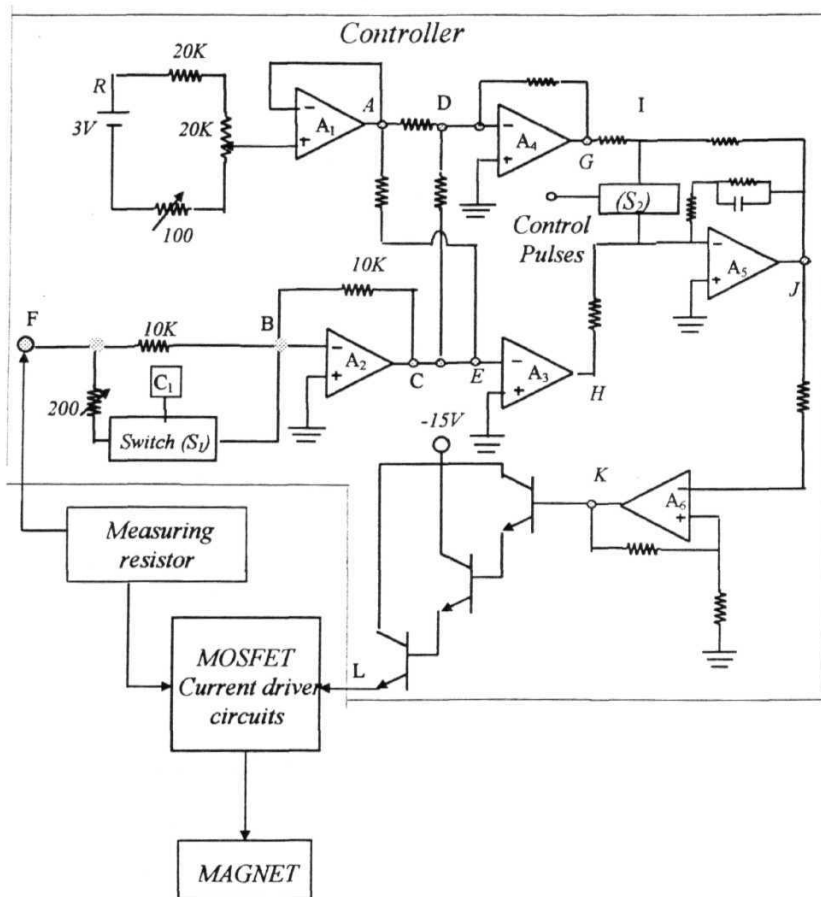


Figure 2.19. The total circuit diagram of the controller.

2.4.1.5. Evolution field control

The input signals corresponding to the different evolution periods are obtained by varying the gain of the amplifier A_3 , with the help of the feedback signal and by closing the solid state switch S_f (CD4066). When the switch is closed, its gain, originally at unity, increases to a value A , (the subscript f refers to the feedback) and hence the controller compares $A V_f$ with V_r (the subscript r refers to the reference). Thus the current through the magnet during evolution period is proportional to the ratio $V_r A_f R_s$, whereas the current during polarization and detection periods is proportional to the ratio V_r / R_s . The control signal to the switch S_f , a TTL pulse, is obtained from the pulse programmer setup. The details of the pulse programmer will be discussed in chapter-3. The output of A_3 is further amplified by A_6 before giving it to a Darlington pair of transistors. The total controller circuit is shown in figure 2.19.

2.4.2. Working of the controller

2.4.2.1. Polarization and Detection fields

The reference voltage V_R is taken from the power pack R , through the variable resistors. In the present case, a 3V power pack gives the necessary *dc* voltage. The calibrated potentiometers ($20\text{K}\Omega$ and 100Ω) are varied to get the required reference signal for the polarization and detection fields (high fields require high reference voltage). This reference is given to a buffer (A_1) for obtaining good current driving capabilities. Thus, the signal at A (figure 2.19) is V_R . The feedback signal (V_f) from the measuring resistor is given at F, which is connected, through a $10\text{K}\Omega$ resistor, to the inverting amplifier (A_2) directly. The switch S_f (CD4066) is open during the polarization period and hence the feedback voltage (V_f) is maximum at the input of the amplifier A_2 . The instantaneous variations in the magnetic field sensed by the R_{me} , are carried to the adder (A_5) through A_2 in the negative sense, since it is an inverting amplifier. The output at C is $-V_f$. This voltage is added with the reference output $+V_R$ (at A) at the point E located just before the adder, which is nothing but a unit gain inverting operational amplifier (A_5). The output of the adder at H is

$$- [(V_R + (-V_F))] = -(V_R - V_F) \quad (164)$$

This 'error' value is again amplified by the high gain ($\cong 1000$) PID type pole zero pair amplifier (A_3) in order to nullify the fluctuations in the magnetic field. This PID type amplifier is an inverting amplifier and the output of this is given by

$$- A_P [-(V_R - V_F)] = A_P (V_R - V_F) \quad (1.65)$$

Case-1

If V_F is positive (when the fluctuation leads to a higher field), $(V_R - V_F)$ is negative, and this negative value will appear at J and further amplified by the noninverting, 3-gain operational amplifier A_6 , and fed to the Darlington pair of transistors at K . This negative voltage will decrease the current passing through MOSFETs, since the output of the Darlington pair of transistors at L is connected to the gate driver circuits of the MOSFETs. Compensating amplifier has no role to play in the polarization and detection periods, since the switch S_2 is open throughout this period.

Case-2

If V_F is negative (fluctuations lead to a lower field), the output $(V_R - V_F)$ is positive, and this positive value will appear at J and further amplified by the noninverting, 3-gain operational amplifier A_6 , and fed to the Darlington pair of transistors at K . This signal will increase the current passing through MOSFETs, since the output of the Darlington pair of transistors (at L) is connected to the gate driver circuits of the MOSFETs.

2.4.2.2. Evolution Period operation

The reference voltage is kept unchanged and the feedback voltage is connected to an additional load, in the evolution period by giving a control pulse to switch S_1 . The variable resistor permits the possibility of a variable current through the magnet during evolution period. The pulse duration controls the evolution period. The reduction in the input to A_2 at B leads to reduction in the value of $-V_F$ at C . This

voltage is added with the reference output $+V_R$ before the adder, which is an inverting operational amplifier (A3). The output of the adder at H now, is given by

$$- [V_R + (-V_F')] = -(V_R - V_F') \quad (1.66)$$

This difference in voltages is again amplified by the high gain PID type pole zero pair amplifier (A5). This PID type inverting operational amplifier with a gain A_P gives the reduced output

$$-A_P[-(V_R - V_F')] = A_P(V_R - V_F') \quad (1.67)$$

Here the value of V_F' is much smaller and hence the final output of the controller is more negative and this leads to the reduction of current through the MOSFET current driver network. This field continues, as long as the switch S_1 is ON. V_F' can be varied using a single variable resistor (a 10 turn 200 K Ω potentiometer) and hence the evolution field can be varied by this arrangement.

2.4.2.3. ON/OFF periods and compensation

The large reduction in the feedback signal during OFF period increases the difference, and this in turn leads to, a more negative control signal to MOSFET gate drivers and finally decreases the magnetic field to a low value (evolution field). Thus, during this sudden switch OFF period (from high polarization to low evolution field), the feedback voltage suddenly changes from the maximum value ($V_R = V_F$) to a lower value V_F' . This variation is not simple in the presence of large inductive load of the magnet. Similarly, the large time constant of the pole-zero pair amplifier does not allow fast switching of the current. To handle this complication the compensation amplifier (A4) is introduced in the controller and A5 is disabled temporarily during transits by introducing heavy negative feedback through the solid state switch S_2 (CD4066). But this will change the voltage level at the output of the controller and it will again take long time before it settles at a required value after the pole zero pair is reintroduced by opening this switch S_2 . This may even result in a long ringing time of the amplifier.

The gain of A_4 is adjusted to compensate for the reduction in the gain at A_5 , thereby keeping the output of A_5 at the correct level during the transit periods (ON/OFF periods). After the transit periods, A_5 is fully enabled and A_4 is removed from the loop by opening the switch S_2 , thus again allowing A_5 to control the current in the magnet. The control signal for S_2 is obtained from the pulse programmer.

The switch S_1 (CD4066) is made open immediately after the evolution period. As in the case of the switch OFF period, due to the time constant involved in the PID type pole-zero amplifier, it is difficult to get the correct control signal from PID amplifier, for a period time after switching ON the field. Moreover, in the case of switch ON period, the sudden increase of voltage across the magnet by pumping the energy stored in the capacitor to flow into the magnet, complicates the switching process (overmodulation of the current is expected). The alternative path through the compensating amplifier (A_4), which acts as an inverting amplifier with high gain, is used to get a correct control signal to the MOSFET current driving network. Now, the PID type pole-zero amplifier becomes a unit gain amplifier, since the $1K$ resistor closes the path when the switch S_2 is closed. The control pulse C_1 is applied immediately after the evolution period, which is present (pulse ON) until the compensation is necessary. By adjusting the variable resistor present in A_4 , the gain can be adjusted such that the compensated output is equal to the value needed for the detection field.

2.5. MOSFET current driver circuits

Semiconductor devices such as Metal Oxide Semiconductor Field Effect Transistors (MOSFETs) are used in this circuit to control electric currents (of around 6 to 7 Amp), since they combine the advantages of bipolar transistors as well as switching components. The current in MOSFETs is independent of drain-source voltage at a constant gate input voltage. This property naturally leads to the selection of MOSFETs for this application. Since a single MOSFET cannot control the required currents, 20 MOSFETs connected in parallel have been used following Schweikert's procedure [25]. The current required in this case (for 3 to 4 MHz of polarization and

detection frequencies) is around 5.5 to 7 Amps. The MOSFET current driver circuit is shown in figure 2.20, along with the gate **drivers**. A regulated signal coming from the electronic PID control circuit, fed to the gates of the MOSFETs, set the value of the current flowing through the MOSFETs. It is important to choose the linear region of the current characteristics of the MOSFETs to have best regulation of the current.

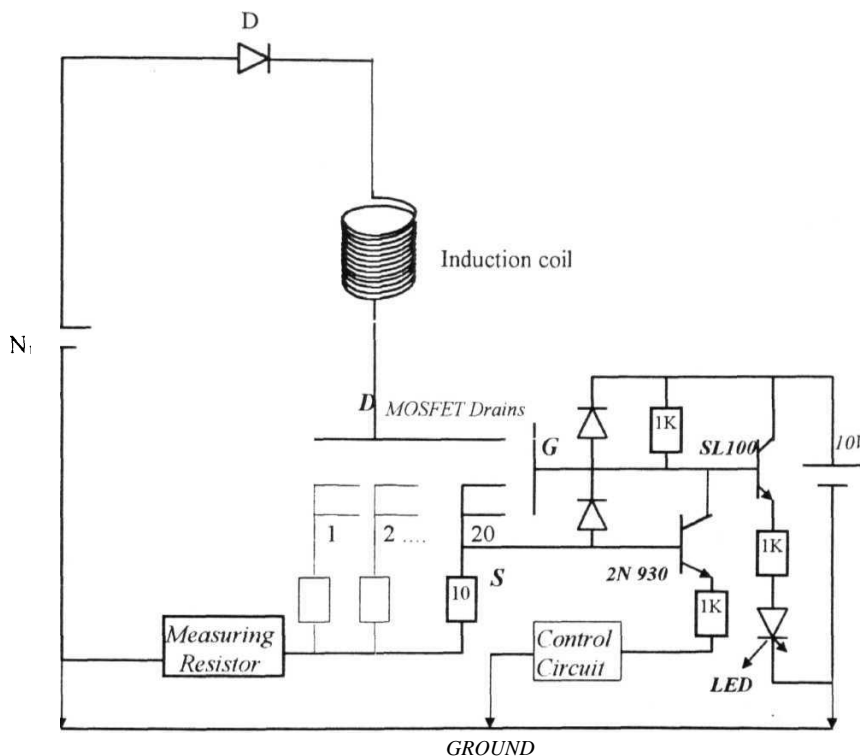


Figure 2.20 Independent gate driver circuits for MOSFET current driver circuits.

Parallel connection of many MOSFETs leads to oscillations when the control is done for intermediate values between maximum and minimum currents, due to unfavorable driving, higher cut-off frequencies and differences in the input capacitance values. Moreover, the threshold voltages for different MOSFETs are generally

different Therefore, each MOSFET is driven with an independent gate driver circuit, in order to decouple the gates, and also to avoid mismatches. An added advantage of these gate driver circuits is due to their partial linearization of the voltage-current characteristic, which is not linear at small drain currents. An LED added to this circuit helps in identifying the function of the particular gate driver and any possible damage in the circuitry. The rectangles in the figure represents resistors and the numbers refer to the value of the resistance in Ohms.

The MOSFETs, the switch S, the diodes D_1 and D_3 and the sampling resistor R_s are all mounted on a thick aluminum plate, cooled by running chilled water (through copper tubing).

2.6. MOSFET switch

Most of the groups [12,36,44] have used the GTO Thyristor to employ the energy storage principle. The control electrode (gate) of the GTO can be triggered by a pulse in order to pass high currents between the anode and cathode. Special GTO thyristors, were used, which needs a trigger pulse to disconnect current flow between anode and cathode, instead of physically disconnecting them. This necessitates a special gate driver circuit. In the present work, a single MOSFET is used in place of a GTO thyristor to allow and disconnect the path to the energy storage capacitor network from the induction coil. The MOSFETs procured from International Rectifiers (IRFPG40) are capable of withstanding such high currents, with a proper gate control signal.

2.7. MOSFET switch driver circuit

Optical couplers (or opto-couplers) are designed to provide isolation between different voltage levels, and hence, to protect the components from high-voltage transients. Hence they allow interfacing systems of different voltage levels, different grounds, etc. that would otherwise be incompatible. A *Darlington transistor opto-*

coupler (TIL 113) is used (shown in figure 2.21) for this purpose since it show high current transfer ratios (300 in the present case) and increased output current capabilities. The speed in this case is 30 kHz, which is less than a single transistor coupler, but the transfer ratio is about 10 times larger than that of a single transistor coupler.

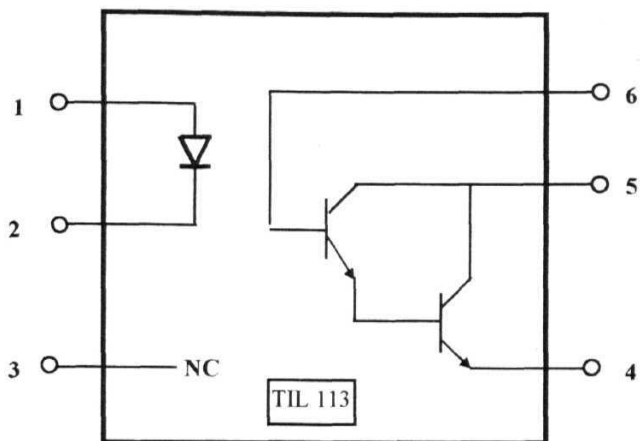


Figure 2.21 Optical Darlington transistor coupler (TIL 113)

The opto-coupler is used here, to isolate the high voltage capacitor network from a low voltage induction coil. It also provides an optical path for the pulse, which is applied to the gate of the MOSFET switch such that, the switch is closed, whenever it is necessary to pump the capacitor energy into the induction coil. The gate current characteristics of the MOSFET is very crucial, in designing this optically coupled MOSFET switch. Opto-coupler switch driver input voltages are also found to be very crucial and a minimum of 10V is needed for a good performance, in the present case.

A single MOSFET which can withstand 1000V and more than 7 Amp (IRFPG40, International rectifiers) is used here. The opto-coupler (Motarola make, TIL 113) and the connections are shown along the MOSFET switch in figure 2.21. The source (S) of the MOSFET is connected to the induction coil and the drain (D) is

the energy storage capacitor network. The required gate trigger pulses are fed through the optical coupler. The two transistors shown in the right hand side of the optical coupler gets a base voltage through an optical path.

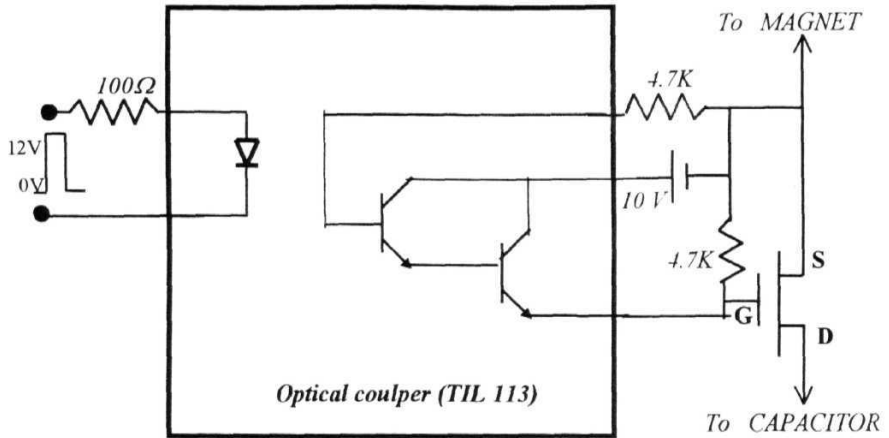


Figure 2.22. MOSFET switch with its Gate driver circuit.

The input terminals (pins 1 and 2) get pulses from a pulse amplifier (0-15V). The transistors are ON when there is a pulse in the inputs. A +10V power supply is connected to the collectors of the transistors with respect to the source (S) voltage. A pulse of about +10V with respect to the source voltage is fed to the gate G of the MOSFET. This closes the path between the capacitor and the magnet. This set up is not only economical but also very simple to achieve. For higher current values, more MOSFETs can be connected in parallel.

2.8. Working of the Field Cycling Network

The overall operation of the field cycling network in different periods of the NMR experiment is explained [here](#). Different portions of the field cycling network are drawn in order to explain the particular operation, and to highlight the specific role-played by each sub-unit.

2.8. 1. Polarization and Detection Periods

MOSFET current driver circuits are switched ON by applying suitable control signals to the gates of the 20 MOSFETs through their individual gate drivers.

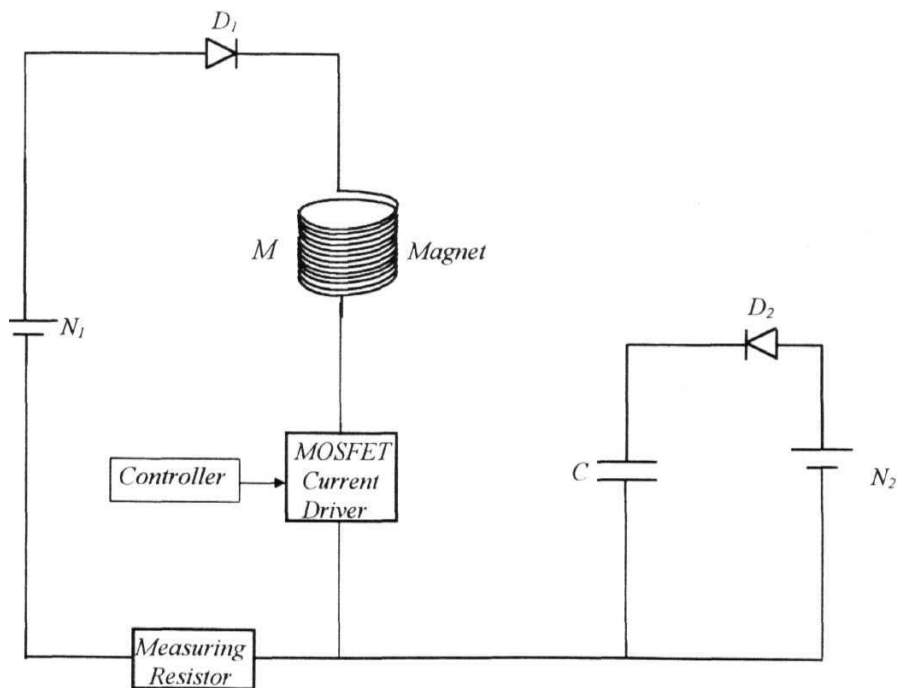


Figure. 2.23. High field operation (polarization and detection periods).

During high fields, the available energy from the power supply is dissipated in the magnet, and the current driver circuits. The energy storage capacitor (C) is isolated from the network as shown in figure 2.23, by a decoupling diode. The signal from the measuring resistor is fed to the controller in the negative sense such that the oscillations are nullified in the process. The pole zero pair amplifier of the controller gives the drift-free, modulation-free constant signal to the gates of the MOSFETs. The details of these circuits have already been discussed in the previous sections. This cycle is repeated at regular intervals depending on the relaxation times of the system under investigation. In the present case, the operation is simplified by making the polarization and detection field levels equal. The function of the field cycling network is similar during high polarization and detection periods as well as low values of the current during the evolution period. Any value of the evolution field can be set between zero to the detection field, and is controlled at that particular value in the constant current mode of operation.

2.8.2. *Switch OFF operation*

During the transit from high to low fields (turn *off* of the field), the control signal corresponding to the required low field is given to the gates of the MOSFET current driver circuit, resulting in the reduction of the current and also the generation of high voltage across the coil. The components involved in this operation are shown in figure 2.24. The energy storage capacitor C is precharged to U_{co} by N_2 and is further charged with this excess voltage to a higher value U_c , during this period. If the precharged voltage is close to U_c , the capacitor charges quickly to the maximum value resulting in a faster decay of the current through the coil $I(t)$, with an initial value of current I_0 , and is given by the equation,

$$I(t) = [I_0 \cos \omega t - I_1 \sin \omega t] e^{-\lambda t} \quad (1.68)$$

and the voltage $U_C(t)$ in this case is given by the equation 1.69 [12,25],

$$U_C(t) = U_{C0} - [I_0(\omega \sin \omega t - \lambda \cos \omega t) + I_1(\lambda \sin \omega t + \omega \cos \omega t)] e^{-\lambda t} + \frac{\lambda I_0 - \omega I_1}{(\omega^2 + \lambda^2)C}$$

where

(169)

$$\lambda = \frac{R}{2L}; \quad \omega = \sqrt{\frac{1}{L-C} - \lambda^2} \quad \text{and} \quad I_1 = \frac{U_C - \frac{3}{2}RI_0 - U_N}{\omega C}$$

and U_N , is the over modulated voltage of the capacitor C, arises due to the sudden increase of the energy available for storage, which necessitates protective measures.

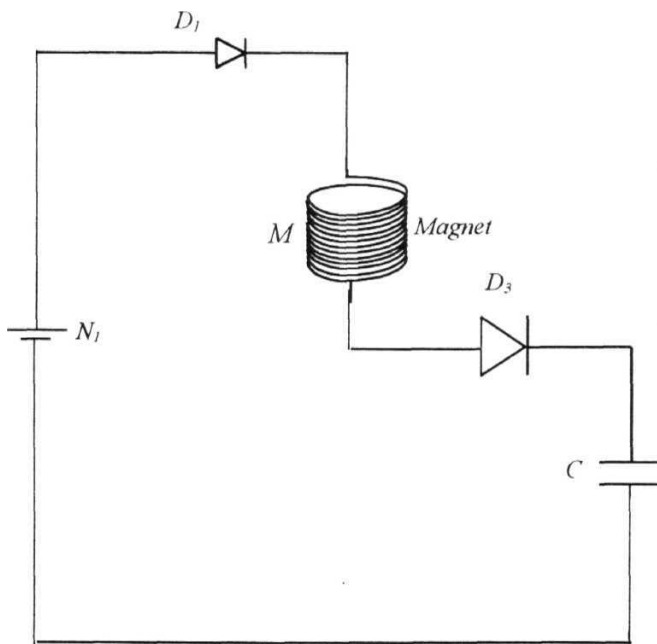


Figure. 2 24. Switch OFF operation

2.8.3. Evolution Period

As soon as the expected lower current level is reached, the MOSFET current driver circuits control the field, and hence a steady evolution field is obtained. Thus, the operation in both the high and low fields is indistinguishable, as regards the operation of the control circuit. The components involved in this operation are shown in figure 2.25. The modulation-free stable evolution field is obtained by properly adjusting the signal from the controller.

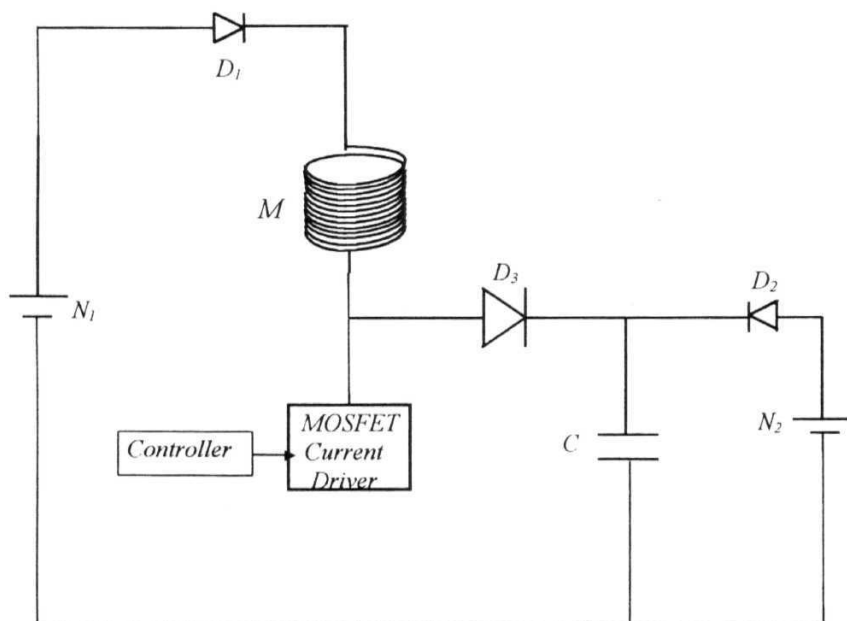


Figure. 2.25. Low field operation (evolution field operation)

2.8.4. Switch ON operation

After allowing the magnetic field (current through the induction coil) to stay in the low evolution level, for a sufficiently long time, the magnetic field is brought to a

higher value by suddenly releasing the energy stored in the condenser C (by applying a pulse to the gate of the MOSFET switch) to flow through the magnet (M), and also by giving the required control signal to the MOSFET current driver circuit. The compensation procedure incorporated in the controller helps the magnetic field to settle faster at the preselected detection (or polarization) field **value**. During the switch ON period of the magnetic field an adjustable compensation is given to the gates of the MOSFET current driver circuit.

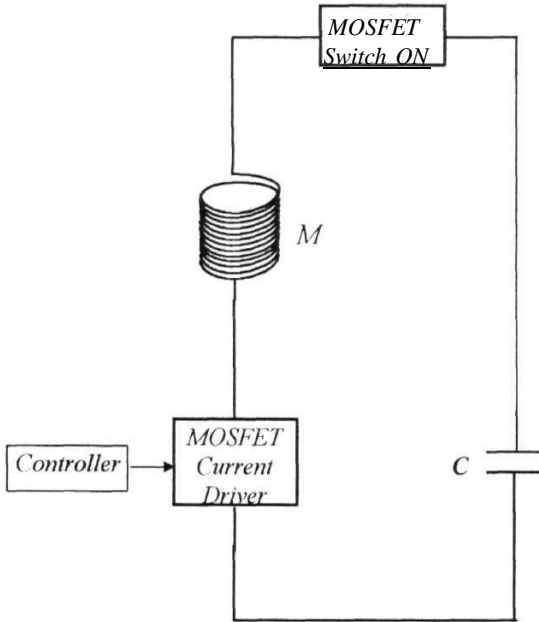


Figure 2.26. Switch ON operation

Now, the current increases from the minimum value to the required high value, with the help of the excess energy provided by the capacitor C . The current, $I(t)$, increases from the initial value I_0 with time, given by

$$I(t) = [I_0 \cos \omega t + I_1 \sin \omega t] e^{-\lambda t} \quad (170)$$

and the voltage $U_c(t)$, across the capacitor with capacitance C , with the precharged voltage U_{c0} is given by [12,25]

$$U_c(t) = U_{c0} + [I_0(\omega \sin \omega t - \lambda \cos \omega t) - I_1(\lambda \sin \omega t + \omega \cos \omega t)]e^{-\lambda t} + \frac{\lambda I_0 + \omega I_1}{(\omega^2 + \lambda^2)C} \quad (1.71)$$

where

$$\lambda = \frac{R}{2L}; \quad \omega = \sqrt{\frac{1}{L-C} - \lambda^2} \quad \text{and} \quad I_1 = \frac{U_{c0} - \frac{1}{2}RI_0}{\omega C}$$

where L and R are the inductance and resistance of the solenoid. The components involved in this operation are shown in figure 2.26.

2.8.5. Detection Period

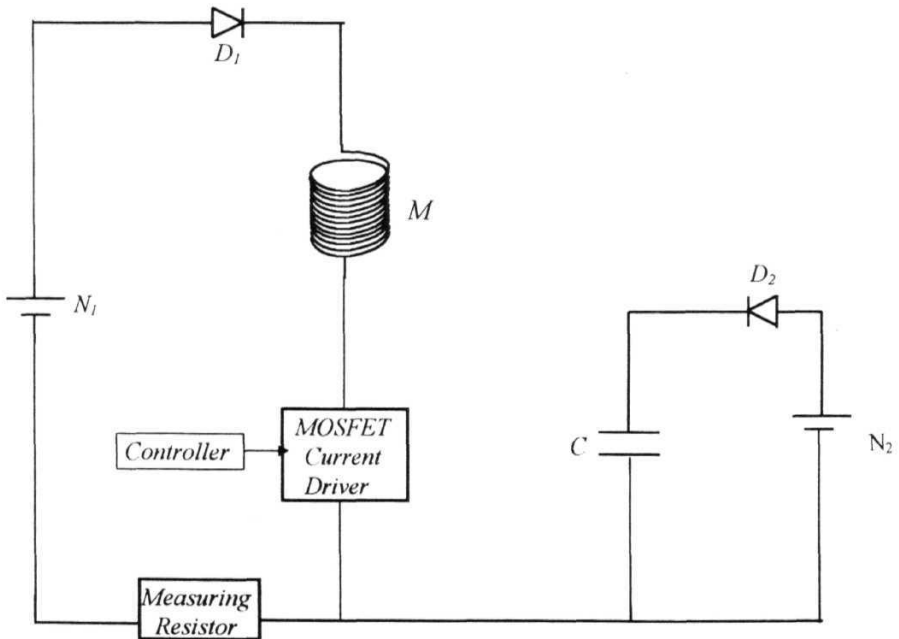


Figure. 2.27. Detection field operation

Finally, when the detection field is reached, the MOSFET switch is switched ON (by applying a suitable pulse to the gate) and the MOSFET current driver circuit is switched ON to regulate the field, resulting in the initial condition (polarization field). This cycle is repeated at regular intervals depending on the relaxation times of the systems under investigation. The components involved in this operation are shown in figure 2.27.

2.9. Standardization and Calibration

After obtaining the expected field cycles, with switching times less than 2 ms, all the important variable resistors used in the controller are fixed on a separate control panel, in order to provide an easy access to the operator. Keeping the requirements of the spin-lattice relaxation time measurements in mind, the drift-free, modulation-free stable magnetic field during the detection period were visually observed and measured with the help of a digital storage oscilloscope, by simply observing at the voltage across the measuring resistor.

As explained earlier, various field cycling operations such as, the variation of the amplitude and duration of the evolution field, can be obtained by adjusting the potentiometer present in the feedback path of the controller. Two potentiometers, one for coarse and the other for fine adjustments, present in the reference amplifier of the controller, are used to adjust the amplitude of the detection and polarization fields. A potentiometer kept in the compensation amplifier is used to adjust the current to a value equal to the detection field, during the switch ON period. All these potentiometers are calibrated such that the field cycling procedure can be optimized and evolution and detection frequencies can be easily varied. A 10 turn calibrated potentiometer is used to vary the evolution frequencies directly.

Alternatively, the voltage drop measured across the measuring resistor is calibrated to get the detection frequency as well as the evolution frequency. While calibrating, the spectrometer is tuned for different detection fields (for different currents flowing through the magnet), and the current values are determined for

evolution frequencies. The voltages measured across the measuring resistor were tabulated. Since the field varies linearly with the current, voltage drop across the measuring resistor can be used directly to get a chart giving the Larmor frequencies and the corresponding voltage values. By measuring the frequencies by both these methods, it is possible to obtain the evolution frequencies without any error.

Depending on the detection frequencies, FID length, temperature and phase of the liquid crystal different pulse sequences are applied to get a good S/N. For example, at low evolution fields, *one pulse sequence* (chapter-1) is favorable due to the large variation of the nuclear magnetization, which is taking place far away from the baseline. At evolution frequencies close to the detection frequencies, the *inversion recovery pulse sequence* is used due to its large magnitude variation of the magnetization. The compensation level is adjusted for different evolution currents in order to get **overmodulation** free, oscillations free magnetic field.

Chapter 3

Field Cycling NMR Spectrometer

The block diagram of the home built FCNMR spectrometer consists of six major units is shown in figure 3.1 and listed below, which have many sub-units as described in the following sub-sections.

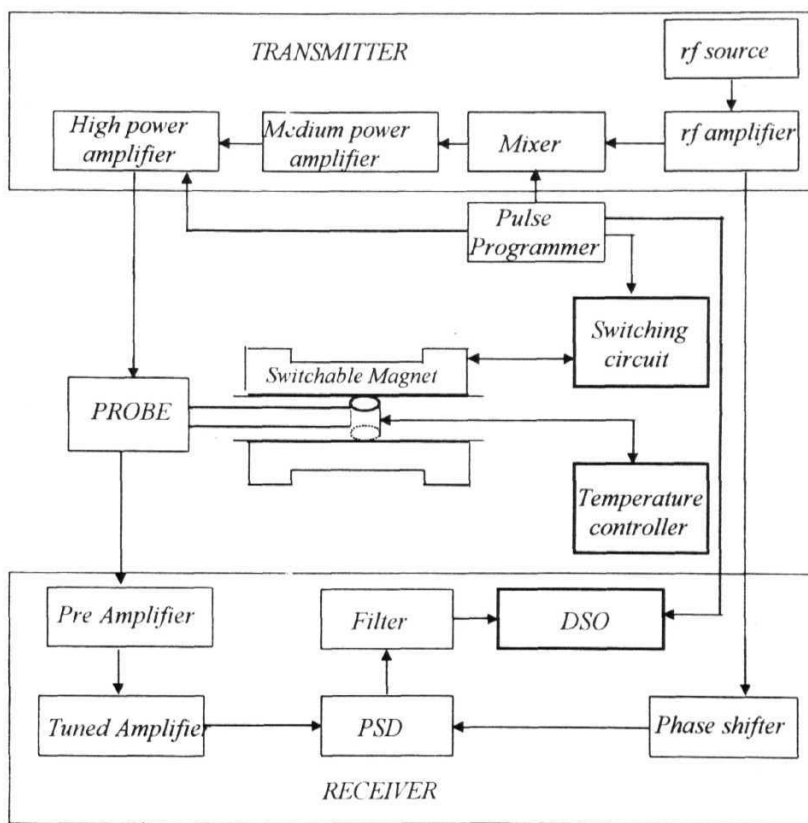


Figure. 3.1. Block diagram of the FCNMR Spectrometer.

- > The *transmitter* gives high power *rf* pulses, which has mixing and amplifying circuits.
- > The *probe* for matching the transmitter and receiver, and for providing good S/N at low frequencies around 3 MHz
- The *receiver* that could take care of the long dead time and noise problems arising especially at the low //ranges (around 3 MHz).
- A home built ***Field Cycling Network***, which is already described with its complete fabrication details in chapter-2.
- > A *pulse programmer setup* which is capable of producing pulses for transmitter, receiver and for synchronization of field cycling network with the *rf* pulse sequences and
- A temperature control facility consisting of a double wall cryostat, heater, air blower, measurement and control thermocouples and a **multimeter**

The *transmitter* should be capable of providing high power *rf* pulses (typically in the range of a few hundreds of watts with sharp rising and falling edges) of short duration (1-100 μ sec). The ON/OFF ratio of the //pulses should be very large so as to ensure that there is no leakage of //voltage into the receiver during the transmitter OFF time. The *rf* field (H_1) provided by the transmitter should be as homogeneous as possible, over the sample volume. The transmitter essentially consists of a //source, a pulse programmer capable of generating the required pulse sequences, a pulsed *rf* mixer, a medium power amplifier and a gated high power amplifier.

The power from the transmitter should be efficiently transferred to the spin system (sample coil) by an impedance matching network. This matching network along with the sample coil is termed as **the probe**. The signal induced in the sample coil after the transmitter pulse is very small (typically in μ V), and hence, it should be amplified by the *receiver* to a few hundred times, and then demodulated to recover the decaying pattern. Apart from this, the receiver should be capable of withstanding overload voltages and also recover fast from these voltages (due to leakages during pulse ON periods). The recovery time of the receiver from overloading should be as short as possible to ensure that the signal is not lost during this 'dead time' of the

receiver. Moreover, the receiver should be capable of detecting only the carrier wave in order to increase the signal strength. The various sub-units are described in detail below.

3.1. Transmitter

3.1.1. rf generator

The *rf* voltage obtained from a variable frequency *rf* synthesizer (commercial unit of Kikusui make, Model No.4100, capable of generating *rf* voltage of high spectral purity, from 0.1 kHz to 110 MHz with a stability of about 1 in 10^9 s), is amplified using 2N2369 transistors to a required level of about 3 V peak to peak. The *rf* amplifier circuit [73] is shown in figure 3.2.

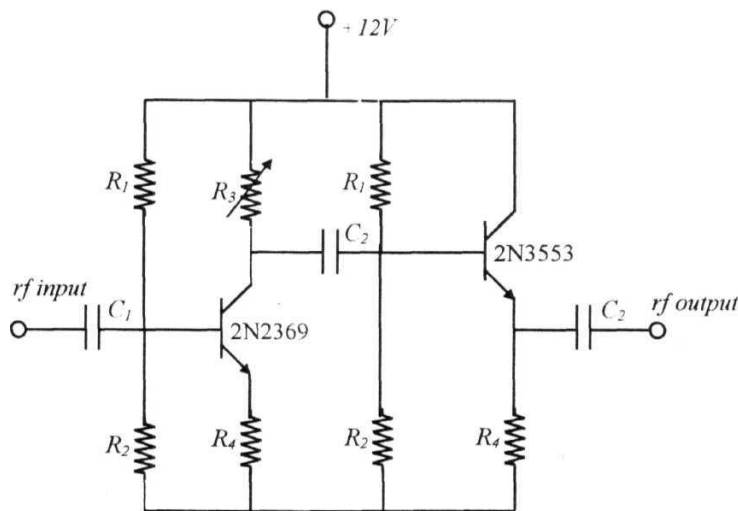


Figure. 3.2. *rf* amplifier

The //thus obtained is power divided into two parts, the first part is used for pulse modulation and the other as reference (through a phase shifter), for the phase sensitive detector (PSD). The details of the PSD would be discussed later.

3.1.2. Pulse and delay generators

The pulses and the necessary delays are obtained from a commercial four channel digital delay generator (EG&G make, Model No.9650) and a homemade pulse generator [73] panel built using IC74121's. The pulses obtained from these units are also used for triggering the oscilloscope and the gated high power amplifier. The pulse generator circuit is shown in figure 3.3. R is the variable resistor and C is the series capacitor network.

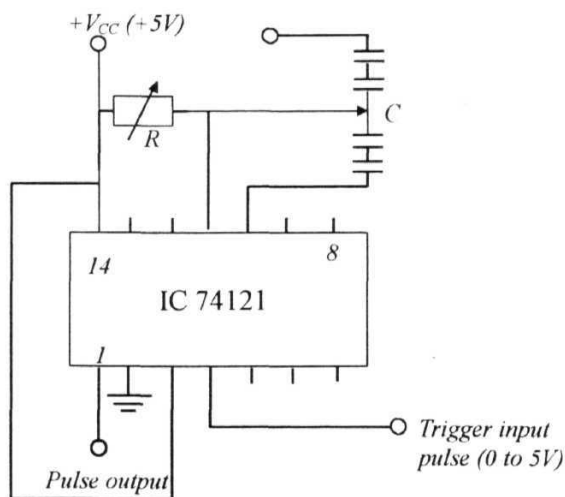
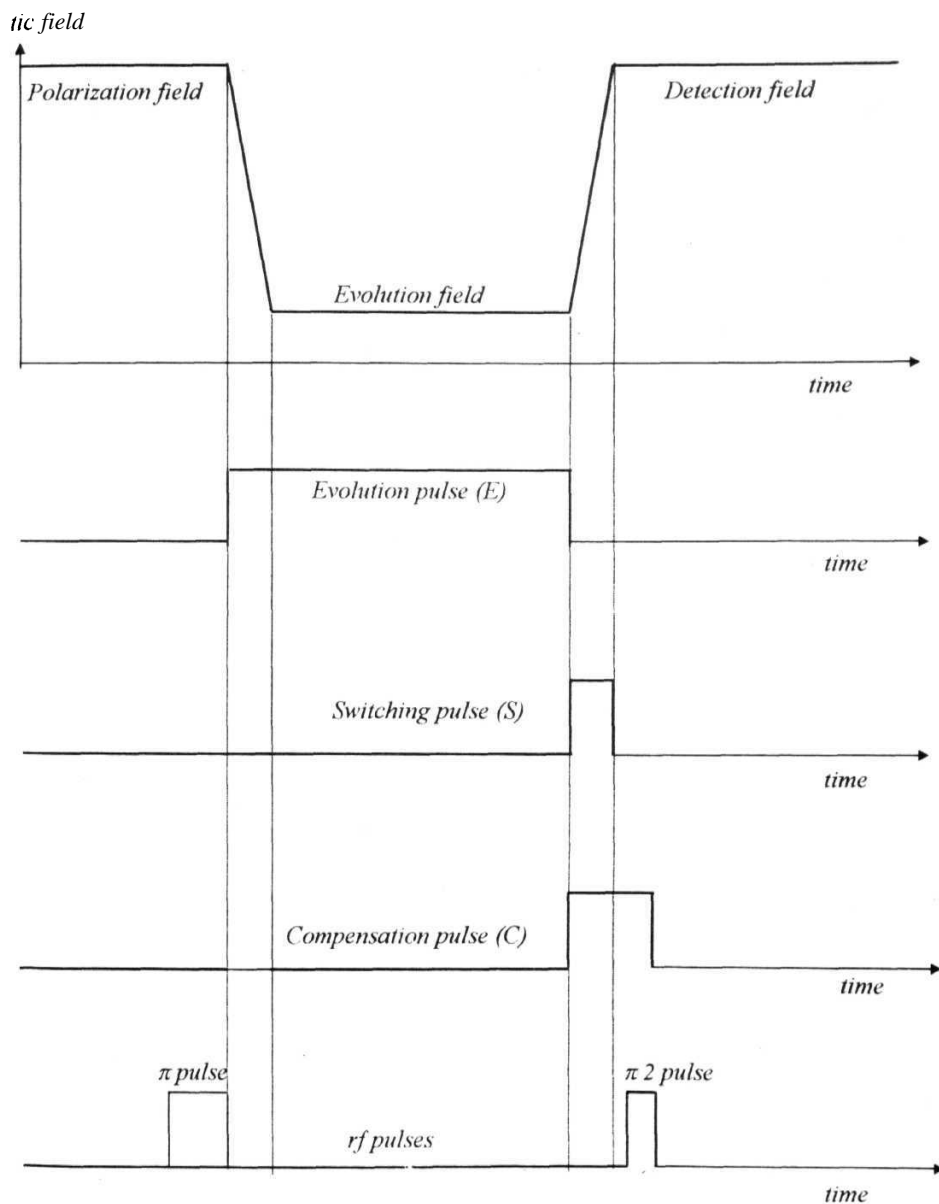


Figure. 3.3. The pulse generator circuit using IC 74121

The required pulses for FCNMR spectrometer (for switching the magnetic field as well as for the application of the rf pulse sequences) is given in the timing diagram given in figure. 3.4

Figure 3.3. Timing diagram of the pulses used in the FCNMR spectrometer



Complicated //pulse sequences (pulse sequences used for the measurement of //) could be generated, using a combination of home made pulse generators and delay generators. The typical interconnection procedure adopted for a two-pulse sequence is shown in figure 3.5. Clock pulses with the required repetition rate are obtained from one channel of the four-channel commercial digital delay generator (Channel D, with a delay of 0 sec, in DG-1, EG&G make), which is kept in the internal trigger mode. This trigger pulse is directly given to the pulse generator (PG-1) which in turn can produce 0 to +5V pulses with variable width. Another trigger pulse with an adjustable delay, which is taken from one channel of the delay generator having four channels (C-channel, of DG-2) and used to trigger the second pulse generator (PG-2). These two pulses are added using an OR gate and fed to the transmitter through the mixer and high power amplifier.

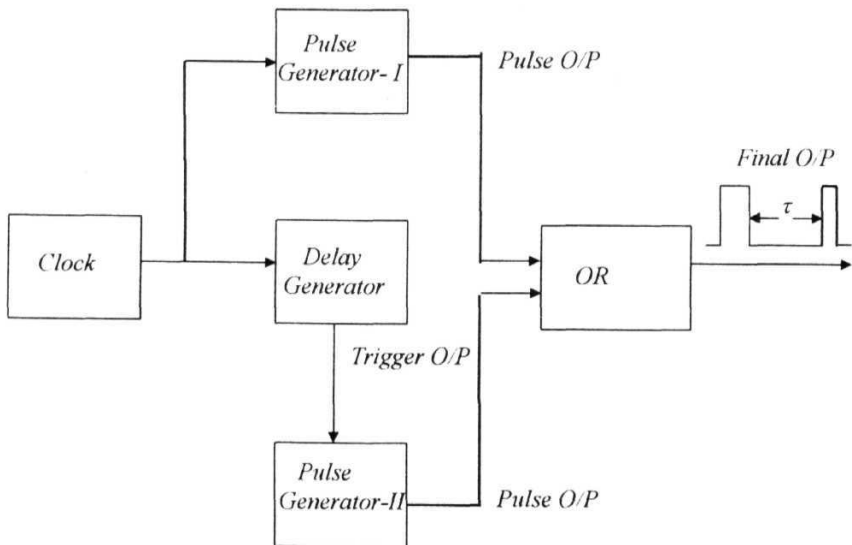


Figure. 3.5. Pulse and delay generators set up for two-pulse sequence

The pulses used for the operation of the field cycling network and for the *inversion recovery sequence* could be obtained using the setup shown in figure 3.6. **Two** digital delay generators, one in the internal trigger mode (DG-1) and the other in

the external trigger mode (DG-2), along with four pulse generators (PG-1, PG-2, PG-3, and PG-4) are used for this purpose. Here, the outputs are labeled with letters *E*, *S*, *C*, *rf* and DSO, to specify the application of the specific pulse (figure 3.3).

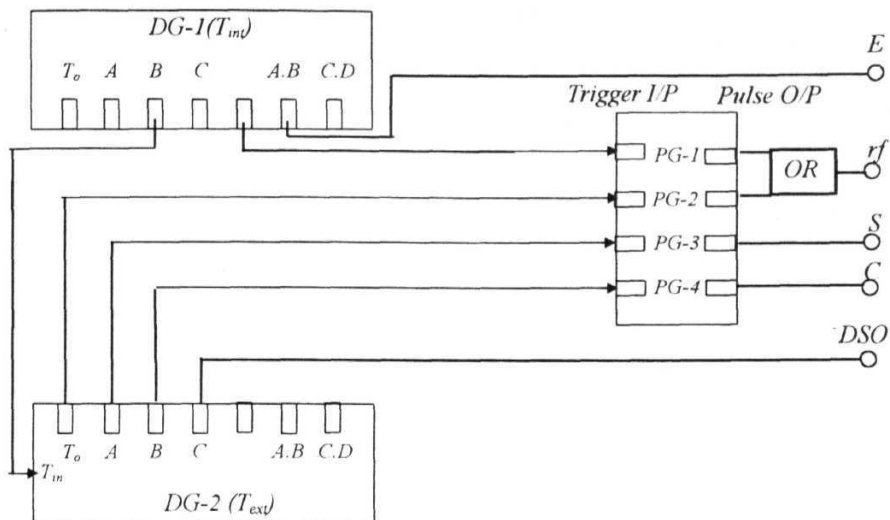


Figure 3.6. Arrangement of pulse and delay generators for FCNMR two pulse sequence

3.1.3. Double Balanced Mixer

The pulse modulation with ω is done using commercial double balanced mixers (DBM Mini Circuits, Model No SRA-3H). These DBMs consist of three ports IF, LO and RF isolated from each other. A current driving circuit designed by McLachlan [75] is used to drive the DBMs for better isolation. By varying the gating pulse current using this circuit, it is possible to increase the amplitude of the pulsed *rf*. The circuit is shown in figure 3.7a.

Pulse amplifier circuit

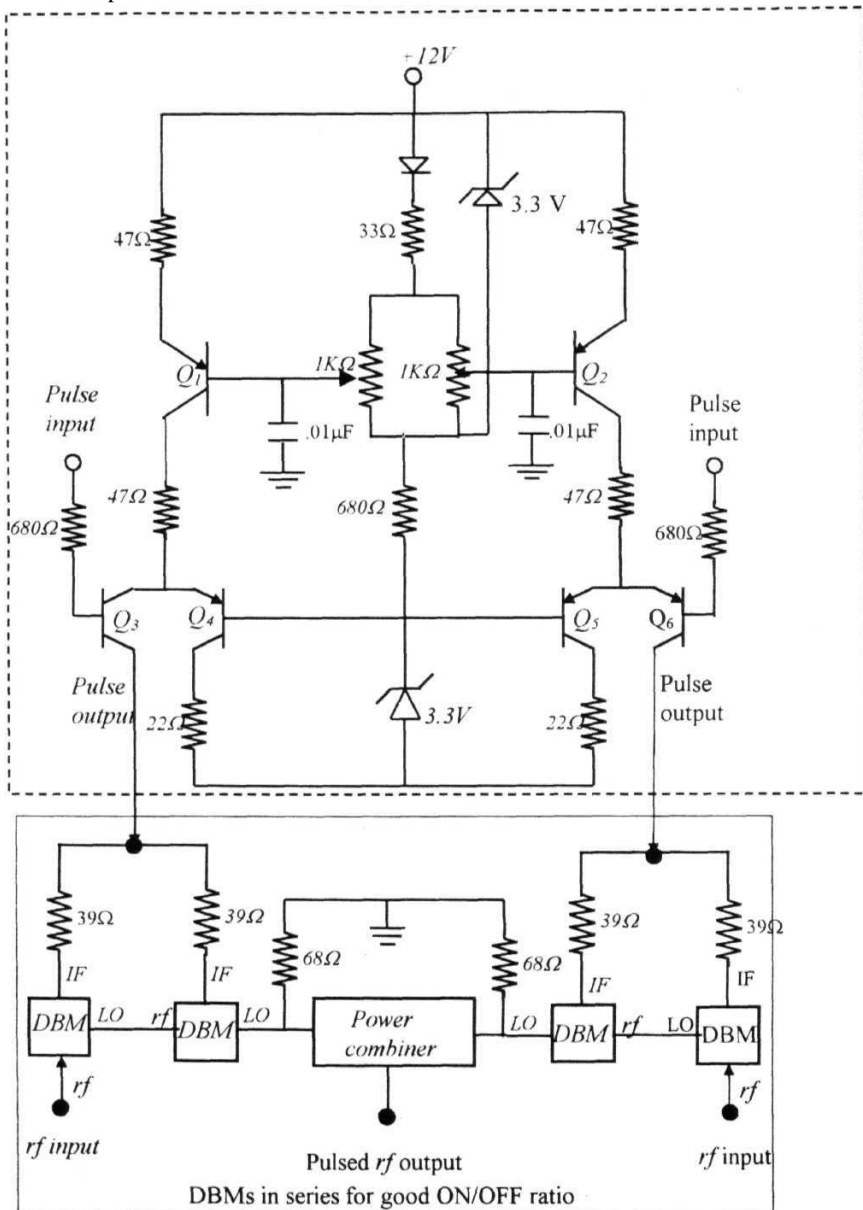


Figure. 3.7a. Double balanced mixer and the pulse amplifier circuit

The transistors Q_1 and Q_2 are independent current drivers. Their collector currents are adjusted by the $1\text{K}\Omega$ trimpot. When the transmitter pulses are not present, the collector currents switch ON the transistors Q_4 and Q_3 respectively and hence no pulses appear at the IF inputs of the DBMs. During the pulse ON period (since the transistors used are *pnp* type the TTL pulses are inverted before being given at the inputs of the current driver circuit) Q_3 and Q_4 are ON and the collector currents of Q_1 and Q_2 are steered to the IF ports of the corresponding DBMs. The two channels present in this circuit are useful when two different pulses with different phases can be modulated simultaneously.

Operation of a simple double balanced mixer is described below and shown in figure 3.7b.

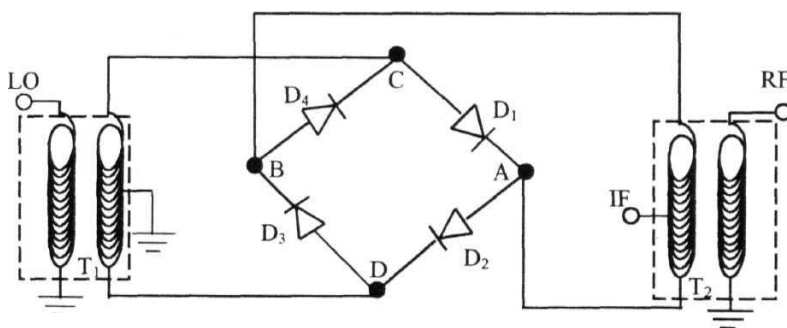


Figure 3.7b. Double Balanced Mixer (DBM)

If the diodes D_1 and D_2 are matched and the transformers T_1 and T_2 are symmetrical, the voltage at A is equal to the voltage at the center tap of T_1 , i.e., ground. Similarly if D_3 and D_4 are matched, the voltage at B is equal to ground. Thus the secondary' ends of the transformer T_2 are at ground potential and hence LO port is isolated from both RF and IF ports. Now, looking from the RF port, the voltage at C is equal to the voltage at D i.e., ground, since all the diodes are matched. Hence, no rf voltage appears at the LO port. Due to symmetry, the voltage at the IF ports is the

same as that, at C and D i.e., zero. Thus, there is no //output at the IF port and hence, all the three ports are isolated. With the pulses at the IF port and a //signal at the *rf* port, the current at the IF port rises suddenly during the pulse ON period. This turns on the diodes and hence the *rf* appears at the LO port. When the transmitter pulse is OFF, as explained above, the IF and *rf* ports are isolated, resulting in a pulse modulated *rf* with negligible rise and fall times (less than 0.1 microsecond). Addition of one more DBMs in the series results in a better ON/OFF ratio and hence a better S/N at the cost of higher insertion loss.

3.1.4. Medium power amplifier

The fluctuation spectrum of different mechanisms mediated through the dipolar interaction in solids results in considerable increase of line width and hence results in very short FIDs. As explained earlier, the inhomogeneity in the Zeeman magnetic field leads to a further shortening of T_2 to T_2^* . In order to excite all the spins equally in such a broadened spectrum, the pulse width should be as small as possible. Normally pulsed //with the voltage of a range of few kW is needed to get a $\pi/2$ pulse width of about 3-4 μ sec for a proton. This is achieved in two stages. The gated //obtained from the NAND gates is amplified to 20 Vpp using a gated medium power amplifier which subsequently, is used to drive a gated high power amplifier to get the required pulsed *rf* power. In the present case, a commercial *rf* amplifier (ENI, Model 310L, RF power amplifier) is used for this purpose. A peak voltage of 20 V is obtained at the output of this medium power amplifier (typical input of about 200 mV of pulsed *rf*).

3.1.5. High power amplifier

This amplifier is constructed, using 3E29 dual tetrode tubes operating in a push-pull configuration [66] and is gated with a 0 to -150V pulse amplifier. The 0 to -150V synchronous, gating pulses and the input pulsed *rf* are given to the tubes through a wide band input transformer (model NH0900B of North Hills make). This is capable of amplifying pulsed *rf* with negligible rise and fall times, the 3 dB bandwidth

Figure. 3.8. High power //amplifier and pulse amplifier circuits

High power amplification and good ON/OFF ratio is accomplished by biasing the grids of the dual tetrodes with 0V during pulse ON period and -150V during the pulse OFF period. The working of the pulse amplifier can be understood as follows. During the pulse OFF period, the transistor T_1 is OFF, resulting in -150V at the bases of T_2 , T_3 and T_4 . Since both, the *pnp* transistors T_2 and T_3 are conducting and the *nnp* transistor, T_4 is not conducting, -150V appears at the grids of the tubes. Thus, during the pulse OFF period, no amplification is done resulting in an improved ON/OFF ratio. During the pulse ON period, T_1 conducts making the voltage at the base of T_2 , T_3 and T_4 from -150V to 0V. Thus T_2 and T_3 are OFF and T_4 is ON, resulting in 0V at the grids of the tubes. The output of the amplifier is taken through another wide band transformer (North Hills NH1703BA). Since the plates of the tetrodes are at about 800V, very high amplification (~ 10) of the input pulsed //is achieved during the pulse ON period.

3.2. Matching network

The most important part of a pulsed NMR spectrometer is the matching network (probe) which couples the power from the transmitter to the sample coil during the pulse ON period and converts the precessing magnetization into a detectable signal at the input of the receiver immediately following the pulse. The matching network should be capable of coupling the sample coil to the transmitter during the pulse ON period and should also couple the sample coil to the receiver during the pulse OFF period. It should also decouple the receiver from the transmitter during the pulse ON period. The important considerations during the construction of the probe are discussed here. The amplitude of H_1 and hence the $\pi/2$ pulse width, is determined by the transmitter coil and the final S/N is determined by the sensitivity of the receiver coil. One crucial factor in the design of the size of the sample is that, since $H_1 \propto (V)^{-1/2}$, where V is the effective volume of the sample, a probe built for a larger sample would have a smaller H_1 for the sample power. Moreover, for a good signal to noise ratio ($S/N \propto (f)^{-1/2}$, where f is the filling factor of the coil), it is necessary that the probe should have a filling factor close to unity. Finally, the receiver coil in the probe should not give rise to spurious signals (for example, from the mechanical oscillations of the inadequately secured rf coil or generation of acoustic waves and signals, which interfere with the actual signals).

The above requirements can be fulfilled by using tunable circuits consisting of LCR networks. Either the crossed coil method [67] proposed by Bloch et al., where separate transmitter and receiver coils are used or the single coil method [68,69] proposed by Clark and McNeil, where a single coil is used for both the transmitter and the receiver, can be used for this purpose. The single coil arrangement is simpler and has advantages over the other one in terms of the maximum power efficiency. Since the coil is common to both the transmitter and the receiver, care should be taken to protect the receiver from leakage of rf pulses from the transmitter, i.e. the probe should isolate the receiver from the transmitter. This can be achieved by using crossed diodes and $\lambda/4$ transmission lines which appear as short-circuit to high voltages and

open circuit to the small signals. Two matching circuits available in the literature are used in the present studies and their relative merits are discussed here. Both the circuits are single coil circuits, which are easier to handle, and also efficient compared to the crossed coil probe.

3.2.1. Series resonant circuit

This matching network [68] consists of three resonant circuits, L/C , L_2C_2 and L_3C_3 each tuned independently at the Larmor frequency (Figure.3.9).

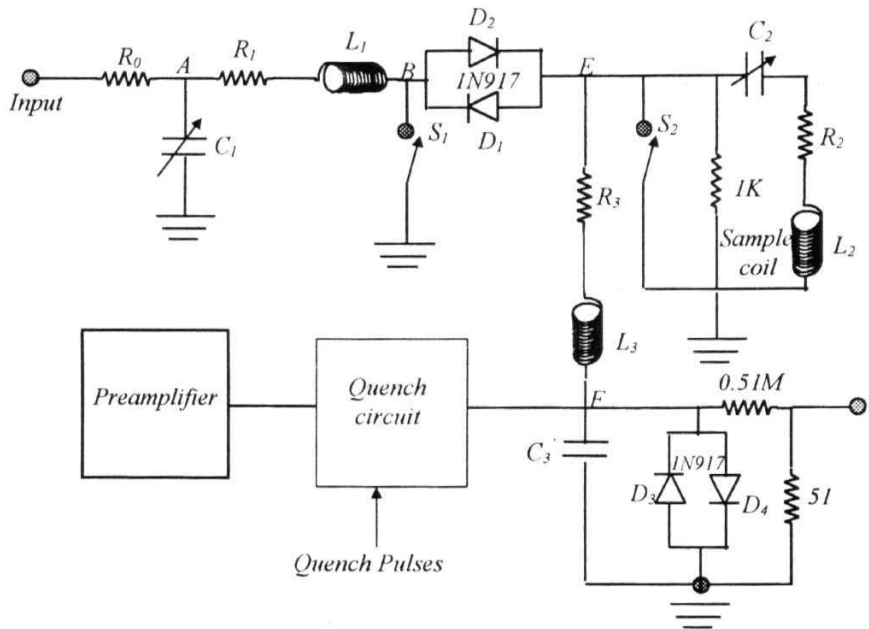


Figure 3.9. Series resonant circuit [68]

The crossed diodes (D_1) at the input act as a short circuit to the small signal voltages (during pulse OFF period). The series combination, L_2C_2 represents a low impedance path in parallel with that of L_3C_3 so that the entire transmitter voltage is dropped across L_2 and a very little voltage is fed into the receiver during the pulse ON period.

Moreover, since the diode pair (D_2) represents short circuit to ground, the voltage at E is dropped across L_3 before reaching the receiver. After the transmitter pulse, the diode pair D_1 effectively disconnects it from E and D_2 acts as an open circuit to the low voltage induced resonant signals, thereby forcing the signal into the receiver through L_3C_3 . Hence, L_2C_2 and L_3C_3 represent a composite series circuit tuned at the **Larmor** frequency. The FID is received at F (a high impedance point to ground). The tuned input receiver circuit (L_3C_3) provides a good coupling of L_2 to the receiver and hence increases the **S/N**. Thus, the circuit ensures an efficient transfer of power from the transmitter to the sample coil and also a good protection of the receiver from destructive overloads.

3.2.2. Parallel resonant circuit

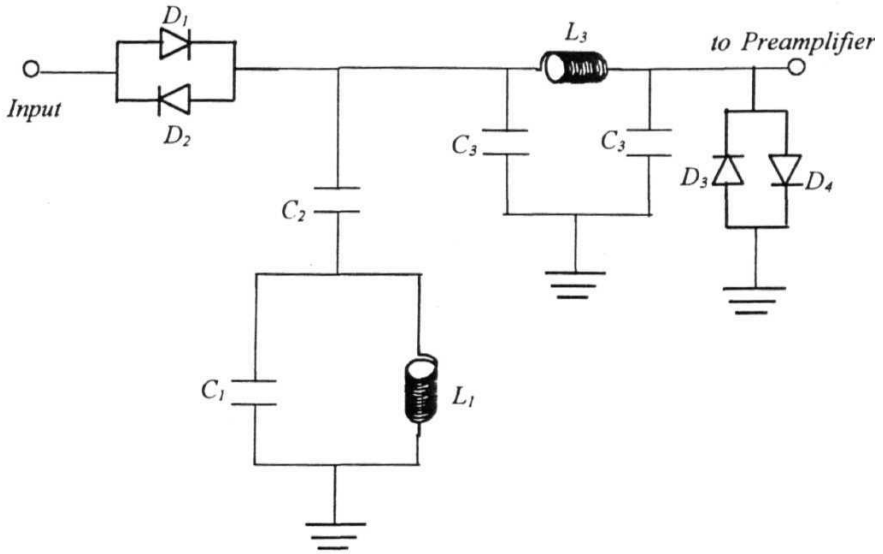


Figure. 3.10. Parallel resonant circuit [69]

The second circuit [69], given in figure 3.10, which consists of a series resonant tank circuits (L_1C_1), in series with a capacitor C_2 . The crossed diodes at the input of the circuit allow the high power rf voltages to pass through the sample coil,

while acting as an open circuit to the small signals induced in the coil. The diodes at the output of the circuit allow any //power leaked into the ground, thus protecting the receiver from the *rf* pulses, while acting as open circuit to the small NMR signals, thereby forcing them to pass entirely into the receiver. These crossed diodes also remove low level noise and other transients originating in the transmitter and hence improve the S/N of the system. In addition, the presence of the quarter wave network before the diode pair offers high impedance for transmitter pulses thus protecting the receiver from further overload [77]. The input and output impedances of the tuned coil is chosen to be equal to 50 Ohms. C_2 is chosen to be as small as possible in order to minimize the degradation of the L/C ratio and in turn the quality factor Q of the circuit. The conditions for tuning the circuit are given by [77] the equations 3.72.

$$\omega(C_1 + C_2) = \omega L$$

$$C_2 = (RQ\omega^3 L)^{-\frac{1}{2}} \quad (3.72a)$$

$$L_3\omega = \frac{1}{C_3\omega} = 50\Omega \quad (3.72b)$$

Here, Q is the quality factor of the coil which is made as large as possible to optimize the S/N and power transfer efficiency. On the other hand, a very large Q would result in a long ringing time and hence, a long dead time of the receiver, even after the turn OFF of the *rf* Hence for broad signals, it is advantageous to reduce Q at the cost of a lower S/N. L is determined from equation 3.72b and C_1 from equation 3.72a. The tuning of the circuit is done by slowly changing the values of the circuit elements, for maximum power at the coil. Fine tuning can be done **further**, by observing the ringing pattern after the pulse. The $\lambda/4$ circuit acts as the impedance transformer network. When shorted at one end, the $\lambda/4$ line transmits the low voltage signals at the designed frequency and hence attenuates all other frequencies (equivalent to a selective filter).

Two different types of $\lambda/4$ networks are used [77] depending on the recovery time requirements. The first one consists of an inductor L_3 , and two capacitors C_3

(connected as a π section) wherein the active elements are chosen to offer an impedance of 50 Ohms at the designed frequency (equation 3.72b). The signal strength is maximized by tuning the capacitor C_3 . Tuning is easier in this circuit, since there is just one capacitor, which has to be tuned. This type of $X/4$ **network**, which is built for this matching **network**, is shown with the probe containing a parallel resonant circuit.

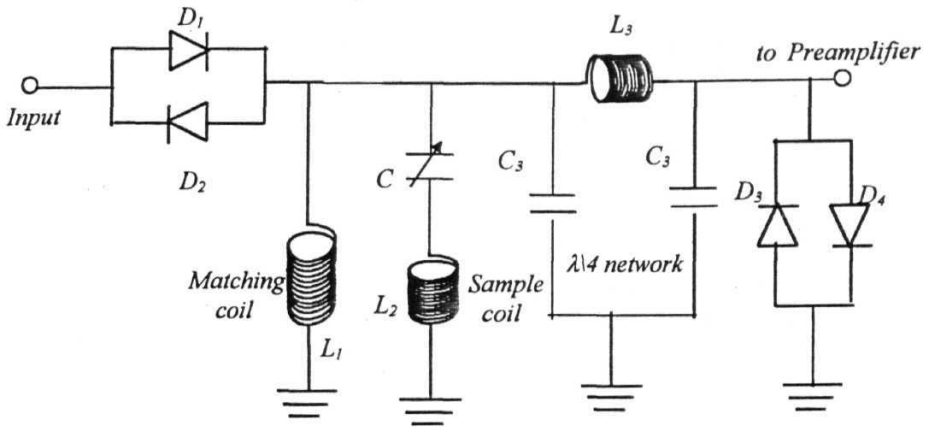


Figure. 3.11. Matching network used in the FCNMR spectrometer

Another type of $X/4$ network, which is built for this matching network, has 4 cables (RG 58) having the length of 15 meters each. This is very useful and convenient in the case of FCNMR receiver, where the detection is done at a single **frequency** (3 MHz). The details are given in the literature [77].

3.3. Receiver

The receiver consists of a fast recovery preamplifier, a tuned amplifier, a phase sensitive detector, a filter and a signal averager for signal acquisition and averaging purposes. The details of these sub-units are given below.

3.3.1. Fast recovery preamplifier

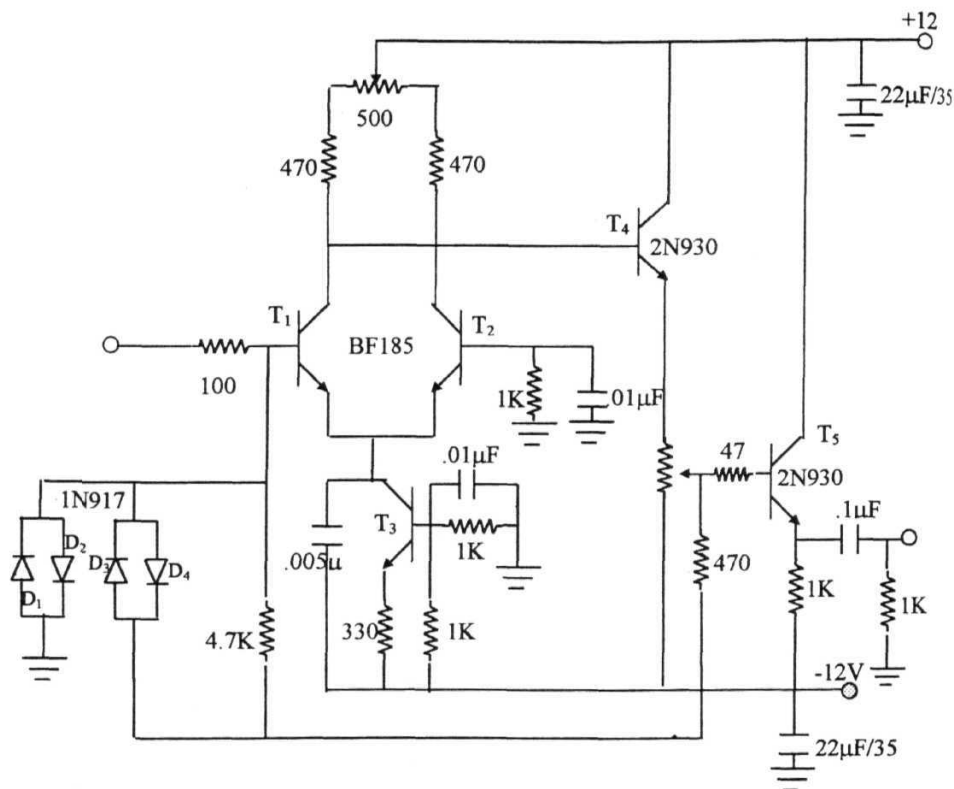


Figure. 3.12. Fast recovery preamplifier [70]

The receiver should have a large gain of about 10^5 , in order to amplify the very weak NMR signals available across the sample coil (few microvolts) before demodulation. Despite the precautions **taken**, the receiver is always overloaded by the large *rf* pulses from the transmitter, resulting in two problems. The first is the long dead time of the receiver and the second, the baseline shift after the detection due to asymmetry of saturation together with *ac* coupling. A fast recovery pre-amplifier [70]

is used to overcome these problems. The circuit diagram of the fast recovery preamplifier is shown in figure 3.12. The values of the resistors in Ohms are given adjacent to the resistors.

The preamplifier possesses high sensitivity and short recovery times, besides a large bandwidth. The *dc* level of the feedback circuit is adjusted by a variable resistor (10 K) such that the positive and negative limit of the *rf* pulses are symmetric about the baseline. The gain is adjusted to about 10 and a bandwidth from 1 kHz to 15 MHz. The diodes **D₁** and **D₂** protect the input of the receiver from large //pulses. The diodes **D₃** and **D₄** in the feed back circuit limit the high voltage *rf* pulses to the receiver to a very low value (**less** than $\pm 0.5V$).

3.3.2. *Tuned Amplifiers*

A narrow band double tuned amplifier (Matec Make, Model: 252) and a tuned amplifier (Matec make, Model: 625) are used to **amplify** the signal coming from the fast recovery preamplifier. The output of these amplifier stages is fed to a PSD.

3.3.3. *PSD and phase shifter*

The amplified NMR signal from the probe consists of all frequency components, along with the frequency of interest, and hence has to be demodulated before signal averaging. The Phase Sensitive Detector (PSD) has a shorter bandwidth and hence a better **S/N** [71] than the other detectors such as the diode detector. Since, PSD is sensitive to the phase of the signal, it is **useful** in obtaining phase information also. A commercial double balanced mixer (DBM) is used as a PSD in the present case. The signal of frequency f , is applied at the LO port of the DBM (HP make, Model No. 10534A). The reference *rf*, with frequency f_0 is fed into the ***rf* port**. The detected output, which is proportional to the frequency $f+f_0$ and the difference of the frequencies of the two inputs, f_0-f , is taken out from the IF port of the DBM. Thus, when the frequency of the reference is same as the signal, an output, corresponding to zero frequency is obtained. The signal strength is **further** maximized by decreasing the

phase difference between two inputs. When the phase difference between the two inputs are zero, maximum output is obtained. A commercial phase shifter (Merrimac make) is used for this purpose, where the phases of the output with respect to the input can be varied from 0 to 360° by using a variable power supply (0 to 30V). The PSD and phase shifter arrangement is shown in figure.3.13.

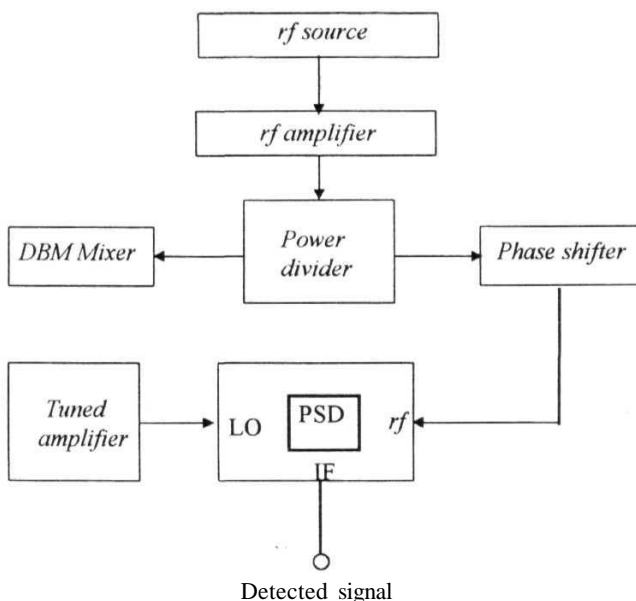


Figure. 3.13. Phase sensitive detector and phase shifter arrangement.

3.3.4. Filter and signal averager

It is known that the detected signal has a component at $2f_0$ along with the dc component, which could also be removed by this RC filter. A RC filter is used to filter the noise and other unwanted components in the signal. A digital storage oscilloscope (Tektronox, Model: 2230) is used for averaging the filtered FID signal.

3.4. Temperature Controller

The temperature control circuit developed by Chiu et al., [72] was modified and used to build a temperature control setup for the FCNMR spectrometer, which essentially consists of

- 1) An error amplifier followed by a PID type pole zero pair amplifier
- 3) Power amplifier using 2N3055 transistors.
- 4) Copper-Constantan thermocouples for feedback and measurement
- 5) A digital multimeter to measure the *thermo-emf* (temperature)
- 6) A double wall evacuated glass Cryostat and
- 7) A heater and air blower set up (fan or an air-compressor)

The temperature control setup is shown in figure 3.14. In liquid crystals, the orientational ordering of the molecules is sensitive to the temperature, and hence a good temperature control facility is essential. The narrow cylindrical bore of the field cycling magnet and heat radiated into the bore necessitates a more constrained cryostat setup. A commercially available electric fan and an air compressor are used, depending on the temperature requirements, to blow air into the cryostat. A double-walled cryostat, is designed to fit into the small bore of the cylindrical magnet (diameter of the outer wall should be less than 5 cm) and is shown along with the heater set up in figure 3.14. The sample is kept inside the double-walled evacuated glass cryostat, which is used to minimize heat loss (or gain) to (from) the surroundings. It is also important to keep the sample coil at the center of the cylindrical magnet, where maximum homogeneity of the magnetic field can be obtained.

The electronic circuit capable of controlling current through the heater coil, which automatically varies the current in order to control the amount of heat generated by the heater coil is explained here. A drift-free modulation-free control signal is obtained through two operational amplifier stages of the temperature controller as shown in figure 3 14.

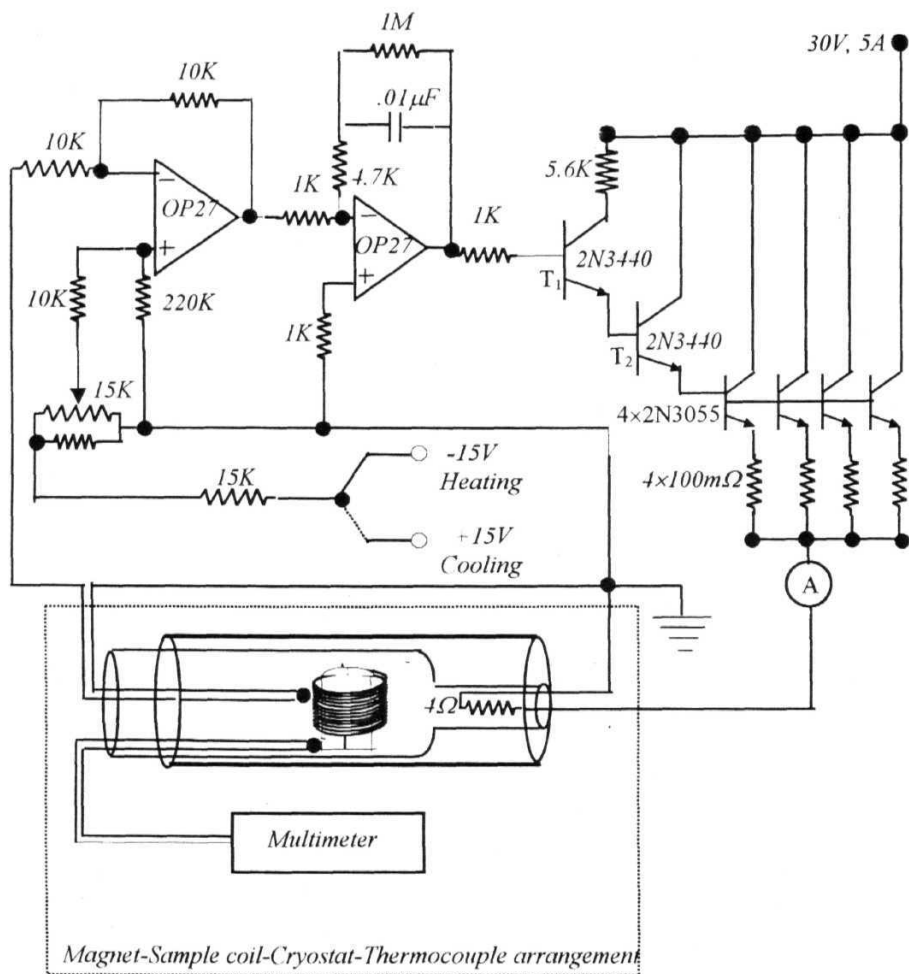


Figure. 3.14. Temperature controller and Cryostat arrangement

The first stage of the circuit acts as a simple error amplifier. This takes the input reference signal through a 10 turn calibrated helipot, and the thermo-emf sensed by the thermo couple junction kept on the sample tube. The difference (error) is

amplified and any variation in the set temperature would be removed by increasing or decreasing the current through the heater coil.

The second stage, which is a **PID** type pole-zero amplifier designed for the field-cycling control circuit, is found to be very **useful** here. A modulation free control signal is obtained using this, which in turn is fed to the bases of the power transistors. When the reference voltage is more than the sensor voltage, a positive voltage appears at the output of the error amplifier, thereby turning ON the power transistors. This leads to an increase in the current flowing through the heater coil and hence, the temperature increases to the set value. The increase in the sensor voltage reduces the difference at the inputs of the error amplifier, thus making the output of the error amplifier less positive and less current pass through the heater coil. This heating decreases once the temperature is higher than the required value. This increase and reduction of heating, controls the temperature to stay at a constant value. Apart from the thermal mass inside the cryostat there are other factors like the rate of airflow, position of the sensor, and the position of the heater coil, are crucial for the good performance of the temperature controller. A temperature stability of 0.2 K within the time about 30 minutes is obtained.

3.5. Automation

The FCNMR spectrometer is connected to a PC through IEEE488 interface bus for automatic controlling of the spectrometer for data transfer. A digital storage oscilloscope and the delay generators are also interfaced with the PC for signal averaging and measurement of FID amplitudes.

Conclusions of the unit - I

- A simple Field Cycling Network capable of providing reasonable field cycling is achieved.
- Some of the important units were built for the transmitter, receive, probe and temperature controller and partially automated with the help of a computer. Thus FCNMR spectrometer capable of operating at a detection frequency of about 3 MHz is fabricated and standardized.
- The performance of the spectrometer was tested by measuring J values in standard samples.
- The FCNMR spectrometer has been routinely used for collecting, proton T_1 data as a function of frequency and temperature, in liquid crystals. Spin-lattice relaxation time experiments had been performed on the homologous series 4O.m, (butyloxybenzylidene alkylanilines) as a part of this Ph. D thesis. The results are presented in chapter-6. A binary mixture of liquid crystals, 8CN and 7BCB has been studied and the results are presented in chapter-7. FCNMR spectrometer has been used by other researchers [78,79] in the same laboratory, for the frequency and temperature dependent T_1 measurements in liquid crystals.
- It is important to mention that, the conventional NMR spectrometer available in this laboratory, which is capable of providing proton T_1 from 3 MHz to 50 MHz enhances the time window by another decade. The T_1 data collected at 3 MHz using both the spectrometers is useful to understand the functioning of the FCNMR spectrometer and the reliability of the NMRD data. The specifications of the spectrometers (FCNMR and NMR) are given in the tables 1 and 2.

Table 1. Specifications of the FCNMR spectrometer

1. Operating frequency range	0 kHz to 3 MHz
2. Polarization and detection frequency	3 MHz to 4 MHz
3. Maximum OFF time	1 ms
4. Maximum turn ON time	2 ms
5. Field stability	1 in 10^5
6. Field homogeneity	1 in 10^{-5}
7. Bandwidth	1 MHz
8. Pulsed //power	Up to 1 kV (peak to peak) into 50 Ohms.
9. Typical n^2 pulse width	4-8 μ s for proton
10. ON/OFF ratio of r_f pulse	100dB
11. Transmitter isolation	60dB minimum
12. Recovery time	15-20 μ s
13. Interface bus with PC	GPIB
14. Temperature range	77K to 400 K (with 0.2 K stability).

Table 2. Specifications of the NMR spectrometer

1. Operating frequency range	3 kHz to 50 MHz
2. Field stability	1 in 10^6
3. Field homogeneity	1 in 10^{-5}
4. Bandwidth	2MHz
5. Pulsed //power	Up to 1 kV (peak to peak) into 50 Ohms.
6. Typical $\pi/2$ pulse width	2-5 μ s for proton
7. ON/OFF ratio of <i>rf</i> pulse	100dB
8. Transmitter isolation	60dB minimum
9. Recovery time	15-20 μ s
10. Interface bus with PC	GPIB
11. Temperature range	77K to 500 K (with 0.2 K stability in one hour).

References for the Unit - I

- 1 R. V. Pound, *Phys. Rev.* **81**, 156 (1951).
- 2 Schumacher, *Phys. Rev.* **112**, 837 (1958).
3. A. Abragam and W. G. Proctor, *Phys. Rev.* **109**, 1441 (1954).
- 4 P. S. Pershan, *Phys. Rev.* **117**, 109 (1960).
- 5 B. C. Johnson and W. I. Goldberg, *Phys. Rev.* **145**, 380 (1966).
6. G. P. Jones, J. T. Daycock, and T. T. Roberts. *J. Phys. E (Sci. Just)* **2**, 630 (1968)
- 7 R. Blinc, M. Luzar, M. Mali, R. Osredkar, J. Seliger and M. Vifan, *J. Physique Colloque* **37**, C3-73 (1976)
- 8 D. T. Edmonds, *Phys. Rep.* **29**, 233 (1977).
9. M. Packard and R. Varian *Phys. Rev.* **93**, 941 (1954).
- 10 A. Bloom and D. Mansir, *Phys. Rev.* **94**, 41 (1954)
- 11 A. G. Redfield, W. Fite and H. E. Bleich, *Rev. Sci. Instr.* **39**, 710 (1968).
12. F. Noack 'NMR Field Cycling spectroscopy - principles and applications' in *Progress in NMR Spectroscopy*, **18**, 171 (1986), and references therein.
13. E. Rommel, K. Mischker, G. Osswald, K. H. Schweikert and F. Noack, *J. Mag. Res.* **70**, 219 (1986).
14. T. P. Das, and E. L. Hahn, *Solid State Physics, Suppl.* **1**, Academic Press, New York (1958).
- 15 L. C. Hebel and C. P. Slichter, *Phys. Rev.* **113**, 1504 (1959)
16. Y. Masuda and A. G. Redfield, *Phys. Rev.* **125**, 159 (1962).
17. Y. Masuda and A. G. Redfield, *Phys. Rev.* **133A**, 944 (1964).
- 18 A. G. Redfield, *Phys. Rev.* **130**, 589 (1963).
19. A. G. Redfield, *Phys. Rev.* **162**, 367 (1967)
- 20 R. E. Slusher and E. L. Hahn, *Phys. Rev.* **116**, 332 (1968).
- 21 D. T. Edmonds, *Bull. Mag. Res.* **3**, **53** (1981).
22. P. Van Hecke and G. Jannsens, *Phys. Rev.* **B17**, 2124 (1978)
- 23 P. Coppen, L. Van Gerven, S. Clough and A. J. Horsewill, *J. Phys. C* **16**, 567 (1983).
- 24 M. Perger, A. M. Raaen and I. Svare, *J. Phys.* **C16**, 181 (1983).

- 25 K. H. Schweikert, *Ph. I) Thesis*, Universitat Stuttgart, Germany (1990).
26. I. Solomon, *Phys. Rev.* 99, 559 (1955).
- 27 I. Solomon and N. Bloembergen, *J. Chem. Phys.* 25, 261 (1956).
- 28 J. Seliger, R. Orsedgar, M. Mali and R. Blinc, *J. Chem. Phys.* 65, 2887 (1976).
- 29 S. H. Koenig, R. G. Bryant, K. Hallenga and G. S. Jacob, *Biochemistry*, **17**, 4348 (1978).
30. M. Vilfan, J. Seliger, V. Zagar and R. Blinc, *Phys. Lett.* 79 A, 186 (1980).
31. F. Winter and R. Kimmich, *Mol. Phys.* 45, 33 (1982)
32. F. Winter and R. Kimmich, *Biochem Biophys. Acta* **719**, 292 (1982).
- 33 R. Blinc, M. Vilfan and J. Seliger, *Bull. Magn. Res.* 5, 51 (1983).
- 34 J. Dolinsek, T. Apih and R. Blinc, *J. Phys. Cond. Matter* 4, 7203 (1992).
35. R. Kimmich, *Bull. Magn. Res.* 1, 195 (1980).
36. R. Kimmich, *"NMR: Tomography, Diffusometry, Relaxometry"*, Heidelberg: Springer-Verlog (1997), and references therein.
- 37 Proceedings of the *"Field Cycling NMR Relaxometry - Symposium"*, Berlin (1998).
38. R. Zamer, E. Anoardo, O. Mensio, D. Pusiol, S. Becker and F. Noack in *"Field Cycling NMR Relaxometry - Symposium"*, Berlin, p92 (1998).
39. A. G. Krushelnitsky, D. V. Markov, A.A. Kharitonov, A. E. Mefeld and V. D. Fedotov in *"Field Cycling NMR Relaxometry - Symposium"*, Berlin, 20 (1998)
40. D. J. Pusiol and E. Anoardo, in *"Field Cycling NMR Relaxometry - Symposium"*, Berlin, 29(1998).
- 41 J. Struppe, T. Liesener, F. Noack and M. Vilfan in *"Field Cycling NMR Relaxometry - Symposium"*. Berlin, 32 (1998).
- 42 J. Kryzyszek, M. Notter, and A. L. Kwiram, *J. Phys. Chem.* 98, 3559 (1995).
43. G. Sturm, D. Killian, A. Lotz and J. Voitlander in *"Field Cycling NMR Relaxometry - Symposium"*, Berlin, 86 (1998).
- 44 C. Job, J. Zajicek and M. F. Brown, *Rev. Sci. Instrum.* 67(6), 2113 (1996).
45. G. Scauer, W. Nusser, M. Blanz, and R. Kimmich *J. Phys. E: Sci Instrum* 20, 43 (1987)
- 46 M. Blanz, T. J. Rayner, J. A. S. Smith, *Meas. Sci. Technol.*, 4, 48 (1993).
- 47 G. Grossel, F. Winter and R. Kimmich, *J. Phys. E: Sci Instrum* **18**, 358 (1985).

48. G. R. Kumar, P. Chaddah, *Cryogenics* 27, 229 (1987).
49. K. H. Schweikert, R. Krieg and F. Noack, *J. Magn. Reson* 78, 77 (1988)
50. A. G. Redfield, W. Fite and H E Bleich, *Rev. Sci. Instr.* 39, 710 (1968)
51. R. Kimmich and F. Noack *Z. Naturforsch* **25a**, 1680, (1970).
52. R. D. Brown and S H. Koenig, *IBM Research Rep. RC6712*, York Town Heights (1977).
53. W. Wolfel, *Ph. D Thesis*, Universitat Stuttgart, Germany (1978).
54. V. Graf *Ph. I) Thesis*, Universitat Stuttgart, Germany (1980).
55. G. Voigt and R. Kimmich, *Polymer*, 21, 1001 (1980).
56. J. Hak, *Arch. Electrotech.* 30, 736 (1936).
57. D. B. Montgomery, *Solenoid Magnet Design*, Wiley, New York (1969)
58. L. Cesnak and D. Kabat, *J. Phys (E)* 5, 944 (1972).
59. G. Grossel, F. Winter and R Kimmich, *J. Phys. E: Sci Instrum* 18, 358 (1985)
60. M. Packard, R. Varian, A Bloom and D. Mansir *Phys. Rev.* 93, 941 (1954).
61. C. W. Lander, *Power Electronics*, McGraw-Hill, New York (1981).
62. O. Feustel and W. Schmidt, *Sensorhalbleiter und Schutzelemente* Vogel Verlag, Wurzburg (1982)
63. H. Buri, *Leistungshalbleiter*, Brown, Boverie and Cie, Mannheim (1983)
64. M. Kubat, *Power Semiconductors*, Springer, Berlin (1984)
65. R. Felderhoff, *Leistungselektronik*, Hanser, Munchen (1984).
66. I. J. Lowe and C. E. Tarr, *J Phys.*, E1,320 (1968).
67. F. Bloch , *Phys. Rev* 70,460, (1946).
68. W. G. Clark and J. A. McNeil, *Rev. Sci. Instrum* , 44, 844 (1973).
69. D. C. Ailion, “ *Methods of Solid State Physics*”, ed., J. N. Mundy, S. J. Rothman, K. H. Fluss, and L. C. Sumedskjaer (Academic Press) **21**, 439 (1983).
70. B. Ramadan, Ng. T. C. and E Tward, *Rev. Sci. Instr.*, 45, 1174 (1974).
71. T. C. Farrar and E. D. Becker, ‘*Pulse and FT NMR*’, Academic Press, New York (1971)
72. U. T. H. Chiu, D. Griller, K. V. Ingold, and P. Knittel, *J. Phys.* **E12**, 274 (1979)
73. K. Venu, *Ph. D thesis*, University of Hyderabad, India (1986).
74. A. S. Sailaja, *Ph.D Thesis*, University of Hyderabad, India (1994); A. S. Sailaja, D. Loganathan and K. Venu, *Proc. Ind. Acad. Sci. India*, **66(A)**, 161 (1996).

75. McLachlan, *J. Magn. Reson.*, 47, 490 (1982).
- 76 T. Jeener and P. Broekaert, *Phys. Rev.*, **157**, 232 (1967).
- 77 E Fukushima and S. B. W. Roeder, '*Experimental Pulsed NMR: Anuts and bolts approach*', Addison Wesley, Reading, Massachusetts (1981).
- 78 M. Venkata Reddy, *M. Phil Thesis*, University of Hyderabad, Hyderabad India (1999).
79. V. Satheesh, *Ph. D Thesis*, University of Hyderabad, Hyderabad, India (2000).

Unit II

Molecular Dynamics of Liquid Crystals

Studied by FCNMR Technique

Chapters 4 to 7 are presented in Unit-II. This unit deals with the molecular dynamics of liquid crystals studied in two different types of systems.

In order to understand the microscopic molecular level behavior responsible for macroscopic physical properties of liquid crystals, a systematic study was carried out, on the well known homologous series of liquid crystalline systems, called 4O.m (Butyloxybenzylidene Alkylanilines). In particular, molecular dynamics is studied as a function of terminal end chain properties. Before presenting (Chapter-6) the actual results obtained from the present Proton Nuclear Magnetic Relaxation Dispersion (NMRD) studies, the background necessary to understand and analyze the results have been discussed in chapters 4 and 5. Chapter-4 deals with the physics of liquid crystals, with a special reference to structure-property relationships. Chapter-5 presents the nuclear magnetic relaxation theory of liquid crystals.

A study of molecular dynamics of binary liquid crystalline mixtures (8CN+7BCB) exhibiting the Induced Smectic A_d Phase (ISP) was carried out with the aim of understanding the dynamic environment and factors responsible for the stability of the nematic and smectic A_d phases. Chapter-7 presents the results obtained from the pure systems 8CN and 7BCB and their binary mixtures. Recent experimental and theoretical developments on the ISP have also been presented. Molecular dynamic parameters obtained as a function of composition have been presented and compared with the theoretical results.

Chapter 4

Structure - Property Relationships in Liquid Crystals

Section A of this chapter consists of, an introduction to liquid crystals, types of liquid crystals and molecular engineering of liquid crystalline phases. Thermal stability of the nematic phase is analyzed as a function of terminal alkyl chain properties. A plot between the number of carbon atoms in the alkyl terminal chain and the nematic temperature range in systems under the present NMRD study clearly indicate *odd-even effects, chain length effects* alongwith the '*symmetry effect*'. In order to show the effect of symmetry of two terminal chains, a new parameter called the 'deviation from the symmetry' is defined. It has been observed that, maximum stability is seen when the 'deviation from the symmetry' is close to zero. References for this section are given separately at the end.

A major portion of Section B presents different theories of liquid crystals based on the 'mean field', the 'Onsagar' and the 'generalized' models. Theoretical models explaining the isotropic-nematic and nematic-smectic A phase transitions have been briefly discussed, with a special reference to end chain parameters. An attempt has been made to gather information available in the literature, which link end chain parameters to the physical properties connected with the molecular dynamics. For instance, the elastic constants, directly connected with the collective director fluctuations in liquid crystals, have been discussed based on the experiments, theories and simulations performed so far. Similarly, results obtained from different studies on the rotational dynamics and self-diffusion have also been discussed. References have been listed at the end of the section B separately.

Section A

Chemical structure and Thermal stability in Liquid Crystals

4.1. Introduction

The molecules composing a solid generally possess positional order and orientational order, meaning that, the centers of mass of the molecules occupy specific locations and the molecular axes point in certain directions. When the solid melts to a liquid, both positional and orientational orders vanish. In this state, there are no preferred locations for the centers of mass, or preferred directions for the molecular axes (figure 4.1a). The molecules in the solid may change their positions and orientations slightly due to thermal motion, but their positions are generally fixed at specific lattice points and motion is with respect to the perfect geometrical lattice. In the liquid state, molecules diffuse freely throughout the sample and the centers of mass move in random directions

There are substances which do not directly pass from crystalline solid to isotropic liquid and vice versa, but adopt an intermediate structure which flow like a liquid and yet possesses the anisotropic physical properties similar to that of crystalline solids. This kind of a phase is termed as the liquid crystalline phase, **mesophase** or mesomorphic phase and the materials, **mesomorphs**. Molecules diffuse freely throughout the sample while maintaining some positional and orientational order. In general, it is accepted that liquid crystals represent a state of higher order than classical isotropic liquids. The simplest case of liquid crystalline phase is the **nematic** phase in which there is a higher probability of the molecular axes of neighboring molecules pointing in an average direction, called the *director*. In the **smectic** phase there is a higher probability of the centers of mass lying in layers, with molecules moving freely

from one lattice site to another. Considering the fact that solids have elastic properties and liquids a viscous nature, a visco-elastic nature can be conveniently assigned to liquid crystals.

Liquid crystals are beautiful and extremely useful physical systems, thus providing scientists and engineers, one of the fascinating fields of scientific and industrial research. There are very many basic books [1-7], which give details of various aspects of liquid crystalline physics and phase transitions.

Liquid crystal molecules are organic in nature and many of them are elongated in shape. These elongated units are more or less parallel to each other in mesophases, and this long range orientational ordering is the reason for their anisotropic physical properties. A measure of degree of this orientational ordering is called the *order parameter*. Their visco-elastic nature and easy response to electric, magnetic and surface forces have generated innumerable applications.

The following physical phenomena have made liquid crystal studies more important than the other physical systems in the recent times [5,7].

- Spaces of low dimensionality
- Wide variety of phase transitions and critical domains
- Coupled order parameters
- Multicritical points
- Anisotropic scaling behaviors
- Defect mediated transitions
- Multiple reentrant phases
- Induced Smectic Phases (ISP) formed in binary mixtures
- Transitions induced by collective fluctuations
- Ferroelectric phases and glass transitions
- Incommensurate layer spacing and **dimers**
- > Solitons in liquid crystalline phases
- Cybotactic clusters and frustration

These phenomena can be studied at easily accessible temperatures in liquid crystals. Besides their technical applications in optic and electronic displays, liquid crystals can certainly be regarded as a paradise for the physics of phase transitions.

4.2. Types of Liquid Crystals

Liquid crystalline phases can be obtained by heating or cooling substances, which are called ***thermotropic*** liquid crystals. Liquid crystals can also be obtained by dissolving certain substances in a controlled amount of solvent (such as water). This type of material is called a ***lyotropic*** liquid crystal.

There are two known classes of thermotropic liquid crystals based on molecular anisotropy. The more common variety called *calamitic* liquid crystals, are made up of molecules with a rod-like shape. The other kind called, *discotic* liquid crystals [2] are made up of molecules with a disc-like shape. The first kind of liquid crystals has a molecular length, usually a few times larger than the molecular width. They form nematic, smectic, and cholesteric phases.

4.2.1. Nematic and Smectic Phases

In the ***nematic phase***, the molecular centers of gravity are disordered as in the case of an isotropic liquid, but we have a statistically parallel orientation of the long axes of the molecules along the axis called the *director*, n (figure 4.1a). The nematic phase has a freedom of mobility concerning rotation about different axes and translation (figure 4.1a). External fields and forces easily affect molecules in the nematic phase.

The molecules are arranged in *Smectic A* (S_A) phase in such a way that their ends stay in a line, to form layers in which the long axes of the molecules tend to be orthogonal to the layer planes. The molecules not only align but also have their cores closely packed. Rotational motion of the molecules is fairly free, but there is no long-

range regularity in packing the centers of gravity of the molecules in the planes of the smectic layers. As a result they form phases in which the molecules spend most of the time in layers, but can move freely within a layer. The layers are therefore liquid like in nature. Movement of molecules from one layer to another occurs quite freely, and the layers themselves are quite free to slide and move over on another [3]. These types of liquid crystals are known as layer structures without order. Figure 4.1a describes the dynamic degrees of freedom of nematic and smectic liquid crystals.

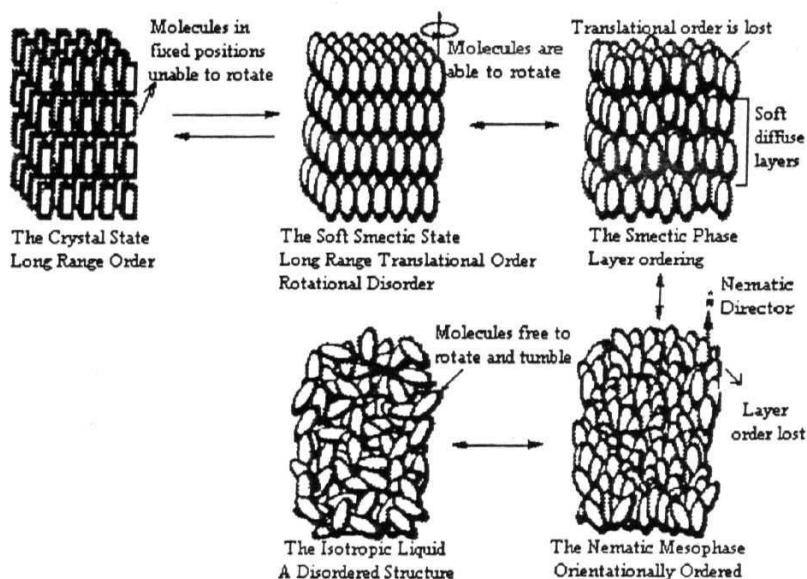


Figure 4.1a Melting process of a rod-like liquid crystalline material. Various dynamical degrees of freedom are described with respect to the *director* (n) axis [7].

There are different smectic A phases (A_1 , A_d , A_{1f}), based on the layer spacing and dipole moments. In the case of the smectic A_d phase, the layer spacing is longer than the molecular length. Factors responsible for the formation of the smectic A_d phase are discussed in chapter-7.

The layer thickness in the smectic A phase is often somewhat **less** than the molecular length. This has been attributed to slight interpenetration of the layers which

often have liquid-like hydrocarbon chains at the interfaces, or to departures of terminal alkyl chains from their fully extended (*all-trans*) configuration. Another interesting view suggested is that the difference in layer thickness might arise through a gyroscopic motion [4] of the elongated molecules about the central part.

Smectic C (S_C) phase is a tilted analogue of the S_A phase. The smectic C layers have a liquid like, unstructured arrangement of the lath-like molecules which are tilted with respect to the layer plans at angles which vary from compound to compound. For a given compound also, the degree of tilting may either vary with temperature over the range of the phase, or stay relatively constant [3].

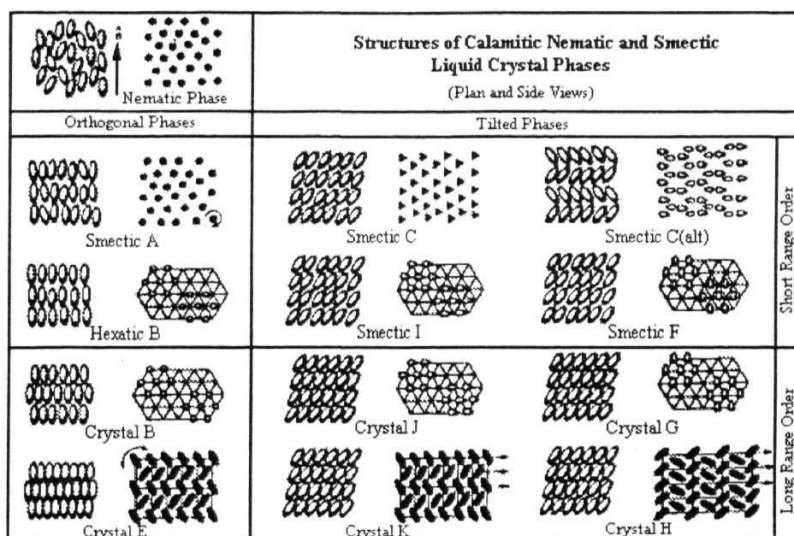


Figure 4.1b. Structures of different mesophases in calamitic liquid crystals [7].

There are layer structures with an order unlike smectic A and C phases. The molecules, which tend to lie orthogonal to the layer planes, are called *smectic B* phase. And, layer spacing should therefore be the same as the molecular length in this highly structured S_B phase. The dimension of the hexagonal net however, being small in relation to the size of the molecules, molecular rotation can hardly be regarded as free, but probably co-operative. The layers of the S_B phase cannot undergo bending or

curving deformations, necessitating a splay deformation of the parallel molecular alignment which also has a consequence on the microscopic texture which an S_B phase tends to adopt [5]. Figure 4.1b describes the structures of different mesophases seen in liquid crystals.

In certain homologous series S_G phase is formed when alkyl chains are present. This is also considered as tilted phase, the layer being highly structured. Layer spacing is smaller than the molecular length. The molecules undergo rapid, though restricted reorientational motion [3]. The arrangement in the layers can be described as monoclinic, compared with the orthorhombic, orthogonal arrangement of the S_E phase. There are other smectic (E, F, G, I, J, K) phases, as shown in figure 4.1b.

4.3. Chemical Structure and thermal stability

It is known that the anisotropic shape and the resulting anisotropic forces of a rod-shaped molecule can give rise to the formation of the liquid crystal phases [5,10-12]. The requirement that the molecule of a nematogen possesses a fairly rigid core structure, usually with terminal substituents associated with it. Chemists, [5,10-12] have been trying to understand the factors, which relate molecular structure to liquid crystal properties. For certain properties like liquid crystal transition temperatures this has been reasonably successful, but for others such as elastic constants and molecular dynamics, there is still much work to be done. A typical calamitic liquid crystal forming molecule [5] has the idealized molecular structure shown in figure 4.2.

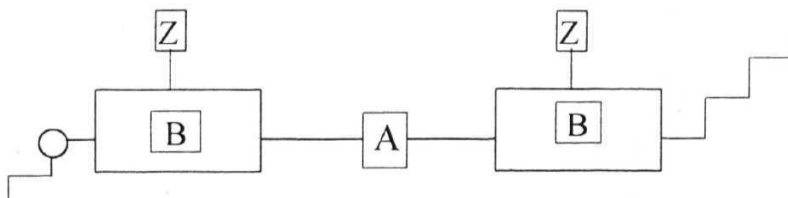


Figure 4.2. Idealized structure of a typical calamitic liquid crystal forming molecule

Where, B, B are ring systems, Z, Z are lateral substituents and A is the linking group. Alkoxy (O is an oxygen atom) and alkyl chains are also shown in figure 4.2, where the segments represent the C-C bonds between the methylene groups present in the end chains.

4.3.1. Physical properties and substituents

4.3.1.1. Role of the core

Aromatic rings connected either directly or through a linking unit are very useful in providing rigidity to the molecule. The ring system strongly affects liquid crystal stability and other physical properties like dielectric anisotropy, birefringence, elastic constants and viscosity [3]. Theoretically, a ring system, which would allow a linear configuration, could be used. Decreased ring flexibility has the effect of increasing transition temperature [5].

4.3.1.2. Role of linking groups

The principle object of introducing a linking group between ring systems is to increase the length of the molecule as well as to alter the polarizability and flexibility of the molecules [3,10-12]. Generally, two or multiples of two atoms are used in the linking group to preserve the linearity of the molecule and the linking points of the rings are usually *para*, again to preserve the linearity of the molecule.

Generally, more polar the linking group is the higher is viscosity [5]. If the linking group is an alkyl chain, the homologous series shows *odd-even effects* in the properties with the number of carbon atoms. Multiple bonds usually present in the linking unit restrict the freedom of rotation, and preserve the rigidity and elongation of the molecules [3,10-12]. Such multiple bonds can also conjugate with the phenylene rings, enhancing the anisotropy of polarizability. Extension of the linking unit greatly

enhances the nematic-isotropic transition temperature, i.e., increases the thermal stability of the nematic order.

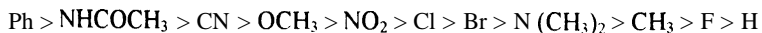
4.3.1.3. Role of the lateral substituents

It is possible to broaden the molecule [10-12,5] by introducing substituents in place of hydrogen in a position, along the side of the aromatic core structure. For a range of substituents with varying size, polarizability and polarity, the nematic-isotropic transition temperatures fall in proportion to the size of the substituent. These effects have been rationalized in terms of the molecules giving a reduction in intermolecular attractive forces. In smectic phases lateral attractions are important, thus the group efficiency order is different from that of nematic phase. For smectic A phases, the order is reported as [5]



4.3.1.4. Role of the terminal substituents

Most of the liquid crystal molecules contain at least one terminal alkyl chain. Generally any terminal group which extends the molecular long axis, as long as it does not increase the molecular width, will increase the thermal stability of the nematic phase. The theories of Maier and Saupe [10] suggest, that the nematic-isotropic transition temperature of the compound is related to the molecular polarizability of the molecule, which is invariably related to the terminal group and its influence on the conjugation within the molecule. The nature of the terminal substituents or end groups in the molecule of the mesogen has profound influence on the liquid crystal properties of the compound. An average order of terminal group efficiency [5] in enhancing the nematic-isotropic transition temperature could be represented as:



4.3.2. *Nematic phase stability and terminal chains*

The study of transition temperatures as a function of end chains has attracted scientists since long [3]. Such studies have been well documented for a large number of homologous series [10-12,19]. Some of the important observations made on the studies of alkyl and alkoxy groups are summarized here [3,5]. These observations are illustrated using the data available on the homologous series of liquid crystals, butyloxy benzylidene alkylanilines (abbreviated as 4Om, with m varies from 1 to 12). The molecular dynamics studies carried out on some of these systems are presented in Chapter-6. Observations made in this chapter would be discussed again in Chapter-6, in order to correlate the dynamical parameters with the phase stability and physical properties.

4.3.2.1. Odd-Even effects

In the compounds with alkyl and alkoxy end chains it is known that nematic-isotropic transition temperatures show *odd-even effects*. Particularly, this alternation is most pronounced for short alkyl chain lengths. Odd-even effects can be explained by the odd carbon atom alkyl chain having a terminal **CH₃**, which extends the long molecular axis, whereas in an even number carbon chain, the terminal chain lies off axis. As the alkyl chain becomes longer, the effect becomes less marked. If the nematic-isotropic transition temperatures are high, the curves are of the falling type; if the nematic-isotropic transition temperatures are low, the curves rise.

4.3.2.2. Alkyl chain length

In the case of 4Om series, the nematic phase temperature range varies as a function of the end alkyl chain length. This is shown in figure 4.3.

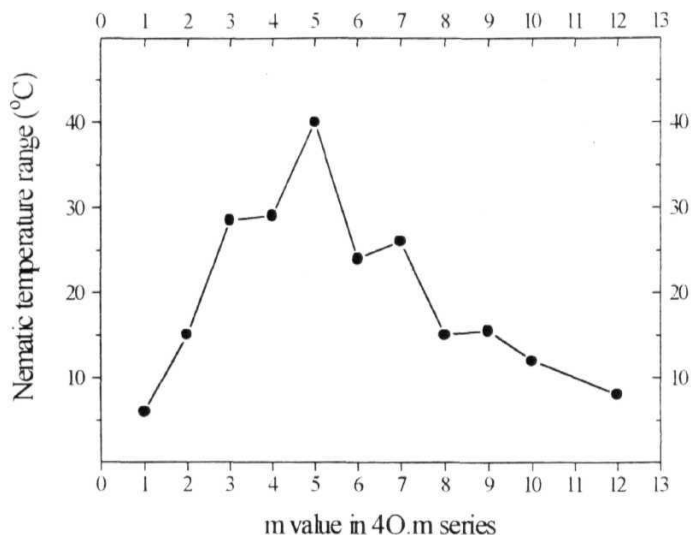


Figure 4.3. Variation of nematic temperature range as a function of alkyl chain length in the homologous series Butyloxybenzylidene Alkylanilines (4O.m).

The nematic temperature range is considered here, as a representative of the nematic phase stability instead of the transition temperatures. The nematic phase stability increases with chain length initially, and decreases with chain length at the cost of smectic A (and/or Smectic C) phase stability.

The alkyl chain length increases the stability of the smectic phases whereas the alkoxy chain length enhances the nematic stability alone. The conjugative interactions between O-alkyl functions and the rings increase the anisotropy of the polarizability and intermolecular attractions for the system, leading to higher transition temperatures for alkoxy compounds. The intermolecular repulsion for the two systems would differ, since a $-\text{CH}_2-$ and $-\text{O}-$ function differs, electronically. Thus, in aromatic systems, alkoxy groups always give rise to a higher liquid crystal thermal stability compared to alkyl analogues, this being due to increased conjugation and rigidity in the system. In most cases, the oxygen atom is directly bonded to the aromatic core.

4.3.2.3. Symmetric end chains

When the liquid crystal molecules have two end chains, the phase transition temperatures are higher for the systems with equal chain length (symmetric) than that of the systems having end chains of different lengths (asymmetric) [21]. When alkyl and alkoxy chains are present in a single system, the balancing of these end chains affect the phase transition temperatures as well as the temperature ranges of nematic and smectic A phases. The molecular weights of terminal chains could be considered as the measure of this 'balancing', and if they are nearly equal, the system is **balanced**. In other words, the system is symmetric about the molecular short axis.

The term 'nematic phase stability' can be attributed to the isotropic to nematic transition temperature as well to the temperature range of nematic phase. For example, if the transition temperature were to be considered as the only scale, a nematic phase existing between 100 and 102° C would be seen as highly stable than the nematic phase existing between 20 to 80° C. Hence, it is reasonable to consider both the factors and define a parameter called, 'the stability factor (S_{nem})',

$$S_{nem} = T_{mid} * \Delta T_{nem} \quad (4.1)$$

T_{mid} here, is the mid-nematic temperature and ΔT_{nem} , the nematic temperature range. Similarly, a parameter representing the balancing (symmetry) of alkyl and alkoxy chain present in the 4O.m series is defined, based on the molecular weights of these end chains. In the case of alkoxy chain the molecular weight of the oxygen atom is also taken into **consideration**. The 'balancing factor' (B) is defined as

$$B = \frac{M_{alkyl} - M_{alkoxy}}{M_{alkyl} + M_{alkoxy}} \quad (4.2)$$

where, M_{alkyl} is the molecular weight of the alkyl chain and M_{alkoxy} , is the molecular weight of the alkoxy chain. Here the value of B quantifies the deviation from symmetry. B=0 represents a system with a perfect balancing of alkyl and alkoxy chains. B>0 represents the alkyl chain domination and B<0, represents the alkoxy

chain domination. The ‘balancing effect’¹ seen in the 4O_m series is shown in figure 4.4 The systems with balanced (symmetric) end chains show high nematic stability than the unbalanced (asymmetric) ones.

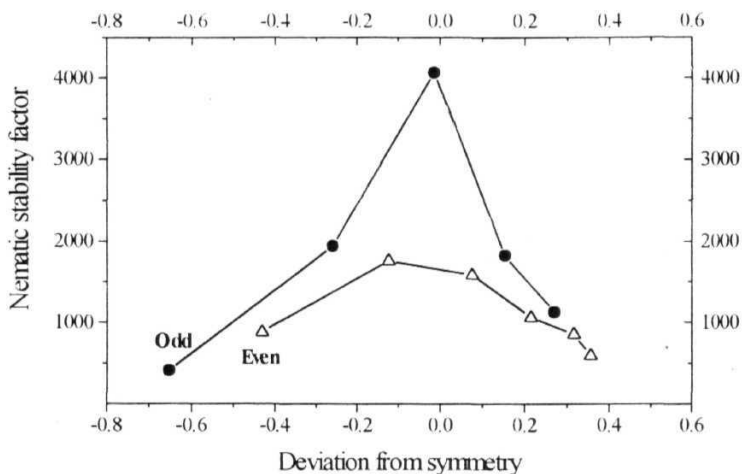


Figure 4.4. Effects of the symmetric terminal end chains on the stability of the nematic phase. Odd and even systems are plotted separately with different symbols.

From the figure 4.4, it can be said that the stability factor (M_{nem}) is higher for odd systems than for the even ones. The transition entropies and transition energies measured in the nO_m homologous series [20] peak when the alkyl chains are balanced. This is discussed in Chapter-6. A similar analysis of another homologous series [19] having alkoxy groups at both ends also shows similar trends.

The reasons for the odd-even alteration of transition temperatures are explained in the literature [3]. If the alkyl chain adopts an extended all *trans* conformation, the axial **polarizability** increases about twice as much at right angles on passing from an even to an odd member of the alkyl-substituted series; on passing from odd to an even number, the two polarizabilities increase at about the same manner [3]. At comparable molecular weights, the anisotropic polarizability therefore, is greater for odd than for

even members and their nematic-isotropic transition temperatures and temperature ranges are higher. Such arguments explain the rising type of the nematic-isotropic transition temperature curve, because of the increasing molecular polarizability along the series. Though the assumption of regularly extended conformation for a flexible chain is unreasonable, the regularity of alternation of T_{NI} values can be explained only if some preference for such conformation does exist. The damping of alternation at longer chain lengths is explained by a statistical increase in population of non-extended conformations giving a decreasing difference in the anisotropic polarizabilities for odd and even numbers.

Extending the length of the terminal n-alkyl chain increases the smectic forming tendency (starts from 8 to 9 carbon atoms) relative to the nematic forming tendency (pure nematics are possible below 6 to 7 carbon atoms in the end chains) of a system. Eventually a stage is reached where nematic properties are extinguished (about 14 to 15 carbon atoms) and the compounds are purely smectic. Plots of transition temperature against chain length for S_A-N and S_A-I transitions are therefore very similar to those of nematic-isotropic transition [3]. Depending on the core structure, the smooth curves can either rise or fall with alternation, as the series is ascending [5]. Systems having two terminal alkyl chains usually [5] have pronounced smectic phases.

4.4. References

1. P.G. de Gennes. *"The Physics of Liquid Crystals"*, Clarendon Press, Oxford (1974).
2. S. Chandrasekhar, *"Liquid Crystals"* Cambridge University Press (1977).
3. *"The Molecular Physics of Liquid Crystals"*, ed by G. R. Luckhurst and G. W. Gray, Academic Press, London. (1979) .
4. G. Vertogen and W. H. de Jeu. " *Thermotropic Liquid Crystals, Fundamentals* ", Springer-Verlog, Heidelberg (1988).
5. B. Bahadur (Ed) *"Liquid Crystals Applications and uses"*, Vol. I, World Scientific (1993).

6. S. Martellucci and A. N. Chester (ed.), *"Phase Transitions in Liquid Crystals"*, Plenum Press, New York, (1992); J. Collings and J. Y. Patel (ed), *'Hand Book of Liquid Crystal Research"*, Oxford University Press, Oxford, New York, (1997).
7. D. Demus, J. Goodby, G. W. Gray, H. -W. Spiess and V. Vill (Eds.), *"Handbook of Liquid Crystals"*, Vol. **1-3**, WILEY- VCHP (1998);
8. D. Demus, S. Diele, M. Klapperstuck, V. Link and H. Zschke, *Mol. Cryst. Liq. Cryst.* 15, 161 (1971).
9. W. Maier and A. Saupe, *Z. Naturforsch*, **15a**, 287, (1960) and references therein.
10. G. W. Gray in *"Molecular Structure and the Properties of Liquid Crystals"*, Academic Press Inc., New York, (1962).
11. G. W. Gray, *"Advances in Liquid crystals"* , (G.H. Brown, Ed.) Vol. 2, Academic Press Inc., New York, (1976).
12. G. W. Gray in *" Liquid Crystals and Plastic Crystals"*, (G W Gray and P.A. Winsor, Eds.) Vol.1, Chapter.4.1, Ellis Harwood, Chichester, England, (1974).
13. T. Inukai and H. Sato, *DE-OS* 2751,403 (1977).
14. J. P. Schroeder and D. W. Bristol, *J. Org. Chem.*, 38, 3160(1973).
15. W. H. de Jeu, J. van der Veen and W. J. A. Goossens, *Solid State Commun.* 12, 405(1973)
16. S. Mercelja, *J. Chem. Phys.*, 60, 3599, (1974).
17. G. W. Gray and P. A. Winsor, *Mol. Cryst. Liq. Cryst.*, 26, 305 (1974).
18. J. W. Emsley (ed.) *"Nuclear Magnetic resonance of Liquid Crystals"*, D Reidel Publishing Company, Italy (1983).
19. V. Vill, University of Hamburg, *Liquid Cryst (Database) Demo Version 2.0* (1998).
20. G. W. Smith and Z.G. Gardlund, *J. Chem. Phys.*, **59(2)**, 3214 (1973).
21. Osman, *Z. Naturforsch*, **31b**, 801 (1976).

Section B

Theories and experiments on Phase Transitions, Physical properties and Molecular Dynamics in Liquid Crystals

4.5 Introduction

Present understanding of the role played by the terminal alkyl chains on physical properties and molecular dynamics of liquid crystals is given importance throughout this section. In this regard, an attempt is made to give a brief account of the theoretical models developed so far, which explain liquid crystalline phase transitions and physical properties. Experimental results obtained on end chain structure, physical properties and molecular dynamics are also summarized in this section.

Molecular field theories can provide information about the structure and properties of liquid crystals, because they enable an understanding of the onset of liquid crystalline order at the microscopic level. The primary aim of these theories is to understand and obtain information into the molecular origin of various effects in liquid crystals. New theories to predict and explain the individual molecular structural components and packing, which determine the relative stabilities of the partial orientational and partial positional ordering of the molecules in different liquid crystalline phases, were developed recently [1]. Different approximations were used to calculate the molecular field. There are two basic approaches viz.,

1. Non-spherical excluded volume models (Onsager approach) and
2. Maier-Saupe (mean field approach) model based on anisotropic van der Waals attractive forces between molecules.

4.6. Order parameter

In a nematic liquid crystal, as has already been mentioned, the direction of the average orientation of the long axis of the molecules can be specified by a unit vector called the *director*, n . The physical properties of the nematic phase clearly show that n and $-n$ are equivalent, i. e. n is an apolar vector. Hence the orientational order in a uniaxial nematic phase can be described as a second rank tensor [1], but for practical purposes it is convenient to define a *scalar order parameter*,

$$S = \left\langle \frac{3 \cos^2 \theta - 1}{2} \right\rangle \quad (4.3)$$

where θ is the polar angle made by the long axis of the molecule with n , and the angular brackets indicating a statistical average. It is clear that S goes to zero for an isotropic distribution of molecules, and takes the value one, when all the molecules are strictly parallel to one another. In the nematic phase, S has intermediate values, which is a function of temperature.

Apart from having flexible chains attached to one or both ends, the rigid core of the molecule generally has a low symmetry. However, for the sake of developing theories for nematic phase, it is usually assumed that the molecules are cylindrically symmetric. It is clear from the equation that, $S > 0$ if the molecules make relatively small angles θ with n . On the other hand, if θ lies close to 90 degrees for most of the molecules, $S < 0$. These two distributions are so different that they cannot have the same free energy. A free energy between isotropic and nematic phases can be described by the Landau expansion given by [2],

$$\Delta F = \frac{A}{2} S^2 + \frac{B}{3} S^3 + \frac{C}{4} S^4 + \dots \quad (4.4)$$

A, B, C are temperature and pressure dependent coefficients. The cubic term makes nematic-isotropic (N-I) phase transition to have first order character [2] and there is a non-vanishing cubic term in S .

4.7. Onsagar approach (repulsive forces)

4.7.1. Isotropic-Nematic transition

The first statistical model for orientational phase transition was developed by Onsagar [3]. According to this model, when the number density of hard rods progressively increases, beyond some value of the density, the rods can pack efficiently only if they are orientationally ordered. The free energy of the hard rod system was assumed to be entirely entropic in origin. The loss of entropy when the orientational order sets in at the transition is compensated by the gain in translational entropy due to the greater freedom of movement of the particles. Isotropic-nematic (I-N) phase transition can be accomplished only by a variation of the density, since the excluded volume models are athermal. So, based on the excluded volume model one can briefly say [1] that, stabilizing is assisted by packing entropy, and rotational entropy is responsible for destabilizing the nematic phase. Mutual exclusion of volume of two rods oriented with an angle was considered when calculating the free energy, on which Onsagar made virial expansion and retained only the second virial coefficient

Various authors extended Onsagar's model to real systems since it is valid only for very long rods and for low densities. Lasher's numerical calculations [4] show that in the limit of large length to breadth ratio (L/D), the N-I phase transition which is located by equating free energy in the nematic and isotropic phases, is characterized by a value $S_{NI}=0.784$. Zwanzig [5] could calculate higher virial coefficients, by restricting the molecules to take only three mutually perpendicular orientations. Flory and Ronca [6] had used a lattice model, and had made calculations at relatively high densities. However all these models are useful to describe the N-I phase transition, only if the molecules have very large L/D values (about 100) as in main chain polymeric compounds and their solutions in suitable solvents.

In the low molecular weight liquid crystals, the L/D of the molecule is only about 3 to 5, and further the density of the medium is quite high. In this case, the

Scaled Particle Theory (SPT) [7] has been used to get good approximation for free energy. Gibbs free energy is calculated by introducing at any point in the medium, a scaled spherocylinder oriented along a particular direction. The volume excluded to an **unscaled** molecule is defined by the scaled molecule. The N-I phase transition is located by equating the Gibbs free energy as well as the pressure of the ordered and disordered phase. The calculated phase transition temperatures are in good agreement with the experimental data, on certain simple liquid crystals when L/D is 2.5.

However when the equation of state predicted by SPT is compared with the results of Monte Carlo (MC) and Molecular Dynamics (MD) [8,9] simulations on the isotropic phase, for L/D values 2 and 3, SPT overestimates the pressure and densities. In order to extrapolate the 'exact' results of the computer simulation studies, to the region of the nematic-isotropic transition, a method originally proposed by Andrews [10] for an assembly of hard spheres has been extended to spherocylinders [11]. Frenkel et al., [12,13] have done Monte Carlo simulation studies on the hard ellipsoid system. By computing the equations of state and free energies of different phases, they have constructed a 'phase diagram' for hard ellipsoids of different axial ratios. It was observed that a nematic phase occurs for both prolate and oblate ellipsoids with axial ratios >2.5 or $<1/2.5$ respectively.

A more recent Monte Carlo simulations by Bolhuis and Frenkel [14], gives a detailed connection between L/D and the mesophases formed, explicitly for various cases of shape anisotropies and densities. The phase diagram is shown in figure 4.5. The phase diagram showing the (L/D) - I ratio's from 0 to 100 at various densities (ρ) are given, which show the isotropic, nematic, smectic, and AAA staked phases along with the usual ABC stacked solid. A link could be established by this work [14], with the hard-sphere phase diagram for small L/D and with the Onsagar limit for $L/D \rightarrow \infty$ and it was found that the nematic phase is stable from about $L/D \approx 3.7$. Smectic phases become stable from $L/D \approx 3.1$. **Isotropic-smectic** and the **nematic-smectic** phase transitions starts off as a strong first order transition for $L/D > 3.7$. For $L/D \approx 7$, AAA stacked crystalline phases become stable and AAA-ABC transition is first order.

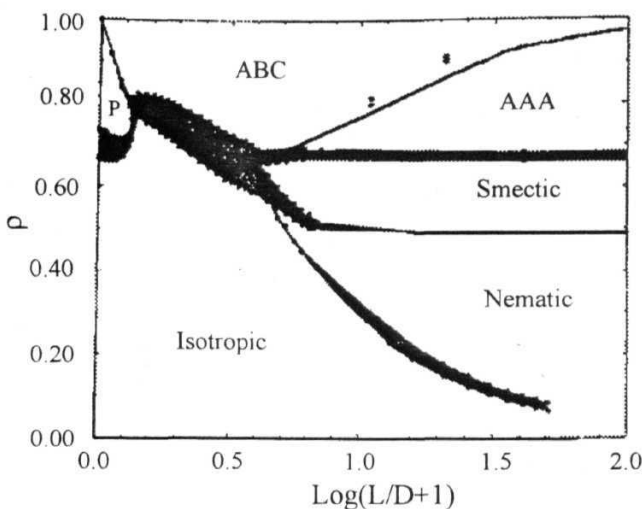


Figure 4.5 Summary of the phase diagram of hard spherocylinders with L/D between 0 and 100. In order to give equal emphasis to all parts of the phase diagram, ρ has been plotted as a function of $\log(L/D+1)$ [14].

Between $L/D \approx 4$ and $L/D \approx \infty$ the first order smectic-solid transition is located at the almost constant reduced densities 0.66 and 0.68. In the Onsager limit, it was determined that the **nematic-smectic** transition at density 0.47 is in good agreement with the predicted value 0.46. It was also observed that the phase diagram of long rods not only depends on the L/D , but also on the exact shape of the particles. For example, hard ellipsoids do not form smectic phases, even in the Onsager limit, whereas hard spherocylinders clearly form stable smectic phases.

A recent Monte Carlo study by Wilson [15] describes the molecular structure and properties of the liquid crystal molecule. Functions like distortions in the bond length, bond angle, and dihedral angle within the molecule together with each non-bonded interaction between adjacent atoms were used to construct a molecular mechanics force field. Every conformation in the end chain has a steric energy (E_s) associated with it, which measures how the conformation differs from the hypothetical

structure, where all the features have their ideal values. The structure of the molecule can be optimized with the minimization of the $\langle E_i \rangle$.

Dynamics of the orientational correlations near the I-N phase transition were studied by Allen and Warren [16] using Monte Carlo simulations. Slowing down of the collective reorientations (DF modes) and the growth of short-range static orientational correlations were observed near the transition. In the vicinity of the phase transition, it was found that the amplitude and the decay time for DF modes, proportional to k^{-2} for all but the lowest values of k . In fact the proportionality constants are quite insensitive to the temperature. These results also indicate that all but the longest wavelength dynamical properties remain unaffected by the approach of the nematic-isotropic phase transition. The upper limit of the wavelength of director fluctuations is related to the transition temperatures by setting up of the dimensions of the simulation box.

The density functional approach has been used by several authors, to discuss the N-I phase transition in systems of hard ellipsoids [17,18,19]. In this approach, free energy is assumed to be a function of the local density $p(R)$ along with the usual thermodynamic variables, such as the average density and temperature. A simple scaling argument has been proposed by Lee [20] to write an Onsager type free energy for ensembles of both hard spherocylinders and ellipsoids of revolution. A good agreement with the computer simulation on the packing fraction at the N-I phase transition is obtained by this method.

4.8. Mean field approach (attractive potentials)

Maier and Saupe [21] had developed a mean field theory of the nematic phase by assuming that anisotropic dispersion forces (anisotropic van der Waals forces between molecules) are entirely responsible for the orientational order, regardless of the shape anisotropy of the molecules. The attractive anisotropic energy dominates over counteracting orientational (rotational) entropy. The molecules supposed to

possess an anisotropic polarizability are determined by these attractive interactions. According to the theory of Maier-Saupe, stabilizing is governed by rotational energy and destabilizing is attributed to the rotational entropy.

Rull et al., [22] have shown clearly that attraction could have a drastic effect on the stability of the liquid crystalline phases in simple model systems. The calculations lead to a first order N-I transition at $S_{NI} = 0.42$, a universal value. It is useful to note that Krieger and James [23] had derived the same model for describing rotational transitions in solids. Experimentally, however S_{NI} varies in the range of .25 to .5 for different compounds. Molecular flexibility is included in the mean field theory [24] due to strong correlation between orientational order and internal conformational degrees of freedom.

4.8. J Nematic-Smectic A phase transition

The S_A phase is characterized by a periodic density modulation along the direction perpendicular to the layers. The interesting behavior of the **smectic** state can be deduced from the analogy with the superconductors. For example, just as superconductors expel magnetic fields, **smectics** expel bend and twist. The bend and twist constants K_{22} and K_{33} should therefore diverge, upon approaching the smectic state from the nematic, just as the magnetic field is expelled from a superconductor. The energy of the deformation of the director has to be taken into account, in the theory of phase transitions, and therefore Frank-Oseen elastic contributions in the free energy have to be included. It is then, clearly shown that the bend and twist elastic constants K_{33} and K_{22} exhibit an increase near the **nematic-smectic A** phase transition temperature [25] due to pretransitional smectic fluctuations (formation of small domains with smectic order) called cybotactic groups. According to the theoretical approach of the extended analogy with superconductors including the smectic fluctuations, these cybotactic groups should be anisotropic and characterized by two coherence lengths of the smectic order parameter, ξ_{\parallel} and ξ_{\perp} , in the directions parallel and perpendicular to the director, respectively.

Smectic A behavior occurring with increasing alkyl chain length, is the basis for the theories on the nematic-smectic A phases transition and the importance of such effects are well documented [1]. Effect of alkyl chain length on the formation of different smectic phases is shown in figure 4.6. The aromatic moieties have large polarizabilities and thus the dispersion interaction energy is very strong between the cores. This could naturally lead to the formation of layered arrangement phase if the alkyl chains are sufficiently long and serve to efficiently separate the aromatic cores in layers.

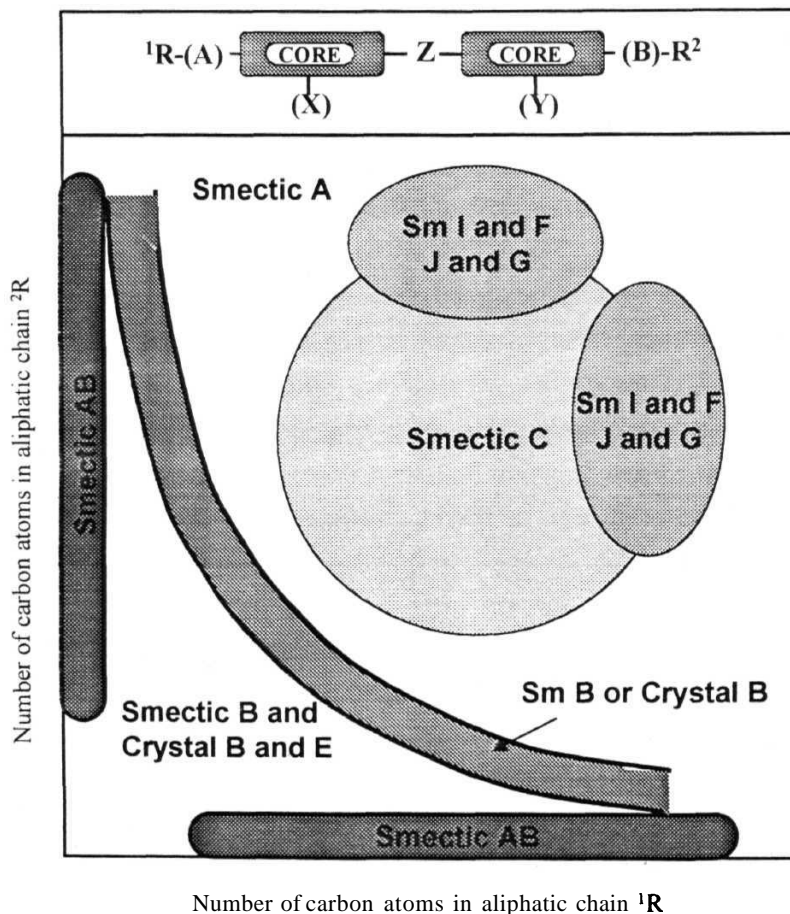


Figure 4.6. Effect of terminal chain length on smectic phase formation.

The Landau theory of smectic A to nematic phase transition (N-S_A) was developed by de Gennes and McMillan [26]. A density wave with amplitude and phase was considered i.e., the order parameter has two components just as superconductors do. The elastic constant for layer compression is much larger than the curvature elastic constants in nematics and in the first approximation it can be assumed that the layers are incompressible.

The Landau-Ginzburg free energy can be written in the form

$$F = \alpha |\psi|^2 + \frac{\beta}{2} |\psi|^4 + \frac{1}{2M_v} \left(\frac{\partial \psi}{\partial z} \right)^2 + \frac{1}{2M_r} |\nabla_{\perp} \psi - i q_s \delta n \psi|^2 \quad (45)$$

in which gradient terms in ψ have been included where the gradient operator is taken in the plane of the layers. Further, as Halperin and Lubensky [29] have shown, the above free energy expectation value of the director fluctuations δn^2_{ψ} is proportional to $1/|\psi|$. Inserting this back into the free energy relation, it is clear that the latter acquires a term in $1/|\psi|$. This means that the director fluctuations always make the N-S_A transition to have a first order character. But this effect is so small that it was experimentally confirmed only recently [27]. The coupling between smectic order parameter and the orientational order parameter leads to a renormalization of the fourth order term coefficient of the free energy. When the width of the nematic phase is large, N-S_A phase transition is of the second order and the nematic orientational order is saturated. When the nematic phase range is short, the nematic order is far from saturated, and the transition is of the first order.

Using a dynamical method, Anisimov et al., [27] had experimentally studied the N-S_A phase transition. Molecular length here, plays a crucial role in driving the N-S_A transition towards a Landau tricritical point (LTP), where the effect of the cubic term is dominant and the quartic term in the free energy vanishes. The shorter the molecular species, the less likely they were to exhibit the smectic A phase and hence, the temperature range of the nematic phase is larger, and the more likely the transition was to be of the second order. The effect of layering could lead to an enhancement of the orientational order parameter in the smectic phase relative to the nematic phase A

brief account of the McMillan theory is discussed here. Starting from the anisotropic pair interaction energy, a single particle potential may be conveniently written as

$$u_i(z_i, \cos \theta_i) = -V_0 [S + \alpha \sigma \cos(2\pi z_i/a)] (3\cos^2 \theta_i - 1)/2 \quad (4.6)$$

where α is the layer thickness. The McMillan parameter a is given by

$$\alpha = 2 \exp [-(\pi a/a)^2] \quad (4.7)$$

in which the range of dispersion interaction, r_0 is of the order of the length of the rigid core of the molecules. S is the orientational order parameter and σ an order parameter, which couples translational and orientational orders. i.e.,

$$\sigma = \langle \cos(2\pi z/a) \text{ if } \cos^2 \theta - 1/2 \rangle \quad (4.8)$$

where the statistical average is taken over the distribution function f_i , and σ is a measure of the amplitude of the density wave in the smectic phase. And as is known, the order parameter

$$S = \langle (3\cos^2 \theta - 1)/2 \rangle \quad (4.9)$$

The following solutions are obtained by McMillan for these equations.

- 1) $S = \sigma = 0$ i.e., the isotropic phase
- 2) $S \neq 0, \sigma = 0$ i.e., **nematic** phase
- 3) $S \neq 0, \sigma \neq 0$ i.e., the smectic A Phase

(4.10)

It is clear from the above equations (4.5-4.7) that a (called the McMillan parameter) is a measure of the strength of the layering interactions and from its definition it is clear that for a given core length r_0 , a increases with increase of the layer spacing 'a' which is nearly equal to the molecular length. In other words, a increases with the chain length in a homologous series.

In most homologous series, the smectic A to nematic transition point reaches a maximum value for some chain length and tends to decrease for higher homologous. For small values of r_0/a the attractive interactions are strongly localized and the smectic phase clears directly into the isotropic liquid. For larger values, a nematic

phase appears, that is separated from the smectic phase by a first order phase transition. At the McMillan number $T_N/T_{SN} = 0.886$ a tricritical point is predicted, where this transition becomes the second order. Predicted first order behavior of the phase transition is due to a coupling of the smectic order parameter to the orientational order. The existence of a tricritical point is well established now, for a variety of systems [1]. There have been studies on the coupling of the smectic order parameter with the second harmonic of the density wave [28] and with the director fluctuations [29]. Other extensions of the McMillan theory include

- A model in which both attractive interactions and hard rod features of spherocylinders are incorporated [30]
- A model, which allows short-range order [31].
- > A theory for binary mixtures which include intermolecular repulsions and attractions [32,33] and,
- A model which takes into account the statistics of flexible end chains [34].

Following McMillan, most attempts at theoretical description of smectics have focused on a mean field type treatment of the attractive intermolecular forces. Exceptions are the work of Dowell [35], who have shown in the context of the lattice model, that the addition of semiflexible side chains to a rigid molecular core can also account for smectic behavior in systems with purely repulsive interactions. Dowell's work also shows that it is not necessary to invoke dipolar forces to have stable Smectic A_1 , smectic A_d phases. Dipolar forces however, increase the stability of these phases in systems with Lennard-Jones interactions. The details of the models developed by Dowell are described separately under the category of generalized models.

A theory for the stability of the nematic phase of parallel cylinders was developed by Mulder [36]. A more generalized theory for binary mixtures was developed by Sear and Jackson [37] based on the model by Mulder, and it was concluded that adding cylinders of different lengths decreases the tendency to smectic ordering. It has been shown that adding cylinders of different lengths to one component nematic phase of cylinders postpones the nematic-smectic A transition, decreasing the range of smectic A phase.

4.9. Generalized models

A combination of both types of ingredients (attractive and repulsive) has been considered in the so-called generalized van der Waals theory (GVDW) [7]. A significant feature of the GVDW approach is that the contributions of the short ranged and long ranged pair interactions are coupled. This combination leads to the point that the full polarizability of each molecule is concentrated in its center. It would immediately be clear that for parallel molecules, it is not only the excluded volume that is more favorable, but that the attractive forces also contribute to the stability of the orientational order, because of the shorter distance between the attractive centers. The important assumptions made in the GVDW theory include 1. The molecules are rigid and axially symmetric, 2. Short-ranged forces are dominated by hard core repulsions. 3. Long ranged attractions are comprised essentially of an angle dependent dispersion interaction.

The failure of the models such as the scaled particle theory (SPT) has been attributed to the neglect of short range orientational and translational correlations resulting from intermolecular interactions. In other words, it can be said that these models have not considered the soft repulsions. It was shown by Dowell [35], that at short ranges of separation between intermolecular segments, soft repulsions are very significant in any reasonably realistic model potential such as his use of the Lennard-Jones (LJ) potential. A realistic transition temperature and a relative density change could be got, by including both soft repulsions and attractions in the realistic LJ potential, which makes the **isotropic-nematic** transition more like the weakly first-order order-disorder transition observed experimentally, rather than the strongly first order condensed phase-gas phase transition proposed by hard rod models. *Soft repulsions 'soften' the nematic-isotropic transition.*

Dowell introduced [35] a general partition function derived via combinatorial lattice statistics, for condensed phases with partial or total orientational and positional ordering of the molecules. In this case, partition function could be in one, two or three dimensions, permitting the modeling of **nematic**, smectic A and ordered **smectic** phases. The lengths of the core and tails can be varied as well as the flexibility of the

intramolecular bonds in the **tails**. Using this model, the configurational properties of the system, those that depend on both the temperature and the positions of the molecules and the relative stabilities were studied. The hindered rotation of the **semiflexible** bond about the core long axis is actually associated with the internal degrees of freedom of the molecule and with the configurational degrees of freedom of the system of molecules. *A symmetrical **distribution** of semiflexible bonds about the core long axis has also been assumed.* The relative stabilities of isotropic, nematic, smectic A, and reentrant nematic phases are studied as a function of temperature, tail flexibility and chain length. **Thermodynamic** and ordering properties such as, the smectic A order parameter, core and tail **intermolecular** orientational order parameters, density and entropy were also calculated using this generalized model.

As a special case, Dowell used the general partition function to the smectic A liquid crystal, in which the molecules have a certain positional ordering in one dimension (layering) of the system and also have some orientational **order**. There is a liquid like positional order within each layer. This partition function can be reduced to the nematic partition function when the smectic A order parameter goes to zero and can be reduced to the partition function for an isotropic liquid when both the smectic A order parameter and the nematic order parameter go to zero.

This model [35] showed that the differences in packing between rigid cores and chains can in some ranges of temperature and **pressure**, *force **the** molecules in the system to form smectic A layers in such a way that cores tend to pack with cores and tails tend to pack with tails.* And as the tails become more rigid and rod like as the temperature decreases, the segregated packing of the smectic A is no longer advantageous and thus disappears, allowing the re-entrant nematic at the temperatures below that of the smectic A phase.

4.9.1. Formation of the mesophases

It is also possible to understand [35] the transitions through simple arguments. At a high temperature T , the system volume V is large enough for the molecules to

pack randomly, and thus the drive for maximum entropy leads to the existence of a *stable isotropic phase*. As T lowers, V decreases, and the molecules must order partially, to fit in to the volume, and there is thus a transition to a *stable nematic phase*. As T decreases, V decreases further, and there is a weakly first order transition to a *stable S_A phase*. No stable smectic A phase is observed by Dowell when terminal chains are very short, which is consistent with experimental observations. When the number of segments in the terminal chains are less than that of the number of segments in the core, the packing of the tail segments seems to act as a minor perturbation to the packing of the cores. This is so negligible that the segregated packing of cores with the cores and tails with the tails (S_A phase) is no longer necessary, and the drive to maximize entropy favors the more disordered nematic phase over a smectic A phase.

4.9.2. Role of dipolar forces

Though the attractive dipolar forces are not essential, it was shown [35] that attractive forces increase the stability of the mesophases in systems with Lennard-Jones (LJ) interactions. Dipolar forces also shift the temperature ranges of these phases closer to the ambient, thus making them easier to discover and observe experimentally. Dipolar forces added to the LJ system orient the cores more and pull the molecules closer to hard repulsive separation distances, thereby producing a return to a phase diagram whose qualitative features are more similar to those of the steric system. It was also shown that the LJ forces to the steric system increases the temperatures at which the S_A phases are stable. Adding dipolar forces to the pure LJ system, increases the temperatures still further, bringing the S_A and low temperature nematic (RN) phases into temperature ranges closer to the ambient and thus more accessible to experimental discovery and observation.

4.10. Theoretical explanation for odd-even effects

The flexible chains increase the entropy of melting; they serve to lower the melting point and to increase the liquid crystalline range. Considering flexibility due

to end chains, Mercelja [38] has incorporated the configurational statistics of the end chains in the theory of the **nematic** phase in a **Flory-type** calculation [6]. In addition to having the **conformational** energy, each C-C bond in the end chain is subjected to a mean field, which depends both on the orientational order of the rigid central part and that of the end chain. A detailed calculation of ordering, by doing exact summation over all the conformations of a chain in the molecular field, had shown 'odd-even' effects in both the transition temperatures and the order parameters (T_{NI} and S_{NI}) in a homologous series. The results [38] are in well agreement with the experimental trends [1a]. It is also clear from simple geometric considerations that a strong odd-even effect for lower homologous is caused by a high probability of occurrence of the *all-trans* configuration for short chains. The increase in conformational flexibility for the higher homologues is seen as a smearing out of this effect. The anisotropic interaction between the rigid structures of the molecule therefore, is rather strong and the addition of end chains decreases the average anisotropic interaction. This is true in the case of homologous series with higher transition temperatures [1a]. In the case of the homologous series with lower transition temperatures, the addition of end chains increases the average anisotropic interaction between molecules. The orientation of the $C_{n-2}-C_{n+3}$ bond in the chain can take, with respect to the C_n-C_{n-1} bond, either a *trans* conformation, which has the lowest energy, or two *gauche* conformations, which have considerably higher energy. The '*all-trans*' configuration indeed has the state of 'perfect order' for the chain; the other possible conformations giving rise to flexibility.

Pink [39] developed a model including the various states of hydrocarbon chains, (not only the ground states but also the excited states) and showed that, while the even-odd effect in transition temperature can be understood as a consequence of the even-odd effect in the chain order parameter ($\langle S \rangle$) with respect to the molecular axis, the even-odd effect in the rigid segment order parameter is the consequence of at least such an effect in the mean-square deviation, $\langle S^2 \rangle - \langle S \rangle^2$. These calculations have since been refined by Luckhurst [40], and used to make successful calculations for compounds which have two rigid cyanobiphenyl moieties linked by flexible spacers, in which the odd-even alteration in T_{NI} is very strong.

4.10.1 Intrachain constraints and rotational dynamics

Dowell [35] explained the effect of end chain flexibility on the mesophase stability and particularly, the effects of intrachain constraints on the alkyl end chain flexibility, comparing his approximate but computationally simple method with a full statistical methods, based on Merce'lja's model [38].

It is known that, in the liquid crystalline molecules consisting of a long rigid core and terminal alkyl and alkoxy chains, there is essentially a free rotation of the molecule about the core long axis, thereby giving an effective rod like, cylindrical shape of the core. The alkyl chains are semiflexible, since it costs a finite, but easily achievable, energy to make rotations about any carbon-carbon bond between -CH₂- and -CH₃ units in given terminal chain. There are three rotational energy minima for a given carbon-carbon bond in these terminal chains: a *trans* rotational state and two *gauche* rotational states. The net energy difference between these states is E_g , with the *gauche* states having the higher energy. The statistical distribution of *trans* and *gauche* rotational states as a function of E_g and the temperature are the origin of the *intrachain* constraints on the terminal chain flexibility. It has been emphasized that there is an appreciable fraction of *gauche* states in n-alkyl chains in mesophases and isotropic liquid phases. If all these segments are in an all-*trans* configuration the material becomes a crystalline solid.

Dowell theoretically showed [35], how intra chain constraints explain the odd-even effects with more accuracy. He considered the fraction of semiflexible bonds in the tail chain bent out of the direction of the long axis of the core of the molecule. In other words, the fraction of bonds bent out of the direction of the long axis of the all-*trans* state of the tail chain of the molecule is considered. This approach is different from earlier theories in the following way. The rotation of the semiflexible bond is coupled directly to the direction of the long axis of the core of the molecule. Consequently, since the *gauche* energy is assigned for each bond rotated out of the core long axis, it includes in a rather approximate manner certain *intermolecular* constraints on the intramolecular *trans-gauche* flexibility. That is, it

reflects in a close fashion that it should be harder to make a rotation out of the core long axis since such a rotated bond would run into more **interference**

4.10.2. Intrachain constraints and physical properties

Dowell could explain odd-even effects in the phase stabilities of **nematic**, **smectic A_d**, **smectic A₁** and isotropic phases based on the intrachain constraints. Other properties like the average core orientational order parameter, tail intermolecular orientational order, the average tail intrachain orientational order, reduced entropy changes and reduced density changes of the system at the **nematic-isotropic** phase transition also showed odd-even effects with tail chain length in Dowell's calculations.

The observed magnitude of odd-even effects of tail intermolecular orientational order parameters are larger than the odd-even effects in the core orientational order parameters. This is consistent with the fact that the alteration of the number of -CH₂- units (or carbon atoms) in the chain itself is the origin of the odd-even effects. *The observed changes in core order parameters leads to a conclusion that the tails affect the cores.* The core order parameters are larger than the chain intramolecular order parameters by an order of magnitude, since it is easier to orient cores than **semiflexible tails** *Since the cores and tails are attached, an ordering of the cores affect the ordering of the tails.* The magnitudes of entropy and density changes observed in this theoretical results are well in agreement with the experimental values. *These results imply that the intra-chain constraints are by far, the major factor responsible for odd-even effects in these systems and thus account for most of the magnitude of these odd-even effects.* The small differences seen in these results with the experimental observations [35] indicates that intermolecular constraints on the end chain flexibility also make some contribution to the odd even effects seen experimentally.

4.10.3. Other models and computer simulations

Lebwohl and Lasher [41] and later Jansen et al., have performed Monte Carlo simulation studies on a lattice version of the Maier-Saupe theory. A study of molecular dynamics simulations [43] of a flexible solute dissolved in a Gay-Berne solvent show that the increase in the anisotropic environment which favors *all-trans* conformation is balanced by an increase in density which favors conformations with more *gauche* links. Moving from nematic to the smectic phase by lowering the temperature generates a large increase in the number of *all-trans* configurations. This study shows very clearly that smectic ordering enhances the *all-trans* configurations. There have also been simulations [44] on collections of mesogenic molecules which use their full structure, and atom-atom pair potentials, and the comparison of various computed ensemble averages with their experimental counterparts. Palke et al., [44] had used the molecular dynamics trajectory to calculate averaged nuclear spin dipolar couplings, and these are used to test the maximum entropy (ME) and additive potential (AP) methods [45], which have been used to obtain the probability distribution for internal bond rotations.

4.11. Theories and experiments on elastic constants

Elastic constants in nematic liquid crystals (K_n , K_{22} and K_{33}) can be measured through creating director field deformations by an external field or by surface anchoring and analyzing these deformations by optic, capacitance, thermal conductivity, electric conductivity, or by magnetic resonance methods. It is possible to get information on elastic constants by observing director fluctuation (DF) modes using optical or NMR methods. Elastic constants have been measured by several experimentalists [1e], and there are certain theoretical attempts to explain these constants based on the molecular structure.

Although there are no general quantitative relations between the elastic constants and molecular structure, there are experimental observations, which connect the molecular properties with the elastic constants. It is also observed that the short-

range **intermolecular** forces are responsible for the elastic properties. A quantitative comparison of experimental elastic constants obtained from different studies is shown in figure 4.7 [1f].

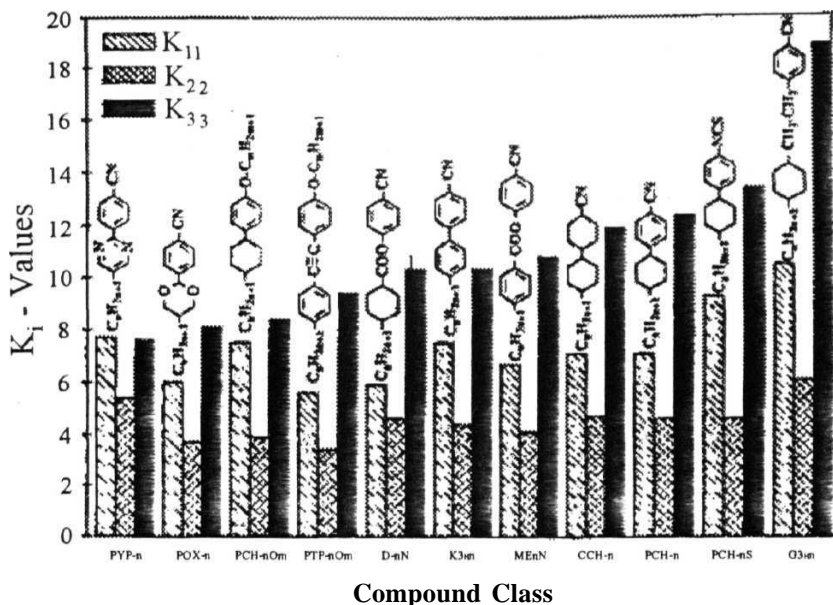


Figure 4.7. Elastic constants K_{11} , K_{22} and K_{33} of important liquid crystals at a fixed reduced temperatures ($T_{red} = 0.95$) [1f].

4.11.1. Molecular length and elastic constants

The splay and bend elastic constants K_{11} and K_{33} are often of comparable magnitude, and their ratio is often close to 1 near I-N phase transition temperature (T_{NI}). The twist elastic constant K_{22} is usually smaller in low molecular mass liquid crystals. The splay/bend ratio is correlated with the molecular **length/width** ratio for rigid molecules as follows [66]

$$K_{33} : K_{11} = L^2 : W^2, \text{ with } K_{33} > K_{11} \quad (4.11)$$

If long, flexible alkyl chains are incorporated in the molecular model structure, the trend is reversed, ($K_{33} < K_{11}$). In practice both cases are observed. In the nCB series,

$K_{33} > K_{11}$ is observed. The bend/splay ratio gradually decreases with increasing alkyl chain length [58]. In, 4-cyanophenyl-4-n-alkyloxycyclohexanoates the K_{33}/K_{11} ratio decreases from about 1.8 for propyl homologue to about 1.15 for the octyl homologue. Odd-even effects are found in the ratios of K_{33}/K_{11} with the number of chain segments. As a general trend, this ratio is closer to 1 near the N-I transition (at low order parameters) than deeper in the higher ordered nematic phase. The twist/splay ratio is found to be quite constant (except for pretransitional effects in the vicinity of smectic phases). Theoretically it is expected to be 1/3, but experiments show that K_{22}/K_{11} is typically of the order of 1/2.

4.11.2. Order parameters and elastic constants

The variation of elastic constants (increasing with decreasing temperature), with temperature is attributed to the changes in the order parameter S , and the molar volume V_{mol} . Hence, Saupe [42] introduced reduced elastic constants

$$C_i = K_{ii} V_{\text{mol}}^{7/3} S^{-2}; \quad i = \{1, 2, 3\} \quad (4.12)$$

According to this theory C_i should be practically independent of temperature, and Frank elastic constants scale with the square of the nematic order parameter, while their ratios should be constant material parameters. In the qualitative estimation of relative values of elastic constants, Saupe had obtained $K_{11} : K_{22} : K_{33}$ ratio of -7 : 11 : 17. This non-physical result is due to an over simplified assumption about the molecular shape and the interactions. Experimentally for large number of nematics (far from smectic phases) it has been an established fact that $K_{11} = K_{33}$. The twist elastic constant K_{22} is generally smaller than the other two. The ratios of the elastic constants moreover, are independent of temperature only to a very rough approximation. It is necessary that anisotropic molecular shapes and short range order be included in a more elaborate microscopic description of nematic elasticity.

Another expression obtained for the elastic constants $[1c]$ as a function of the different order parameters P_2 and P_4 is given by the relation,

$$K_i = K_i^{22}(P_2)^2 [1 + (K_i^{24}/K_i^{22})(P_4/P_2)], \quad (4.13)$$

where \tilde{K}_i are elastic constants (K_n , K_{22} and K_{33}) and P_2 and P_4 are order parameters. The contributions from these order parameters are given with superscripts 22 and 24 respectively. The results obtained for the nematic medium showed that the elastic constants obtained are linearly dependent on the temperature and essentially constant over the narrow thermal range of the nematic liquid. The order parameters P_2 and P_4 on the other hand, vary significantly over the same temperature range. Thus the temperature dependence of K_i/P_2^2 , $i = 1, 2, 3$ are determined by the relative magnitude and sign of P_4 .

The theoretical elastic constants obtained for PAA and MBBA are compared [1c] with experimental values. For the intermolecular potential appropriate to PAA, the ratio $K_i^{24}P_4/K_i^{22}P_2$ is the largest, for the bend elastic constant, which is consistent with the experimental fact that K_{33} for PAA shows the largest deviation from P_2^2 temperature dependence. More explicitly, as T is increased from 390 to 410 K, P_2^2 decreases by a factor of 2, whereas K_{33} decreases almost threefold. This is because P_4/P_2 also decreases over the same range and the contribution of K_i^{24} to K_{33} is at least 20% of the K_i^{22} terms. Thus independent measurements of order parameters provide information complementary to the data, on elastic constants. On the other hand in MBBA, the P_4/P_2 ratio is found to decrease significantly over the narrow thermal range from 293 K to 320 K of the nematic. In fact, the ratio actually vanishes (since P_4 goes to zero) and goes to negative. In the neighborhood of $P_4=0$ value, K_i are determined exactly by the P_2^2 contributions. Since $K_{11}=K_{33}$ on the P_2^2 level, this suggests that K_{33} should approach K_{11} from above, as P_4/P_2 decreases toward the top of the nematic range. This behavior is indeed observed in the case of MBBA, for which P_4/P_2 not only decreases but also vanishes. Chanrasekhar et al., [46] and Boehm and Martire [47] have analyzed a system in which the rods are restricted to only 3 orthogonal orientations. The important result, which connects the end chain effects on the order parameters and elastic constants, is that if the molecular polarizability increases, K_i^E (E represents energy) grow faster than the K_i^S (S represents entropy) and account in this way for a decreasing value of K_{33}/K_{11} .

Poniewierski and Stecki [50,51] have applied the density functional theory in order to relate in a quantitative way, the elastic constants to characteristic properties

of a statistical ensemble of molecules with the given nematic interaction potential. Considering the difficulties involved in the calculation of the multiple pair correlation functions needed to calculate the elastic constants in the theory proposed by Poniewierski and Stecki, an alternative approach is used. This approach is to perform MD simulations of a statistical ensemble of particles [52-55], in which the classical equations of motion are solved for the multi-particle system.

A qualitative comparison of different theoretical approaches in the study of hard spherocylindrical system has been reported by Poniewierski and Holyst [56]. While the order parameters obtained using the different models coincide fairly well, the agreement between values of the elastic constants is rather poor. In general, because of the complexity of the assumptions and approximations and the sensitivity of the elastic constants to details of the orientational distribution and correlation functions, quantitative and even qualitative comparison of molecular statistical approaches and experiment are usually unsatisfactory. At present it seems that all such theories, despite providing an insight into the properties of Gay-Berne [1] and other model fluids, are far from reaching the goal of providing a microscopic understanding of nematic elasticity.

Regardless of a molecular interpretation, a theoretical relation between nematic elastic constants and the order parameter can be established by a Landau-deGennes expansion of the free energy and by a comparison with the Frank-Oseen elastic energy expression, given by,

$$K_{11}=K_{33}=S^2(2L_1+L_2) \quad (4.14)$$

and

$$K_{22}= 2S^2L_1 \quad (4.15)$$

where L_1 and L_2 are expansion parameters.

The behavior of nematic elastic constants in the vicinity of the **nematic-smectic** transition has been analyzed by means of the Ginzburg-Landau Hamiltonian [57]. At the transition to the smectic A phase, a critical divergence of K_{22} and K_{33} is

predicted Also Monte Carlo simulations of the N-S_A transitions have also been studied by many authors [58].

4.11.3. Cybotactic clusters and elastic constants

Thus, if the nematic has no smectic like short-range correlations, $K_{33} > K_{11}$. If the molecules have a tendency to form layered cybotactic groups, as in the case of mixtures exhibiting the induced smectic A phase, at lower temperatures [48,49], $K_{33} < K_{11}$. However, a long range layering order cannot sustain a **curl n** distortion, and hence, both K_{22} and K_{33} diverge when the smectic A-nematic transition point is approached.

4,12, Anisotropic physical properties and molecular dynamics

Anisotropic physical properties that are generally affected by the terminal chains would be discussed in this sub-section. Properties of liquid crystals can be distinguished into scalar and non-scalar [1]. While the order parameter, transition temperature and transition entropies are scalar properties, dielectric, diamagnetic, optical, elastic and viscous coefficients are non-scalar properties. Scalar properties, like positional, orientational and conformational orders, are important to characterize various states and the orientation of the groups within the molecule.

4.12.1. Optical anisotropy

Existence of random refractive index fluctuations led to a milky and opaque appearance of nematic liquid crystal. Similar to anisotropic polarizability and electric permittivity (ϵ_c) nematic liquid crystals have an optical anisotropy (Δn), called 'birefringence'. It was experimentally observed that Δn increases with decreasing temperature, simply following the behavior of the order parameter, S . One can estimate the relative variations of the order parameters from the anisotropy in the refractive index. The refractive index of the extraordinary wave (decreasing with an increase in temperature) shows strong temperature dependence, which is probably due

to the temperature dependence of density along with the changes in the S. Odd-even effects in An are observed in the homologous series of systems [1].

4.12.2. Anisotropic viscosity coefficients

The viscous behavior of liquid crystals has pronounced effects on the dynamics of the liquid crystal molecules. Since viscosity is a collective property resulting from the interaction of the molecules with one another, it is strongly dependent on the molecular environment. There are five (three among them are shear viscosities) anisotropic viscosity coefficients, depending on the relative orientation of the molecules with respect to the flow of the material. When the oriented liquid crystal is placed between two plates which are then sheared, the director is perpendicular to the flow pattern and parallel to the velocity gradient, the viscosity connected with this being η_1 . η_2 is the viscosity coefficient when the director is parallel to the flow pattern and perpendicular to the viscosity gradient. And, η_3 is viscosity coefficient when the director is perpendicular to both flow pattern as well as the velocity gradient. η_1 , η_2 and η_3 are referred as the Miesowicz viscosities and are difficult to determine. In addition to these, the rotational viscosity, γ_1 , is that, where a rotation of the molecule around an axis perpendicular to the director takes place. This has values typically ranging from .02 Pa s to 0.5 Pa s [1f]. Longer alkyl chains, more number of aromatic rings and the lateral functional groups lead to higher viscosity values [1e]. Strong polar interaction also leads to higher viscosities. These general observations are often superseded by the structural rigidity of the molecules, exceptional intermolecular attractions or repulsions and pretransitional phenomena.

4.12.3. Anisotropic rotational motions

The rod-like molecules in the nematic phase are free to rotate about their long axis and to some degree about the short axis [1d]. The dielectric relaxation times measured for rotations about their short axes are much longer ($\sim 10^6$ to 10^8 times per second) than those about their long axis ($\sim 10^{11}$ to 10^{12} times per second) [1e]. In the case of smectic A phase these values do not change much.

Considering the anisotropic rod-like nature of the liquid crystal molecule different types of reorientations (or rotations) are proposed in the literature [59]. The various possible relaxation mechanisms in the liquid crystal system **10.4 (MBBA)** are shown in Figure 4.8.

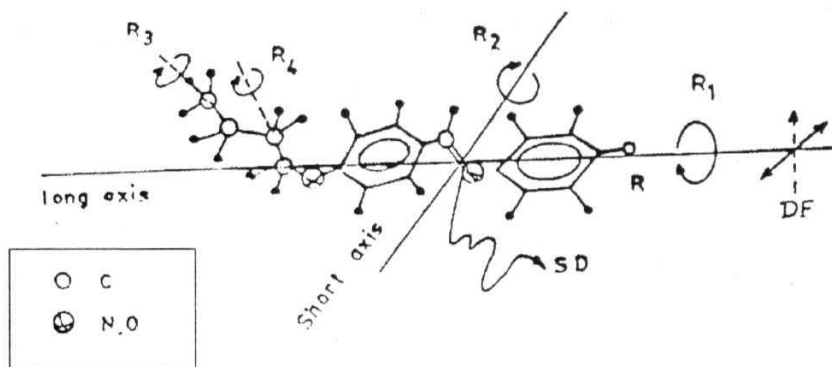


Figure 4.8 Typical molecular structure of nO.m system (10.4). Various dynamic degrees of freedom are also specified. Rotations about long and short molecular axes (R_1 and R_2), segmental rotations (R_4) and the three-fold rotations about the short axis (R_3) are specified with labels. Self-diffusion (SD) and director fluctuations (DF) are also described [1d].

Apart from director fluctuations (DF) and self-diffusion, there are four different rotations [1d] that seem to be important in the rod-like molecules with end chains, in mediating the spin-lattice relaxation. R_1 represents the rotational tumbling about the long axis (with typical time scales of the order of about 10^{11} to 10^{12} seconds). R_3 and R_4 represent the rotations of the CH_3 groups about the three-fold axis and the rotations of the CH_2 segments about the C-C bonds, respectively. Both R_3 and R_4 are expected to have a time scale of the order of 10^{-10} seconds [1]. Contributions from R_1 , R_3 and R_4 are not much to the nematic T_1 data, due to their smallness of the correlation times compared to the inverse Larmor frequency, which

in practice is between 10^{-3} and 10^{-8} seconds [1d]. The only rotational mechanism, which could be effective, is the rotation (R_2), about the short axis (with correlation times of the order of 10^{-6} - 10^{-8} seconds).

4.12.4. Anisotropy in Self-Diffusion

Self-Diffusion (SD) is a thermally activated molecular motion, which does not affect the orientational ordering of the mesophase. The available experimental and theoretical results on SD are mostly inconsistent, although there are few systematic studies using field gradient technique by Noack and coworkers [60]. It is generally observed from the experimental results that the diffusion constants are anisotropic, and the diffusion D_{\perp} , which is measured in the direction perpendicular to the director is smaller than the D_{\parallel} , which is measured in the direction parallel to the director. The values [60] of these two diffusion constants are in the range between $10^{-11} \text{ m}^2 \text{ s}^{-1}$ and $10^{-10} \text{ m}^2 \text{ s}^{-1}$. The anisotropy ratio $\sigma = D_{\perp}/D_{\parallel}$ is a material parameter which is typically around 0.5 for nematic phases. Very often the average diffusion constant $\langle D \rangle = (2D_{\perp} + D_{\parallel})/3$ is defined which is expected to be equal to the diffusion constant in the isotropic phase.

Various theories are discussed in the literature [60] assuming the validity of Fick's law for SD in liquid crystals, in order to explain diffusion properties in terms of the molecular properties. There are different experimental techniques ranging from very simple tracer techniques, to methods of measuring the diffusivity of a liquid into a porous matrix using NMR [61]. Experimental results are not satisfactory and not sufficient to explain the theoretical observations. Blinc et al., [62] have experimentally shown that the diffusion tensor components are coupled to the order parameter S . The average diffusion constant $\langle D \rangle$, and the limiting values D_{\parallel}^0 , D_{\perp}^0 of a perfectly ordered cluster ($S=1$) is of the form

$$D_{\perp} = \langle D \rangle (1-S) + S D_{\perp}^0 \quad (4.16)$$

$$D_{\parallel} = \langle D \rangle (1-S) + S D_{\parallel}^0 \quad (4.17)$$

Modified equations are given by [60] as

$$D_{\perp} = \langle D \rangle \{ 1 - [(1-\gamma)/(2\gamma+1)] S \} \quad (4.18)$$

$$D_{\parallel} = \langle D \rangle \{ 1 + [2(1-\gamma)/(2\gamma+1)] S \} \quad (4.19)$$

where, $\gamma = D_{\perp}^0 / D_{\parallel}^0 = \pi d / 4L$, d is the diameter and L is the length of the molecule. The predicted macroscopic anisotropy ratio a , is hence independent of $\langle D \rangle$. From the above relations, for a mesophase system of $S = 0.6$ with $d/L = 3$, $\sigma = 0.5$ can be obtained. Due to the non-availability of sufficient experimental data, it is common to describe the results by the modified Arrhenius law, $D_j = D_j^0 \exp (-E_j/kT)$, where j is either \parallel or \perp and E_j is the activation energy. Recent theoretical developments [63-64] using molecular dynamics and Monte Carlo simulations are very useful in understanding the microscopic structure dependence on diffusion.

The importance of density measurements in understanding transport properties is described by Allen [63]. Diffusion coefficient D_{\parallel} (in the direction parallel to the director) increases with density in the nematic phase initially, reaches a maximum value and then decreases. This decrease of diffusion with further increase of density is attributed to the increased collision rate at such higher densities. The diffusion constant D_{\perp} decreases monotonically in the usual manner. This effect seems to be associated with the density variation of the nematic order parameter near the phase transition.

Allen has explained [15] the various dynamical features like director fluctuations, reorientations (becoming slower in nematic phase), and the elastic constants of long rod like molecules using molecular dynamics simulations. Slowing down of director fluctuations and the growth of orientational correlations, limited to the ranges of few molecular diameters is found for hard ellipsoid fluids at the nematic-isotropic transition, which is more like a weakly first order transition. This molecular dynamics study [15] shows how orientational domain size affects the collective fluctuations.

There are certain important experimental methods, which could provide the diffusion constants. Tracer techniques directly measure mass transport, and in liquid

crystals, this has been achieved by radioactive tracers or optical tracers. Another important indirect method used to measure self-diffusion constants is the quasi-elastic neutron scattering, with crucial requirements on instrumental resolution in terms of energy and momentum. Using the nuclear spin-echo methods using NMR pulsed field gradients the most reliable data was obtained in the recent years. The observed self diffusion constants by various groups using NMR and tracer techniques, show the Arrhenius type temperature dependence consistently [60] for both D_{\parallel} and D_{\perp} with slightly different activation energies (20 to 70 kJ mol⁻¹) and hence, temperature independent anisotropy ratios from 0.5 to 0.7.

Systematic studies of diffusion constants in the homologous series of nematic liquid crystals show very interesting trends [60]. Odd-even effects are seen in these systems in a manner similar to the clearing temperatures. It is important to compare the diffusion constants at the same temperature. In the PAA homologous series it was seen that $D_{\perp} > D_{iso}$ and also $D_{\parallel} > D_{\perp}$ independent of the odd-even effects. There are similar results from QNS studies, which cannot be explained by the existing theories. nCB systems studied by Noack and coworkers using field-cycling magic angle technique [60] showed that the results were consistent with the theories. Generally, it is found that longer the terminal chain length is lesser the diffusion constants. Slowing down of diffusion in longer chain lengths leads to the formation of the smectic A phases. In the smectic phases the activation energies for diffusion mechanisms are different ($E_{\perp} < E_{\parallel}$) from that of nematic phases. The anisotropy ratio changes from the nematic value $\sigma \gg 1$ to $\sigma \ll 1$. In the homologous series alkanoylbenzylidene aminoazobenzenes the values go up to 10 in the smectic A phase.

4.13. References for section B

1. a) P. G. de Gennes, "*The Physics of Liquid Crystals*", Clarendon Press, Oxford (1974); b) S. Chandrasekhar, "*Liquid Crystals*" Cambridge University Press, Cambridge, (1977); c) "*The Molecular Physics of Liquid Crystals*", (eds.) G. R. Luckhurst and G. W. Gray, Academic Press, London, (1979); d) G. Vertogen and W. H. de Jeu, "*Thermotropic Liquid Crystals, Fundamentals*", Springer-Verlog, Heidelberg (1988); e) D. Demus, J. Goodby, G. W. Gray, H.-W. Spiess, and V. Vill (eds) *Hand Book of Liquid Crystals*, Vol.1, 2A, 2B and 3 (1998). f) N. V. Madhusudhana in "*Liquid Crystals Applications and uses*", Bahadur (Ed.) Vol. I, World Scientific (1993), g) S. Martellucci and A. N. Chester (ed), "*Phase Transitions in Liquid Crystals*", Plenum Press, New York, (1992); h) P. J. Collings and J. Y. Patel (eds), "*Hand Book of Liquid Crystal Research*", Oxford University Press, Oxford, New York, (1997).
2. L. D. Landau and E. M. Lifshitz. "*Statistical Physics*" Part 1, Pergamon Press, Oxford (1980).
3. L. Onsager, *Ann. N. Y. Acad. Sci.*, 51, 627, (1949).
4. G. Lasher, *J. Chem. Phys.*, 53, 4141 (1970).
5. R. Zwanzig, *J. Chem. Phys.*, 39, 1714 (1963).
6. P. J. Flory, *Proc. Roy. Soc., London*, **A234**, 73, (1956)
7. M. A. Cotter in "*The Molecular Physics of Liquid Crystals*", (ed.) G. R. Luckhurst and G. W. Gray, Academic Press, London, (1979).
8. J. Vieillard-Baron, *Mol. Phys.*, **28**, 809, (1974)
9. I. Nezbeda and T. Baublik, *Czech. J. Phys.*, **B28**, 353 (1978).
10. F. C. Andrews, *J. Chem. Phys.*, 62, 272, (1975).
11. Savithramma and N. V. Madhusudana, *Mol. Cryst. Liq. Cryst.*, 62, 63, (1980).
12. D. Frenkel and B.M. Mulder, *Mol. Phys.*, **55**, 117 (1985).
13. D. Frenkel, B.M. Mulder and J. P. McTague, *Phys. Rev. Lett.*, 52, 287, (1984).
14. P. Bolhuis and D. Frenkel, *J. Chem. Phys.*, **106**, 666 (1997).
15. M.R. Wilson, *Liq. Cryst.*, 21, 437 (1996).
16. M. P. Allen and A. A. Warren, *Phys. Rev. Lett.*, 78, 1291 (1997).

41. P. A. Lebwohl and G. Lasher, *Phys. Rev.*, **6A**, 426, (1972); H. J. F. Jansen, G. Vertogen and J. G. J. Ypma, *Mol. Cryst. Liq. Cryst.*, **38**, 87, (1977).
42. A. Saupe, *Z. Naturforsch. Teil a*, **15**, 810, (1960).
43. J. Alejandro, J. W. Emsley, D. J. Tildesley and P. Carlson, *J. Chem. Phys.*, **101**, 7027 (1994)
44. W. E. Palke, D. Catalano, G. Celebre and J. W. Emsley, *J. Chem. Phys.*, **105** (16), 7026 (1996)
45. G. Celebre, G. De Luca, M. Longeri, D. Catalano, C. A. Veracini and J. W. Emsley, *J. Chem. Soc. Faraday Trans.*, **87**, 2623, (1992).
46. S. Chandrasekhar, R. Shashidhar, and N. Tara, *Mol. Cryst. Liq. Cryst.*, **10**, 337, (1970).
47. R. E. Boem and D. E. Martire, *Mol. Phys.*, **36**, 1, (1978).
48. N. V. Madhusudana and K. P. L. Moodithaya, *Mol. Cryst. Liq. Cryst.*, **90**, 357 (1983)
49. B. S. Scheuble, G. Baur and G. Meier, *Mol. Cryst. Liq. Cryst.*, **68**, 57 (1981).
50. A. Poniewierski and J. Stecki, *Mol. Phys.*, **38**, 1931 (1979).
51. J. Stecki and A. Poniewierski, *Mol. Phys.*, **41**, 1451 (1981).
52. M. P. Allen and D. Frenkel, *Phys. Rev.*, **A37**, 1813 (1988); **A42**, 3641 (1990).
53. M. Whittle, A. J. Masters, *Mol. Phys.*, **11**, 247 (1991).
54. J. Stelzer, L. Longa, H. R. Trebin, *Mol. Cryst. Liq. Cryst.*, **262**, 455 (1995).
55. J. Stelzer, *Dissertation*, Stuttgart (1994).
56. A. Poniewierski and J. Holyst, *Phys. Rev.*, **A41**, 6871 (1990).
57. K. Rosciszewski, *Acta Phys. Pol. Ser. A*, **64**, 277 (1983).
58. R. Stannarius in “*HandBook of Liquid Crystals*”, Vol.1, 2A, 2B and 3, (Eds.) D. Demus, J. Goodby, G. W. Gray, H.-W. Spiess and V. Vill (1998)
59. G. Vertogen and W. H. de Jeu, “*Thermotropic Liquid Crystals Fundamentals*”, Springer-Verlog, Heidelberg, Ch.11, 211 (1988).
60. F. Noack in “*Hand Book of Liquid Crystals*”, Vol.1 and 3 (eds.) D. Demus, J. Goodby, G. W. Gray, H.-W. Spiess, and V. Vill. and references therein.
61. C. Choi, J. Peterelji and M. M. Pinar, *J. Chem. Phys.*, **109**, 1860, (1998)
62. R. Blinc, Pirs, I. Zupancic, *Phys. Rev. Lett.*, **30**, 546 (1973).
63. M. P. Allen, *Phys. Rev. Lett.*, **65**, 2881 (1990)

Chapter 5

Nuclear Magnetic Relaxation Dispersion (NMRD) Theory of Liquid Crystals

Theoretical models required for analyzing the proton NMRD data are presented in this chapter under different sections. A brief introduction to the basic NMRD methodology is given in section 5.1. Other sections deal with different dynamic processes mediating spin relaxation in liquid crystals. In section 5.2, various models describing the contribution from director fluctuations (DF) to the total spin relaxation are presented. Section 5.3 deals with the self-diffusion (SI) mechanism and section 5.4, with the rotational motions (R). References are given at the end of the chapter.

5.1. Nuclear Magnetic Relaxation Dispersion (NMRD)

The interest in molecular dynamics in thermotropic liquid crystals is driven by a desire for an understanding of the description of the fourth state of matter (liquid crystals). On the other hand, the lyotropic interest is derived from a wish to understand which physical processes of membrane systems are of prime importance for the biological function [1]. The molecular motions in liquid crystals are of two fundamental types [1-3]. The first one is translational motion. In the nematic phase, molecules as a whole can undergo three-dimensional translational self-diffusion (SD). However, in the smectic phase one expects to observe a distinct anisotropy in the translational diffusion process, with the exchange between layers being slower than the lateral in-plane diffusion. The motion in the lyotropics, on the other hand, is strictly two-dimensional. This is because the hydrophobic nature of the lyotropic mesogens strongly suppresses their passage through an aqueous region [1].

The presence of translational diffusion makes the task easier for both theoreticians and experimentalists [1], because it helps justify the molecular field description of liquid crystals which assumes that the behavior of each molecule is

determined by a near interaction potential, independent of its position within the structure. Furthermore, what is expected now is that, any structural correlations between adjacent layers in many smectic and lamellar phases are averaged out. This implies that microscopically aligned samples would exhibit uniaxial symmetry about the common macroscopic direction and that the molecular order and dynamics in each layer can be considered to be two dimensional in character.

The second mode of motion involves a change of orientation of the molecule relative to the symmetry axis of the phase. This change may be a result of a reorientation (R) of the whole molecule, and in flexible molecules, a **conformational** change due to internal motion [1-3]. The combination of these two mechanisms complicates the details of the molecular dynamics as the processes take place on a similar time scale [5]. The orientation of the molecules in space may also change as a result of collective molecular motions, for example, through director fluctuations (DF). It is important to realize the fact that this is a basic problem and that the separation of internal conformational motions and director fluctuations (DF) from overall molecular rotation (R) is not simple [5]. The only hope that this can be achieved lies in the expectation that the two processes occur on different time scales, the independent reorientations (R) being significantly faster than the collective director fluctuations (DF). Thus, techniques having a small intrinsic time window are expected to be less susceptible to the effects of collective motions than those with a large time window like the field cycling NMR technique [5].

It is now important to note the assumption that the translational and orientational molecular motions are effectively decoupled and may be considered independently of each other. This gives a simple approach to a difficult problem. The experimental observations that the translational diffusion and the rotational motions of the molecules occur at different time scales suggest that such an assumption is not wrong and this is an appropriate simplification [5]. As has been mentioned earlier, the intrinsic time scale decides the usefulness of the technique, which in turn depends on the physical phenomena under study. Certain techniques, which are useful in studying molecular dynamics and their intrinsic time scales [5], are mentioned here.

- > In the UV and Visible light absorption experiments, the intrinsic time scale is the time taken to absorb a photon from the radiation field ($\tau_{int} < 10^{-14}$) and this process clearly occurs instantaneously before the molecule can change its position or orientation.
- IR absorption or the Raman scattering experiment has an intrinsic time scale (τ_{int}) of about 10^{-12} s, so that the band shape of the line of a molecular vibration is modulated by the fast components of the molecular motions.
- The fluorescence experiment has $\tau_{int} \approx 10^{-9}$ - 10^{-8} s, reflecting the lifetime of the excited state and is useful in monitoring reorientations (R).
- For the magnetic resonance experiments, intrinsic time scale is determined by the anisotropy of the magnetic interaction tensors and consequently varies with the nature of the observed spins and their environment. ESR experiments utilize nitroxide spin labels, which give $\tau_{int} \approx 10^{-9}$ s. Thus the spectral line-shapes are particularly sensitive to the rotational motions in liquid crystalline systems. ^2H NMR line shape experiments have a time window of about 10^{-5} s, and hence, the features are not affected by orientational motions. But, the relaxation rate measurements can provide information about the orientational dynamics.
- The dielectric relaxation technique has a variable time window, as this experiment measures the electric field frequency dispersion. This technique measures the macroscopic property of the system, while the NMR technique probes the system at the microscopic level.
- Quasi-elastic neutron scattering has a very short time window and this technique is also useful in studying translational and orientational motions.

There are thus, two distinct classes of experimental techniques, which are useful in studying rotational motions [1]. The techniques like the ESR and the NMR are utilize magnetic interactions, and optical spectroscopy and dielectric methods rely on the interaction of fluctuating electric fields with the sample. The Redfield theory [7] can directly relate the relaxation rates to the spectral densities $J(\omega)$ which are the Fourier transforms of the correlation **functions** of the spin Hamiltonian. These spectral densities may be sampled at a number of discrete **Larmor** frequencies, depending on the availability of magnets or field cycling NMR experiments [5] The Redfield theory

relates the measured relaxation rates and spectral densities in the extreme narrowing condition $1 \gg \omega\tau_c$ only. However, as the slow motion regime where $\omega\tau_c \approx 1$, is reached, the contributions to the relaxation rates from higher terms, which are neglected in the Redfield approach [7] become increasingly important. The correct relation between the relaxation rates and dynamic process must now be calculated from an explicit application of this stochastic Liouville formulation for the time evolution of the density matrix. In this context, it is important to note that the slow motion regime, $\tau_c \gg 1$, may be reached for certain motional processes in experiments monitoring the fast motions at very high Larmor frequencies or on lowering this Larmor Frequency, as is done in field cycling experiments, to access the slow fluctuations.

It is well known that the interaction between nuclei having magnetic moment (μ) and a dc magnetic field (H_0) results in equally spaced energy levels [6,8]. If the spin vector of the nucleus is the operator I , the nuclear angular momentum operator J is expressed in terms of I by

$$J = \frac{J}{\hbar} \hbar I \quad (5.1a)$$

and this nucleus has a permanent magnetic moment μ , given by

$$\mu = \gamma J \quad (5.1b)$$

where γ is the gyromagnetic ratio of the nucleus. The value of the γ is positive, if μ and J are parallel, and negative if they are antiparallel. The energy of the nucleus in the presence of the magnetic field H_0 (applied in the direction z) is $-\mu \cdot H_0$ and the dipole axis of the nucleus precesses about H_0 with angular frequency $-\omega_0$. We call the motion of the dipole as Larmor precession, and ν_0 defined by,

$$\nu_0 = \frac{\gamma H_0}{2\pi} \quad (5.2)$$

the Larmor frequency. The energy difference between consecutive energy levels is $\pm \hbar \omega_0$ and hence in order to raise the nuclear spins from one level to the next level, the nuclei needs to be irradiated with a time dependent electromagnetic waves of frequency, ν_0 (this frequency lies in the radio-frequency range). The macroscopic

process, which causes the evolution of the system from the initial, non-equilibrium, excited state to the final equilibrium state through energy exchange with the surroundings is termed as 'relaxation'. Depending on the agents of the energy exchange, the relaxation process can be a 'spin-spin' or a 'spin-lattice' relaxation process. These are explained here.

When a spin system is made to interact with a strong magnetic field applied in the z-direction, and a suitable *rf* pulse is used to create the non-equilibrium situation, the individual spins precess about the z-axis, while the spin system is settling down to its equilibrium state (figure 1.4, chapter 1, page no: 17). The precessional motion of the spin is influenced by the internal field arising from interactions with spins of neighboring particles. This internal field does not contribute to the total energy of the system. However, it has the effect that the particles do not precess with the same angular velocity, and so the transverse components of magnetization, M_x and M_y tend to zero. This relaxation process leading to the redistribution of energies within the system without changing the entropy of the system is called the spin-spin relaxation (figure 1.5, chapter 1, page no: 17). The time constant associated with this process is called the spin-spin relaxation time (T_2) or transverse relaxation time. The process of energy exchange between the perturbed spin system and other degrees of freedom of the system (lattice or bath) through fluctuations in the surrounding electromagnetic fields, resulting in a change of entropy of the system, is called spin-lattice relaxation. Here, the longitudinal magnetization M_z evolves to reach the Boltzmann equilibrium. The time constant associated with this process is called the spin-lattice relaxation time (T_1) or longitudinal relaxation time (figure 1.6, chapter 1, page no: 18).

The 'lattice' can be of many forms such as molecular rotations, self-diffusion, lattice vibrations, collective fluctuations, etc. The measurement of T_1 gives information about the time modulation of the fluctuation fields surrounding the spin system, $B_{loc}(t)$, which are dipolar fields arising due to the interaction with the surrounding dipoles. Different time dependent correlation times and their Fourier intensities (spectral densities) are used to describe various atomic and molecular interactions, which lead to fluctuating local fields. The characteristic time, τ_c

associated with these motions can be obtained by measuring the correlation functions over a time interval or the related power spectrum over a frequency range. Thus, a frequency dependent study of relaxation rate probes the power spectrum for possible information about the fluctuating molecular dynamics. One can obtain spectral density, $J(\omega) \propto 1/T_1$, from the measurement of $1/T_1$, which is the Fourier transform of autocorrelation function for the corresponding motions. Theoretically, there are two different approaches, which lead to the expressions for spectral densities, and hence the spin-lattice relaxation rates, viz., 1). The quantum mechanical time dependent perturbation method developed by Bloembergen et al., [9] and 2). Density matrix formalism due to Wangness and Bloch [10].

The description of nuclear spin system under the influence of rf pulses in liquid crystals requires a quantum mechanical formalism that specifies the state of a spin system by a state function or by a density operator. The full Hamiltonian H of a molecular system is usually complex. Fortunately, magnetic resonance experiments can be described by a much-simplified spin Hamiltonian. The nuclear spin Hamiltonian acts on the spin variables and is obtained by averaging the full Hamiltonian over the lattice coordinates. In contrast to solids, intermolecular interactions are normally averaged to zero in liquid crystals, due to rapid translational and rotational diffusion in liquid crystalline phases [2]. Although the density matrix formalism is a general method, it is particularly suitable for systems in which the lattice may be described classically and in which motional narrowing occurs [6,8].

Generally, the spin-lattice relaxation rate is given by

$$\frac{1}{T_1} \propto J_m \equiv \int_0^\infty G_m(\tau) e^{i\omega\tau} d\tau \quad (5.3)$$

$G_m(\tau)$, here quantifies the correlation between the random functions $B_{loc}(t)$ at times t and $t + \tau$, and is given by the ensemble average of the corresponding fluctuating Hamiltonian as

$$G_m(\tau) = \langle B_{loc}^*(t) B_{loc}(t + \tau) \rangle_{av} \quad (5.4)$$

Considering the fluctuations in $B_{loc}(t)$ to be stationary and Markovian in time, the correlation function can be written as

$$G_m(\tau) = \langle |B_{loc}(0)|^2 \rangle e^{-\frac{\tau}{\tau_c}} \quad (5.5)$$

where τ_c is the correlation time. The corresponding spectral density function is a Lorentzian [6,8] i.e.,

$$J(\omega) \propto \frac{\tau_c}{1 + \omega^2 \tau_c^2} \quad (5.6)$$

5.7.1 Laboratory-Frame Spin-Lattice Relaxation

Various interactions involved in the nuclear spin relaxation are briefly described here with their corresponding Hamiltonians.

Considering an ensemble of systems consisting of two arbitrary spins I and S , the interaction mechanism is assumed to be a dipolar interaction. When spin-lattice relaxation refers to the z -components of the magnetizations, the stationary part of the Hamiltonian is given as the Zeeman expression

$$H_0 = -\hbar\omega_I I_z - \hbar\omega_S S_z \quad (5.7)$$

where $\omega_I = \gamma_I B_0$ and $\omega_S = \gamma_S B_0$ and γ_I and γ_S are the gyromagnetic ratios of the nuclei.

The spin interaction Hamiltonian H_I is identified with that for dipolar coupling H_d . This Hamiltonian is expanded into terms consisting of the fluctuating functions $F^{(k)}$ and the spin-operator expressions $O^{(k)}$ [3,6,8],

$$H_d = f_d \sum_{k=-2}^2 F^{(k)} O^{(k)} \quad (5.8)$$

where $f_d = \frac{\mu_0}{4\pi} \gamma_I \gamma_S \hbar^2$

When the spin operator terms are transformed to the interaction representation, and labeling the multiple quantum order with the subscript k , and the spin transition

with the subscript I , the dipolar Hamiltonian in the interaction frame (\mathcal{H}_d) can be written as [3]

$$\mathcal{H}_d = f_d \sum_{k,l} F^{(k)} O_l^{(k)} e^{-i\omega_l^{(k)} t} \quad (5.9)$$

A system of two unlike spins I and S , $\gamma_I \neq \gamma_S$, is considered. The //pulses are tuned to the I spins whereas the off-resonant S spins merely take effect as the interaction partners and are not subject to rf excitation. It is also assumed that S -spins are in their thermal equilibrium irrespective of what happens to I spins. This situation may arise when the resonant nuclei (spin I), are *dipolar coupled to quadrupole* nuclei or unpaired electrons (spin S) suffering additional and independent relaxation mechanisms. The S -spin relaxation is assumed to be much faster than that, due to the mutual dipolar coupling of the I and S spins and virtually never leaves its equilibrium value [3]. For a fixed inter-dipole distance r , the spin-lattice relaxation rate of the I spins in terms of the reduced intensity function,

$$J(\omega) = \int_{-\infty}^{+\infty} G(\tau) e^{-i\omega\tau} d\tau \quad (5.10)$$

is

$$\frac{1}{T_1} = \left(\frac{\mu_0}{4\pi} \right)^2 \frac{1}{15r^6} \gamma_I^2 \gamma_S^2 \hbar^2 S(S+1) [J(\omega_I - \omega_S) + 3J(\omega_I) + 6J(\omega_I + \omega_S)] \quad (5.11)$$

Like-Spin limit

When the spin system consists of like-spins, i.e., $I = S$, $\gamma_I = \gamma_S = \gamma$, $\omega_I = \omega_S = \gamma H_0$, for a fixed internuclear distance r , in terms of reduced intensity function the relaxation rate is given by

$$\frac{1}{T_1} = \left(\frac{\mu_0}{4\pi} \right)^2 \frac{1}{5r^6} \gamma^4 \hbar^2 I(I+1) [J(\omega_0) + 4J(2\omega_0)] \quad (5.12)$$

This is the well known *Bloembergen-Purcell-Pound* (BPP) formula [9,6]. For systems consisting of more than two dipolar coupled spins, the dipolar Hamiltonian is a sum over all pairs and the relaxation rate due to each of these pairs can be summed over

provided that pair motions are independent of each other (with vanishing cross correlations). The relaxation rate is

$$\frac{1}{T_1} = \frac{3}{2} \left(\frac{\mu_0}{4\pi} \right)^2 \frac{\gamma^4 \hbar^2}{r^6} I(I+1) \sum_j [J_j^{(1)}(\omega_0) + J_j^{(2)}(2\omega_0)] \quad (5.13)$$

where j runs over all dipoles interacting with the reference nuclei. The relaxation curves for like spins are nonexponential in accordance with the **Bloch** equation for the **z-magnetization**. Typical behavior of T_1 with temperature is shown in figure 5.1 [3,13].

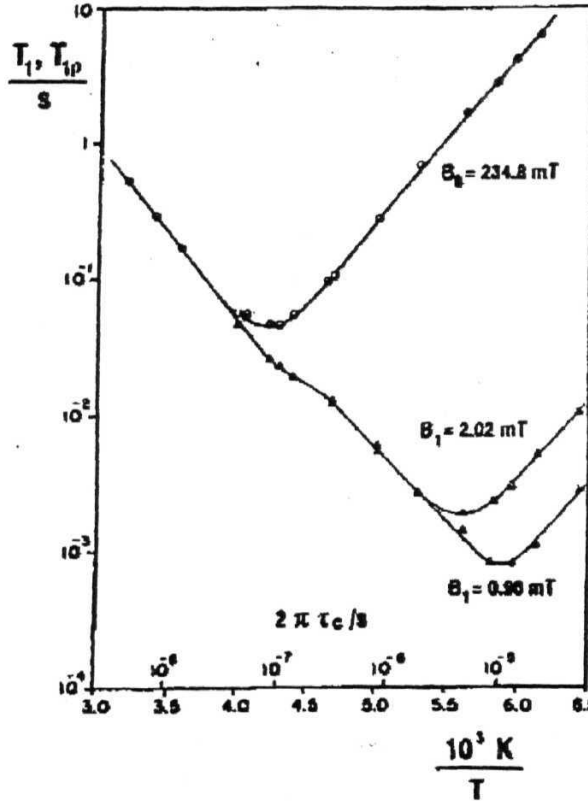


Figure 5.1. Temperature dependences of the proton spin-lattice relaxation time in the laboratory frame, T_1 , and in the rotating frame $T_{1\rho}$, of crystal water in gypsum. The dipolar-coupling fluctuations arise from 180° rotational flips. The lines were calculated with the aid of equations 5.13 (T_1) and 5.19 ($T_{1\rho}$). The condition for minima is $\omega_0\tau_c \approx 0.62$ and $\omega_1\tau_c = 1$ for T_1 and $T_{1\rho}$, respectively [3].

5.1.1.2. Scalar Coupling

For unlike spins I and S , $\gamma_I \neq \gamma_S$, scalar-coupling relaxation can arise due to, 1). Dipolar-interaction induced equilibration, 2). Due to nuclei coupled to unpaired electrons having a finite residency probability in the resonant nucleus (like the Fermi contact interaction) and 3). **Indirect** spin-spin coupling of the resonant nucleus to a quadrupole nucleus. The additional spin-lattice relaxation (for nucleus I) term based on zero-quantum transitions is obtained [3],

$$\left(\frac{1}{T_1}\right)_{scal} \propto A^2 S(S+1) J(\omega_S - \omega_I) \quad (5.14)$$

where $J(\omega) = F\{G(r)\}$ and $G(r)$ are the respective reduced intensity and correlation function for scalar interaction ($G(0)=0$)

5.1.1.3. Quadrupolar coupling

Nuclei with an electric-quadrupole moment are subject to "quadrupolar relaxation", which tends to be stronger than dipolar coupling so that it is a strong source of relaxation. Restricting the treatment to **spin-1** case, based on quadrupole-coupling **Hamiltonian** $H_I=H_q$, one finds the spin-lattice relaxation of the observable $Q=I_z$, [8,11]

$$\frac{1}{T_1} = \frac{3}{80} \left(\frac{e^2 q Q}{\hbar} \right)^2 \left(1 + \frac{\eta^2}{3} \right) [J(\omega_0) + 4J(2\omega_0)] \quad (5.15)$$

which is determined by a single and a double-quantum transition intensity **function** as expected in view of the quadrupolar-interaction Hamiltonian. Considering the longitudinal quadrupolar order too, the observable is $Q - I_z^2 + 2/3$. The resulting weak-collision quadrupolar order relaxation rate is [12],

$$\frac{1}{T_q} = \frac{9}{80} \left(\frac{e^2 q Q}{\hbar} \right)^2 \left(1 + \frac{\eta^2}{3} \right) J(\omega_0)$$

Note that this rate is governed by the single quantum transition spectral-density term.

5.1.1.4. Chemical-Shift Anisotropy

The anisotropy of the chemical shift tensor produces transverse field components that induce single quantum spin transitions. Chemical shift Hamiltonian, fluctuates due to molecular reorientations and the spin-lattice relaxation rate expression derived for axially symmetric molecules is given by [3,6,8],

$$\frac{1}{T_1} \propto \gamma^2 B_0^2 (\sigma_{33} - \sigma_i)^2 J(\omega_0) \quad (5.17)$$

i.e., the chemical shift anisotropy spin coupling constant varies proportionally to the external magnetic field.

5.1.2. *Rotating-Frame Spin-Lattice Relaxation by Dipolar Coupling*

As regard as the dipolar coupled pairs of like-spins, the same treatment is followed, as in the previous case, with the exception, lying in the interaction frame, which now is the tilted rotating frame with the z-axis aligned along the effective field B_E . Rotating frame experiments (will be explained later), are usually carried out while the magnetization is locked along the (rotating) effective field. The angular frequencies of interest are

$$\begin{aligned} \omega_0 &= \gamma B_0; \\ \omega_I &= \gamma B_I; \\ \omega_e &= \gamma B_e = \sqrt{(\omega_0 - \omega_c)^2 + \omega_I^2} \end{aligned} \quad (5.18)$$

in the limit $\omega_0 \gg \omega_e$, which represents the actual situation in practically all applications. The effective spin-lattice relaxation rate for dipolar coupling of the like spins in the rotating frame when the spin-lock pulse is resonant ($\omega_c = \omega_0$; $\omega_e = \omega_I$) is given by

$$\frac{1}{T_{1\rho}} = \left(\frac{\mu_0}{4\pi} \right)^2 \frac{1}{10r^6} \gamma^4 \hbar^2 I(I+1) [3J(2\omega_I) + 5J(\omega_0) + 2J(2\omega_0)] \quad (5.19)$$

The temperature dependence of $T_{1\rho}$ calculated on the basis of this equation is shown in the figure 5.1 [3].

5.2 Director Fluctuations and Spin Relaxation

Collective director fluctuations (DF) are elastic deformations in liquid crystalline medium, which are perceived as **hydrodynamic** phenomena and are influenced by molecular properties such as elastic constants and viscosities of the liquid crystalline **medium**. Director fluctuations, in principle, therefore, do provide information on anisotropic intermolecular interactions, and the elastic constants of the medium. DF modes also exist in the isotropic phases of liquid crystalline materials, with a finite coherence length, giving rise to pretransition phenomena [14].

These long-range collective motions were first recognized by de Gennes [15] and the hydrodynamic description of the **nematic** phase was confirmed by light scattering experiments [17,18]. The first frequency dependent relaxation time measurements made by Orsay liquid crystal group [16] had proved that the relaxation rate in **nematics** did not obey the Lorentzian like behavior expected from the BPP theory [9]. Pincus derived [19] the first expression for γ due to director fluctuations in the nematic phase and predicted the ω^{-1} behavior for spin-lattice relaxation. NMR experiments by many authors [20-24] have proved that the proton spin-lattice relaxation behavior is more complex than the one predicted by **Pincus's** theory. The original theory by Pincus [19] and the subsequent models by others [25,26] were developed by treating an assembly of partially ordered rigid cylindrical molecules. A detailed description of these theories along with the latest developments of spin relaxation theories of director fluctuations are given in the book by Dong [2]. A brief account of the theoretical developments is presented here.

5.2.1. Curvature elastic constants

While dealing with large scale phenomena such as the DF modes, it should be kept in mind that the characteristic distances involved are large compared with the molecular dimensions, and the energy involved per molecule is small in comparison with the strength of the intermolecular interactions. It is hence, appropriate to ignore

completely, the **molecules** and regard the liquid crystal as a *continuum medium with curvature elasticity*.

The nematic director $n(r,t)$ is considered to be aligned along the direction of the applied magnetic field (in the present case, the **Zeeman** magnetic field). The orientations of the molecule vary in space, giving rise to fluctuations of the director around the equilibrium direction in an average direction n_0 , parallel to the z-axis, which is given by

$$n(r,t) = n_0 + \delta n(r,t) \quad (5.20)$$

Three distinct curvature strains in terms of six components are defined below, and any arbitrary deformation in the medium can be considered as a combination of these three basic deformations [27,2] namely, splay, bend **and** twist (figure 5.2). At any point r in the liquid crystal sample, a coordinate system with its z-axis along the director is chosen. The local director $n(r)$ may be expressed as $n_0 + \delta n$, with δn being given by two components $n_x(r)$ and $n_y(r)$ along the x- and y- axes, respectively. The components of curvature strains are defined as follows

$$\begin{aligned} a_1 &= \partial n_x / \partial x, \\ a_2 &= \partial n_x / \partial y, \\ a_3 &= \partial n_x / \partial z \\ a_4 &= \partial n_y / \partial x, \\ a_5 &= \partial n_y / \partial y \\ a_6 &= \partial n_y / \partial z \end{aligned} \quad (5.21)$$

The **splay**(K_{11}) deformation is described by a_1 and a_5 , and gives a non-zero $\nabla \cdot n(r)$; the **twist** (K_{22}) deformation is described by a_2 and a_4 and gives a non-zero $n(r) \cdot \nabla \times n(r)$; the **bend** (K_{33}) deformation is described by a_3 and a_6 and gives a non-zero $n(r) \times [\nabla \times n(r)]$. Viscoelastic properties of the liquid crystalline medium are described in figure 5.2.

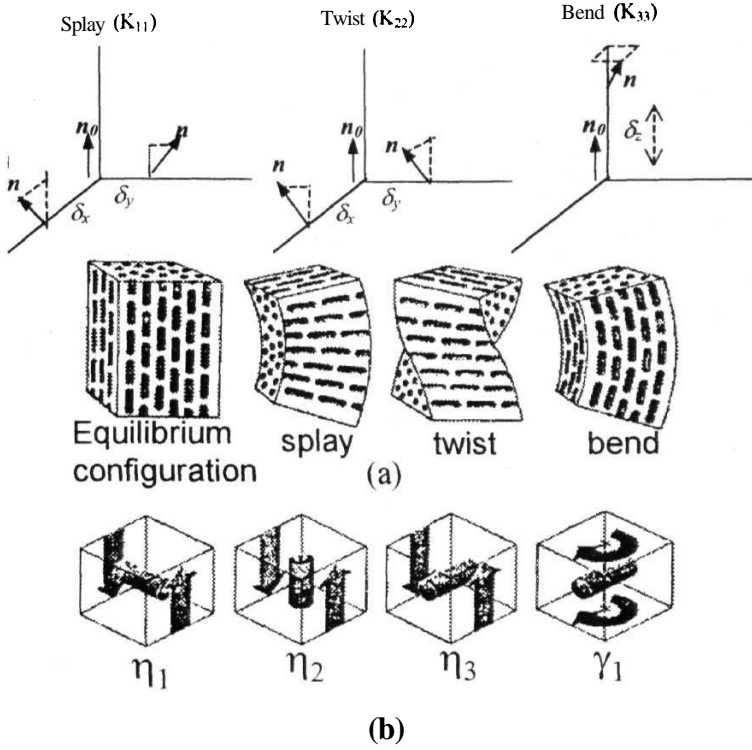


Figure 5.2. Three types of deformation splay, twist and bend are illustrated along with the equilibrium configuration (a). The Miesowich viscosities (η_1, η_2, η_3) and the rotational viscosity (γ_1) are also illustrated (b).

In terms of these curvature strains, the local director is given at the point r by

$$n_x = a_1 x + a_2 y + a_3 z + O(r^2), \quad (5.22a)$$

$$n_y = a_4 x + a_5 y + a_6 z + O(r^2), \quad (5.22b)$$

$$n_z = 1 - O(r). \quad (5.22c)$$

Frank has shown the Gibbs free energy density (ϵ), for the deformation, relative to its value in a state of uniform orientation [28] as

$$f = K_1(a_1 + a_5) + K_2(a_1 - a_4) + \frac{1}{2}K_{11}(a_1 + a_5)^2 + \frac{1}{2}K_{22}(a_2 - a_4)^2 + \frac{1}{3}K_{33}(a_3^2 + a_6^2) + K_{12}(a_2 - a_4)(a_1 + a_5) \quad (5.23)$$

Where K_i , K_{ii} and K_{ji} are curvature elastic constants. The above expression can be simplified due to symmetry considerations, since **nematics** are apolar, $K_I = K_{I2} = 0$. Furthermore, there exists a reflection symmetry about a plane that contains the z-axis, $K_2 = K_{I2} = 0$. Thus the free energy density is simplified as

$$f = \frac{1}{2}[K_{11}(a_1 + a_5)^2 + K_{22}(a_2 - a_4)^2 + K_{33}(a_3^2 + a_6^2)] = \frac{1}{2}[K_{11}(\nabla \cdot \vec{n})^2 + K_{22}(\vec{n} \cdot \nabla \times \vec{n})^2 + K_{33}[(\vec{n} \cdot \nabla)\vec{n}]^2] \quad (5.24)$$

In a smectic A phase, deformations that do not preserve interlayer spacing of the layered structure, would cost a great amount of energy. For a dislocation free system, it can be shown that $\nabla \cdot \vec{n} = 0$. Thus, both twist and bend deformations are absent in the system. In other words, $a_2 - a_4 = 0$, and $a_3 + a_6 = 0$. Under these conditions, K_{22} and K_{33} are found [27] to diverge in the **nematic** phase as the temperature approaches a **nematic-smectic** A phase transition. The **diamagnetic** susceptibility of a liquid crystal is anisotropic due to the shape anisotropy of the liquid crystal molecule. The presence of a magnetic field leads to an additional term in / [27],

$$f_m = -\frac{1}{2}\chi_{\parallel}B^2 - \frac{1}{2}\Delta\chi(\vec{n} \cdot \vec{B})^2 \quad (5.25)$$

where $\Delta\chi = \Delta\chi_{\parallel} - \Delta\chi_{\perp}$ and $\Delta\chi_{\perp}$ are the two components of the susceptibility tensor per unit length, along and perpendicular, to the direction \vec{n}_0 . If $\Delta\chi > 0$, the director would align along the magnetic field ($B \parallel \vec{z}$). Only the second term here, has a dependence on the orientation of this direction. In particular, this function is minimized when \vec{n} is collinear with the field, and if $\Delta\chi$ is positive. Fluctuation of the local director increases this function by

$$\Delta f_m = \frac{1}{2}\Delta\chi(n_x^2 + n_y^2)B^2 \quad (5.26)$$

So, the static free energy F of a nematic liquid crystal undergoing long wavelength distortion in a magnetic field is

$$F = \frac{1}{2} \int d^3r \left\{ K_{11} \left(\frac{\partial n_x}{\partial x} + \frac{\partial n_y}{\partial y} \right)^2 + K_{22} \left(\frac{\partial n_x}{\partial x} - \frac{\partial n_y}{\partial y} \right)^2 + K_{33} \left[\left(\frac{\partial n_x}{\partial z} \right)^2 + \left(\frac{\partial n_y}{\partial z} \right)^2 \right] + \Delta\chi B^2 (n_x^2 + n_y^2) \right\} \quad (5.27)$$

The fluctuations are expressed in terms of a set of periodic distortion modes, so as to emphasize the spatial dependence of the orientation of the local director [29]. It is convenient to Fourier expand $n_x(r)$ and $n_y(y)$ using

$$n_\alpha(\vec{r}) = \frac{1}{V} \sum_{\vec{q}} n_\alpha(\vec{q}) \exp[-i\vec{q} \cdot \vec{r}] \quad (5.28)$$

where V is the sample volume. The mode amplitudes are

$$n_\alpha(\vec{q}) = \int n_\alpha(\vec{r}) \exp[i\vec{q} \cdot \vec{r}] d^3r \quad (5.29)$$

In terms of these Fourier components, the free energy (per unit volume) becomes

$$F = \frac{1}{2V} \sum_{\vec{q}} \left\{ K_{11} |n_x(\vec{q})q_x + n_y(\vec{q})q_y|^2 + K_{22} |n_x(\vec{q})q_y - n_y(\vec{q})q_x|^2 \right. \\ \left. + (K_{33}q_z^2 + \Delta\chi B^2) [|n_x(\vec{q})|^2 + |n_y(\vec{q})|^2] \right\} \quad (5.30)$$

The above quadratic form, when **diagonalized** by transforming $(n_x, n_y) \rightarrow (n_1, n_2)$ to yield two uncoupled modes $n_1(q)$ and $n_2(q)$ $n_1(q)$ lies on the (q, n_0) plane and describes a periodic distortion involving splay and bend deformations, while $n_2(q)$ is perpendicular to the (q, n_0) plane and describes a periodic distortion involving twist and bend deformations, i.e.,

$$q_{||}^2 = q_z^2 \text{ and} \quad (5.31)$$

$$q_{\perp}^2 = q_x^2 + q_y^2 \quad (5.32)$$

The equation for F is rewritten as

$$F = \frac{1}{2V} \sum_{\vec{q}} \sum_{\alpha=1}^2 K_\alpha(\vec{q}) |n_\alpha(\vec{q})|^2 \quad (5.33)$$

where

$$K_{\alpha}(\vec{q}) = K_{\alpha\alpha}q_{\perp}^2 + K_{33}q_{\parallel}^2 + \Delta\chi B^2 \quad (5.34)$$

The $n_{\alpha}(q)$ are transverse modes responsible for bringing the instantaneous director n to its equilibrium orientation. They relax with exponential damping [27] according to

$$\frac{\partial}{\partial t} n_{\alpha}(\vec{q}) = -\frac{1}{\tau_{\alpha}(\vec{q})} n_{\alpha}(\vec{q}) \quad (5.35)$$

where $\alpha = 1, 2$ and the time constants

$$\tau_{\alpha}(\vec{q}) = \frac{\eta_{\alpha}(\vec{q})}{K_{\alpha}(\vec{q})} \quad (5.36)$$

The viscosities depend on the wave vector q and are closely related to the twist viscosity (shown in figure 5.2b). The effect on relaxation due to the wave vector dependence has been examined in **Smectic A** phases and was found to be small [30]. The wave vector dependence is ignored here. The equipartition theorem of energy is used, to obtain the mean square amplitude of each transverse mode,

$$\langle |n_{\alpha}(\vec{q})|^2 \rangle = \frac{K_B T V}{K_{\alpha}(\vec{q})} \quad (5.37)$$

In the one constant approximation ($K_{11} = K_{22} = K_{33} = K$, $\eta_1 = \eta_2$), $K_{\alpha}(q)$ reduces to $Kq^2 + \Delta\chi B^2$. Furthermore, director fluctuation modes of different wave vectors are uncorrelated (strictly true in the limit of infinitely large volume, $V \rightarrow \infty$) i.e.

$$\langle n_{\alpha}(\vec{q}) n_{\alpha}^*(\vec{q}') \rangle = \delta_{\vec{q}\vec{q}'} \langle |n_{\alpha}(\vec{q})|^2 \rangle \quad (5.38)$$

The spectral densities are obtained from the correlation functions associated with the fluctuations leading to the modulation of the **intermolecular** dipolar interaction. Those correlation **functions** have to be transformed from the magnetic field fixed frame (laboratory form) to the director fixed frame and finally to the molecular fixed frame through proper Wigner rotation matrix elements [26]. Such transformation results in

$$\begin{aligned}
G(t) &= \langle F_h(0) F_h^*(t) \rangle \\
&= f_h(\Delta) \langle F_1(0) F_1(t) \rangle \\
&= f_h(\Delta) S^2 \langle \delta n(r, 0) \delta n(r, t) \rangle
\end{aligned} \tag{5.39}$$

where S is the **nematic** order parameter. A is the angle between the magnetic field and the director. The functions $f_h(A)$ are given by

$$\begin{aligned}
f_0(\Delta) &= 18 (\cos^2 \Delta - \cos^4 \Delta) \\
f_1(\Delta) &= 1/2 (1 - \cos^2 \Delta + 4 \cos^4 \Delta) \\
f_2(\Delta) &= 2(1 - \cos^4 \Delta)
\end{aligned} \tag{5.40}$$

The spectral density is given by

$$J_h(p\omega) = f_h(\Delta) S^2 \int_{-\infty}^{\infty} e^{-ip\omega t} \langle \delta n(r, 0) \delta n(r, t) \rangle dt \tag{5.41}$$

Introducing the Fourier components of the director fluctuations of the nematic order (equation 5.28) the spectral density is given by

$$J_h(p\omega) = f_h(\Delta) S^2 \int_{-\infty}^{\infty} e^{-ip\omega t} dt \sum_q \sum_{\alpha=1}^2 \langle |n_\alpha(\vec{q})|^2 \rangle e^{-t/\tau_\alpha(q)} \tag{5.42}$$

5.2.2 The one constant expansion for $J_1(\omega_0)$

Following the Pincus's [19] work, the expression for $J_1(\omega_0)$ was extended and refined by several authors [26,31,32] using the one constant approximation. This leads to a simple expression for the relaxation time of each mode

$$\tau_q = \eta / K q^2 \tag{5.43}$$

Considering the upper cut-off frequencies of the modes to be infinity, these theories predicted $\omega^{-1/2}$ dependence for the relaxation rate due to the DF modes. However, since the director fluctuation modes are restricted by a longest and shortest possible wavelengths, the existence of an upper and lower bound for frequencies are to be considered. The upper cut-off frequency is necessary due to the fact that the shortest wavelength cannot be smaller than the length of the molecule (and hence the

upper cut-off frequency is a function of molecular dimensions though it is inconsistent to allow up to the inverse of the molecular length since it is assumed that molecules undergo free rotational diffusion about the local director). The lower cut-off frequency should be considered especially at sub MHz frequencies as suggested by Blinc et al., [29,30] and by Noack et al., [33].

The spectral density function $J_1(\omega)$ is obtained, considering only the upper cut off frequency by Fourier transforming the correlation function with one constant approximation,

$$G(t) = 3S \frac{K_B T}{2\pi^2 K} \int_0^{q_c} dq \exp(-tKq^2 / \eta) \quad (5.44)$$

The resultant spectral density is given by

$$J_1(\omega) = \frac{3KTS^2}{2\pi^2 K} \int_{-\infty}^{\infty} dt \int_0^{q_c} dq e^{-tKq^2 / \eta} e^{-i\omega t} \quad (5.45)$$

$$= A_c S^2 \omega^{-\frac{1}{2}} U\left(\frac{\omega_c}{\omega}\right) \quad (5.46)$$

where

$$A_c = \frac{3KT}{2\pi^2 K}, \omega_c = \frac{q_c^2}{\eta} \quad (5.47)$$

and the cut off function $U\left(\frac{\omega_c}{\omega}\right)$ is given by

$$U\left(\frac{\omega_c}{\omega}\right) = \frac{1}{2\pi} \ln \frac{\left(\frac{\omega_c}{\omega}\right) - \left(\frac{2\omega_c}{\omega}\right)^{\frac{1}{2}} + 1}{\left(\frac{\omega_c}{\omega}\right) + \left(\frac{2\omega_c}{\omega}\right)^{\frac{1}{2}} + 1} + \frac{1}{\pi} \left\{ \tan^{-1} \left[\left(\frac{2\omega_c}{\omega}\right)^{\frac{1}{2}} - 1 \right] + \left[\left(\frac{2\omega_c}{\omega}\right)^{\frac{1}{2}} + 1 \right] \right\} \quad (5.48)$$

5.2.3. Anisotropic elastic Constants

For nematic liquid crystals, which have underlying smectic phases, the elastic constants are no more isotropic when they are studied close to N-S_A phase transition temperature. The one constant approximation therefore, is not adequate in evaluating the spectral density in such cases. A fully anisotropic spectral density expression was first derived by Brochard [34] and Blinc et al., [35,29]. Different elastic constants are

introduced in equations describing damping time and mean square amplitude of modes, and the summation over the modes is replaced by integration over cylindrical volume with the limit between zero and upper cut-off frequencies ($q_{zc} = \pi/l$, $q_{\perp c} = \pi/a$, l and a being of the order of the molecular length and width respectively) instead of originally assumed spherical volume [19] The resulting spectral density can be written as

$$J_h(p\omega) = f_h(\Delta) S^2 \frac{1}{(2\pi)^3} \sum_a \int_0^{q_{zc}} \int_0^{q_{\perp c}} \frac{kT}{(K_{33}q_z^2 + K_a q_{\perp}^2)} \times \frac{2\tau_a(q) 2\pi q_{\perp}}{1 + p^2 \omega^2 \tau_a^2(q)} dq_{\perp} dq_z \quad (5.49)$$

Neglecting the wave vector dependence of visco-elastic coefficients, the above equation can be simplified for different limiting cases given below. The cut off frequencies are given by

$$\omega_{ac} = \frac{K_1 q_{\perp c}^2}{\eta_a} \quad (5.50)$$

$$\omega_{zc} = \frac{K_3 q_{zc}^2}{\eta_3} \quad (5.51)$$

Case. 1

$$\omega \ll \omega_{ac}, \omega_{zc}$$

$$J_h(p\omega) = \sum_{a=1}^2 C' \frac{\sqrt{2\pi}}{2K_a} \sqrt{\frac{\eta_a}{K_{33}}} \frac{1}{\sqrt{(p\omega)}} \quad (5.52)$$

$$\text{where} \quad C' = \frac{(f_h(\Delta) S^2 K T)}{2\pi^2} \quad (5.53)$$

This case is valid for normal range of Larmor frequencies below 100 MHz. The spectral density results in a square root dependence of frequency.

Case. 2

$$\omega_{ac} \gg \omega \gg \omega_{zc}$$

In this case

$$J_h(p\omega) = \frac{C' \pi q_{zc}}{4K_1 p\omega} \text{ and hence} \quad (5.54)$$

$$J_h(p\omega) \propto \frac{1}{\omega} \quad (5.55)$$

Case. 3

$$\omega \gg \omega_{ac}, \omega_z$$

$$J_h(p\omega) = \frac{q_{\perp c}^2 q_{zc}^2}{2p^2 \omega^2} \left[\frac{1}{\eta_1} + \frac{1}{\eta_2} \right] \quad (5.56)$$

and hence

$$J_h(p\omega) \propto \frac{1}{\omega^2} \quad (5.57)$$

Case. 4

$$\omega_{zc} \gg \omega \gg \omega_{ac}$$

$$J_h(p\omega) = \frac{C' q_{\perp c}^2}{2K_{33}^2 q_{zc}^2} (\eta_1 + \eta_2) \quad (5.58)$$

Here, the spectral density is independent of frequency.

The expression by Blinc [29] does not reduce to the one constant approximation [19]. The new expression (which is the modified version of Blinc's equation) was derived by Vold and Vold [36] which differ from that given by Blinc's equation [29], in which the upper limit of the integral over q_{\pm} has been modified to represent an ellipsoidal volume of integration. The spectral densities are derived by Vold and Vold [36] which is given in the equation 5.59.

The differences appear only in the cut-off region of frequencies. The effects of including the anisotropies in the viscoelastic constants are of significance when smectic phases are considered, since in this case major differences are observed between the various K_{ii} and the η_i . The frequency dependence predicted by Vold and Vold [36] for range of elastic constants considering only the upper cut off frequencies is shown in figure 5.3. Here the variation of K_{33} between 1×10^{-12} and 1×10^{-2} dyne with other parameters chosen as $S = 1$, $T = 298.2\text{K}$, $\eta_1 = \eta_2 = 0.5$ Poise, $K_{11} = K_{22} = 10^6$ dyne and cut-off wave length of 30 Å results in a cut-off frequency of 140 MHz.

$$\begin{aligned}
J_h(p\omega) = & \frac{3K_B TS^2}{8\pi\sqrt{2}\omega} \sum_a \frac{1}{K_a} \left[\frac{\eta_a}{K_3} \right]^2 \left\{ \frac{1}{2\pi} \ln \frac{B_a^2 - B_a\sqrt{2} + 1}{B_a^2 + B_a\sqrt{2} + 1} + \frac{1}{\pi} \tan^{-1}(B_a\sqrt{2} - 1) \right. \\
& + \frac{1}{\pi} \tan^{-1}(B_a\sqrt{2} + 1) + \frac{\frac{B_a\sqrt{2}}{2\pi}}{\sqrt{2D(\sqrt{1+A_a^4\mu A_a^2})}} \\
& \ln \left[\frac{\sqrt{1+A_a^4} + \sqrt{2D(\sqrt{1+A_a^4\mu A_a^2}) + D}}{\sqrt{1+A_a^4\mu} \sqrt{2D(\sqrt{1+A_a^4\mu A_a^2}) + D}} \right] \mu \frac{\frac{B_a\sqrt{2}}{\pi}}{\sqrt{2D(\sqrt{1+A_a^4\pm A_a^2})}} \\
& \times \left[\tan^{-1} \frac{\sqrt{2D} - \sqrt{\sqrt{1+A_a^4\mu A_a^2}}}{\sqrt{\sqrt{1+A_a^4\pm A_a^2}}} + \tan^{-1} \frac{\sqrt{2D} + \sqrt{\sqrt{1+A_a^4\mu A_a^2}}}{\sqrt{\sqrt{1+A_a^4\pm A_a^2}}} \right] \Bigg\} \quad (5.59)
\end{aligned}$$

where $A_a^2 = K_a q_{\perp c}^2 / \eta_a \omega$ and $B_a^2 = K_3 q_{zc}^2 / \eta_a \omega$

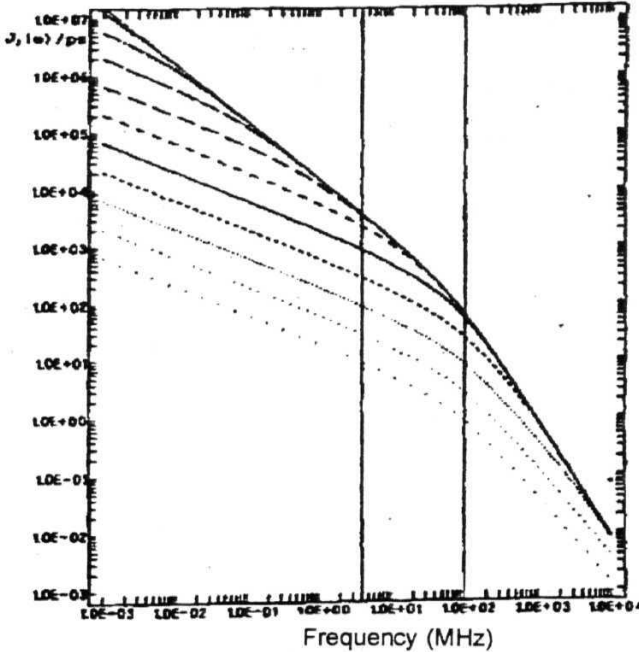


Figure 5.3. Variation of spectral densities $J_I^{DF}(\omega)$ with Larmor frequencies for different elastic constants, K_{11} , K_{22} and K_{33} . The region in between the vertical lines is the region typically covered by conventional NMR [36]. The lower frequency region from 1kHz can be covered by FCNMR.

The plot (figure 5.3) is divided into three regions (the region in between the vertical lines is typically covered by conventional NMR experiments. Low frequency region from 1 kHz can be covered by FCNMR experiments). The solid line in the figure corresponds to the isotropic case and represents the well known $\omega^{-1/2}$ behavior, for the frequencies far below the cut-off frequency. For the Larmor frequency well above the cut off frequency ω_c , the absolute value of $J_1(\omega)$ is small and drops off as ω^{-2} .

5.2.4. Generalized Model (Upper and Lower cut off frequencies)

Vold and Void's model [36] for DF modes based on the anisotropic visco-elastic constants with only upper cut-off frequencies is modified in this laboratory [38] by introducing both the lower and upper cut-off frequencies along with the anisotropic nature of the elastic constants. The relaxation rate now, for Zeeman order, R_{IDF} is proportional to the spectral density $J_1(\omega)$ for director fluctuations given by [38]

$$J_1(\omega) = c_1(\Delta_\perp) \sum_{\alpha=1}^2 \eta_{\alpha} \int_{q_{cl}}^{q_{ch}} dq_z \int_{q_{cl}}^{q_{ch}} \frac{q_\perp dq_\perp}{(K_\alpha q_\perp^2 + K_3 q_z^2) + \omega^2 \eta_\alpha^2} \quad (5.60)$$

$$J_1(\omega) = c_1(\Delta) \sum_{\alpha} \frac{\sqrt{\eta_{\alpha}}}{K_{\alpha} \sqrt{K_3} \sqrt{\rho \omega}} [f(D_{ch}, A_{ch}) - f(D_{cl}, A_{ch}) - f(B_{ch}, A_{cl}) + f(B_{cl}, A_{cl})] \quad (5.61)$$

where

$$f(D, A) = B \tan^{-1}(D^2 + A^2) + \frac{B \sqrt{1+A^4} + A^2}{2\sqrt{2}D} \ln \left| \frac{\sqrt{1+A^4} + \sqrt{2} \sqrt{1+A^4 - A^2 D + D^2}}{\sqrt{1+A^4} - \sqrt{2} \sqrt{1+A^4 - A^2 D + D^2}} \right|$$

$$- \frac{B_{\alpha} \sqrt{1+A^4} - A^2}{\sqrt{2}D} \left\{ \tan^{-1} \left(\frac{\sqrt{2}D - \sqrt{1+A^4 - A^2}}{\sqrt{1+A^4} + A^2} \right) + \tan^{-1} \left(\frac{\sqrt{2}D + \sqrt{1+A^4 - A^2}}{\sqrt{1+A^4} + A^2} \right) \right\} \quad (5.62)$$

and $f(B, A)$'s can be obtained by replacing D by B in this equation

$$D_{ch}^2 = B_{ch}^2 - A_{ch}^2, \quad D_{cl}^2 = B_{cl}^2 - A_{ch}^2 \left(\frac{q_{zcl}}{q_{zch}} \right)^2 \quad (5.63)$$

$$A_{DF} = \frac{3}{2} \frac{\gamma^4 h^2}{r^6} \frac{S^2 k_{\beta} T}{(2\pi)^2} ; \quad q_{lch(l)} = \frac{2\pi}{\lambda_{lcl}(h)} \quad \text{and} \quad q_{zch(l)} = \frac{2\pi}{\lambda_{zcl}(h)} \quad (5.64)$$

$$A_{ah(l)}^2 = \frac{K_a q_{\perp ch(l)}^2}{\omega \eta_a}, B_{ah(l)}^2 = \frac{K_a q_{\perp ch(l)}^2}{\omega \eta_a} \quad (5.65)$$

λ_{lcl} and λ_{acl} are the upper cut off wavelengths of DF modes along and perpendicular directions of the director respectively with the corresponding cut-off frequencies given by

$$v_{sch(l)\alpha} = \frac{K_3 q_{sch(l)}^2}{2\pi \eta_a} \quad \text{and} \quad v_{\perp ch(l)\alpha} = \frac{K_a q_{\perp ch(l)}^2}{2\pi \eta_a} \quad (5.66)$$

$$C_1(\Delta) = f_h(\Delta) \frac{2S^2 K_B T}{(2\pi)^2} \quad (5.67)$$

Here $f(\Delta)$ describes the angular dependence and S is the **nematic** order parameter.

This new expression differs from the one derived by **Vold** and **Vold** [36] (where DF modes were assumed to be extending down to zero frequency) in the two terms involving low frequency cut-off. $J_l(\omega)$ values for different frequencies were computed [38] considering the typical values expected in the liquid crystalline medium as given below

$$\begin{aligned} K_a &= 10^{-6} \text{ dyne} \\ \eta_a &= 0.5 \text{ Poise} \\ \lambda_{acl} &= \lambda_{\perp cl} = 30 \text{ }^\circ \text{A} \\ \lambda_{sch} &= \lambda_{\perp ch} = 1 \times 10^4 \text{ }^\circ \text{A} \\ C &= 5 \times 10^{-3} \text{ S}^{\frac{3}{2}}. \end{aligned} \quad (5.68)$$

and for the different values of K_{33} (or K_3). The constant $C \propto A_{DF}$. Here $J_l(\omega)$ varies as $v^{1/2}$ ($\omega = 2\pi\nu$, where ν is Larmor frequency) between upper and Lower cut-off frequencies for the isotropic case ($K_{33} = 10^{-6}$ dyne). The plots obtained for different K_{33} values and lower cut off frequencies are presented in the reference [36]. This model have been used in the analysis of the nematic **NMRD** data. Upper and lower cut-off frequencies are varied. Experimental elastic constants (K_{11} , K_{22} and K_{33}) are also used in the model fitting (chapter 6 and 7).

5.2.5. Smectic Phases

In the smectic phases, the elastic constants K_{33} and K_{22} (for bend and twist) deformations diverges to infinity. Application of Vold and Vold's equation [36] for $J_1(\omega)$ suggests that relaxation by director fluctuations should be entirely absent in smectics. However, substantial experimental evidence exists [20,35,39,40] in favor of such a mechanism. Vilfan et al., have developed [30] a theory analogous to equations (14-22), but by including additional elastic constants B and D which denote restoring forces for fluctuations in the smectic layer thickness and reorientation of the director with respect to the normal to the layers. The theory also includes the possibility of critical behaviour of the elastic constants K_{22} and K_{33} close to the smectic A-nematic phase transition. It was found that for frequencies above 1MHz, the frequency dependence expected for smectic A director fluctuations is similar to that for the nematic cases [30].

In addition to the nematic phase energy density (f_n), the smectic (f_s) and the nematic-smectic interaction (f_i) terms are needed to derive an expression for spin relaxation. Thus, the free energy of the system is written as the summation of all these contributions [27]

$$F = f_n + f_s + f_i \quad (5.69)$$

The smectic term is given by

$$f_s = \alpha(T)|\psi|^2 + \beta(T)|\psi|^4 \quad (5.70)$$

The nematic-smectic interaction term is given by

$$f_i = \left(\nabla^2 + iq_s \delta \hat{n} \right) \psi^* \frac{1}{\gamma_{sm}} \left(\nabla - iq_s \delta \hat{n} \right) \psi \quad (5.71)$$

where α and β are coefficients of expansion of f_s in powers of ψ , the smectic order parameter, which is a complex quantity.

$$\psi = |\psi| \exp(i\phi) \quad (5.72)$$

where $|\psi|$ is the amplitude of the density wave associated with the **smectic** phase and ϕ determines the location of the layers. M is the mass tensor with two components $M_{||}$ and M_{\perp} (along and perpendicular to the normal to the layers, respectively). $Q_s = 2\pi d$, where d is the distance between smectic layers. The co-efficient p is always positive and α vanishes at a second order transition temperature T_{AN}

Mean square amplitude of the director fluctuations for the q^h mode and its decay time have been derived by Brochard [34] and by Schaetzing and Lister [41], using the free energy and equipartition of energy,

$$\langle |n_1(q)|^2 \rangle = \frac{K_B TV}{\left[K_{11} q_{\perp}^2 + K_{33} q_z^2 + \left(\frac{M_{||} q_{\perp}^2 + M_{\perp} q_z^2}{\Psi_0^2 q_z^2 q_{\perp}^2} \right)^{-1} \right]} \quad (5.73)$$

$$= \frac{K_B TV}{\left[K_{11} q_{\perp}^2 + K_{33} q_z^2 + B \left(\frac{q_1}{q_2} \right)^2 \left[1 + \frac{\beta}{\delta} \left(\frac{q_z}{q_{\perp}} \right)^2 \right]^{-1} \right]} \quad (5.74)$$

$$|n_2(q)|^2 = \frac{K_B TV}{[K_{22} q_{\perp}^2 + K_{33} q_z^2 + \delta]} \quad (5.75)$$

Where $q_1 = (q_x + q_y)^{1/2}$ and q_2 are the components of the deformation wave vector q in the directions 1 and $||$ to the **smectic** layers respectively and

$$B = \frac{\Psi_0^2 q_s^2}{M_{||}} \quad (5.76)$$

$$\delta = \frac{\Psi_0^2 q_s^2}{M_{\perp}} \quad (5.77)$$

with Ψ_0 is the equilibrium value of smectic order parameter. Coefficients B and S denote restoring forces for fluctuations in the layer thickness and, for fluctuations of the director orientations away from the normal A_0 to the layers, respectively. In the nematic case both B and δ vanish, and in smectic case, B is about ten times larger than δ which can be estimated using $B = K_{||}/d^2$ [41]. It is useful to note that $1/M_{||}$ is a measure of the compressions to the layers.

The damping time constants corresponding to the above mean square fluctuation are given by

$$\tau_1(\vec{q}) = \frac{n_1(q)}{\left\{ K_{11}q_{\perp}^2 + K_{33}q_z^2 + B\left(\frac{q_1}{q_2}\right)^2 \left[1 + \frac{B}{\delta} \left(\frac{q_1}{q_2}\right)^2 \right]^{-1} \right\}} \quad (5.78)$$

$$\tau_2(\vec{q}) = \frac{\eta_2(q)}{K_{22}q_{\perp}^2 + K_{33}q_z^2 + \delta} \quad (5.79)$$

here, η_1 and η_2 are the two effective viscosity coefficients which are independent of q . If the high and low frequency cut-offs are ignored [30] then,

$$j_1^{DF}(\omega) = \frac{3}{V(2\pi)^2} \sum_0^{\infty} dq_z \int_0^{\infty} \frac{\tau_{\alpha}(\vec{q})}{1 + [\omega\tau_{\alpha}(\vec{q})]^2} \langle |\eta_{\alpha}(\vec{q})|^2 q_{\perp} dq_{\perp} \rangle \quad (5.80)$$

Integration from q_{min} , which is given by the inverse dimension of a uniformly oriented sample, to q_c . These finite limits are useful because of the result at very low frequencies, especially important for field cycling NMRD studies. The integration over q -space is preferred for the deformation modes with $\alpha=1$ and completely for $\alpha=2$ to give [30].

$$J_1^{(2)}(\omega) = \frac{3k_B T \eta_2}{4\sqrt{2}\pi K_{22}\sqrt{K_{33}}\delta} \left\{ 1 + \left[1 + \left(\frac{\omega}{\omega_{s2}} \right)^2 \right]^{\frac{-1}{2}} \right\} \quad (5.81)$$

and

$$J_1^{(1)}(\omega) = \frac{3k_B T \eta_2}{4\sqrt{2}\pi K_{11}^{\frac{3}{2}}\sqrt{\delta}} \quad (5.82)$$

where

$$Y = \int_0^1 x^{-1} \left[x^2 + \frac{(1-x^2)\delta}{B} \right]^{\frac{1}{2}} \left[1 - x^2 + \left(\frac{K_{33}x^2}{K_{11}} \right) \right]^{\frac{3}{2}} \left[1 + \left\{ 1 + \left(\frac{\omega}{\omega_{s1}} \right)^2 \left[\frac{1 + (1-x^2)\delta}{Bx^2} \right] \right\}^{\frac{1}{2}} \right]^{\frac{1}{2}} dx \quad (5.83)$$

and

$$\omega_{sa} \equiv \frac{\delta}{\eta_a} \quad (5.84)$$

($\alpha=1, 2..$) are the characteristic upper and lower cut-off frequencies in the direction perpendicular to the director.

The relaxation rate due to DF modes in the smectic A phase is now obtained as

$$T_1^{-1}{}_{DF} = \frac{9}{8} r^4 \hbar^2 J_1(\omega) \quad (5.85)$$

Since the contribution from $J_2(\omega)$ is insignificant, it is neglected [19,30,42]. The frequency dependence of $J_1^{DF}(\omega)$ in a smectic A phase depends on the values of ω_{sa} and on the ratios of K_{33}/K_{11} and SB .

It was found [30] that $J_1^{DF}(00)$ behaves like that of nematics when the Larmor frequency is larger than $\omega_{s1}=\omega_{s2}=\omega_s$. On the other hand, for $\omega_o < \omega_s$, the smectic order influences $J_1^{DF}(\omega)$ by producing a leveling off, of the frequency dispersion curve at low frequencies, which is similar to the one predicted in the nematics with lower cut-off frequencies, [43] introduced. It is noted that ω_{lc} is at least several orders of magnitude smaller than ω_s .

The field-cycling NMR technique being applied by Noack and co-workers [45], to study T_1 frequency dispersion (v) curve for a wide range of frequencies in the smectic A phase. At a particular temperature, the NMRD profile can be fitted to a sum of three relaxation contributions namely SD, R and LU (layer undulations).

$$\frac{1}{T_{1\text{exp}}} = \frac{1}{T_1^{LU}} + \frac{1}{T_1^{SD}} + \frac{1}{T_1^R} \quad (5.86)$$

Blinic et al., [47] were the first, to study proton T_1 frequency dispersion in the smectic phases using field-cycling NMR technique. The dispersion curves in the smectic A phases are found to be different i.e director fluctuations produce a linear

dispersion profile in the smectic A phase. Considering the anisotropic nature of the elastic constants, Blinc et al., [35] predicted such a linear behavior.

$$\text{If } K_{33} = K_{22} = K_{11}$$

$$J_1^{DF} = \frac{3K_B T q_{zc}}{4\pi K_{11}} \omega^{-1} \quad (5.86)$$

$$= \frac{3K_B T}{2K_{11}\xi\omega^{-1}} \quad (5.87)$$

where ξ is the coherence length in the z-direction. Thus, in the smectic B phase the following is found

$$\frac{1}{T_1^{DF}} = B_{DF} \nu^{-1} \quad (5.88)$$

where

$$B_{DF} = \frac{9}{8\pi} \left(\frac{\gamma^2 \hbar}{r^3} \right) \frac{K_B T S_o^2}{K_{11}\xi} \left[d_{oo}^2(\beta) \right]^2 \quad (5.89)$$

In the present NMRD analysis of smectic A and A_d phases, only the smectic layer undulation modes (LU) are considered. The FCNMR data at kHz region requires this contribution to fit the data. Linear frequency dependence is assumed in this analysis. The simplified equation used for fitting the LU contribution is given in the chapter - 6.

5.3. Self Diffusion

Self-diffusion [48] or translational displacements of molecules as a consequence of Brownian motions is to be distinguished from ***interdiffusion***[49] of molecules, which is the intermingling of different species which are initially separated. The translational diffusion constants can be determined by several methods [50]. Field gradient NMR diffusometry is the direct technique used to study self-diffusion (SD). The precession frequency of the nuclear spins changes with the position of the spins for a sample placed in a magnetic field-gradient [8]. For normal liquids, the spin-spin relaxation is dominated by the translational diffusion and the application of this method to nematics is difficult because of strong magnetic dipole-dipole interactions making T_2 rather short. Using a special sequence of spin echoes, that removes most of the dipolar interaction, Blinc and coworkers had measured self-diffusion constants in the nematic phase of MBBA [52,53] and this method has been used by the others to study self-diffusion in liquid crystals [51].

The indirect NMR methods involve measurements of spin-lattice relaxation times (T_1 , T_{1D} , $T_{1\rho}$) [54,55]. From the frequency and temperature dependence studies of these relaxation times it is possible to obtain information on the self-diffusion constants using suitable theories [56-59,42,43].

5.3. J. Isotropic Phase

Torrey's theory [56,57] for isotropic self-diffusion can be extended to the anisotropic systems appropriately. The correlation functions for the intermolecular dipolar interactions, modulated by the self-diffusion of the molecule are given by

$$K_{\alpha}(t) = \sum_j \langle F_{ij}^{\alpha}(t) F_{ij}^{\alpha*}(t + \tau) \rangle_{AV(t)}, \alpha = 1, 2 \quad (5.90)$$

Here $\langle \rangle_{AV(t)}$ represents the time average. The functions F_{ij}^{α} , which are the space part of the non-secular component [6] of the dipolar interaction are given by

$$F_y^1(t) = \frac{\sin \theta_y \cos \theta_y e^{i\phi_y}}{r_y^3} \quad (5.91)$$

$$F_y^2(t) = \frac{\sin^2 \theta_y e^{2i\phi_y}}{r_y^3} \quad (5.92)$$

where r_y , θ_y and ϕ_y are the spherical coordinates of spin j relative to spin i . In evaluating the spectral density functions [56,57] the time averages in equation 5.90 replaced by the ensemble average. Thus,

$$K_\alpha(t) = \iint P(r, r_0, t) F_{ij}^\alpha(r_0) F_{ij}^{\alpha*}(r) f(r_0) dr_0 dr \quad (5.93)$$

where $P(r, r_0, t)dr$ is the probability that the spin j located at r_0 at $t=0$, relative to the spin i , will lie at time t , within the volume element dr at r , relative to the new position of i . $f(r_0)$ is the initial spin density. $N \int f(r_0) dr_0$ is the probability that at time $t=0$, spin j is located in dr_0 at r_0 , relative to spin i . N is the total number of spins. The function $P(r, r_0, t)$ can be found from the theory of random flights [48]. The theory of random flights (also called random walk) applicable to hard identical spherical molecules, each having spin at its center is due to Torrey [56,57], who assumed that the positions of the spins are satisfactorily equivalent. Hence the probability of finding a spin, which was initially at the origin, in the element of volume d^3r at the point r after one flight is expressible as $P_1(r)d^3r$. Then it is known [48], that

$$P_n(r)dr = \frac{1}{8\pi^3} \int (A(q))^n e^{-ir \cdot q} dq \quad (5.94)$$

Here the integration is over the entire q space, and $A(q)$ is the Fourier transform of $P_1(r)$ given by

$$A(q) = \int P_1(r) e^{ir \cdot q} dr \quad (5.95)$$

On employing the three dimensional Dirac delta function

$$\delta(r) = \frac{1}{8\pi^3} \int P_1(r) e^{-i(r \cdot q)} d^3r. \quad (5.96)$$

From equation 5.90 and $P_0(r) = S(r)$. This was the probability of the spin not being at $r=0$ and the integral of $S(r)$ is over all the space at unity. If $r(t)$ denotes the position at

time t of a spin, $P(r, t)$ then, is the conditional probability density that, if the spin is at the origin at time $t = 0$, it would be at r at time t . If $\omega_n(t)$ is the probability that n flights take place in time t , the relation then is

$$P(r, t) = \sum_n P_n(r) \omega_n(t). \quad (5.97)$$

The poisson distribution for $\omega_n(t)$ is to be assumed as

$$\omega_n(t) = \frac{1}{n!} \left[\frac{t}{\tau} \right]^n e^{-\frac{t}{\tau}} \quad (5.98)$$

where T is the mean time between flights. From the above equations (by substituting (5.98) and (5.94) in (5.97), the expression for $P(r, t)$ and hence $P(r, r_0, t)$ can be calculated. Transforming to a relative centroidal coordinate system with $r = r_i - r_j$; $R = 1/2(r_i + r_j)$, where r_i and r_j are the position vectors of spins i and j relative to a common origin, and finally integrating over all positions and substituting for the correlation functions with appropriate initial spin density, $f(r_0)$, the spectral density can be obtained

For isotropic diffusion, which corresponds to uniform spin density, the correlation function $A(r)$ is given by

$$K_1(t) = \frac{n}{4\pi} \iiint \frac{\sin \theta_0 \cos \theta_0 \sin \theta_1 \cos \theta_1}{r_0^3 r_1^3} e^{i(\phi_0 - \phi)} \times \exp \left[-iq(r - r_0) - \frac{2t}{\tau} [1 - A(q)] \right] dr_0 dq. \quad (5.99)$$

where $n = f(r_0)$ represents the uniform spin density. Expansion of $e^{-iq \cdot r}$ and $e^{iq \cdot r_0}$ in terms of Legendre and Bessel functions results in

$$e^{iqr \cos \phi} = \left[\frac{\pi}{2qr} \right]^{\frac{1}{2}} \sum_{n=0}^{\infty} (2n+1) i^n J_{n+\frac{1}{2}}(qr) P_n(\cos \phi) \quad (5.100)$$

Equation (5.99) can be simplified to

$$K_1(t) = \frac{8\pi n}{15a^3} \int_0^{\infty} \exp \left[-\frac{2t}{\tau} [1 - A(q)] \right] J_{3/2}^2(aq) \frac{dq}{q} \quad (5.101)$$

where ' a ' is assumed to be the closest possible distance of approach of two nuclei. The corresponding spectral density is given by

$$J_1(\omega) = 2 \int_0^\infty \cos(\omega t) K_1(t) dt$$

$$= \frac{8\pi m \tau}{15a^3} \int_0^\infty J_{3/2}^2(aq) \frac{[1 - A(q)]}{[1 - A(q)]^2 + \left(\frac{\omega \tau}{2}\right)^2} \frac{dq}{q} \quad (5.102)$$

A similar calculation for $K_2(t)$ results in

$$K_2(t) = 4K_1(t) \text{ and} \quad (5.103)$$

$$J_2(\omega) = 4J_1(\omega).$$

The possible choices of $A(q)$ can be limited to three cases.

Case (I): $\omega \tau \gg 1$

Since τ is assumed to vary with temperature as $\tau = \tau_0 e^{E_a/T}$ for a thermally activated process, this case corresponds to the low temperature asymptote of T . Hence $|A(q)| \ll 1$ can be neglected and the spectral density can be simplified as

$$T_1^{-1} \propto J_1(\omega) = \frac{32\pi m}{15a^2 \omega^2 \tau} \int_0^\infty J_{3/2}^2(aq) [1 - A(q)] \frac{dq}{q} \quad (5.104)$$

i.e.,

$$J_1(\omega) \propto (\omega^2 \tau)^{-1} \quad (5.105)$$

Thus

$$T_1 \propto \omega^2 \tau = \omega^2 \tau_0 e^{\frac{E_a}{kT}} \quad (5.106)$$

Case(ii): $COT < 1$

In this case $\omega \tau \approx 0$ and hence the spectral density is given by

$$J_1(\omega) = \frac{8\pi m \tau}{15a^3} \int_0^\infty J_{3/2}^2(aq) \frac{1}{[1 - A(q)]} \frac{dq}{q} \quad (5.107)$$

Since the integral in the above equation always converges, the spin-lattice relaxation rate is given by

$$T_1^{-1} \propto J_1(\omega) \propto \tau \quad (5.108)$$

or

$$T_1^{-1} \propto \frac{1}{\tau} = \frac{1}{\tau_0} e^{-\frac{E_a}{kT}} \quad (5.109)$$

This case corresponds to higher temperature asymptote for T_1 , which is just the opposite of case (i). It is seen that the frequency ω , is in between these two cases, there exist a particular r for which the relaxation rate is maximum (and hence T_1 is maximum).

Case (iii): $r \rightarrow \infty$

This is a special case for which the mean flight path is long. The function $[1-A(q)]$ vanishes for $q=0$ and approaches unity for a large q . The value of $P_1(r)$ is very small and hence,

$$J_1(\omega) = \frac{8\pi m}{45a^3} \left[\frac{\frac{\tau}{2}}{1 + \left(\frac{\omega\tau}{2}\right)^2} \right] \quad (5.110)$$

Thus

$$T_1^{-1} = \frac{8\pi m}{45a^3} \gamma^4 \hbar^2 I(I+1) \left[\frac{\frac{\tau}{2}}{1 + \left(\frac{\omega\tau}{2}\right)^2} + \frac{2\tau}{1 + (\omega\tau)^2} \right] \quad (5.111)$$

The two equations above have well known forms appropriate to an exponentially decaying function with correlation time $\tau_c = \tau/2$ and the T_1 minimum obtained from equation (5.111) when $\omega\tau = \sqrt{2}$ is given by

$$T_{1\min}^{-1} = \frac{16\sqrt{2}\pi}{45} \gamma^4 \hbar^2 I(I+1) \frac{n}{a^3 \omega} \quad (5.112)$$

Case (iv):

Assuming special forms for $P_i(r)$ and $A(q)$, say

$$P_i(r) = \frac{1}{4\pi D \tau r} \exp \left[\frac{-r}{(D \tau)^{1/2}} \right] \quad (5.113)$$

where D is the diffusion coefficient corresponds to $A(q) = [1 + D \tau q^2]^{-1}$, which is the simple form for $A(q)$, satisfying all the conditions that can be imposed for an acceptable form. Substituting in equation (5.107), the spectral density is obtained as

$$J_1(\omega) = \frac{16\pi m}{15a^3} \text{Re}[J] \quad (3.114)$$

where J is the Bessel function given by

$$J = \int_0^\infty \frac{1 + D \tau q^2}{2Dq^2 - i\omega(1 + D \tau q)} J_{3/2}(aq) \frac{dq}{q} \quad (5.115)$$

Simplifying the equation (5.114) [56, 57] results in

$$J_1(\omega) = \frac{8\pi m}{15a^3 \omega} f(\alpha, x) \quad (5.116)$$

The function $f(\alpha, x)$ is given by

$$f(\alpha x) = \frac{2}{x^2} \left[v \left(1 - \frac{1}{u^2 + v^2} \right) + \left(v \left(1 + \frac{1}{u^2 + v^2} \right) + 2 \right) e^{-2v} \cos 2u \right. \\ \left. + u \left(1 - \frac{1}{u^2 + v^2} \right) e^{-2v} \sin 2u \right] \quad (5.117)$$

with u and v defined in terms of α and x as

$$\begin{pmatrix} u \\ v \end{pmatrix} = \frac{\sqrt{\frac{\omega \alpha^2}{2d}}}{(4 + \omega^2 \tau^2)^{1/4}} \sqrt{\left\{ 1 \mp \frac{\omega \tau}{\sqrt{(4 + \omega^2 \tau^2)}} \right\}} \quad (5.118)$$

and

$$\alpha = \frac{\langle r^2 \rangle}{12a^2}; \quad x = \sqrt{\frac{\omega \alpha^2}{2d}} \quad (5.119)$$

$$\text{Let } \omega = \frac{\frac{\omega\tau}{2}}{\sqrt{1 + \left(\frac{\omega\tau}{2}\right)^2}} = \frac{\alpha x^2}{\sqrt{1 + \alpha^2 x^4}} \quad (5.120)$$

Then u and v can be expressed as

Hence the expression for the relaxation rate (in terms of $J_1(\omega)$ and $J_2(2\omega)$) is given by

$$(T_1^{-1})_{\text{Torrey}} = \frac{4}{5} \gamma^4 \hbar^2 I(I+1) \frac{n\pi}{a^3 \omega} \phi(\alpha, x) \quad (5.122)$$

where

$$\phi(\alpha, x) = f(\alpha, x) + f(\alpha, \sqrt{x}) \quad (5.123)$$

In the limit $\omega\tau \gg 1$, the spectral density term reduces to ω^{-2} law. And for $\omega\tau \ll 1$, it can be shown that $T_1^{-1} \propto \omega^{1/2}$, i.e.,

$$T_1^{-1} \sim C - F\omega^{1/2} \quad (5.124)$$

where C , and F are constants related to the diffusion coefficient D and are given by [61]

$$F = -4.77 \times 10^{-14} (1 + \delta) D^{-3/2} \quad (5.125)$$

$$C \propto D^{-1}$$

5.3.2. *Nematic Phase*

The orientational ordering in liquid crystals leads to anisotropy in diffusion coefficients, D_{\parallel} and D_{\perp} which are the diffusion constants, along and perpendicular to the director. Zumer and Vilfan [58] have extended Torrey's theory [56,57] for isotropic liquids to anisotropic media by taking into account the anisotropy of molecular diffusion, the cylindrical shape of the molecule and the specific distribution of spins along the long molecular axis to obtain the relaxation rate for **self-diffusion**

Following the notation of Torrey, the random correlation functions which on Fourier transform give the spectral densities are given by

$$F^{\alpha} [r_{ij}(t)] = F^{\alpha}_{\xi} [r(t)] \quad (5.126)$$

where

$$F_s^a(r) = \frac{e^{i\alpha\phi}}{\left[\rho^2 + (z + \xi)^2\right]^{5/2}} \left\{ \rho(z + \xi) \right\}, d=1 \quad (5.127)$$

Here, ξ_j , ξ_i and ξ_l are the vectors from the molecular centers to the j^{th} and i^{th} spins. ρ , z and ϕ are the cylindrical coordinates of r , the distance between the centers of nearest neighbor molecules. The anisotropic diffusion tensor, given by,

$$\begin{pmatrix} D_{\perp} & 0 & 0 \\ 0 & D_{\perp} & 0 \\ 0 & 0 & D_{\parallel} \end{pmatrix} \quad (5.128)$$

can be written in terms of the components of D^0 , the diffusion coefficient of a perfectly ordered mesophase [59]. The anisotropic diffusion constant describes the solution of the diffusive motion i.e.

$$\frac{1}{4\pi(D_{\perp}^2 D_{\parallel}^2 t^3)^{1/2}} \exp\left(-\frac{z^2}{4D_{\parallel}t} - \frac{\rho^2}{4D_{\perp}t}\right) \quad (5.129)$$

here, D_{\parallel} and D_{\perp} are the diffusion coefficients along and perpendicular to the director, n_o . The proper choice of $p_l(r)$ is

$$p_l(r) = \frac{1}{4\pi D_{\perp} \tau} \left[\rho^2 + \frac{D_{\parallel}}{D_{\perp}} z^2 \right]^{-1/2} \exp\left\{ -\left[\frac{z^2}{D_{\parallel} \tau} + \frac{\rho^2}{D_{\perp} \tau} \right]^{1/2} \right\} \quad (5.130)$$

and the corresponding Fourier transform,

$$A(q) = \left(1 + D_{\perp} \tau q_{\perp}^2 + D_{\parallel} \tau q_{\parallel}^2 \right)^{-1} \quad (5.131)$$

where τ is the mean time in between flights which gives the mean square jump length

$$\langle r^2(t) \rangle = (4D_{\perp}^o + 2D_{\parallel}^o) t \quad (5.132)$$

The effective diffusion constants are given by

$$D_{\perp}^o = \frac{\langle r_{\perp}^2 \rangle}{4\tau}, \text{ and } D_{\parallel}^o = \frac{\langle r_{\parallel}^2 \rangle}{2\tau} \quad (5.133)$$

here, D_{\perp}^o and D_{\parallel}^o are the macroscopic self diffusion constants of the perfectly aligned liquid crystalline phase. Substituting equations (5.133), in equation (5.131), $A(q)$ can be obtained. Considering the static pair correlation function (which partly correlates the final positions of the two molecules) to be of a simple square well function [58],

$g(\rho, z)=1$; $|z| \leq 1$ and $p = d$ or $|z| \neq 0$; $p < d$ and $|z| \leq 1$ and the spins to be distributed uniformly along the long molecular axis, the relaxation rate can be obtained as [58],

$$T_1^{-1} = \frac{9}{8} r^4 \hbar^2 \frac{n\tau}{d^3} Q \left[\omega_\tau, \frac{\langle r_\perp^2 \rangle}{a^2}, \frac{D_\parallel^2}{D_\perp^2} \right] \quad (5.134)$$

The frequency dependence of Q for the typical liquid crystal molecules (in the frequency range $\omega\tau = 0$ to 10) is shown in figure 5.4 (for three different values of r_\perp^2/d^2 viz 1.0, 1 and 0.01).

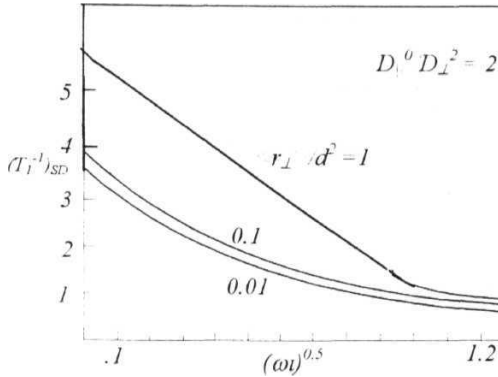


Figure 5.4. Frequency dependence of $Q \propto (T_1^{-1})_{SD}$, for three different jump lengths in the nematic phase [58].

The assumed values of molecular parameters are given below

$$l = 25 \text{ \AA} \\ d = 5 \text{ \AA} \text{ so } l/d = 5 \quad (5.135)$$

D_\parallel^2/D_\perp^2 is taken from experimental data [53] and it is found that these two do not differ much for different systems.

The observed features are

1. When $\omega\tau \rightarrow 0$, the ratio r_\perp^2/d^2 increases from 0.01 to 1 and hence, the relaxation rate due to SD increases

2. For low values of $(\text{or, } T_{1SD}^{-1} \propto (\omega\tau)^{1/2})$ and in the high frequency limit $T_{1SD}^{-1} \propto (\omega\tau)^{-1}$ and are similar to the isotropic case. It is observed that the ratio R of T_{1SD} to T_{1aniso} is equal to a constant 1.4, as the frequency is increased till $\omega\tau \sim 0.1$. This is shown in figure 5.5,

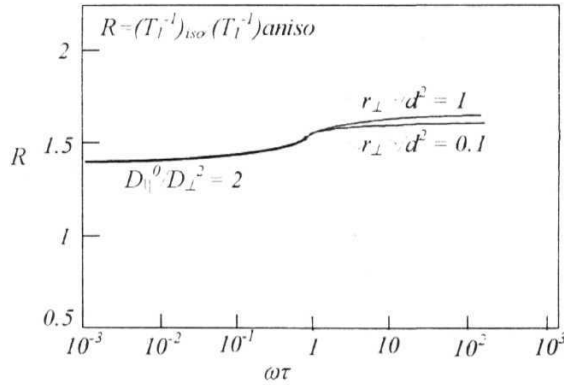


Figure 5.5. Frequency dependence of the ratio $R = T_{1SD} / T_{1aniso}$, in the nematic phase [58].

where the ratio $R = T_{1SD} / T_{1aniso}$ plotted as a function of $\omega\tau$ when $D_{iso} = D_{\perp}^0, r_{iso} = d$ and T is equal in both the cases. Thus, the relaxation due to SD in nematic phase is 1.4 times smaller than that of the isotropic diffusion, and is given by

$$T_{1SD}^{-1} = \frac{1}{1.4} (T_{1Torrey}^{-1}) \quad (5.136)$$

where $(T_{1Torrey}^{-1})$ is the equation (5.122) for isotropic liquids.

5.13. Smectic A phase

A random flight model where the time spent for a jump is much shorter than the average time interval between the two successive jumps has been considered by Zumer and Vilfan [60] to derive an expression for spin relaxation due to self-diffusion process in the smectic A phase. Considering a system of molecules of length l , and diameter d , with $d/l \ll 1$ and assuming that the spins are distributed along the long molecular axis, this model had calculated the T_{1SD}^{-1} for smectic A phase with a nematic order close to 1. Inter layer jumping is also considered by a thermally activated random jump process, wherein the molecules are assumed to jump only to one of the two adjacent layers, the jump length being equal to the interlayer distance. The time spent for a jump is assumed to be much smaller than the average time between two successive inter layer jumps. Based on these factors and assumptions, the spin lattice relaxation rate for self diffusion in smectic A phase is calculated by Vilfan and Zumer [60]

$$T_{1SD}^{-1} = \frac{3}{2} \gamma^4 \hbar^2 I(I+1) [J_1(\omega, \Delta) + J_2(2\omega, \Delta)] \quad (5.137)$$

where A is the angle between the director within each layer and the field.

The spectral density can be written as the Fourier transform of the correlation function for intra molecular dipolar Hamiltonian as

$$J_a(\omega) = \frac{\eta}{16\pi^3} \int \text{Re} \left[\langle I_{\xi}^{(a)*}(q) I_{\xi}^{(a)}(q) \rangle \right] S_s(q, \frac{\omega}{2}) \quad (5.138)$$

where $S_s(q, \omega)$ is the Fourier transform of the one particle auto correlation function $G(r, t)$. The functions $I_{\xi}^{(a)}(q)$ which are auto correlation functions, are different for the inter-layer and the intra-layer diffusion and are given by equation 5.127 [60,61]. Using the same notation as in the **isotropic** case, the distribution function $P_l(r)$, and the Fourier transform are given by [60]

$$P_l(z) = \frac{1}{2} [\delta(z+l) + \delta(z-l)] \quad (5.139)$$

and

$$A_{\perp}(q_{\perp}) = \frac{1}{1 + D_{\perp}^0 \tau_{\perp} q_{\perp}^2}; \quad (5.140)$$

$$A_{\parallel}(q_{\parallel}) = \cos(q_{\parallel} l) \quad (5.141)$$

The static pair correlation function has to be written as a product corresponding to the long range and short range positional order i.e.,

$$g(r) = g_l(r) g_o(r) \quad (5.142)$$

where $g_l(r) = g_l(z)$ and $g_o(r)$ is of the form of a square well (as in the nematic case). Finally, considering a distribution of spins to be uniform along the long molecular axis, the expression for the relaxation rate due to SD is obtained as

$$T_{1SD}^{-1} = \frac{9}{8} \gamma^4 \hbar^2 \frac{\eta \tau_{\perp}}{d^3} R \left(\omega \tau_{\perp}, \frac{\langle r_{\perp}^2 \rangle}{d^2}, \frac{D_{\parallel}}{D_{\perp}}, \frac{l}{d}, \Delta \right) \quad (5.143)$$

5.3.4. Smectic B and ordered smectics

The director fluctuations are frozen in these systems with additional degrees of ordering within each layer. There are fast local motions with large amplitudes [62], and self diffusion with weaker dynamical correlations are the mechanisms, mediating spin relaxation in these systems.

The self diffusion process is described [63] by two thermally activated jump processes, interlayer and intra-layer, with jump length equal to d , similar to the S_A phase. The molecules are represented by rigid cylinders with the nuclei distributed along the molecular axis. In addition, the possible correlations in the layer stacking is considered in deriving the relaxation rate as [63]

$$T_{1SD}^{-1} = \alpha \tau_{\perp} P_1(\omega \tau_{\perp}, \frac{D_{\perp}}{D_{\parallel}}, \frac{l}{d}, \frac{a}{d}, \Delta) \quad (5.144)$$

where $\alpha = \frac{9\gamma^4 \hbar^2 n}{8d^3}$

α measures the strength of the intermolecular dipolar interactions and P_I is a dimensionless function to be evaluated numerically. ' a ' is the quantity which measures the distance of closest approach between two nuclei belonging to two neighboring molecules lying in two adjacent layers.

For typical values of $l/d \approx 5$, and $a/d \approx 0.5$, the dispersion of T_{1SD} in crystalline B phase and hexatic B phase is similar to the dispersion in S_A phase as long as the relative layer motion is not too fast (5.143). At higher frequencies, $\omega\tau_L \gg 2$, the dispersion can be approximated to the Torrey's expression (equation 5.122). The dispersion curves of S_B phases follow the Torrey's well known low frequency dependence, $C_o - C_I \omega^{1/2}$ only for $A \neq 0$, and $\omega\tau_L \ll 10^2$. In intermediate frequencies corresponding to the conventional NMR range ($\omega\tau_L \geq 10$), the diffusion induced T_I^{-1} has ω^2 dependence given by

$$T_{1SD}^{-1} = 4(C^{(1)} + C^{(2)})\alpha \frac{D}{d^2 \omega^2} \quad (5.145)$$

where $C^{(1)} = 0.005$ and $C^{(2)} = 0.346$.

In the frequency region of interest (ranging from 20 kHz to 50 MHz), experimental proton NMRD data obtained in the nematic and smectic phases are fitted to equation (5.136).

5.4, Reorientations

Nuclear magnetic interactions are time dependent since they are modulated by changes in the position and orientation of a molecule. These molecular motions depend on the intermolecular and intramolecular forces, which are governed by electrostatic intermolecular potentials. To get information about these forces and dynamics it is important to study the time dependent characteristics of the nuclear spin. In a highly **anisotropic** liquid crystal medium, by treating the position and orientation of the molecule as a random variable the molecular dynamics can be studied through the stochastic approach.

Motional processes considered in the very beginning of the NMR relaxation theory as an isotropic continuous rotational diffusion, however this is a rare event in nature [11]. There are numerous attempts to understand anisotropic continuous rotational diffusion motion described by diffusion tensors [11,64-66]. Reorientations of molecules or molecular groups may be restricted by microstructural constraints. When the intermolecular forces are strong, molecules tend only to reorient through a sequence of collisions and no free rotations of the molecules can occur. This situation is explained by, discrete-coupling-state jump models in which the spin system is supposed to perform random jumps between a well-defined set of discrete spin-interaction states [2,3].

In a liquid crystal, since the molecules are large and the viscosity is high the inertial effects due to free rotations may be neglected and molecular reorientation may be assumed to occur via collisions only. In treating the orientation as a Markov stochastic variable, there are two limiting cases [2,3] based on the correlation between the orientation before and after the jump of the molecule, namely, 1. Very strong correlation limit (the small step rotational diffusion model) and 2. Lack of any correlation (the strong collision model), in which orientations of the molecules are randomized by collisions subject to a Boltzmann distribution. Nordio et al., [67-69] proposed a model for rotational diffusion in the presence of ordering potential. For the reorientation of the long axis of a nematogen, the small step rotational diffusion model seems to have a physical basis [2]. There are many models [2] related to the small step diffusion model. One such model is based on restricted rotational diffusion of a rod-shaped molecule in a conical volume [70], which is suitable to study the motion of the lyotropic lipid molecules anchored on a lipid-water interface in lipid bilayers. The other model is the "anisotropic viscosity model" [71,72], which treats the rotational diffusion tensor of molecules being time-independent in a laboratory frame. "Third rate model" is an extension of the anisotropic viscosity model, which includes fast rotations of molecules about the long axis.

Further constraints on dynamics may arise by the topology of the molecular environment, and such constraints lead to reorientations mediated by translational displacements of molecules diffusing along curved surfaces. In the "strong adsorption

limit", translational diffusion of adsorbate molecules along surfaces was shown to obey the Levy-Walk statistics [73]. There are many proton NMR experimental studies and some direct site specific measurements of spectral densities using deuterium resonant lines [2,54,55]. The strong collision model has been used in several studies on liquid crystals to interpret spectral densities [74,75]. The ratio J_1/J_2 of spectral densities is considered to be important. This ratio has a value unity in the isotropic phase due to the absence of the orientational order parameters. This ratio depends on the angle between the symmetry axis of the interaction tensor and that of the molecule [74] (higher the angle, lower the ratio). The diffusion in the cone model has been used in partially deuterated samples [76,75] and is used to understand the temperature dependence of $J_1(\omega)$ and $J_2(2\omega)$ in the nematic phase of 5O. 7-d₄. The small step rotational diffusion model has been used to extract rotational diffusion constants $D_{||}$ and D_{\perp} from the experimental deuterium spectral densities in liquid crystals [76-83]. The third rate model [35] has been used to explain the ratio J_1/J_2 of spectral densities for solute and liquid crystal molecules. There are similar significant studies [80,84,85] seen in the recent literature [2].

Dong [2] have used the decoupled model to study the chain conformational dynamics assuming the independent rotations of segments about different C-C bonds and thus internal rotations about different axes are highly correlated. This work also proves that the overall motion of an average IVIBBA molecule is well described by the third-rate model. There are models to describe the internal rotations in an alkyl chain of a nematogen. The superimposed rotations model proposed by Backmann et al., [74] is used, to describe phenyl ring rotation in mesogens [77]. The assumption made in this model is that internal motions are completely decoupled from the overall reorientation of the molecules. Wallach [86] too, has made an assumption that free diffusive rotations occur about each carbon-carbon bond in the chain and are independent of each other. Tsutsumi has proposed a decoupled model [87] for internal dynamics in liquid crystals. Wittebort and Szabo [88] have considered all energetically allowed conformations to solve the master equation that describes conformational transitions using a time domain extension of the rotameric model of Flory [89]. Nordio et al. [90] have introduced coupling between conformational changes and molecular reorientations. Though the earlier nuclear spin relaxation

theories [58,91,92] neglected the internal dynamics, the site-specific experimental studies [74,76,81,93,94,95] led to the development of models considering internal as well as overall motions.

5.4.1. *Nematic Phase*

The rod like molecules in the nematic phase are free to rotate about their long axis and to some degree about the short axis, **concomitantly**, the relaxation times for rotations about their short axes are much longer ($\sim 10^5$ to 10^6 times per second) than those about their **long** axis ($\sim 10^{11}$ to 10^{12} times per second). The third type of [96] of rotational motion which is important in anisotropic rod like liquid crystal systems with flexible end chains are the reorientations of the end chains. Now, the different correlation times of interest are τ_l and τ_s for rotations of the entire molecules about their long and short axes respectively and τ_{CH2} and τ_{CH3} for rotations of **CH₂** and **CH₃** groups. The rotations about the short axis contribute to spin relaxation at conventional NMR **frequencies**, hence, only τ_s is of major significance. The rotations about long axis and the rotations of the end chains are much faster and are not significant in conventional NMR **frequencies** in the nematic phase.

The relaxation rate for rotation about the short molecular axis is written in the BPP form [9] as

$$\frac{1}{T_{1RS}} = \epsilon C \left(\frac{\tau_s}{1 + (\omega \tau_s)^2} + \frac{4\tau_s}{1 + (4\omega^2 \tau_s^2)} \right) \quad (5.146)$$

where ϵ measures the anisotropy of local reorientations around the short axis. The constant C for a molecule consisting of aliphatic groups in the core and aromatic groups in the end chains is given by

$$C = \frac{9}{8} \gamma^4 \hbar^2 \frac{1}{15} \sum_k \frac{U_k (3l_k^2 - 1)^2}{r_k^6} \quad (5.147)$$

where U_k stands for the ratio of protons belonging to k^h group, to the total number of protons in the molecules. l_k 's are cosines of angle between internuclear vector r_k of k^h group and the long axis. In the limit $\omega \tau \ll 1$, give rise to frequency independent **contribution**. ϵ is assumed to be equal to 1.

5.4.2. Smectic phases

In the high temperature smectics like S_A , the contribution to the relaxation process arises from the rotations about the short axis and is, as the same as in the nematic case. In the low temperature ordered smectic phases, the rotations around the long axis may become important. In case the director n , makes an angle A with the external field, the relaxation rate is given in $\omega\tau_l \ll 1$ limit as

$$\frac{1}{T_{1RF}} = \frac{9}{8} \gamma^4 \hbar^2 \sum_k \frac{U_k (3I_k^2 - 1)^2}{8r_k^6} (1 + 3 \cos^2 \Delta) \quad (5.148)$$

Here U_k stands for the relative weight of the proton belonging to the k^{th} group and Δ , for the cosine of the angle between the inter nuclear vector r_k of the k^{th} group and the long molecular axis. In ordered smectics, rotations around the short molecular axis are known to be frozen [97]. The isotropic tumbling of the end chains [96] also contributes to T_1 in the ordered phases. The relaxation rate due to the isotropic tumbling of end chains is given by a BPP type expression

$$\frac{1}{T_{1RF}} = C \left[\frac{\tau_{cl}}{1 + (\omega\tau_{cl})^2} + \frac{4\tau_{cl}}{1 + (4\omega^2\tau_{cl}^2)} \right] \quad (5.149)$$

Here the constant C represents the relative weights of end chain protons with respect to the total number of protons. Thus $1/C$, as a function of τ_{cl} , shows a minimum at $\omega\tau_{cl} = 0.616$ and at the minimum relaxation rate, is given by

$$(T_1^{-1})_{min} = 1.43(C''/\omega) \quad (5.150)$$

Earlier analysis of the frequency dependent T_1 data (4 to 50 MHz) collected on these 40. m systems in this laboratory are presented in the theses [98,99]. In the present NMRD data analysis the BPP type contribution (isotropic approximation) is used with a single correlation time. In the nematic and smectic A phases this correlation time is associated with rotations about the short axis. In the ordered smectic phases this correlation time can be attributed to the rotation about the long axis or to the segmental motions. Earlier temperature dependent T_1 results on nO.m systems [98,99,100] are found useful in the interpretation of the present NMRD data.

5.5. References

1. G. R. Luckhurst and C. A. Veracini (Eds.) "*The Molecular Dynamics of Liquid Crystals*", Kluwer Academic Publishers, Dordrecht (1994).
2. R. Y. Dong, "*Nuclear Magnetic Resonance of Liquid Crystals*", Springer-Verlog, New York (1997) and references therein.
3. R. Kimmich, "*NMR: Tomography, Relaxometry and Diffusometry*", Springer-Verlog, Heidelberg (1997).
4. J. W. Emsley, (Ed.) "*Nuclear Magnetic Resonance of Liquid Crystals*", Reidel Publishing com., Dordrecht, Holland (1985).
5. G. L. Hoatson and Y. K. Levine in "*The Molecular Dynamics of Liquid Crystals*", (Eds.) G. R. Luckhurst and C. A. Veracini, Chapter 1, Kluwer Academic Publishers, Dordrecht (1994).
6. C. P. Slichter, "*Principles of Magnetic Resonance*", Springer-Verlog, New York, (1990).
7. A. G. Redfield, *Adv. Magn. Reson.*, 1, 1 (1965).
8. A. Abragam, *Principles of Nuclear Magnetism*, Clarendon Press, Oxford, (1961).
9. N. Bloembergen, E. M. Purcell, and R. V. Pound, *Phys. Rev.*, 73, 679 (1948).
10. R. K. Wangness and F. Bloch, *Phys. Rev.*, 89, 728 (1953).
11. H. W. Spiess in "*NMR basic principles and progress*", Vol. 15, Springer, Berlin pp 56-214 (1978).
12. J. P. Jacobson, H. K. Bildsoe, and K. Schaumburg, *J. Mag. Reson.*, 23, 153 (1976)
13. D. C Look, I. J. Lowe, *J. Chem. Phys.*, **44**, 2995 (1966).
14. G. R. Luckhurst, *J. Chem. Soc. Faraday Trans.*, **284**, 961 (1988).
15. P. G. de Gennes, *Compt. Rend.*, **266B**, 15 (1968).
16. Orsay Liquid Crystal Group, *Phys. Rev. Lett.*, 22, 1361, (1969).
17. I. Haller and J. D. Lister, *Phys. Rev. Lett*, 25, 1550 (1970).
18. M. Wager and B. Cabane, *J. Phys. (Paris), Colloq.*, 30, C4-72 (1969).
19. P. Pincus, *Solid State Commun.*, 7, 415 (1969).
20. J. W. Doane and J. J. Visitainer, *Phys. Rev. Lett.*, 23, 1421 (1969).
21. R. Blinc, D. L. Hogenbloom, D. E. O'Reilly, and E. M. Peterson, *Phys. Rev. Lett.*, **23**, 969 (1969).

22. R. Y. Dong and C. F. Schwerdtfeger, *Solid State Commun.*, 9, 707 (1970)
23. C. E. Tarr, M. A. Nickerson, and C. W. Smith, *Appl. Phys. Lett.*, 17, 318 (1970).
24. C. R. Dybowski, B. A. Smith, and C. G. Wade, *J. Phys. Chem.*, 75, 3834 (1971).
25. T. Lubensky, *Phys. Rev. A*, 2, 2497 (1970).
26. J. W. Doane and D. L. Johnson, *Chem. Phys. Lett.*, 6, 291 (1970).
27. P. G. deGennes, *"The Physics of Liquid Crystals"* Oxford University Press, London, (1974); E. B. Priestley, P. J. Wojtowicz, and P. Sheng, *"Introduction to Liquid Crystals"*, Plenum Press, New York (1975).
28. M. J. Stephen and J. P. Straley, *Rev. Mod. Phys.*, 46, 617 (1974)
29. R. Blinc, *NMR Basic Principles Progr.*, 13, 97 (1976)
30. M. Vilfan, M. Kagoj, and R. Blinc, *J. Chem. Phys.*, 86, 1055 (1987).
31. J. W. Doane, and D. S. Morai, *Chem. Phys. Lett.*, 11, 339 (1971).
32. J. W. Doane, C. E. Tarr, and M. A. Nickerson, *Phys. Rev. Lett.*, 33, 620 (1974)
33. F. Noack, M. Notter, and W. Weiss, *Liq. Cryst.*, 3, 907 (1988); D. Pusioli and F. Noack, *Liq. Cryst.*, 5, 377 (1989).
34. R. Brochard, *J. Phys. (Paris)*, 34, 411 (1973).
35. R. Blinc, M. Luzar, M. Vilfan, and M. Burger, *J. Chem. Phys.*, 63, 3445 (1975)
36. R. L. Vold, and R. R. Vold, *J. Chem. Phys.*, 88, 4655, (1988)
37. R. L. Vold and R. R. Vold, in *"The Molecular Dynamics of Liquid Crystals"*, (Eds.) G. R. Luckhurst and C. A. Veracini, Kluwer Academic Publishers, Dordrecht (1994)
38. K. Venu and V. S. S. Sastry, in *"Field-Cycling NMR Relaxometry Symposium"*, Berlin, p39 (1998)
39. G. J. Kruger, H. Spiescheke, R. Van Steenwinkel and F. Noack, *Mol. Cryst. Liq. Cryst.*, 40, 103, (1977).
40. L. S. Selwyn, R. R. Vold, and R. L. Vold, *Mol. Phys.*, 55, 287, (1985)
41. R. Schaefgen and J. D. Lister, *"Advances in liquid crystals"*, Academic, New York. Vol. 4, p. 147 (1979)
42. R. L. Vold and R. R. Vold, in *"The Molecular Dynamics of Liquid Crystals"*, (Eds) by G. R. Luckhurst and C. A. Veracini. p207, Kluwer Academic Publishers. Dordrecht (1994)
43. I. Zupancic, V. Zagar, M. Rozmarin, F. Levstik, F. Kogovsek, and R. Blinc, *Solid State Commun.*, 18, 1591 (1976)

44. M. Vilfan, R. **Blinc**, and J. W. Doane, *Solid State Commun.*, **11**, 1073 (1972).
45. F. Noack, *Progr. NMR Spectrosc.* 18, 171 (1986).
46. N. J. Heaton, *Ph. D thesis*, University of Southampton (1986).
47. R. Blinc, M. Luzar, M. Mali, R. Osredkar, J. Seliger, and M. Vilfan, *J. Phys. (Paris) Colloq.* 37, C3-73 (1976).
48. S. Chandrasekhar, *Rev. Mod Phys.*, 15,1(1943).
49. J. Crank, *"The Mathematics of diffusion"*, Clarendon Press, Oxford (1975).
50. G. J. Kruger, *Phys. Rep.* **82**, 229 (1982).
51. F. Noack, *Mol. Cryst. Liq. Cryst.*, **113**, 247 (1984).
52. R. Blinc, J. Pirs, and I. Zupancic, *Phys. Rev. Lett.*, 30,546 (1973).
53. I. Zupancic, J. Pirs, R. Blinc, and J. W. Doane, *Solid State Commun.*, 15, 227 (1974).
54. C. G. Wade, *Annu. Rev. Phys. Chem.* **28**, 47 (1977).
55. R. Y. Dong, *Isr. J. Chem.*, 23, 370 (1983).
56. H. C. **Torrey**, *Phys. Rev.*, 92, 962 (1953).
57. H. C. Torrey, *Phys. Rev.*, 96, 690 (1954).
58. S. **Zumer** and M. Vilfan, *Phys. Rev.* **A17**, 424 (1978).
59. R. Blinc, M. Burgar, M. Luzar, J. Pirs, I. Zupancic and S. Zumer, *Phys. Rev. Lett.*, **33**, 1192(1974).
60. M. Vilfan and S. Zumer, *Phys. Rev.* **A21**, 672 (1980).
61. J. F. Harmon and B. N. Muller, *Phys. Rev.* **182**, 400 (1969).
62. A. M. Levelut, F. Moussa, J. Doucet, J. J. Benettar, M. Lambert and B. Dornier, *J. Phys. (Paris)* 42, **1651** (1981).
63. S. Zumer and M. Vilfan, *Phys. Rev.* **A28**, 3070 (1983).
64. D. E. Woessner, *J. Chem. Phys.*, 36, 1 (1962).
65. D. E. Woessner, *J. Chem. Phys.*, 37,647 (1962).
66. D. E. Woessner, B. S. Snowden, G. H. Meyer, *J. Chem. Phys.*, 50,719 (1969).
67. P. L. Nordio and P. Busolin, *J. Chem. Phys.*, 55, 5485 **91971**).
68. P. L. Nordio, G. Rigatti, and U. Segre, *J. Chem. Phys.*, 56, **2117** (1972).
69. P. L. Nordio, G. Rigatti, and U. **Segre**, *Mol. Phys.*, 25, 129 (1973).
70. C. C. Wang and R. Pecora, *J. Chem. Phys.*, 72, 5333 (1980).
71. C. F. Polnaszek, G. V. Bruno, and J. H. Freed, *J. Chem. Phys.*, 58, **3185** (1973).
72. C. F. Polnaszek, and J. H. Freed, *J. Phys. Chem.*, 79, 2283(1983).

73. O V Bychuk, B O'Shaughnessy, *J. Chem. Phys.*, **101**, 772 (1994)
74. P A Beckmann, J W Emsley, G R Luckhurst, and D L Turner, *Mol. Phys.*, 50,699(1983).
75. R Y Dong and K R Sridharan, *J. Chem. Phys.*, **82**, 4838,(1985).
76. L. S. Selwyn, R R Vold, and R. L Vold, *J. Chem. Phys.*, 80, 5418 (1984)
76. R. Y. Dong, *J. Chem. Phys.*, **88**, 3962 (1988).
77. R. Y. Dong, *Mol. Cryst. Liq. Cryst.*, **141**, 349 (1986).
78. R Y Dong, *Liq. Cryst.*, 4, 505 (1989).
79. R Y Dong and G M Richards, *Mol. Cryst. Liq. Cryst.*, **141**, 335 (1986).
80. J. W Emsley and K. Hamilton, *Liq. cryst.*, 5, 1019 (1989).
81. R Y. Dong and G M. Richards, *J. Chem. Soc. Faraday Trans. 2*, 84, 1053 (1988).
82. R Y. Dong and G. M Richards, *J. Chem. Soc. Faraday Trans. 2*, **88**, 1885 (1992).
83. G. M. Richards and R. Y. Dong, *Liq. Cryst.*, 5, 1011 (1989).
84. R Y. Dong. *Phys. Rev.*, **A42**, 858 (1990).
85. J. M Goetz, H, L Hoatson. and R. L. Vold, *J. Chem. Phys.*, 97, 1306 (1992)
86. D. Wallah, *J. Chem. Phys.*, 47, 5258 (1967)
87. A. Tsutsumi, *Mol. Phys* 37. 111 (1979)
88. R. J. Wittebort, and A Szabo, *J. Chem. Phys.* 69. 1722 (1978).
89. P. J. Flory, "*Statistical Mechanics of Chain Molecules*" Interscience, New York, (1969)
90. A Ferrarini, G. J Moro, and P L. Nordio, *Liq. Cryst.* 8. 593 (1990).
91. J H. Freed, *J. Chem. Phys.*, 66,4183 (1977)
92. P. Ukleja, J Pirs, and J W Doane, *Phys. Rev.*, **A14**, 414 (1976)
93. R. Y Dong and G. M Richards, *J. Chem. Phys.*, 91. 7276, (1989).
94. R Y Dong, J Lewis, E Tomchuk, and E Bock, *J. Chem. Phys.* 69, 5314 (1978)
95. C. R J Coundell, J W. Emsley, G R Luckhurst, D. L Turner, and J. Charvolin . *Mol. Phys.*, **52**, 499 (1984)
96. R Blinc, M Vilfan, M Luzar, J Seliger, and V Zagar, *J. Chem. Phys.* 68, 303 (1978)
97. J Seliger, R Orsedkar, V. Zagar and R Blinc. *Phys. Rev. Lett.*, 38, 411 (1977)

98. A. S. Sailaja, *Ph.D Thesis*, University of Hyderabad, India (1994).
- 99 G Ravindranath, *Ph. D Thesis*, University of Hyderabad, India (1990);
 G. Ravindranath, K. Venu and V. S. S. Sastry, *Chem. Phys.*, **140**, 299 (1990);
 G. Ravindranath, K. Venu, V. S. S. Sastry and G. Padmavathi, *Phase Trans.*,
 12,129 (1988); G. Ravindranath, K. Venu and V. S. S. Sastry, *Z. Phys. B:*
 Cond. Matter 78, 235 (1990)
100. E. Heinze, S. Grande and A. Loshe, *Ann. Phys.*, 35, 145 (1978); E. Heinze and
 S. Grande, *Chem. Phys. Lett*, 58, 87 (1978).

Chapter 6

Field Cycling NMR Studies of Molecular Dynamics in Butyloxy Benzylidene Alkylanilines (40.m)

Chapter 6 deals with the study of the relationship between end chain structure and molecular dynamics in the homologous series, Butyloxybenzylidene Alkylanilines (40 m). These systems belong to the well known, nO.m series of Liquid crystals. The chapter consists of 9 sections.

Section 6.1: Motivation and objectives of the present study are described towards the beginning of the section. Earlier structure-property studies on nO.m systems as well as NMRD studies on other homologous series of systems are reviewed next. Experimental details and the models followed in the NMRD data analysis in terms of different contributions (DF, SD, R and LU) to the total relaxation rate are also presented

Sections 6.2 to 6.8: Experimental data obtained from different liquid crystalline systems (40.2, 40.3, 40.4, 40.5, 40.7, 40.8 and 40.9) of the 40.m series are presented in these sections. These systems are treated independently and the results obtained from the NMRD data analysis are presented separately for different phases. Dynamic parameters obtained from the analysis are presented in tables for each system and phase.

Section 6.9 Structure-Dynamics relationships obtained from the present study are presented in this concluding section. Different dynamic parameters obtained as a function of end chain properties are compared and plotted independently. Relative contributions of the three important dynamics (DF, SD and R) are plotted as a function of chain length at different frequencies.

Section 6.1

6.1. Earlier studies and present objectives of molecular dynamics in Liquid Crystals

6.1.1. Introduction

The systems under the present NMRD study belong to the well known N(p-n-alkoxybenzylidene) p-n-alkylaniline homologous series (*nO.m* series), which have two terminal chains, where *n* is the number of carbon atoms in the alkoxy end chain and *m* is the number of carbon atoms in the alkyl end chain. This homologous series (*nO.m*) has the molecular structure depicted in the scheme given in figure 6.1.

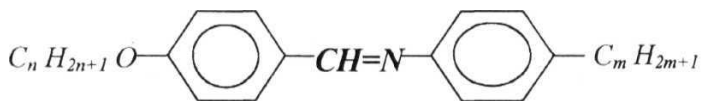


Figure 6.1. General molecular structure of the *nO.m* homologous series of systems.

The present NMRD studies are carried out on the systems, 40.2, 40.3, 40.4, 40.5, 40.7, 40.8 and 40.9, i.e., keeping $n = 4$ as constant in the above molecular structure and changing the alkyl chain length, by choosing systems having *m* from 2 to 9. This series exhibits a series of smectic (S_A , S_C , S_E , and S_G) phases and a nematic phase with variable stabilities. The present experimental work includes frequency dependent proton T_1 study (NMRD) using FCNMR technique in different phases of these systems. Earlier work done in this laboratory [1,2] using conventional NMR techniques (T_1 , $T_{1\rho}$) is also used in the analysis in order to get the complete picture of molecular dynamical parameters. Temperature dependent data are available at high frequencies (4 to 50 MHz) on these (40.2, 40.3, 40.4, 40.5, 40.7, 40.9) systems. Phase sequences of the 40.*m* systems are shown in figure 6.2.

6.1.2. Motivation and objectives

The homologous series *nO.m* of systems are chosen, keeping the following reasons and expectations in mind. Some of the reasons listed below are general in nature to any molecular dynamics study of liquid crystals.

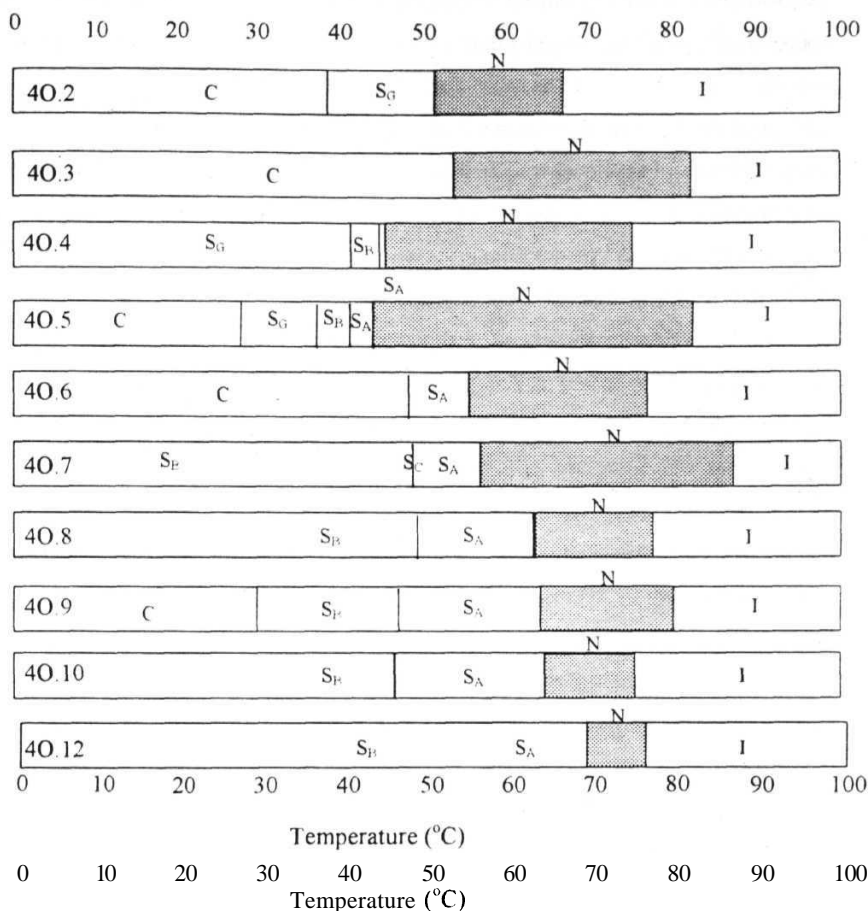


Figure 6.2 Phase sequences of the 40.m systems. The temperature range of the nematic phase for each system is shown with the shaded area.

1). This homologous series (nO.m) have been studied extensively, using all possible techniques, by various groups [6] in order to elucidate the microscopic structure and its relationship to the macroscopic physical properties. For example, the most studied MBBA (10.4), using almost all the physical techniques, including NMRD studies [3,4] belongs to this nO.m series. Using the vast amount of data on structural and physical properties available, it is expected to be easier to explain the more complex, microscopic molecular dynamics in these homologous systems. They have rich polymorphism and have convenient temperature regions to work with. The transition

temperatures of different **mesogens** were measured [5] using calorimetry and optical microscopy, by varying n from 1 to 7 and m from 4 to 8, which are verified later by other studies also. Databases are also available on some of these systems [6].

2) In particular, the **4O.m** series, has a special significance because it shows very stable nematic phases over a wide temperature region, and very easily accessible for experimentation. These systems exhibit nematic phases having temperatures from 45.2° C (40.4) to 83° C (40.7) and the nematic temperature range varies from about 39°C (40.5) to 8°C (40.12). Such a broad variation in the nematic phase temperature range and transition temperatures in this series is not only useful but also convenient for temperature dependent studies. These systems exhibit increasing smectic A phase stability when the chain length is gradually increased.

3). The controversy over the nature of the **nematic-smectic A** transition, is another important reason to study, since these systems exhibit continuously differing N-S_A transition order. In **4O.m** liquid crystals, this particular transition shows a second order, and a weakly first order nature depends on the chain length of the molecules, which were different from the theoretical predictions. The refractive index and density studies carried out by Potukuchi [7] have demonstrated the presence of a tricritical point for nematic-smectic A transition and also has shown that the McMillan parameter for the $nO.m$ homologous series is different from the other results for other series of liquid crystals. The order of the nematic to smectic A transition has shown different behaviors. A first order transition is observed in 60.4, 60.8, **7O.1**, and 70.4 systems. A weakly first order transition is observed in 50.8 and a second order phase transition in 40.4, 40.6, 40.7, 40.8 and **4O.10** systems. These observations suggest that alkoxy end chain play an important role in this transition. These observations highlight the importance of these systems and the molecular level dynamical properties would be more **useful** to understand this behavior.

A variety of pretransitional effects in the nematic phase near the second order nematic-smectic A transition result from the thermally excited **fluctuations** in the smectic order. The smectic A density correlated over a relatively short range (called cybotactic clusters) appears and decays **away**. de Gennes [8] has suggested that the

N-S_A transition should be identical to the **superfluid-normal transition**. It was disputed by Halperin et al., [9], who have argued that it should be similar to the superconductor-normal transition with director fluctuations (DF) driving the transition to the first order. The influence of the coupling between the orientational order and **translational** order on the order of the **N-S_A** transition was studied by Longa [10]. Contrary to the first order nature seen in the nCB, nS5 homologous series and other systems and mixtures with short nematic temperature ranges, the **nO.m** homologous series of systems showed a first order, second order and weakly first order transitions. Since it is possible to get information on director fluctuation from NMRD studies, the systematic study on these systems, would be useful to understand molecular dynamic processes responsible for such phase transitions.

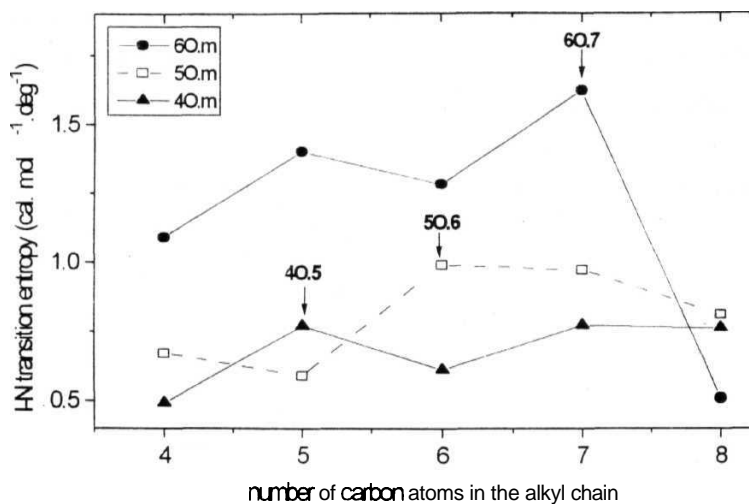
4). A variation of the end chain length from **m** = 2 to **m** = 9, gives an opportunity to probe dynamics of different nematic phases and compare the results in terms of the usually observed odd-even effects, chain length effects and symmetry effects as explained below.

a) Odd-odd systems (40.3, 40.5, 40.7 and 40.9) and odd-even systems (40.2, 40.4 and 40.8) which could give information about the famous 'odd-even effects' in **dynamics**, which were already shown by Noack et al., [4] and Dong et al., [11] in liquid **crystals**. It is well known that odd-even effects are seen in almost all macroscopic physical properties studied in liquid crystals.

b) It is also known that the chain length alters the phase stabilities of the nematic and smectic phases. This homologous series provides an opportunity to study shorter (40.2, 40.3) and longer (40.8 and 40.9) chain **systems**, within the odd or even **systems**.

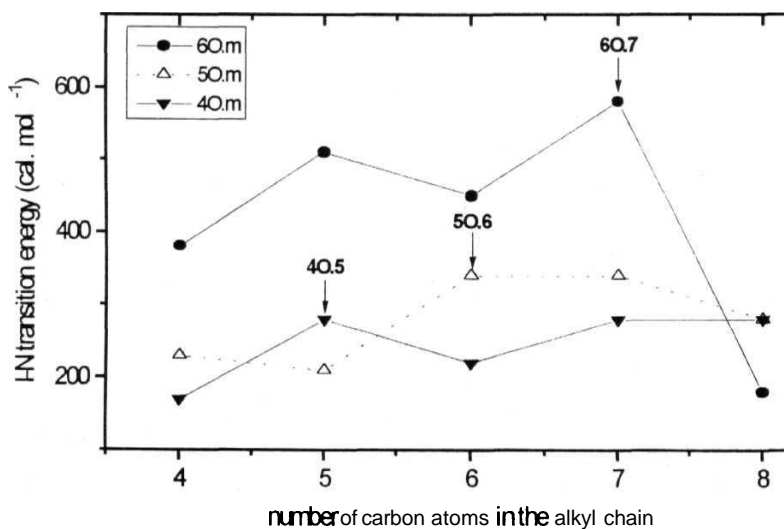
c) There is another property that can be taken seriously, based on the existing experimental **data**, though it is not frequently mentioned in the literature on liquid crystals i.e., 'balancing of the terminal **chains**' or "symmetric and non-symmetric end **chains**". The effect of symmetry on the nematic phase stability in **40.m** systems is presented in **chapter-4 Transition** energies as well as transition entropies [5] of **these** systems seem to show a kind of symmetry effects as shown in figure 6.3.

Balancing effects in nO.m series



(a)

Balancing effects in nO.m series



(b)

Figure 6.3. Isotropic-nematic transition entropies (a) and transition energies (b) for nO.m homologous series. Systems having symmetric end chains show a maximum in transition entropy and energy when comparing the immediate neighbors of the same series. The data are taken from the literature [5].

The general trend in these figures seems to show either a peak or a deviation when the end chains are close to **balanced**. The present family of the systems gives an opportunity to study molecular dynamics of balanced-odd (40.5) and balanced-even (40.4) systems, without changing the molecular length too **much**. It is known that the longer chain **smectic** systems showed **conformational** jumps and hence the orientational disorder in these **systems**. Cybotactic clusters were seen above N-S_A transition in longer chain systems.

5). Moreover, no systematic NMRD studies over wide frequency range were done on this particular family (40 m) so far. There exist some experimental efforts by this group, using the conventional NMR technique [1,2] and by others [12] using the deuterium NMR relaxation time measurements on this series. There has been no attempt to see the low frequency spectral densities, which could give direct information about the connection between phase stabilities and collective director fluctuations on this homologous series.

6). Since collective motions are superimposed on simultaneous non-collective rotations and translational reorientations of individual molecules, a clear distinction of these, require a very wide nematic range NMRD studies. It has been established that these collective motions dominate at a low kHz regime and that individual motions dominate at conventional high frequencies. The available data is insufficient for an understanding of the molecular level microscopic behavior, and also in correlating the rich theoretical understanding on liquid crystal physics.

There is no clear understanding of the three dynamical properties (DF, SD, R) on the end chain structure, as yet. It has been reported that [13], near the I-N transition, rotations about the short axis is an important mechanism in mediating the spin relaxation. The low temperature nematic, close to N-S_A transition is dominated by DF and SD mechanisms, where rotations contributes lesser. A systematic study at the high temperatures closer to the I-N transition sufficiently away from the region where pre-transitional effects dominate the spin relaxation, are to be useful means of separating the R, about the short axis from the collective DF modes.

7). The DF contribution and the value of the constant (ADF) in nematic liquid crystals are considered to be important factors. Procuring some information on the cut-off frequencies is also important. With the available computational facilities it has been possible to implement model fitting with very many parameters. The modifications introduced by Blinc [14], Doane and Johnson [15], Vold and Vold [16] and several others, to the basic model proposed by Pincus et al., [17] lead to a more generalized model [18]. Model fitting for the DF contribution can be done using these models. The anisotropic elastic constants model could be implemented if the experimental elastic constants are available for the system.

In the present series, the experimental data available on 40.4 [30] has made such an attempt possible. The differences between the one constant approximation model and the anisotropic elastic constants model in implementing them, for the NMRD data would be interesting. Introduction of upper as well as lower cut-off frequencies makes DF contributions more meaningful. NMRD studies on PAA [49] have shown a decreasing ADF value with an increasing chain length. There are nevertheless, observation [12] in the literature that the A_{DF} decreases with chain length, in homologous series.

6.1.3 Review of earlier studies on nO.m compounds

Experimental attempts on different homologous series were carried out by various groups with typical objectives such as, the effect of molecular structure on polymorphism and changes in the molecular parameters, as one runs through the homologous series. There have been attempts to look for the physical systems to test the validity of theoretical models built, to explain static/dynamic features of liquid crystals. Optical microscopy, miscibility, and X-ray diffraction methods were used by Goodby et al., [19], for studying different homologous of nO. m series.

Pisipati and coworkers [7] have studied the nO.m **series** of systems using thermal microscopy, density, ultrasonic velocity, refractive index, magnetic resonance, DSC, and the XRD techniques. There are a number of publications [7] on

these studies. The static physical properties of all the available possible phases in this series had been studied, and various relevant physical properties and critical exponents were **explained**. The results showed that the I-N, I-S_A, N-S_C, N-S_G, S_C-S_C, S_B-S_G and S_A-S_F phase transitions are of the first order phase **transitions**.

The **SA-SC** transition had showed a second order behavior in all the nO.m systems studied by Pisipati and coworkers [7]. The results from **density**, ultrasonic, X ray, dielectric, ultrasonic relaxation, NMR, ESR, DSC, **IR** and refractive index studies on the system 40.4 had shown a first order I-N, S_A-S_B and a second order N-S_A transition. 40.7 and 40.8 systems showed second order N-S_A, S_A-S_C transitions as observed from the calorimetric, light scattering and X-ray studies. ESR line width studies of 40.6 had shown the pretransitional effects near the N-S_A transitions. Density and ultrasonic studies had shown the weak first order nature of 40.12, and a second order nature on 40.10. The density and refractive index studies on 40.m systems had been carried out by Potukuchi et al., [7].

Takahashi et al., [20] have studied variation of specific volume with temperature in the 50.m series by changing m from 4 to 14. Neutron scattering experiments were used to study the co-operative nature of the molecular motions in S_B and S_O phases of 50.7 [21]. Limmer et al., [22] have performed line width measurements on three nO.m compounds 50.6, 70.5 and 70.6.

6.1.4. Earlier NMR relaxation measurements in Homologous series

Normally it is difficult to isolate the individual contributions (due to each dynamical mechanism) from a T_1 study of a narrow frequency range except for a few fortuitous cases. However, the earlier work on a few liquid crystal systems had reported the identification of different dynamical processes in a limited **frequency** range. It was shown particularly, that the frequency dependent studies of relaxation times combined with temperature dependent studies could be **effectively** used to obtain information about these mechanisms. There have been several studies on molecular dynamics through conventional NMR relaxation measurements in liquid crystals [1,2,12,16,23,24,25].

The FCNMR technique has been used to investigate molecular dynamics in liquid crystals by Noack and coworkers [11]. Proton spin relaxation studies on **nematic** homologs of PAA were carried out by Nagel et al., [26]. From these studies certain differences in dynamics were observed with the changes in the chain length. Shorter chain molecules (PAA) show higher values of T_1 , than the longer chain molecules (PAB, HAB) at any particular nematic temperature. The DF contribution (quantified by the constant A_{DF}) varies with the chain length in the PAA series [27]. Longer chain molecules have a higher value of A_{DF} .

Another important conclusion arrived at, in the case of PAA and PAB studies is that, the chain protons also contribute to the value of the A_{DF} , contrary to the belief that, only the core involves in the collective fluctuations. This was also verified by a line shape analysis of these compounds [26]. The behavior of activation energies and upper cut-off frequencies obtained for the DF modes were used to support these conclusions. The decrease of the upper cut-off frequency with increasing chain length in PAA series ($8.1 \times 10^9 \text{ s}^{-1}$ for PAA and PAA-d₆, $6.4 \times 10^9 \text{ s}^{-1}$ for PAB, $1.1 \times 10^9 \text{ s}^{-1}$ for HAB) suggests that the whole molecule undergoes DF dynamics. The square root region shifted with the chain length, in different systems studied [11] reveal that, longer the chain length of the molecule, longer the region having square root dependence.

It is generally observed from these studies that, due to the modulation of the inter-proton dipolar interaction, the proton spin-lattice relaxation times are sensitive to the following mechanisms.

1. *Director fluctuations* (DF) are dominant at very low frequencies (below few MHz) in the nematic phase with the usual square-root dependence on the proton Larmor frequency. It has weak temperature dependence. In the smectic A phase the DF mechanism is replaced by the smectic layer undulation modes (LU), which are generally described by a linear dependence with Larmor frequency.

2. The second mechanism, is the anisotropic translational *self-diffusion* (SD), which is strongly temperature dependent, and generally dominates the high frequency relaxation from 10 MHz to a few 100 MHz in the **nematic phase**
3. *Rotations about the short axis* (R) dominate the intermediate frequency **range** The R contribution is frequency independent, generally **up to 1 MHz** and frequency dependent, upto a few **MHz** These rotations are generally observed in the **nematic phase** close to the I-N phase transition [13].
4. **Reorientations** about the long axis and the ring flips were observed in the high frequency regime from a few tens of MHz to a few hundred **MHz** Segmental rotations and conformational jumps have also been observed by many researchers [12] at high frequencies. These rotations are best studied, by the deuterium NMR methods and by angular dependent studies There are various rotational models available, in the literature [12].
5. *Order fluctuations* (OF) dominate the *I*) value near the transitions This has inverse temperature **dependence**
6. *Dipolar* effects lead to a shallow region at low frequencies below 10 kHz
7. The *cross relaxation* process becomes effective when the dipolar proton splitting frequencies and the quadrupolar nitrogen transition frequencies overlap, allowing a resonant exchange between the two spin systems, thus shortening the relaxation time at special frequencies

6.1.4.1. Earlier observations on Order and Director Fluctuations (OF and **DF**)

The orientationally ordered nematic liquid crystal phase is similar to the case of the Heisenberg ferromagnet and is a spontaneously broken continuous orientational symmetry of the high temperature isotropic phase [27]. As a consequence, the spectrum of collective fluctuations of the nematic director field is expected to be gapless in the long wavelength limit, and the so-called Goldstone mode should exist

The spectrum of eigen modes of these excitations consists of one branch of propagating acoustic waves and of two pairs of over damped, non-propagating modes. These can be further separated into low and a high frequency branches. The branch of low frequency modes corresponds to a slow collective **orientational** relaxation of an elastically deformed **nematic** structure, whereas the fast modes correspond to over damped shear waves, which are similar to the shear wave modes in ordinary liquids. In the long wavelength limit, the relaxation rates for both the modes are proportional to q^2 , which is characteristic of hydrodynamic modes. Here, q is the wave-vector of the over damped mode.

In 1968, de Gennes [8] had introduced the concept of orientational normal modes, similar to the phonon collective excitations in 3D solids, which can be considered as plane, wave like, spatially coherent excitations of the director field $n(r, t)$. In contrast to the phonons in solids, collective modes in liquid crystals are always over-damped due to high viscosity. Soon after de Gennes suggestions, Blinc [14] and Pincus [17] showed the characteristic square root frequency behavior of T_1 in **nematics** and the failure of BPP theory of liquids in liquid crystals. This $T_1 \propto \omega^{-1/2}$ behavior (ω is the Larmor frequency) is a direct result of the gapless Goldstone mode nature, of the director fluctuations [27].

There have been attempts to study the **pre-transitional** dynamic behavior and order fluctuations (OF) near the I-N phase transition using the NMRD technique. NMRD studies by Wolfel et al., [28] on PAA and T_1 measurements by Dong et al., [29] on MBBA, showed a critical dependence of T_1 with frequency near phase transition. This behavior is in contrast with the frequency independent behavior of T_1 , for a very long temperature range in the isotropic phase. Measurements between 7 MHz to 30 kHz in PAA, show this critical behavior, indicating the short-range order fluctuations (called cybotactic clusters) in the isotropic phase close to the I-N phase transition. Order fluctuations lose their importance, once the long-range nematic order is formed in the medium.

In the nematic phase sufficiently away from the phase transition temperature, director fluctuations (DF) become very important. The experimental efforts by Doane

et al., [15] and Blinc et al., [14] could not lend them to a single interpretation on frequency dependent τ , data of MBBA (10.4) The limited frequency NMRD studies (from 4 MHz to 100 MHz) on 10.4, by Doane et al., favored the DF domination whereas Blinc et al., had recommended the SD domination Both the groups had come up with different arguments for corresponding behaviors in order to eliminate the difficulties in fitting the NMRD data. Doane et al., had proposed a high frequency cut-off for DF modes, and Blinc, a step-width parameter for SD mechanism. Doane remodified his theory considering both DF modes and local diffusive reorientations of proton spins. which lead to a cross correlation term also But the proton NMRD work using the field-cycling technique on MBBA and other systems by Noack's group [11] established the fact that, SD and R are the very important dynamical processes in conventional NMR frequencies in nematic liquid crystals, and DF modes are more effective at low frequencies Anisotropy can be best probed by the angular dependent spin relaxation studies, and the angular dependent NMRD studies by Noack et al.. [11] established the effect of local fields beyond doubt, and permitted a detailed analysis of DF at low frequencies

6.1.5. Experimental Details

In this sub-section an attempt is made to give general experimental details like sample preparation, pulse sequences used in NMRD data collection, theoretical models, fitting procedures, data analysis etc , in order to avoid repetition of the same details when each liquid crystal system is discussed in the forthcoming sections.

The 40 m samples were purchased from a commercial source (M/S Frinton Laboratories. USA) and used without further purification Samples were sealed under vacuum (10^{-5} Torr) after removing the dissolved oxygen, by the freeze-pump-thaw method. Phase transition temperatures were verified with the observed changes in the amplitude and shape of the FID. In order to orient the nematic director \mathbf{n} of the system, parallel to the Zeeman magnetic field, the samples were heated to the isotropic phase first, and slowly cooled to the temperature in the presence of the Zeeman magnetic field Proton NMRD data were collected in the nematic phases at fixed temperatures using the FCNMR spectrometer The temperature dependent data

collected earlier in this laboratory [1,2] was also used in the analysis in order to get a complete picture on the dynamical properties in different mesophases.

The inversion-recovery *rf* pulse sequence and the saturation-burst *rf* pulse sequences were used on the conventional pulsed NMR spectrometer. Inversion recovery sequence and single pulse methods were used on FCNMR spectrometer. The details of the pulse sequences and the data fitting procedures are presented in chapter 1. The estimated errors in T_1 measurements at frequencies below 1 MHz are found to be less than 7%, and at above 1 MHz there are around 5%.

6.1.6. Data analysis

It has been established that, the proton T_1 measurements are expected to show dominant contributions to $J_1(\omega)$ from the three mechanisms (DF, R and SD), which are essentially distinguished by their characteristic frequency dependent behaviors. Effective contributions to the spectral densities from these dynamics could be seen at the Larmor frequency and at twice the Larmor frequency. The total spin lattice relaxation rate (R_{1Tot}) therefore, can be written as

$$R_{1Tot} = R_{1DF} + R_{1SD} + R_{1R} \quad (6.1)$$

Detailed expressions for each contribution are given in chapter-5. The data were analyzed, fitting them to the above equation 6.1, using the non-linear least square analysis, based on the Levenberg - Marquardt algorithm [52].

6.1.6.1. Nematic Director fluctuations (DF)

The data analysis was done using two different procedures for the DF contribution. The first method is based on the *one constant approximation (isotropic elastic constants model)*. The second method is based on the *anisotropic elastic constants model*, using a generalized expression [18] incorporating all the modifications made by Doane and Johnson [15], Brochard [53] Vold and Vold [16],

and **Blinic et al.**, [14] on the Pincus model [17]. In the present NMRD data analysis, the generalized equation for DF modes [18] is used for both the **analysis**

6.1.6.1.1. Isotropic elastic constants model

In the first method, elastic constants are fixed as $K_{11} = K_{22} = K_{33} = 10^6 \text{ dyne}$. For the *director fluctuations* with lower and upper cut-off frequencies, the model parameters are the amplitude A_{DF} , lower cut-off frequency ν_{cl} and upper cut off frequency, ν_{ch} . The well known square-root frequency dependence on the relaxation time between upper and lower cutoff frequencies is the basis for the identification of the DF **contribution**. Details of the theoretical formulation of this model are given in chapter-5, section 5.2.

6.1.6.1.2. Anisotropic elastic constants model

In the second procedure (called the *anisotropic elastic constants model* or *generalized model*) an **expression**, considering the influence of upper and lower cut-offT wavelengths for the director **modes**, as well as the anisotropy in elastic constants were used in calculating the DF parameters. Based on this model the relaxation rate due to director fluctuations (R_{DF}) is given by [18]

$$R_{DF} = A_{DF} \sum_a \frac{\sqrt{\eta_a}}{K_a \sqrt{K_a} \sqrt{\rho \omega}} \left[f(D_{ab}, A_{ab}) - f(D_{ai}, A_{ai}) - f(B_{ab}, A_{ai}) + f(B_{ai}, A_{ai}) \right] \quad (6.2)$$

where

$$A_{DF} \propto f(\Delta) \frac{2N^2 k_b T}{(2\pi)^2}$$

The cut-offT frequencies are give by

$$\nu_{zch(l)u} = \frac{K_3 q_{zch(l)}^2}{2\pi\eta_u} \quad \text{and} \quad \nu_{zcl(l)u} = \frac{K_a q_{zcl(l)}^2}{2\pi\eta_u}$$

The complete description of the **functions** and parameters involved in this model has also been described in chapter-5. The experimental elastic constants measured by Tolmachev et al., [30] for 40.4 are used in deducing the elastic constants for other 40.m systems. These elastic constants are given as the input parameters in the model for the DF contribution. It is known that S (order parameter) is proportional to the square of the density [31] and the anisotropy of the refractive index [33]. Elastic constants are proportional to S^2 [32].

A systematic study of the refractive index and density on 40.m systems by Potukuchi [7] were used in estimating the relative values of S in 40.m systems. Using 40.4 elastic data as the reference, the values of the elastic constants for other 40.m systems were calculated, following the variations in the density and refractive index values at required temperatures. Figure 6.4, shows the density variations in the 40.m systems.

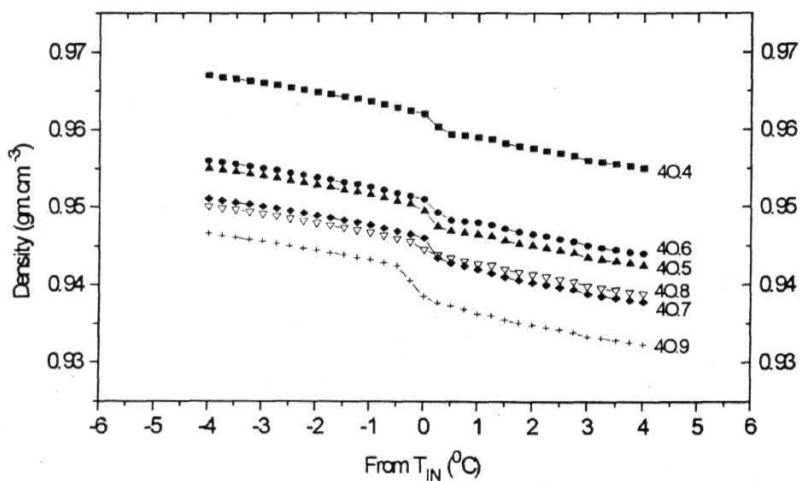


Figure. 6.4. Densities near isotropic-nematic phase transition in 40.m systems [7].

The general trend of **decreasing** density with increasing chain length, as well as the odd-even alteration, is observed in these **phases** 40.4, the system with symmetric end chains shows an increase of density in the isotropic as well as in nematic **phases** The density decreases with the increasing **alkyl** chain length. Odd and even systems follow smooth curves [7] in the isotropic and nematic phases with **temperature** There is no slope change in the interface between the nematic to smectic A transition when the alkyl chain is **short** The systems 40.8, 40.6, 40.4, as well as 40.5 and 40.7. show no slope change at the interface

The density data **in** the interface between the S_A - S_B also [7] shows a very different behavior from that of the I-N interface Odd systems show high values of density in both S_A and S_B phases. Near the transition, all even systems except 40.8 show a linear behavior 40.8 shows a lower value than the expected value. The system 40.9 also deviates from the linear behavior with respect to the other odd systems In general, symmetric end chain systems show higher densities. Figure 6.5 shows anisotropy in the refractive index of the 40.m systems

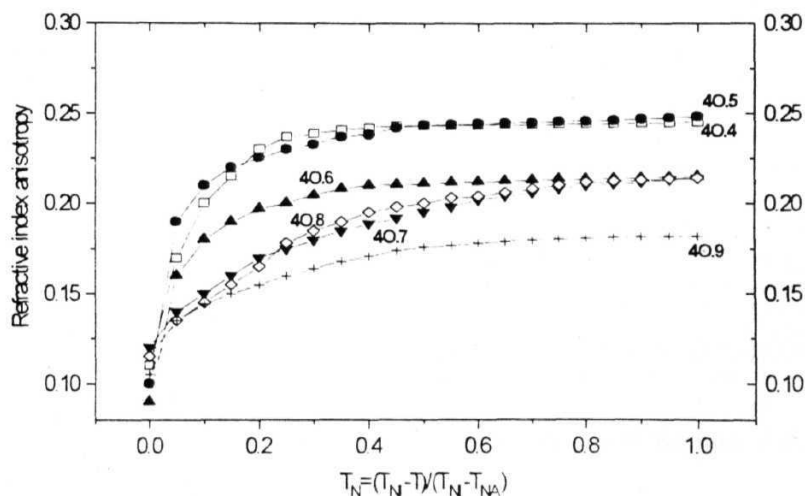


Figure 6.5 **Anisotropy** in the refractive index as a function of reduced nematic temperature T_N in the 40.m systems [7]

The data were plotted as a function of reduced temperature, T_N [7] such that one can easily compare the behavior of refractive index anisotropy in all the nematic phases, which have nematic phases in different temperature regions. It is interesting to note that the refractive index data shows a completely different behavior when compared to the density data, within the 40.m homologous series. Though the general trend of decreasing density and decreasing anisotropy with chain length is observed, the refractive index anisotropy shows very strong anomalies which could not be explained by the simple packing effects (chain length effects) or by odd-even effects.

The NMRD data were analyzed, considering the equations (5.62-5.67 for DF) given in chapter-5, under certain assumptions, to reduce the number of parameters to be determined from the data. The values of viscosity coefficients η_1 and η_2 were assumed to be 0.5 P. Though these values differ from compound to compound and are temperature dependent, the order of magnitude remains the same, if the molecular structure is essentially similar. Further, since these quantities appear as ratios K/η in R_{IDF} , its variation should be much less from the assumed values [13]. In addition, since the long wavelength cut-off values of DF modes should not depend on the anisotropy at molecular level, it was also assumed that $\lambda_{zch} = \lambda_{\perp ch}$. Then four parameters connected with R_{IDF} , viz. $\lambda_{zcl}, \lambda_{\perp cl}, \lambda_{zch}$ and ADF are left to be evaluated from the data. The parameters K_{11}, K_{22} and K_{33} are given as input parameters. In the fitting program, the input variables connected with the cut-off wavelengths are given in terms of wave vectors (q 's). The equations connecting wave vectors, cut-off frequencies and cut-off wavelengths are also described in chapter-5. The subscript l in the term $\lambda_{\perp cl}$ refers to the direction perpendicular to the director. The subscript p is also used often, with the same meaning of the subscript l . The subscript z refers to the direction parallel to the nematic director.

6.1.6.2. Smectic layer undulation modes (LU)

In the case of smectic A phase, layering leads to a sudden increase of bend (K_{33}) and twist (K_{22}) elastic constants. The strong mechanism, which influences the

spin relaxation at low **Larmor** frequencies are the layer undulation modes (LU). Theoretical formulation for this contribution and the parameters involved, are also described in chapter-5. **Important** parameters involved in fitting the NMRD data in the smectic A phase includes the upper and lower cut-off frequencies and the constant **A_{LU}**. **In** the present experimental NMRD data the contribution from LU is very small, due to the fact that the experiments are performed only from 50 kHz. The contribution from LU becomes very weak at this frequency. A presence of this contribution is essential however, to explain the NMRD data in the smectic A phase, particularly to explain the small region having a steep variation below about 200 kHz. The simplified equation used to **fit** the LU contribution is given here (equation 6.3) [48]

$$R_{1LU} = \frac{9}{8} \gamma^4 \hbar^2 J_1(\omega) = \frac{9}{8} \gamma^4 \hbar^2 \frac{A}{\omega} \left[\arctg\left(\frac{\omega_l}{\omega}\right) - \arctg\left(\frac{\omega_0}{\omega}\right) \right] \quad (6.3)$$

Where γ is the gyromagnetic ratio for protons, \hbar is the Planck's constant divided by 2π , $J_1(\omega)$ is the spectral density and A is the adjustable parameter which depends on the temperature, **nematic** order parameter and material physical **constants**. ω_0 and ω_l are the lower and upper cut-off frequencies of the collective modes, respectively, depending on the effective viscosity, splay elastic constant and smallest and largest wave vectors present in the system. This equation if further simplified by defining a new constant, **A_{LU}**, which is the new adjustable parameter given by

$$A_{LU} = \frac{9}{8} \gamma^4 \hbar^2 A$$

The values of **A_{LU}**'S obtained in present analysis are not accurate, since the NMRD data collected on smectic A phases have shown, a very short frequency **region**, having this linear behavior. **In** the present analysis, the **functional** behavior (linear behavior) is given priority rather than the other parameters such as cut-off frequency and the constant **A_{LU}**.

6.1.6.3. Rotations about the short axis (*R*)

Various theoretical models used, to get information about the rotational dynamics, in the analysis of the NMR data are listed below [12].

- > The simple Woessner approach [37] of rotating ellipsoids.
- > The small-step rotational diffusion in the ordering potential proposed by Nordio and Brown [35].
- The anisotropic viscosity model [36] of Freed et al., in combination with fast spinning around the molecular long axis [16,34], the so called **Vold** and Vold's 'third rate model' and
- > Extensions of **Woessner's** formalism (and the small step rotational **diffusional** model) made by Dong et al., [12], with the inclusion of correlated uncoupled chain mobilities.

Graf et al., [4] have argued that the rotations about the short molecular axis are very significant in nematics since they are much slower than that of the rotations about the long axis. It has been argued that the rotations of segments and **methylene** groups occur parallel with the fast rotation, about the **long** axis and their contribution, moreover, is not important in NMR **frequencies** in the nematic phase. The correlation times obtained for rotations suggest that the rotations seen in the nematics are about the short molecular axis. For 10.4 the observed values of τ_R from NMRD studies are 2.4×10^{-7} s at 18°C , and 5.7×10^{-8} s at 45°C . These values are comparable with dielectric studies [13,41]. It is observed from dielectric experiments that the correlation time corresponding to the reorientation about a short molecular axis can have the value of the order of 10^{-6} – 10^{-8} seconds [13]. Near the **I-N** transition all these motions (**R**, SD and DF) become equal at medium frequencies [4]. Based on the above observations made in the literature, rotations about the short axis are considered in the present analysis of nematic NMRD data.

In the case of *rotations about the short molecular axis*, the explicit model parameters used are, the amplitude *C* and the rotational correlation time τ_R , assuming a simple BPP type (Eq. 5.146) contribution. Rotations about the short molecular axis are important at high temperature nematic phase closer to the **I-N** transition. Since the

data is not collected **above** 50 MHz, and no attempt is **made** to collect angular dependent data, the more advanced models proposed by Nordio [35], Vold and Vold [34], Dong [12] and others were not **implemented**, for R contribution in the present NMRD analysis

Apart from the contribution from rotations (R), with a single correlation time for the rotations about the short axis, it is expected that there are other rotational diffusive motions. It is assumed that in the present NMRD analysis between 50 kHz to 50 MHz these fast motions can contribute with a frequency independent **behavior**. Comparing with the strong SD contribution, which shows frequency dependence in the current frequency range, the faster rotations are difficult to detect. Keep in mind the importance of the parameters connected with the rotations about the short axis, and the complications involved in fitting so many parameters with the data available in the narrow frequency region, the contributions from faster rotations are not **considered** in model fitting. The three contributions, DF, SD and R about the short axis are sufficient to explain the present NMRD data in 4O.m systems.

Smectic A Phase

In the present systems, NMRD data does not show discontinuity between **nematic** and smectic A phases in the conventional NMR frequencies. This shows that there are common mechanisms in nematic and smectic phases, which dominate spin relaxation in this frequency range. SD is one such mechanism, which dominates **the** conventional NMR frequency range. R about the short axis, seen in the nematic phases of these systems as well as the other rotational diffusive motions may also be present in the **smectic A** phase, owing to the fact that the smectic A phase is again a fluid like **phase**. The simple BPP type equation is used in fitting the R contribution in the smectic A phase too.

6.1.6.4. Self-Diffusion (SD)

Vilfan et al., [40] have developed a **theory** for SD in liquid crystals, which is a modified version of the Tonrey's theory [39] developed **for** isotropic liquids, using

Chandrasekars' random flight model. Theoretical details of this model have been described in chapter-5. Significant observations made in the literature, useful in handling the NMRD data are discussed here.

It was generally found that the high frequency spectrum (from few tens of MHz to a few hundred MHz) of NMRD data was mainly determined by self-diffusion mechanism [11]. In the case of self-diffusion, the model parameters are B (the amplitude), and D (the average diffusion constant). In the present NMRD studies, the complete profile of the diffusion curve could not be obtained due to lack of data at high frequencies, above 50 MHz. Same equation (5.136) is used for SD mechanism in both nematic and smectic phases.

In order to avoid mistakes in calculating the SD constants, restrictions are imposed [4] on the jump time τ_{SD} , by providing the average self-diffusion constant suited to the isotropic approximation of R_{ISD} , and by imposing the Einstein relation $D^2 = 6 D \tau_{SD}$. The low frequency asymptote $TJSD (\omega \rightarrow 0)$ and the dispersion frequency $1/(2\pi\tau_{SD})$ are correlated thus, i.e., in the fit they cannot be shifted independently.

6.1.7. Ordered smectic Phases

Dynamic mechanisms identified, which are responsible for relaxation in N, S_A and S_C phases are different from the mechanisms identified for relaxation in SB, S_G and other solid smectic phases. In the N, S_A, and S_C phases the important mechanisms, along with the nematic DF modes and smectic layer undulation modes, are SD and R about the short axis. In the case of ordered smectic phases and solid phases of the liquid crystalline materials, the contribution from DF and LU becomes negligible, in the frequency region of interest. Different types of rotations along with the SD mechanism are important in these phases. This argument is well supported by the T_I and T_{ID} measurements made by Heinze and Grande [41] on nO.m systems. The negligible discontinuities of temperature dependent F/ data in the N-S_A and S_A-S_C transition regions and an almost non-discontinuity in the T_{ID} values at these transitions supports this view.

The observed jumps at the transition to S_B or S_C phases in both $T_{1\rho}$ and T_1 at frequencies between 5-50 MHz [41] clearly demonstrates the difference between the dynamic properties of the highly ordered smectic phases (B and G) and the fluid-like smectic phases (A and C). In the long chain systems for example, in 70.4, temperature dependent T_1 and $T_{1\rho}$ studies at 32 MHz were carried out by Heinze and Grande [41], in the temperature range from 60°C to -150°C. This work clearly demonstrates the typical motional processes responsible for spin relaxation in the highly ordered phases. The T_1 data can be described based on the following observations made by these studies [41]. The typical behavior of the temperature dependent $T_{1\rho}$ and T_1 data obtained from these studies are shown in figure 6.6.

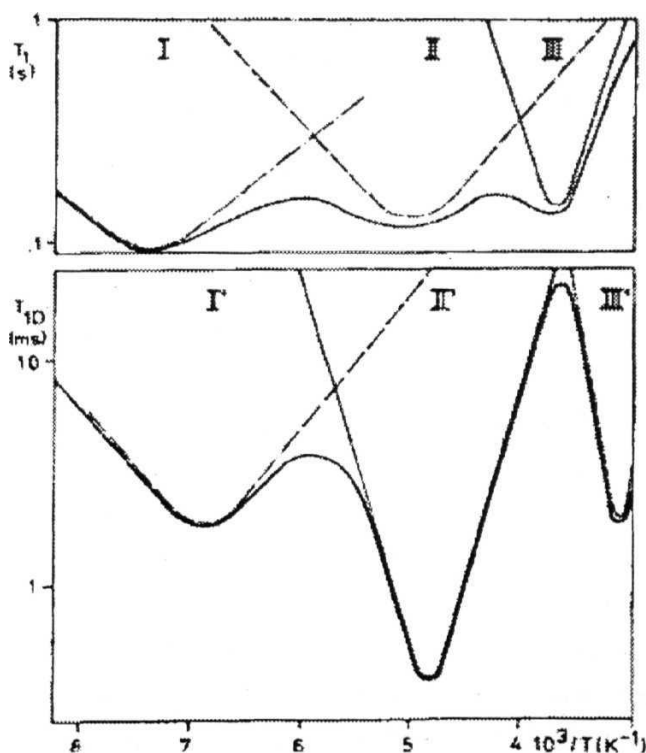


Figure 6.6 Typical behavior of $T_{1\rho}$ and T_1 data as a function of temperature in the system. 70.4 Theoretical curves explaining the behavior of the data are also shown in the figure [41].

Different temperature regions of the T_1 data shown in figure 6.6 and their theoretical explanation are given below.

- > In the high temperature (smectic G or Smectic B phase) region, called region-III, T_1 decreases with decreasing temperature. This region is explained by the rotation of the molecule as a whole (with a single correlation time 3×10^{-9} s at -18°C , with an activation energy of about 8 kcal/mole) about the long axis. A minima in the T_1 is seen at about -15°C .
- The relaxation in the next region from -25 to -105°C (region-II) is due to the chain **segmental** motions. A minima is seen around 80°C , due to chain **segmental** motions.
- The lowest temperature range (region -I) showing a minima at around -130°C in the T_1 data is due to the three-fold CH_3 reorientation (with a correlation time of 3×10^{-9} s at 133°C with an activation energy of about 2 kcal/mole). **Region-I** overlaps with **region-II** and similarly, **region-II** overlaps with **region-III**. At any temperature, different contributions to spin relaxation could be separated out by fitting the T_1 data to an equation considering these mechanisms.

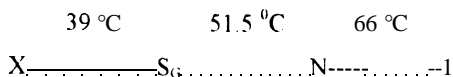
Similarly, different temperature regions of the T_{1D} data obtained from 70.4 are also shown in figure 6.6 and their theoretical explanation are given below [41].

- > The high temperature region (region -III') of S_G and S_B phases (from 60°C to -20°C) SD mechanism with a correlation time of about 10^{-5} s and an activation energy of about 12 kcal/mole is observed (S_B showing higher correlation time).
- The lower temperature region (**region-II'**) of T_{1D} data is explained by the rotation of the whole molecule. The lowest temperature region (**region-I**) in the T_{1D} data, is explained using intra molecular rotations.

These observations are useful in explaining the temperature dependent T_1 data in the ordered smectic phase. In the present experimental studies, no model fitting was attempted to explain the temperature dependent T_1 data of smectic B, or smectic G phases. But, the NMRD data is analyzed, considering the contributions from rotations and diffusion. From these observations, it is natural to expect SD domination at low frequencies and rotations about the long axis, at conventional NMR frequencies in these phases.

6.2. NMRD study of Butyloxybenzylidene ethylaniline (4O.2)

The first system studied in the 4O.m series is butyloxybenzylidene ethylaniline (4O.2). 4O.2 has the phase sequence given by [6],



This system has a stable nematic phase over 14.5 °C and an ordered smectic G phase over 9 °C. between an isotropic liquid phase and a solid phase.

6.2.1. Experimental Details

Proton NMRD measurements were carried out as a function of frequency in the nematic phase of 4O.2, at temperature 61 °C. The data from 55 kHz to 3 MHz was obtained, using the field-cycling NMR spectrometer, and the high frequency data from 3 to 50 MHz was obtained using a conventional NMR spectrometer [2]. The estimated error in τ measurements at frequencies below 1 MHz is found to be less than 7% and at above 1 MHz it is around 5%. NMRD data from 55 kHz to 50 MHz at temperature 61 °C in the nematic phase of 4O.2, is illustrated in figure 6.7. The observed NMRD data in the nematic phase of 4O.2 has the following features.

1. The relaxation times are range from 52 milliseconds at 55 kHz. to 444 milliseconds at 50 MHz. and τ decreases with decreasing frequency in the entire frequency range studied

2. τ data in the logarithmic scale (figure 6.7) shows a steep variation as a function of Larmor frequency. At low proton Larmor frequencies, the data shows a longer region having a square-root behavior, which extends upto intermediate frequencies, indicating the presence of the DF mechanism at this frequency range. The NMRD data slightly

deviates from this behavior from 2 MHz and a slightly different slope was observed at higher frequencies.

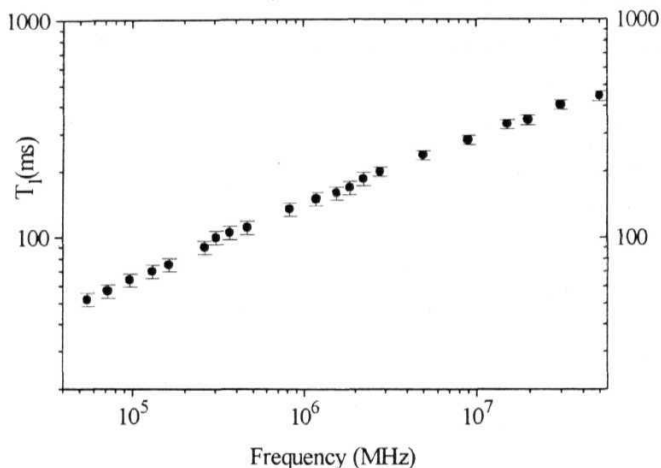


Figure 6.7. Frequency dependence of the spin-lattice relaxation time (T_1) in the nematic phase of 40.2 at temperature 61 °C.

3. Thus, the NMRD data in the nematic phase of 40.2 at 61 °C, shows two **different** regions with different slopes, and hence, a look at the data suggests that there are at least two possible mechanisms with different frequency dependence. The temperature dependent data at spot frequencies at 5, 9, 15, 19.5, 29.8, and 50 MHz are shown in figure 6.8.

In the conventional NMR region, the temperature dependent T_1 data shows an interesting behavior with two different regions in the nematic phase, from 5 MHz to 50 MHz. The first region close to the I-N phase transition shows almost a constant T_1 value with a lowering of the temperature. This trend continues for about 10 °C at lower frequencies. This region close to the I-N phase transition becomes shorter in the case of higher frequency data from 30 MHz onwards. The second region, with strong temperature dependence is observed closer to the N- S_C transition. The nematic phase range having strong temperature dependence in T_1 data is longer at high frequencies,

rather than low frequencies. This trend suggests that the SD mechanism becomes more dominant only at higher frequencies around 30 MHz. SD necessarily dominates the nematic phase near the N-S_G transition in all frequencies, from and above 30 MHz.

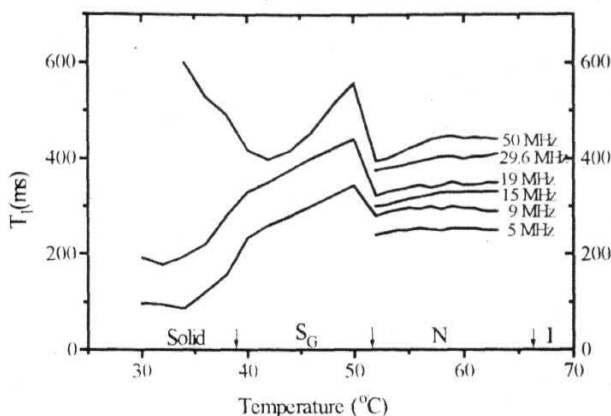


Figure 6.8. The behavior of the spin-lattice relaxation time (T_1) as a function of temperature at different frequencies in 40 2. The arrows denote the transition temperatures.

A sudden increase of T_1 is observed near the nematic to smectic G phase transition. Data in the ordered S_G phase shows strong temperature dependence as well as frequency dependence in the conventional NMR frequency range. T_1 decreases with an increase in temperature, and decreases with a decreasing frequency. It is interesting to note a minimum in the temperature dependent data at each frequency in an ordered smectic G or solid phase. The minimum observed at a lower temperature at the lowest frequency (5 MHz) shifts towards a higher temperature in the higher frequencies (50 MHz).

6.2.2. Data analysis

6.2.2.1. Nematic Phase

6.2.2.1.1. Isotropic elastic constants model

The frequency dependent relaxation rates ($R_I - 1/T_I$) at 61 °C, in the nematic phase of 40.2, were fitted to an equation assuming contributions from all the three dynamic processes namely SD, R and DF. The DF contribution to the NMRD data was fitted in two different ways. The value of A_{DF} and the lower cutoff frequency were varied to get a good fit. The DF contribution is quantified by the constant $A_{DF} = 6.68 \times 10^{-6} \text{ s}^{-2}$ in the case of the one constant approximation method. The estimation of upper cut-off frequencies become complicated, since the DF contribution becomes negligible at the expected cut-off frequency ranges. In the present case, the upper cut off frequency should be above than 100 MHz, assuming the molecular length to be the parameter deciding this cut-off. The lower cut-off frequency is about 8.1 kHz, and the corresponding upper cut-off wavelength for the director modes is about 3927 °A.

The dynamic parameters obtained from this fit are summarized in table 6.1. The qualitative picture of the fitting, in the nematic phase of 40.2, reveals that the DF dominates the spin relaxation upto 5 MHz. Relative contributions of DF, R and SD are shown in figure 6.9. The T_I data at 5 MHz shows almost no temperature dependence, which is attributed to the strong contribution from the DF mechanism. Rotations (R) about the short axis shows a frequency independent behavior ranging from 50 kHz to 5 MHz. A frequency dependent behavior of R, upto 30 MHz also contributes to the spin relaxation, along with the DF and SD. SD is more important than R throughout the dispersion. The DF mechanism becomes weaker, from 30 MHz onwards. The increasing slope of temperature dependent data, with an increasing frequency above 30MHz also supports this view.

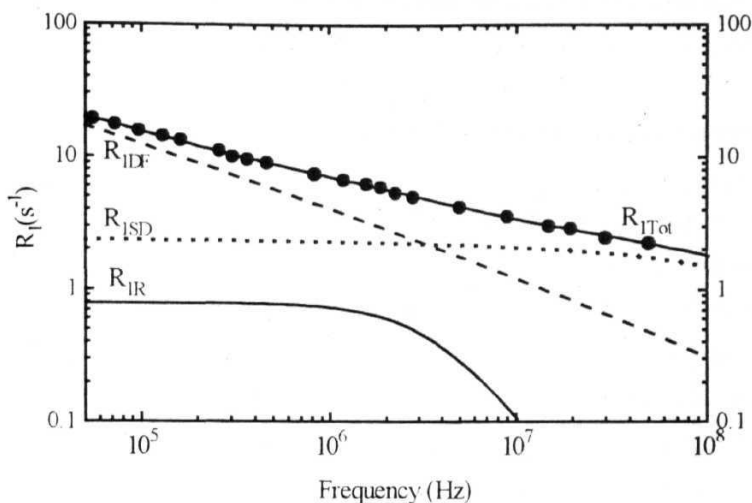


Figure 6.9, Proton relaxation rate ($R_1 \approx 1/T_1$) as a function of frequency in the nematic phase of 4O.2 at 61 °C and the model fit to three individual contributions to the relaxation rate director fluctuations (DF), self-diffusion (SD), and molecular reorientations about the short axis (R). The isotropic elastic constants model is assumed for DF contribution.

The NMRD data fitting gives the relative contribution of the various dynamical processes at different frequencies. A more quantitative picture of the relative contributions can be obtained at different frequencies by calculating the percentage contribution due to various mechanisms. For example at 50 kHz, the contribution from the DF mechanism to the total relaxation, is about 84%. The contribution from R and SD are about 4% and 12% **respectively**. The contributions at 1 MHz are 56% due to DF, 33% due to SD and 11% due to R. Contribution from SD becomes more important than DF, above 5 MHz. The contributions at 5 MHz are 41% due to DF, 52% due to SD and 7% due to R. At 10 MHz the contribution from R becomes 3% **only**. DF and SD contribute 35% and 62% respectively, to the spectral density. At

20 MHz, the DF contribution becomes 28.5% and the remaining 70.5% relaxation is almost due to the SD mechanism, and 1% is from R. At the maximum measured frequency (50 MHz) the contributions from SD and DF are 78% and 22%, respectively.

Reorientations about the short molecular axis

In the case of *rotations about the short molecular axis*, the explicit model parameters used, are the amplitude C and the rotational correlation time τ_R , assuming a simple BPP type contribution, neglecting the effects, due to molecular anisotropy. The values obtained for the R mechanism is given in the table 6.1. The correlation time obtained for rotations about the short molecular axis in the nematic phase of 40.2 is 5.53×10^{-9} seconds. The contribution to the total relaxation rate from R , is given by the value $C = 10.9 \times 10^7 \text{ s}^{-1}$. Rotations about the molecular short axis seem to be temperature independent or weakly temperature dependent, in the nematic phase.

Self-Diffusion

In the case of *self-diffusion*, the model parameters obtained are given in table 6.1. The parameter B , is equal to $4.2 \times 10^3 \text{ s}^{-2}$, the average diffusion constant D is obtained as $2.63 \times 10^{-6} \text{ m}^2 \text{ s}^{-1}$. The frequency independent contribution from SD is restricted to lower frequencies upto 10 MHz, in the nematic phase of 40.2. The stronger temperature dependence observed in the high frequency data can be accounted by the presence of SD process at high frequencies.

6.2.2.1.2. Anisotropic elastic constants model

In the second procedure, an expression considering the influence of upper and lower cut-off wavelengths for the director modes as well as, the anisotropy in elastic properties was used in calculating the DF parameters. The complete description of the functions and parameters involved in this generalized model have been described in chapter 5. The experimental elastic data obtained for 40.4 [30] is used to get elastic

data for 4O.2, by extrapolation. The elastic constants calculated for 4O.2 ($K_{11} = 1.2 \times 10^6$, $\Delta V = 0.812 \times 10^{-6}$ and $K_{33} = 1.76 \times 10^6$ dyne) at 61 °C are used in the model fitting. The details of the calculation of the elastic constants are given in the section 6.1. The fitting is shown in figure 6.10.

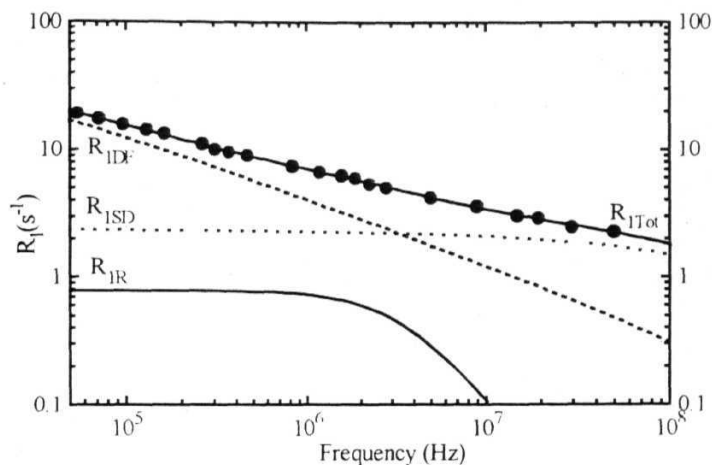


Figure 6.10. Proton relaxation dispersion ($R_1=1/T_1$) data as a function of frequency in the nematic phase of 4O.2 at 61 °C and the model fit to three individual contributions to the relaxation rate: director fluctuations (DF), self-diffusion (SD), and molecular reorientations about the short axis (R). The anisotropic elastic constants model is considered for DF contribution.

The constant A_{1DF} obtained for 4O.2 is $4.3831 \times 10^{-6} \text{ s}^{-2}$, a value smaller than that obtained from the isotropic elastic constants model. The lower cut-off frequency in this case is less than 1 kHz. The upper cutoff frequencies in the directions parallel and perpendicular to the director are $11.2 \cdot 10^8 \text{ Hz}$ and $9.95 \cdot 10^8 \text{ Hz}$, respectively. The parameters obtained from both these methods are given in table 6.1.

The contributions obtained for SD and R are different from the picture obtained from the isotropic elastic constants model. The values of B and D are decreased. Correlation time for rotations is increased by an order of magnitude. In this case, the DF contribution dominates for upto 3 MHz, with the square root behavior.

Table 6.1

Model Parameters	Isotropic elastic constants model	Anisotropic elastic constants model
Nematic director fluctuations (DF)		
K_{11} (in 10^{-6} dynes)	1	1.22
K_{22} (in 10^{-6} dynes)	1	0.81
K_{33} (in 10^{-6} dynes)	1	1.76
A_{DF} (in 10^{-6} s^{-2})	3.5	4.3831
q_{zcl} (in 10^5 l/Am)	3.6	4
f_{zcl} (in kHz)	0.412	0896
λ_{zch} (in Å)	17450	15700
q_{zch} (in 10^7 l/Am)	6.8	4.48
f_{zch} (in MHz)	1400	1120
λ_{zcl} (in Å)	9.24	14
$q_{\perp ch}$ (in 10^7 l/Am)	6.4	5.59
$f_{\perp ch}$ (in MHz)	1300	995
$\lambda_{\perp ch}$ (in Å)	9.81	11.23
Translational self-diffusion (SD)		
B (in 10^9 s^{-2})	4.234	3.667
D (in $10^{10} \text{ m}^2 \text{ s}^{-1}$)	2.63	1.98
Rotations about the short axis (R)		
C (in 10^8 s^{-2})	1.09	0.32
τ_R (in 10^{-9} s)	5.53	24.4

Self-diffusion (SD) mechanism, which is frequency independent upto 3 MHz, becomes responsible for the frequency dependence seen in the experimental NMRD data, above 3 MHz SD is strong at higher frequencies, than at frequencies below 10 MHz Temperature dependent T_1 data above 10 MHz, shows a stronger variation, due to the increased domination of the SD. Rotations about the short axis show frequency independent behavior upto 1 MHz and then, becomes frequency dependent upto 10MHz

6.2.2.2. *Ordered smectic phase (S_G)*

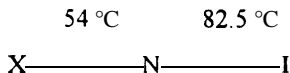
The observed increase of T_1 , at the transition from nematic to the smectic G phase of 4O2, in the frequency range between 5-50 MHz, clearly demonstrates the basic difference between dynamic properties of the highly ordered smectic G phase and the fluid like nematic phase Slowing down of the diffusion process and the absence of the DF mechanism are responsible for the sudden increase of T_1 in the smectic G phase in the conventional NMR frequencies In the smectic G phase of the 4O.2, T_1 data shows strong temperature dependence.

Using the detailed experimental observations made by Grande and Henize [24] in the nO m systems, it is possible to qualitatively explain the present temperature dependent T_1 data in the ordered smectic phases and solid phases The typical behavior shown by nO.m systems earlier has been described in the previous section From the present behavior of the data in the S_G phase at the measured temperature ranges, one can conclude that the major contribution comes from rotations of the molecule around the long axis and from segmental motions

Since there are two terminal chains and many CH_2 groups present in the 4O.2 system, several rotational diffusion modes could be present, leading to as many values of the correlation times possible The frequency dependent T_1 data measured in the S_G phase supports this view. This contribution is responsible for the frequency dependence in the S_G phase at conventional NMR frequencies from 10 MHz to 45 MHz

6.3. NMRD study of **Butyloxybenzylidene propylaniline (40.3)**

The next system, studied in the 40. m homologous series is butyloxybenzylidene propylaniline (40.3). It has the phase sequence given by [42]



A stable, very wide **nematic** phase (28.5 °C) was observed between isotropic (I) and **solid (X)** phases in 40.3.

6.3.1. *Experimental Details*

Proton spin-lattice relaxation time (T_1) measurements were carried out as a function of **Larmor** frequency in the nematic phase of 40.3 at temperature 69 °C. The data from 50 kHz to 3 MHz were obtained using the field-cycling NMR spectrometer, and the high frequency data from 3 to 50 MHz were obtained using a conventional NMR spectrometer [2]. The errors in T_1 measurements at **frequencies** below 1 MHz are found to be less than 7% and at above 1 MHz they are around 5%. Experimental NMRD data for the nematic phase is shown in figure 6.11. The temperature dependent data at spot frequencies 9, 15, 19.5, 29.8 ,39.6, and 50 MHz is shown in figure 6.12. The observed NMRD data in the nematic phase of 40.3 has the following features.

1. The relaxation times range from 45 milliseconds at 65 kHz, to 550 milliseconds at 50MHz. T_1 increases with increasing frequency throughout the nematic phase.
2. T_1 in the logarithmic scale varies slowly as a function of Larmor frequency, with a maximum slope in the low frequencies below 100 kHz. The slope decreases in the intermediate frequencies from 100 kHz to 800 kHz, and there is a steeper region after this (800 kHz to 3 MHz). Finally a region with a slow variation is seen from 6 to 40 MHz.

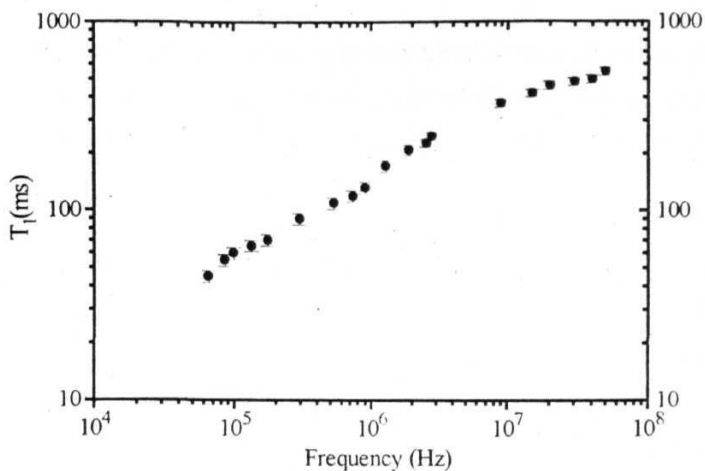


Figure 6.11. Frequency dependence of the spin-lattice relaxation time (T_1) in the nematic phase of 40.3 at temperature 69 °C.

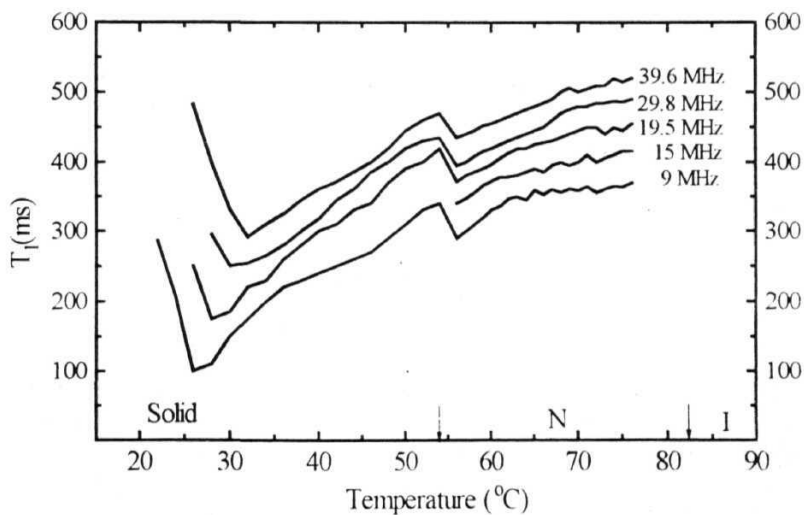


Figure 6.12. The behavior of the spin-lattice relaxation time (T_1) as a function of temperature at different frequencies in 40.3. The arrows denote the transition temperatures.

3. Thus, the NMRD data in the nematic phase of 40.3 at 69 °C, shows at least three different regions with different slopes. Hence, a first look at the data suggests that there are three possible mechanisms with different frequency dependencies.
4. In the conventional NMR region from 5 MHz to 50 MHz, the T_1 data shows a strong temperature dependence (the T_1 in the nematic phase decreases by more than 100 ms between the maximum or minimum temperature, at all the frequencies). This dependence becomes stronger at higher frequencies, making the 50 MHz temperature dependent data to show a higher slope than the 5 MHz data. This trend indicates that the major mechanism is probably self-diffusion, which should be stronger, at higher frequencies.
5. T_1 shows a sudden jump towards a higher value at the nematic to crystal phase transition and decreases quickly with temperature. The data in the crystal phase also shows strong frequency dependence. The T_1 value increases with frequency and decreases with temperature, within the frequency. A minimum is observed in the temperature dependent data, which moves towards the lower temperature region, when the frequency is lowered. The minimum seen at 28 °C at 5 MHz moves to 34 °C at 50 MHz. With regard to the general trends in the T_1 profiles, this behavior in the solid phase differs from the other solid systems under study, which would be discussed in the subsequent sections.

6.3.2. Data analysis

6.3.2.1. Nematic Phase

6.3.2.1.1. Isotropic elastic constants model

The frequency dependent relaxation rates ($R = 1/T_1$) at 69 °C in the nematic phase of 40.3 were fitted to an equation assuming a contribution from all the three dynamic processes, viz., SD, R and DF. The DF contribution to the relaxation was fitted in two different ways. The first method is based on the one constant

approximation, assuming $K_{11} = K_{22} = K_{33} = 1 \times 10^{-6}$ dyne. The value of the constant A_{DF} and the cut-off frequencies for the DF modes were varied to get a good fit. The DF contribution is quantified by the constant $A_{DF} = 3.2122 \times 10^{-6} \text{ s}^{-2}$.

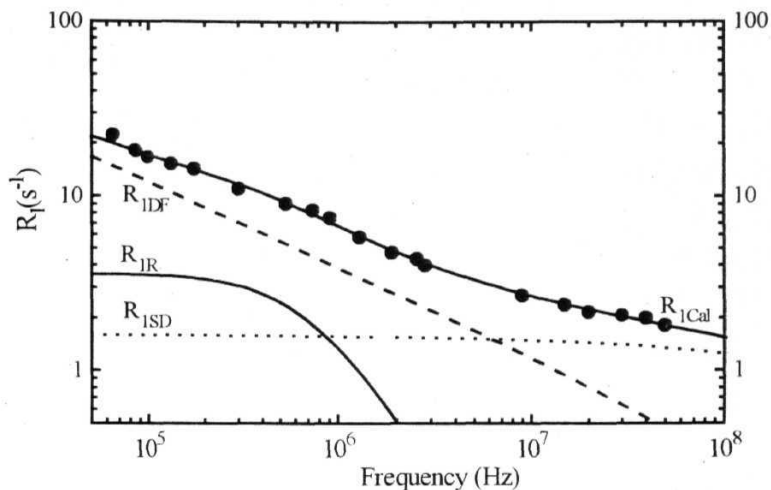


Figure 6.13. Proton relaxation rate ($R_1 = 1/T_1$) as a function of frequency in the nematic phase of 40.3 at 69 °C and the model fit to three individual contributions to the relaxation rate: director fluctuations (DF), self-diffusion (SD), and molecular reorientations about the short axis (R). The isotropic elastic constants model is assumed for DF contribution

The lower cut-off frequency is about 412 Hz, and the corresponding upper cut-off wavelength for the director modes is about 17450 Å. A constant value corresponding to lower cutoff wavelength of about 10 Å was given for upper cut-off frequency in the model fitting in order to get a good fit. The NMRD fitting is shown in figure 6.13. The dynamic parameters obtained from this fit are summarized in table 6.2. A qualitative picture of the fit, in the nematic phase of this system reveals that the DF modes completely dominate the spin relaxation at very low frequencies (in the kilo Hertz regime) and SD becomes significant from about 6 MHz. From 6.5 MHz

onwards, diffusion dominates the DF mechanism and it solely responsible for relaxation above 30 MHz

Table 6.2

Model Parameters	Isotropic elastic Constants model	Anisotropic elastic constants model
Nematic director fluctuations (DF)		
K_{11} (in 10^{-6} dynes)	1	1.06
K_{22} (in 10^{-6} dynes)	1	0.706
K_{33} (in 10^{-6} dynes)	1	1.53
A_{DF} (in 10^{-6} s ⁻²)	3.2122	3.5375
q_{zcl} (in 10^5 l/Am)	3.6	3.418
f_{zcl} (in kHz)	0.412	0.557
λ_{zch} (in Å)	17450	50480
q_{zch} (in 10^7 l/Am)	6.8	6.8
f_{zch} (in MHz)	1400	1400
λ_{zcl} (in Å)	9.24	924
q_{lch} (in 10^7 l/Am)	6.4	6.4
f_{lch} (in MHz)	1300	1300
λ_{lch} (in Å)	9.81	9.81
Translational self-diffusion (SD)		
B (in 10V)	6.386	6.409
D (in 10^{-10} m ² s ⁻¹)	5.07	5.42
Rotations about the short axis (R)		
$\overline{C^2}$ (in 10^8 s ⁻²)	0.30	0.286
τ_R (in 10^{-9} s)	119	112.56

Rotations about the short axis seem to be more important than diffusion below 1 MHz and become negligible above 2 MHz. At the conventional NMR frequencies, SD mechanism is very important. This interpretation is also supported by the strong

temperature dependence of the T_1 data at conventional NMR frequencies in the nematic phase.

A more quantitative picture of the relative contributions can be obtained by calculating the percentage contribution at different frequencies, due to various mechanisms. For example at 100 kHz, the contribution from DF mechanism in the total relaxation is about 82%. The contribution from SD and R are about 6% and 12% respectively. At 500 kHz, the contributions from DF, R and SD are about, 59.6%, 26%, and 14.4% respectively. The contributions at 1 MHz are 57.2% from DF, 24.3% from SD and 18.5% from R. The SD mechanism takes over the R mechanism from about 1 MHz onwards. This trend continues, and finally R becomes negligible right from 2 MHz. The contributions at 2 MHz are 52% due to DF, 36% due to SD and 12% due to R. At 6 MHz, DF modes and SD mediate spin relaxation equally and there is no contribution from rotations about the short molecular axis. At 20 MHz, it is estimated that the contribution from DF becomes one third and SD contributes the remaining two-thirds to the spectral density. Accuracy of various parameters differ widely, since the optimization procedure has to handle many parameters which have analytical dependence, and also because some of these constants are strongly correlated. In the present analysis the errors estimated for the model parameters are about 10%.

Reorientation's about the short molecular axis

In the case of *rotations about the short molecular axis*, the explicit model parameters used, are the amplitude C and the rotational correlation time τ_R . Since there is no region in the NMRD data where one can see the frequency behavior recommended for rotations, the deviations from the square root dependence is only an indication of the presence of rotations. It is not very difficult in the case of 40.3, with two steps seen at high frequencies. The SD should, in principle, take care of high frequency dispersion. The values obtained are given in table 6.2. The correlation time obtained for rotations about the short molecular axis in the nematic phase of 40.3 is 1.19×10^{-7} seconds. It is observed from the dielectric experiments [33,34,41] that in the

presence of the nematic orientational order the correlation time corresponding to the **reorientation** about a short molecular axis can have correlation times of the order of 10^{-8} to 10^{-6} seconds

Self-Diffusion

In the case of **self-diffusion**, the model parameters are B (the amplitude), and D (the average diffusion constant). The theory and equations have been given in chapter 5. The frequency independent contribution from SD changes to frequency dependent, from 10 MHz. The complete profile of the diffusion curve could not be obtained due to the lack of data at high frequencies above 50 MHz. The strong temperature dependence at the highest frequency of 50 MHz, the T_1 data observed, is due to the strong domination of SD process. The diffusion constant $D = 5.07 \times 10^{-10} \text{ m}^2 \text{ s}^{-1}$ obtained here is in good agreement with the diffusion constants obtained for typical nematic liquid crystals [43].

6.3.2.1.2. Anisotropic elastic constants

The complete description of the functions and **parameters**, involved in this generalized model [18] have been described in chapter 5. The experimental elastic data given by Tolmachev et al., [30] for 40.4 is extrapolated, keeping in mind the general trends followed by other homologous series of nematic liquid crystals, in order to obtain elastic constants for the 40.3 system. It is well known that $K \propto S^2$ and hence the value of A_{DF} is attributed to the changes in the value of S also. In this model, the ADF value obtained is $3.5317 \times 10^{-6} \text{ s}^{-2}$, which is not very different from the value obtained from the isotropic elastic constant model

The lower cut-off frequency in this case is 557 Hz, close to the value obtained from the one constant elastic constants model. The upper cut-off frequencies in the directions parallel and perpendicular to the director are same as that of the other **model**. The parameters obtained from both these methods are given in table 6.2. The correlation time obtained for rotations about the short molecular axis in the nematic

phase of 40.3, is 11.26×10^{-8} seconds. The contribution to the total relaxation rate from R is quantified by the value $C = 2.86 \times 10^7 \text{ s}^{-1}$.

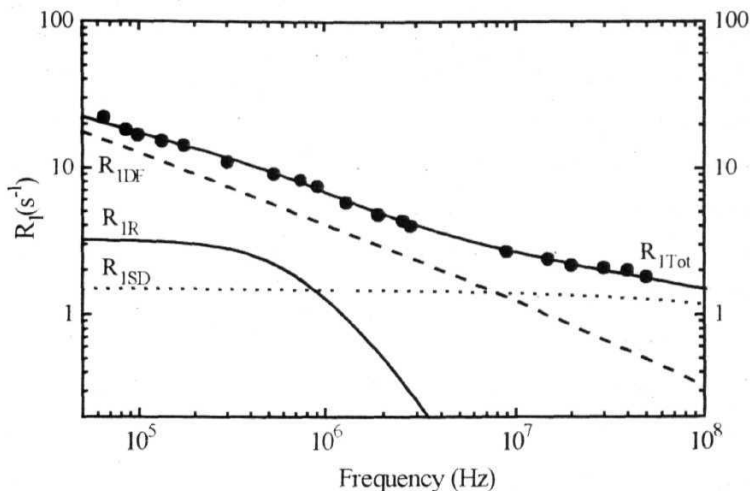


Figure 6.14. Proton relaxation rate ($R_1 = 1/T_1$) as a function of frequency in the **nematic** phase of 40.3 at 69 °C and the model fit to three individual contributions to the relaxation rate: director fluctuations (DF), self-diffusion (SD), and molecular reorientations about the short axis (R). The anisotropic elastic constants model is considered for DF contribution.

In the case of *self-diffusion*, the model parameter B is equal to $6.409 \times 10^{10} \text{ s}^{-2}$, and A the average diffusion constant is equal to $5.42 \times 10^{-10} \text{ m}^2 \text{ s}^{-1}$. Diffusion parameters (B and D) obtained with the anisotropic elastic constants model for DF modes are almost the same as that of the parameters obtained in the case of the isotropic elastic constants model.

In comparison with the first model, the qualitative picture show differences, too. DF contribution in the second model is stronger than that of the first model. Diffusion does not change much, though the quantitative picture does show some

differences. The increase in DF is at the cost of reduction in the contribution from **R** only. Functional behavior of **R** does not change much, but the percentage contribution decreases from the value obtained from the first model. This increase in the DF contribution affects the percentage contribution of **R** and the value of **B** slightly. For example, the percentage contribution from SD at 50 MHz now, is about 8% lesser than the previous value. By performing the analysis using both models, a clear understanding of the role of elastic constants in the evaluation of the dynamic parameters can be had. It is very interesting to note that the value of A_{DF} is strongly dependent on the anisotropy of the elastic constants.

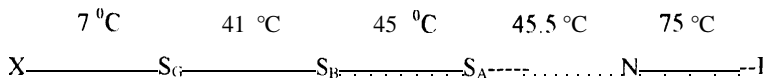
6.3.12. Solid phase

In the solid phase, diffusion becomes negligible and DF modes are not possible. The increase in the relaxation times with decreasing temperature in the system 40.3 indicates that the hindrance to faster rotations (at higher frequencies) increase at lower temperatures. In the case of 40.3, the minima are close to the nematic to solid transition temperature for all the measured temperatures.

The relaxation in the highly ordered smectic phases and the solid phases can be best described, using three dynamical processes generally seen [24] in the chain molecules, 1. Rotation of the molecule as a whole around its long molecular axis, 2. Chain segmental motions and 3. CH_3 three fold rotations. Experimental relaxation rate in the solid system 40.3 can be explained, based on these contributions. The shifting of minima towards high temperatures with increasing Larmor frequency (strong minima at that frequency) could be interpreted as that, the reorientations about the long axis and the segmental motions could be better observed at high frequencies, when temperatures are high. In other words, the rotations about the long axis are faster at high temperatures, and hence, data at high frequencies have to be collected in order for their effect to be seen clearly. By decreasing the temperature, the reorientations about the long axis, can be slowed down, and the minima could be observed at the current (lower) frequencies.

6.4. NMRD study of Butyloxybenzylidene Butylaniline (40.4)

The next system in the 40.m series is *butyloxybenzylidenebutylaniline* (40.4). This system has the phase sequence given by [6]



Stable nematic (a range of 31 °C) and smectic G (a range of 34 °C) phases along with a shorter smectic B (4.5 °C) and a very short smectic A phase (0.5 °C) are seen between the isotropic liquid and solid (X) phases. The mesophase range is very wide compared to the other shorter chain systems in the 40.m series

6.4.1. Experimental Details

Proton spin-lattice relaxation time (T_1) measurements were carried out as a function of frequency in the nematic phase of 40.4 at a temperature of 67 °C. The data from 50 kHz to 3 MHz was obtained using field cycling NMR spectrometer and high frequency data from 3 to 50 MHz was obtained using conventional NMR spectrometer [2]. The estimated errors in T_1 measurements at frequencies below 1 MHz are found to be less than 7% and at above 1 MHz they are around 5%. It is important to mention here, that the temperature dependent data has strong pretransitional effects in the case of 40.4. Experimental NMRD data for the nematic phase, is shown in figure 6.15. The temperature dependent data at spot frequencies at 5, 9, 15, 20, 30, and 39.6 MHz are shown in figure 6.16. The observed NMRD data in the nematic phase of 40.4 has the following features

1. The relaxation times range from 51 milliseconds at 55 kHz to 413 milliseconds at 39.6 MHz. T_1 decreases with decreasing frequency, as observed in the entire frequency range studied.

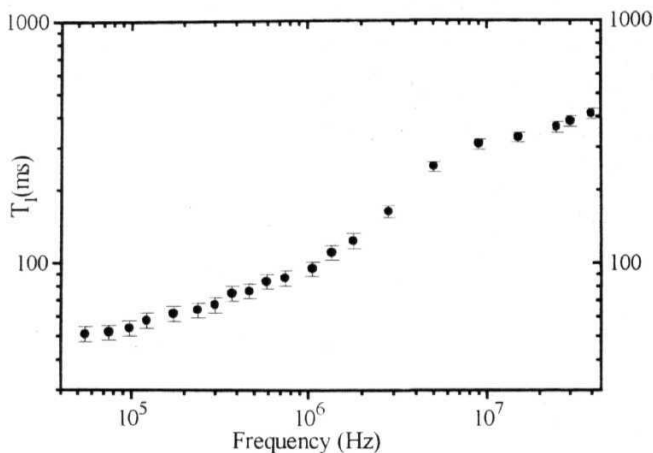


Figure 6.15 Frequency dependence of the spin-lattice relaxation time (T_1) in the nematic phase of 40.4 at temperature 67 °C. Data points are represented by circles. Error bars are also given along with the data points.

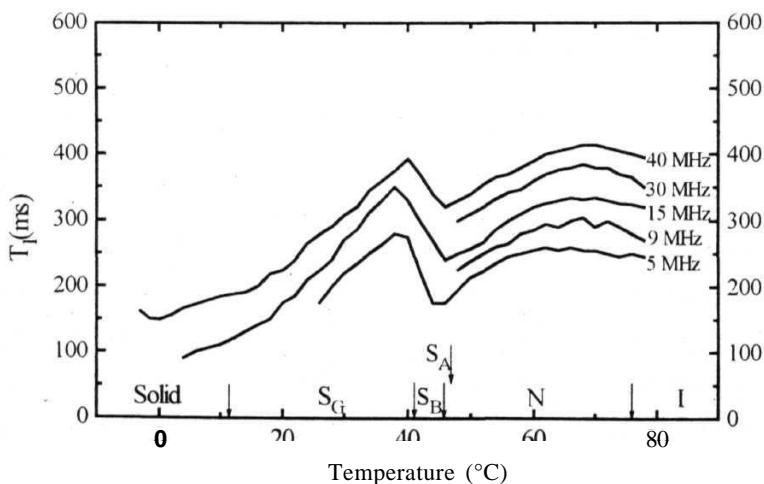


Figure 6.16. The behavior of the spin-lattice relaxation time (T_1) as a function of temperature at different frequencies in 40.4. The arrows denote the transition temperatures.

- 2 γ in the logarithmic scale shows variation as a function of Larmor frequency with lesser slope in the low frequencies (below 800 kHz). The slope increases in the intermediate frequencies (from 1 to 10 MHz) and finally reaches a region with lower slope in the higher frequencies (10 to 40 MHz).
- 3 Thus NMRD data in the nematic phase of 40.4 at 67 °C shows at least three different regions with very different slopes. The typical square-root behavior at low frequencies is very weak in 40 4
- 4 In the conventional NMR region from 5 MHz to 39.6 MHz, the T_1 data shows an interesting behavior with three different regions. The first region close to the I-N phase transition shows an increasing γ value with the decreasing temperature. This trend continues for about 5 °C and the second region is seen with weak temperature dependence. This region continues for about 15 °C and the third region, showing very strong temperature dependence extending up to nematic to smectic A phase transition, is observed. The temperature independent region decreases with increasing frequency.
- 5 γ data shows a sudden increase towards a higher value at the smectic A to Smectic B phase transition. This value decreases with temperature after reaching a maximum value near the S_R to S_Q phase transition. The data in the highly ordered S_R and S_G phases also shows strong frequency dependence. The γ value increases with frequency and decreases with temperature within the frequency in the S_G phase. A region showing minima is observed in the temperature dependent data, which moves towards the lower temperature region, when frequency is reduced, in the S_G phase.

6.4.2. Data analysis

6.4.2.1. Nematic Phase

6.4.2.1.1. Isotropic elastic constants model

It is important to introduce the contribution from the rotation about the short molecular axis (R), in the analysis, in order to explain the low and intermediate frequency data upto 2 MHz. Similarly, the low frequency cut-off is necessary to fit the low frequency data in the kHz, range satisfactorily. The frequency dependent relaxation rate ($R \propto 1/T_1$) at 67 °C, in the nematic phase of 40.4, is also fitted to two different models, the equation assuming contributions from all the three dynamic processes, viz., SD, R and DF.

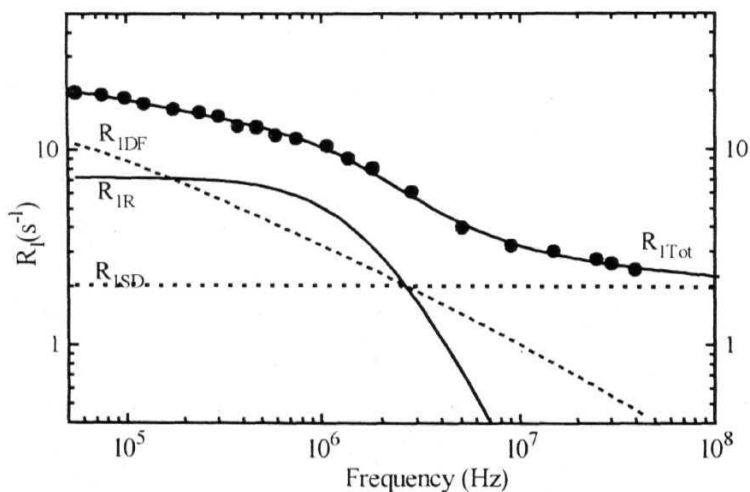


Figure 6.17. Proton relaxation rate ($R_1 \propto 1/T_1$) as a function of frequency in the nematic phase of 40.4 at 67 °C and model fit (equation 6.1) to three individual contributions to the relaxation rate: director fluctuations (DF), self-diffusion (SD), and molecular reorientations about the short axis (R). Isotropic elastic constants are assumed in evaluating the DF contribution.

Table 6.3

Model Parameters	Isotropic elastic constants model	Anisotropic elastic constants model
Nematic director fluctuations (DF)		
K_{11} (in 10^{-6} dynes)	1	0.9
K_{22} (in 10^{-6} dynes)	1	0.6
K_{33} (in 10^{-6} dynes)	1	1.3
A_{DF} (in 10^{-6} s ⁻²)	2.57	2.2988
Q_{zcl} (in 10^5 l/Am)	1.46	1.46
F_{zel} (in kHz)	20	8.8
λ_{ech} (in Å)	2480	4306
Q_{zch} (in 10^7 l/Am)	6.8	4.68
F_{zch} (in MHz)	1400	900
λ_{zcl} (in Å)	9.24	13.4
Q_{Jch} (in 10^7 l/Am)	6.4	5.64
F_{Jch} (in MHz)	1300	1012
λ_{Jch} (in Å)	9.81	11.14
Translational self-diffusion (SD)		
B (in 10^9 s ⁻²)	513	506
D (in 10^{-10} m ² s ⁻¹)	363	318
Rotations about the short axis (R)		
C (in 10^8 s ⁻²)	1.245	1.238
τ_R (in 10^{-9} s)	5.816	5.878

The value of A_{DF} and the cut-off frequencies were varied to get a good fit. The DF contribution is quantified by the constant $ADF = 2.808 \times 10^{-6}$ s⁻² in the case of one constant approximation method. This value for ADF is very less, since the domination of the DF contribution is confined to very low frequencies, and the higher frequency

dispersion is due to R and SD. The lower cut-off frequency is about 24 kHz, and the corresponding upper cut-off wavelength for the director modes is about 24800 Å. The typical errors estimated in evaluating the dynamic parameters are about 10%.

Relative contributions

Relative contributions from various mechanisms to the measured R_1 data are shown in figure 6.17. The dynamic parameters obtained from this fit are summarized in table 6.3.

A qualitative picture of the fit, in the nematic phase of 40.4 reveals that the DF modes dominate, spin relaxation at the very low frequencies upto 200 kHz. R about short axis dominates the relaxation with a frequency independent behavior from 200 kHz to 500 kHz and with a frequency dependent behavior upto 3 MHz. SD becomes important, from about 2.8 MHz, where all the three mechanisms become equally important. At high frequencies, diffusion is the major mechanism responsible for relaxation. This interpretation is supported by the strong temperature dependence of the T_1 data at conventional NMR frequencies throughout the nematic phase. The relatively weaker temperature dependence at intermediate frequencies, about 5 MHz is probably due to the presence of DF and R, along with the SD mechanism.

From the NMRD data fitting, the percentage contribution from various dynamical processes at different frequencies, can be calculated. For example at 55 kHz, the contribution from the DF mechanism to the total relaxation, is about 52.5%. The contribution from R and SD are about **36.5%** and 11% respectively. At 100 kHz, the contributions from DF, R and SD are about, 48%, 40%, and 12% respectively. The contributions at 175 kHz are 43.2% from DF, 43.2% **from** R and 13.6% from SD. The R mechanism takes over the DF mechanism, from 175 kHz onwards. This trend continues, and finally R becomes equal to SD and DF at 2.8 **MHz**. **The** contributions at 1 MHz are 31% due to DF, 49% due **to** R and 20% due to SD. At 9 MHz, the contribution from R becomes 6% and SD contributes about 62% and DF contributes by about 32% **to the** spectral density. At **the** highest

measured frequency (39.6 MHz), DF contribution becomes very less (16.5%) and the remaining relaxation is almost due to the SD (about 83.5%) mechanism. This view is well supported by the strong temperature dependence of the τ data at 39.6 MHz.

Reorientation's about the short molecular axis

In the case of *rotations about the short molecular axis*, the explicit model parameters used are the amplitude C and the rotational correlation time τ_R , assuming a simple BPP type contribution. The correlation time obtained for rotations about the short molecular axis in the nematic phase of 40.4 is 5.8157×10^{-8} seconds. It has also been observed from the dielectric experiments that the correlation time corresponding to the reorientation about a short molecular axis can have the value of the order of 10^{-6} – 10^{-8} seconds [41].

Presence of strong contribution from rotations about the short axis at kHz region is the mechanism, probably leading to the temperature dependent dipolar relaxation times (T_{1D}) [2]. Generally T_{1D} shows temperature independent behavior when the DF dominates upto few MHz, as seen in the other 40 m systems. Activation energy associated with the temperature dependent of T_{1D} is 7.6 kCal/mol [2]. This value is in agreement with the generally observed activation energy associated with the rotational motion about the molecular short axis [32,33].

Self-Diffusion

The frequency independent contribution from SD extends to higher frequencies in the case of 40.4. The complete profile of the diffusion curve could not be obtained due to the lack of data at high frequencies above 40 MHz in 40.4. The strong temperature dependence of T_1 at 39.6 MHz is observed probably due to the domination of SD process at high frequencies. Relaxation in the intermediate frequency region is due to the SD, assisted by DF.

The diffusion constant is $32.4 \times 10^{15} \text{ cm}^2 \text{ s}^{-1}$, a higher value comparing with the other 40 m systems, but within the range of the diffusion constants obtained for typical nematic liquid crystals (0.4×10^{-8} to $3 \times 10^{-5} \text{ cm}^2/\text{sec}$) [43].

6.4.2.1.2. Anisotropic elastic constants model

The second method based on the anisotropic elastic constants model gives a slightly different picture of the dynamical parameters. The experimental elastic data given by Tolmachev et al., [30] for 40.4 is used directly in the model fitting for DF. The complete description of the functions and parameters involved in this more generalized model, considering cut-off frequencies as well as anisotropy in the elastic constants have been described in **chapter-5**, section 5.2. The relative contributions observed from the analysis are depicted in figure 6.18.

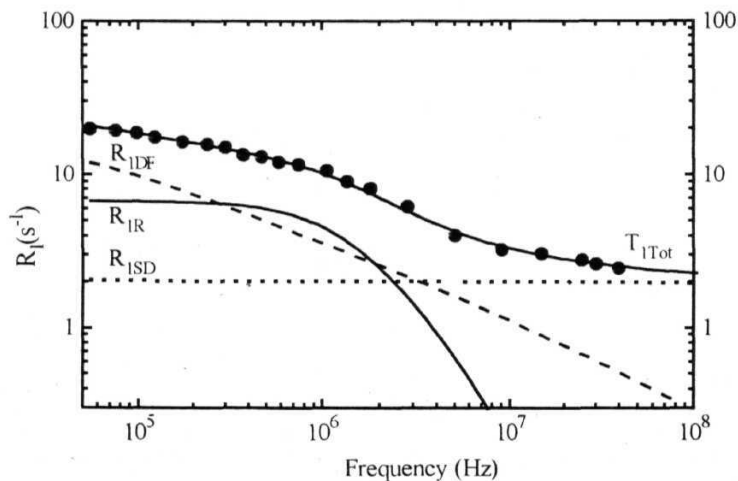


Figure 6.18. Proton relaxation rate (R / T) as a function of frequency in the nematic phase of 40.4 at 67 °C and model fit (equation 6.1) to three individual contributions to the relaxation rate: director fluctuations (DF), self-diffusion (SD), and molecular reorientations about the short axis (R). Experimental elastic constants are considered in evaluating the DF contribution.

The constant A_{DF} , obtained for 40.4 is $2.2988 \times 10^{-6} \text{ s}^2$, which is smaller than that of the value obtained from the isotropic elastic constants model. The lower cut-off frequency obtained in this case is 8.8 kHz. The upper cut-off frequencies in the directions parallel and perpendicular to the director are $9 \times 10^8 \text{ Hz}$ and $10 \times 10^8 \text{ Hz}$, respectively. The DF mechanism contributes effectively to the spin relaxation from 50 kHz to 3 MHz along with R. From 2 MHz onwards SD becomes more dominant than DF. The behavior of the NMRD data from 50 kHz to 2 MHz can be attributed to the combined effect of R and DF mechanisms. Above 2 MHz, frequency dependence results from SD and DF. R contribution becomes negligible, from 10 MHz onwards.

The correlation time obtained for rotations about the short molecular axis in the nematic phase of 40.4 from this model is $5.878 \times 10^{-8} \text{ seconds}$. The contribution to the total relaxation rate from R is quantified by the value $C = 1.238 \times 10^8 \text{ s}^{-1}$. While the correlation time for rotations show a slight variation, the contribution to the total relaxation increases at the cost of the DF contribution in this model.

In the case of *self-diffusion*, the values B and I are obtained as $506 \times 10^9 \text{ s}^2$ and $318 \times 10^{-10} \text{ m}^2 \text{ s}^{-1}$ respectively. The behavior of the SD contribution is almost the same as that of the previous model. SD shows its frequency behavior at much higher frequencies and hence the NMRD behavior of the nematic phase of 40.4 is characteristic the SD behavior only at high frequencies around 30 MHz.

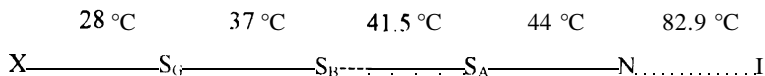
6.4.2.2. Comparison with the ordered smectic phases

Mechanisms identified for relaxation in N, S_A and S_C phases are different from the mechanisms identified for relaxation in S_B , S_G and solid phases. In the N, S_A , and S_C phases the important mechanisms are SD and R about the short axis, along with the nematic DF modes and smectic undulation modes. The negligible discontinuities of η' in the N- S_A and S_A - S_C transition regions and an almost non-discontinuity in the $T_{1\rho}$ values at these transitions supports this view, in contrast with the strong discontinuities found near N- S_B , S_A - S_B and S_A - S_G transitions regions.

Slowing down of diffusion process and the absence of DF mechanism are responsible for the sudden increase of T_1 in the smectic G phase near the S_B - S_G transition, in the conventional NMR frequencies [2j]. The increasing nature of T_1 in the S_B phase for few degrees is probably attributable due to the decreasing contribution from SD and R, of the whole molecules. A detailed discussion of the data in the smectic B phase in 40.4 is difficult due to the short temperature range of this phase. In the smectic G phase of the 40.4 the T_1 data show frequency as well as temperature dependence with the presence of a T_1 minimum. The mechanism, probably responsible for the T_1 behavior is the rotation of the core, as well as, the **segmental** motions of the chains. The contribution from the CH_3 rotations of the end chains are not be very efficient [24], when compared to the other two motions (rotations about the long axis and segmental motions) at these temperatures. Since there are two end chains and many CH_2 groups present in the system, several rotational diffusion modes could be present, leading to as many values of the correlation time, possible.

6.5. NMRD study of Butyloxybenzylidene Pentylaniline (40.5)

The system, next studied in 40.m series is *butyloxybenzylidenepentylaniline* (40.5). This system has the phase sequence given by [7],



A wide and stable nematic (39 °C) phase is seen from 82.9 °C to 44 °C. This highly stable nematic phase seen in the system with fairly symmetric end chains is an interesting point, to be noted.

6.5.7. Experimental Details

Proton spin-lattice relaxation time (7)) measurements were carried out as a function of frequency in the nematic phase of 40.5 at temperature 70 °C. The data from 65 kHz to 3 MHz was obtained using the field cycling NMR spectrometer and the high frequency data from 3 to 30 MHz was obtained, using the conventional NMR spectrometer [1]. The estimated errors in 7) measurements at frequencies below 1 MHz are found to be less than 7% and at above 1 MHz, around 5%. This temperature (70 °C) is chosen, since there are no pre-transitional effects found in the temperature dependent 7) data and this temperature is sufficiently away from N-I phase transition. The experimental NMRD data for nematic phase of 40.5 is shown in figure 6.19.

The observed NMRD data in the nematic phase of 40.5 has the following features.

1. The relaxation times ranging from 65 milliseconds at 65 kHz, to 469 milliseconds at 30 MHz, with a decreasing T_1 with decreasing frequency are observed in the entire frequency range studied.

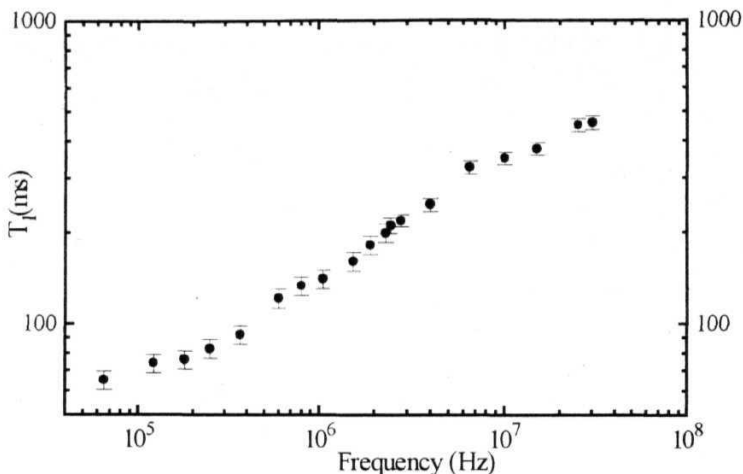


Figure 6.19. Frequency dependence of the spin-lattice relaxation time (T_1) in the nematic phase of 40.5 at temperature 70 °C. Error bars are also shown.

2. T_1 , in the logarithmic scale shows (figure 6.19) variation as a function of the Larmor frequency with lesser slope in the low frequencies. The slope increases in the intermediate frequencies. At low proton Larmor frequencies, the plot shows a very short region having a square-root behavior, indicating the presence of weaker DF contribution. NMRD data deviates from this behavior, from 1 MHz and a sharp variation is observed after this frequency.

3. Thus, the NMRD data in the nematic phase of 40.5 at 70 °C shows at least three different regions with different slopes, and hence, from the first look at the data suggests that there are three possible mechanisms with different frequency dependence.

4. In the conventional NMR region from 4 MHz to 30 MHz, the T_1 data in the nematic phase shows an interesting behavior with two different regions. The temperature dependent data at spot frequencies 4, 6.5, 10, 15, 20, 25, and 30 MHz are shown in figure 6.20.

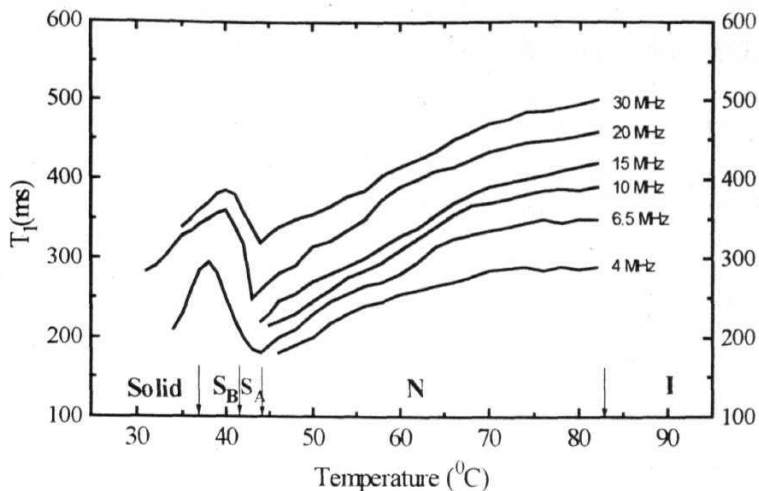


Figure 6.20. The behavior of the spin-lattice relaxation time T_1 as a function of temperature at different frequencies in 40.5. The arrows denote the transition temperatures

The first region closer to the I-N phase transition shows an almost constant T_1 behavior, with decreasing temperature. This trend continues for about 10 °C and another region with strong temperature dependence follows this region at lower temperatures. This second region is seen for about 35 °C, extending upto the nematic to smectic A phase transition. This trend is observed in all frequencies upto 30 MHz. Stronger temperature dependence is seen at higher frequencies.

5. T_1 data shows a sudden increase towards higher value at the smectic A to smectic B phase transition and this value increases with a decrease in temperature, finally reaching a maximum value near the S_A to S_B phase transition. The data in the highly ordered S_B and S_C phases show a strong temperature dependence and weak frequency dependence in the conventional NMR frequency range. The T_1 values slightly increases with frequency and strongly decreases with temperature within the frequency in the S_B and S_C phases

6.5.2. Data analysis

6.5.2.1. Nematic Phase

6.5.2.1.1. Isotropic elastic constants model

The frequency dependent relaxation rate ($R-T_1$) at 70 °C, in the nematic phase of 40.5, was fitted to an equation assuming contributions from **all** the three dynamic processes, viz., SD, R and DF (equation 6.1). The DF contribution to the NMRD data was fitted in two different ways. The first method is based on the *one constant approximation* with an assumption that $K_{11} = K_{22} = K_{33} = 1\text{e}^{-6}$ dyne (in this work it is also called as *isotropic elastic constants* model). The value of ADF and the lower cut-off frequency were varied to get a good fit. The DF contribution is quantified by the constant $A_{DF} = 3.47 \times 10^{-6} \text{ s}^{-2}$ in the case of the one constant approximation method. The estimation of the upper cut-off frequency becomes difficult in this case. A constant value was given in the model fitting in order to get a good fit. The lower cut-off frequency calculated from the analysis is 24 kHz. and the corresponding upper cut-off wavelength for the director modes is about 24800 Å. The physical significance of the lower cut-off frequency is conflicted in the literature [44] due to the presence of dipolar fields, and hence a correlation of the lower cut-off frequency (ν_{cel}) with the generally assumed domain size is not simple.

Contributions from various mechanisms to the measured R_1 data are shown in figure 6.21. The dynamic parameters obtained from this model fit are summarized in table 6.4. The uncertainty in determining the model parameters is about 10%. A qualitative picture of the NMRD model fit in the nematic phase of 40.5 reveals that, the DF modes dominate the spin relaxation, at low frequencies upto 6 MHz.

Rotations about the short axis, with a frequency independent behavior from 65 kHz to 300 kHz, and with a frequency dependent behavior upto 1 MHz, contribute to spin relaxation, alongwith the DF. SD becomes more important than R, from about 1 MHz and becomes the most dominating mechanism from 10 MHz. DF and SD

contribute equally at 6.5 MHz, where R has a negligible contribution. At high frequencies SD is solely responsible for relaxation, from about 10 to 30 MHz

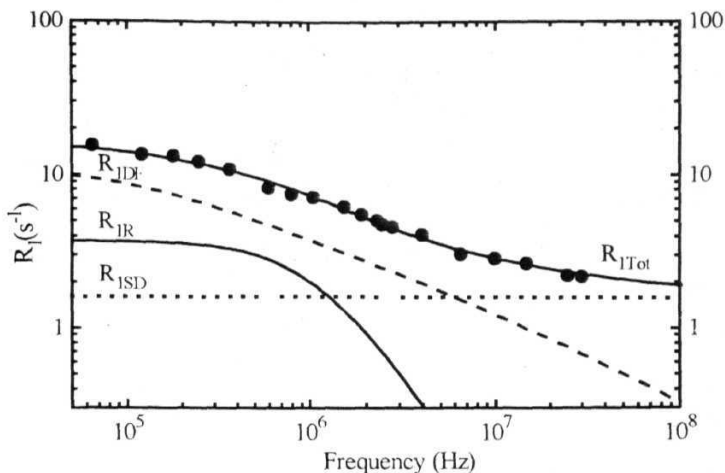


Figure 6.21. Proton relaxation rate (R , $1/T$) as a function of frequency in the nematic phase of 40.5 at 70 °C and model fit (eqn.6.1) to three individual contributions to the relaxation rate: director fluctuations (DF), self-diffusion (SD), and molecular reorientations about the short axis (R). Isotropic elastic constants model is assumed in evaluating the DF contribution.

From the NMRD data fitting, the percentage contributions of the various dynamical processes at different frequencies can be quantified. For example at 65 kHz, the contribution from DF mechanism to the total relaxation is about 65.5%. The contribution from R and SD are about 23.5% and 10% respectively. At 370 kHz, the contributions from DF, R and SD are about, 52%, 32%, and 16% respectively. This trend continues, and finally R becomes equal to SD and DF at 2.8 MHz. The contributions at 1 MHz are 49% due to DF, 28% due to R and 23% due to SD. The contribution from SD and R becomes equal at 1.2 MHz. At 6.5 MHz, the contribution from R becomes negligible, where SD and DF contributes equally to the spectral density. At the highest measured frequency (30 MHz), DF contribution becomes 32%

and the remaining 68% relaxation is due to SD mechanism. This analysis is consistent with the strong temperature dependence, characteristic of SD, seen in the T_c data at higher frequencies.

Table 6.4

Model Parameters	Isotropic elastic constants model	Anisotropic elastic constants model
Nematic director fluctuations (DF)		
K_c (in 10^{-6} dynes)	1	0.8
K_{22} (in 10^{-6} dynes)	1	0.55
K_{33} (in 10^{-6} dynes)	1	1.2
A_{DF} (in 10^{-6} s $^{-2}$)	3.47	2.66
q_{zcl} (in 10^5 l/Am)	2.53	1.756
f_{zcl} (in kHz)	24	11.77
λ_{zch} (in Å)	2480	3578
q_{zch} (in 10^7 l/Am)	6.8	3.024
f_{zch} (in MHz)	1400	349
λ_{zcl} (in Å)	9.24	20.77
q_{zch} (in 10^7 l/Am)	6.4	5.4
f_{zch} (in MHz)	1300	930
λ_{zcl} (in Å)	9.81	11.6
Translational self-diffusion (SD)		
B (in 10^9 s $^{-2}$)	456.6	444.8
D (in 10^{-10} m 2 s $^{-1}$)	363.1	349.6
Rotations about the short axis (R)		
τ_R (in 10^8 s $^{-2}$)	0.45	0.482
τ_R (in 10^{-9} s)	82.1	64.1

The correlation time obtained for rotations about the short molecular axis in the **nematic** phase of 40.5 is 8.21×10^{-8} seconds. Contribution to the total relaxation rate from R is quantified by the value $C = 4.5 \times 10^7 \text{ s}^{-1}$.

Self-Diffusion

In the case of *self-diffusion*, the model parameter B (the amplitude) is equal to $4.566 \times 10^{11} \text{ s}^{-2}$, and D (the average diffusion constant) is equal to $36.3 \times 10^{-5} \text{ m}^2 \text{ s}^{-1}$. The frequency independent contribution from SD extends to higher frequencies in 40.5. The complete profile of the diffusion curve could not be obtained due to lack of data at high frequencies, above 30 MHz. The diffusion constant obtained in this case is higher than the D value obtained from direct methods. One probable reason for such a difference (about an order of magnitude) is probably due to the non-availability of the NMRD data in the region of frequencies, where one can see the complete dispersion of SD

6.5.2.1.2. Anisotropic elastic constants model

The second method, with the anisotropic elastic constants ($K_{11} = 0.8 \times 10^{-6}$, $K_{22} = 0.55 \times 10^{-6}$ and $K_{33} = 1.2 \times 10^{-6}$ dyne) model for DF contribution gives a slightly different picture. The model fit is shown in figure 6.22. The elastic constants are calculated by extrapolating experimental data for 40.4 [30]. The details of the calculation of the elastic constants have been given at the beginning of the chapter (section 6.1). The constant A_{DF} obtained for 40.5 is $2.6597 \times 10^{-6} \text{ s}^{-2}$, which is smaller than the value obtained from the one constant approximation model. The lower cut-off frequency in this case is 11.7 kHz. The upper cut-off frequencies in the directions parallel and perpendicular to the director are $3.5 \times 10^8 \text{ Hz}$ and $9.3 \times 10^8 \text{ Hz}$, respectively. The parameters obtained from both these methods are given in table 6.4

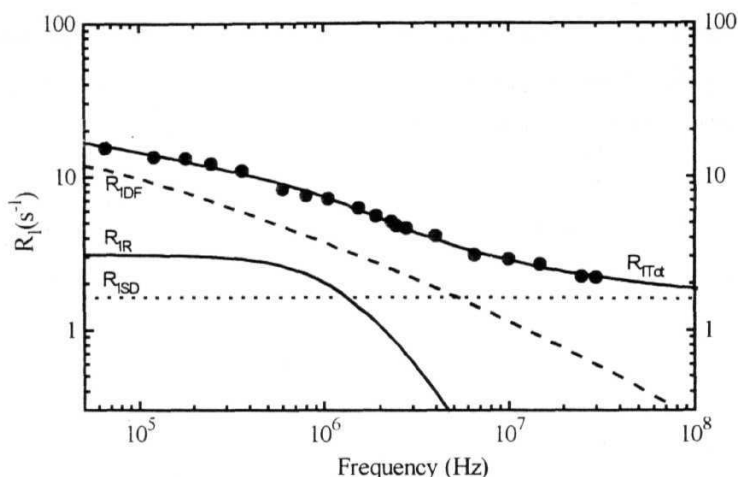


Figure. 6.22. Proton relaxation rate ($R_l - I T_l$) as a function of frequency in the nematic phase of 40.5 at 70 °C and model fit (eqn. 6.1) to three individual contributions to the relaxation rate: director fluctuations (DF), self-diffusion (SD), and molecular reorientations about the short axis (R). Anisotropic elastic constants model is considered for DF contribution.

The correlation time obtained for rotations about the short molecular axis in the nematic phase of 40.5 is 8.21×10^{-8} seconds. The contribution to the total relaxation rate from R is quantified by the value ($\tau = 4.5 \times 10^7 \text{ s}^{-1}$). The correlation time changes slightly when comparing with the earlier analysis. In the case of *self-diffusion*, the model parameter B is equal to $4.566 \times 10^{11} \text{ s}^{-2}$, and D , the average diffusion constant is equal to $36.3 \times 10^{-5} \text{ m}^2 \text{ s}^{-1}$. Diffusion parameters (B and D) obtained with the anisotropic elastic constants model for DF modes are almost the same as that of the parameters obtained in the case of the isotropic elastic constants model.

6.5.2.2 Smectic A phase

NMRD data measured in the smectic A phase from 65 kHz to 30 MHz, is shown in figure 6.23. This data was fitted with the theoretical equation incorporating three dynamical processes namely, the smectic layer undulation modes (LU), SD and R. Thus, the spin-lattice relaxation rate (R_{1Tot}) in the S_A phase can be written as

$$R_{1Tot} = R_{1LU} + R_{1SD} + R_{1R} \quad (6.4)$$

where R_{1LU} given by equation 6.3, represents the contribution to total R_1 , from the smectic layer undulation modes. Different contributions to the relaxation rate in the smectic A phase of 40.5 shown in figure 6.24.

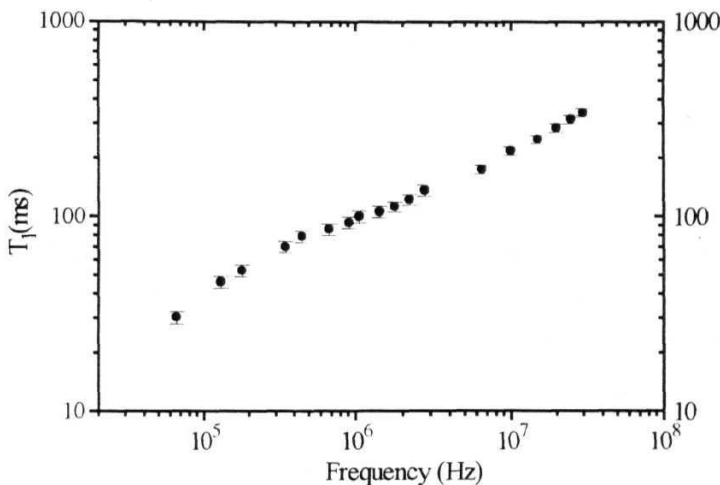


Figure 6.23. Frequency dependence of the spin-lattice relaxation time (T_1) in the smectic A phase of 40.5 at temperature 43 °C. Error bars are also shown in figure.

LU contribution in the smectic A phase is dominant, only upto 200 kHz, in 40.5. Diffusion becomes more important, and strongly contributes to relaxation in the S_A phase of 40.5. SD contribution is almost frequency independent upto 10 MHz. R also contributes to the relaxation rate, till about a few MHz. From 6.5 MHz, SD mediates the relaxation completely, where R and DF become negligible.

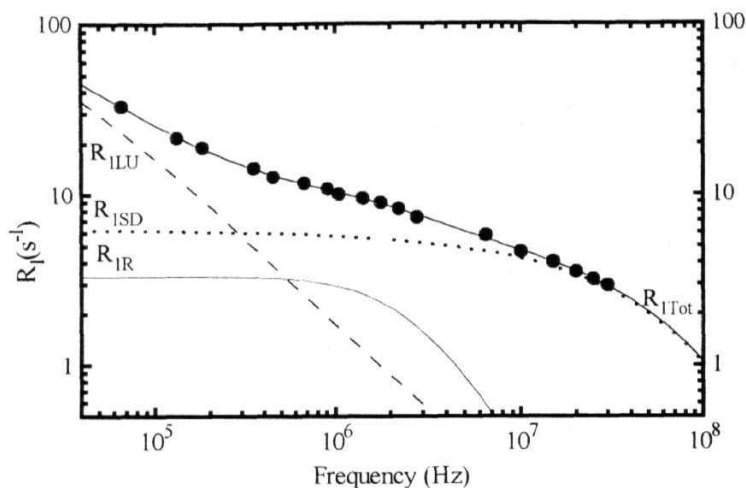


Figure 6.24. Proton relaxation rate (R_1 / T_1) as a function of frequency in the smectic A phase of 40.5 at 43 °C and model fit (eqn. 6.4) to three individual contributions to the relaxation rate: layer undulations (LU), self-diffusion (SD), and molecular reorientations about the short axis (R).

The $T_{1\rho}$ data in the smectic A phase [1] shows temperature dependence. This is qualitatively different from the $T_{1\rho}$ data obtained from the higher homologous 40.6, 40.7 and 40.9, where $T_{1\rho}$ data in the S_A phase are almost temperature independent. The strong SD contribution in the S_A phase of 40.5 at low frequencies as observed in the present analysis is consistent with the temperature dependent $T_{1\rho}$ behavior. The model parameters obtained for SD and R about the short axis in the S_A phase are given in the table 6.5. The parameters for LU are not presented here due to the large uncertainty in evaluating them in the present NMRD frequency range. It is known that [11,48,51] LU mechanism strongly contributes at lower frequencies, where the T_1 data was not collected due to the experimental limitations. The estimated errors in the evaluation of the dynamic parameters for SD and R are around 10%

Table 6.5.

Translational self-diffusion (SD)	
B (in 10^9 s^{-2})	1.14
D (in $10^{11} \text{ m}^2 \text{ s}^{-1}$)	2.1753
Rotations about the short axis (R)	
C (in 10^8 s^{-2})	0.91
TR (in 10^{-8} s)	4.1644

6.5.2.3. Ordered *smectic* Phases

The NMRD data obtained in the case of 40.5 smectic B phase is shown in figure 6.25 NMRD data is fitted to SD and R mechanisms, as shown in figure 6.26. The models used in the evaluation of the contributions from SD and reorientations are presented in the chapter 5

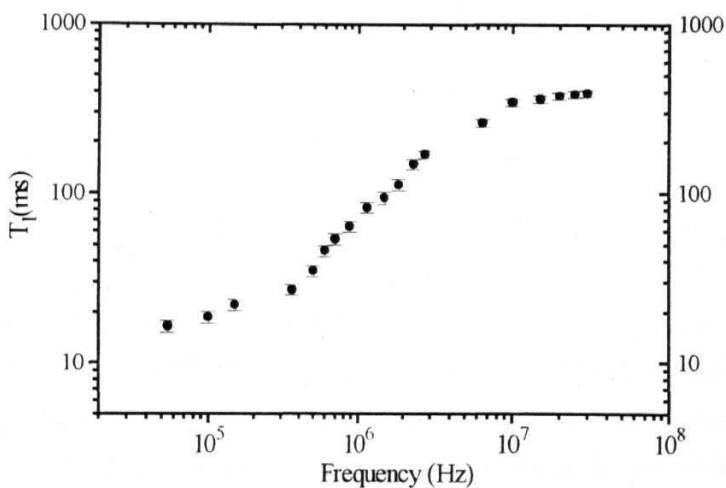


Figure 6.25 Frequency dependence of the spin-lattice relaxation time (T_1) in the smectic B phase of 40.5 at temperature 40 °C Error bars are also shown.

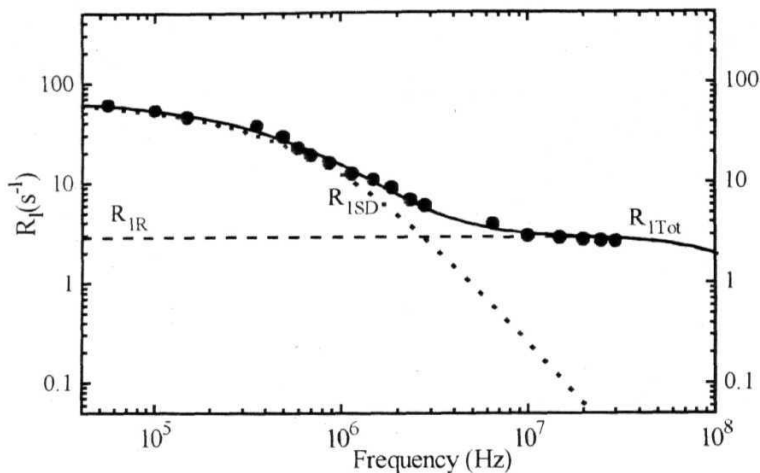


Figure 6.26. Proton relaxation rate (R_1 / T_1) as a function of frequency in the smectic B phase of 40.5 at 40 °C and model fit to the individual contributions to the relaxation rate: self-diffusion(SD), and molecular reorientations (R).

Table 6.6

Model Parameters	From 40.5-S _B
B (in 10V)	1.4056
D (in $10^{-13} \text{ m}^2 \text{ s}^{-1}$)	2.412
C' (in 10^9 s^{-1})	4.659
τ_R (in 10^{-10} s)	6.055

The low frequency region is completely dominated by the SD mechanism and the higher frequency relaxation, by rotations. This interpretation is consistent with the observations made with the temperature dependent data [2]. In the highly ordered smectic B phase, the diffusion constant becomes very small ($D = 2.41 \times 10^{-9} \text{ cm}^2/\text{s}$) and relaxation dispersion is explained by the SD process. A relatively small, frequency independent contribution comes from R at low frequencies. The strong temperature

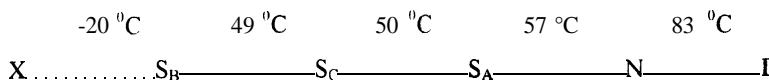
dependence seen in the high frequency τ_c data is consistent with this view. The temperature dependence of $T_{1\rho}$ at these temperatures represents the SD mechanism. The explanation given for the $T_{1\rho}$ data for the S_B phase is also consistent with the NMRD analysis. The dynamic parameters are given in table 6.6. Typical errors in estimating the dynamic parameters in this case is about 15%.

Rotations in the ordered smectic (S_B and S_G) phases can be best described using three different rotational dynamic processes generally present in the chain molecules [24]. The observations made by earlier studies [24] that have been described in the introductory section of this chapter (section 6.1), are useful in understanding the contributions of various dynamic processes to τ_c and $T_{1\rho}$ in the ordered smectic phases and also in the solid phases. The sudden increase of τ_c , observed near the transition from smectic A to smectic B in both $T_{1\rho}$ and τ_c at frequencies between 5-30 MHz clearly demonstrates the basic difference between the dynamic properties of highly ordered smectic phases and the fluid like nematic and smectic A phases. Slowing down of the diffusion process and the absence of the DF mechanism are responsible for the sudden increase of τ_c in the smectic G phase near the SB-SG transition, in the conventional NMR frequencies. In the smectic B and smectic G phases of the 40.5, the τ_c data shows a weak frequency dependence and strong temperature dependence.

The probable mechanisms responsible for the $R_{1\rho}$ behavior shown in the NMRD data analysis are due to the rotation of the core, to a large extent and due to the segmental motions of the chains. In 40.5, anisotropic rotational diffusion motions of the end hydrocarbon chains, of the entire molecule, or of just the core rigid portions, are possible at these temperatures. From the behavior of the data in the S_B and S_G phases at the measured temperature ranges, it can be concluded that, the major contribution is from the rotations of the molecule around the long axis and from the segmental motions.

6.6. NMRD study of Butyloxybenzylidene Heptylaniline (40.7)

The next system, studied in the 40.m series is *butyloxybenzylidene heptylaniline* (40.7). This system has the phase sequence given by [7],



A stable and wide nematic phase (26 $^{\circ}\text{C}$) seen from 83 $^{\circ}\text{C}$ to 57 $^{\circ}\text{C}$ and a smectic A phase with a temperature range of about 7 $^{\circ}\text{C}$ is observed in 40.7. A smectic C phase of about 1 $^{\circ}\text{C}$ along with a very wide S_B phase ranges from 49 $^{\circ}\text{C}$ to -20 $^{\circ}\text{C}$ were also seen.

6.6.1. Experimental Details

Proton spin-lattice relaxation time (T_1) measurements were carried out as a function of frequency in the nematic phase of 40.7, at a temperature of 75 $^{\circ}\text{C}$. The data from 50 kHz to 3 MHz was obtained using the field-cycling NMR spectrometer, and the high frequency data from 3 to 30 MHz were obtained using the conventional NMR spectrometer [1]. The estimated errors in T_1 measurements at frequencies below 1 MHz are found to be less than 7% and at above 1 MHz, around 5%.

Experimental NMRD data for nematic phase are shown in figure 6.27. The temperature dependent data at spot frequencies at 6.5, 10, 15, 20, and 30 MHz are shown in figure 6.28. The observed NMRD data in the nematic phase of 40.7 has the following features.

1. The relaxation times range from 49.5 milliseconds at 50 kHz to 480 milliseconds at 30 MHz

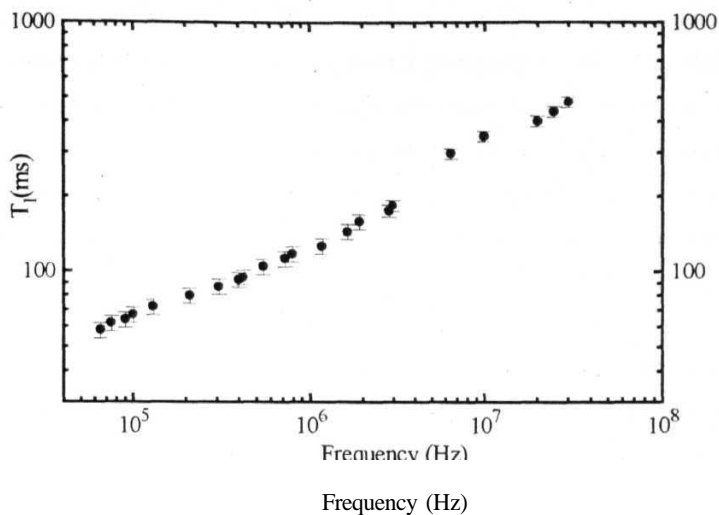


Figure 6.27. Frequency dependence of the spin-lattice relaxation time (T_1) in the nematic phase of 40.7 at temperature 75 °C. Error bars are also shown.

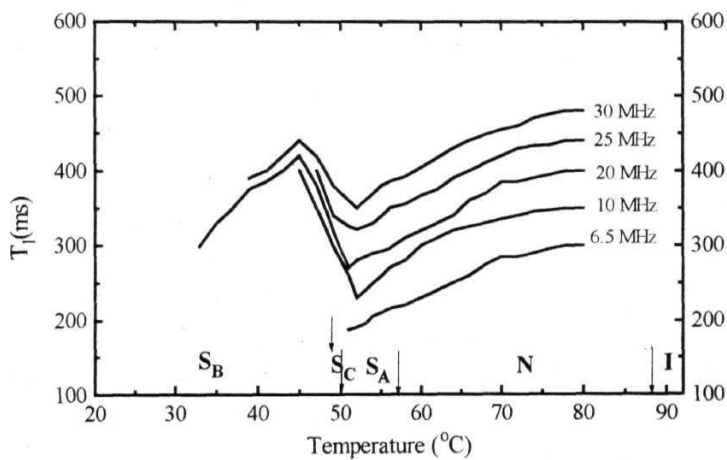


Figure 6.28 The behavior of the spin-lattice relaxation time (T_1) as a function of temperature at different frequencies in 40.7. The arrows denote the transition temperatures

2. T_1 in the logarithmic scale (figure 6.28) shows a steep variation as a function of the Larmor frequency at low frequencies, from 50 kHz to 1 MHz. The slope increases in the intermediate frequencies (from 1 MHz to 10 MHz) and finally reaches another region with lesser slope at higher frequencies (10 to 30 MHz). The plot between relaxation rate and frequency (in Hz) at low proton Larmor frequencies, show a slightly longer region having a square-root like behavior, indicating the presence of a longer region with DF mechanism. The NMRD data deviates from this behavior, from about 2 MHz.

3. Thus NMRD data in the nematic phase of 40.7 at 75 °C shows at least two different regions with different slopes, and hence a first glance at the data suggests that there are at least two possible mechanisms with different frequency dependencies.

4 In the conventional NMR region from 6.5 MHz to 30 MHz, the T_1 data shows an interesting behavior with two different regions. The first region close to the I-N phase transition show, almost a constant T_1 value with decreasing temperature. This trend continues for about 10 °C and the second region with strong temperature dependence is seen below this temperature range. This region continues for about 16 °C extending upto the nematic to smectic A phase transition. The temperature independent region decreases with increasing frequency.

5. NMRD data in the smectic A phase shows three regions with different slopes. The first region (though very short) with steep behavior is seen below 150 kHz. The second region with a lesser slope is observed from 200 kHz to 6.5 MHz and finally, it reaches a different region with very weak frequency dependence above 6.5 MHz.

6. This behavior indicates the presence of three mechanisms. The short region having a very high slope is probably due to the LU mechanism. The observed continuity between the nematic and smectic A phase (in the temperature dependent T_1 data) suggests that there are common mechanisms, which influence spin relaxation in the conventional NMR frequencies. The T_1 in the smectic A phase shows strong temperature dependence This behavior is almost similar, at all the frequencies.

7. A sudden increase towards higher value of I) at the smectic A to Smectic B phase transition is seen in the data and this value increases with decreasing temperature. The data in the ordered S_B phase shows strong temperature dependence and weak frequency dependence in the conventional NMR frequency range.

6.6.2. Data analysis

6.6.2.1. Nematic Phase

6.6.2.1.1. Isotropic elastic constants model

It is important to introduce the contribution from the rotation about the short molecular axis (R), along with the SD and DF in the analysis in order to explain the intermediate frequency range from a few hundred kHz to a few MHz. Similarly, the low frequency cut-off is necessary to fit the low frequency data at kHz range satisfactorily. So, the frequency dependent relaxation rates ($R = 1/\tau$) at 75 °C in the nematic phase of 40.7 were fitted to the following equation assuming a contribution from all the three dynamic processes, viz., SD, R and DF.

$$R_{tot} = R_{DF} + R_{SD} + R_{R}$$

The value of A_{DF} and the cut-off frequencies were varied to get good fit. The DF contribution is quantified by the constant $ADF = 3.457 \times 10^{-6} \text{ s}^{-2}$ in the case of the one constant approximation method. The lower cut-off frequency is about 18 kHz, and the corresponding upper cut-off wavelength for the director modes is 39800 Å.

Relative contributions

The contributions from various mechanisms to the measured R_i data are shown in figure 6.29. The dynamic parameters obtained from this fit are summarized in table 6.7. The uncertainty in obtaining the dynamic parameters is found to be about 10%. A qualitative picture of the fit in the nematic phase of 40.7 reveals that the DF

modes dominate the spin relaxation upto 6 MHz. R about the short axis with frequency independent behavior from 50 kHz to 1 MHz and with a frequency dependent behavior upto 3 MHz, contributes to spin relaxation alongwith the DF and SD. SD becomes more important than R, from about 2.2 MHz and becomes the most dominant mechanism, from 7 MHz. DF and SD contributes equally at 7 MHz, where R has a negligible contribution. At high frequencies SD is the dominating mechanism over DF for relaxation, from 20 to 30 MHz.

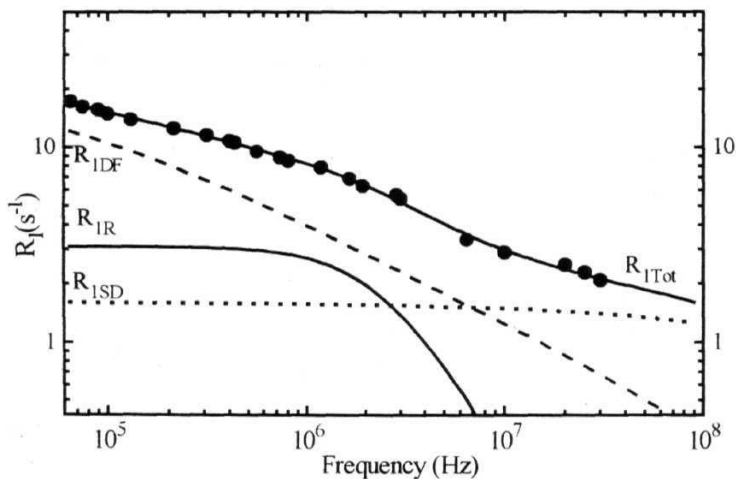


Figure 6.29. Proton relaxation rate ($R_1 - 1/T_1$) as a function of frequency in the nematic phase of **4O.7** at 70 °C and model fit to three individual contributions to the relaxation rate: director fluctuations (DF), self-diffusion (SD), and molecular reorientations about the short axis (R). Isotropic elastic constants are assumed in evaluating the DF contribution.

Table 6.7

Model Parameters	Isotropic elastic Constants model	Anisotropic elastic constants model
Nematic director fluctuations (DF)		
K_{11} (in 10^6 dynes)	1	0.633
K_{22} (in 10^6 dynes)	1	0.422
K_{33} (in 10^6 dynes)	1	0.915
A_{DF} (in 10^{-6} s ⁻²)	3.458	1.38
q_{zcl} (in 10^5 1/Åm)	1.6	1.04
f_{zcl} (in kHz)	8.1	3.15
λ_{zch} (in Å)	3900	6033
q_{zch} (in 10^7 1/Åm)	6.8	6.8
f_{zch} (in MHz)	1400	1340
λ_{zcl} (in Å)	9.24	9.24
$q_{\perp ch}$ (in 10^7 1/Åm)	6.4	6.4
$f_{\perp ch}$ (in MHz)	1300	1300
$\lambda_{\perp cl}$ (in Å)	9.81	9.81
Translational self-diffusion (SD)		
B (in 10^9 s ⁻²)	6.386	444.8
D (in 10^{-10} m ² s ⁻¹)	5.07	349.6
Rotations about the short axis (R)		
C (in 10^8 s ⁻²)	0.912	484
τ_R (in 10^{-9} s)	33.89	3.73

A more quantitative picture of the relative contributions can be obtained by calculating the percentage contribution due to various mechanisms. For example at 50 kHz, the contribution from DF mechanism to the total relaxation is about 65.5%. The contributions from R and SD are about 23.5% and 10% respectively. At 370 kHz, the contributions from DF, R and SD are about, 52%, 32%, and 16% respectively.

This trend continues, and finally R becomes equal to SD and DF at 2.8 MHz. The contributions at 1 MHz are 49% due to DF, 28% due to R and 23% due to SD. The contributions from SD and R become equal at 1.2 MHz. At 6.5 MHz, the contribution from R becomes negligible, where SD and DF contributes equally to the spectral density. At the highest measured frequency (30 MHz) the DF contribution becomes 32% and the remaining 68% relaxation is almost due to SD mechanism. This view is consistent with the strong temperature dependence expected for SD of the T_1 data.

The correlation time obtained for rotations about the short molecular axis in the nematic phase of 40.7 is 3.389×10^{-8} seconds. The contribution to the total relaxation rate from R is **quantified** by the value $C = 9.124 \times 10^7 \text{ s}^{-1}$. Presence of strong contribution from DF modes in the nematic phase at low frequencies in the kHz region lead to the temperature dependent dipolar relaxation times (T_{1D})[1].

In the case of *self-diffusion*, the model parameters are B (the amplitude obtained as $6.38 \times 10^9 \text{ s}^{-2}$), and D (the average diffusion constant obtained as $5.07 \times 10^{-6} \text{ m}^2 \text{ s}^{-1}$). The strong temperature dependence at high frequency data observed is due to the presence of SD process at high frequencies.

6.6.2.1.2. Anisotropic elastic constants

The complete description of the functions and parameters are involved in this generalized model (called anisotropic elastic constants model) have been described in chapter 5. The experimental elastic data given by Tolmachev et al., [30] for 40.4 is deduced, keeping the general trends followed by other homologous series of nematic liquid crystals in mind, in order to obtain elastic constants for the 40.7 system. NMRD fitting with anisotropic elastic constants is shown in figure 6.30. In this model the A_{DF} value obtained is $1.38 \times 10^{-6} \text{ s}^{-2}$ which is lesser compared to the value obtained from the isotropic elastic constant model. The lower cut-off frequency in this case is 3.15 kHz, which is smaller than the value obtained from the one constant elastic constants model. Model fitting is better in the case of the anisotropic elastic constants model.

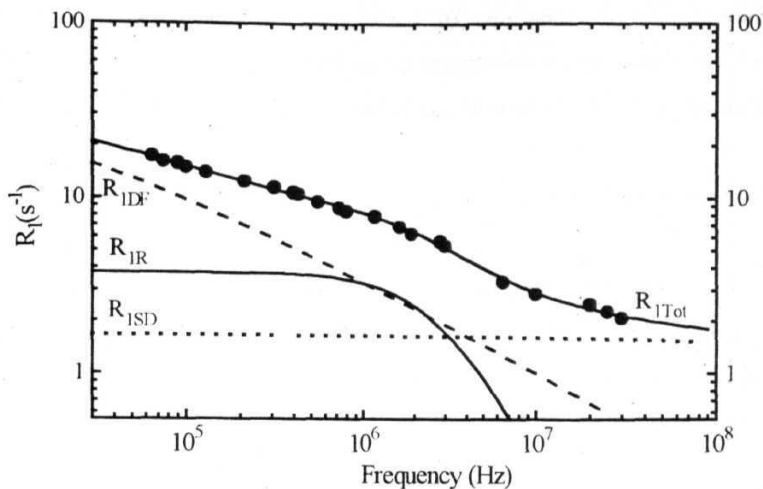


Figure 6.30. Proton relaxation rate ($R_1 - 1/T_1$) as a function of frequency in the **nematic** phase of 40.7 at 70 °C and model fit to three individual contributions to the relaxation rate: director fluctuations (DF), self-diffusion (SD), and molecular reorientations about the short axis (R). Anisotropic elastic constants model is considered for DF contribution.

The correlation time obtained for rotations about the short molecular axis in the nematic phase of 40.7 is 3.73×10^{-9} seconds. The contribution to the total relaxation rate from R is quantified by the value $C = 48.4 \times 10^9 \text{ s}^{-1}$. In the case of *self-diffusion*, the model parameter B is equal to $44.48 \times 10^{10} \text{ s}^{-2}$ and D , the average diffusion constant is equal to $349.6 \times 10^{-10} \text{ m}^2 \text{ s}^{-1}$. Diffusion parameters (B and D) obtained with the anisotropic elastic constants model for DF modes are very different from **the** parameters obtained in the case of the isotropic elastic constants model.

DF mechanism dominates spin relaxation from 50 kHz to 1 MHz. where the contribution from the R frequency independent. From 1 MHz. R and DF contribute equally and this explains the slight deviation in the experimental NMRD data from 1MHz to 3 MHz From 3 MHz onwards, SD contribution becomes comparable with the DF contribution. From 3 to 4 MHz, all the three mechanisms contribute almost equally. R loses its important from 7 MHz SD becomes the most dominating

mechanism from 4 MHz onwards. DF contribution becomes very less from 20 MHz. where SD is responsible for the frequency dependence in the NMRD data. Percentage contributions can be calculated from this fitting.

6.6.2.2. Smectic A phase

The NMRD data collected in the smectic A phase (figure 6.3 1) was fitted with the theoretical equation incorporating the three dynamical processes namely 1. Smectic layer undulation modes (LU), 2. SD and 3. Rotations about the short axis. The details of the theoretical formalism are given in chapter-5.

Each of these contributions has characteristic frequency and temperature dependencies, which have already been discussed, in the introductory section. Different contributions to the relaxation rate are shown in figure 6.32

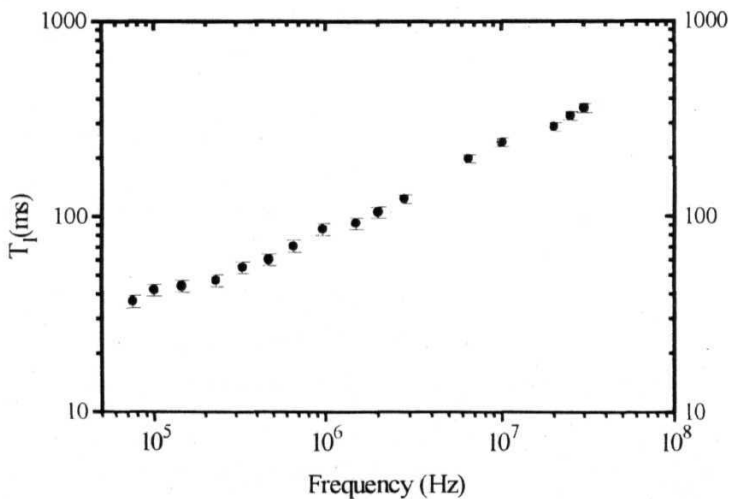


Figure 6.31. Frequency dependence of the spin-lattice relaxation time (T_1) in the smectic A phase of 40.7 at temperature 54 °C. Errors bars are also shown.

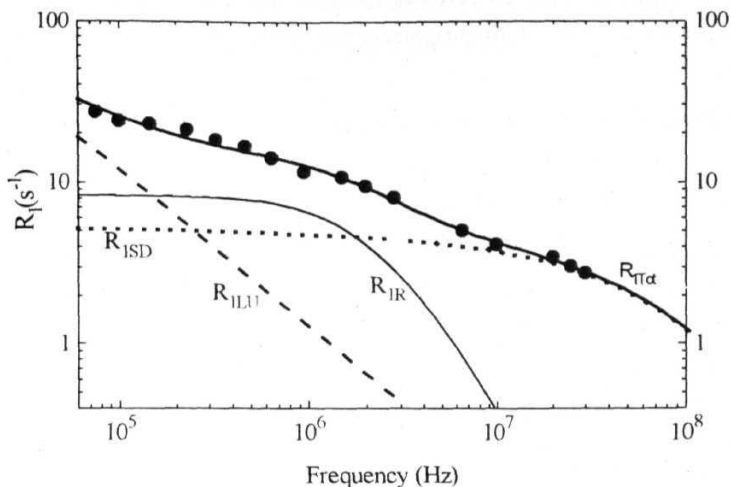


Figure 6.32. Proton relaxation rate (R_1 $1/T_1$) as a function of frequency in the smectic A phase of 40.7 at 54 °C and model fit (equation 6.4) to three individual contributions to the relaxation rate: layer undulations (LU), self-diffusion (SD), and molecular reorientations about the short axis (R).

The parameters are given in table 6.8. LU contribution in the smectic A phase is dominant upto 150 kHz in 40.5. The dynamic parameters related to the LU mechanism are not given keeping the large uncertainties in evaluating the values in the present frequency range where LU contribution is very weak. The dynamic parameters are obtained within the error limit of about 10% in this case also.

R becomes more important from 150 kHz to 2 MHz in this case and strongly contributes to the relaxation in the S_A phase of 40.7. From 6.5 MHz, SD mediates the relaxation completely where R and LU becomes negligible. SD contribution is almost frequency independent upto 3 MHz. The T_{1D} data in smectic A phase shows temperature independence. This is qualitatively different from the T_{1D} data obtained from the other homologue 40.5, where T_{1D} data, in the S_A phase is almost

temperature dependent. Weak contribution of SD in the S_A phase of 40.7 at low frequencies is consistent with the temperature independent T_{LD} behavior.

Table 6.8

Translational self-diffusion (SD)	
$B(\text{in } 10^9 \text{ s}^{-2})$	1.384
$D(\text{in } 10^{-11} \text{ m}^2 \text{ s}^{-1})$	3.369
Rotations about the short axis (R)	
$C(\text{in } 10^8 \text{ s}^{-1})$	1.826
$\tau_R(\text{in } 10^{-8} \text{ s})$	4.549

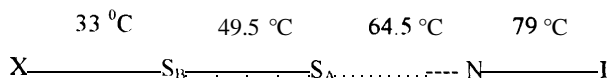
6.6.2.3. Comparison with the ordered smectic phase

The observations made in the literature [24] which have been described in the introductory section of this chapter, are useful in understanding the contributions of various dynamic processes to T_1 and T_{LD} in the highly ordered smectic B phases. The observed increase of T_1 at the transition from smectic A to smectic B in both T_{LD} and T_1 at frequencies between 5-30 MHz clearly demonstrates the difference between the dynamic properties of highly ordered smectic phases and the fluid like nematic and smectic A phases.

Slowing down of diffusion process and the absence of the DF/LU mechanism are responsible for the sudden increase of T_1 in the smectic B near the S_A - S_B transition, in the conventional NMR frequencies. In the smectic B phase of the 40.7 the T_1 data shows strong temperature dependence. The probable mechanisms responsible for the T_1 behavior shown in the data are the rotation of the core, and due to the **segmental** motions of the chains. From the behavior of the data in the S_B phase at the measured temperature ranges, it can be concluded that, the major contribution comes from the rotations of the molecule around the long axis and from the segmental motions.

6.7. NMRD study of Butyloxybenzylidene Octylaniline (40.8)

The next system under study in the 40.m series is *butyloxybenzylidene octylaniline* (40.8). This system has the phase sequence given by [7],



6.7.7. Experimental Details

Proton spin-lattice relaxation time (T_1) measurements were carried out as a function of the Larmor frequency in the nematic phase of 40.8 at temperature 71°C . The NMRD data from 50 kHz to 3 MHz was obtained using the field cycling NMR spectrometer and the high frequency data from 3 to 45 MHz was obtained using the conventional NMR spectrometer. The estimated errors in T_1 measurements at frequencies below 2 MHz found to be less than 7% and at above 2 MHz, around 5%

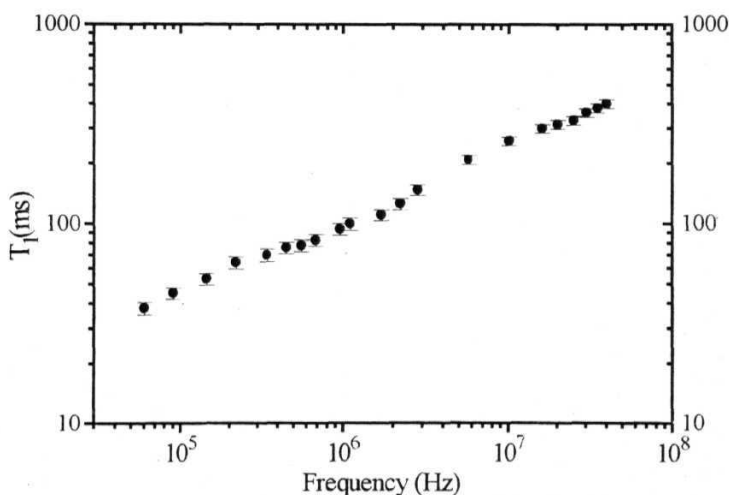


Figure 6.33. Frequency dependence of the spin-lattice relaxation time (T_1) in the nematic phase of 40.8 at temperature 71°C . Error bars are also shown.

The experimental NMRD data is shown for the **nematic** phase in figure.6.33. The observed NMRD data in the nematic phase of 40.8 has very interesting features. The relaxation times range from 38 milliseconds at 50 kHz to 400 milliseconds at 40 MHz. T_1 in the logarithmic scale shows a steep variation as a function of Larmor frequency at low frequencies, from 50 kHz to 300 kHz. The slope decreases in the intermediate frequencies (from 400 kHz to 900 kHz). Another region with increased slope at the intermediate frequency range from 1 to 10 MHz is seen, which is followed by a region with very small variation from 10 to 45 MHz. Thus, the NMRD data show four different regions, indicating the presence of three different processes with different frequency dependencies.

At low proton Larmor frequencies, the NMRD data show a region having square-root behavior indicating the presence of stronger DF mechanism at this frequency range. The NMRD data deviates from this behavior from about 500 kHz and a slight slope change follows this region indicating the presence of another mechanism along with DF.

6.7.2. Data analysis

6.7.2. 1. Nematic Phase

6.7.2.1.1. Isotropic elastic constants model

The frequency dependent relaxation rate ($R = 1/T_1$) at 68 °C in the nematic phase of 40.8 was fitted to an equation assuming contributions from all the three dynamic processes, viz., SD, R and DF. The total spin lattice relaxation rate (R_{1Tot}) can be written as

$$R_{1Tot} = R_{1DF} + R_{1SD} + R_{1R}$$

In **40.8** the DF contribution to the NMRD data was fitted in two different ways. **The** first method is based on the one constant approximation (K_{11} K_{22} K_{33} = $1e^{-6}$ dyne). The value of A_{DF} and the cut-off frequencies were varied to get a good fit.

The DF contribution is quantified by the constant $A_{DF} = 4.14 \times 10^{-6} \text{ s}^2$ in the case of one the constant approximation method. The lower cut-off frequency is about 860 Hz, and the corresponding upper cut-off wavelength for the director modes is about 12000 Å.

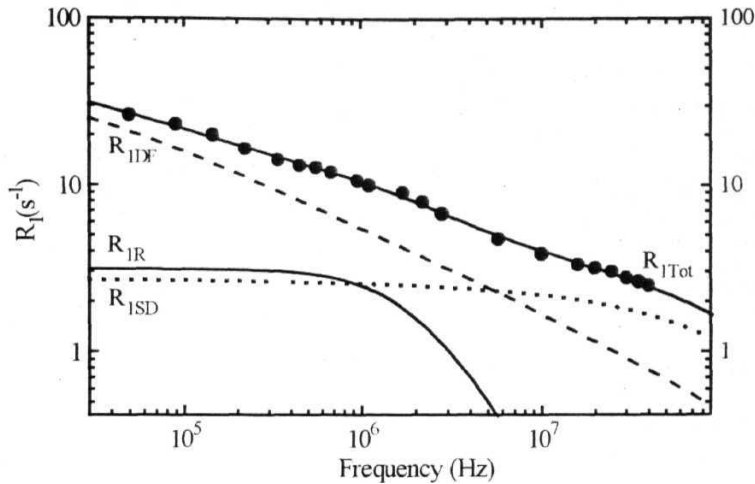


Figure 6.34. Proton relaxation rate ($R_1 = 1/T_1$) as a function of frequency in the nematic phase of 40.8 at 71 °C and model fit to three individual contributions to the relaxation rate: director fluctuations (DF), self-diffusion (SD), and molecular reorientations about the short axis (R). Isotropic elastic constants model is assumed for DF contribution.

Upper cut-off frequencies and other dynamic parameters are given in table 6.9. The errors estimated in evaluating the dynamic parameters are about 10 %. The contributions from various mechanisms to the measured R_1 data are shown in figure 6.34. A qualitative picture of the fit in the nematic phase of 40.8 reveals that the DF modes dominate the spin relaxation at low frequencies which extend upto 5.7 MHz. R about the short axis with a frequency independent behavior from 50 kHz to 800 kHz and with a frequency dependent behavior upto 10 MHz contributes to the spin relaxation along with the DF. Frequency independent SD becomes more important than R, from about 1 MHz and becomes the most dominating mechanism from 5.7 MHz. DF and SD contribute equally at 5.7 MHz, where R has a negligible

contribution. At high frequencies SD and DF contributes to the spin relaxation from 15 to 30 MHz. This interpretation is supported also by the weak temperature dependence of the T_1 data at high NMR frequencies.

Table 6.9

Model Parameters	Isotropic elastic constants model	Anisotropic elastic constants model
Nematic director fluctuations (DF)		
K_1 (in 10^{-6} dynes)	1	0.635
K_{22} (in 10^{-6} dynes)	1	0.422
K_{33} (in 10^{-6} dynes)	1	0.917
A_{DF} (in 10^{-6} s $^{-2}$)	4.639	2.026
q_{zcl} (in 10^5 l/Am)	0.94	1.04
f_{zcl} (in kHz)	2.18	0.589
λ_{zch} (in Å)	6680	10668
q_{zch} (in 10^7 l/Am)	6.8	5.5
f_{zch} (in MHz)	1400	882
λ_{zcl} (in Å)	9.24	11.4
$q_{\perp ch}$ (in 10^7 l/Am)	6.4	6.8
$f_{\perp ch}$ (in MHz)	1300	1470
$\lambda_{\perp cl}$ (in Å)	9.81	9.24
Translational self-diffusion (SD)		
B (in 10^9 s $^{-2}$)	1.516	3.256
D (in 10^{-10} m 2 s $^{-1}$)	0.7122	1.642
Rotations about the short axis (R)		
C (in 10^8 s $^{-2}$)	0.70	0.9797
τ_R (in 10^{-9} s)	44.37	39.55

A more quantitative picture of the relative contributions can be obtained by calculating the percentage contribution due to various mechanisms. For example at 50 kHz, the contribution from DF mechanism to the total relaxation is about 76.5% and the contribution from R and SD are about 14.4% and 9.1% respectively. At 200 kHz, the contributions from DF, R and SD are about 63.4%, 22.4%, and 14.2% respectively. At 600 kHz DF contributes about 51.7% and R and SD contributes 28.9% and 19.32% respectively. This trend continues, and finally R becomes equal to SD at 1.8 MHz. The contributions at 2 MHz are 43.8% due to DF, 26.8% due to R and 29.4% due to SD. The contributions from SD and DF become equal at 4.8 MHz. At 10 MHz, the contribution from R becomes very less and the contributions are 38.6%, 55.8% and 5.5 % from DF, SD and R, respectively. At the highest measured frequency (40 MHz) DF contribution becomes 27% and about 72.5% relaxation caused by the SD mechanism. R contribution is (0.5 %) negligible.

The correlation time obtained for rotations about the short molecular axis in the nematic phase of 40.8 is 3.958×10^{-8} seconds. The contribution to the total relaxation rate from R is quantified by the value $C = 9.8 \times 10^7 \text{ s}^{-1}$. Presence of a smaller contribution from rotations about the short axis and the strong DF contribution in the kHz region leads to the temperature independent dipolar relaxation times (T_{1D}) [45]. In the case of *self-diffusion*, the model parameters obtained are B (the amplitude obtained as $3.05 \times 10^9 \text{ s}^{-2}$), and D (the average diffusion constant obtained as $1.56 \times 10^{-6} \text{ m}^2 \text{ s}^{-1}$)

6.7.2.1.2. Anisotropic elastic constants

In the second procedure an expression, considering the influence of upper and lower cut-off wavelengths for the director modes, as well as the anisotropy in elastic properties, was used in calculating the DF parameters. Complete description of the functions and parameters involved in this generalized model have been described in chapter 5. section 5.2.

The elastic constants are calculated by extrapolating experimental elastic data [30] obtained in the nematic system 40.4 at different temperatures. The constant A_{DF} , obtained for 40.8 is $2.026 \times 10^{-6} \text{ s}^{-2}$, which is much smaller than that of the value obtained from the isotropic elastic constants model. The lower cut-off frequency obtained in this case is 589 Hz. The upper cut-off frequencies in the directions parallel and perpendicular to the director are $8.82 \times 10^8 \text{ Hz}$ and $14.7 \times 10^8 \text{ Hz}$, respectively. The relative contributions observed from the analysis are depicted in figure 6.35.

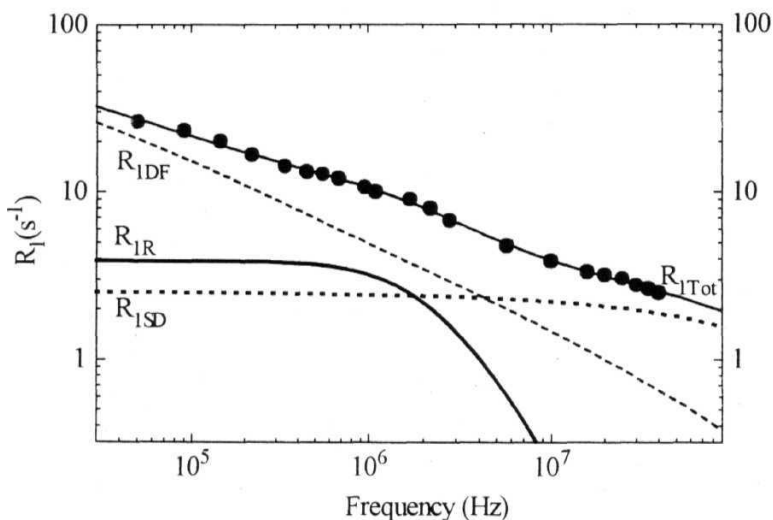


Figure 6.35. Proton relaxation rate ($R_1 - 1/T_1$) as a function of frequency in the nematic phase of 40.8 at 71 °C and model fit to three individual contributions to the relaxation rate: director fluctuations (DF), self-diffusion (SD), and molecular reorientations about the short axis (R). Anisotropic elastic constants model is considered for DF contribution.

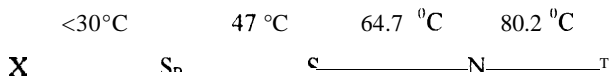
DF mechanism dominates the spin relaxation from 50 kHz to 4 MHz, where DF becomes equal to the SD contribution. From 15 MHz onwards, SD becomes more dominant. At 45 MHz the percentage contributions are 25% and 75% due to DF and

SD, respectively The behavior of the NMRD data from 600 kHz to 2 MHz arises from the combined effect of SD and R mechanisms. Below 600 kHz the frequency dependence is due to the DF alone. R and SD contribute to the relaxation with a frequency independent behavior below 600 kHz. R contribution becomes negligible from 8 MHz onwards Model fitting in the **nematic** phase of 40.8, becomes better in the case of anisotropic elastic constant model. From 5.7 to 20 MHz, SD and DF contributions mediate relaxation, where SD contribution is dominant. SD becomes the major mechanism above 20 MHz The SD contribution from 50 kHz to 10 MHz is almost frequency independent, and it becomes frequency dependent from 10 to 45 MHz

The correlation time obtained for rotations about the short molecular axis in the nematic phase of 40.8 in this model is 3.95×10^{-8} seconds. The contribution to the total relaxation rate from R is quantified by the value $\tau^{-1} = 9.7 \times 10^7 \text{ s}^{-1}$. While the correlation time for rotations show a slight variation; the contribution to the total relaxation increases considerably at the cost of the DF contribution in this model. In the case of *self-diffusion*, the values B and D are obtained as $3.256 \times 10^{-9} \text{ s}^{-2}$ and $1.642 \times 10^{-10} \text{ m}^2 \text{ s}^{-1}$ respectively. The behavior of the SD contribution is not very different from the earlier analysis though SD shows its frequency dependence at much lower frequencies Though there are some differences in the quantitative picture, the qualitative picture of the dynamics are not very different, with the type of approximation (one constant or anisotropic elastic constants model) used The value of A_{DF} is found to be very sensitive to the anisotropy of the elastic constants.

6.8. NMRD study of Butyloxybenzylidene Nonylaniline (40.9)

The system studied next in the 40.m series is *butyloxybenzylidenenonylaniline* (40.9). This system has the phase sequence given by [7]



This system has a stable smectic A phase over a region of 17.7 °C alongwith a reasonably stable high temperature nematic phase of 15.5 °C.

6.8.1. Experimental Details

Proton spin-lattice relaxation time (T_1) measurements were carried out as a function of frequency in the nematic phase of 40.9 at temperature 75 °C. The data from 50 kHz to 3 MHz was obtained using the field cycling NMR spectrometer and the high frequency data from 3 to 30 MHz was obtained using the NMR spectrometer [1]. The estimated errors in T_1 measurements at frequencies below 1 MHz are found to be less than 7 % and at above 1 MHz, around 5 %. Temperature dependent T_1 and T_{1D} in the nematic and smectic phases were performed earlier in this laboratory [1]. Experimental NMRD data are shown for nematic phase of 40.9 in figure 6.36. Temperature dependent T_1 data at spot frequencies at 6.5, 10, 15, 20, 25, 30, 40 and 45 MHz are shown in figure 6.37. The observed NMRD data in the nematic phase of 40.9 has the following features.

1. The relaxation times ranging from 32 milliseconds at 50 kHz to 502 milliseconds at 45 MHz. T_1 decrease with decreasing frequency in the entire frequency range studied.

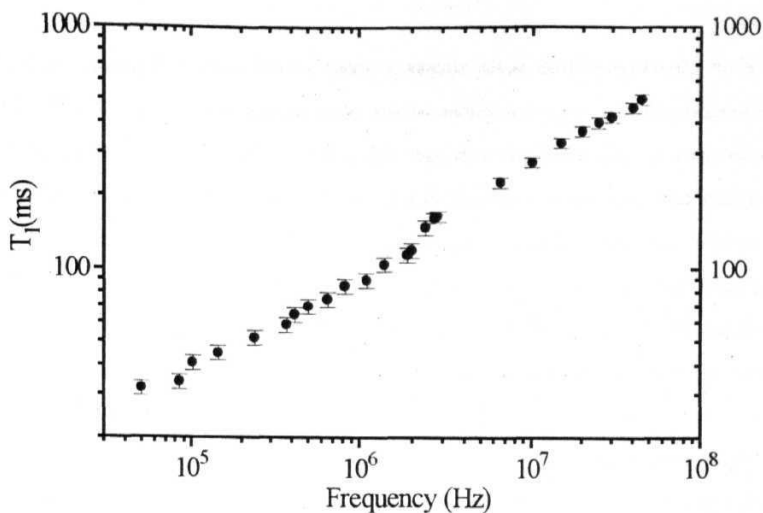


Figure 6.36. Frequency dependence of the spin-lattice relaxation time (T_1) in the nematic phase of 40.9 at temperature 75 °C. Error bars are also shown.

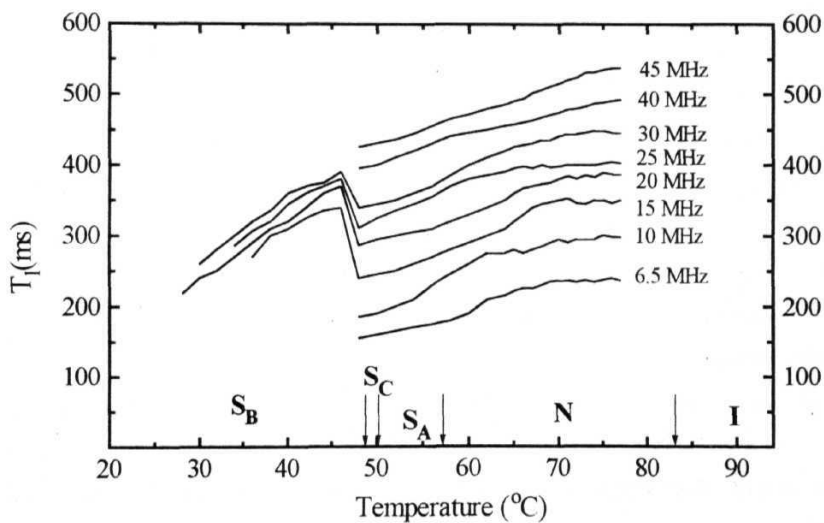


Figure 6.37. The behavior of the spin-lattice relaxation time T_1 as a function of temperature at different frequencies in 40.9. The arrows denote the transition temperatures.

2. 7), in the logarithmic scale shows a steep variation as a function of the Larmor frequency and the slope increases in the intermediate frequencies, finally reaching a region with a different slope at higher frequencies. The plot between relaxation times and frequency (in Hz) at low proton Larmor frequencies, show a longer region having a square-root like behavior, which extends up to intermediate frequencies. This indicates the presence of a longer region with the domination of the DF mechanism at this low frequency range. The NMRD data deviates from this behavior, from about 2 MHz and slightly different slopes were observed at higher frequencies.

3. Thus, the NMRD data in the nematic phase of 40.9 at 75 °C shows at least two different regions with different slopes, and hence a first look at the data suggests that there are at least two possible mechanisms with different frequency dependence.

4. In the conventional NMR region from 6.5 MHz to 45 MHz, temperature dependent T_1 data shows an interesting behavior with two different regions in the nematic phase itself.

a). The first region close to the I-N phase transition shows almost a constant T_1 with temperature for a range of about 10 °C, particularly at lower frequencies. This trend is different in different frequencies. This temperature independent region close to the I-N phase transition becomes shorter in the case of higher frequencies above 30 MHz.

b). The second region with a stronger temperature dependence closer to the N-SA transition is observed in the nematic phase. This region is longer at higher frequencies. This trend suggests that the SD mechanism becomes more dominant only at high frequencies, around 30 MHz.

5. The SD domination also dominate the smectic A phase near the N-S_A transition. There is no sharp change observed at the transition between the N-S_A in the collected T_1 . The strong temperature dependence seen in the nematic phase continues in the smectic A phase also.

6. 7), in the **smectic** A phase shows similar behavior in all the frequencies from 6.5 to 45 MHz. The continuity between **nematic** and smectic A phase in the high frequency 7) data suggests that there are common mechanisms which vary continuously with temperature, irrespective of **layering**. This should be either SD or R, and cannot be DF.

7. The **NMRD** data collected in the **S_A** phase of 40.9 shows (figure 6.40) a different behavior. A strong frequency dependent region is seen below 150 kHz. Another region with a different slope is seen from about 150 kHz to 400 kHz. A third region with a steep variation is seen from around 700 kHz to 20 MHz. Finally, there is a small region that shows a lesser slope from 20 MHz to 45 MHz.

8. A sudden increase towards higher value T_l , at the smectic A to Smectic B phase transition is witnessed, and this occurs within the smectic A phase from at least 2 degrees above this transition. The data in the ordered **S_B** phase shows strong temperature dependence and weak frequency dependence in the conventional NMR frequency range. 7) decreases with increasing temperature and decreases with decreasing frequency.

9. The temperature dependent data has shown a weaker **pre-transitional** effect.

10. The NMRD data collected from 100 kHz to 45 MHz in the **S_B** phase exhibits a different behavior, suggesting that the dynamics are very different from that of the nematic and smectic A phases. Three different regions are observed in the NMRD data in the smectic B phase of 40.9. The first region below 400 kHz shows weaker frequency dependence. The second region from 400 kHz to 6.5 MHz, shows a steep variation, and finally reaches a region of lesser slope with frequency dependence.

6.8.2. Data analysis

6.8.2.1 Nematic Phase

6.8.2.1.1. Isotropic elastic constants model

NMRD data analysis was performed assuming isotropic elastic constants ($K_{11} = K_{22} = K_{33} = 1 \times 10^6$ dyne) for DF modes. The contributions from various mechanisms to the measured R_1 data are shown in the figure 6.38. The dynamic parameters obtained from this fit are summarized in table 6.10. The errors estimated in evaluating the dynamic parameters are around 10 %.

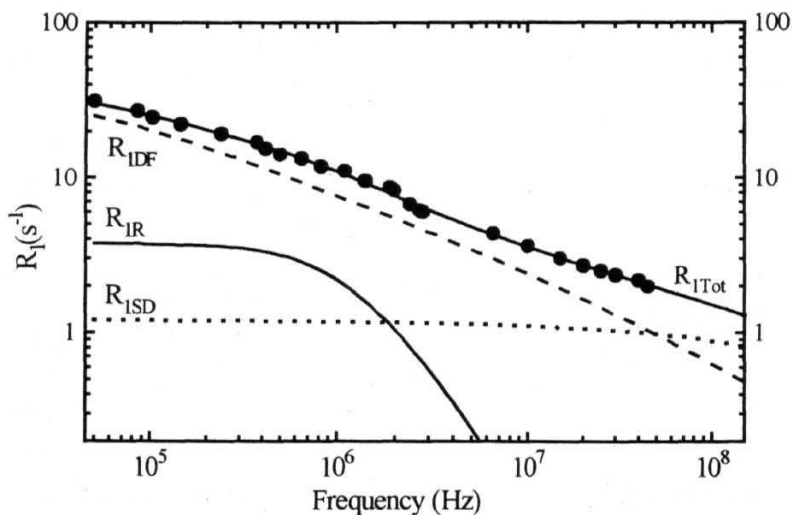


Figure 6.38. Proton relaxation rate ($R_1 = 1/T_1$) as a function of frequency in the nematic phase of 40.9 at 75 °C and model fit (eqn.6.1) to three individual contributions to the relaxation rate: director fluctuations (DF), self-diffusion (SD), and molecular reorientations about the short axis (R). Isotropic elastic constants are assumed in evaluating the DF contribution.

Table 6.10

Model Parameters	Isotropic elastic constants model	Anisotropic elastic constants model
Nematic director fluctuations (DF)		
K_{11} (in 10^{-6} dynes)	1	0.516
K_{22} (in 10^{-6} dynes)	1	0.344
K_{33} (in 10^{-6} dynes)	1	0.745
A_{DF} (in 10^6 s ⁻²)	6.680	1.573
q_{zcl} (in 10^5 1/Å)	1.6	0.257
f_{zcl} (in kHz)	8 1	0.157
λ_{zch} (in Å)	3927	24429
q_{zch} (in 10^7 1/Å)	6.8	4.51
f_{zch} (in MHz)	1400	482
λ_{zcl} (in Å)	9.24	13.92
q_{lch} (in 10^7 1/Å)	6.4	5.69
f_{lch} (in MHz)	1300	1030
λ_{lcl} (in Å)	9.81	11
Translational self-diffusion (SD)		
B (in 10^9 s ⁻²)	3.635	1.428
D (in 10^{-10} m ² s ⁻¹)	3.838	0.78
Rotations about the short axis (R)		
C (in 10^8 s ⁻²)	0.496	0.873
τ_R (in 10^{-9} s)	75.58	67.61

The DF contribution is quantified by the constant $A_{DF} = 6.68 \times 10^{-6}$ s^{*2} in the case of the one constant approximation method. In the present case, the upper cut-off frequencies could not be varied and hence they are fixed. The DF contribution needs to be 30 percent of the total relaxation in order to get a reasonable value for upper

cut-off frequency [46]. It should be much more than 100 MHz, assuming molecular length as the parameter deciding this cut-off. The lower cut-off frequency is about 8.1 kHz, and the corresponding upper cut-off wavelength for the director modes, is about 3927 Å

Relative contributions

A qualitative picture of the NMRD data fitting in the nematic phase of 40.9 shows that, the DF modes dominate the spin relaxation upto 45 MHz. Rotations about the short axis show frequency independent behavior from 50 kHz to 400 kHz and frequency dependent behavior upto 3 MHz. SD becomes more important than R, from about 2 MHz and becomes comparable to DF, from 30 MHz. Even at high frequencies, DF is the dominating mechanism over SD. This interpretation is supported by the weaker temperature dependence observed in the T_1 data at conventional NMR frequencies below 30 MHz. An increasing slope of temperature dependent T_1 data, with increasing frequency suggests that DF domination over SD decrease with increasing frequency.

A more quantitative picture of the relative contributions can be obtained by calculating the percentage contributions (at specific frequencies) to the total relaxation. For example at 50 kHz, the contribution from DF mechanism to the total relaxation is about 83.5%. The contribution from R and SD are about 12.5% and 4% respectively. At 400 kHz, the contributions from DF, R and SD are about, 72%, 20.7%, and 7.3% respectively. Finally R becomes equal to SD at 1.26 MHz. The contributions at 1 MHz are 69% due to DF, 20% due to R and 11% due to SD. At 8 MHz, the contribution from R becomes negligible. DF and SD contribute 69% and 29% respectively to the spectral density. At 30 MHz DF contribution becomes 56% and the remaining 44% relaxation is almost due to the SD mechanism. At the maximum measured frequency (45 MHz) the contributions from SD and DF are equal.

In the case of *rotations about the short molecular axis*, the explicit model parameters used are the amplitude C and the rotational correlation time τ_R , assuming a

simple **BPP** type contribution [38]. The correlation time obtained for rotations in the nematic phase of 40.9 is 7.558×10^{-8} seconds. The contribution to **the total** relaxation rate from **R** is **quantified** by the value $C = 4.96 \times 10^7 \text{ s}^{-1}$. Presence of strong contribution from DF modes in the nematic phase at low frequencies in the kHz region leads to the temperature independent dipolar relaxation times (T_{1D}) []].

In the case **of self-diffusion**, the values are obtained for the diffusion constant $D = 3.838 \times 10^{-10} \text{ m}^2 \text{ s}^{-1}$ are in good agreement with the values obtained from the direct methods in the nematic phases at this temperature range [49]. The frequency independent contribution from SD is extends to frequencies up to about 10 MHz in the nematic phase and a frequency dependent behavior is seen above this frequency.

6.8.2.1.2. Anisotropic elastic constants model

The complete description of the **functions** and parameters involved in the more generalized model, considering cutoff frequencies as well as anisotropy in the elastic constants have been described in chapter-5. The elastic constants for 40.9 are calculated by extrapolating experimental elastic data [30] obtained in the nematic system 40.4 at different temperatures. The constant ADF obtained for 40.9 is $1.5729 \times 10^{-6} \text{ s}^{-2}$, which is much smaller than that of the value obtained from the isotropic elastic constants model. The lower cut-off frequency obtained in this case is 156 Hz. The upper cut-off frequencies in the directions parallel and perpendicular to the director are $4.82 \times 10^8 \text{ Hz}$ and $10.3 \times 10^8 \text{ Hz}$ respectively. The parameters obtained for SD and R contributions are different when comparing with the earlier analysis. It is interesting to note that the anisotropy in the elastic constants influences the relative contributions as well as the dynamic parameters in the case of 40.9. Estimated elastic constants for 40.9 (table 6.10) are much smaller than the values assumed in the case of one constant approximation (10^{-6} dyne) and more anisotropic than the other shorter chain systems in the **40.m** series.

Relative contributions

The relative contributions observed from the analysis based on anisotropic elastic constants for DF modes are depicted in figure 6.39. The dynamic parameters are presented in the table 6.10. Typical errors in evaluating these parameters are about 10 %. DF mechanism dominates the spin relaxation from 50 kHz to 6.5 MHz, and become equal to SD contribution. From 20 MHz onwards SD become more dominating. At 45 MHz the percentage contributions are 30% and 70% due to DF and SD respectively. The behavior of the NMRD data 400 kHz to 1 MHz is due to the combined effect of SD and DF mechanisms. R and SD contribute to relaxation with a frequency independent behavior below 400 kHz. R contribution becomes negligible from 4 MHz onwards.

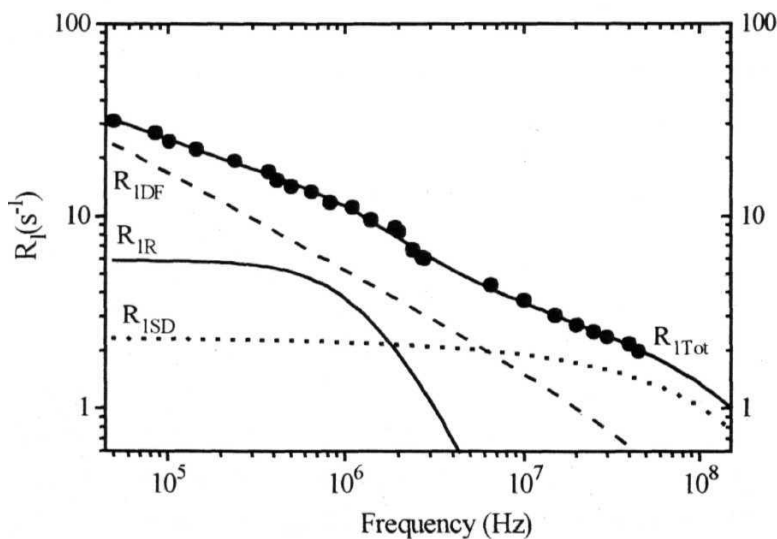


Figure. 6.39. Proton relaxation rate ($R_l = 1/T_l$) as a function of frequency in the **nematic** phase of 40.9 at 75 °C and model fit (eqn. 6.1) to three individual contributions to the relaxation rate: director fluctuations (DF), self-diffusion (SD), and molecular reorientations about the short axis (R). Anisotropic elastic constants are considered for the evaluation of DF contribution.

The correlation time obtained for rotations about the short molecular axis in the nematic phase of 40.9 in this model is 6.761×10^{-8} seconds. The contribution to the total relaxation rate from R is quantified by the value $C = 8.73 \times 10^7 \text{ s}^{-1}$. While the correlation time for rotations show a slight variation, the contribution to the total relaxation increases considerably at the cost of the DF contribution in this model.

In the case of *self-diffusion*, the values B and D are obtained as $1.427 \times 10^9 \text{ s}^{-2}$ and $0.802 \times 10^{-10} \text{ m}^2 \text{ s}^{-1}$, respectively. The frequency independent contribution from SD is restricted to lower frequencies upto 8 MHz in the nematic phase. The behavior of the SD contribution is very different from the earlier analysis. SD shows its frequency behavior at much lower frequencies and hence the NMRD behavior of the nematic phase of 40.9 is characteristic to the SD behavior. The stronger temperature dependence seen in the T_1 at high frequencies is caused by the presence of this SD. The higher frequency region from 10 to 45 MHz is mediated by SD assisted by DF.

6.8.2.1.3. Comparison with high frequency study

A comparison of the present NMRD study of the nematic phase of 40.9 with the earlier 7) data analysis using a limited frequency range demonstrates the merits and demerits of both the studies. The frequency dependent data from 6.5 MHz to 40 MHz was fitted [1] to various models. It was observed that the analysis of the frequency dependence data of such a small region could not give a completely acceptable picture, though it predicted the domination of the DF contribution in the conventional NMR frequencies. But, the suggested linear behavior of DF contribution with frequency is controversial. The second mechanism predicted by the earlier work (rotations) for high frequency dispersion is different from the present result (*self-diffusion*). The temperature dependent high frequency data could be best explained by SD+DF contributions rather than DF+R contribution as proposed by the previous study [1]. The high frequency data (6.5 MHz to 45 MHz) was fitted [1] very well to the following models.

Model - 1: $A\omega^{1/2} + B$ (assuming DF with a square root frequency dependence and rotations with frequency independent behavior) model is the first one fitted the frequency dependent T , data. Fitting was very good in all temperatures [2]. But the constants obtained were unphysical and hence, this model fitting was not acceptable.

Model -2: In the second model, in addition to the DF and R contributions, SD contribution was added in the first model [2]. This was also fitted very well but the diffusion constants and the other model parameters obtained were unphysical. This model therefore, was not accepted.

Model - 3: A replacement of the square-root dependence with the linear dependence in the DF term in the second model given above, also lead to good fitting, but the temperature dependence and the coefficients obtained were found to be unphysical.

Model - 4: Finally, the first model with linear frequency dependence in the DF term fitted well and no temperature dependence was observed. This fitting was considered **meaningful**. The activation energy associated with the R mechanism was found to be less. The temperature dependence seen in the constant A_{DF} , was attributed to the diffusion assisted DF.

In contrast to the above interpretation, the present NMRD data analysis in the nematic phase of 40.9, using a composite model incorporating DF (anisotropic elastic constants with upper and lower cutoff frequencies), SD and R leads to a better and unique fit, which also gives realistic model parameters. Moreover, the temperature dependence seen in the T , data is also explained reasonably well.

6.8.2.2. Smectic A phase

The NMRD data collected in the smectic A phase (figure 6.40) was fitted with the theoretical equation incorporating the three dynamical processes namely 1). Smectic layer undulation modes (**LU**) (equation 6 3), 2). SD and 3). Rotations about the short axis. The details of the theoretical formalisms for SD and R have been given

in chapter-5. The total spin lattice relaxation rate (R_{Tot}) can be written as

$$R_{Tot} = R_{LU} + R_{SD} + R_R$$

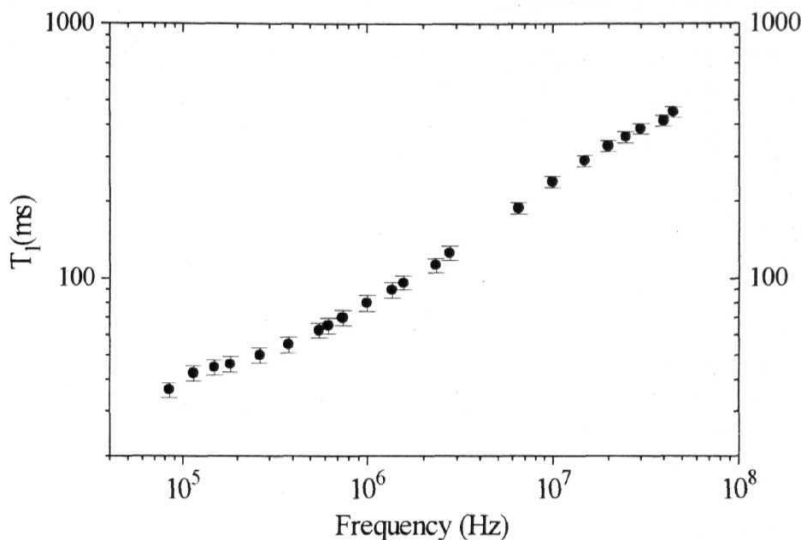


Figure 6.40. Frequency dependence of the spin-lattice relaxation time (T_1) in the smectic A phase of 40.9 at temperature 58 °C. Error bars are also shown in figure.

Different contributions to the relaxation data (figure 6.40) in the S_A phase at 58 °C are shown in figure. 6.41. The parameters for SD and R are given in table 6.11. LU contribution in the smectic A phase is dominates upto 150 kHz in 40.9. R becomes more important from 150 kHz to 2 MHz than LU and SD contributions. SD contributes strongly to the relaxation in the S_A phase of 40.9 in the conventional NMR frequencies from about 2 MHz and becomes the sole mechanism responsible for spin relaxation. SD contribution is frequency independent upto 2 MHz and frequency dependent from 2 to 45 MHz. The T_{1D} data collected earlier [2] in the smectic A phase of 40.9 shows no temperature dependence. This is qualitatively different from the T_{1D} data obtained from 40.5 where T_{1D} data in S_A phase is temperature dependent.

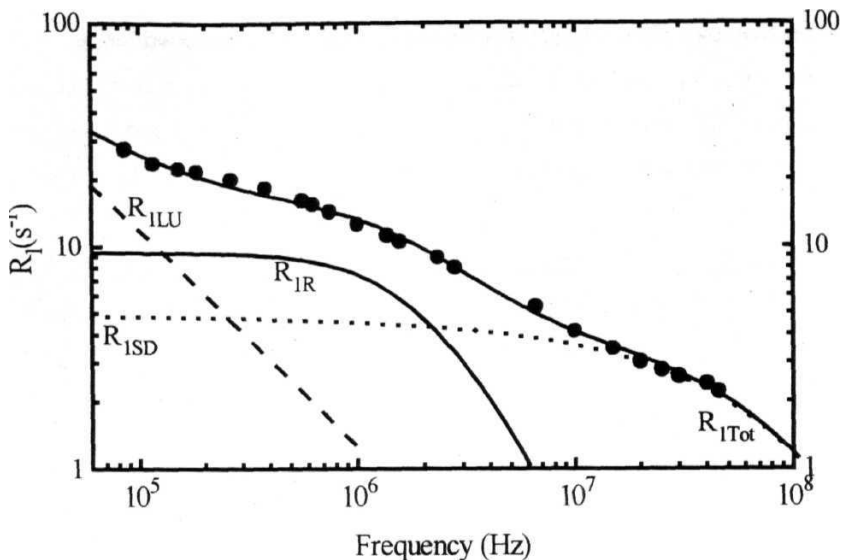


Figure 6.41. Proton relaxation rate ($R_1 = 1/T_1$) as a function of frequency in the smectic A phase of 40.5 at 58 °C and model fit to three individual contributions to the relaxation rate: layer undulations (LU), self-diffusion (SD), and molecular reorientations about the short axis (R).

As observed by Schweikert and Noack [47], and Bender et al., [48], it is important to incorporate the R mechanism (about short axis) to explain the intermediate frequency range in the nematic and smectic A phases. Whenever such contribution was not considered NMRD data in the smectic A phase does not seem to fit well [51]. It is also possible to have another R contribution (about long axis) to explain the NMRD behavior at very high frequencies (above 100 MHz).

In the present systems (40. m) R about the short axis seems to be very important in order to explain NMRD data obtained in the nematic and smectic A phases for the present range of frequencies. Rotations about the long axis and segmental motions are also expected to contribute at the high frequencies [12]. It needs to have an almost frequency independent behavior in the measured frequency range (below 50 MHz). But, in the present analysis such a contribution is not

included, since the data fits reasonably well without such contribution. So the present analysis is confined to R about short axis with single correlation time. The parameters obtained for LU contribution are not given in the table 6.11, due to the fact that the dynamic parameters obtained (given manually) are not reliable since the complete dispersion of LU is not observed in the present analysis. The linear behavior of relaxation rate with frequency was given priority rather than the constants and cut-off frequencies. Errors estimated in the evaluation of parameters for SD and R are about 10%

Table 6.11

Translational self-diffusion (SD)	
B (in 10^8 s^{-2})	1.753
D (in $10^{-12} \text{ m}^2 \text{ s}^{-1}$)	1.71
Rotations about the short axis (R)	
C (in 10^9 s^{-2})	2.408
τ_R (in 10^{-9} s)	1.1372

6.8.2.3. *Ordered smectic phase (SB)*

NMRD data collected in the SB phase of 40.9 was fitted to SD and R mechanisms. The data is shown in figure 6.42. The data fitting is shown in figure 6.43. The dynamic parameters are given in table 6.12. Typical errors in the values of the parameters related to SD and R are about 15% in the case of S_B phase. The low frequency region is completely dominated by the SD mechanism and the high frequency relaxation is dominated by rotations about the long axis. This interpretation is consistent with the observations made with the temperature dependent data (figure 6.37). The observed increase in T , and T_{ID} , near the transition from smectic A to smectic B, in the conventional NMR frequencies clearly demonstrates the difference between the dynamic properties of highly ordered smectic phases and the fluid like nematic and smectic A phases.

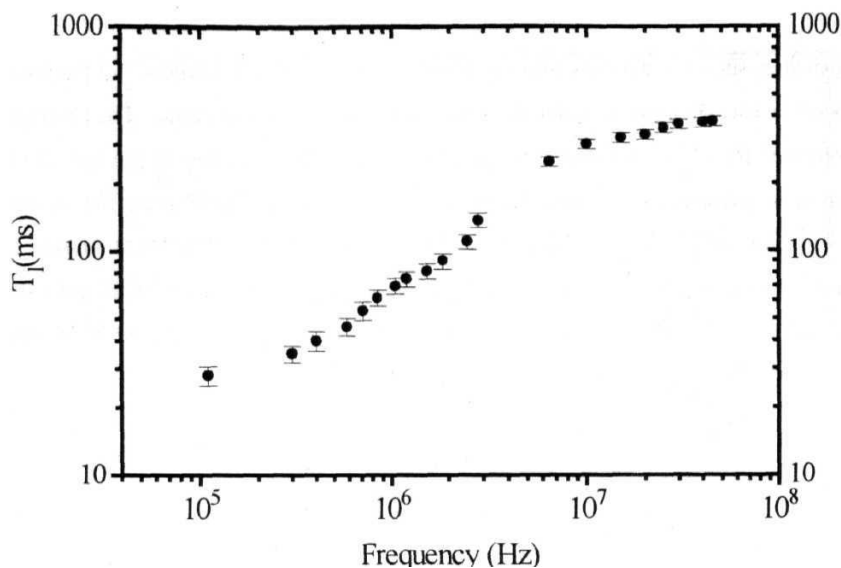


Figure 6.42. Frequency dependence of the spin-lattice relaxation time (T_1) in the smectic B phase of 4O.9 at temperature 40 °C. Error bars are also shown.

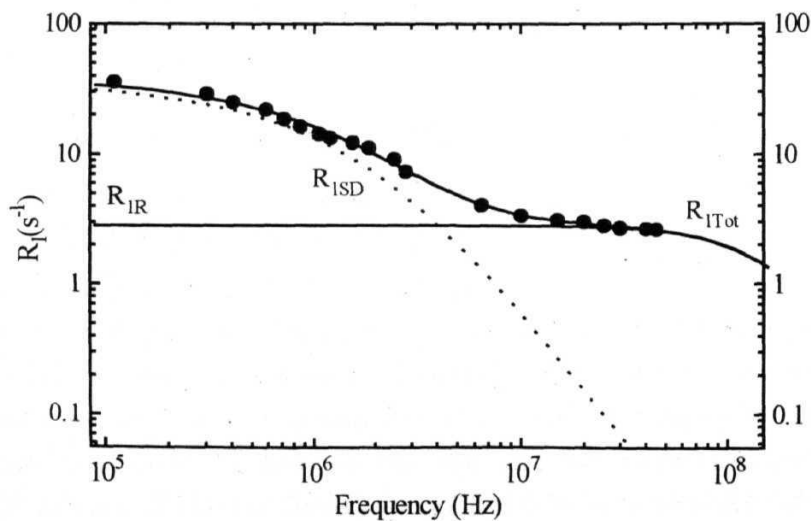


Figure 6.43. Proton relaxation rate ($R_1 = 1/T_1$) as a function of frequency in the smectic B phase of 4O.9 at 40 °C and model fit to the individual contributions to the relaxation rate: self-diffusion (SD), and molecular reorientations (R).

Table 6.12

Model Parameters	From 40.9-S_B
B (in 10^8 s^{-2})	1.615
D (in $10^{-14} \text{ m}^2 \text{ s}^{-1}$)	5.241
C (in 10^9 s^{-1})	4.659
τ_R (in 10^{-10} s)	6.055

Slowing down of the diffusion process and the absence of DF/LU mechanisms are responsible for the sudden increase of T_i in the smectic B near the S_A-S_B transition, in the conventional NMR frequencies. In the smectic B phase of the 40.9 the T_i data shows strong temperature dependence. In 40.9, anisotropic rotational diffusion motions of the end hydrocarbon chains, of the entire molecule, or of just the core rigid portions are probable at these temperatures. From the behavior of the data in the S_B phase, at the measured temperature ranges, one can conclude that the major contribution comes from rotations of the molecule around the long axis and from the segmental motions. Contributions from the rotations of the CH₃ rotations are negligible

Since there are two alkyl end chains and many CH₂ groups present in the system, several rotational diffusion modes could be present, leading to as many values of the correlation time. The T_{1D} data measured in the S_B shows temperature dependence. Reduction of T_{1D} in the S_B phase suggests that, the SD mechanism becomes more efficient since SD sufficiently slows down and influences the dipolar relaxation more efficiently at low frequencies.

In the highly ordered smectic B phase, the diffusion constant becomes very small ($D = 5.24 \times 10^{-9} \text{ cm}^2/\text{s}$). The relaxation dispersion at low frequencies is explained by the SD process, where one can see a relatively small but frequency independent contribution from R. The temperature dependence seen in the high frequency T_i data with small frequency dependence is consistent with this view. The explanation given for the T_{1D} data, for the S_B phase is also consistent with the NMRD analysis.

R contribution is responsible for the frequency dependence in the **S_B** phase at conventional NMR frequencies from 10 MHz to 45 MHz. The correlation time associated with the rotation about the long axis obtained from this analysis is **6.06×10⁻¹⁰s**, which is reasonable when compared to correlation times obtained from NMR studies by Heinze and Grande [24] on **nO.m** systems. The value obtained by them for rotations about the long axis at temperature **-18 °C** in the smectic B phase of 70.4 is **3×10⁻⁹ s**. The value obtained for 40.9 is about an order of magnitude smaller than the value obtained by Heinze and Grande [24]. This difference is probably due to the difference in the temperatures of observation.

The activation energy associated with the T_i data in **S_B** phase is found to be **5.6 ± 0.5 k Cal/mole** [1]. This is in good agreement with the value obtained for the rotations about the long axis in the smectic B phase of 70.4. Heinze and Grande [24] had obtained the value of the activation energy for this dynamics in the system 70.4 as **6.5 kCal/mole**. It is therefore, reasonable to say that the rotational contribution obtained in the smectic B phase of 40.9 is mainly due to the rotations about the long axis. The segmental motions are expected to contribute at lower temperatures. The segmental motions observed at lower temperatures in 40.9 with a correlation time of the order of **2×10⁻¹² s** and the associated activation energy for the segmental motions are obtained as **2.8 kCal/mole** [1].

Hence, it is concluded that the contribution for relaxation in the **S_B** phase is predominantly due to the R about the long axis. There should be a weaker contribution from the segmental motions. The experimental correlation times associated with **CH₃** three-fold rotation in the **nO.m** series obtained from earlier studies [24] are range from **2.3×10⁻¹³s** (with activation energy 2.75 kCal/mole in 70.4) to **13×10⁻¹³s** (with activation energy 2.1 **kcal/mole** in 70.4). Comparing the present results with the literature values for **CH₃** rotations one can say that there is no major contribution that could come from CH₃ three fold rotations.

Section 6.9 - Conclusions

End chain Structure and Molecular Dynamics in 40.m homologous series of Liquid Crystals

The results obtained from the NMRD studies of the 40.m series were discussed in detail considering the systems individually in the preceding sections (sections 6.2 to 6.8). These studies could explain the dynamic behavior of mesophases in each system. It was demonstrated that the individual contributions in mediating spin-lattice relaxation time at different frequencies could be separated out by measuring NMRD at fixed temperature. It was also shown that temperature dependent studies were very useful in obtaining clues about the type of dynamics dominating spin relaxation. In this section, an attempt is made to correlate the dynamic parameters obtained from the NMRD studies of 40.m systems to the structural parameters which generally influence molecular properties.

6.9.1. Effect of end chain length on T_1

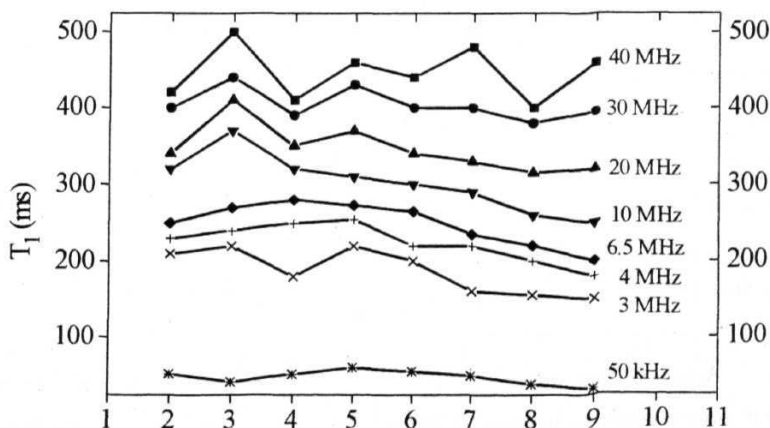


Figure 6.44. Spin-lattice relaxation time (T_1) as a function of chain length, in the homologous series, 40.m. The data is obtained at a fixed temperature ($T \approx 65^\circ \text{C}$).

The figure 6.44. shows an interesting variation of T_1 with chain length at a fixed **nematic** temperature (65 °C) and at different frequencies. Since, the **nematic** temperature ranges vary with chain length, it is difficult to obtain T_1 data at a fixed temperature. In the present case, the T_1 values are estimated through extrapolation by simply following the temperature dependence of T_1 at different frequencies and systems.

It can be observed from figure 6.44 that the T_1 values at low and intermediate frequencies below 20 MHz depends on the chain length. The T_1 value increases initially from 40.2 to 40.5 and decreases to low values at longer chain lengths. The absence of such reduction at higher frequencies above 20 MHz suggests that the dynamics observed at high frequencies does not show any systematic variation on the chain length. In other words, there is a strong contribution due to some slow dynamic process, which increases with chain length. This particular dynamics (identified as DF, in the present case) seems to be effective with an increase in chain length. But, it is important to note that there are other properties (odd-even alteration and symmetric end chains) which probably complicate the effect of the chain length. It can be seen in the above figure (6.44) that for the system with $m = 2$ lower T_1 value is observed, which increase until $m = 5$ is reached, and then decrease upto $m = 9$. It also possible to say that the systems having symmetric end chains (40.3, 40.4 and 40.5) behaves differently. This is probably due to the weaker DF contribution and a stronger contribution from rotations about the short axis and self-diffusion from the symmetric systems. This behavior leads to a sharp increase in T_1 in the symmetric systems. This can be justified by the fact that the DF mechanism involves more number of molecules and hence the strong presence of such dynamics would effectively mediate spin relaxation than any other dynamics involving individual molecules, such as **R** and SD. Hence, a weaker DF mechanism increases the T_1 values.

A comparison between earlier results on PAA series [49] and the present **40.m** series would be interesting. In the PAA series shorter chain molecules (PAA) show higher values of T_1 , than longer molecules (PAB, HAB) at any particular nematic temperature. In the **40.m** series, high T_1 values are observed when the end chains are close to balanced. At the same time, the T_1 values decrease **with** increasing

chain length when the end chains are **imbalanced**. The PAA series deals with balanced systems and by increasing the ***n*** value, the length of the chains increases at both the ends simultaneously. In the case of the **40.m** series, alkoxy chain length is fixed and the **alkyl** chain length increases. The effect of chain length alone is seen in the PAA **series**, whereas in the **40.m** series, the effect of symmetry complicates the effect of chain length. Even in the case of **40.m** series it is observed that **T₁** decreases with an increase in chain length.

6.9.2. Director fluctuations **and** end chains

The mode spectrum of DF modes depends on many factors, which include viscoelastic properties of the medium, molecular length, domain size, temperature, and degrees of ordering in the sample [12]. It is important to compare the values of ***A_{DF}***, which are sensitive to the viscoelastic constants of the medium. In the present work, the value of ***A_{DF}*** is calculated in two different ways (using the isotropic and anisotropic elastic constants models). The ***A_{DF}*** values obtained from the NMRD analysis (one constant model for DF contribution) are presented in figure 6.45.

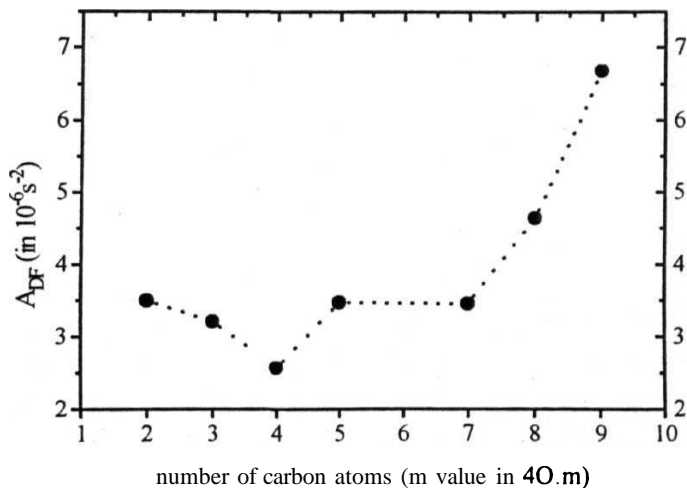


Figure 6.45. Effect of end chain symmetry on the values of ***A_{DF}***. The ***A_{DF}*** values are calculated using the isotropic elastic constants model.

Odd-even effects are observed in the values of A_{DF} . The values of A_{DF} decreases first with the chain length and then increases with chain length drastically, when the length of the chain is long. ADF value is minimum when $m = 4$. When the number of carbon atoms in the **alkyl** and alkoxy end chains are equal or close to equal, the value of A_{DF} decreases. The decrease of ADF in the intermediate chain lengths also coincides with the increase of T_i values for systems having similar chain lengths.

Refractive index anisotropy measured [7] in this **40.m** series is useful in understanding the present results. The maximum value of anisotropy in the refractive index indicates the highest degree of ordering (since refractive index anisotropy is directly proportional to the nematic order parameter S). The higher value of anisotropy observed in system 40.4 could be due to the weaker DF contribution.

From the values observed for A_{DF} and from the arguments given above, it is possible to conclude that the systems with a higher nematic stability and higher value of order parameters show a weaker DF contribution. In the present **40.m** family, higher stability coincides with the symmetry of the end chains. The balanced end chains leading to better stability, probably results from the fact that they show weaker collective director fluctuations.

The ADF values obtained from the anisotropic elastic constants model show a different behavior with the alkyl chain length. ADF decreases with increasing alkyl chain length. ADF values show odd-even effects, which are more pronounced in the case of the anisotropic elastic constants model. Effects of length and symmetry of end chains seem to complicate each other, as well as the odd-even effects in the ADF values. Earlier experimental observations [12] in a homologous series (**nOCB**) are in agreement with these results. A_{DF} appears to decrease slightly with increasing chain length in the **nOCB** series. NMRD studies in the PAA series had concluded that the longer molecules have a higher value of A_{DF} , which is contrary to the results obtained from the **nOCB** series.

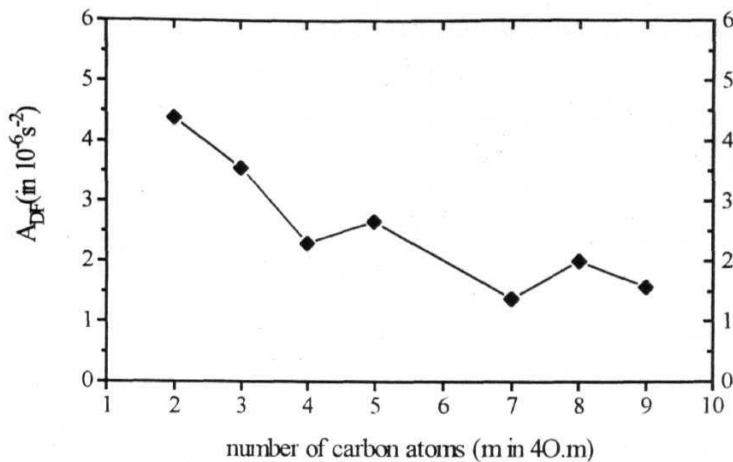


Figure 6.46. Effect of end chain length on the values of A_{DF} . The values of A_{DF} are calculated by the anisotropic elastic constants model. Experimental elastic constants are given as input parameters in the model fit.

Comparing the behavior of ADF values obtained from the isotropic and anisotropic elastic constants models it is possible to conclude that, the value of A_{DF} is very sensitive to the values of the elastic constants (K_{11}, K_{22} and K_{33}). Incorporation of experimentally observed (and extrapolated) elastic constants in the model fitting assigns different meaning to the ADF values, and a comparison of A_{DF} values would be **meaningful** only if the one constant approximation method is adopted. It is clear from these studies that the value of ADF is critically dependent on the choice of model used and the anisotropy of the elastic constants.

Although ADF behaviors are different as observed from these models, the relative contributions from DF modes to the total relaxation are not very different. Comparison of relative contributions from different dynamics to the total relaxation is more important and useful. The percentage contributions of SD, R and DF would be discussed in the sub-section 6.9.5

6.9.3. Self-Diffusion and end chain length

Diffusion constants are known to vary strongly with temperature. In the present case the **nematic** temperatures, at which the NMRD data was collected are not very different. This gives an opportunity to discuss the importance of end chain structure and properties, in the alteration of the diffusion process. The diffusion constants (*D*) obtained from NMRD studies are generally not as accurate as the *D* values obtained from the direct methods.

The *D* values obtained for 40.4 and 40.5 are of an order of magnitude higher than the values obtained for the other **40.m** systems. This anomalous increase of *D* in the systems 40.4 and 40.5 calls for confirmation, by more direct experiments like the Pulsed Field Gradient NMR method. This increase is probably due to the symmetry of the end chains. Any motion on a molecular level must reflect the shape of the instantaneous potential mean torque on each molecule. Both rotation and translation are expected to be sensitive to the nature of anisotropic interactions, which determine the formation of various liquid crystalline structures [12]. Systems 40.4 and 40.5 not only show high stability, but also very high values of the order parameter when compared to other systems in the **40.m** series. The anisotropy in the **refractive** index measurements made by Potukuchi [7] reveals that the nematic order parameter for 40.4 and 40.5 are much more than the values obtained for the other **40.m** systems.

6.9.4. Rotations about the short axis

The qualitative picture of the NMRD analysis shows that the rotations about the short axis are very effective in symmetric **systems**. **DF** seems to be more effective in systems having very long end chains as well as in systems having unbalanced end chains (non-symmetric end chains). The correlation times associated with the rotations about the short axis as well as the contribution from this mechanism need to be correlated with the end chain structure. The values obtained from the present NMRD analysis on **40 m** systems are tabulated along with the values obtained from the NMRD studies of nematic and **smectic** systems.

Table 6.13

System	Mesophases	Correlation time x 10 ^{ns} seconds	Temperature (in °C)
6OCB+8OCB	Nematic	0.8	47
	Reentrant nematic	2	27
	Smectic A	4	37
IS 1912	Smectic C	9.5	70
		3.5	100
MBBA	Nematic	24	18
		14.5	27
		9.4	35
		5.7	45
CB7	Nematic	0.25	32
PCH7	Nematic	0.5	47
CCH7	Nematic	1	48
TBBA	Nematic	.05	205
TBBA	Smectic A	0.1	185
40.9	Nematic	6.76	75
	Smectic A	11.3	58
40.8	Nematic	3.95	71
40.7	Nematic	0.373	70
	Smectic A	4.5	54
40.5	Nematic	6.4	70
	Smectic A	4.16	43
40.4	Nematic	0.58	67
40.3	Nematic	11.2	69
40.2	Nematic	2.44	61

The quantitative picture obtained here, as well as in the previous NMRD studies by Noack and coworkers [49] are well supported by the observations made by more simple experiments using dielectric relaxation [41]. The general observation made in the literature [13,32,33,41] says that the correlation times of the order of 10^{-6} – 10^{-8} s are possible for the rotations about the short molecular axis. In the NMRD studies, rotations about the short axis with correlation times of about 10^{-7} to 10^{-8} s are easily detectable and the shorter correlation times are generally not observable, probably due to the strong domination of the DF mechanism at the shorter time scales of about 10^{-6} s. Dielectric relaxation measurements are sensitive to this time scale, since DF modes do not contribute to the dielectric relaxation [41]. In the present study, slower rotations could be detected probably due to weakening of the DF in the symmetric end chain systems. The constant C, which quantifies the contribution from R, is shown in figure 6.47.

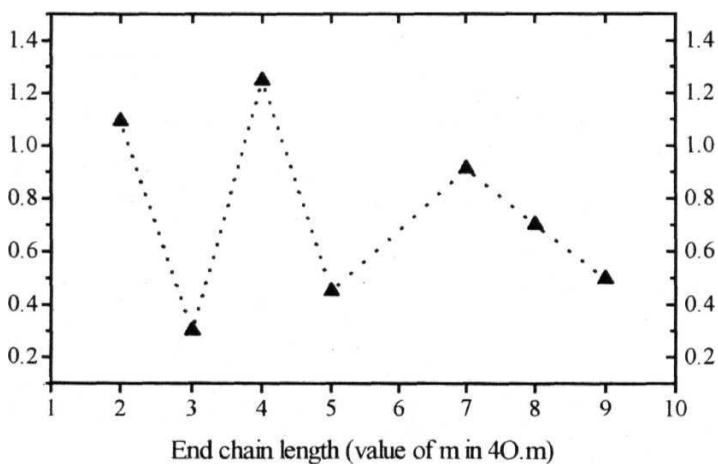


Figure 6.47 A plot between C (represents the contribution from the rotations about the short axis) and the number of carbon atoms in the **alkyl** end chain. A strong odd-even effect is observed in the value C, which is more pronounced for shorter chain systems.

This **figure** (6.47) shows that strong odd-even effects are observed in the value of C . Balancing effects are also seen. Both these effects complicate each other. It is interesting to note that the balanced even system 40.4 shows a peak in the value of C . It is known that shorter chain systems show a stronger **odd-even** effect in almost all macroscopic physical properties. A correlation between the microscopic molecular level dynamic behavior and the macroscopic static physical properties emerge from these studies, though the explanation is not simple as in the case of the microscopic behavior.

In order to understand this complex behavior of the dynamic properties, it is possible to separate odd-even contributions by simply plotting the results of odd and even systems separately. Such a plot is shown in figure 6.48. In order to show the relative variations of all the parameters, and the trends, various parameters are plotted in figure 6.48 in arbitrary units in the logarithmic scale.

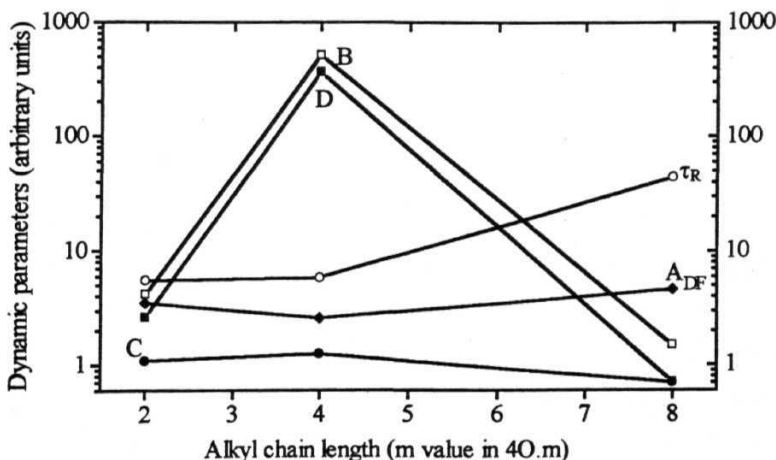


Figure 6.48. Different dynamic parameters are plotted (in arbitrary units) as a function of end chain length. Only even systems are considered here. Here, D is diffusion constant, τ_R the rotational correlation **time**, B and D are the constants representing the contributions from SD and R. ADF is the contribution from DF.

This figure (6.48) demonstrates the effects of symmetry of the end chains, which overlap with the effects of chain length. In the above figure, only even systems are plotted. Effects of the chain length can be linked with the nature of the end conformer, which is bent in the case of even systems. It can be assumed that the bent conformer interacts more efficiently with the ordering potential rather than the linear conformer, and this may, in principle, affect the rotations and translations in nematic liquid crystals. A closer look at the above figure leads to the following observations and arguments.

1. Strong balancing effects are seen in the dynamic parameters corresponding to the diffusion mechanism.
2. By comparing the values of τ_R obtained from 40.2 and 40.8, one can say that τ_R increases with the chain length. In other words, the rotations become slower when the chain length is more. Interaction of the chain with the nematic ordering potential increases with the end chain length, and this leads to a slowing down of rotations. Balancing of the end chains in the case of 40.4 probably decreases the activation energy associated with the rotations about the short axis, and hence more number of molecules involves in the rotations. The increase in the value of C for 40.4 is consistent with this picture.
3. Decrease of the value of A_{DF} in the symmetric system can also be explained on similar lines. Reduction in the activation energy associated with the rotations probably favors this motion instead of DF modes at this time scale. This situation reduces the need and importance of the DF modes at these frequencies. This reduces the overall contribution from DF modes to the relaxation.

The results obtained in the low frequency dielectric relaxation studies [41], on the rotations about the short axis in the homologous series $nS5$ ($n = 5, 6, 7, 8, 9, 10$) are very useful and relevant here. Chrusciel et al., [41] had studied properties such as, dielectric relaxation time, correlation times associated with the rotations, and transition enthalpy, near the I-N phase transition and other transitions (figure 6.49).

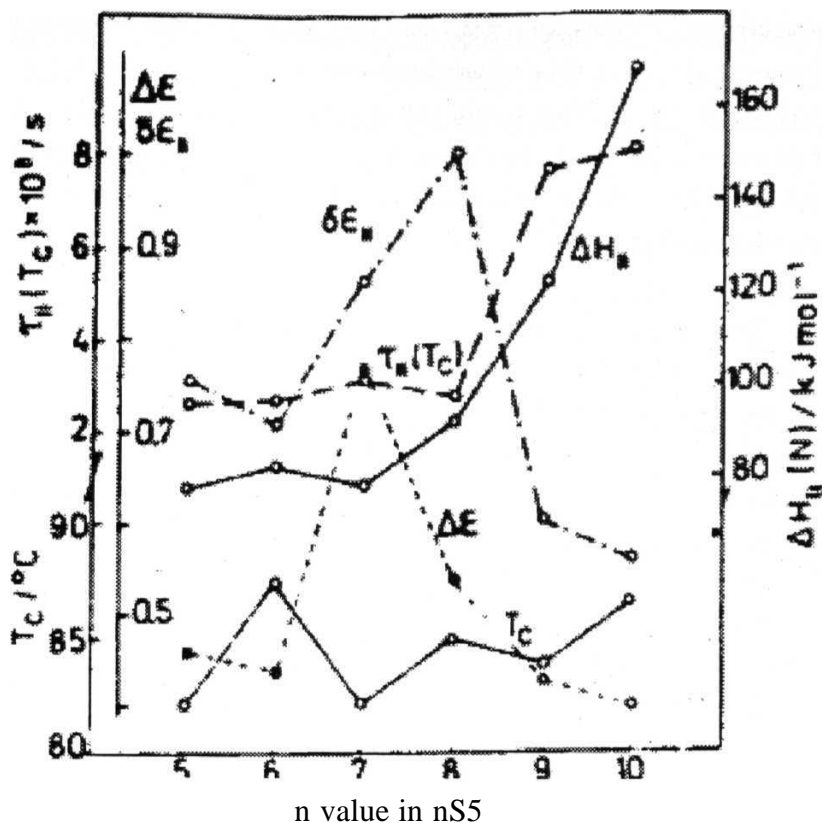


Figure 6.49. The clearing temperatures and all dielectric and molecular dynamics parameters obtained for the rotations about the short axis, as a function of chain length in the homologous 4-n-pentylphenyl-4'-n-alkoxythiobenzoate (in short nS5). Here, the symbol || refers to the rotations about the short axis. (after Chrusciel et al [41])

Relaxation times (τ) corresponding to the rotations about the short axis show a low value, leading to an anomalous behavior when the end chains are **balanced**. Relaxation times are very shorter for systems with $n = 5, 6, 7$ and 8 when compared with longer chain systems. This means that the rotations about the short axis become efficient when the end chains are close to balanced. It is also observed in these studies that, the activation enthalpy (ΔH) associated with this dynamics also show a

similar behavior. The balanced systems show lower values of activation enthalpy and the longer chain systems, those are unbalanced lead to very high values of activation enthalpies. Though the effect of balancing is not mentioned in the work [41], it is natural to consider this effect, due to the fact that the usual trends expected from chain length and odd-even alternation cannot produce such a change in the trends in the static and dynamic parameters.

The correlation times associated with the rotations about the short axis in the *nS5* series [41] range from 2×10^{-8} s to 10×10^{-8} s. Current results obtained for **40.m** series are comparable with the values obtained from the studies on the *nS5* series (figure 6.49). This comparison of correlation times not only proves the importance of balancing effects but also supports the view that, the rotations observed in the NMRD studies of **nematic** phases in the **40.m** series are nothing but the rotations about the short axis. In the case of low frequency dielectric relaxation measurements are direct in nature, whereas in the case of NMRD studies of the **40.m** series of liquid crystals the R contribution is partially masked by DF at lower frequencies and SD at higher frequencies.

Separation of individual rotations from collective rotational motions (DF) is considered as one of the difficulties faced by experimentalists [50]. Present study reveals that the separation is not very difficult if a proper system and a proper experimental technique like the present one is chosen. In the present work, information about the faster rotations could not be arrived at, mainly because of the non-availability of the NMRD data from 50 MHz to a few hundred MHz. A NMRD study of wider frequency from few kHz to a few hundred MHz can in principle separate out the collective rotations from individual rotations about the short axis, and faster rotations from the slower individual rotations.

6.9.5. Relative percentage contributions

So far, different dynamical parameters have been discussed quantitatively based on the model parameters by comparing their absolute values. The discussion

was general in nature, and the relative contributions at different time scales of these dynamics, as a function of the molecular structure have not been compared. The following figures 6.50a to 6.50/, clearly demonstrate the complete picture of dynamic behavior as a function of time window.

The quantitative results as a function of chain length presented earlier, such as D , B , τ_R , C , A_{DF} , cut-off frequencies and etc., have strong theoretical basis but they are very complicated. For example, A_{DF} depends on visco-elastic constants of the medium and choice of these constants changes the value of A_{DF} . Moreover, explanation based on these parameters necessitates lot more information about the ordering potential and intermolecular interactions.

Though, the values of the dynamic parameters show differences in the analysis, the relative contributions are model independent, except for 40.9. A quantitative analysis of relative contributions as a function of chain length would be more interesting and informative. Relative contributions of DF, SD and R can easily compared if the percentage contribution to the total relaxation can be estimated for different systems at a specific frequency of interest.

Figures 6.50a to 6.50/, show the percentage contributions of director fluctuations (DF), self-diffusion (SD) and rotations about the short axis (R) in the nematic phases of the 4O.m systems at spot frequencies, 40 MHz, 30MHz, 20 MHz, 15 MHz, 10 MHz, 5 MHz, 2 MHz, 1MHz, 500 kHz, 200 kHz, 100 kHz and 50 kHz. The frequencies at which the dynamics show significant variation are chosen here. From these figures it is possible to see, how the SD mechanism which is the most dominant one at 40 MHz becomes least important at 50 kHz. Similarly, the DF mechanism, which is a weaker one at 40 MHz in most of the systems, becomes very dominant at 50 kHz. Rotations about the short axis, shows negligible contribution in all the systems at 40 MHz. This remains insignificant at higher frequencies 15 MHz. Importance of R increases from 10 MHz onwards, and R contribution becomes comparable with SD and DF from 2 MHz to 200 kHz. Below 200 kHz DF dominates the relaxation upto the lowest frequency measured.

Figure 6.50a.

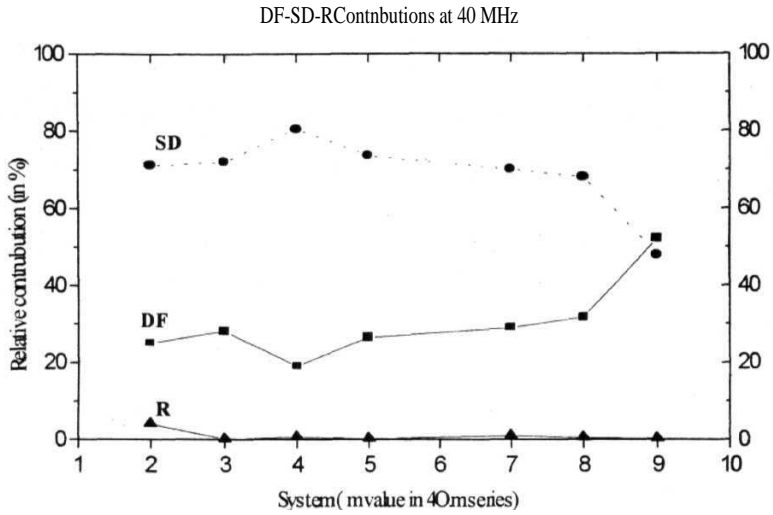


Figure 6.50b.

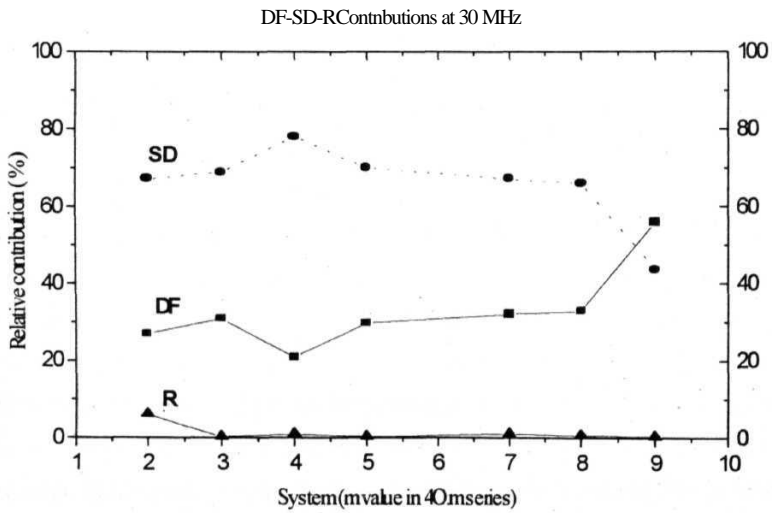


Figure 6.50c.

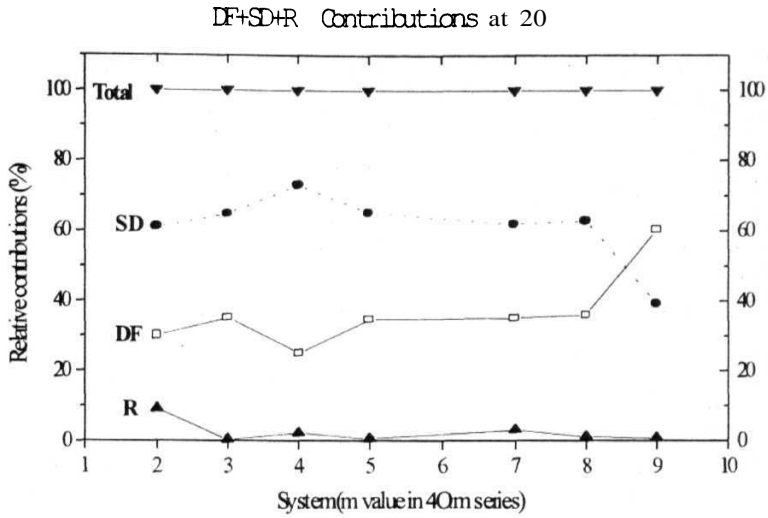


Figure 6.50d.

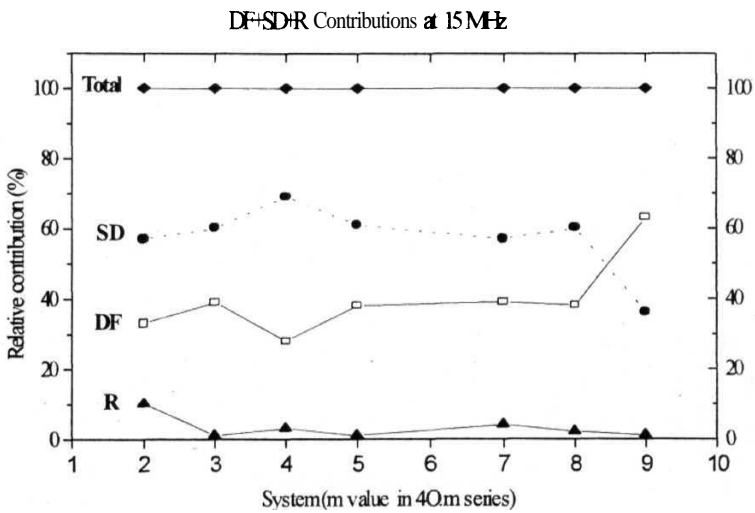


Figure 6.50e.

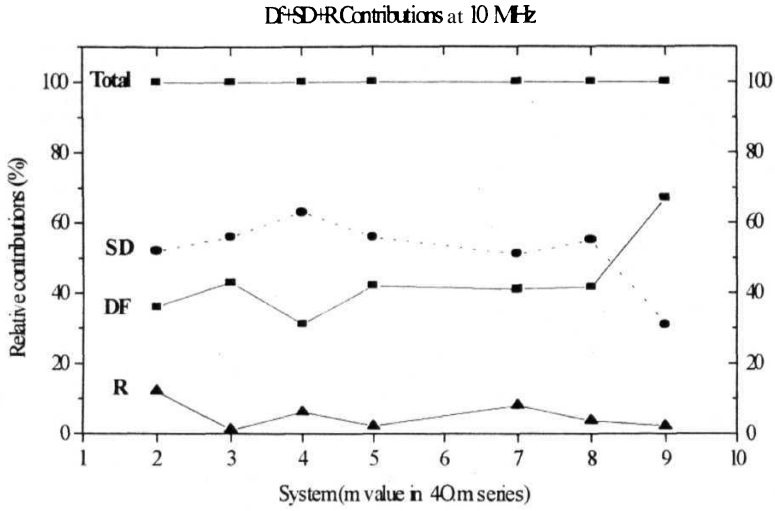


Figure 6.50f.

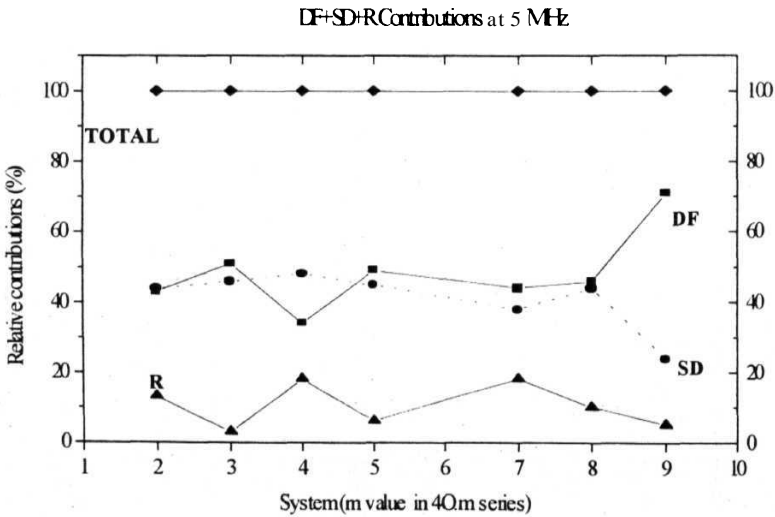


Figure 6.50g.

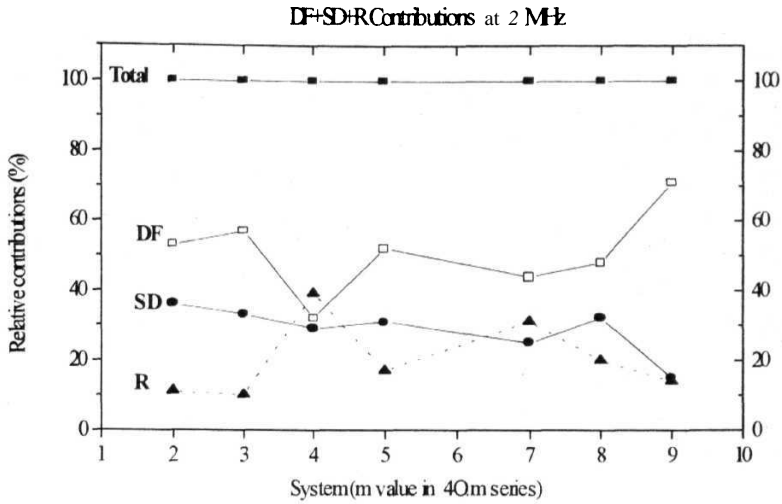


Figure 6.50h.

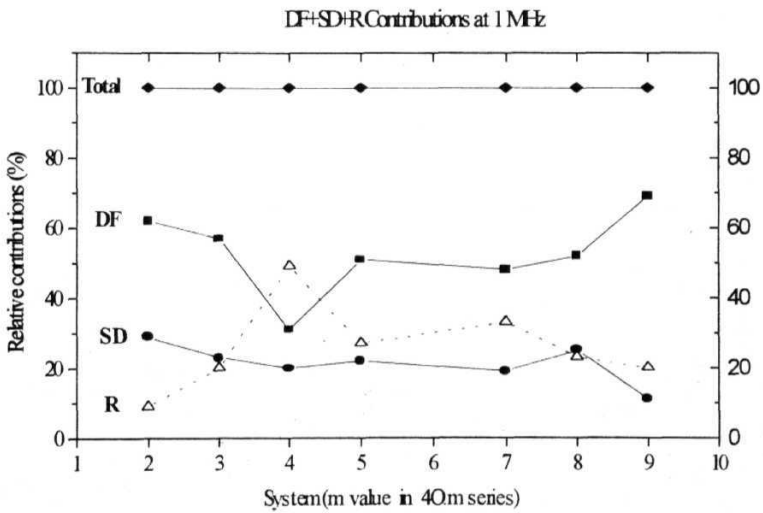


Figure 6.50i.

DF+SD+R Contributions at 500kHz

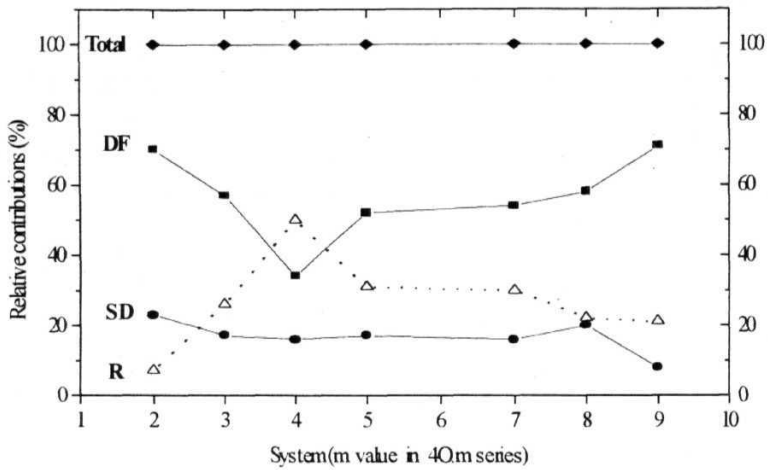


Figure 6.50j.

DF+SD+R Contributions at 200kHz

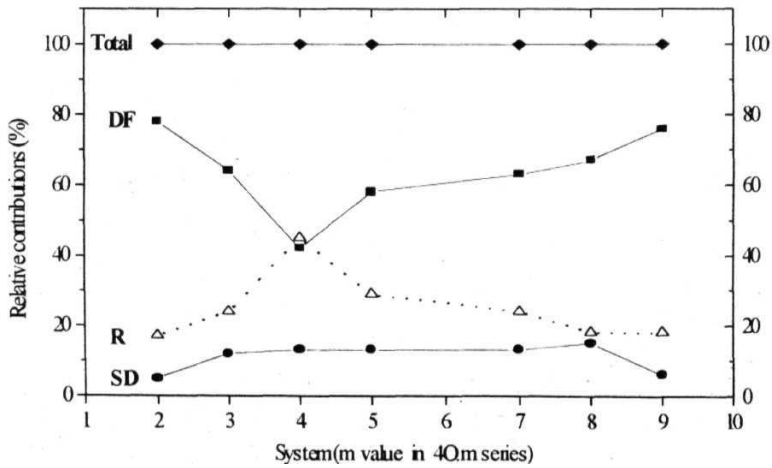


Figure 6.50k.
DF+SD+R Contributions at

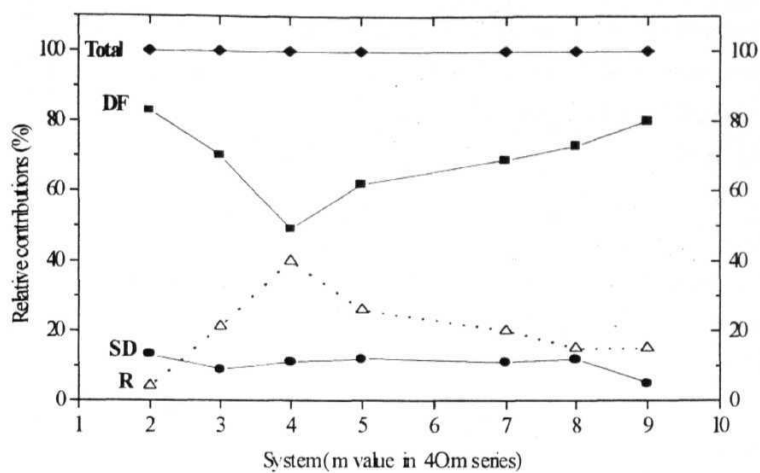
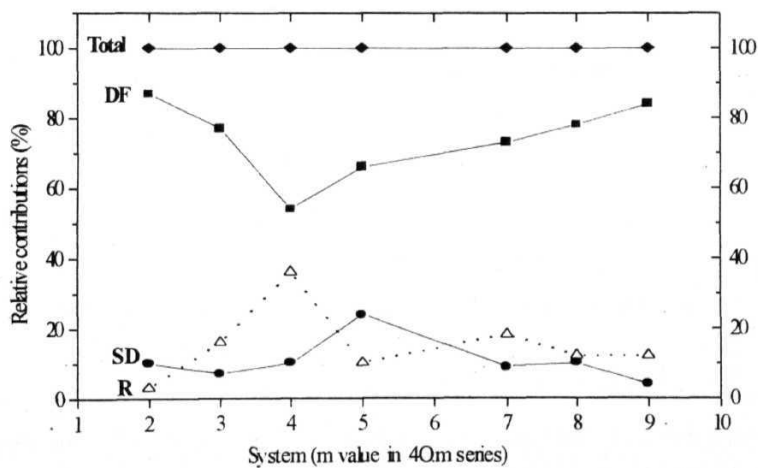


Figure 6.50l.
DF+SD+R Contributions at 50kHz



6.10. References

1. G. Ravindranath, *Ph. D Thesis*, University of Hyderabad, India (1990);
G. Ravindranath, K. Venu and V. S. S. Sastry, *Chem. Phys.*, **140**, 299 (1990);
G. Ravindranath, K. Venu, V. S. S. Sastry and G. Padmavathi, *Phase Trans.*,
12,129 (1988), G. Ravindranath, K. Venu and V. S. S. Sastry, *Z Phys. B:*
Cond.Matter 78, 235 (1990).
2. A. S. Sailaja, *Ph. D thesis*, University of Hyderabad, India (1994).
3. V. Graf, F. Noack and M. Stohrer *Z.Naturforsch.* **32a**, 61 (1977).
4. F. Noack and K. H. Schweikert, in "*The Molecular Dynamics in Liquid Crystals*",
(eds.) G. R. Luckhurst and C. A. Varacini, Kluwer Academic Publishers, London,
(1994).
5. G. W. Smith and Z. G. Gardlund *J. Chem. Phys.* 59, 3214 (1973).
6. V. Vill, *LiqCryst Database*, Demo Version 3. 4, Universitat Hamburg, Germany
(1999).
7. D. M. Pothukuchi, *Ph.D Thesis*, Nagarjuna University, INDIA (1989); A. R.
Alapati D. M. Potukuchi, N. V. S. Rao, V. G. K. M. Pisipati, A. S. Paranjpe and
U. R. K. Rao, *Liq. Cryst.* 3, 1461 (1988). V. G. K. M. Pisipati, S. B. Rannavare
and J. H. Freed, *Mo/. Cryst. Liq. Cryst. Lett.* 4, 181 (1987).
8. P. G. de Gennes "*The Physics of Liquid Crystals*", Clarendon Press, Oxford
(1974).
9. B.I. Halperin, T. C. Lubensky and S. K. Ma, *Phys. Rev. Lett.*, **32**, 292 (1974).
10. J. Longa, *Chem. Phys.*, 85, 2974 (1986); *Z Phys B-Condensed Matter* 64, 357
(1986).
11. F. Noack, Becker and J. Struppe, "*Field Cycling NMR Spectroscopy and
Applications*" *Prog. In NMR Spectroscopy* (1997).
12. R.Y. Dong, "*Nuclear Magnetic Resonance of Liquid Crystals*", Springer-Verlog
(1997).
13. G. Vertogen and W. H. de Jeu, in "*Thermotropic Liquid Crystals, Fundamentals*"
Springer Series in Chemical Physics, (ed.) F.P. Schafer, Springer-Verlag, Berlin,
Vol. 45(1988).
14. R. Blinc, M. Vilfan, M. Luzar, J. Seliger and V. Zagar, *J. Chem. Phys.*, 68, 303
(1978). R. Blinc, *NMR Basic Principles Progress*, **13**, 97 (1976).

15. J. W. Doane and D. L. Johnson, *Chem. Phys. Lett.* 6, 291 (1970).
16. **R R Vold** and R. L. Vold, *J. Chem. Phys.* 88, 4655 (1988); R. R. Vold and **R L Vold**, in *"The Molecular Dynamics in Liquid Crystals"*, (eds.) G. R. Luckhurst and C. A Veracini, Kluver Academic Publishers, London, 207 (1994) and references therein.
17. P. Pincus, *Solid State Commun.*, 7, 415 (1969).
18. K. Venu and V. S. S. Sastry, *"Symposium on Field Cycling Relaxometry (Techniques, applications and Theories)"*, Berlin, 39 (1998).
19. J. W. Goodby, G. W. Gray, A. L. Leadbetter and M. A Mazid in *"Liquid Crystals of one and two dimensional order"*, (eds.) W. Helfrich and G. Heppke, Springer - Verlag, New York (1980).
20. M. Takahashi, S. Mita and S. Kondo *Mol. Cryst. Liq. Cryst.* **147**, 99 (1987)
21. R. M. Richardson, A. J. Leadbetter, J. B. Hayter, W. G. Sterling, G. W. Gray and A. Tajbakhsh, *J. de Phys.*, 45, 1061 (1984).
22. St. Limmer, J. Schiffler and M. Findeison, *J. de. Phys.* 45, 1149 (1984).
23. C. Dybowski, B. Smith, and Ch. Wade, *J. Phys. Chem.*, 75, 3834 (1971).
24. E. Heinze and S. Grande, *Chem. Phys. Lett.*, 58, 87 (1978); E. Heinze and S. Grande and A. Loshe, *Ann. Phys.* **35**, 145 (1978).
25. C. G. Wade, *Ann. Rev. Phys. Chem.*, 28, 47 (1977).
26. G. Nagel, W. Wolfel and F. Noack, *Israel J. Chem.* 23, 380 (1983).
27. R. Blinc and I. Musevic in *"Hand Book of Liquid Crystals"*, Vol 2A, (eds.) D. Demus, J. Goodby, G. W. Gray, H.-W. Spiess and V. Vill, Wiley-VCH, Chap. III, 170 (1998).
28. W. Wolfel, F. Noack, and M. Stohrer, *Z Naturforsch*, **30a**, 437 (1975).
29. R.Y. Dong, E. Tomchuk and E. Bock *Can. J. Phys.*, 53, 610 (1975).
30. A. Tolmachev, A. Fedoryako and L. Lisetski. *Mol. Cryst. Liq. Cryst.* **191**, 395 (1990)
31. W. Wedler, in *"Hand Book of Liquid Crystals"*, Vol. I, (eds.) D. Demus, J. Goodby, G. W. Gray, H.-W. Spiess and V. Vill, Wiley-VCH, Chap 6, 334 (1998).
32. D. Dunmur and K. Toriyama in *"Hand Book of Liquid Crystals"*, Vol. 1, (eds.) D. Demus, J. Goodby, G W Gray, H -W. Spiess and V. Vill, Wiley-VCH, Chap. 4, 253 (1998).

33. D. Dunmur and K. Toriyama in *"Hand Book of Liquid Crystals"*, Vol. I, (eds.) D. Demus, J. Goodby, G. W. Gray, H.-W. Spiess and V. Vill, Wiley-VCH, Chap. 3, 217 (1998).
34. R. R. Vold and R. L. Vold, in *"The Molecular Dynamics in Liquid Crystals"*, (eds.) by G. R. Luckhurst and C. A. Veracini (Kluwer Academic Publishers, London, 1994), 207, and references therein; R. R. Vold and R. L. Vold, *J. Chem. Phys.* 88, 4655 (1988).
35. P. L. Nordio, P. Busolin, *J. Chem. Phys.*, 55, 5485 (1971); R. Y. Dong, *"Nuclear Magnetic Resonance of Liquid Crystals"*, Springer-Verlog (1997), Chap. 6, 7, 8 and references therein.
36. J. H. Freed, *J. Chem. Phys.*, 66, 4183 (1977).
37. D. E. Woessner, *J. Chem. Phys.*, **36**, 1 (1962).
38. N. Bloembergen, E. M. Purcell and R. V. Pound, *Phys. Rev.* 73, 679 (1948).
39. H. C. Torrey *Phys. Rev.* 97, 962 (1953).
40. M. Vilfan, R. Blinc and J. W. Doane *Solid State Commun.*, **11**, 1073 (1972)
M. Vilfan and S. Zumer *Phys. Rev.* **A21**, 672 (1980). M. Vilfan, J. Seliger, V. Zagar and R. Blinc *J. Chem. Phys.* 86, 1055 (1980).
41. J. Chrusciel, S. Wrobel, B. Gestblom and W. Haase, in *"Modern topics in liquid crystals"*, (ed.) A. Buka, World Scientific, 31 (1993)
42. Kei Murase, *Bull. Chem. Soc. Jpn.* 45, 1772 (1971).
43. F. Noack in *"Hand Book of Liquid Crystals"*, Vol. I, (eds.) D. Demus, J. Goodby, G. W. Gray, H.-W. Spiess and V. Vill, Wiley-VCH, Chap. 13 (1998).
44. F. Noack, St. Becker, and J. Struppe, in *"Annual reports on NMR spectroscopy"*, (ed.) G. A. Webb, 33, 1 (1997).
45. J. R. Owers-Bradley, I. D. Calder, J. B. Ketterson and W. P. Halperin, *Mol. Cryst. Liq. Cryst.*, 76, 165 (1981)
46. J. Struppe and F. Noack, *Liq. Cryst.*, 20, 595 (1996).
47. K. H. Schweikert and F. Noack, *Z. Naturf. a*, 44, 597 (1989).
48. H. Bender, F. Noack, M. Vilfan and R. Blinc, *Liq. Crystals*, 5, 1233 (1989).

49. F. Noack and K.H. Schweikert, in *"The Molecular Dynamics in Liquid Crystals"*, (eds.) G.R. Luckhurst and C.A. Varacini (Kluver Academic Publishers, London, (1994), 233, and references therein; F. Noack in *"Hand Book of Liquid Crystals"*, Vol. 1, (Eds.) D. Demus, J. Goodby, G W.Gray, H.-W. Spiess and V. Vill, Wiley-VCH, Chap 13, 582 (1998), and references therein.
50. G.L.Hoatson and Y.K. Levine, in *"The Molecular Dynamics in Liquid Crystals"*, (eds.) G R Luckhurst and C. A Varacini, Kluver Academic Publishers, London, Chap. 1(1994).
- 51 J. L Figueirinhas, A. Ferraz, A C. Ribeiro, H. T. Nguyen and F. Noack, *Ferroelectric**, **146**, 123 (1993).
- 52 W H Press, B P Flennerly, S. A Teukolsky and W. T. Vetterling, *"Numerical Recipes, The art of Scientific Computation"*, Cambridge University Press, Cambridge (1986).
53. F. Brochard,./ *Phys. (Paris)*,34, 411 (1973).

Chapter 7

NMRD Studies of Binary Liquid Crystal Mixtures exhibiting Induced Smectic A_d Phases

Chapter 7 presents a study of molecular dynamics as a function of molecular composition in novel binary liquid crystalline mixtures of nematic liquid crystals 8CN and 7BCB, which exhibit Induced Smectic Phase (ISP). Frequency and temperature dependent spin-lattice relaxation time measurements were carried out in pure systems and mixtures at specific compositions. This work is done in collaboration with another researcher in the same laboratory. Data analysis was done considering four different dynamic processes, namely Director Fluctuations (*DF*), Self-Diffusion (*SD*), Rotations about the short axis (*R*) and Frustration (*F*), in mediating the spin relaxation. Formation and segregation of molecular associations (**dimers** and clusters) is termed as 'Frustration' in this work.

Section 7.1 gives a brief account of liquid crystalline mixtures. Theoretical and experimental understanding of phase diagrams and physical properties of the liquid crystalline mixtures are reviewed. *Section 7.2* presents the physics of frustrated liquid crystals. The factors responsible for the frustration, such as **dimerization** and the end chain length are discussed. Present understanding of the systems under study (8CN + 7BCB) is also presented in this section.

Sections 7.3 and 7.4 presents the results obtained from the NMRD studies of pure nematic liquid crystals 8CN and 7BCB. *Sections 7.5 and 7.6* presents the results obtained from the NMRD studies of nematic and induced smectic phases of the binary liquid crystal mixtures of 8CN and 7BCB at two different contributions.

Section 7.7 presents the summary and conclusions of this study. Molecular dynamics as a function of composition and the percentage contributions of different mechanisms to the spin relaxation are also presented.

7.1. Liquid crystal mixtures

7.1.1. Introduction

A single compound, which fulfils the liquid crystal specification for even the simplest type of display, has not yet been found [1,2]. For a simple watch display, the basic requirements are that the nematic temperature range should be -10°C to $+60^{\circ}\text{C}$, together, with a high positive dielectric anisotropy to allow a low voltage operation. For displays with modest information content, e.g., simple calculators, it is necessary to use a multiplexed addressing scheme. For this, a sharp threshold voltage is required and to achieve this, the ratio of elastic constants K_{33}/K_{11} should be low [2].

Thus, mixture optimization for even the simplest displays can be a challenge. Many physical properties need to be simultaneously adjusted towards target values and it is not often possible to adjust one parameter without affecting another. In some cases, the properties vary linearly with concentration, but in others they do not. Generally, the melting point of a binary mixture of compounds is less than its constituent components. From the point of view of applications, however, the main interest in the theory is in predicting the variation of the nematic-isotropic transition temperature with composition and the temperature variations of the component order parameters in the nematic phase. Understanding of the molecular level processes, which are responsible for the variation of the physical properties, is one of the important aims of molecular dynamics study, in binary liquid crystals exhibiting a variety of phases like the re-entrant nematic, nematic gap, induced smectic and induced nematic phases. Before going into the details of the present NMRD study on the binary mixtures of 8CN+7BCB, an attempt is made to explain the various parameters responsible for such interesting phase diagrams here.

7.1.2. Theoretical review of binary liquid crystal mixtures

7.1.2.1. Linear and non-linear behaviors of phase diagram

The Schrodter van Laar equation [4] (7.1) relates the melting point of a mixture to the mole fraction (X_A) of component A.

$$\ln X_A = H_A / R [(1/T_A) - (1/T)] \quad (7.1)$$

where, H_A and T_A are the latent heat and melting point of a pure compound, R , the gas constant. For a mixture of N components there are N such equations, which, when solved for the condition shown in the equation give the temperature and mole fractions of the eutectic composition.

Nematic-Isotropic transition temperature (T_{NI}) in certain binary mixtures do not exhibit a linear dependence with respect to the mole fraction of the constituents, but show the negative deviation from the values interpolated by a linear relation. **Osman et al.**, [5] have found experimentally, that such non-ideal behavior is closely related to molecular packing or to the molecular geometry.

Humphries-James-Luckhurst (HJL) extended [6] the Maier-Saupe theory [7] to the multi-component systems of nematogens, and taking account of only the intermolecular attractive interaction, they could explain the negative deviation from linearity by adjusting the interaction parameter. Later, based on the generalized van der Waals theory, the **MS-HJL** theory was extended by Cotter and Wacker [8] to the multi-component systems, considering both intermolecular attraction and repulsion.

Nakagawa and Akahane [9] have studied the nematic-isotropic transition of binary mixtures of nematogens and calculated phase diagrams on the basis of the generalized van der Waals theory, to compare them with experimental results. It was shown that such non-ideal behavior of T_{NI} in certain binary mixtures results from the imbalance between the attractive and repulsive interactions for both the components. And for the binary mixtures of a homologous series of nematogens, linearity is expressed by

$$T_{NI} = x_1 T_{NI1} + x_2 T_{NI2} \quad (7.2)$$

should be found if the relationship

$$u_{11} l_1^2 = u_{22} l_2^2 \quad (7.3)$$

holds true. Here, x , and T_{NI} are the mole fraction and the **nematic-isotropic** transition temperature of the f component respectively. u_{ii} is the anisotropic attractive interaction coefficient between i^{th} kind of molecules, l_i , the effective molecular length of an i^{th} kind of molecule. The equation 7.3 explains the balance between the repulsive and attractive interactions. From the microscopic point of view, these results seem to imply that the similarity of the molecular structures or geometries of each of the kind of molecule result in the linearity found in the phase diagrams. If the equation 7.3 is not satisfied, a non-ideal behavior appears.

7.1.2.2. Molecular flexibility

The importance of molecular flexibility is emphasized on, in this study. Effects of alkyl end chains on the nematic-isotropic transition temperature in the binary mixtures have been studied by Nakagawa and Akahane [9]. A balance relation between the length of the flexible end chain and that of the rigid core was obtained and it was concluded that the balance between molecular flexibility and rigidity bears on the thermodynamic stability of **nematic** phase in a binary mixture of nematogens. And it is important to note that the similarity of molecular structures or geometries of the constituent molecules seem to be crucial for the thermodynamic stability of the nematic phase in a binary mixture of nematogens, in consistency with the study of Osman et al., [5]. There have been theories for binary mixtures using extensions of Maier-Saupe theory, lattice models of hard rods and hybrid models [2].

7.1.3. Theoretical models for the Induced Smectic Phases (ISP)

A molecular model for the induced smectic phase formed in the cyano compounds has been proposed by de Jeu et al., [10]. The dipole-induced dipole interaction as well as. the charge transfer complex formation in which, the cyano compound acts like an electron acceptor are responsible for the occurrence of the induced smectic A phase.

Kyu et al., [11] have recently developed a model for ISP, based on the combination of the **Flory-Higgins** (FH) theory [7,12] for isotropic mixing and the **Maier-Saupe-McMillan** (MSM) theory [13] for induced smectic ordering in non-smectic liquid crystal mixtures, such as **nematic** mixtures. It was also shown [11], that the strong nematic interaction between the dissimilar mesogens could give rise to a more stable nematic phase in the nematic mixtures. The ISP is also an outcome of such a strong mesogenic interaction.

The total free energy of mixing, for a binary nematic mixture may be expressed in terms of a simple addition of the free energy of mixing of isotropic liquids (g^I), and the free energy of anisotropic ordering of the liquid crystals undergoing ISP transition (g^S).i. e., $g = g^I + g^S$, where g represents the **dimensionless** total free energy density of the system. The free energy of isotropic mixing can generally be described by the Flory-Higgins theory [13] as

$$g^I = \frac{G^I}{nkT} = \frac{\Phi_1}{r_1} \ln \Phi_1 + \frac{\Phi_2}{r_2} \ln \Phi_2 + \chi \Phi_1 \Phi_2 \quad (7.4)$$

where k is the Boltzmann constant and T , the absolute temperature. r_1 is the number of sites occupied by one liquid crystal molecule and is equal to unity, for a low molar mass liquid crystal, whereas, r_2 represents the number of segments or sites occupied by a single chain. Φ_1 and Φ_2 are the volume fractions of the component 1 and 2, respectively. χ is known as the Flory-Higgins interaction parameter, which is generally assumed to be a function of reciprocal absolute temperature.

Free energy density of the anisotropic ordering of the nematic liquid crystal mixtures undergoing induced smectic ordering is represented in terms of the Maier-Saupe-McMillan mean field theory [7,11,12] as

$$g^S = \frac{G^S}{nkT} = -\Sigma_1 \Phi_1 - \Sigma_2 \Phi_2 - \frac{1}{2} \nu_{11} s_1^2 \Phi_1^2 - \frac{1}{2} \nu_{22} s_2^2 \Phi_2^2 - \nu_{12} (s_1 s_2 + \beta \sigma_1 \sigma_2) \Phi_1 \Phi_2 \quad (7.5)$$

where, $2\}$ and Σ_2 represent the decrease of entropy due to the alignment of individual liquid crystal molecules of component 1 and the mesogenic group of compound 2,

respectively. β represents a **dimensionless** cross-interaction strength between two dissimilar **mesogens** undergoing the induced **smectic** ordering and thus will be called, hereafter, the induced smectic interaction parameter. Physical meaning of this parameter is similar to the McMillan parameter (α) described in the chapter 4. β , here, is related to the formation of a single smectic due to strong cross-mesogenic interaction of dissimilar mesogens. The magnitude of β is twice the α value of the pure smectic.

As in the case of α in the McMillan theory [12], the magnitude of the induced smectic interaction parameter β generally determines whether a phase transition occurs, from a smectic to an isotropic phase directly or through a **nematic phase**. s_1 and s_2 are the nematic order parameters and σ_1 and σ_2 , the smectic order parameters. v_{11} and v_{22} are the nematic interaction parameters of the pure components whereas, v_{12} represents the cross-nematic interaction between the dissimilar mesogens, which is defined as

$$v_{12} = c\sqrt{v_{11}v_{22}} \quad (76)$$

Kyu et al., [11] have derived equations for the order parameters s_1 and s_2 and σ_1 and σ_2 , which depend on the volume fraction, smectic cross-interaction strength (β) and the nematic interaction parameters (v_{11} , v_{22} , and v_{12}). v_{11} and v_{22} are given to be inversely proportional to temperature. Induction of smectic A phase is critical about the temperature dependence of the coupling term involving cross-nematic interaction (c or v_{12}), and the cross-smectic interaction parameter which is present in the equation 7.6. Relative strength of the cross-nematic interaction of the dissimilar mesogens with respect to similar mesogens is represented by the value of c . If the value of c is less than 1, the cross interaction is weak, thus the nematic phase is favored and no smectic phase is induced. When c is greater than 1, where cross-interaction becomes stronger than that in the same mesogens, the nematic becomes more stable in the mixture relative to that in the pure constituent nematics. This situation gives rise to an *Induced Nematic Phase*. Depending on the magnitude

of the coupling between the cross-nematic interaction parameter c and the cross smectic interaction parameter β a *smectic phase may be induced in a nematic mixture*.

The interaction parameters associated with the **Flory-Higgins** theory do affect the induced nematic phase boundaries, though there is some effect on the induced smectic boundaries (the width of the induced smectic boundary changes with FH interaction parameters). Similar to the McMillan parameter α , the liquid crystal phase transition occurs in the smectic-nematic-isotropic sequence when β is greater than 1.96 (keeping $c = 1.2$ as constant). Different phase diagrams had been obtained by **Kyu et al.**, [11] with the proper choice of parameters. For example, when β changes from 1.2 to 1.5, the stability of the ISP increases and the convexity of the smectic-island formed gets slightly sharper. When β increased to 2, the smectic-isotropic transition occurs in the intermediate compositions without passing through the nematic phase. In the high compositions of either constituent, the transition occurs from an isotropic to the pure nematic, through the I+N coexistence regions in the descending order of temperature. It is interesting to note that the induced nematic phase in the I+N regions is more stable than that in the pure components. This model was able to reproduce the experimental phase diagrams of certain ISP's with a reasonably good precision. The experimental phase diagram and theoretically evaluated temperatures are plotted in figure. 7. 1a.

Kyu et al., [11] have evaluated temperature dependent order parameters in the mixtures, as a function of composition (figure 7.1b). From the order parameters the free energy of anisotropic ordering (figure 7.2) and the phase diagram were calculated. The concave free energy curves obtained for the mixtures suggest that the nematic phase is more stable in the mixture as compared to that, in the pure state. Upon lowering the temperature, a subtle change in the curvature was noticed at certain intermediate compositions. This implies that the two free energy curves, attribute to the induced nematic and smectic orderings. The anisotropic free energy is lowest at the middle composition and at lower temperatures suggesting that the induced smectic phase is most stable in the mixture.

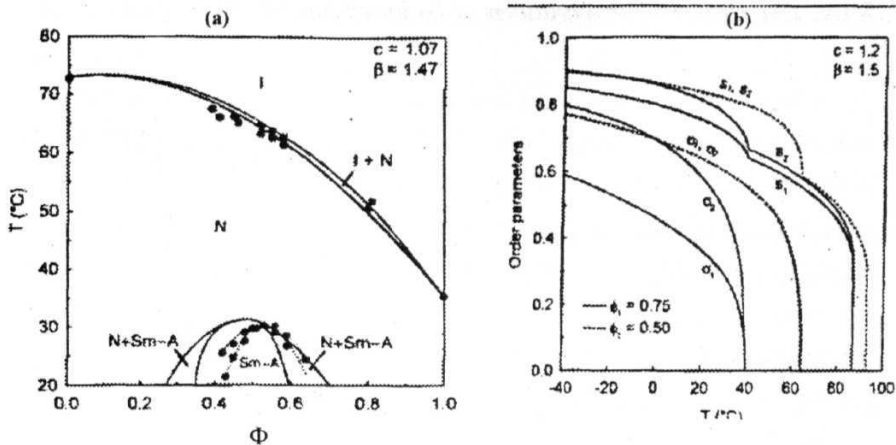


Figure 7.1. (a) Phase diagram of the binary mixture of 4-n-pentyl-4'-cyanobiphenyl and 4-n-methoxy azoxybenzene in compared with the calculated coexistence curves for induced nematic and induced smectic coexistence phase boundaries (b). Temperature dependence of the nematic and smectic order parameters for a mixture comprised of two nematic liquid crystals with $T_{N,1} = 60\text{ }^{\circ}\text{C}$; $T_{N,2} = 50\text{ }^{\circ}\text{C}$; $c = 1.2$ and $\beta = 1.5$ exhibiting an ISP for two compositions $\Phi_1 = 0.5$ (dashed lines) and $\Phi_2 = 0.75$ (solid lines) [11].

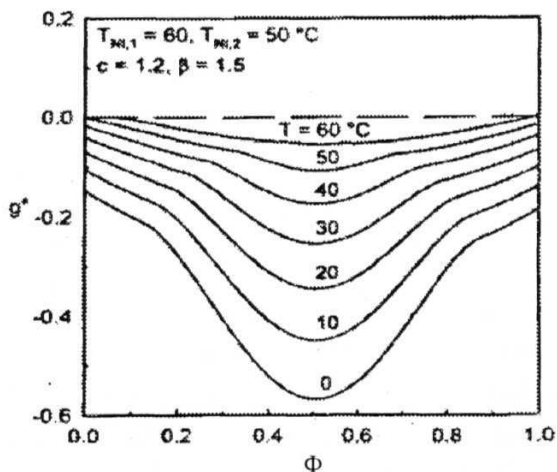


Figure 7.2. Variation of combined nematic and induced smectic free energies versus composition at various temperatures for a mixture of two nematic liquid crystals with $T_{N,1} = 60\text{ }^{\circ}\text{C}$; $T_{N,2} = 50\text{ }^{\circ}\text{C}$; $c = 1.2$ and $\beta = 1.5$ [11].

7.1.4. Experimental observations of Induced Smectic Phases

It is known that the induced smectic A (A_i) phases, which have the maximum thermal stability for the mixture with a 50 mole percent composition usually results [3,14,15,16]. These types of compounds are used in practically all mixtures of technological importance and care must be taken to avoid the occurrence of the induced smectic A phase in the operational temperature range of the displays. However, it is advantageous if the induced smectic A phase occurs at low temperatures, which usually decreases the value of K_{33}/K_{11} , the ratio of bend and splay elastic constants [17,18], thus increasing the sharpness of the electro-optic response of voltage in TN devices.

Different types of induced phases are observed in the literature [3]. Nematic or smectic phases may be injected to the system containing non-mesogenic compounds. For this to happen, at least one component should have a distinct anisotropic shape. The shape of the molecule should allow, for the compound to be included into the category of quasi-mesogens and donors. The second component should have rather strong acceptor properties. The phases of higher order are injected by acceptor-donor interaction as described by Matsunaga et al., [19].

Alkyl chain length, odd-even effects and polarity of the end group are the crucial factors in deciding the type of induction, to take place. The incorporation of shorter molecule into the free space between the bulky swallow tailed-ends of the molecules injects the smectic A phase [3].

Induction of the smectic phase is accompanied by changes in the transition temperatures, transition enthalpy, entropy, volumes, densities, specific heat capacities, viscosities and elastic constants [1-3]. Non-additive changes in the density, with mixing, lead to changes in properties like the refractive index and dielectric properties. These changes are found to be non-linear with composition. The volume averaged order parameter is also independent of the concentration. Loosening of nematic phase occurs due to steric effects, though the underlying induced smectic A is

not disturbed [3]. Compounds with even alkyl chains are more smectogenic than the odd ones.

7.1.5. Nematic gap

Another important observation, which is exactly opposite to the induced smectic phase, is known as, the 'nematic gap' [3]. While **ISP** refers to the stability of the smectic order, nematic gap refers to the destabilization of the smectic order and a transformation of the system to a system of lower order (nematic). This phenomenon occurs in the binary mixtures of two polar systems, where one possesses a monolayer smectic **A₁** phase and the second, a bilayer smectic **A_d** phase. Chemical structure and the layer organization of the constituents play a crucial role in destabilizing the smectic order. If the layer spacing and molecular organization of constituents is very different, the probability of the formation of the nematic gap is more. Another important factor is connected with the direction of the dipole moments. If the orientation of the dipole moments of the linking groups is in accordance with the dipole moment of the terminal group, a nematic gap appears. It has also been experimentally observed that the systems exhibiting such nematic gap shows lower transition enthalpies for the transitions between **S_A-I** and **S_A-N** phases. The ratio of the transition temperatures T_{S-I}/T_{S-N} is also very small for both compounds of the mixture forming nematic gap. It is generally observed, that the mixture of a two ring polar smectic **A₁** system with a short aliphatic end chain and two-or-three ring polar smectic **A_d** compounds with longer aliphatic chain could create a nematic gap.

7.2. Frustration, Dimerization and Molecular Dynamics in Induced Smectic Phases

7.2.1. Introduction

Frustration and reentrance are connected to each other in condensed phases, which indicates the presence of wide a variety of conflicting goals arising from random interactions in a many body system. Frustrated liquid crystalline phases are different from normal mesophases in terms of their short-range structure and transport properties [20]. Before going to the microscopic dynamic behavior of the frustrated liquid crystals it is useful to define the term frustration in liquid crystals and the other systems.

7.2.2. Frustration

Ising Hamiltonian of N spins at N sites, with random nearest neighbor interactions reveals, the nature of the frustration in any physical many body systems. The statistical mechanics of this system reveals a sharp transition in the limit, N tends to infinity, to a non-ergodic state the spin glass state, where different regions of phase space becomes irretrievably separated by energy barriers. As the temperature is lowered, these regions proliferate. Frustration is also found in the systems with ferromagnetic and **antiferromagnetic** competing interactions on a square lattice. When competing next nearest neighbor interactions are introduced, reentrant transitions result. It typically occurs for a narrow range of coupling constants [20].

7.2.3. Frustration in Liquid crystals

In liquid crystals, the reentrant transition occurs at the **nematic-smectic A** phase ranges of temperatures. The Hamiltonian, in this case consists of two-particle dipolar potential that has competing ferroelectric and **antiferroelectric** interactions. The dipoles are oriented parallel to the layer normal. The system is analyzed in terms

of three dipoles or triplets. When dipolar forces between two cancel, the third dipole experiences no **force**. It is free to permeate from layer to layer, "frustrating" **smectic order**. However, by allowing displacements of the three dipoles relative to each other in the layering direction, a population of triplets is generated that has net short range dipole. They interact with neighboring triplets within a plane via short-range antiferroelectric or ferroelectric interactions thus stabilizing the layered structure. The energy fluctuations associated with an ensemble of triplets can be evaluated. If an **Ising** criterion is satisfied, it is concluded that the ensemble stabilizes a layered structure. If the criteria cannot be satisfied, it is concluded that a disordered state prevails (**nematic**). Berker [21-24] calls this theory of frustration, the spin-gas model instead of spin-glass model, due to the fact that the medium is liquid.

7.2.4. Mean field and Frustration strategies

In the mean field strategy with competing interactions, the system democratically chooses a compromise state in which all the members of the system are slightly unhappy [20]. In contrast, in the frustration strategy, the system chooses a configuration where all the members are locally satisfied. After the locally satisfied regions are brought into contact, the magnitude in the energy fluctuations is monitored. If these are large, the system is unfrustrated and orders to **find** the optimum configuration. If these are small, no solution exists and the system is called frustrated.

Entropy is important for stabilizing many body systems that have a large number of degenerate states. The members of the frustrated system are not locked into a single state and hence, contribute to the entropy but not the symmetry. In reviewing the Berker theory [21,22,23,24] the picture that emerges is that the reentrant nematic in polar compounds is a frustrated smectic A (no solution) or a frustrated nematic phase. It is not non-ergodic since it is a three dimensional fluid. In order to set up their ensemble of triplets, notches are installed in each layer. The notches allow them to consider configurations where dipoles are displaced on atomic length scales out of the layer. In this scheme, when two dipoles are in an **antiferroelectric** orientation and in the same notch, there is a near cancellation of

forces between the "dimer" and the third member of the triplet that is now free to permeate parallel to the layers. The triplet does not stabilize a layered phase structure. Triplets that are displaced relative to each other, have a net dipole and so can stabilize a layered structure through short-range ferroelectric or anti ferroelectric interactions.

Using a criterion from the distorted **Ising** system and classifying the energy as strongest, intermediate and weakest and monitoring variance in the energy, stability can be defined. When the sign of strongest and intermediate interactions are the same, the dominant interaction stabilizing the layer is ferroelectric, associated with smectic **A₁** and when opposite, it is anti ferroelectric, associated with **A_d**. If the criterion cannot be satisfied, then the nematic state results (disordered state). The frustration theory with the inclusion of next nearest neighbor interactions and orientational order seems to be a better theory for a better understanding of frustrated liquid crystal phases and incommensurate phases of liquid crystals.

7.2.5. Dimerization and the formation of the ISP

Due to the large dipoles present in the polar molecules, two polar molecules form a **dimer** and hence an incommensurate layer spacing is possible [20]. As the **dimer** proportion increases in the layered mesophase, the dipolar interactions stabilizing the layered phase would be weakened, and eventually the smectic stability collapses, which leads to the formation of the nematic phase at the cost of smectic regions. By mixing two liquid crystals of different length scales or polarities, the dipolar interactions can be enhanced and the formation of layered phases at the cost of nematic phase is also possible. While the weakening of dipolar forces forms the reentrant phases, strengthening of dipolar phases leads to induced smectic phases (ISP). The dipole-induced dipole interactions are found to be the major dipolar forces responsible for the ISPs. The dimerization is limited to the extent that the proportion is not sufficient to collapse the dipolar attractive forces. When this limit is exceeded either by changing the ratios or by varying the temperature, the ISP loses its stability and forms an island of the smectic **A_D** phase.

7.2.6. *Role of the alky/ chains on the stability of the frustrated phases*

The connection between phase stabilities and interactions is studied by various researchers [1]. The pressure studies by Cladis et al., [25], on some pure liquid crystals have revealed that the maximum pressure a smectic A_d phase supported was a sensitive function of the number of methylene groups interacting in the smectic layers. In the frustration picture, presumably, the fewer the number of methylene groups, the less deep the potential minima associated with the notches and the more susceptible the system is to permeation. The theories by Cladis et al., [20], Gray and Lydon [26] and Leadbetter et al., [27] had described various schemes of dimer formation and bilayer structures.

Dowell [28] had explained various features such as different orientational and positional ordering found in the nematic, smectic A, reentrant nematic, multiple smectic A, and smectic A_d phases. A model consisting of hard repulsive rods, inter molecular site-site segmental attractions arising from London dispersion forces and soft repulsion of semiflexible chains along with dipole-dipole and dipole-induced dipole interactions in the polar molecules was developed by Dowell. A general partition function derived via combinatorial lattice statistics, for condensed phases with partial or total orientational and positional ordering of the molecules was introduced. In this, partition function can be in one, two or three dimensions, permitting the modeling of nematic, smectic A and ordered smectic phases. The relative stabilities of isotropic, nematic, smectic A, and reentrant nematic phases are studied as a function of temperature, tail flexibility and chain length. Moreover, thermodynamic and ordering properties like the smectic A order parameter, core and tail intermolecular orientational order parameters, density and entropy were also calculated using this generalized model.

Relative stabilities of isotropic, nematic, reentrant nematic, smectic A], and smectic A_d phases were explained by a molecular theory proposed by Dowell [29]. These stabilities were discussed as a function of temperature, pressure, chain length and flexibility, and orientational and positional order of the molecules for different

phases. The explanation for the formation of frustrated phases based on end chain length is given in the following paragraphs.

Very long chain lengths

At a high enough temperature T , the system volume V is large enough for the molecules to pack randomly, and thus the drive for maximum entropy leads to the existence of a stable isotropic phase. As T is lowered, V decreases, and the molecules must order partially to fit in the volume. There is thus a transition to a stable nematic phase. As T decreases V decreases further, and there is a weakly first order transition to a stable S_A phase (in this case for very long terminal chains, it is the S_{Ad} phase). In the S_{Ad} temperature range tails are flexible and V is small enough for the molecules to pack with the lowest energy, i.e., cores tend to pack with other cores and tails pack with other tails. The **semiflexible** tail chains bend and twist well around each other, but do not pack well with the rigid cores. As T decreases even further, there is a transition from S_{Ad} to a low temperature nematic phase. As T decreases, the tail become less flexible and more closely resembles a rigid extension of the rigid core. The difference in packing cores and tails thus decreases; the need for segregated packing of cores with cores and tails with tails, diminishes and is now overcome by the entropy of unsegregated packing, thereby leading to the reappearance of a stable nematic phase. This transition is precipitated by subtle changes in the flexibility on the end chains. This is evidenced by the fact that, while the end chains are less flexible at the transition, they are still somewhat flexible and are certainly not completely rigid as shown by Dowell in his theoretical studies.

Intermediate chain length

The theoretical results obtained are similar with the above results except that the higher temperature N phase has been replaced by an S_{A1} phase. At these lengths the differences in packing cores and tails is large enough to force a total positional alignment of oriented molecules. As T is lowered, the tails become less flexible and the differences in packing cores and tails decrease initially just so, that some

positional alignment is needed and finally, no positional alignment is needed (reentrant nematic phase).

Very short chains length

No stable **smectic A** phases are observed, when terminal chains are very short, consistent with the experimental observations. When the number of segments in the terminal chains are less than that of the number of segments in the core, the packing of the tail segments seems to act as a minor perturbation to the packing of the cores-so minor that the segregated packing of cores with the cores and tails with the tails in an **S_A** phase is no longer necessary, and the drive to maximize entropy, favors the more disordered nematic phase over a smectic A phase. Effect of chain length on the formation of **ISP** is shown in figure 7.3b.

7.2.7. Factors responsible for the ISP in the mixture of 8CN+7BCB

Details of the parameters responsible for the induction and reentrance of new phases in the binary mixtures of liquid crystals are discussed in section 7.1, Details particular to the binary mixtures exhibiting an induced smectic **A_d** phase and pure nematic systems 7BCB (4-cyanobiphenyl 4-heptylbenzoate) and 8CN (4-cyanophenyl 4-octylbenzoate) would be discussed briefly, with the aim of highlighting microscopic features, which influence molecular dynamics in these systems. The phase diagram of the liquid crystal mixture of 8CN and 7BCB is shown in figure. 7.3a

X-ray investigations carried out by Dabrowski et al., [3] on the binary mixtures of 8CN and 7BCB revealed the presence of cybotactic smectic like clusters with a size of around 30 Å in the nematic phases with underlying smectic **A_d** phases. It is also observed that the layer spacing in the induced smectic **A_d** phase is also of the same order. These studies confirmed not only the presence of dimers but also the frustrated nature of nematic phases, which have underlying smectic **A_d** phases. The theoretical explanation given for frustrated nematic phases of 8CN and 7BCB and the induced smectic phase of their mixtures with the experimental evidences on these systems would be discussed here. Dabrowski et al., have compared and used Berker's

spin gas model, as well as Longa and de Jeu's mean field model, in explaining the induction of the smectic A_d phase.

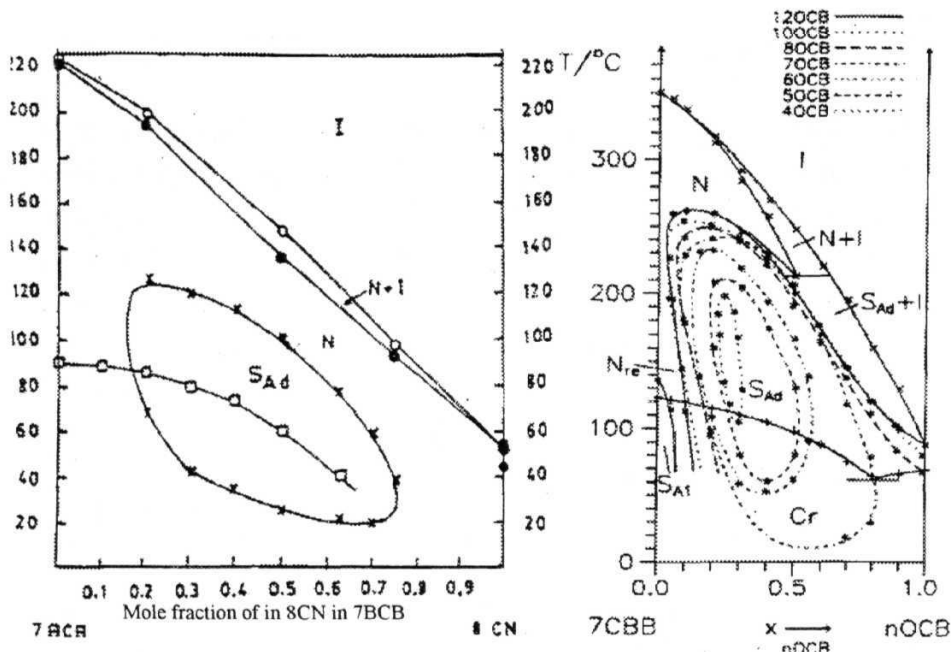


Figure 7.3. (a). Phase diagram showing ISP in the binary mixture of nematic liquid crystals 8CN and 7BCB. (b). Enhancement of the size of the 'induced smectic island' due to end chain length in the binary liquid crystal mixtures (nOCB; $n = 4, 5, 6, 7, 8, 10, 12$ in 7CBB) [3]. Similar enhancement is observed in the case of 7BCB + nCN mixtures also.

Induction of the smectic A_d phases in the binary mixture 8CN+7BCB is controlled by many parameters. Both 8CN and 7BCB have no smectic phases in the pure form. A mixture of these shows a smectic A_d island surrounded by a nematic sea. The pure compound 7BCB has the tendency to form the smectic A_d phase, which is generally high in the longer chain A/BCB systems. Similarly, the chain length and the polarity of the end group of 8CN are significant in forming the ISP (similar to nOCB + 7CBB mixtures). If chain length is decreased in the nCN system, the size of the island shrinks. The polar end group in the system 8CN is also important in the formation of the smectic A_d phase in order to change the monomer-dimer equilibrium

already present in the pure 7BCB system. The steric interactions cause a cage effect for short molecules. Steric forces prohibit close packing of the host molecules (7BCB) and cause the existence of cavities in the host structure, to be filled by short molecules of guest compound (8CN).

The role of **alkyl** chain length, very important in the case of these systems is in agreement with the mean field model proposed by Longa and de Jeu [10] and the frustrated spin gas model proposed by Berker [21-23]. These also consider the alkyl chain length, an important **factor**. The presence of molecules with long alkyl chains in these systems, provide a possibility for different conformations, thus stabilizing the smectic **A_d** phase caused by the denser packing of molecules in layers due to the ability of these paraffin sublayers to prevent the molecules from moving between layers. This view is consistent with the observations that long chain polar molecules form smectic **A_d** phases. Figure 7.3b shows the effect of chain length on the ISP in a similar system (7CBB+nOCB). With the increase of length of the alkyl chain, the size of the induced smectic island **increases**. Even in the systems the minimum chain length ($n>7$) needs to have a smectic **A_d** phase,

de Jeu and Longa's model [10] postulates the need of monomers and **dimers** in stabilizing the smectic **A_d** phase by effective packing. Calculations made by Madhusudana [30] show that longer molecules with terminal polar group (like 7BCB) associate (dimers) themselves in an anti-parallel direction forming the partially bilayered structure with a layer spacing of about 1.4 times of the molecular length (figures 7.4 and 7.5). The concentration of the dimers increases with a decrease in **temperature**.

One of the crucial factors deciding the stability of the smectic **A_d** phase is the concentration of dimers. There is a critical range of **dimer** concentration required for the formation of a smectic **A_d** phase. Another factor is the packing of the dimers, which in turn is controlled by the temperature. At lower temperatures an unfavorable packing of dimers leads to a disappearance of the smectic **A_d** phase. **Moreover**, at high temperatures, reduction in the dimer concentration as well as the increase of

thermal disorder leads to the disappearance of the smectic A_d phase. Thus, a smectic island is formed surrounded by the nematic sea [3].

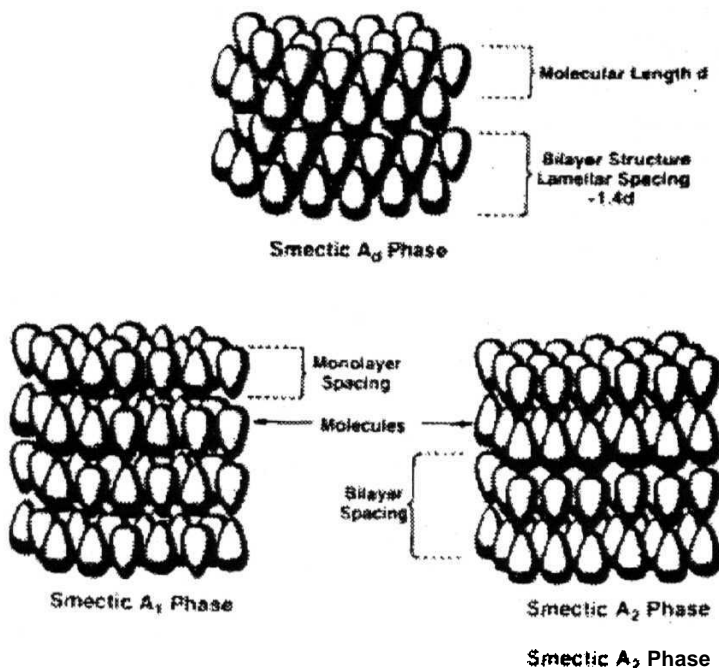


Figure 7.4. Organization of molecules in smectic A_d phase and the typical layer spacing of about $1.4d$ (d is the molecular length). Other types of smectic A phases (smectic A_1 and smectic A_2) are also shown [1e].

Comparing with the pure 7BCB and 8CN, the dimer concentration is necessarily more in the case of the mixture, since a parallel alignment of molecules becomes difficult, due to the steric interactions between the molecules having different lengths. This is the prime reason for the induction of the bilayer smectic A_d phase. The concentration of dimers does not seem to increase with the addition of 8CN in 7BCB

Similarly, Berker's spin gas model can also explain the induction of the smectic A_d phase in the binary mixture of 8CN and 7BCB. In contrast to the mean field theory, Berker's theory does not consider the role played by the 8CN monomers

and 7BCB **dimers** individually and considers them as parts of the '**correlated triplet**'¹ which is formed due to the dipolar short range ferroelectric or antiferroelectric **order**

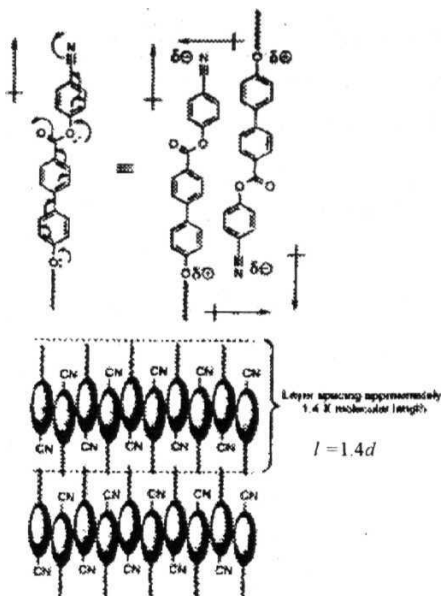


Figure 7.5. Formation of dimers caused by a quadrupolar coupling between the longitudinal dipoles. Molecular structure and dipoles of typical liquid crystal molecules with cyano end group are also shown [1 e].

According to the frustration theory this triplet association is energetically favorable and leads to the minimization of energy, which is necessary for the formation of the induced **smectic A_d** phase. Molecules in this triplet occupy energetically preferred positions (notches) in the direction of the long molecular axis (z-axis). The number of such notches depends on the length of the **alkyl** end chains. Depending on entropy and energetic properties, the triplets may or may not combine, to form a percolating network or a smectic (**A_d**) layering in the x-y plane. The layer spacing and pair length in this model have a statistical nature, which is connected with the concentration of the constituent molecules and their microscopic configurations.

Theoretical calculations of the pair potentials for the nearest neighbor molecules in the triplet, had been made by considering van der Waals forces (which favor parallel, ferroelectric ordering) and steric forces (which favor antiparallel, antiferroelectric ordering of molecules). Since both these forces are expected in the molecular system, a competition of these factors is characterized by the ratio B/A ($B/A < 1$ refers to the domination of the steric force and $B/A > 1$ refers to the domination of the van der Waals attractive forces). Here, A reflects the term of the chain-chain van der Waals attraction and hindrance, and B reflects a dipolar interaction. Short molecules with a strong steric contribution leads to a value of B/A , close to 2. For longer molecules the value of B/A is close to 1.5.

The phase diagram obtained for the ISP are similar to the phase diagrams predicted by the theoretical model of Markov [31], Indekeu and Berker based on the spin-gas model. These observations can be summarized, by saying that the structures of the smectic A phases of different kinds are determined by a fine balance between repulsive steric forces and attractive forces resulting from localized or distributed dipoles of the molecules, as well as dispersion interactions of rigid cores and aliphatic chains. Another important parameter involved in the stability of the smectic A_d phase is a/l , where a , is the average lateral separation and l , the molecular length

In the present system, (8CN+7BCB) and in similar systems (n CBB+ n OCB) the steric forces increase, by mixing the molecules of dissimilar lengths and the average value of a/l increases, by mixing the shorter system 8CN with the long molecular system 7BCB. Such a situation favors smectic A_d phase. Though both the models seem to explain the induced the smectic A_d phase in the present mixtures, dielectric measurements on certain systems, show higher values of changes in the dielectric constants, than the values predicted by the de Jeu and Longa's model.

The controversy over the selection of the model is an open question, which calls for experimentation, in order to understand the microscopic behavior of the molecules. NMRD can provide clues to understand the microscopic behavior of these systems. The nature of the pure system 7BCB, which has a smectic A_d forming tendency is also an important factor to be considered. Increasing the length of the end

chain (8BCB) as well as mixing the shorter polar molecule 8CN plays almost the same role. This virtual smectic A_d nature of the pure system 7BCB can be studied by the NMRD technique in order to understand the molecular level processes, leading the system to have such a tendency.

7.2.8. Molecular dynamics in frustrated phases

The various degrees of freedom of the molecule are treated in the previous chapter, and their contributions to the spin relaxation were discussed in detail as a function of end chain structure. It is known that due to the modulation of the inter-proton dipolar interaction, spin-lattice relaxation is sensitive to the following mechanisms, namely director fluctuations (DF), smectic layer undulation modes (LU), self-diffusion(SD), rotations about the short axis (R) In the case of frustrated phases having dimers and clusters, there are additional mechanisms [36,37], which are also important in mediating spin relaxation.

The following properties of smectic A_d , are expected to show their signature in the NMR relaxation also. First the existence of the mixture of monomers and dimers in the smectic A_d phase, in a given percentage, in which dimers would combine and dissociate in pairs of head-to-head molecules after a mean life-time [34]. Secondly, the existence of aggregates of three or more molecules which, due to the anti-parallel paring form a frustrated system [21-24]. In these aggregates, several molecules can permeate within the microscopic range, thus releasing the frustration of the remaining molecules, as described by Netz et al., [35,36,37]. X-ray studies on the systems having a strong polar group show that the nematic phases retain locally, some of the smectic order observed in the underlying smectic A mesophases. In the smectic A_d phase, too, a creation and segregation of groups of molecules leads to a Lorentzian like contribution [36], to the spin relaxation.

7.3. NMRD study of the polar liquid crystal 8CN

Molecular structure of the polar liquid crystal, *4-cyanophenyl 4-octylbenzoate* (8CN) is depicted in the figure 7.6.

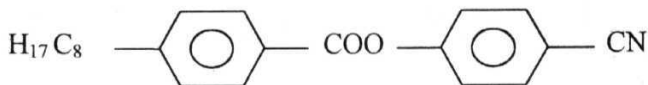
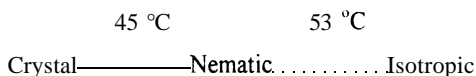


Figure 7.6. Molecular structure of the liquid crystal 8CN.

The strong polar nature of the molecule is due to the end group CN. This system has an **alkyl** end chain with 8 carbon atoms. The phase sequence of 8CN is given below.



This system has a very narrow nematic phase range and has no **smectic** phase, between isotropic and solid phases.

7.3.1. Experimental Details

The system 8CN was procured from Prof. R. Dabrowski (Military Technical Academy, Warsaw, Poland) and used without further purification. The sample was sealed under vacuum (10^{-5} Torr) after removing the dissolved oxygen, by the freeze-pump-thaw method. Phase transition temperatures were verified with the observed changes in the amplitude and shape of the FID. In order to orient the nematic director of the system parallel to the **Zeeman** magnetic field, samples were heated to the isotropic phase first, and slowly cooled to the temperature of 50 °C, where the NMRD experiment was performed. Proton NMRD data was collected in the frequency range of 50 kHz, to 3 MHz using the field cycling NMR spectrometer built as a part of this thesis. Further, high frequency NMRD data from 3 MHz to 50 MHz was collected, using a home built conventional NMR **spectrometer**. The data point at 3 MHz was collected using both the spectrometers as a check.

Inversion-recovery *rf* pulse sequence, and saturation-burst *rf* pulse sequence were used on the conventional pulsed NMR spectrometer. Inversion-recovery //pulse sequence and single pulse methods were used on FCNMR spectrometer depending on the magnetization available for detection. The details of the pulse sequences and the data fitting procedures have been presented in **chapter-1**. The estimated errors in T_1 measurements at frequencies below 1 MHz is found to be less than 7% and above 1 MHz are is around 5%. Temperature was controlled, employing a gas-flow type cryostat and a home built PID controller, within 0.1 °C on the conventional NMR spectrometer and within 0.2 °C on the FCNMR spectrometer. Temperature dependent data at the spot frequencies at 4, 10, 20, 30, 40 and 50 MHz were collected throughout the nematic phase and to some extent in isotropic and crystal phases. This work was done in collaboration with another researcher in the same group.

NMRD data obtained on pure nematic liquid crystal 8CN at 50 °C from 40 kHz to 50 MHz is depicted in figure 7.7.

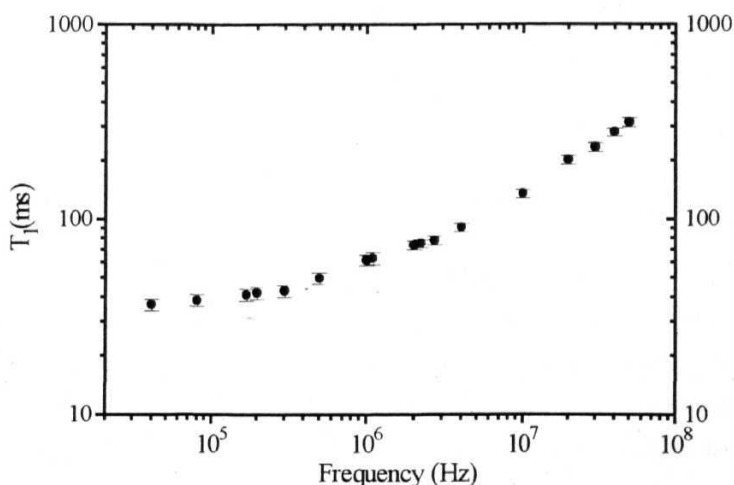


Figure 7.7. Proton T_1 as a function of Larmor frequency (NMRD) in the nematic phase of pure 8CN at temperature 50 °C.

The NMRD data plotted in the logarithmic scale has the following features. T_1 values ranging from 36 milliseconds at 40 kHz to 315 milliseconds at 50 MHz are obtained. T_1 show a small variation from 40 kHz to 150 kHz and the slope increases from 200 kHz to about 10 MHz. There is another region with a still higher slope seen from 10 to 50 MHz. Thus, T_1 behavior with frequency show three regions with different slopes, and this suggests that at least two or three mechanisms are responsible for the relaxation. Temperature dependent data in 8CN at spot frequencies show (Figure 7.8) a very interesting behavior, through a transition from one phase to the other.

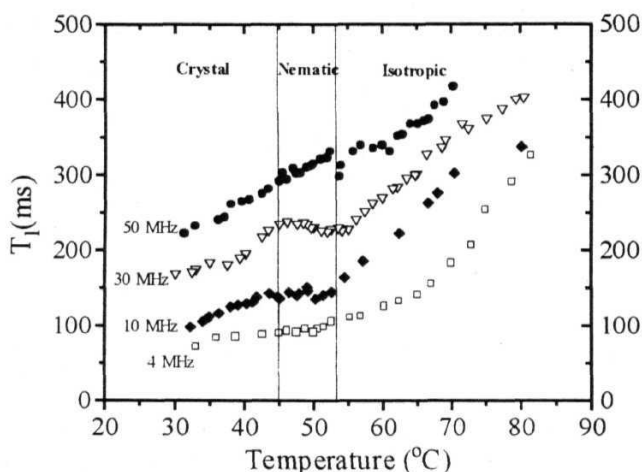


Figure 7.8. Proton spin-lattice relaxation time(T_1) as a function of temperature in 8CN

In the isotropic phase of 8CN, the relaxation time generally shows increasing T_1 values with an increase in temperature. The slope of temperature dependence seems to increasing with a decreasing frequency. Temperature and frequency dependence of T_1 in the isotropic phase from 4 MHz to 50 MHz is as expected, as the general behavior seen at the high frequency regime ($\omega \gg \tau^{-1}$) in liquid crystals. Interpretation of temperature dependent data is not straight forward, since many different contributions to the relaxation rate compete with the orientational fluctuations. Self-diffusion is one such mechanism, responsible for the temperature and frequency dependence at high frequencies. Since there are many non-equivalent

protons in each molecule, which are fixed in the **alkyl** end chain and the aromatic core, which may lead to different correlation times

7.3.2. Data analysis

It is well established, that the proton ^1H measurements in **nematic** phases are expected to show dominant contributions to $J_1(\omega)$ from the three mechanisms (DF, R and SD), which are essentially distinguished by their characteristic frequency and temperature dependent behaviors. The total spin lattice relaxation rate (R_{1Tot}) therefore, can be written as

$$R_{1Tot} = R_{1DF} + R_{1SD} + R_{1R} \quad (7.7)$$

Detailed expressions for each contribution has been given in the chapter-5. The data was analyzed, fitting them to the above equation using the non-linear least square analysis based on the Levenberg-Marquardt algorithm [38].

7.3.2.1. Nematic Director fluctuations (DF)

The NMRD data analysis was done for 8CN using two different approaches for DF contribution. The first method is based on the *one constant approximation (isotropic elastic constants model)*. The second method is based on the *anisotropic elastic constants model*, using a generalized expression [39] incorporating all the modifications made by Brochard [40], Vold and Vold [41], and Blinc et al [42] on the **Pincus** model [43].

Isotropic elastic constants model

In the first method, elastic constants are fixed as $K_{11} = K_{22} = K_{33} = 10^{-6}$ dyne. For the *director fluctuations* with lower and upper cut-off frequencies, the model parameters are the amplitude A_{DF} , lower cut-off frequency ν_{cl} and upper cut-off frequency, ν_{ch} . The well known square-root frequency dependence on the relaxation time between upper and lower cut-off frequencies. is the basis for the identification of

the DF contribution. The physical significance of the lower cut-off frequency is conflicted, due to the presence of dipolar fields, and hence it is difficult to correlate ν_{zel} with the generally assumed domain size. Details of the theoretical formulation of this model have been given in chapter-5.

Anisotropic elastic constants model

In the second procedure (called the *anisotropic elastic constants model*, or the *generalized model*) an expression, considering the influence of upper and lower cut-off wavelengths for the director modes as well as the anisotropy in elastic constants was used in calculating the DF parameters. Based on this model, the relaxation rate due to director fluctuations (R_{1DF}) is given by

$$R_{1DF} = A_{DF} \sum_{\alpha} \frac{\sqrt{\eta_{\alpha}}}{K_{\alpha} \sqrt{K_3} \sqrt{\rho \omega}} \left[f(D_{ah}, A_{ah}) - f(D_{al}, A_{ah}) - f(B_{ah}, A_{al}) + f(B_{al}, A_{al}) \right] \quad (7.8)$$

where

$$A_{DF} \propto f(\Delta) \frac{2S^2 k_b T}{(2\pi)^2}$$

The cutoff frequencies are given by

$$\nu_{zch(l)\alpha} = \frac{K_3 q_{zch(l)}^2}{2\pi\eta_{\alpha}} \quad \text{and} \quad \nu_{-ch(l)\alpha} = \frac{K_{\alpha} q_{-ch(l)}^2}{2\pi\eta_{\alpha}}$$

The values of viscosity coefficients η_1 and η_2 were assumed to be 0.5 P. Though these values differ from compound to compound and are temperature dependent, the order of magnitude remains the same if the molecular structure is essentially similar. Four parameters connected with R_{1DF} , viz. λ_{zel} , λ_{Lcl} , λ_{zch} and ADF are evaluated from the NMRD data. In the fitting program, the input variables connected with the cut-off wavelengths are given in terms of wave vectors (q 's). The equations connecting wave vectors, cut-off frequencies and cut-off wavelengths have also been described in chapter-5. The subscript l in the term λ_{Lcl} refers to the

direction perpendicular to the director (and also perpendicular to the long axis of the molecule). The subscript z refers to the direction parallel to the nematic director.

7.3.2.2. Rotations about the short molecular axis and Self-diffusion

In the case of rotations about the short molecular axis, the explicit model parameters used, are the amplitude C and the rotational correlation time τ_R , assuming a simple BPP type [44] contribution. It is assumed that in the present NMRD analysis between 50 kHz to 50 MHz, these fast motions can contribute with a frequency independent behavior. Comparing with the strong SD contribution, which shows a frequency dependence in the current frequency range, faster rotations are difficult to detect. Keeping in mind, the importance of the parameters connected with the rotations about the short axis, and the complications involved in fitting so many parameters with the data available in the narrow frequency region, contributions from faster rotations are not considered, in model fitting. The three contributions, DF, SD [45] and R about the short axis are sufficient, to explain the NMRD data in the 8CN system.

7.3.3. Results and Discussion

Isotropic elastic constants model

The frequency dependent relaxation rate $(R = 1/T_1)$ at 50° C in the nematic phase of 8CN was fitted to an equation, assuming a contribution from all the three dynamic processes, viz., SD, R and DF. The data analysis is performed based on the *one constant approximation* with an assumption that $K_{11}=K_{22}=K_{33}=1\text{e}^{-6}\text{dyne}$. The value of A_{DF} and the lower cut-off frequency were varied to get a good fit. Contributions from various mechanisms to the measured R_1 data are shown in figure 7.9. The DF contribution is quantified by the constant $A_{DF}=10.81\times10^6\text{ S}^{-2}$ in the case of the one constant approximation method. The estimation of upper cut-off frequency becomes difficult in this case. A constant value, corresponding to an upper cut-off frequency of about 640 MHz was given in the model fitting in order to get a good fit.

The lower cut-off frequency calculated from the analysis is 57.8 kHz, and the corresponding upper cut-off wavelength for the director modes is about 1470 Å. The physical significance of the lower cut-off frequency is conflicted in the literature [5] due to the presence of dipolar fields, and hence it is difficult to correlate lower cut-off frequency (ν_{cl}) with the generally assumed domain size. In the case of pure 8CN, which is a strong polar compound the lower cut-off frequency is higher than the value obtained for the general nematic liquid crystals. This system has a very narrow nematic phase of just about 8 °C and hence the pretransitional effects due to transition from isotropic and to the crystal phase probably complicate the low frequency dynamics.

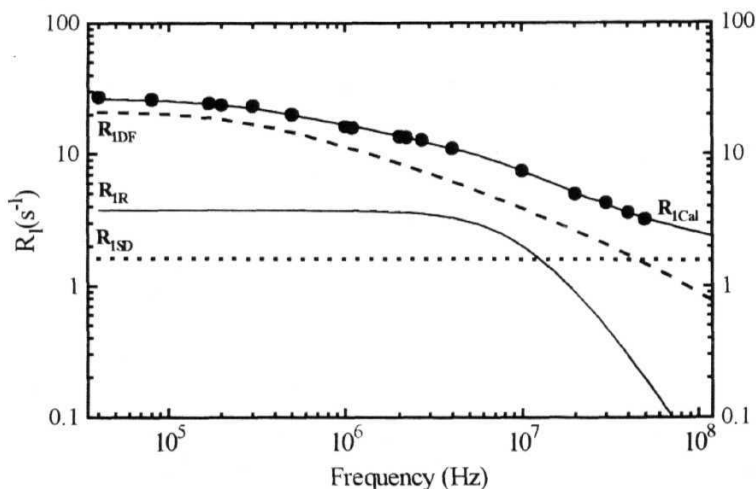


Figure 7.9. Various contributions (R_{1DF} , R_{1SD} , R_{1IR}) [7.7] to the experimental spin-lattice relaxation rate ($R_1=1/T_1$) in the nematic phase of 8CN at temperature 50 °C. In evaluating [7.8] the contribution from DF (R_{1DF}) isotropic elastic constants are assumed.

A qualitative picture of the NMRD fitting in the nematic phase of 8CN reveals that the DF mechanism dominates the spin relaxation upto 40 MHz and SD becomes dominant only from 50 MHz. Rotations about the short axis, with frequency independent behavior from 40 kHz to 4 MHz and with a frequency dependent behavior from 5 MHz to 50 MHz, is seen alongwith the DF contribution. SD

becomes more important than R, from about 11 MHz and becomes the most dominating mechanism from 50 MHz. DF and SD contribute equally at around 45 MHz, where R has a negligible contribution. The dynamic parameters obtained from this fit are summarized in table 7.1.

Table 7.1

Model Parameters	Isotropic elastic Constants model	Anisotropic elastic constants model
Nematic director fluctuations (DF)		
K_{11} (in 10^{-6} dynes)	1	0.7
K_{22} (in 10^{-6} dynes)	1	0.35
K_{33} (in 10^{-6} dynes)	1	0.95
A_{DF} (in 10^{-6} s $^{-2}$)	11.75	5.95
q_{zcl} (in 10^5 1/Am)	4.263	5.3786
f_{zcl} (in kHz)	58	87
λ_{zch} (in Å)	1470	1168
q_{zch} (in 10^7 1/Am)	4.5	3.66
f_{zch} (in MHz)	640	404
λ_{ccl} (in Å)	14	17
$q_{\perp ch}$ (in 10^7 1/Am)	3.96	4.6
$f_{\perp ch}$ (in MHz)	499	674
$\lambda_{\perp cl}$ (in Å)	16	13.65
Translational self-diffusion (SD)		
B (in 10^9 s $^{-2}$)	4.56	4.37
D (in 10^{-10} m 2 s $^{-1}$)	3.63	2.64
Rotations about the short axis (R)		
C (in 10^8 s $^{-2}$)	4.42	3.17
τ_R (in 10^{-9} s)	8.5	9.13

The DF domination upto 30 MHz is well supported by the temperature dependent data (figure 7.8) of the nematic phase in 8CN. The 7) data from 4 to

30 MHz, shows an almost temperature independent behavior, which is very much consistent with the result obtained in favor of DF mechanism in the NMRD model fitting. The temperature dependent T_1 data at 50 MHz. is very different from the lower frequency T_1 data (from 4 to 30 MHz), which shows a stronger temperature dependence. This is also consistent with the outcome of the NMRD data analysis, which shows SD, as the dominant mechanism at 50 MHz.

The correlation time obtained for rotations about the short molecular axis in the nematic phase of 8CN is 8.5×10^{-9} seconds. The contribution to the total relaxation rate from R is given by $C = 4.42 \times 10^8 \text{ s}^{-1}$. In the case of *self-diffusion*, the model parameter B (the amplitude) is equal to $4.37 \times 10^{-9} \text{ s}^{-2}$, and D (the average diffusion constant) is equal to $2.645 \times 10^{-10} \text{ m}^2 \text{ s}^{-1}$. Diffusion starts showing its frequency dependence only at a very high frequency. Though this method is indirect in nature, when compared to the field gradient NMR method, the values obtained here are comparable with the D values obtained from the direct methods, in nematic liquid crystals.

Anisotropic elastic constants model

In the second method, with the anisotropic elastic constants ($K_{11} = 0.7 \times 10^{-6}$, $K_{22} = 0.35 \times 10^{-6}$ and $K_{33} = 0.95 \times 10^{-6}$ dyne) model for DF contribution gives a slightly different picture. The model fitting to equation 7.7 is shown in figure 7.9. The elastic constants are taken from the literature [46,1h] for 7CN and extrapolated for 8CN following the similar procedure followed for 4O.m systems. The order parameters, density and refractive index anisotropy are available in the literature [46], which are useful in estimating the elastic constants. The constant A_{DF} , quantifying the DF contribution in 8CN is $5.94 \times 10^{-6} \text{ s}^{-2}$, which is much smaller than the value obtained from isotropic elastic constants model. The lower cut-off frequency in this case is 87 kHz. The upper cut-off frequencies in the directions parallel and perpendicular to the director are $4.04 \times 10^8 \text{ Hz}$ and $6.74 \times 10^8 \text{ Hz}$, respectively. The parameters obtained from both these methods are given in table 7.1. Different contributions to the experimental relaxation rate are shown in figure 7.10.

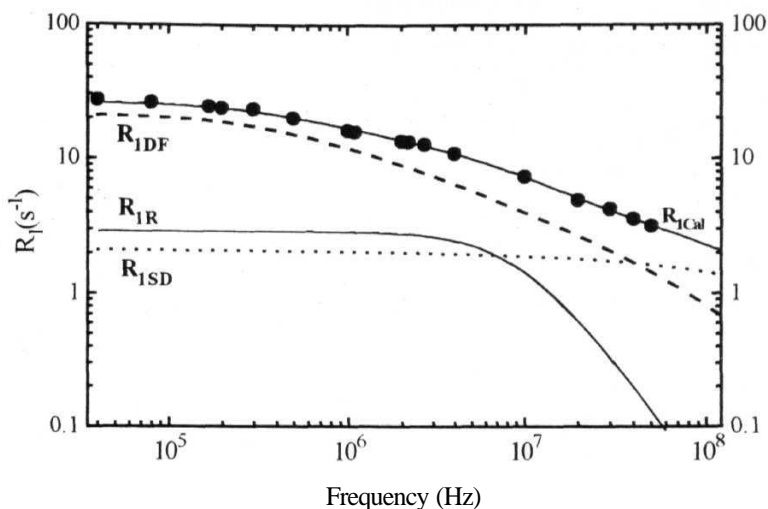


Figure 7.9, Various contributions (R_{1DF} , R_{1SD} , R_{1R}) [7.7] to the experimental spin-lattice relaxation rate ($R_1=1/T_1$) in the nematic phase of 8CN at temperature 50 °C. In evaluating [7.8] the contribution from DF (R_{1DF}) anisotropic (experimental) elastic constants model is considered

The correlation time obtained for rotations about the short molecular axis in the nematic phase of 8CN is 9.13×10^{-9} seconds. The contribution to the total relaxation rate from R is quantified by the value $C = 3.17 \times 10^8 \text{ s}^{-1}$. The correlation time and the value of C , for rotations, do not change with the choice of DF model. In the case of *self-diffusion*, the model parameter B , is equal to $4.37 \times 10^9 \text{ s}^{-2}$, and D , the average diffusion constant is equal to $2.645 \times 10^{-10} \text{ m}^2 \text{ s}^{-1}$.

From the NMRD data fitting one can quantify the percentage contributions of the various dynamical processes DF, SD and R at different frequencies. Though the dynamic parameters corresponding to the DF modes are different with the choice of the model used, the relative contribution did not change much in the analysis of 8CN. The percentage contributions are given below.

1. At 40 kHz, the contribution from DF mechanism to the total relaxation is about 81%, which is same in the case of both the models. The contribution from R and SD are about 11% and 8%, respectively. At 100 kHz, the contributions from DF, R and SD are about 80%, 11.5%, and 8.5%, respectively.
2. At 500 kHz, 75% is from DF mechanism and 15% and 10% comes from R and SD respectively. This trend continues upto 5 MHz, where R starts showing frequency dependence with a decreasing contribution. The contributions at 1 MHz (70%, 17% and 12% from DF, R and SD, respectively) is very different from the contributions at 10 MHz (54%, 26%, and 19% from DF, SD and R).
3. The contribution from SD and R become equal at 5 MHz. From 20 MHz, the contribution from R becomes negligible. SD and DF contribute equally to the spectral density at 40 MHz. At the highest measured frequency (50 MHz), the DF contribution becomes 44% and 51.5% relaxation is due to the SD mechanism. This view is consistent with the strong temperature dependence, characteristic of SD, seen in the T_1 data at higher frequencies at 50 MHz.

7.4. NMRD study of frustrated nematic liquid crystal 7BCB

Molecular structure of the polar liquid crystal, *4-cyanobiphenyl 4-heptylbenzoate* (7BCB) is depicted in figure 7.10.

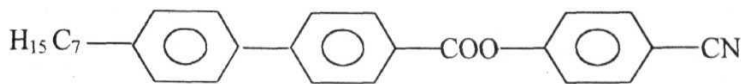
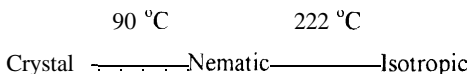


Figure 7.10. The molecular structure of the liquid crystal 7BCB.

This system has three benzene rings and an alkyl end chain with 7 carbon atoms. The phase sequence of 7BCB is given below.



This system has a very wide nematic phase range (132 °C) and has no smectic phase between the isotropic and solid phases.

7.4.1. Experimental Details

The system 7BCB was also procured from Prof. R. Dabrowski (Military Technical Academy, Warsaw, Poland) and used without further purification. Sample preparation method and experimental details are described in the section 7.3. Proton NMRD data was collected in the pure nematic system 7BCB at a spot temperature 120 °C in the frequency range from 40 kHz to 3 MHz using the field cycling NMR spectrometer. The high frequency NMRD data from 3 MHz to 50 MHz was collected using a home built conventional NMR. spectrometer.

The estimated errors in T_1 measurements at frequencies below 1 MHz are found to be less than 7% and above 1 MHz, around 5%. Temperature was controlled employing a gas-flow type cryostat and a home built PID controller within 0.2 °C on the conventional NMR spectrometer and within 0.4 °C on the FCNMR spectrometer.

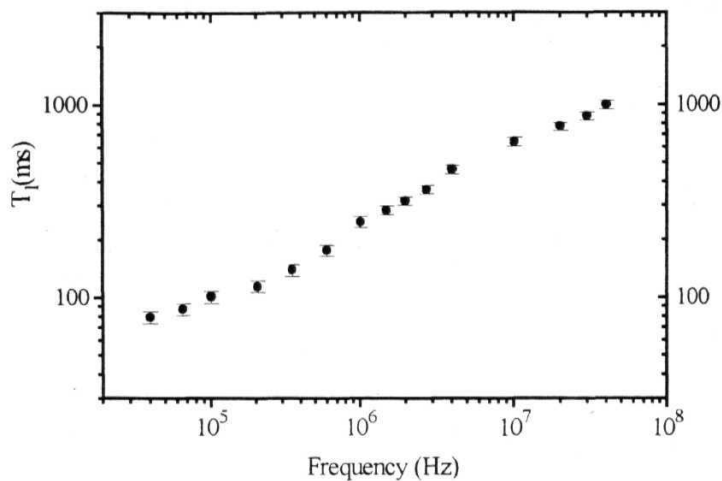


Figure 7.11. Proton T_1 as a function of Larmor frequency (NMRD) in the nematic phase of pure 7BCB at temperature 120 °C.

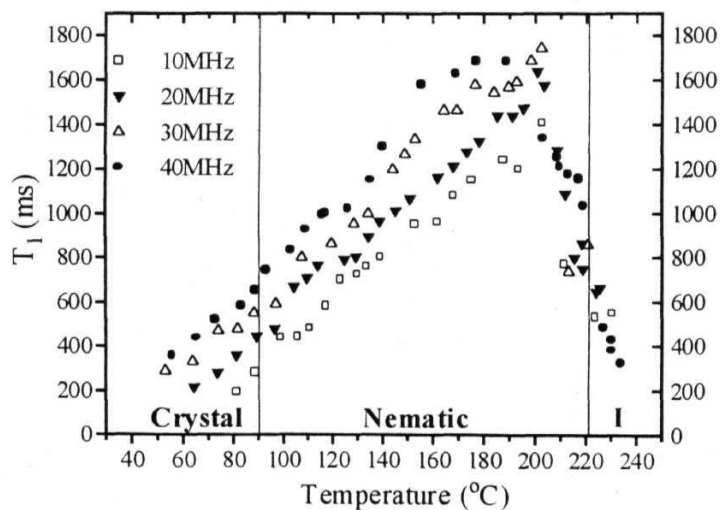


Figure 7.12. Proton spin-lattice relaxation time (T_1) as a function of temperature in 7BCB at various frequencies.

Temperature dependent data at the spot frequencies at 4, 10, 20, 30, 40 and 50 MHz was collected throughout the nematic phase. NMRD data obtained on pure nematic liquid crystal 7BCB at 120 °C from 40 kHz to 50 MHz is depicted in figure 7.11. The NMRD data plotted in the logarithmic scale has the following features. T_1 values ranging from 79 milliseconds at 40 kHz to 1000 milliseconds at 50 MHz are obtained. T_1 shows a smaller variation from 40 kHz to 400 kHz and the slope increases from 600 kHz to about 3 MHz. There is another region with a smaller slope seen from 3 to 50 MHz. Temperature dependent data in 7BCB at spot frequencies show (Figure 7.12) a very different behavior in the nematic phases, when compared to the data in the previous system 8CN. Above the isotropic to nematic phase transition the relaxation time shows strongly decreasing T_1 values.

The temperature dependent data in the nematic phase of 7BCB is similar in all experimental frequencies. The data shows a strong temperature dependent behavior, which is an indication of very strong contribution from SD process. The nematic T_1 data of 7BCB from 10 to 50 MHz shows a similar variation with temperature, after the formation of the crystal phase near the transition.

7.4.2. Data analysis

7.4.2.1. NMRD model for frustration and other dynamics

Different models used in the analysis of NMRD data in order to evaluate the contributions from DF, SD and R about the short axis are described in the chapter -5. Here, the additional mechanism called "Frustration" and the theoretical procedure to evaluate the dynamic parameters related to this special kind of mechanism seen in the frustrated liquid crystal phases, alone will be described.

It is known that [3] the nematic system 7BCB has the **smectic-forming** tendency and was considered as the 'virtual **smectic A_d** phase'. X-ray studies on the systems having strong polar group show that the nematic phases retain locally, some of the smectic order observed in the underlying smectic A mesophases. The existence of aggregates (clusters) of three or more molecules, which form due to the

anti-parallel paring form a frustrated system. In these aggregates, several molecules can permeate within the microscopic range thus releasing the frustration of the remaining molecules as described by Netz et al., [26].

As mentioned in the section 7.2, there is an additional mechanism which contributes to spin-lattice relaxation in the systems having **dimers** and frustration. An additional term is used by Sabastiao et al., [36] in order to incorporate this contribution. This additional term for the frustrated nature of the medium (with a notation, F) is used in this NMRD analysis. In the present analysis BPP type expression (same as R about short axis) is used for this contribution.

Thus, the proton T_1 measurements in the nematic phase of 7BCB are expected to show dominant contributions to $J_1(\omega)$ from the four mechanisms (DF, R, SD, and F), which are essentially distinguished by their characteristic frequency and temperature dependent behaviors. The total spin lattice relaxation rate (R_{1Tot}) therefore, can be written as

$$R_{1Tot} = R_{1DF} + R_{1SD} + R_{1R} + R_{1F} \quad (7.9)$$

The data was analyzed, by fitting to the above equation using the non-linear least square analysis based on the Levenberg-Marquardt algorithm [38].

In the case of **frustration** contribution (F) and *rotations about the short molecular axis* (**R**), the explicit model parameters used, are the amplitudes F and C and the rotational correlation times τ_{cs} (the subscript *cs* refers to the creation and segregation of the molecular associations) and τ_R , assuming a simple Lorentzian like contribution (BPP) [44]. Comparing with the strong DF, R, F and SD contributions, which show frequency dependence in the current frequency range, the faster rotations are difficult to detect, with their frequency independent nature. Keeping in mind, the importance of the parameters connected with the rotations about the short axis, and the complications involved in fitting so many parameters with the data available in the narrow frequency region, the contributions from faster rotations are not considered, in model fitting.

7.4.3. Results and Discussion

The frequency dependent relaxation rate ($R - 1/T_1$) at 120 °C in the **nematic** phase of 7BCB was fitted to the equation (7.9) The value of A_{DF} and the cut-off frequencies were varied to get a good fit in the case of DF, and correlation times τ_R and τ_{cs} along with the other parameters B , D , C and F were varied in the case of the other three mechanisms The DF contribution is quantified by the constant $A_{DF} = 1.9 \times 10^{-6} \text{ s}^2$. This value is much smaller than the value obtained for 8CN. It is observed in the literature that the presence of frustration and dimerization leads to a decrease in the DF domination [3]. The lower cut-off frequency calculated from the analysis is 6.4 kHz, and the corresponding upper cut-off wavelength for the director modes is about 4428 Å. Contributions from various mechanisms to the measured R_1 data are shown in figure 7.13.

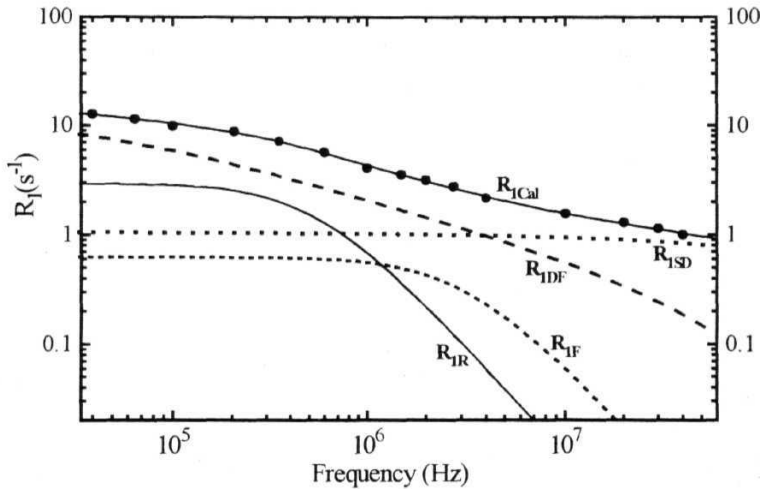


Figure 7.13. Various contributions (R_{1DF} , R_{1SD} , R_{1R} and R_{1F}) (eqn. 7.9) to the experimental spin-lattice relaxation rate ($R_1 = 1/T_1$) in the nematic phase of 7BCB at temperature 120 °C. In evaluating (eqn.7.8) the contribution from DF (R_{1DF}) the isotropic elastic constants are assumed.

The upper cut-off frequencies and wavelengths for DF modes are calculated from the q values obtained from the NMRD analysis. Upper cut-off frequency in the direction parallel to the director is 135 MHz, and in the direction perpendicular to the director is 117 MHz. The corresponding wavelengths representing the smallest possible wavelength of the DF modes are 30 and 32.7 Å, respectively in the directions parallel and the perpendicular to the nematic director. The values obtained here are consistent with the model assuming the presence of the smectic like clusters of three or more molecules. The X-ray measurements in the nematic phases of binary mixtures 8CN+7BCB have shown that, the molecular aggregates of size 33.6 Å is present in the system. The smectic A_d phase formed in the mixture showed layer spacing of about 33.5 Å. These results that the virtual smectic A_d phases forms dimers and clusters. It is also known that the clusters present in the nematics with an underlying smectic A_d increases [37] the value of K_{11} making the elastic constants K_{11} and K_{33} almost equal. This situation makes the one elastic constants model closer to the real situation.

A quantitative picture of the NMRD data analysis in the nematic phase of 7BCB reveals that the DF mechanism dominates the spin relaxation upto 3 MHz and SD becomes dominant from 4 MHz onwards. SD domination from 4 MHz to 50 MHz as observed in the NMRD analysis is well supported by the strong temperature dependence of T_1 in this frequency range. Rotations about the short axis, with frequency independent behavior from 40 kHz to 200 MHz and with a frequency dependent behavior from 200 kHz to 3 MHz, is seen alongwith the DF and SD contributions. SD becomes more important than R, from about 700 kHz and becomes solely responsible for the dispersion seen in the data, from 20 MHz.

The dynamic process of creation and segregation of molecular aggregates termed here as the frustration (F) is important from 1 MHz to 10 MHz, where the total effect of DF, SD and F contributions, is responsible for the NMRD data variation. Though the contribution from F is less than SD and DF at this frequency range, this contribution is necessary to fit the NMRD data well. F contribution is frequency independent up to 1 MHz and becomes frequency dependence from 1 to 10 MHz.

The correlation time obtained for rotations about the short molecular axis in the **nematic** phase of 7BCB is 0.175×10^{-8} seconds. The contribution, to the total relaxation rate from R is given by $C = 1.68 \times 10^7 \text{ s}^{-1}$. In the case of *self-diffusion*, the model parameter B , (the amplitude) is equal to $2.104 \times 10^9 \text{ s}^{-2}$, and D (the average diffusion constant) is equal to $2.548 \times 10^{-10} \text{ m}^2 \text{ s}^{-1}$. The value obtained for D here, is comparable with the D values obtained in the nematic liquid crystals [1]. The correlation time associated with the creation and segregation of the cybotactic smectic clusters is 3.02×10^{-8} seconds. The constant quantifying the contribution from the **frustration** term, F is $2.063 \times 10^7 \text{ s}^{-1}$. The dynamic parameters obtained from this fit are given in table 7.2.

Table 7.2. Dynamic parameters obtained from the NMRD analysis of 7BCB

Model Parameters	Results obtained
K_{11} (in 10^{-6} dynes)	1
K_{22} (in 10^{-6} dynes)	1
K_{33} (in 10^{-6} dynes)	1
A_{DF} (in 10^{-6} s^{-2})	1.9
q_{zcl} (in 10^5 l/Am)	1.48
f_{zcl} (in kHz)	6.4
λ_{zch} (in Å)	4428
q_{zch} (in 10^7 l/Am)	2.1
f_{zch} (in MHz)	138
λ_{zcl} (in Å)	30
$q_{\perp ch}$ (in 10^7 l/Am)	1.92
$f_{\perp ch}$ (in MHz)	117
$\lambda_{\perp ch}$ (in Å)	32.74

Various contributions to the spin relaxation could be obtained by calculating the percentage contributions at different frequencies.

1. At 40 kHz, the contribution from the DF mechanism to the total relaxation in the **nematic** phase of 7BCB is about 63% to the total relaxation, which is much smaller than the value obtained for 8CN (81% at 40 kHz). The contribution from SD, R and F are about 8.5 %, 23.5% and 5% respectively. At 100 kHz, the contributions from DF, SD, R and F are about, 55.5%, 10%, 28%, and 6% respectively.
2. At 500 kHz, 48% is from the DF mechanism and 25%, 17% and 10% result from R, SD and F, respectively. In the case of 8CN the major mechanism at 500 kHz is DF with 75% contribution. R starts showing frequency dependence from 200 kHz onwards.
3. At 1 MHz, the contributions from DF, SD, R and F are 48%, 22%, 15.5% and 13%, respectively. The contribution from SD can be seen to be dominating over R, at this frequency.
4. The contribution from SD and R becomes equal at 600 kHz. From 2 MHz, the contribution from R becomes negligible. SD and DF contribute equally to the spectral density at 4 MHz.
5. SD and DF become equal (44% each) at 3.5 MHz and SD dominates at 10 MHz than all the other mechanisms. The percentage contributions at 10 MHz are 60% from SD, 35% from DF, 4% from F and 0.5% from R.
6. At 20 MHz, the contributions from R and F become negligible. The contributions from DF and SD are 26.5% and 72% respectively. At 50 MHz, 85% contribution is from SD and 15% from DF. The contribution from DF deviates from the square root behavior at high frequencies.
7. At the highest measured frequency (50 MHz), DF contribution becomes 44% and a 51.5% relaxation is results from SD mechanism. This view is consistent with the strong temperature dependence, characteristic of SD, seen in the T_1 data at higher frequencies at 50 MHz.

7.5. NMRD studies of the binary mixture of 70% 8CN + 30% 7BCB

Phase sequence of the binary **nematic** mixture of 70% of 8CN and 30% of 7BCB is given by

30 °C
60 °C
100 °C
 Crystal ——— Smectic A_d ——— Nematic Isotropic

This system has a nematic phase with a temperature range of about 40 °C and a smectic A_d phase of about 30 °C in between the isotropic and crystal phases. This composition is chosen for NMR study, since it has sufficiently wide nematic as well as smectic A_d phases. It is important to understand the dynamics of the nematic medium, which possesses an underlying smectic A_d phase and the one without this, in order to get possible information about the factors responsible for the stability of the phases with and without layering.

7.5.1. Experimental Details

The pure systems 8CN and 7BCB obtained from Prof. R. Dabrowski are used to prepare mixtures of required mole concentrations. Proton NMRD data was collected in the frequency range of 20 kHz to 3 MHz using the field cycling NMR spectrometer at temperature 84 °C. The high frequency NMRD data from 3 MHz to 50 MHz was collected using a home built conventional NMR spectrometer. The estimated errors in T_1 measurements at frequencies below 1 MHz are found to be less than 7% and above 1 MHz around 5%. Temperature was controlled employing a gas-flow type cryostat and a home built PID controller within 0.2° C on the conventional NMR spectrometer and within 0.4° C on the FCNMR spectrometer. Temperature dependent data at the spot frequencies at 4, 10, 20, 30, 40 and 50 MHz was collected throughout the nematic phase.

NMRD data obtained on the nematic system of 70% 8CN + 30% 7BCB, from 20 kHz to 50 MHz, is depicted in figure 7.14. The NMRD data plotted in the logarithmic scale has the following features.

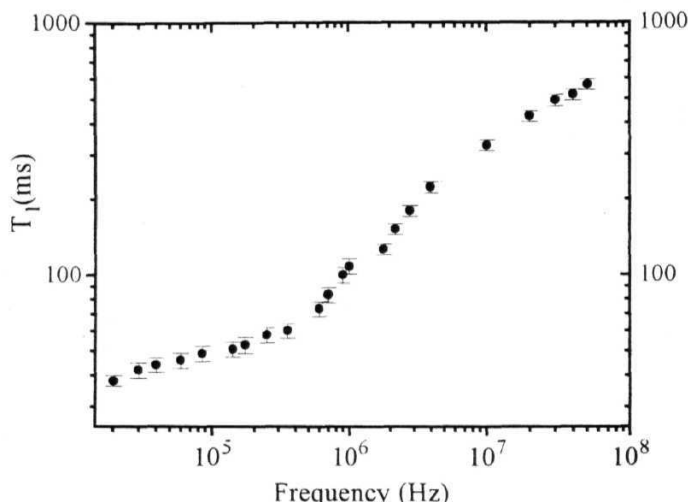


Figure 7.14. Experimental NMRD data in the nematic phase of binary mixture 70% 8CN + 30% 7BCB at temperature 84 °C. Error bars are also shown.

T_1 values ranging from 38 milliseconds at 20 kHz to 568 milliseconds at 50MHz are observed. T_1 shows a lesser slope in the frequency from 20 kHz to 400 kHz and the slope increases in the range from 600 kHz to about 10 MHz. There is another region with lesser slope seen from 10 to 50 MHz. Thus, the T_1 behavior with frequency shows three regions with very different slopes suggesting that at least three mechanisms are responsible for the relaxation. Above the isotropic to nematic phase transition the relaxation times show a strongly decreasing trend.

The temperature dependent data in the nematic phase of the binary mixture is shown in figure 7.15. The T_1 data in the nematic phase at high frequencies shows stronger temperature dependence than the lower frequencies. In contrast to the strong temperature dependent T_1 data from 4 to 50 MHz in the nematic system 7BCB, and

almost no temperature dependent data below 40 MHz in the case of nematic phases of pure 8CN, this system shows temperature dependence, which is intermediate

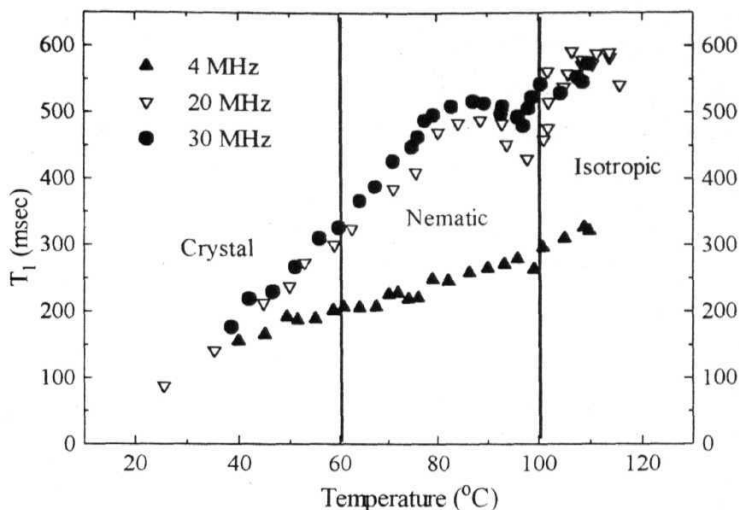


Figure 7.15. Temperature dependent T_1 data at three different frequencies in the binary mixture of 70% 8CN + 30% 7BCB.

Temperature dependent data in the nematic phase also shows pretransitional effects below the isotropic to the nematic phase transition, which leads to an increase of T_1 with decreasing temperature. With increasing temperature, T_1 reaches a maximum in the mid-nematic temperature range and finally decreases at lower nematic temperatures

7.5.2. Nematic Phase

It is important to mention here that the nematic phases as well the underlying smectic A_d phases are frustrated in nature [20]. The existence of two processes, which are described below, important to be considered as significant [36,37], in order to explain NMRD in the smectic A_d phase as well as in the frustrated nematic phase or in the virtual smectic A_d phases.

1. Existence of a mixture of monomers and dimers in a given percentage, in which the dimers would combine and dissociate in pairs of head-to-head molecules, after a mean lifetime [3].
2. Existence of aggregates of three or more molecules which, due to the anti-parallel paring would form a frustrated system. In these aggregates, several molecules can permeate within the microscopic range thus releasing the frustration of the remaining molecules as described by Netz et al [35].

In the case of binary mixtures of 70% 8CN+30% 7BCB the situation is more complex, since there are different factors responsible for frustration. Mixing two molecules of different length scales, and the strong polar nature are the main sources of frustration. Presence of dimers in the pure 7BCB is well known in the literature [3]. Formation of smectic like clusters is also expected in this nematic mixture. Assuming the nematic phase of 8CN as a pure nematic system with no clusters and dimers, the addition of the second compound 7BCB creates a new situation. This mixture should have dimers of 7BCB, and molecules of different molecular lengths, a favorable condition for the formation of clusters [3]. The first and second processes [36,37] are possible in the case of this mixture. Thus, a considerable concentration of 7BCB in the liquid crystal 8CN leads to two different mechanisms, which can influence the NMR relaxation.

In the case of the induced smectic phase of this mixture one can assume both the processes contributing to NMR relaxation. Thus, the proton T_1 data in the nematic phase as well as the induced smectic A_d phase are expected to show dominant contributions to $J_1(\omega)$ from these four mechanisms (DF or LU, R, SD, and F), which are essentially distinguished by their characteristic frequency and temperature dependent behaviors. Therefore, total relaxation rate (R_{1Tot}) can be written as

$$R_{1Tot} = R_{1DF} + R_{1SD} + R_R + R_F \quad (7.9)$$

7.5.2.1. Results and Discussion

The frequency dependent relaxation rate ($R = 1/T_1$) at 84 °C, in the **nematic** phase of the mixture was fitted to an equation assuming a contribution from all the four dynamic processes, viz., SD, R, F and DF. The value of A_{DF} and the cutoff frequencies were varied to get a good fit in the case DF, and correlation times τ_R and τ_{cs} along with the other parameters B, D, C and F were varied in the case of other three mechanisms. Contributions from various mechanisms to the measured R_1 data are shown in figure 7.16

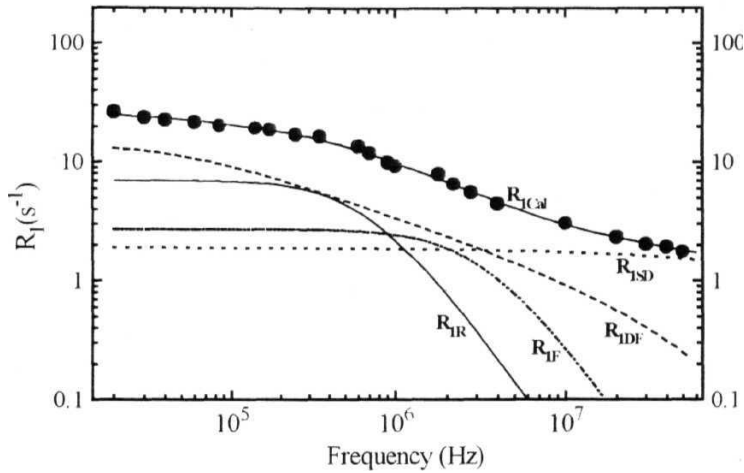


Figure 7.16. Different contributions to the experimental spin-lattice relaxation rate ($R_1 = 1/T_1$) in the nematic phase of 70% 8CN + 30% 7BCB at 84 °C. The solid line connecting the data points (closed circles) is the total relaxation rate calculated using the equation (7.9)

7.5.2.2. Dynamic parameters for DF modes

DF contribution is quantified by the constant $A_{DF} = 3.1733 \times 10^{-6} \text{ s}^{-2}$. This value is much smaller than the value obtained for 8CN ($A_{DF} = 11.75 \times 10^{-6} \text{ s}^{-2}$) and bigger than the value obtained for the 7BCB ($A_{DF} = 1.9 \times 10^{-6} \text{ s}^{-2}$). The lower cut-off frequency calculated from the analysis is 9.6 kHz. and the corresponding upper cut-off

wavelength for the director modes is about 3600 Å. The uncertainty in evaluating the dynamic parameters is about 10%

Upper cut-off frequency in the direction parallel to the director is 146 MHz, and in the direction perpendicular to the director is 118 MHz. The corresponding wavelengths representing the smallest possible wavelengths of the DF modes are 29.25 Å and 32.66 Å respectively, in the directions parallel and the perpendicular to the nematic director. The values obtained here are consistent with the model assuming the presence of the smectic like clusters of three or more molecules. The X-ray measurements in the nematic phases of binary mixtures 8CN+7BCB showed that the cybotactic clusters of size 33.6 Å are observed [3]. The smectic A_d phase formed in the mixture of 8CN and 7BCB also showed layer a spacing of about 33.5 Å.

A qualitative picture obtained from the NMRD data analysis in the nematic phase of the mixture reveals that the DF mechanism dominates the spin relaxation upto 3 MHz and SD becomes dominant from 10 MHz onwards. Rotations about the short axis, with a frequency independent behavior from 20 kHz to 200 kHz, and with a frequency dependent behavior from 200 kHz to 6 MHz is observed alongwith the DF and SD contributions. R seems to be equally important with the DF contribution in a narrow region from 200 to 800 kHz, the most complicated region in the NMRD data. The region between 200 kHz to 2 MHz is dominated by all the four mechanisms with their corresponding frequency dispersion

The lower values obtained for upper cut-off frequencies, shortens the square root region of DF modes, leaving SD, the most important mechanism above 10 MHz. The complicated behavior of temperature dependent data in the conventional NMR frequencies is due to the presence of different dynamic processes with their correlation times ranging over only two decades. SD domination from 4 MHz to 50 MHz as observed in the NMRD analysis is well supported by the strong temperature dependence of τ_c , in this frequency range.

7.5.2.3. Dynamic parameters for SD, R and F

The dynamic process due to creation and segregation of clusters as well as making and breaking of **dimers** is termed here as frustration (**F**), is important from 40 kHz to 20 MHz The contribution from frustration is important over SD from 40 kHz to 12 MHz, with a frequency independent behavior and strongly responsible for the NMRD data behavior from 1 to 20 MHz The contribution from F is less than SD and DF from 3 MHz to 20 MHz; this contribution is necessary to fit the NMRD data well.

Table 7.3. Dynamic parameters for the **nematic** phase of 70% 8CN+30% 7BCB.

Model Parameters	Results obtained
K_{11} (in 10^{-6} dynes)	1
tf_{22} (in 10^{-6} dynes)	1
K_{33} (in 10^{-6} dynes)	1
A_{DF} (in 10^{-6} s $^{-2}$)	3.1733
q_{zcl} (in 10^5 l/Am)	1.74
f_{zcl} (in kHz)	9.68
λ_{zch} (in A)	3600
q_{zch} (in 10^7 l/Am)	2.14
f_{zch} (in MHz)	146
λ_{zcl} (in A)	29.25
q_{pch} (in 10^7 l/Am)	1.92
f_{pch} (in MHz)	118
λ_{pcl} (in A)	32.36
B (in 10^9 s $^{-2}$)	5.229
D (in 10^{10} m 2 s $^{-1}$)	3.5
C (in 10^8 s $^{-2}$)	0.503
τ_R (in 10^{-7} s)	14
F (in 10^8 s $^{-2}$)	0.914
T_{CS} (in 10^{-8} s)	2.96

The dynamic parameters obtained from the NMRD fit in the nematic phase are summarized in table 7.3. The correlation time obtained for rotations about the short molecular axis in the nematic phase the mixture (70% 8CN + 30% 7BCB) is 0.141×10^{-8} seconds. The contribution to the total relaxation rate from R is given by $C = 1.68 \times 10^7 \text{ s}^{-1}$. In the case of *self-diffusion*, the model parameter B (the amplitude) is equal to $5.03 \times 10^{-9} \text{ s}^{-2}$, and D (the average diffusion constant) is equal to $3.51 \times 10^{-10} \text{ m}^2 \text{ s}^{-1}$. The value obtained for D here, is comparable with the D values obtained in nematic liquid crystals and slightly higher than the value obtained for pure 7BCB. The correlation time associated with the creation and segregation of the cybotactic smectic clusters and dimers is 2.97×10^{-8} seconds. The constant quantifying the contribution from the frustration term, F is $9.14 \times 10^7 \text{ s}^{-1}$, which is much higher than the value obtained for the pure system 7BCB. This shows that the contribution from the frustration phenomenon increases in the nematic phase of the binary mixture of 70% 8CN + 30% 7BCB, which has an underlying smectic A_d phase. It is also important to mention here that the DF contribution, which is very strong in the case of pure 8CN, becomes weaker by adding 30% of the molecules with a smectic-forming tendency.

7.5.2.4. Percentage contributions

Relative contributions to the spin relaxation can be obtained by calculating the percentage contributions.

1. At 20 kHz, the contribution from DF mechanism to the total relaxation in the nematic phase of the mixture of 70% 8CN+30% of 7BCB is about 53% to the total relaxation, which is much smaller than the value obtained for 8CN (81% at 40 kHz) and pure 7BCB (around 62% at 40 kHz). The contribution from SD, R and F are about 7.5 %, 28.5% and 11% respectively. Contribution from R becomes very important at low frequencies, though it is half the value of the DF in the lowest frequency studied. At 100 kHz, the contributions from DF, SD, R and F are about, 44%, 9%, 33.5%, and 13% respectively

2. At 300 kHz, 36.6% is from the DF mechanism and 35.5% arises from R SD and F contribute about 11.5% and 16.5% respectively.
3. At 1 MHz, the contributions from DF is 34% and the second dominant mechanism F contributes about 25% to the total relaxation. R and SD contribute about 22% and 19% respectively.
4. At 5 MHz, R becomes the least important mechanism with a 3% contribution. SD becomes the most important mechanism with 44%. DF and F contribute to about 34% and 18.5% respectively.
5. At 10 MHz, 59% is from SD and 1% from R DF contributes to about 30% of the total relaxation and F, about 9%.
6. At 20 MHz, the contributions from R and F become negligible. The contributions from DF and SD are 24% and 73% respectively. At 50 MHz, 86% contribution is from SD and 13.5% from DF. The contribution from DF deviates from the square root behavior at high frequencies due to the lowering of upper cutoff frequencies.
7. At the highest measured frequency (50 MHz), DF contribution becomes 44% and a 51.5% relaxation results from the SD mechanism. This view is consistent with the strong temperature dependence, characteristic of SD, noticed in the T_1 data at higher frequencies at 50 MHz.

7.5.3. *Smectic A_d phase*

NMRD data collected in the smectic A_d phase is shown in figure 7.17. NMRD data in the logarithmic scale clearly shows three different regions with very different slopes. The first region from 40 kHz to 200 kHz shows variation with a lesser slope than the region succeeding it, from 300 kHz to 4 MHz. This intermediate frequency region shows a steep variation. T_1 data in the smectic A_d phase shows a strong temperature dependence than the nematic phase. This suggests that SD is the most dominating mechanism, in the conventional NMR frequencies from 4 MHz to 50 MHz.

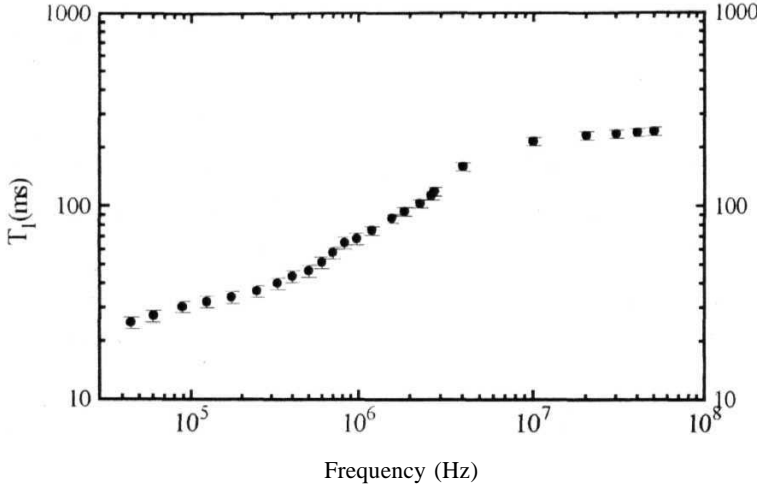


Figure 7.17. Experimental NMRD data in the smectic A_d phase 70% 8CN + 30% 7BCB at temperature 52 °C. Error bars are also shown.

NMRD data in the smectic A_d phase is fitted, considering the mechanisms LU, R, SD and F, the model parameters of which are explained in chapters 5 and 6 and section 7.4. Smectic layer undulations (LU) are considered with their linear dependence on frequency. The NMRD data obtained in the Smectic A_d is fitted to the equation 7.10 and the contributions from different dynamics are shown in figure 7.18.

$$R_{Tot} = R_{LU} + R_{SD} + R_R + R_F \quad (7.10)$$

The qualitative picture of the model fitting clearly demonstrates the importance of the F contribution, which is very important to fit the NMRD data in the smectic A_d phase. Layer undulations (LU) are important to fit the lowest frequency data below 100 kHz, though the major part of the spectrum for LU is not observed since experimental NMRD data was not collected below 40 kHz. The low frequency region from 40 kHz to 400 kHz is explained by rotations about the short axis. R contribution shows a frequency independent behavior from 40 kHz to 200 kHz and shows a frequency dependence from 200 kHz to 7 MHz.

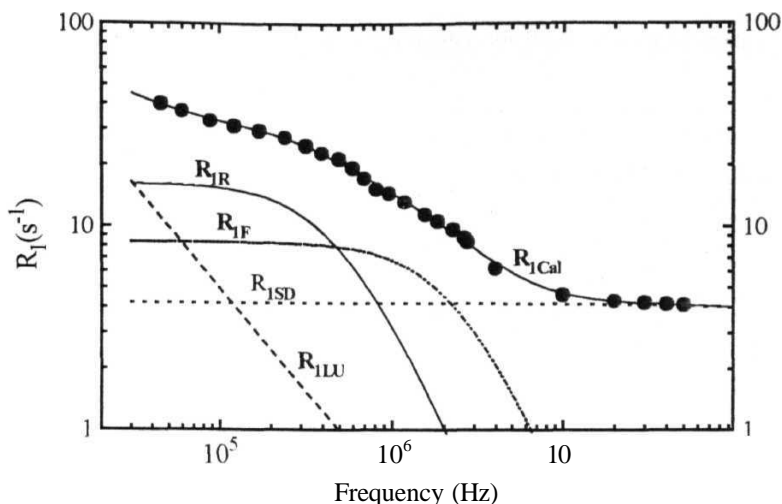


Figure 7.18. Various contributions to the experimental relaxation rate ($R_1 = 1/T_1$) in the binary mixture of 70 % 8CN + 30 % 7BCB. The solid line connecting the data points (closed circles) is the calculated relaxation rate using the equation 7.10. Different contributions (LU, SD, R and F) evaluated are also shown.

F contribution shows a dominance over other mechanisms from 400 kHz to about 1.5 MHz. This contribution is very important though it is frequency independent in the low frequency region from 40 kHz to 1 MHz. From 1 MHz to 20 MHz, the F contribution becomes frequency dependent. SD contribution is the least important contribution at 40 kHz, and starts dominating the other mechanisms gradually when frequency is increased. SD becomes more important than DF from 100 kHz and also dominates R from 1 MHz, finally dominating all the other mechanisms from 2.5 MHz. From 10 MHz onwards the smectic A_d data is completely dominated by the SD contribution. Though one cannot completely rule out the possibility of the contributions from rotations about the long axis as well as the conformational jumps, which are expected to show frequency independent contributions, in the present analysis, no attempt is made to obtain information about the such a faster rotations, due to the constraints in varying the number of parameters.

Table 7.4. Dynamic parameters evaluated from the NMRD analysis of the smectic **A_d** phase of the binary mixture of 70 % 8C + 30 % 7BCB.

Model Parameters	Results obtained
B (in 10^{11} s^{-2})	3.1
D (in $10^{-10} \text{ m}^2 \text{ s}^{-1}$)	0.92
C (in 10^7 s^{-2})	839
τ_R (in 10^{-7} s)	1.94
F (in 10^8 s^{-2})	2.04
τ_{CS} (in 10^{-8} s)	4.11

The dynamic parameters obtained from the analysis are given in table 7.4. Typical error in evaluating the parameters is about 10% in the case of smectic **A_d** phase also (but for the LU parameters). The correlation time obtained for rotations about the short axis is 1.938×10^{-7} seconds and the constant $C = 8.39 \times 10^7 \text{ s}^{-1}$ which is higher than the values obtained in the nematic phase of the same system. The contribution from F is quantified by the correlation time 4.1×10^{-8} seconds and the constant $F = 2.046 \times 10 \text{ s}^{-1}$. The F value obtained in the nematic phase is an order of magnitude smaller than the present value. But the correlation time is almost same. The dynamic parameters for LU are difficult to evaluate since the contribution from LU is very weak in the present frequency range.

Relative contributions can be quantified by calculating the percentage contributions. The percentage contributions are given at certain frequencies, where the results show considerable variations.

1. At 30 kHz, the LU mechanism contributes 36.4% and R contributes 35.7%. 18% results from F and only 9% from SD.

2. At 60 kHz, LU falls to 22% and R becomes the most dominant mechanism with a 43% contribution. F and SD contribute to about 23% and 12% respectively
- 3 Layer undulations become just 8% at 200 kHz, where **R contributes about 47%**, followed by F with 29% SD contributes around 15% to the total relaxation at 200 kHz
- 4 At 500 kHz the F mechanism dominates all the other mechanisms with 39%. R follows the F **with 36%** and SD and LU contributes about 21% and 5% respectively.
5. At 2 MHz, R and LU become very less with 10% and 2%, respectively F and SD become almost equal **with 45% and 43%.**
6. At 6 MHz, **SD** becomes the most dominating mechanism with 76.5%. 20% contribution is due to F. LU and R are negligible, from 6 MHz onwards (1.5% and 2%).
7. SD contribution becomes 90% at 10 MHz, 95% at 15 MHz and 98% at 30 MHz and the remaining relaxation is due to F and LU. At 50 MHz, 99.3% of the spin relaxation is mediated by the self-diffusion mechanisms.

7. 6. NMRD studies of the binary mixture of 40% 8CN + 60% 7BCB

Phase sequence of the binary nematic mixture of 40% of 8CN and 70% of 7BCB is given by

$72\text{ }^{\circ}\text{C}$ $108\text{ }^{\circ}\text{C}$ $156\text{ }^{\circ}\text{C}$
 Crystal ————— Smectic A_d Nematic ————— Isotropic

The system has a nematic phase with a temperature range of about $48\text{ }^{\circ}\text{C}$ and a smectic A_d phase of about $36\text{ }^{\circ}\text{C}$ in between the isotropic and crystal phases. This composition is chosen for NMR study since it has a smectic A_d phase with maximum stability.

7.6.1. Experimental Details

Proton NMRD data was collected in the nematic phase of this mixture at temperature $116\text{ }^{\circ}\text{C}$, in the frequency range of 50 kHz to 3 MHz using the field cycling NMR spectrometer. The high frequency NMRD data from 3 MHz to 40 MHz was collected, using a home built conventional NMR spectrometer

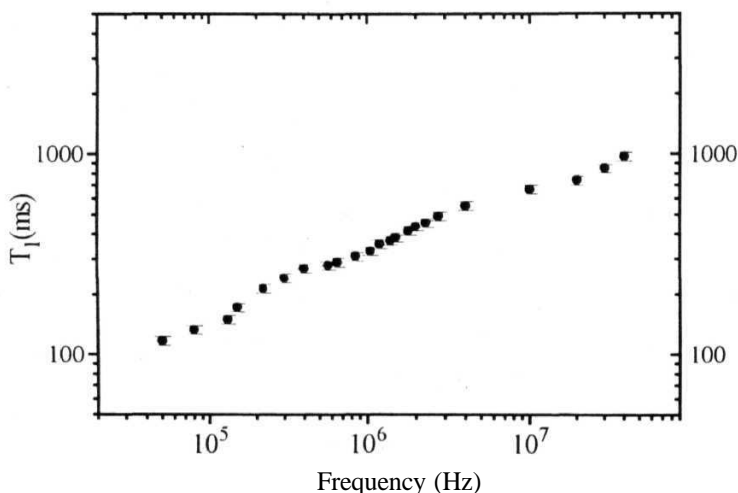


Figure 7.19. Experimental T_1 data as a function of frequency in the nematic phase of binary mixture 40% 8CN + 60% 7BCB at temperature $116\text{ }^{\circ}\text{C}$ Error bars are also shown.

The estimated errors in T_1 measurements at frequencies below 1 MHz are found to be less than 7% and above 1 MHz less than 5%. Temperature was controlled employing a gas-flow type cryostat and a home built PID controller within 0.2° C on the conventional NMR spectrometer and within 0.4 T on the FCNMR spectrometer. Temperature dependent data at the spot frequencies at 4, 10, 20, 30 and 40 MHz were also collected. NMRD data obtained on the nematic system of 40% 8CN + 60% 7BCB, from 50 kHz to 40 MHz, is depicted in figure 7.19. NMRD data plotted in the logarithmic scale has the following features

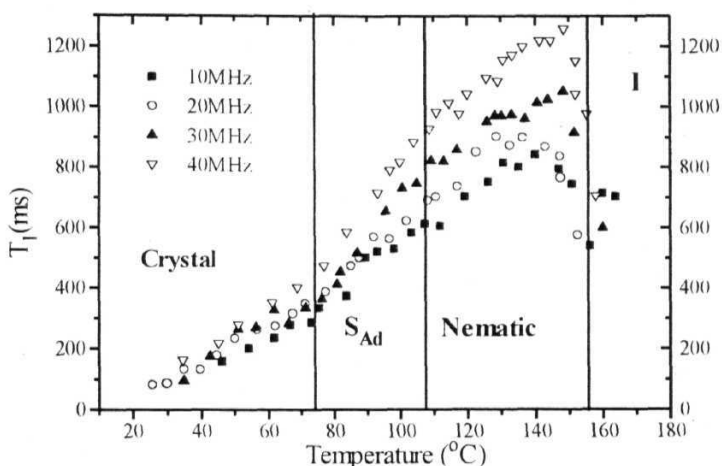


Figure 7.20. Temperature dependent T_1 data at three different frequencies in the binary mixture of 40% 8CN + 60% 7BCB

T_1 values ranging from 117.6 milliseconds at 50 kHz to 975 milliseconds at 40 MHz are observed. T_1 shows a larger slope in the frequency range from 50 kHz to 400 kHz, and the slope decreases in the range from 400 kHz to about 10 MHz. There is another region with a lesser slope seen from 10 to 40 MHz. The temperature dependent data obtained in the binary mixture is shown in figure 7.20.

The temperature dependent data in the nematic phase of this mixture shows a behavior, similar to the one seen in the pure system 7BCB, but the temperature dependence is not as strong as in the case of 7BCB, near the I-N transition. The data at 10 MHz shows weaker temperature dependence than the 40 MHz data. In contrast to the strong temperature dependent T_I data from 4 to 50 MHz in the system 7BCB and almost no temperature dependent data below 40 MHz in the case of pure 8CN, this system shows a temperature dependence intermediate between them, but more like 7BCB. Temperature dependent data also shows pretransitional effects below the isotropic to nematic phase transition, leading to an increase of T_I with decreasing temperature

7.6.2. Data analysis

7.6.2.1. Nematic Phase

The frequency dependent relaxation rate ($R - 1/T$) at 116 °C in the nematic phase of the mixture was fitted to an equation, assuming a contribution from all the four dynamic processes, viz., SD, R, F and DF (equation 7.9). The value of A_{DF} and the cut-off frequencies were varied to get a good fit in the case the DF, and correlation times τ_R and τ_{cs} alongwith the other parameters B, D, C and F were varied in the case of other three mechanisms. Contributions from various mechanisms to the measured R_I data are shown in figure 7.21

7.6.2.1.1. Dynamic parameters for DF modes

DF contribution is quantified by the constant $ADF = 1.4 \times 10^{-6} \text{ s}^{-2}$. This value is much smaller than the value obtained for 8CN ($ADF = 11.75 \times 10^{-6} \text{ s}^{-2}$) and for the other mixture with 70% 8CN and 30% 7BCB ($A_{DF} = 1.75 \times 10^{-6} \text{ s}^{-2}$). It is interesting to know that the value is slightly smaller than the value obtained for 7BCB ($A_{DF} = 1.48 \times 10^{-6} \text{ s}^{-2}$). The lower cut-off frequency calculated from the analysis is 2.3 kHz, and the corresponding upper cut-off wavelength for the director modes is about 7392 Å

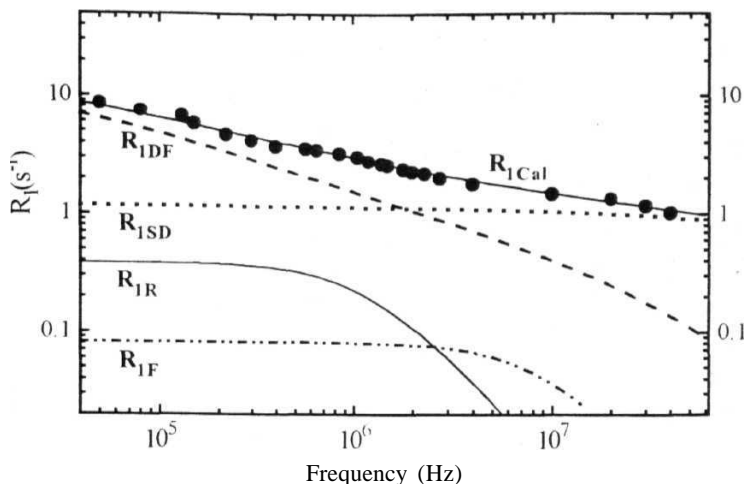


Figure 7.21 Different contributions to the experimental spin-lattice relaxation rate ($R_1=1/T_1$) in the nematic phase of 40% SCN + 60% 7BCB at 116 °C. The solid line connecting the data points (closed circles) is the total relaxation rate calculated using the equation 7.9.

The upper cut-off frequencies and wavelengths for DF modes are calculated from the q values obtained from the NMRD analysis. Upper cut-off frequency in the direction parallel to the director is 115 MHz, and in the direction perpendicular to the director is 127 MHz. The corresponding wavelengths representing the smallest possible wavelengths of the DF modes are 33 Å and 31.42 Å respectively, in the directions parallel and perpendicular to the nematic director. The values obtained here are consistent with the model assuming the presence of the smectic like clusters of three or more molecules. The X-ray measurements in the nematic phases of binary mixtures 8CN+7BCB shows that the cybotactic clusters of size 33.6 Å is observed [3].

A qualitative picture obtained from the NMRD data analysis in the nematic phase of the mixture reveals that the DF mechanism dominates the spin relaxation upto 2 MHz and SD becomes dominant from 2 MHz onwards. Rotations about the short axis, with a frequency independent behavior from 50 kHz to 700 kHz, and with a

frequency dependent behavior from 200 kHz to 10 MHz is observed along with the DF, SD and F contributions

The lower values obtained for upper cut-off frequencies shorten the square root region of DF modes. This leaves SD as the most important mechanism, from 10 MHz SD domination from 4 MHz to 40 MHz as observed in the NMRD analysis is well supported by the strong temperature dependence of η in this frequency range. F contribution is smaller when compared to the contribution in the previous mixture.

7.6.2.1.2. Dynamic parameters for SD, R and F

The correlation time obtained for rotations about the short molecular axis in the nematic phase of the mixture (40% 8CN + 60% 7BCB) is 7.58×10^{-8} seconds. The contribution to the total relaxation rate from R, is given by $C = 0.51 \times 10^7 \text{ s}^{-1}$. It is necessary to mention here that the contribution from R is decreased drastically, probably due to the presence of large number of dimers and clusters in the case of this mixture. This composition has all the ingredients (more concentration of 7BCB molecules should increase the amount of dimer concentration and the presence of considerable amount of 8CN provides steric hindrance due to the competing length scales of the molecules in the mixture) to form stable clusters

In the case of *self-diffusion*, the model parameter B (the amplitude) is equal to $2.32 \times 10^9 \text{ s}^{-2}$, and I (the average diffusion constant) is equal to $2.5 \times 10^{-10} \text{ m}^2 \text{ s}^{-1}$. The value obtained for D here is comparable with the D values obtained in nematic liquid crystals [1]. The correlation time associated with the creation and segregation of the clusters and dimers is 1.02×10^{-8} seconds. The constant, quantifying the contribution from the frustration mechanism, F is $0.8 \times 10^7 \text{ s}^{-1}$, much smaller than the value obtained for the previous mixture. This shows that the frustration phenomena decreases in the nematic phase of the binary mixture of 40% 8CN + 60% 7BCB, which has a very stable underlying smectic A_d phase. From the NMRD data fitting the percentage contributions of the various dynamical processes, DF, SD, R and F are calculated at different frequencies. The dynamic parameters obtained from the NMRD fit in the

nematic phase are given in table 7.5. The estimated error evaluating the parameters is about 10%

Table 7.5. Dynamic parameters obtained from the NMRD analysis of the nematic phase of 40% 8CN + 60% 7BCB.

Model Parameters	Results obtained
K_{11} (in 10^{-6} dynes)	1
K_{22} (in 10^{-6} dynes)	1
K_{33} (in 10^{-6} dynes)	1
A_{JF} (in 10^{-6} s ⁻²)	14
q_{zcl} (in 10^5 l/Am)	0.85
F_{zcl} (in kHz)	2.3
λ_{zch} (in Å)	7392
q_{zch} (in 10^7 l/Am)	1.9
F_{zch} (in MHz)	115
λ_{zcl} (in Å)	33
q_{lch} (in 10^7 l/Am)	2.0
F_{lch} (in MHz)	127
λ_{lcl} (in Å)	31.4
B (in 10^9 s ⁻²)	2.32
D (in 10^{-10} m ² s ⁻¹)	2.5
C (in 10^7 s ⁻²)	0.5
τ_t (in 10^{-8} s)	7.58
F (in 10^7 s ⁻²)	0.8
τ_{CS} (in 10^{-8} s)	1.02

7.6.2.1.3. Percentage contributions

Relative contributions to the spin relaxation can be obtained by calculating the percentage contributions.

- 1 At 50 kHz, the contribution from DF mechanism to the total relaxation in the **nematic** phase of the mixture of 40% 8CN + 60% 7BCB is about 84%, to the total relaxation. The contribution from SD, R and F are about 15 %, 5% and 1% respectively. At 100 kHz, the contributions from DF, SD, R and F are about, 74%, 18%, 6%, and 1.5% respectively.
2. At 400 kHz, 60% is from DF mechanism and 8% results from R. SD and F contributes about 29% and 2% respectively.
- 3 At 1 MHz, the contribution from DF is 51% and the second dominant mechanism. R, F and SD contribute about 7.5%, 3% and 38% respectively. At 2 MHz SD dominates DF mechanism with 48% contribution to the total relaxation. DF contributes to about 45% while R and F become negligible.
4. At 5 MHz, R becomes the least important mechanism with 1% contribution. SD becomes the most important mechanism with 61%. DF and F contribute to about **34.5%** and 3.5% respectively.
5. At 10 MHz, 70.5% results from SD. DF contributes 27% to the total relaxation and F contributes about 2.5%.
6. At 30 MHz, the contributions from R and F become negligible. The contributions from DF and SD are 84% and 15.5% respectively. The contribution from DF is deviating from the square root behavior at high frequencies due to the lowering of upper cutoff frequencies.

7. At the highest measured frequency (40 MHz), DF contribution becomes 87% and 12.5% relaxation is due to SD mechanism. This result is consistent with the strong temperature dependence, characteristic of SD, seen in the T_1 data at higher frequencies

7.6.2.2. Smectic A_d phase

NMRD data collected in the smectic A_d phase is shown in figure 7.22. NMRD data in the logarithmic scale clearly shows three regions with very different slopes. The first region from 50 kHz to 1 MHz shows a variation with lesser slope than the region succeeding it, from 1 MHz to 4 MHz. This intermediate frequency region shows a very steep variation. Temperature dependent data in the smectic A_d phase in this frequency range shows strong temperature dependence than in the nematic phase. This suggests that SD is the most dominating mechanism in the conventional NMR frequencies from 4 MHz to 40 MHz.

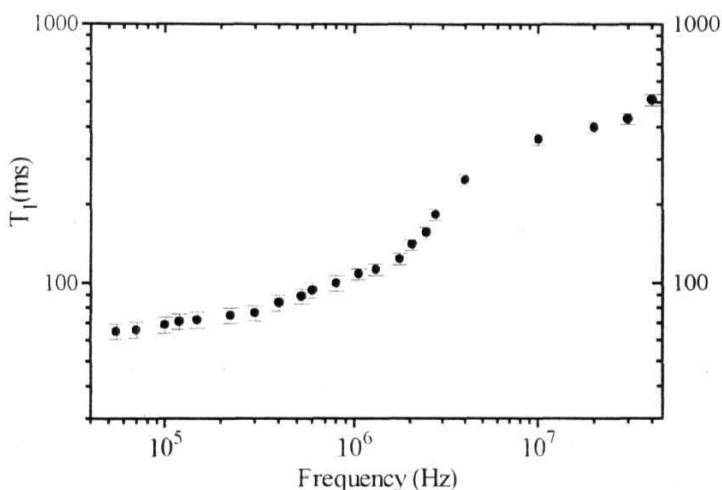


Figure 7.22. Experimental NMRD data in the smectic A_d phase 40% 8CN + 60% 7BCB at temperature 80 °C. Error bars are also shown

NMRD data in the smectic A_d phase is fitted considering the mechanisms LU, R, SD and F (equation 7.10). Smectic layer undulations (LU) are considered with their linear dependence on frequency. Upper and lower cut-off frequencies for LU modes are given as model parameters. Other three mechanisms R and F with their amplitudes and correlation times are obtained from the analysis. In the case of SD, the two parameters B and I (diffusion constant) are allowed to vary. The model fitting is shown in figure 7.23.

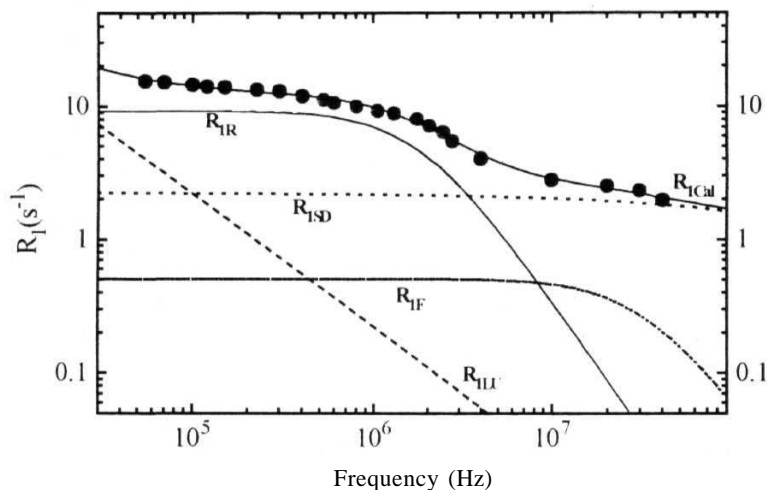


Figure 7.23. Various contributions to the experimental relaxation rate (R_1 / s^{-1}) in the smectic A_d phase of the binary mixture of 40 % 8CN + 60 % 7BCB. The solid line connecting the data points (closed circles) is the calculated relaxation rate using the equation 7.10. Different contributions (R_{ILU} , R_{ISD} , R_{IR} and R_{IF}) evaluated are also shown.

Layer undulation (LU) modes are important to **fit** the lowest frequency data below 100 kHz, though the major part of the spectrum for LU is **not** observed due to the fact that the experimental NMRD data was not available **for** frequencies below 50 kHz. The low frequency region from 50 kHz to 2 MHz is explained by rotations about the short axis. R contribution shows a frequency independent behavior from 50 kHz to 1 MHz, and shows a frequency dependence from 1 MHz to 20 MHz.

F contribution shows a weaker contribution over the other mechanisms upto 500 kHz. and becomes important than SD and LU from 500 kHz to about 10 MHz. This contribution is very important in the high frequency region from 10 MHz to 40MHz with a frequency dependent contribution. SD contribution is less important than LU and R contributions at 50 kHz, and start dominating these mechanisms as the frequency is increased.

Table 7.6. Dynamic parameters evaluated from the NMRD analysis of the smectic A_d phase of 40% 8CN + 60% 7BCB.

Model Parameters	Results obtained
$B \text{ (in } 10^9 \text{ s}^{-2} \text{)}$	5.58
$D \text{ (in } 10^{10} \text{ m}^2 \text{ s}^{-1} \text{)}$	3.19
$C \text{ (in } 10^8 \text{ s}^{-2} \text{)}$	1.8
$\tau_R \text{ (in } 10^{-8} \text{ s)}$	5.1
$F \text{ (in } 10^8 \text{ s}^{-2} \text{)}$	1.8
$Trs \text{ (in } 10^{-9} \text{ s)}$	2.8

At 100 kHz, SD becomes more important than R. From 10 MHz onwards the smectic A_d data is completely dominated by the SD contribution. It is not possible to completely rule out the contribution from rotations about the long axis as well as the conformational jumps, which are expected to show frequency independent contributions in the high frequency region studied here. In the present analysis, parameters connected with R about the long axis were not considered in the model fitting, due to the existing complications and the constraints in varying the number of parameters. It is also difficult to obtain such a weak contribution, since the frequency range of the data collected is not enough to detect and separate out such rotations.

The dynamic parameters obtained from the analysis are given in table 7.6. The uncertainty in the evaluation of the dynamic parameters is about 10%. The dynamic

parameters connected with the LU mechanism are not presented here since the uncertainty is very high due to its weak presence over a very short frequency range. The correlation time obtained for rotations about the short axis is 5.14×10^{-7} seconds and the constant $C' = 1.8 \times 10^8 \text{ s}^{-1}$. These are larger than the values obtained in the nematic phase of the same system. The contribution from F is quantified by the correlation time 1.02×10^{-8} seconds, with the constant $F = 0.8 \times 10^7 \text{ s}^{-1}$.

Relative contributions can be quantified by calculating the percentage contributions.

1. At 30 kHz, the LU mechanism contributes to about 36.4% and R, 35.7%. 18% comes from F and only 9% are due to SD
2. At 60 kHz, LU falls to 22% and R becomes the most dominant mechanism with 43% contribution. F and SD contribute 23% and 12% respectively.
3. Layer undulations become just 8% at 200 kHz, where R contributes about 47% followed by F with 29%. SD contributes 15% to the total relaxation at 200 kHz.
4. At 500 kHz the F mechanism dominates all the other mechanisms with 39%. R follows the F with 36% and SD and LU contributes about 21% and 5% respectively.
5. At 2 MHz, R and LU becomes very less with 10% and 2% respectively. F and SD become almost equal with 45% and 43% respectively.
6. At 6 MHz, SD becomes the most dominating mechanism with 76.5%. 20% contribution is due to F. LU and R are negligible from 6 MHz onwards (1.5% and 2%).
7. SD contribution becomes 90% at 10 MHz, 95% at 15 MHz and 98% at 30 MHz and the remaining relaxation is due to F and LU. At 50 MHz, 99.3% of the spin relaxation is mediated by the **self-diffusion** mechanism.

7.7. Conclusions

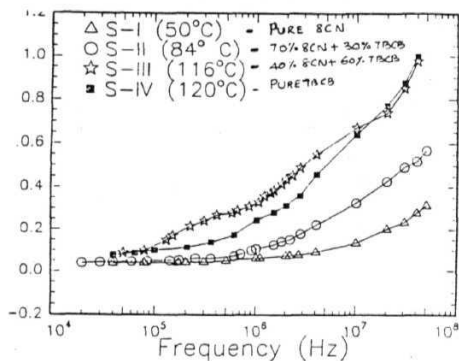
Molecular Dynamics as a function of Composition in the Binary Mixtures of Polar Liquid Crystals

NMRD data analysis of the binary mixtures of 8CN and 7BCB and the **pure** systems were discussed in detail taking **the** systems individually, in the preceding sections, from section 7.3 to section 7.6. It was demonstrated that the individual contributions mediating spin-lattice relaxation at different time scales could be separated out by measuring proton NMRD data at a fixed temperature

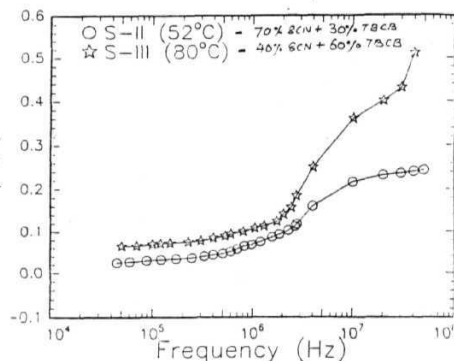
It was also shown that temperature dependent T_1 data is very useful in getting clues about the type of dynamics dominating spin relaxation. For example, in the case of the 7BCB pure nematic system, the strong temperature dependent T_1 data at conventional NMR frequencies implied that SD could be the most probable mechanism. This **view** was quantitatively established by the NMRD analysis, and the self-diffusion constant (D) obtained from the NMRD was in agreement with the values obtained from the direct methods, in similar systems.

7.7.1. Relaxation times and composition

It is interesting to note the behavior of total relaxation in the pure systems and their mixtures. Relaxation times as a function of frequency are plotted (figure 7.24a and b) together to show the difference between the different nematic (figure 7.24a) and **smectic** phases (figure 7.24b) of the mixtures and pure systems. Systems I, **II**, **III**, and IV refers to 100%, 70%, 40% and 0% of the system 8CN in the binary mixture with 7BCB. The temperature dependence of the nematic T_1 data in the pure systems and the mixtures at 30 MHz are shown in figure 7.24c. The pure 7BCB show high values of T_1 with strong temperature dependence. Pure 8CN shows quite an opposite behavior i.e., T_1 is very short and temperature independent.



(a)



(b)

Figure 7.24. Frequency dependent T_1 data in the nematic phases pure systems and their mixtures are plotted together (a) Data obtained from induced smectic smectic A_d phases are plotted separately (b).

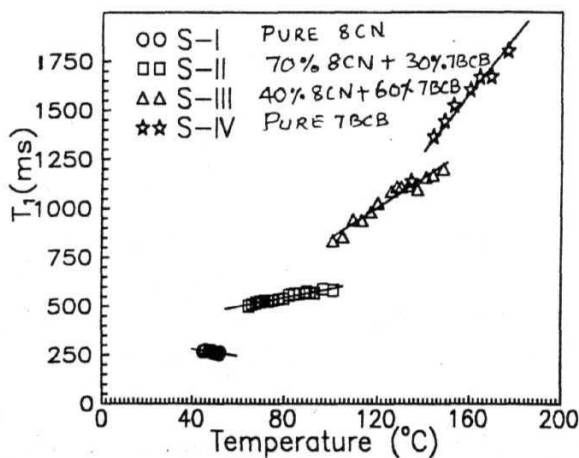
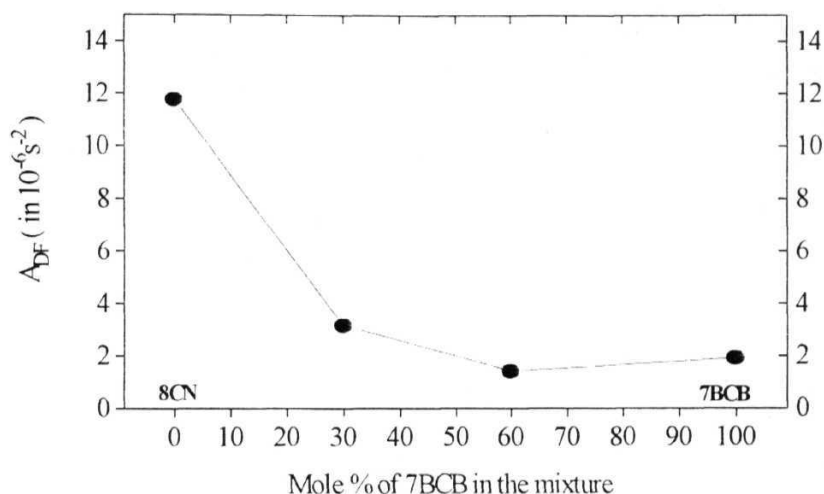


Figure 7.24c. Temperature dependent relaxation times in the nematic phases of the pure systems 8CN and 7BCB and their mixtures at frequency 30 MHz.

7.7.2. Director fluctuations

The mode spectrum of DF modes in the nematic phase depends on many factors which include visco-elastic properties of the medium, order parameter, molecular length [47], domain size, temperature, formation of the cybotactic clusters [34-36], odd-even effects, symmetry of the molecules and the degrees of ordering, in the liquid crystalline system. Variation of A_{DF} , as a function of the concentration of 7BCB in the mixture is shown in figure.7.25.

Figure 7.25. A_{DF} as a function of mole % of 7BCB



It is interesting to note that the value of ADF does not show the linear behavior, with concentration. The pure nematic system 8CN, which does not have the smectic-forming tendency, shows the highest value of A_{DF} . Pure nematic 7BCB, which has a smectic-forming tendency, shows the ADF value lower than 8CN. The mixture of 60% 7BCB with 40% 8CN shows an ADF value lesser than that of the pure 7BCB

From the studies of both 4O.m systems, and the binary mixtures of 8CN and 7BCB, it can be said, that lower the A_{DF} value, higher the stability of the nematic phase. Absence of collective DF modes probably helps the medium to orient better,

and a further reduction of temperature leads to the formation of smectic layers. The theoretical results obtained by Kyu et al., [11] on the formation of induced smectic A_d phases in the binary mixtures have clearly shown that the free energies go through anomalous reduction in the regions where ISP is formed. The nematic phase in the mixtures show a higher stability than the pure nematic systems.

The temperature dependence of the free energy curves, for the anisotropic ordering of the nematic mixtures as a function of composition, obtained by Kyu et al.,[11]. These curves are depicted in figure 7.2 (section 7.1, page 345). The concave free energy curve at 60 °C suggests that the nematic phase is more stable in the mixture as compared to that, in the pure state. Upon lowering the temperature, a subtle change in the curvature can be noticed at certain intermediate compositions. This implies that, the two free energy curves, attribute to the induced nematic and smectic ordering. The anisotropic free energy is lowest, at the middle composition and at lower temperatures, suggesting that the induced smectic phase is most stable in the mixture

The behavior of the A_{DF} shown in figure 7.25 has certain similarities with the theoretical free energy diagram, though the correlation between A_{DF} and free energy is not direct in nature. The non-additive nature of the A_{DF} values is similar to the nematic free energy changes in the mixture. Lowering of the free energy probably leads to reduction of the power spectrum for the DF modes, or vice versa.

This situation has similarities with the 4O.m results on DF modes, where the reasons are connected with the symmetry of the alkyl end chains. The highly stable nematic system 4O.4, having balanced end chains, has shown a weaker DF contribution. In the present binary mixtures, highly stable nematic phases with smectic forming tendencies show similar effects.

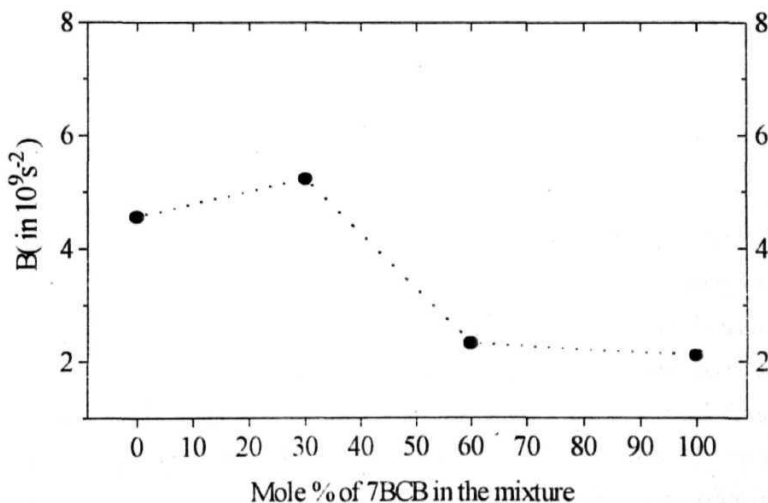
The stability enhanced here is due to the interplay between the strong polar interactions and the steric interactions of the molecules having different length scales. In the case of 4O.m systems the major effects are probably from steric factors connected with the length of the alkyl chain, since the only variation in the 4O.m

systems had been the alkyl end chain length. **Dimers** formed in the present mixtures can be compared to a longer molecule having balanced end chains. Though a logical explanation based on balancing effects on the DF modes is not straightforward in the case of dimers, so many other factors such as the formation of cybotactic clusters, frustration, competing length scales of the molecules and the consequent steric forces complicate the **nematic** medium, once they are mixed.

From the values observed for A_{DF} and from the above arguments made based on the other experimental observations, it is possible to conclude that, the systems with higher nematic stability and higher values of the nematic order parameter, show a weaker DF contribution. In the 4O.m systems, higher stability coincides with symmetry. Balanced end chains lead to better stability, probably due to the fact that they show weaker collective director fluctuations. A_{DF} -value for the non-symmetric systems are higher than the values of A_{DF} , for the symmetric systems. In the mixtures, the minimization of free energy in the nematic mixtures coincides with the reduction in DF contributions. An increase in the order parameters is also observed in the theoretical observations of the ISP formation (Figure 7.1, page 345).

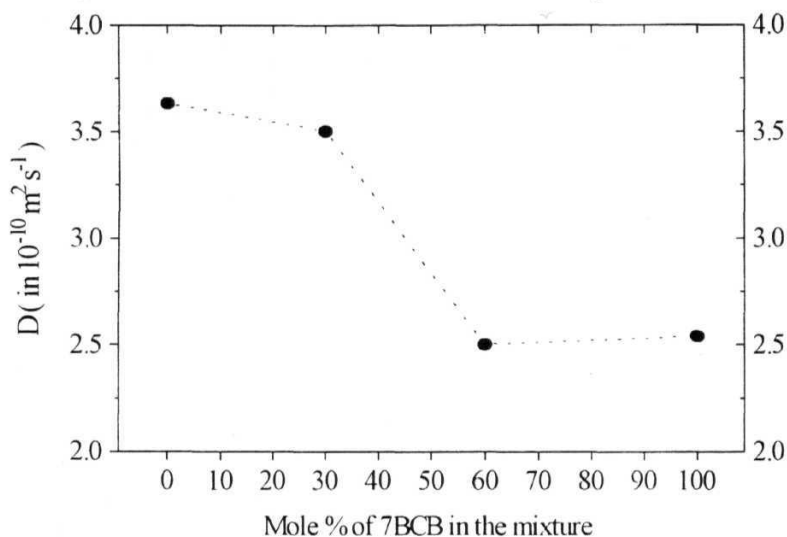
7.7.3. Self-Diffusion

Figure 7.26. Absolute contribution from self-diffusion



Diffusion constants in the nematic phase are known to vary strongly with temperature [1]. In the present nematic mixture, diffusion parameters B and D show nonlinear behavior. The diffusion constant D , and the parameter B , which represent the overall diffusion contribution, are plotted separately as a function of the composition in the figures 7.27 and 7.26. The values of D and B show a sharp decrease at the composition where the induced smectic phase is very stable (60% 7BCB + 40% 8CN).

Figure 7.27. Self-diffusion constants in the nematic phases



7.7.4. Rotations

The correlation times obtained in the NMRD study (Figure 7.29) of the binary mixtures agree well with the observations made in the dielectric studies (10^{-6} – 10^{-8} s are possible for the rotations about the short molecular axis) [1d, 1e]. Present studies of the pure nematic 7BCB system show that the rotations about the short axis has a correlation time of about 10^{-7} s, which indicates that the rotation is slower, in this case. Detection of slow rotations is possible in the case of 7BCB probably due to the weaker domination of the DF mechanism at these time scales. In the pure 8CN system, rotations are observed with a correlation time of about 10^{-8} s, which is about one order of magnitude shorter than the correlation time seen in the pure 7BCB

systems. Shorter molecules are expected to undergo faster rotations about the short axis. In the case of 7BCB, formation of dimers could be another reason for slow rotations, since the effective average length of the **dimer** is about 14 times, the molecular length. Over and above, the system 7BCB has three benzene rings and hence the core of the molecule is longer than the core of the 8CN molecule, which has two benzene rings. Nematic phases of the mixtures show intermediate values of correlation times.

The values of the constant C are plotted as a function of composition in figure.7.28. C is very low for the nematic system, showing a very high nematic stability (60% 7BCB + 40% 7BCB) as well as a **smectic** forming tendency. This could be attributed to the theoretically expected lowering of free energy at this composition.

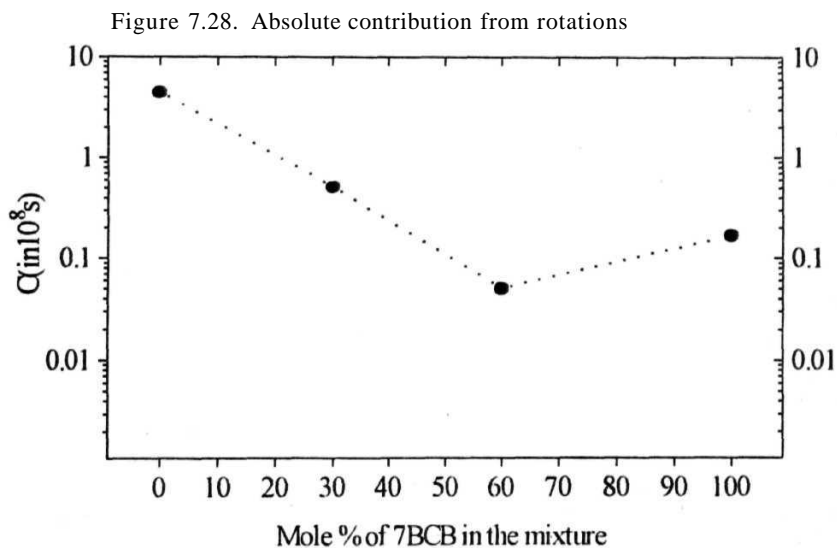
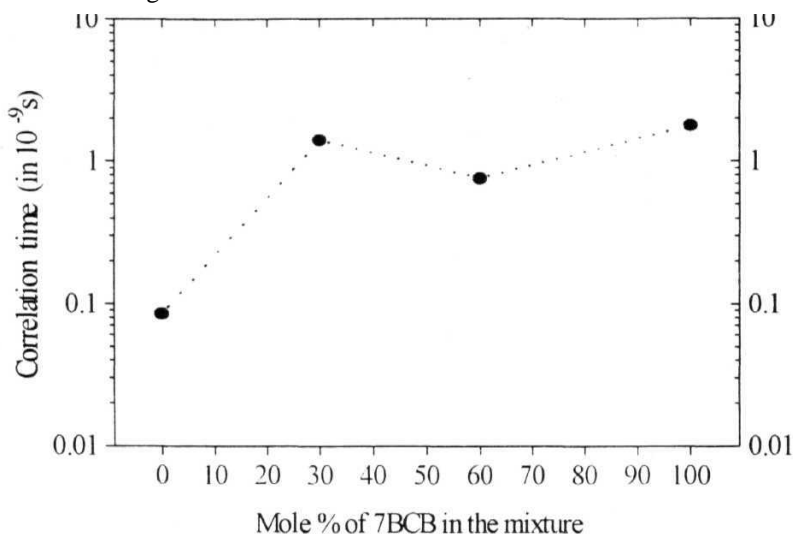


Figure 7.29. Rotational correlation times



7.7.5. Frustration

It is known in that the formation and segregation of the dimers and clusters also contributes to the spin relaxation in frustrated liquid crystals. The clusters are important for releasing the frustration in the system, locally. This additional dynamic process (also called frustration or frustration dynamics) used in explaining the NMRD data in the binary mixtures of the polar liquid crystals is important whenever dimers and clusters of molecules are present. Though the relative contribution from this frustration dynamics to the total relaxation is very less, in the present study it was demonstrated that this phenomenon is very useful in fitting the NMRD data in a better manner.

The correlation time associated with this process and the corresponding amplitude factor, F , are given in the tables, in the concerned sections. The values of the correlation time associated with this mechanism in the nematic phases of mixtures and pure 7BCB varies from $1-3 \times 10^{-8}$ seconds. In the induced smectic phase it shows **a variation** of one **order** of magnitude (the ISP formed in the mixture of 40% 8CN + 60% 7BCB shows the correlation time equal to 28×10^{-8} seconds and the other

mixture forming ISP, 70% 8CN + 30% 7BCB shows the correlation time equal to 4×10^{-8} seconds).

7.7.6. Percentage contributions

Some of the dynamic parameters obtained in the NMRD analysis and the correlation times corresponding to different dynamics might not be accurate, since the present method, for some of these parameters, is indirect in nature. There are direct methods, which could provide information on one or two dynamic parameters. But, NMRD analysis is the only method, which can handle several dynamic parameters over a large time window. While handling such a wide variety of parameters, it is natural to have an uncertainty, over some of these parameters.

Obtaining different dynamical contributions at different time scales is very important an aim of the NMRD studies, which can explain the nature of the microscopic environment, responsible for the stability as well as, the properties of the liquid crystalline medium. Keeping this in mind, an attempt is made to calculate the relative percentage contributions of different dynamics present in the nematic phases of mixtures and the pure systems. The results are presented in the figures 7.30a-7.30m. DF, SD, R and F contributions are shown in a single graph as a function of concentration, for selected frequencies.

The binary mixture of 70% 8CN + 30% 7BCB behave very differently, when compared with the other systems. Almost all the dynamic parameters behave very differently at all the frequencies plotted in the figures 7.30a to 7.30m (50 kHz, 100 kHz, 300 kHz, 500 kHz, 1 MHz, 1.5 MHz, 2 MHz, 5 MHz, 8 MHz, 10 MHz, 20 MHz, 30 MHz and 40 MHz). This particular nematic system has an underlying induced smectic A_d phase with maximum stability. This behavior can be attributed to the enhancement of the nematic stability described as by the theoretical model proposed by Kyu et al., [11]

Figure 7.30a. DF+SD+R+F contributions at 50 kHz

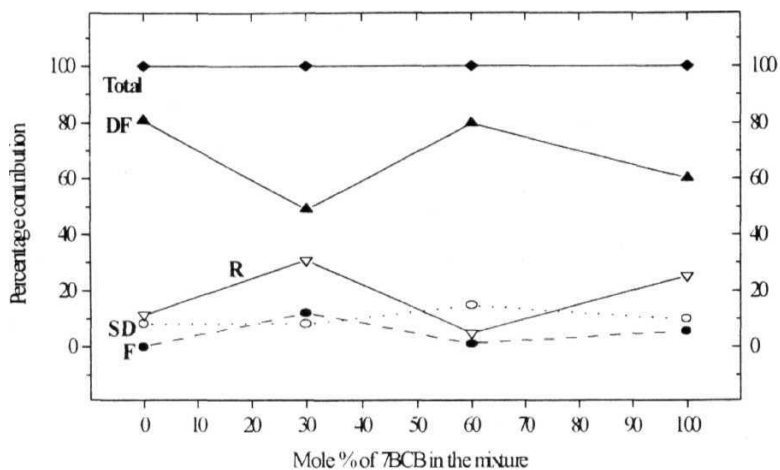


Figure 7.30b. DF+SD+R+F contributions at 100 kHz

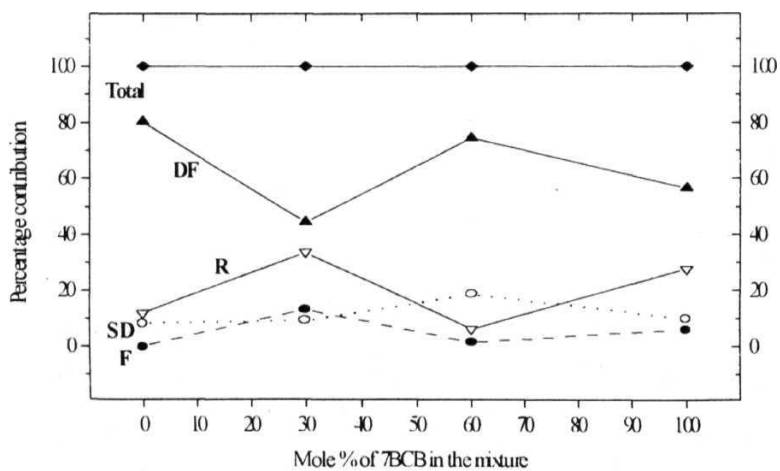


Figure 7.30c. DF+SD+R+F contributions at 300 kHz

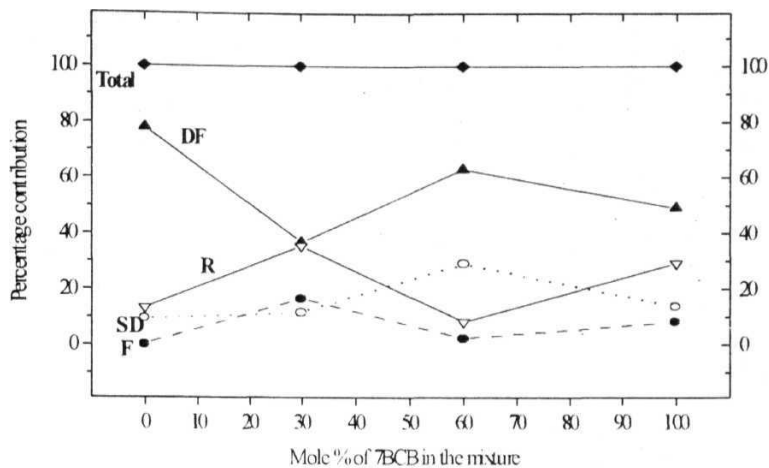


Figure 7.30d. DF+SD+R+F contributions at 500 kHz

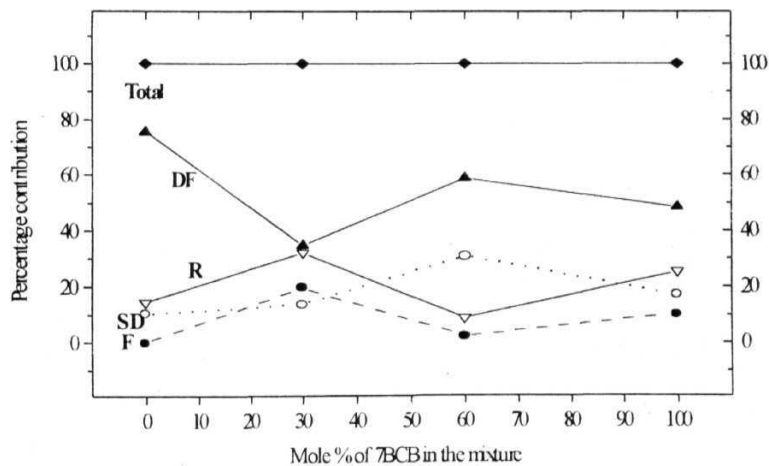


Figure 7.30e. DF+SD+R+F contributions at 1 MHz

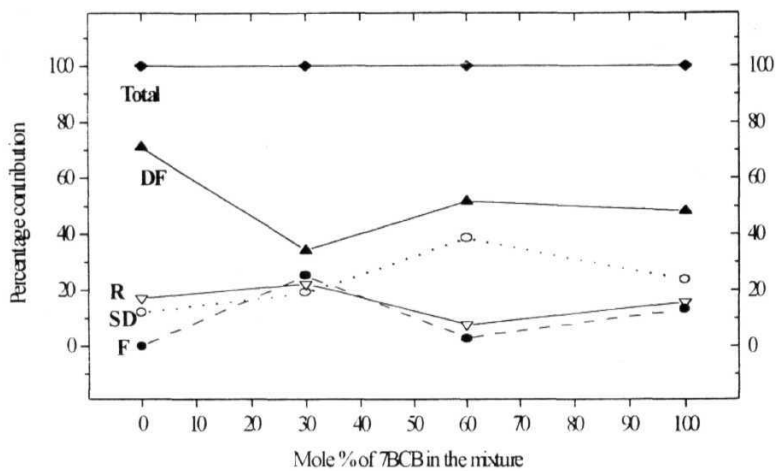


Figure 7.30f. DF+SD+R+F contributions at 15 MHz

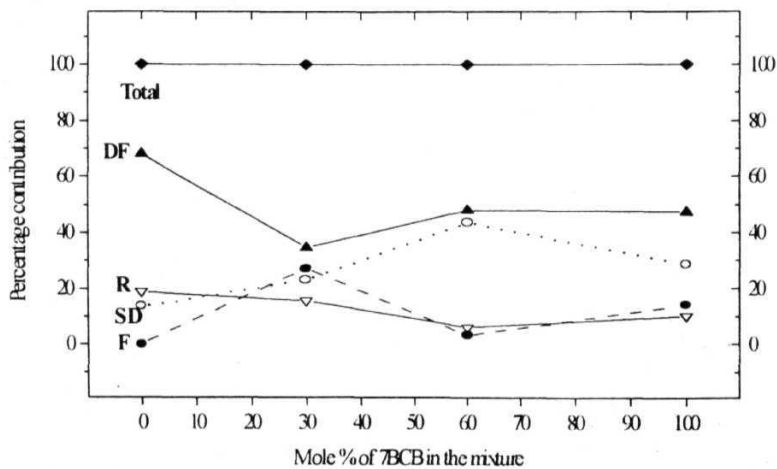


Figure 7.30g. DF+SD+R+F contributions at 2 MHz

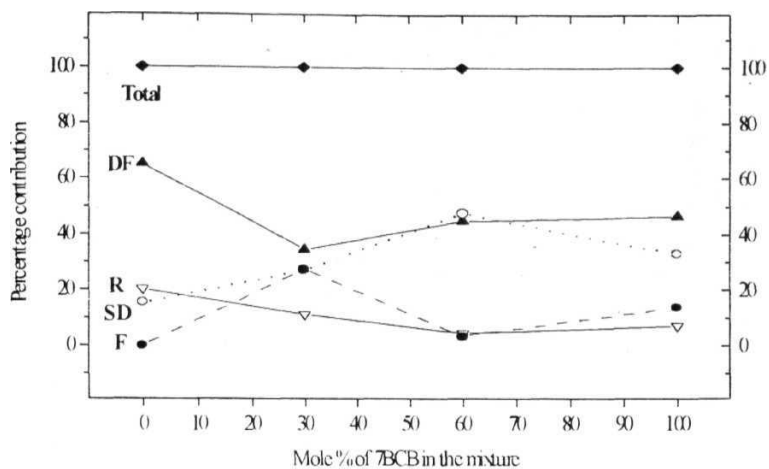


Figure 7.30h. DF+SD+R+F contributions at 5 MHz

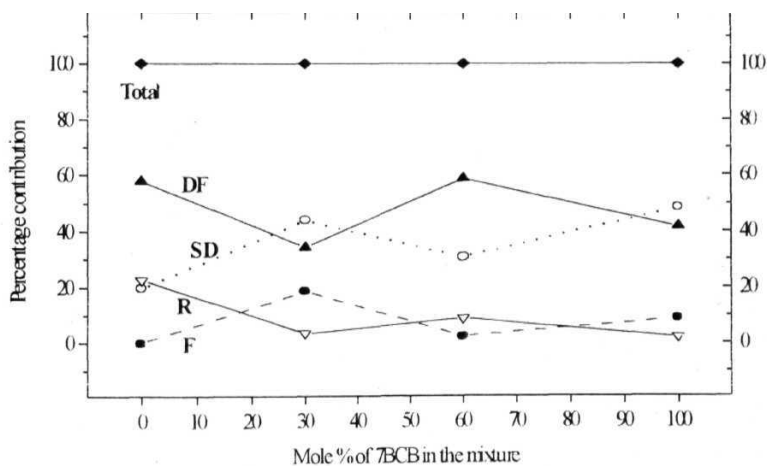


Figure 7.30i. DF+SD+R+F contributions at 8 MHz

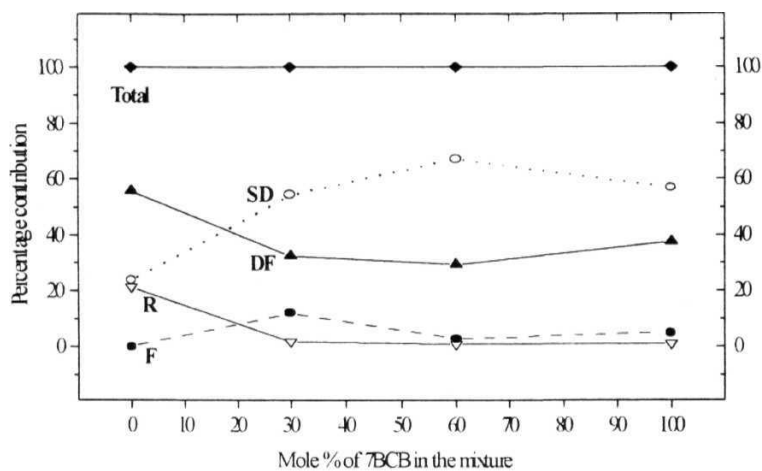


Figure 7.30j. DF+SD+R+F contributions at 10 MHz

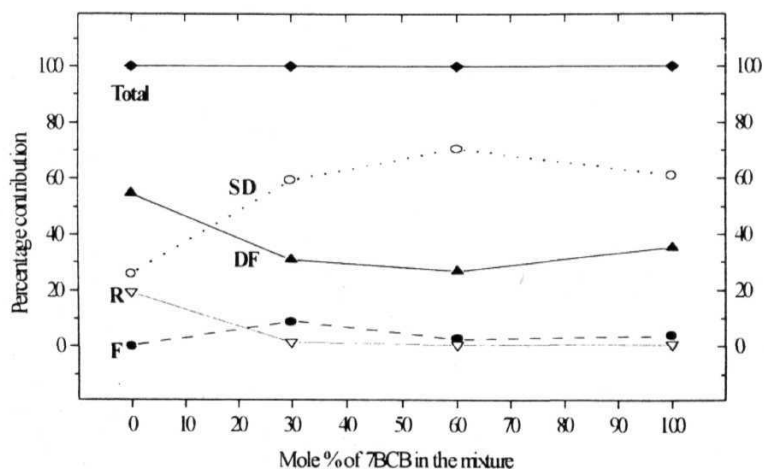


Figure 7.30k. DF+SD+R+F contributions at 20 MHz

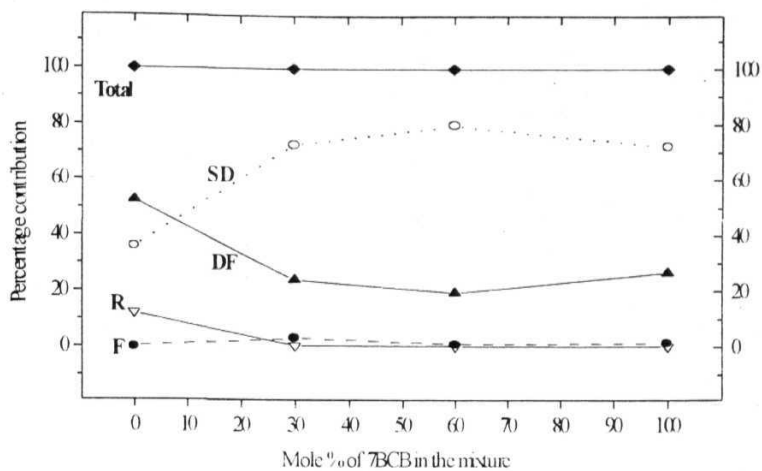


Figure 7.30l. DF+SD+R+F contributions at 30 MHz,

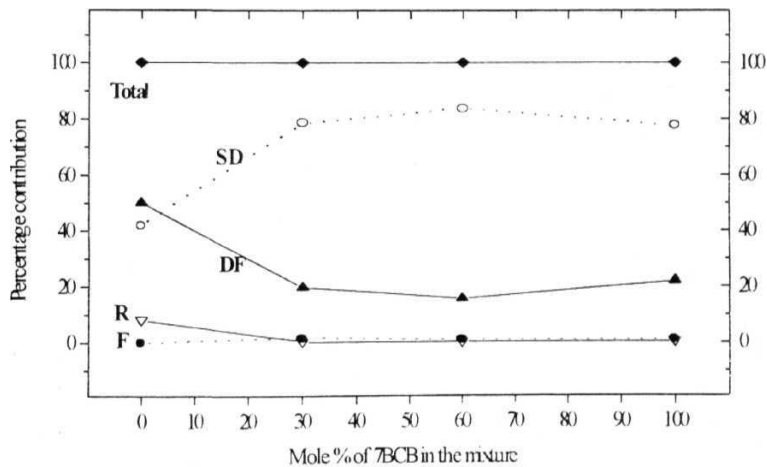
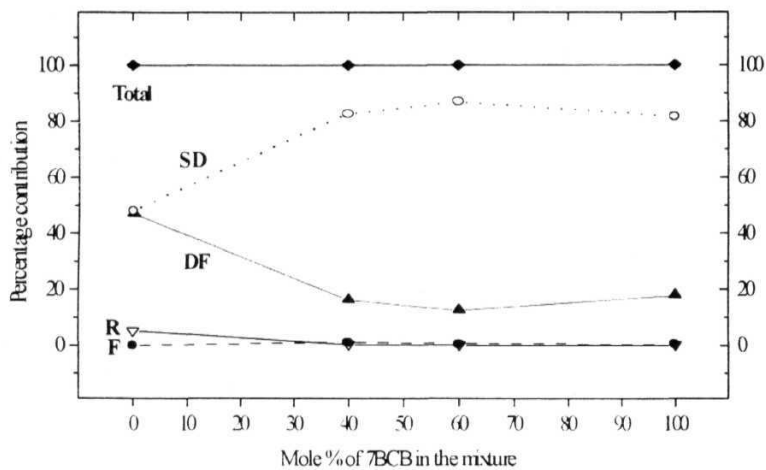


Figure 7.30m. DF+SD+R+F contributions at 40 MHz



7.8. References

1. (a) P. G. de Gennes, *"The Physics of Liquid Crystals"*, Clarendon Press, Oxford (1974); (b) S Chandrasekhar, *"Liquid Crystals"* Cambridge University Press, Cambridge (1977); (c) *"The Molecular Physics of Liquid Crystals"*, (ed.) G. R. Luckhurst and G. W. Gray, Academic Press, London (1979); (d) G. Vertogen and W. H. de Jeu, *"Thermotropic Liquid Crystals, Fundamentals"*, Springer-Verlog, Heidelberg (1988); (e) D.Demus, J.Goodby, G.W Gray, H.-W.Spiess, and V. Vill (eds.) *"Hand Book of Liquid Crystals"*, Vol.1, 2A, 2B and 3 (1998); (f) S Martellucci and A. N. Chester (ed), " *Phase Transitions in Liquid Crystals*", Plenum Press, New York. (1992); (g) P. J. Collings and J. Y. Patel (ed.), *"Hand Book of Liquid Crystal Research"*, Oxford University Press, Oxford, New York, (1997);(h). *"Liquid Crystals Applications and uses"*, Vol. 1, (ed.) Bahadur, World Scientific (1993).
2. N. V. Madhusudana in *"Liquid Crystals Applications and uses"*. Vol. I, (ed.) B. Bahadur, World Scientific (1993) and references therein
3. R. Dabrowski in *"Modern Topics in Liquid Crystals"*, (ed.) A. Buka, World Scientific (1993) and the references therein; Brodzik and R. Dabrowski, *"Induction of smectic A_d island in the binary mixtures"*, I &II (1997). (Communicated),
4. I. Schroder, Z. Phys. Chem. 11, 449 (1983); E. C. H. Hsu, and J. F. Johnson, *Mol. Cryst. Liq. Cryst.*, 20, 177 (1973).
5. M. A. Osman, H. P. Schad and H. R. Zeller,/. *Chem. Phys.*, 78, 906,(1983).
6. R. L. Humphries, P. G. James, and G. R. Luckhurst, *Symp. Faraday Soc.*5,107(1971)
7. W. Maier and A. Saupe, Z *Naturforsch.*, 15A, 287 (1960).
8. M. A. Cotter and D. C. Wacker, *Phys. Rev.* **A18**, 2669 (1978); *Phys.Rev.*,**A18**,676 (1978).
9. M. Nakagawa and T. Akahane,/. *Phys. Soc. Jpn.*, 52, 399 (1983); 52, 2659 (1983).
10. W. H. de Jeu and L. Longa *J. Chem. Phys.*, 84, 6410, (1986).
11. T. Kyu, H.W. Chiu, and T. Kajiyama, *Phys. Rev.*, E 55, 7105 (1997).
12. W.L. McMillan, *Phys.Rev.* **A4**, 1238 (1971)

13. P J Flory, *Principles of Polymer chemistry*, Cornell University Press, Ithaca, (1953).
14. J. W. Park, C S. Bak and M. M. Labes, *J. Am. Chem. Soc.*, **97**, 4398 (1975).
15. C. S. Oh, *Mol. Cryst. Liq. Cryst.*, **42**, 1 (1977).
16. M. Bock, G. Heppke, J Richter and S. Schneider, *Mol. Cryst. Liq. Cryst.*, **45**, 221, (1978).
17. N. V. Madhusudana and K P. L. Moodithaya, *Mol. Cryst. Liq. Cryst.*, **90**, 357 (1983).
18. B. S. Scheuble, G. Baur and G Meier, *Mol. Cryst. Liq. Cryst.*, **68**, 57 (1981).
19. Y. Matsunaga and I. Suzuki, *Bull. Chem. Soc. Jap.*, **57**, 1411 (1984).
20. P. E. Cladis, *Mol. Cryst. Liq. Cryst.*, **165**, 85 (1988).
21. A. N. Berker and J.S. Walker, *Phys. Rev. Lett.*, **47**, 1469 (1981)
22. JO. Indekeu and A.N. Berker, *Physica*, **140A**, 368 (1986).
23. JO. Indekeu and AN. Berker, *Phys. Rev* **A33**, 1158 (1986).
24. JO. Indekeu , *Phys. Rev* **A37**, 288 (1988).
25. P.E. Cladis, *Phys. Rev. Lett.*, **35**, 48 (1975).
26. G. W. Gray and J. E. Lydon, *Nature*, **252**, 221 (1974).
27. A. J. Leadbetter, J. L. A. Durant, and M Rugman, *Mol. Cryst. Liq. Cryst.*, **34**, 231 (1977).
29. F. Dowell, *Phys. Rev* **A28**, 3520 (1983)
30. F. Dowell, *Phys. Rev* **A28**, 3526 (1983).
31. F. Dowell, *Phys. Rev.* **A31**, 2464 (1985).
32. N. V. Madhusudhana and J. Rajan, *Liq. Cryst.*, **7**, 31 (1990).
33. J. F. Marko, J. O. Indekeu, and J. N. Berker, *Phys. Rev.* **A39**, 4202 (1989).
34. D. Guillon and A. Skoulios., *J. Phys.(France)* **49**, 45, 607 (1984); *Mol. Cyst. Liq. Cryst.*, **91**, 341 (1983).
35. R. R. Netz and A. N. Berker, *Phys. Rev. Lett.*, **68**, 333 (1992)
36. P. J. Sebastiao, A. C. Ribeiro, H. T Nguyen and F Noack, *J. Phys.(France) II* **5**, 1707 (1995) and references therein.
37. F. Hordouin., *J. Phys. France* **41**, 41 (1980).
38. W. H. Press, B. P Flannery, S. A. Teukolsky and W T Vetterling, '*Numerical Recipes, The art of Scientific Computation*'. Cambridge University Press, Cambridge (1986).

39. K. Venu and V. S. S. Sastry, "*Symposium on Field Cycling Relaxometry (Techniques, applications and Theories)*", Berlin, 39 (1998).
40. F. Brochard, *J Phys. (Paris)*, 34, 411 (1973).
41. R. R. Vold and R. L. Vold, *J. Chem. Phys.* 88, 4655 (1988); **R R Vold and R L. Vold**, in "*The Molecular Dynamics in Liquid Crystals*", (eds.) G. R. Luckhurst and C. A. Veracini, Kluwer Academic Publishers, London, 207 (1994) **and** references therein
42. R. Blinc, M. Vilfan, M. Luzar, J. **Seliger** and V. Zagar, *J. Chem. Phys.*, 68, 303 (1978). **R. Blinc**, *NMR Basic Principles Progress*, **13**, 97 (1976).
43. P. Pincus, *Solid State Commun.*, 7, 415 (1969)
44. N. Bloembergen, E. M. Purcell and R. V. Pound, *Phys. Rev.* 73, 679 (1948).
45. H. C. Torrey *Phys. Rev.* 97, 962 (1953) M. Vilfan, R. Blinc and J. W. Doane *Solid State Commun.*, **11**, 1073 (1972) M. Vilfan and S. Zumer *Phys. Rev.* **A21**, 672 (1980) M. Vilfan, J. Seliger, V. Zagar and R. Blinc. *J. Chem. Phys.* 86, 1055 (1980).
46. V. Vill, *LiqCrystDatabase*, Demo Version 3. 4, Universitat Hamburg, Germany (1999).
47. R.Y. Dong, "*NuclearMagnetic Resonance ofLiquid Crystals*", Springer-Verlog (1997)

Publications and papers under preparation

1. Field Cycling NMR Spectrometer

A. S. Sailaja , **D. Loganathan** and K. Venu

PROC. NAT. ACAD. SCI. INDIA, 66 (A), SPL ISSUE (50 years of NMR) 1996.

2. Proton Spin Relaxation study of Polar Liquid Crystals with Induced Smectic Phases

V Satheesh, **D.Loganathan**, K.Venu and V.S.S.Sastry R. Dabrowski and M. Brodzik
in “ Liquid Crystals: Physics, Technology and Applications”¹

PROC. SPIE Vol. 3318, p 245-248(1997).

3. Effect of alkyl end chain length on the director fluctuations in Butyloxy Benzyldine

Alkylanilenes (to be communicated)

D. Loganathan, K. Venu and V.S.S. Sastry

4 Symmetry of end chains and the rotations about the short axis in the rod like thermotropic liquid crystals (to be communicated)

D. Loganathan, K. Venu and V. S. S. sastry

5. Odd-even effects in the molecular dynamics of liquid crystals (to be communicated)

D. Loganathan, K. Venu and V. S. S. Sastry

6. Frequency and temperature dependent study of spin-lattice relaxation time in the smectic A phases of the liquid crystals 40.5, 40.7 and 40.9 (to be communicated)

D. Loganathan, K. Venu and V. S. S Sastry

7. Effect of dimer formation and frustration on the molecular dynamics of liquid crystals (to be communicated)

D. Loganathan, V. Satheesh, K. Venu and V. S. S. Sastry

Conferences

- 1) Field Cycling NMR Relaxation Study of a Liquid Crystal (40 5)

D. Loganathan K Venu and V S S Sastry

Presented in the National Conference on The Physics Of the Materials (1997),
University of Hyderabad, Hyderabad

- 2) Field Cycling NMR Relaxation Study of Butyloxy Benzylidene Alkylanilenes (4o.m)

D. Loganathan, Presented in the Special Symposium on Liquid Crystal NMR and

National Symposium on Magnetic Resonance(1998) held at IISc, Bangalore, INDIA

- 3) Slow Motions in Liquid Crystals Studied by Field Cycling NMR Relaxation

D. Loganathan, K. Venu and V. S S. Sastry

Presented in the International Liquid Crystal Conference (1998), France.

- 4) Field Cycling NMR study of Structure and Dynamics in Liquid Crystals

D. Loganathan, K Venu and **V.S.S.** Sastry

Presented in the Field Cycling NMR Relaxometry Symposium (1998), Germany.

- 5) Balancing and Unbalancing of end chains in liquid crystals studied by Field Cycling NMR relaxation

D. Loganathan and A. S. Sailaja

DAE Solid State Physics Symposium. Kurukshethra (1998). INDIA.

- 6) Frustrated Nematic Phases in single component liquid crystals - a Proton MRD study

D. Loganathan, V.Satheesh, A.S.Sailaja, K.Venu and V.S.S.Sastry

Oral Presentation - NMRS Symposium (1999), Dehradun , India.

17. U. P. Singh and Y. Singh, *Phys. Rev.*, **A33**, 2725, (1986).
18. A. Perera, G N. Patey and J. J. Weis, *J. Chem. Phys.*, **89**, 6941, (1988).
19. J. L. Colot, X. G. Wu, H. Xu, and M Baus, *Phys. Rev.*, **A38**, 2022, (1988)
20. S. D Lee, *J. Chem. Phys.*, **87**, 4972, (1987).
21. W. Maier and A. Saupe, *Z Naturforsch*, **14a**, 882, (1959).
22. E. de Miguel, L. F Rull, M. K. Chalam, K. E. Gubbins and F. van Swol, *Mol. Phys.*, **72**, 593,(1991).
23. T. J. Krieger and H. M. James, *J. Chem. Phys.*, **22**, 796, (1954).
24. A. Ferrarini, G. J. Moro, P. L. Nordio, and G. R. Luckhurst, *Mol. Phys.*, **77**, 1 (1992)
25. P. G de Gennes, *Solid State Commun.*, **10**, 753, (1972).
26. W. L. McMillan, *Phys. Rev.*, **A4**, 1238(1971).
27. P. E. Cladis, W. A. Sarloos, D. A. Huse, J. S. Patel, J. W. Goodby and P. L. Finn, *Phys. Rev. Lett*, **62**, 1764 (1989).
28. R. B. Mayer and T. C. Lubensky, *Phys. Rev.*, **A14**, 2307 (1976).
29. B. I. Halperin, T. C. Lubensky and S. K. Ma, *Phys. Rev. Lett.*, **32**, 292(1974).
B. I. Halperin and T. C. Lubensky, *Solid State Commun.*, **14**, 997 (1974).
30. A. Kloczkowski and J. Stecki, *Mol. Phys.*, **55**, 689 (1985).
31. D. A. Badalyan, *Sov. Phys. Crystallogr.*, **11**, 10 (1982).
32. W. Wagner, *Mol. Cryst. Liq. Cryst.*, **98**, 247 (1983).
33. M. Nakagawa and T. Akahane, *J. Phys Soc, Japan*, **54**, 69 (1985).
34. C. D. Mukherjee, B. Bagchi, T. R. Bose, D. Gosh, M. K. Roy and M. Saha, *Phys. Lett.*, **92A**, 403(1982).
35. F. Dowell, *Phys. Rev.* **A31**, 3214 (1985); *Phys. Rev.* **A36**, 5046 (1987); *Phys. Rev.* **A28**, 3526(1983).
36. B. Mulder, *Phys. Rev.*, **A35**, 3095 (1987).
37. R. P. Sear and G. Jackson, *J. Chem. Phys.*, **102**, 2622 (1995).
38. S. Mercelja, *J. Chem. Phys.*, **60**, 3599, (1974).
39. D. A. Pink, *J. Chem. Phys.*, **63**, 2533 (1975).
40. G. R. Luckhurst in *Recent Advances in Liquid Crystal Polymers*, (Ed.) L. L. Chapoy Elsevier, London , P105, (1986).